

The Dissertation Committee for Michael Keith Thompson
Certifies that this is the approved version of the following dissertation:

**The Anchorage Behavior of Headed
Reinforcement in CCT Nodes and Lap Splices**

Committee:

James O. Jirsa, Supervisor

John E. Breen

Richard E. Klingner

Michael E. Kreger

Eric Becker

**The Anchorage Behavior of Headed
Reinforcement in CCT Nodes and Lap Splices**

by

Michael Keith Thompson, B.S., M.S.

Dissertation

Presented to the Faculty of the Graduate School of
the University of Texas at Austin
in Partial Fulfillment
of the Requirements
for the Degree of

Doctor of Philosophy

The University of Texas at Austin

May 2002

The Dissertation Committee for Michael Keith Thompson
Certifies that this is the approved version of the following dissertation:

**The Anchorage Behavior of Headed
Reinforcement in CCT Nodes and Lap Splices**

Committee:

James O. Jirsa, Supervisor

John E. Breen

Richard E. Klingner

Michael E. Kreger

Eric Becker

**The Anchorage Behavior of Headed
Reinforcement in CCT Nodes and Lap Splices**

by

Michael Keith Thompson, B.S., M.S.

Dissertation

Presented to the Faculty of the Graduate School of
the University of Texas at Austin
in Partial Fulfillment
of the Requirements
for the Degree of

Doctor of Philosophy

The University of Texas at Austin

May 2002

To My Parents

Acknowledgments

This document is the result of the contributions from many individuals. The technical staff of the Ferguson Structural Engineering Laboratory were invaluable. They included Blake Stasney, Mike Bell, Wayne Fontenot, Denis Phillip, and Ray Madonna. The administrative and clerical staff were also of immense help: Ruth Goodson, Regina Forward, Wanda Kitts, and particularly Dijaira Smith who processed numerous and varied purchases for the project. Several students also contributed their labor at various times. The help was greatly appreciated.

The early stages of the project were assisted by advice from many contacts with design, construction, and research backgrounds. These included Gregor Wollman, Richard DeVries, Julio Rameriz, Steven McCabe, Richard Wilkison, and Lou Colarusso to name a few. TxDOT personal provided much advice that was very helpful. Furthermore, Donations of headed reinforcement and project literature were made by Kjell Dahl of Headed Reinforcement Corporation and Bob Smith of ERICO.

The early experimental work of this project was assisted by two M.S. degree students: Michele Young who performed much of the early work on the CCT node specimens and Anthony "Tony" Ledesma who performed much of the early lap splice work. They put in many hours of work fabricating and testing the early specimens and analyzing the initial data.

I have particular gratitude to Dean Van Landuyt, the TxDOT project director whose knowledge and encouragement were key components to the completion of this work. His support allowed the direction of this project to proceed into a general study of headed bar behavior in nodes and splices rather than an application specific study. This decision was almost certainly the turning point from which many of the key results of this study emerged. Had this direction not been taken, much less of the behavior of headed bars would have been discovered.

The PhD supervising committee provided much input on the final document. Dr. John E. Breen provided a particularly thorough and knowledgeable reading of this document that helped immensely in the editing of this work. Dr. Breen was involved in the shaping of this research from the beginning and was instrumental in connecting me to this project while it was still just a proposal.

Dr. James O. Jirsa, the project and committee supervisor, contributed valuable experience and insight. He suggested that the direction of the project should focus on general tests of nodes and splices. He helped to decide many of the parameters that were tested and interacted with the author for much of the interpretation of test results and drafting of this document. Furthermore, he has provided much personal support and advice. He has been a mentor and role model through the course of this research.

Much personal gratitude is owed to my parents and family for their advice and support through his graduate career. They have provided incalculable love and care and deserve the recognition of having this work dedicated to them.

Finally, the author expresses his gratitude to Judy Lai. Her patience and love during the writing of this document helped immensely. She gave me much of the strength and perseverance that was needed to complete this work.

The Anchorage Behavior of Headed Reinforcement in CCT Nodes and Lap Splices

Publication No. _____

Michael Keith Thompson, Ph.D.

The University of Texas at Austin, 2002

Supervisor: James O. Jirsa

The behavior of headed reinforcement in concrete was studied using full scale tests of CCT nodes and lap splices. The mechanics of the anchorage behavior were observed and recorded to evaluate the manner in which the capacity of a headed bar is developed. The measured data were used to evaluate existing models of headed reinforcement anchorage as well as the ultimate limit state for anchored bars in CCT nodes. Observations from the CCT node tests provided information on the stages of truss development in a simple strut-and-tie model as well as the stress state of the concrete in the node and adjacent struts. Observations from the lap splice tests provided information on the mechanism of stress transfer between lapped bars. The results indicate that strut-and-tie modeling can be successfully applied to understand the behavior of non-contact lap splices and is necessary in determining the anchorage length of lapped bars. Observations of headed bar anchorage have shown that the final anchorage capacity consists of peak head bearing and reduced bond. A model for anchorage capacity was produced based on this concept. Finally, recommendations for structural concrete design using headed reinforcement were made.

Table of Contents

| | |
|--|------------|
| List of Tables | xiv |
| List of Figures | xvi |
| Chapter 1: Introduction | 1 |
| 1.1 Overview | 1 |
| 1.2 Project Description and Scope | 4 |
| Chapter 2: Bond and Development Length of Deformed Bars | 6 |
| 2.1 Introduction | 6 |
| 2.2 The Mechanics of Bond | 6 |
| 2.2.1 What is Bond? | 6 |
| 2.2.2 Lap Splices | 16 |
| 2.2.3 Confinement of Splitting Stresses | 18 |
| 2.2.4 Effect of Concrete Properties | 23 |
| 2.2.5 Epoxy -Coated Reinforcement | 24 |
| 2.2.6 Measurement of Bond Stress | 25 |
| 2.3 Code Provisions for Deformed Bars | 30 |
| 2.3.1 Quality of Reinforcing Bars: ASTM 615 | 30 |
| 2.3.2 Code Equations for Development Length | 31 |
| 2.3.2.1 ACI 318-02 | 31 |
| 2.3.2.2 AASHTO LRFD Bridge Design Specifications (2nd Ed., 1998) | 34 |
| 2.4 Standard Hooks | 38 |
| Chapter 3: Background on Headed Bars | 44 |
| 3.1 Introduction | 44 |
| 3.2 Historical Development of Headed Bars | 45 |
| 3.3 Headed Bar Fabricators | 48 |
| 3.3.1 Headed Reinforcement Corporation | 49 |
| 3.3.1.1 Friction-Welded Heads | 49 |
| 3.3.1.2 Forged Heads | 50 |
| 3.3.2 ERICO | 51 |
| 3.4 Previous Research on Headed Bars | 54 |

| | |
|---|------------|
| 3.4.1 Caltrans Study | 54 |
| 3.4.2 SINTEF Studies | 58 |
| 3.4.3 University of Kansas Study | 60 |
| 3.4.4 University of Texas Study | 64 |
| 3.4.4.1 Shallow Embedment Pullout Tests | 66 |
| 3.4.4.2 Deep Embedment Pullout Tests | 70 |
| 3.4.4.3 Beam-Column Tests | 74 |
| 3.4.5 Application Studies | 78 |
| 3.4.5.1 Joint Tests | 78 |
| 3.4.5.2 Shear and Confining Reinforcement Tests | 83 |
| 3.4.5.3 Rehabilitation and Retrofit Studies | 85 |
| 3.5 Related Behavioral Topics | 86 |
| 3.5.1 Background on Bearing Capacity | 86 |
| 3.5.1.1 Hawkins | 87 |
| 3.5.1.2 Niyogi..... | 89 |
| 3.5.1.3 Williams | 92 |
| 3.5.2 Deeply Embedded Headed Anchor Bolts | 94 |
| 3.5.2.1 Lee and Breen | 95 |
| 3.5.2.2 Hasselwander and Lo | 97 |
| 3.5.2.3 Furche and Eligehausen..... | 98 |
| 3.6 Code Provisions | 101 |
| 3.6.1 U.S. Mechanical Anchorage Provisions..... | 101 |
| 3.6.2 Canadian Shear Provisions | 102 |
| 3.6.3 ASTM Specification for Weld Connected Heads | 103 |
| 3.6.4 U.S. Bearing Strength Provisions | 105 |
| 3.7 Final Comments | 106 |
| Chapter 4: Background on Strut-and-Tie Modeling..... | 110 |
| 4.1 Introduction | 110 |
| 4.2 Historical Development | 116 |
| 4.3 STM Design Procedure | 119 |
| 4.3.1 Procedure for STM Design..... | 119 |
| 4.3.2 Dimensioning of Nodes, Struts, and Ties..... | 125 |
| 4.3.3 Limitations on Strut-Tie Angle..... | 132 |

| | |
|---|------------|
| 4.3.4 Strength of Nodes | 133 |
| 4.3.5 Strength of Struts | 135 |
| 4.4 Experimental Studies | 138 |
| 4.4.1 Cook and Mitchell (Disturbed Regions)..... | 139 |
| 4.4.2 Beaudre (Deviation Saddles)..... | 139 |
| 4.4.3 Barton, Anderson, and Bouardi (Dapped Beams and Nodes)..... | 141 |
| 4.4.4 Roberts, Sanders, Burdet, and Wollmann (Anchorage Zones)..... | 145 |
| 4.4.5 Zeller (Corbels)..... | 150 |
| 4.4.6 Armstrong, Salas, and Wood (Cantilever Bridge Piers)..... | 151 |
| 4.4.7 Adebar and Zhou (Deep Pile Caps)..... | 152 |
| 4.4.8 Maxwell (Wall with Opening)..... | 154 |
| 4.4.9 Aguilar, Matamoros, and Parra-Montesinos (Deep Beams)..... | 155 |
| 4.5 Final Comments | 157 |
| Chapter 5: CCT Nodes: Specimen Fabrication and Testing Procedures..... | 161 |
| 5.1 Introduction | 161 |
| 5.2 Specimen Details | 162 |
| 5.3 Specimen Instrumentation | 170 |
| 5.4 Load Setup | 174 |
| 5.5 Testing Procedure | 177 |
| 5.6 CCT Node Variables..... | 179 |
| 5.6.1 Bar Size..... | 179 |
| 5.6.2 Strut Angle | 180 |
| 5.6.3 Head Size/Type..... | 180 |
| 5.6.4 Confinement..... | 182 |
| 5.7 Nomenclature and List of Specimens..... | 183 |
| Chapter 6: CCT Nodes: Behavior During Testing..... | 188 |
| 6.1 Unconfined Specimen Behavior..... | 188 |
| 6.1.1 Cracking Behavior..... | 188 |
| 6.1.2 Stress/Strain Development in the Bar..... | 202 |
| 6.1.3 Equilibrium of the Truss Mechanism..... | 209 |
| 6.1.4 Head Slip..... | 211 |
| 6.1.5 Load-Deflection Response | 214 |
| 6.1.6 Modes of Failure | 218 |

| | |
|---|------------|
| 6.1.7 Special Test Results | 228 |
| 6.1.7.1 Specimen CCT-08-45-04.70(V)-1-S2 (Transverse Splitting)..... | 228 |
| 6.1.7.2 Specimen CCT-08-45-04.70(H)-1-S3 (In-Plane Splitting)..... | 231 |
| 6.2 Confined Specimen Behavior | 234 |
| 6.2.1 Cracking Behavior..... | 235 |
| 6.2.2 Stress/Strain Development in the Bar..... | 244 |
| 6.2.3 Stress/Strain Development in the Stirrups | 246 |
| 6.2.3.1 Vertical Splitting Strains Along the Tie Bar | 246 |
| 6.2.3.2 Transverse Splitting Strains Underneath the Tie Bar..... | 253 |
| 6.2.4 Head Slip..... | 261 |
| 6.2.5 Load-Deflection Response | 261 |
| 6.2.6 Modes of Failure | 262 |
| 6.3 Summary of Behavioral Observations..... | 265 |
| Chapter 7: CCT Nodes: Comparison to Failure Models and Formulation of Design | |
| Methodology..... | 268 |
| 7.1 Introduction | 268 |
| 7.2 Trends in the Data..... | 268 |
| 7.2.1 Effect of Relative Head Area | 268 |
| 7.2.2 Effect of Strut Angle | 269 |
| 7.2.3 Effect of Head Shape and Orientation..... | 270 |
| 7.2.4 Effect of Bar Size..... | 275 |
| 7.2.5 Effect of Confinement..... | 275 |
| 7.2.6 Comparison to Hooked Bars..... | 277 |
| 7.3 Comparison of Head Capacity to Theoretical Models | 278 |
| 7.3.1 Comparison to ACI STM Procedures | 278 |
| 7.3.2 Comparison to Modified CCD Approach..... | 284 |
| 7.3.2.1 Comparison to Concrete Breakout Model..... | 284 |
| 7.3.2.2 Comparison to Side Blow-Out Model..... | 286 |
| 7.3.3 Comparison to ACI Bearing Capacity Model..... | 288 |
| 7.4 Development of a Capacity Model for Head Bearing..... | 291 |
| 7.4.1 Effect of Cover/Head Bearing Area Ratio..... | 297 |
| 7.4.2 Effect of Secondary Cover..... | 298 |
| 7.4.3 Effect of Concrete Strength | 300 |

| | |
|--|------------|
| 7.4.4 Effect of Aspect Ratio | 303 |
| 7.4.5 Aggregate Size Effect | 304 |
| 7.4.6 Regression Analysis of Proposed Models | 306 |
| 7.5 Contribution from Bond | 312 |
| 7.6 Summary | 319 |
| Chapter 8: Lap Splices: Specimen Fabrication and Testing Procedures | 322 |
| 8.1 Introduction | 322 |
| 8.2 Specimen Details | 323 |
| 8.3 Specimen Instrumentation | 331 |
| 8.4 Load Setup | 335 |
| 8.5 Testing Procedure | 336 |
| 8.6 Lap Splice Variables | 337 |
| 8.6.1 Head Size/Shape | 337 |
| 8.6.2 Lap Length | 338 |
| 8.6.3 Lap Configuration | 338 |
| 8.6.4 Bar Spacing | 340 |
| 8.6.5 Confinement | 340 |
| 8.7 Nomenclature and List of Specimens | 341 |
| Chapter 9: Lap Splices: Behavior During Testing and Data Trends | 344 |
| 9.1 Cracking Behavior and Failure Modes | 344 |
| 9.1.1 Effect of Lap Length | 351 |
| 9.1.2 Effect of Head Size | 353 |
| 9.1.3 Effect of Lap Configuration | 354 |
| 9.1.4 Effect of Debonding | 356 |
| 9.1.5 Effect of Confinement | 357 |
| 9.2 Stress/Strain Development | 365 |
| 9.2.1 Effect of Head Size | 366 |
| 9.2.2 Effect of Lap Length | 369 |
| 9.2.3 Effect of Confinement | 371 |
| 9.2.3.1 Stress Development in the Hairpins | 373 |
| 9.2.3.2 Stress Development in the Transverse Tie-Down Detail | 375 |
| 9.3 Load-Deflection Behavior | 378 |
| 9.4 Trends in the Data | 381 |

| | |
|--|------------|
| 9.4.1 Effect of Lap Length and Head Area..... | 381 |
| 9.4.2 Effect of Head Shape | 384 |
| 9.4.3 Effect of Bar Spacing | 386 |
| 9.4.4 Effect of Lap Configuration | 387 |
| 9.4.5 Effect of De-Bonding | 388 |
| 9.4.6 Effect of Confinement..... | 390 |
| 9.5 Summary | 393 |
| Chapter 10: Development of a Design Methodology for Headed Bars and Recommendations for Code Provisions | 396 |
| 10.1 Introduction | 396 |
| 10.2 Comparison of Lap Splice Results to Recommended Bearing Model..... | 396 |
| 10.3 Evaluation of Bond Data | 399 |
| 10.4 Combined Bond and Head Bearing | 403 |
| 10.5 Reconfiguration of Proposed Model Into Design Format | 413 |
| 10.5.1 Bond Modification Factor for Head Size | 415 |
| 10.5.2 Equation for Relative Head Area | 418 |
| 10.5.3 Minimum Anchorage Length | 419 |
| 10.6 Recommended Code Provisions | 419 |
| 10.7 Summary | 423 |
| Chapter 11: Design Examples | 425 |
| 11.1 Bracket Design..... | 425 |
| 11.2 Detailing of Precast Panel Closure Strip | 431 |
| 11.3 Bent Cap Extension..... | 434 |
| Chapter 12: Summary and Conclusions | 441 |
| 12.1 Summary | 441 |
| 12.2 Conclusions | 443 |
| 12.2.1 Anchorage Capacity of Headed Bars..... | 443 |
| 12.2.2 CCT Node Behavior..... | 447 |
| 12.2.3 Lap Splice Behavior | 450 |
| 12.3 Suggestions for Future Research | 453 |
| Appendix A: Instrumentation and Mechanical Properties of Reinforcing Bars | 455 |
| A.1 Instrumentation of Reinforcing Bars..... | 455 |
| A.2 Tensile Properties | 456 |

| | |
|--|------------|
| A.3 Flexural Properties | 467 |
| A.4 Calculation of Bar Forces | 471 |
| Appendix B: Distribution Plots for Bearing Capacity Database..... | 474 |
| B.1 Proposed Bearing Capacity Model 1 | 474 |
| B.2 Proposed Bearing Capacity Model 2..... | 479 |
| Appendix C: Summary of CCT Node Data..... | 485 |
| Appendix D: Summary of Lap Splice Data | 489 |
| References | 492 |
| Vita | 502 |

List of Tables

| | | |
|-------------|--|-----------|
| Table 2-1: | ASTM A615 requirements for rebar deformations..... | 31 |
| Table 2-2: | ACI 318-02 multipliers for development length of lap splices | 34 |
| Table 2-3: | AASHTO LRFD multipliers for development length of lap splices | 37 |
| Table 3-1: | HRC head sizes (friction-welded heads)..... | 50 |
| Table 3-2: | Lenton Terminator head sizes and development lengths | 53 |
| Table 3-3: | Setting torques for Lenton Terminator heads..... | 53 |
| Table 4-1: | Allowable stresses for nodes | 134 |
| Table 5-1: | Concrete mix proportions | 168 |
| Table 5-2: | Hardened concrete properties | 168 |
| Table 5-3: | Measured head dimensions for Xtender bars | 182 |
| Table 5-4: | Nomenclature of CCT node test identifiers | 185 |
| Table 5-5: | List of all CCT node tests | 186 - 187 |
| Table 6-1: | Specimen information for data plotted in Figure 6-17..... | 211 |
| Table 6-2: | Specimen information for data plotted in Figure 6-18..... | 212 |
| Table 6-3: | Failure modes of unconfined CCT node specimens | 227 - 228 |
| Table 6-4: | Failure modes of confined CCT node specimens | 265 |
| Table 7-1: | Companion specimens for effect of head shape..... | 271 |
| Table 7-2: | Companion specimens for effect of head orientation..... | 273 |
| Table 7-3: | Statistical data for accuracy of side blow-out model..... | 287 |
| Table 7-4: | Statistical data for accuracy of ACI bearing model..... | 290 |
| Table 7-5: | Summary of sources for collected database of headed bar, anchor bolt, and bearing tests | 293 |
| Table 7-6: | Various models for head capacity..... | 297 |
| Table 7-7: | Statistical data for proposed models of bearing capacity | 306 |
| Table 7-8: | Statistical data for accuracy of model 1 (CCT node tests)..... | 310 |
| Table 7-9: | Statistical data for accuracy of model 2 (CCT node tests)..... | 310 |
| Table 7-10: | Statistical data for accuracy of ACI bond equation in predicting the failure bond | 317 |
| Table 7-11: | Statistical data for accuracy of ACI bond equation in predicting the peak bond | 317 |
| Table 8-1: | Concrete mix proportions | 330 |
| Table 8-2: | Hardened concrete properties | 330 |
| Table 8-3: | Nomenclature of the lap splice test identifiers | 342 |

| | | |
|-------------|---|-----------|
| Table 8-4: | List of all lap splice tests | 343 |
| Table 10-1: | Statistical data for accuracy of recommended bearing model (lap splice tests) | 397 |
| Table 10-2: | Statistical data for accuracy of modified ACI bond stress at failure | 403 |
| Table 10-3: | Research studies of bonded headed bars | 404 |
| Table 10-4: | Statistical data for CCT node and lap splice tests (bond plus head bearing) (current study)..... | 407 |
| Table 10-5: | Statistical data for University of Texas deep embedment tests [42] (bond plus head bearing)..... | 408 |
| Table 10-6: | Statistical data for University of Texas beam-column tests [26] (bond plus bearing)..... | 409 |
| Table 10-7: | Statistical data for University of Kansas pullout tests [119] (bond plus bearing)..... | 409 |
| Table A-1: | Stiffness, A_bE , and yield stress, f_y , for all specimen bar sizes | 462 |
| Table A-2: | Flexural stiffness, IE/r , and radii, r , for all specimen bar sizes | 471 |
| Table C-1: | Summary of CCT node test results | 486 - 488 |
| Table D-1: | Summary of lap splice test results | 490 - 491 |

List of Figures

| | | |
|--------------|--|----|
| Figure 1-1: | Various headed bars compared to a standard hook (#8 size)..... | 2 |
| Figure 1-2: | Reduction of closure strip width using headed bars | 3 |
| Figure 1-3: | Reduction of congestion in a knee joint using headed bars | 3 |
| Figure 1-4: | Simplification of bar details in a deviation saddle using headed bars | 4 |
| Figure 2-1: | Simple concept of bond stresses | 7 |
| Figure 2-2: | Transverse cracking at deformations | 8 |
| Figure 2-3: | Bond and splitting components of rib bearing stresses | 9 |
| Figure 2-4: | Possible splitting crack failures..... | 10 |
| Figure 2-5: | Mechanics of rib bearing on concrete | 12 |
| Figure 2-6: | Models for ring-tension behavior..... | 14 |
| Figure 2-7: | Cohesive crack growth (after Bažant [12])..... | 15 |
| Figure 2-8: | Comparison of various bond model predictions with experimental data (after Tepfers [110] and Gambarova [53])..... | 16 |
| Figure 2-9: | Splitting around lapped bars | 17 |
| Figure 2-10: | Active confinement in a beam end bearing..... | 19 |
| Figure 2-11: | Confinement steel in the vicinity of a splitting crack..... | 20 |
| Figure 2-12: | Crack widths of splitting cracks | 20 |
| Figure 2-13: | Platen restraint in lateral compression studies | 22 |
| Figure 2-14: | Top cast bar effect | 24 |
| Figure 2-15: | Typical pullout specimen..... | 26 |
| Figure 2-16: | Typical beam specimen for bond tests | 27 |
| Figure 2-17: | Typical beam-end test | 28 |
| Figure 2-18: | Typical tensile lap splice specimens | 29 |
| Figure 2-19: | Typical beam specimen for lap tests | 29 |
| Figure 2-20: | Important dimensions for rebar specifications | 30 |
| Figure 2-21: | Standard hook dimensions | 40 |
| Figure 2-22: | Development lengths of standard hooks and straight bars | 41 |
| Figure 2-23: | Stress transfer in a hooked bar..... | 41 |
| Figure 2-24: | Side spall failure of a hooked bar..... | 42 |
| Figure 3-1: | Anchorage of a headed bar | 44 |
| Figure 3-2: | Shear reinforcement tested at University of Calgary | 46 |

| | | |
|--------------|---|-----|
| Figure 3-3: | HRC friction-welded head | 50 |
| Figure 3-4: | The Xtender coupler system | 51 |
| Figure 3-5: | ERICO's Lenton Terminator head | 52 |
| Figure 3-6: | Head-bar connections tested by Caltrans | 55 |
| Figure 3-7: | Head reaction versus embedment depth compared to fully bonded load profiles (after Caltrans data [108])..... | 57 |
| Figure 3-8: | Static pullout test performed by SINTEF..... | 59 |
| Figure 3-9: | Transverse reinforcement patterns studied at Kansas [119]..... | 61 |
| Figure 3-10: | Definition of geometric parameters for University of Texas study..... | 66 |
| Figure 3-11: | Shallow embedment pullout specimen used by DeVries | 67 |
| Figure 3-12: | Projected concrete breakout areas for different situations | 69 |
| Figure 3-13: | Deep embedment pullout specimen used by DeVries and Bashandy..... | 70 |
| Figure 3-14: | DeVries data on side blow-out capacity versus relative head area | 72 |
| Figure 3-15: | Projected concrete side blow-out areas for different situations | 75 |
| Figure 3-16: | Typical exterior beam-column joint studied by Bashandy..... | 76 |
| Figure 3-17: | Photo of cap-beam/column joint reinforcement from U.C. San Diego study [62]..... | 79 |
| Figure 3-18: | Pile/foundation connection studied at University of California, San Diego..... | 80 |
| Figure 3-19: | Cantilever bridge pier tested at the University of Texas | 82 |
| Figure 3-20: | Test specimen for Sleipner A collapse investigation | 83 |
| Figure 3-21: | Bearing of a rigid plate versus bearing of a headed bar..... | 87 |
| Figure 3-22: | Bearing tests on concrete blocks..... | 91 |
| Figure 3-23: | Niyogi's size effect data..... | 92 |
| Figure 3-24: | Minimum and secondary cover dimensions | 94 |
| Figure 3-25: | Test specimen used by Lee and Breen | 96 |
| Figure 3-26: | Definition of head angle | 98 |
| Figure 3-27: | Furche and Eligehausen's transition of failure modes for headed anchors | 100 |
| Figure 3-28: | Definition of notional area | 105 |
| Figure 3-29: | Splitting mechanism in bearing and side blow-out failures | 108 |
| Figure 3-30: | Effect of the secondary cover dimension, c_2 | 109 |
| Figure 4-1: | Examples of strut-and-tie modeling | 111 |
| Figure 4-2: | Deformation response of plain and confined concrete | 112 |
| Figure 4-3: | Beam analysis methods..... | 114 |
| Figure 4-4: | Division of dapped beam into B- and D-regions | 114 |

| | | |
|--------------|---|-----|
| Figure 4-5: | Strut types | 115 |
| Figure 4-6: | Basic node types | 116 |
| Figure 4-7: | The Ritter truss model for shear..... | 117 |
| Figure 4-8: | Morsch's truss model for concentric, concentrated load..... | 118 |
| Figure 4-9: | Truss model for torsion..... | 119 |
| Figure 4-10: | Flowchart for structural design..... | 120 |
| Figure 4-11: | Flowchart for the STM process | 124 |
| Figure 4-12: | Distribution of tie reinforcement | 126 |
| Figure 4-13: | ACI recommendations for dimensioning of nodes | 127 |
| Figure 4-14: | AASHTO recommendations for dimensioning of nodes (after Figure 5.6.3.3.2-1 [1])..... | 128 |
| Figure 4-15: | Hydrostatic and non-hydrostatic nodes | 130 |
| Figure 4-16: | Subdivision and simplification of nodes | 131 |
| Figure 4-17: | Development of tie reinforcement in nodes | 132 |
| Figure 4-18: | Change in strut efficiency factor versus strut angle (AASHTO specifications)..... | 136 |
| Figure 4-19: | Typical deviation saddle tested by Beurpe..... | 140 |
| Figure 4-20: | Isolated CTT node tested by Anderson..... | 143 |
| Figure 4-21: | Isolated CCT node tested by Bouardi..... | 145 |
| Figure 4-22: | Local and general zones of post-tensioned structures | 146 |
| Figure 4-23: | Concrete strains in corbels tested by Zeller..... | 151 |
| Figure 4-24: | Double punch strut test used by Adebar and Zhou | 153 |
| Figure 4-25: | Design specimen for the Purdue study..... | 156 |
| Figure 5-1: | A typical CCT node test..... | 161 |
| Figure 5-2: | Reinforcement layouts for unconfined specimens..... | 164 |
| Figure 5-3: | Reinforcement layouts for confined specimens | 165 |
| Figure 5-4: | Widths of unconfined specimens..... | 166 |
| Figure 5-5: | Cross-section of confined specimen and stirrup geometry | 166 |
| Figure 5-6: | Alignment of heads with bearing plate | 167 |
| Figure 5-7: | Placement of miscellaneous details in the CCT node specimens..... | 169 |
| Figure 5-8: | Placement of instrumentation for a typical specimen | 171 |
| Figure 5-9: | Placement of instrumentation in the nodal region of a typical specimen | 171 |
| Figure 5-10: | Details of the reinforcement and instrumentation for hooked bar specimens | 172 |
| Figure 5-11: | Placement of instrumentation on stirrups of confined specimens..... | 173 |

| | | |
|--------------|--|-----------|
| Figure 5-12: | Equilibrium of CCT node panel with a horizontal reaction at the bearing plate (45° strut angle)..... | 176 |
| Figure 5-13: | Free roller detail used for the final CCT node test setup..... | 177 |
| Figure 6-1: | Development of cracks in a representative test with a large head (CCT-08-45-10.39-2)..... | 191 - 192 |
| Figure 6-2: | Failure of specimen CCT-08-45-10.39-2..... | 192 |
| Figure 6-3: | Crack width measurements from specimen CCT-08-45-10.39-2 | 193 |
| Figure 6-4: | Development of cracks in a representative test with a small head (CCT-08-45-01.85-2)..... | 194 |
| Figure 6-5: | Development of cracks in the hooked bar test (CCT-08-45-Hook2-1)..... | 196 |
| Figure 6-6: | CCT node height in headed bar and hooked bar tests | 197 |
| Figure 6-7: | Development of cracks in a steep strut angle test (CCT-08-55-10.39-1) | 199 |
| Figure 6-8: | Development of cracks in a shallow strut angle test (CCT-08-30-10.39-1) | 200 - 201 |
| Figure 6-9: | Top and bottom fiber strains of the tie bar in specimen CCT-08-45-10.39-2 | 204 |
| Figure 6-10: | “Kinking” of reinforcement caused by dowel action across diagonal shear cracks | 205 |
| Figure 6-11: | Development of bar stress in specimen CCT-08-45-10.39-2..... | 205 |
| Figure 6-12: | Measured bond stresses in CCT-08-45-10.39-2..... | 207 |
| Figure 6-13: | Development of stress for headed and non-headed bars | 208 |
| Figure 6-14: | Components of bar stress provided by bond and head bearing in CCT-11-45-02.85(V)-1..... | 208 |
| Figure 6-15: | Equilibrium of CCT node..... | 209 |
| Figure 6-16: | Equilibrium plot of bar force versus bearing reaction in specimen CCT-08-45-10.39-2 | 210 |
| Figure 6-17: | Bar stress versus head slip for CCT node specimens with #11 bars..... | 212 |
| Figure 6-18: | Bar stress versus head slip for CCT node specimens with #8 bars | 213 |
| Figure 6-19: | Load-deflection and load-slip data for specimens with small and large heads..... | 214 |
| Figure 6-20: | Assumed and possible equilibrium geometries for 30° CCT node specimens | 216 |
| Figure 6-21: | Assumed and possible stress states of CCC nodes | 218 |
| Figure 6-22: | Pullout failure of a non-headed bar (specimen CCT-08-55-00.00-1)..... | 219 |
| Figure 6-23: | Patterns of strut/node rupture | 220 |
| Figure 6-24: | Side view of a failed specimen with a vertically oriented head (CCT-08-55-02.80(V)-1) demonstrating splitting of the diagonal compression strut..... | 221 |

| | | |
|--------------|--|-----------|
| Figure 6-25: | Front view of a failed specimen with a vertically oriented head (CCT-08-55-02.80(V)-1) demonstrating splitting of diagonal compression strut | 222 |
| Figure 6-26: | Splitting failure of a specimen with a small head (CCT-11-55-01.10-1)..... | 223 |
| Figure 6-27: | Zone of crushed concrete in a specimen with a horizontally oriented head (CCT-08-45-04.70(H)-1) after failure (top view)..... | 224 |
| Figure 6-28: | Zone of crushed concrete in a specimen with a horizontally oriented head (CCT-11-45-04.13(H)-1) after failure (side view)..... | 225 |
| Figure 6-29: | Specimen CCT-08-55-02.80(H)-1 after failure..... | 225 |
| Figure 6-30: | Special instrumentation in Specimen CCT-08-45-04.70(V)-1-S2 | 229 |
| Figure 6-31: | Transverse splitting strains in specimen CCT-08-45-04.70(V)-1-S2..... | 231 |
| Figure 6-32: | Special instrumentation in Specimen CCT-08-45-04.70(H)-1-S3..... | 232 |
| Figure 6-33: | In-plane splitting strains in specimen CCT-08-45-04.70(H)-1-S3..... | 234 |
| Figure 6-34: | Spiral confinement detail attempted in specimen CCT-08-45-04.70(V)-1-S1 | 235 |
| Figure 6-35: | Development of cracks in a heavily confined, headed bar specimen (CCT-08-45-04.70(V)-1-C0.012)..... | 237 - 238 |
| Figure 6-36: | Crack patterns overlaid onto probable truss mechanisms for the heavily confined, headed bar specimen (CCT-08-45-04.70(V)-1-C0.012) | 240 |
| Figure 6-37: | Crack width measurements from the heavily confined, headed bar specimen (CCT-08-45-04.70(V)-1-C0.012) | 241 |
| Figure 6-38: | Development of cracks in a lightly confined, headed bar specimen (CCT-08-45-04.70(V)-1-C0.006)..... | 242 |
| Figure 6-39: | Development of cracks in a heavily confined, hooked bar specimen (CCT-08-45-Hook2-1-C0.012) | 243 |
| Figure 6-40: | Strain at 5" vs. bearing reaction in unconfined and confined specimens | 245 |
| Figure 6-41: | Components of bar stress provided by bond and head bearing in CCT-08-45-04.70(V)-1-C0.012..... | 245 |
| Figure 6-42: | Development of vertical tensile strain in the stirrup confinement of the heavily confined, headed bar specimen (CCT-08-45-04.70(V)-1-C0.012) | 247 |
| Figure 6-43: | Development of vertical tensile strain in the stirrup confinement of the lightly confined, headed bar specimen (CCT-08-45-04.70(V)-1-C0.006) | 248 |
| Figure 6-44: | Vertical tensile strains along the tie in the heavily confined, headed bar specimen (CCT-08-45-04.70(V)-1-C0.012)..... | 250 |

| | | |
|--------------|--|-----|
| Figure 6-45: | Vertical tensile strains along the tie in the heavily confined, non-headed bar specimen (CCT-08-45-00.00-1-C0.012)..... | 251 |
| Figure 6-46: | Vertical tensile strains along the tie in the heavily confined, hooked bar specimen (CCT-08-45-Hook2-1-C0.012) | 252 |
| Figure 6-47: | Development of transverse tensile strain in the stirrup confinement of the heavily confined, headed bar specimen (CCT-08-45-04.70(V)-1-C0.012) | 254 |
| Figure 6-48: | Development of transverse tensile strain in the stirrup confinement of the lightly confined, headed bar specimen (CCT-08-45-04.70(V)-1-C0.006)..... | 255 |
| Figure 6-49: | Transverse strains along the underside of the tie in the heavily confined, headed bar specimen (CCT-08-45-04.70(V)-1-C0.012)..... | 258 |
| Figure 6-50: | Transverse strains along the underside of the tie in the heavily confined, non-headed bar specimen (CCT-08-45-00.00-1-C0.012) | 259 |
| Figure 6-51: | Transverse strains along the underside of the tie in the heavily confined, hooked bar specimen (CCT-08-45-Hook2-1-C0.012) | 260 |
| Figure 6-52: | Bar stress versus head slip for unconfined and confined specimens..... | 261 |
| Figure 6-53: | Load-deflection data for specimens unconfined and confined specimens | 262 |
| Figure 6-54: | Failure cracking patterns for non-headed and headed specimens with varying degrees of confinement..... | 264 |
| Figure 7-1: | Effect of relative head area on head capacity | 269 |
| Figure 7-2: | Approximate development lengths for 45° and 30° strut angles | 270 |
| Figure 7-3: | Minimum head size necessary to achieve yield of the tie bar..... | 270 |
| Figure 7-4: | Head slip plots for circular and square heads..... | 271 |
| Figure 7-5: | Effect of head orientation and aspect ratio on head capacity | 273 |
| Figure 7-6: | Shallow and steep faces of the wedge for a rectangular head | 274 |
| Figure 7-7: | Transverse splitting components of shallow and steep wedge face bearing | 274 |
| Figure 7-8: | Horizontal versus vertical head orientation in a CCT node | 274 |
| Figure 7-9: | Effect of bar size on head capacity | 275 |
| Figure 7-10: | Effect of confinement on head capacity | 277 |
| Figure 7-11: | Bar stress from hooked bars compared with headed bars (#8 sizes)..... | 278 |
| Figure 7-12: | Critical node faces for STM stresses | 279 |
| Figure 7-13: | Efficiency factors for node bearing at the face adjacent to the head..... | 279 |
| Figure 7-14: | Distribution of efficiency factors for CCT node bearing results..... | 280 |
| Figure 7-15: | Geometry of the strut/node intersection at the CCT node..... | 282 |

| | | |
|--------------|---|-----|
| Figure 7-16: | Distribution of efficiency factors for strut bearing at the face adjacent to the CCT node..... | 283 |
| Figure 7-17: | Definition of embedment depth and project breakout area for application of concrete breakout model..... | 285 |
| Figure 7-18: | Correlation of measured and calculated values for concrete breakout model..... | 285 |
| Figure 7-19: | Projected side blow-out areas for various CCT specimen series | 287 |
| Figure 7-20: | Correlation of measured and calculated values for side blow-out model..... | 288 |
| Figure 7-21: | Notional areas for bearing analysis of CCT nodes | 289 |
| Figure 7-22: | Correlation of measured and calculated values for bearing model..... | 290 |
| Figure 7-23: | Distribution plot of measured/calculated ratios for bearing model | 291 |
| Figure 7-24: | Relation of concrete power to $2c_1/\sqrt{A_{nh}}$ ratio | 295 |
| Figure 7-25: | Normalized bearing capacity versus $2c_1/\sqrt{A_{nh}}$ ratio..... | 298 |
| Figure 7-26: | Normalized bearing capacity versus cover ratio, c_2/c_1 | 299 |
| Figure 7-27: | Normalized bearing capacity versus concrete strength, f_c' , with trend lines for relationships to f_c' and $\sqrt{f_c'}$ | 300 |
| Figure 7-28: | Normalized bearing capacity versus concrete strength, f_c' , with trend lines for the proposed concrete exponent term..... | 302 |
| Figure 7-29: | Effect of head aspect ratio on capacity..... | 304 |
| Figure 7-30: | Size effect on capacity | 305 |
| Figure 7-31: | Distribution of measured/calculated values for bearing model 1..... | 307 |
| Figure 7-32: | Distribution of measured/calculated values for bearing model 2..... | 308 |
| Figure 7-33: | Probability of unsafe test outcome as a function of exclusion factor..... | 309 |
| Figure 7-34: | Distribution plot of measured/calculated ratios for model 1 (CCT node tests)..... | 311 |
| Figure 7-35: | Distribution plot of measured/calculated ratios for model 2 (CCT node tests)..... | 311 |
| Figure 7-36: | Measured failure bond stress versus relative head area..... | 313 |
| Figure 7-37: | Measured peak bond stress versus vertical compression stress | 315 |
| Figure 7-38: | Measured peak bond stress versus relative head area | 316 |
| Figure 7-39: | Distribution plot of measured/calculated ratios for failure bond..... | 318 |
| Figure 7-40: | Distribution plot of measured/calculated ratios for peak bond..... | 318 |
| Figure 8-1: | A typical lap splice test..... | 322 |
| Figure 8-2: | Reinforcement details of unconfined lap splice specimens | 325 |

| | | |
|--------------|---|-----------|
| Figure 8-3: | The two types of lap splice confinement details tested | 326 |
| Figure 8-4: | Photos of the two lap splice confinement details | 327 |
| Figure 8-5: | Dimensions of the hairpin confinement detail | 328 |
| Figure 8-6: | Dimensions of the transverse tie-down confinement detail | 329 |
| Figure 8-7: | Spacing of strain gages for various lap lengths | 332 |
| Figure 8-8: | Instrumentation of hairpin bars | 333 |
| Figure 8-9: | Instrumentation of transverse tie-down confinement | 334 |
| Figure 8-10: | Load setup for lap splice specimens | 336 |
| Figure 8-11: | Non-contact and contact lap configurations | 339 |
| Figure 9-1: | Crack development in a typical unconfined lap splice test (specimen LS-08-04.04-12-10(N)-1)..... | 346 - 348 |
| Figure 9-2: | Photograph of failed lap splice specimen with cover removed from lap zone (specimen LS-08-04.04-12-10(N)-1) | 348 |
| Figure 9-3: | Causes of cover spalling in lap zone | 350 |
| Figure 9-4: | Features of force transfer in lap zone (photo of specimen LS-08-04.70-12-10(N)-1) | 350 |
| Figure 9-5: | Strut model for lap splices | 351 |
| Figure 9-6: | Photos of concrete wedges in lap splice specimens..... | 351 |
| Figure 9-7: | Crack patterns for large headed specimens with different lap lengths | 352 |
| Figure 9-8: | Crack patterns for specimens of different head sizes ($L_s = 8d_b$) | 354 |
| Figure 9-9: | Crack patterns for contact and non-contact lap splices ($L_s = 5d_b$)..... | 355 |
| Figure 9-10: | Crack patterns for bonded and debonded lap splices | 357 |
| Figure 9-11: | Crack development in a typical hairpin confined lap splice test (specimen LS-08-04.04-12-10(N)-1-H0.6)..... | 358 - 359 |
| Figure 9-12: | Internal cracking with hairpin confinement (specimen LS-08-04.04-12-10(N)-1-H0.6) | 359 |
| Figure 9-13: | Crack development in the transverse stirrup cage test (specimen LS-08-04.04-12-10(N)-1-TTD) | 361 - 363 |
| Figure 9-14: | Crack patterns at failure for unconfined and confined specimens | 364 |
| Figure 9-15: | Components of bar stress provided by bond and head bearing in a typical lap splice specimen (LS-08-04.70-12-10(N)-1)..... | 365 |
| Figure 9-16: | Stress profiles for headed and non-headed lap splices ($L_s = 12d_b$)..... | 366 |
| Figure 9-17: | Bond profiles for a headed bar lap splice (specimen LS-08-04.70-12-10(N)-1)..... | 367 |

| | | |
|--------------|--|-----|
| Figure 9-18: | Bond profiles for a headed bar lap splice (specimen LS-08-00.00-12-10(N)-1)..... | 368 |
| Figure 9-19: | Bond profiles for a headed bar lap splices of varying lap length (specimens LS-08-04.04-08-10(N)-1, LS-08-04.04-12-10(N)-1, and LS-08-04.04-14-10(N)-1)..... | 370 |
| Figure 9-20: | Components of bar stress provided by bond and head bearing in a lap splice of short length (LS-08-04.70-08-10(N)-1) | 370 |
| Figure 9-21: | Bond profiles for a headed bar lap splice confined by hairpins (specimen LS-08-04.04-12-10(N)-1-H0.6) | 372 |
| Figure 9-22: | Bond profiles for a headed bar lap splice confined by transverse and tie-down bars (specimen LS-08-04.04-12-10(N)-1-TTD)..... | 373 |
| Figure 9-23: | Hairpin force versus bar stress (specimen LS-08-04.04-12-10(N)-1-H0.6)..... | 375 |
| Figure 9-24: | Transverse strain versus splice bar stress (specimen LS-08-04.04-12-10(N)-1-TTD)..... | 376 |
| Figure 9-25: | Strain profiles in transverse bars of LS-08-04.04-12-10(N)-1-TTD | 376 |
| Figure 9-26: | Tie-down strain versus splice bar stress (specimen LS-08-04.04-12-10(N)-1-TTD)..... | 377 |
| Figure 9-27: | Strain profile in tie-down bars of LS-08-04.04-12-10(N)-1-TTD | 378 |
| Figure 9-28: | Load-deflection curves for bonded and debonded specimens..... | 380 |
| Figure 9-29: | Load-deflection curves for unconfined and confined specimens | 381 |
| Figure 9-30: | Bar stress versus lap length | 382 |
| Figure 9-31: | Bar stress versus anchorage length..... | 383 |
| Figure 9-32: | Bar stress at the head versus lap length..... | 384 |
| Figure 9-33: | Load-deflection curves for circular and rectangular heads | 385 |
| Figure 9-34: | Concrete cover for various head shapes (after Ledesma [67])..... | 386 |
| Figure 9-35: | The effect of bar spacing on bar stress ($L_s = 5d_b$) | 386 |
| Figure 9-36: | The effect of lap configuration on bar stress ($L_s = 5d_b$)..... | 388 |
| Figure 9-37: | The effect of debonding on bar stress ($L_s = 14d_b$)..... | 389 |
| Figure 9-38: | Bond splitting effect on cover dimensions | 390 |
| Figure 9-39: | Normalized bar stress versus confinement ratio ($L_s = 8d_b$)..... | 391 |
| Figure 9-40: | Normalized bar stress at the head versus confinement ratio ($L_s = 8d_b$)..... | 392 |
| Figure 9-41: | The effect of confinement type on bar stress ($L_s = 12d_b$)..... | 393 |
| Figure 10-1: | Measured/calculated ratio of recommended model versus lap length..... | 398 |
| Figure 10-2: | Distribution plot of measured/calculated ratios for recommended bearing model..... | 398 |
| Figure 10-3: | Bond stress at failure versus lap length | 399 |

| | | |
|---------------|---|-----|
| Figure 10-4: | Peak bond stress distributions for lap splice and CCT node tests..... | 400 |
| Figure 10-5: | Bond stress at failure versus relative head area (lap splice and CCT node data)... | 401 |
| Figure 10-6: | Distribution plot for bond stress at failure data | 402 |
| Figure 10-7: | Distinction between embedment depth and anchorage length..... | 405 |
| Figure 10-8: | Distribution of measured/calculated ratios for CCT node and lap splice tests (bond plus bearing) (current study)..... | 406 |
| Figure 10-9: | Distribution of measured/calculated ratios University of Texas deep embedment tests [42] (bond plus bearing)..... | 408 |
| Figure 10-10: | Measured/calculated ratio versus embedment/cover ratio (University of Texas beam-column and Kansas pullout studies)..... | 410 |
| Figure 10-11: | Strut-and-tie model for beam-column specimen | 412 |
| Figure 10-12: | Strut-and-tie model for Kansas pullout specimen..... | 413 |
| Figure 10-13: | Development of bar stress for a non-headed bar..... | 415 |
| Figure 10-14: | Required relative head area versus anchorage length..... | 417 |
| Figure 10-15: | Head size modification factor versus anchorage length | 417 |
| Figure 11-1: | Loads and dimensions for bracket problem | 426 |
| Figure 11-2: | Column cross-section and free body forces on bracket..... | 426 |
| Figure 11-3: | Spacing of bracket tie bars..... | 427 |
| Figure 11-4: | The available anchorage length within the bracket | 428 |
| Figure 11-5: | Final detail for bracket | 430 |
| Figure 11-6: | Plan and elevation views for precast slab problem..... | 432 |
| Figure 11-7: | Anchorage length of lap splice..... | 432 |
| Figure 11-8: | Final detail for closure strip | 434 |
| Figure 11-9: | Dimensions of bent cap..... | 436 |
| Figure 11-10: | Headed/non-headed bar lap splice | 437 |
| Figure 11-11: | Over-under lap splice..... | 439 |
| Figure 12-1: | Typical CCT node from the test program..... | 441 |
| Figure 12-2: | Plan view of typical lap splice | 442 |
| Figure 12-3: | Critical development point for a CCT node..... | 447 |
| Figure 12-4: | The state of stress at the CCT node..... | 448 |
| Figure 12-5: | Mechanism of stress transfer between opposing lapped bars | 451 |
| Figure A-1: | Placement of strain gage on main rib of bar | 455 |
| Figure A-2: | Steps in the bar instrumentation process..... | 457 |

| | | |
|--------------|--|-----|
| Figure A-3: | Layout of strain gages for #8 and #11 tensile specimens | 458 |
| Figure A-4: | Typical load-strain data from a tensile test (# 8 ERICO ⁽²⁾ bar group)..... | 459 |
| Figure A-5: | Histogram of ³ / ₁₆ " diameter plain wire tensile test data | 463 |
| Figure A-6: | Histogram of # 2 bar tensile test data..... | 463 |
| Figure A-7: | Histogram of # 3 bar tensile test data..... | 464 |
| Figure A-8: | Histogram of # 4 bar tensile test data..... | 464 |
| Figure A-9: | Histogram of # 5 bar tensile test data..... | 465 |
| Figure A-10: | Histogram of # 8 bar tensile test data..... | 466 |
| Figure A-11: | Histogram of # 11 bar tensile test data..... | 467 |
| Figure A-12: | Test setup for bending tests of bars | 468 |
| Figure A-13: | Typical moment-strain data from a bending test (# 8 ERICO ⁽²⁾ bar group)..... | 469 |
| Figure A-14: | Bar cross-section strains and stresses | 472 |
| Figure B-1: | All headed bar and anchor bolt tests listed in database (model 1)..... | 474 |
| Figure B-2: | All bearing block tests listed in database (model 1) | 475 |
| Figure B-3: | University of Texas Deep Embedment Tests [42] (model 1)..... | 475 |
| Figure B-4: | University of Texas CCT node tests (current study) (model 1) | 475 |
| Figure B-5: | Breen, 1964 [31] (model 1) | 476 |
| Figure B-6: | Lee and Breen, 1966 [68] (model 1) | 476 |
| Figure B-7: | Lo, 1975 [58] (model 1)..... | 476 |
| Figure B-8: | Hasselwander, 1977 [58] (model 1)..... | 477 |
| Figure B-9: | Furche and Eligehausen, 1991 [49] (model 1)..... | 477 |
| Figure B-10: | Shelson, 1957 [106] (model 1) | 477 |
| Figure B-11: | Au and Baird, 1960 [24] (model 1)..... | 478 |
| Figure B-12: | Hawkins, 1968 [60] (model 1) | 478 |
| Figure B-13: | Niyogi, 1973 [90, 91] (model 1)..... | 478 |
| Figure B-14: | Williams, 1979 [116] (model 1) | 479 |
| Figure B-15: | All headed bar and anchor bolt tests listed in database (model 2)..... | 480 |
| Figure B-16: | All bearing block tests listed in database (model 2) | 480 |
| Figure B-17: | University of Texas Deep Embedment Tests [42] (model 2)..... | 480 |
| Figure B-18: | University of Texas CCT node tests (current study) (model 2) | 481 |
| Figure B-19: | Breen, 1964 [31] (model 2) | 481 |
| Figure B-20: | Lee and Breen, 1966 [68] (model 2) | 481 |
| Figure B-21: | Lo, 1975 [58] (model 2)..... | 482 |

| | | |
|--------------|--|-----|
| Figure B-22: | Hasselwander, 1977 [58] (model 2)..... | 482 |
| Figure B-23: | Furche and Eligehausen, 1991 [49] (model 2)..... | 482 |
| Figure B-24: | Shelson, 1957 [106] (model 2) | 483 |
| Figure B-25: | Au and Baird, 1960 [24] (model 2)..... | 483 |
| Figure B-26: | Hawkins, 1968 [60] (model 2) | 483 |
| Figure B-27: | Niyogi, 1973 [90, 91] (model 1)..... | 484 |
| Figure B-28: | Williams, 1979 [116] (model 1) | 484 |
| Figure C-1: | Close-up of CCT node | 485 |
| Figure D-1: | Close-up of lap splice | 489 |

Chapter 1: Introduction

1.1 OVERVIEW

In structural concrete, the provisions for anchorage of straight bars and hooks frequently present detailing problems due to the long development lengths and large bend diameters that are required, particularly when large-diameter reinforcing bars are used. In many cases, the requirements for straight bar anchorage and lap splices cannot be provided within the available dimensions of elements. Hooked bars can be used to shorten anchorage length, but in many cases, the bend of the hook will not fit within the dimensions of a member or the hooks create congestion and make an element difficult to construct. Similarly, mechanical anchorage devices can be used to shorten lap splice lengths, but they frequently require special construction operations and careful attention to tolerances.

To address the problems that arise from the use of conventional reinforcing bar solutions anchorage solutions (straight bar development length and hooks), headed bars were developed for use in the construction of concrete platforms for the offshore oil industry. Headed bars (Figure 1-1) are formed by the attachment of a plate or the forging of an upset bearing surface at the end of a straight reinforcing bar. Such bars are anchored by a combination of bond along the straight bar length and direct bearing at the head. Like a hooked bar, they can develop within a short distance, but they do not create as much congestion. Aside from the offshore oil industry, headed bars have not been widely used in the construction of bridges, buildings, or other traditional concrete structures. There is little guidance currently available for the design of headed bar anchorage either in the form of code provisions or published research.

Headed bars can potentially simplify the design and construction of complex bridge details such as closure strips, in which reduced splice lengths can be used to reduce the width of the closure gap (Figure 1-2), knee joints, in which unwieldy hooks can be replaced by compact headed bars (Figure 1-3), and deviation saddle blocks for external post-tensioning of segmental box-girder superstructures, in which complex bend details can be replaced by double headed ties (Figure 1-4).

Project 1855 was funded by the Texas Department of Transportation (TxDOT) to examine the behavior of headed bars in bridge details and to evaluate the feasibility of using headed bars for Texas transportation structures. Additionally, the findings of an extensive literature review and experimental program are to be reported and design guidelines for the use of headed bars are to be developed.

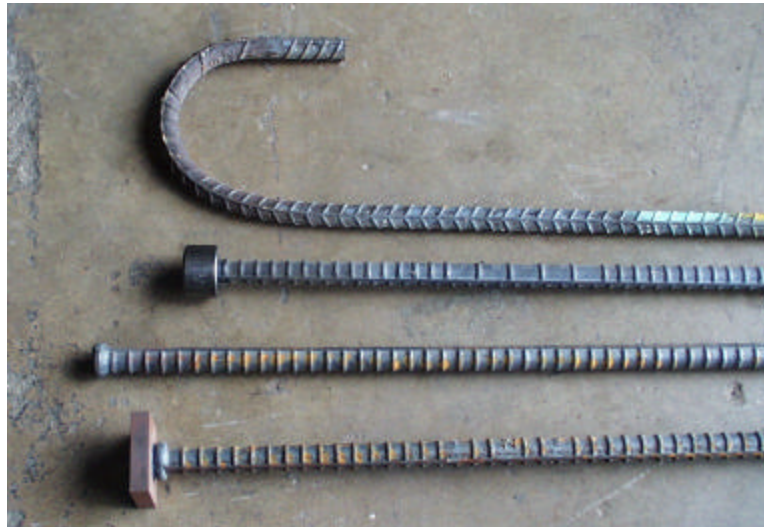


Figure 1-1: Various headed bars compared to a standard hook (#8 size)

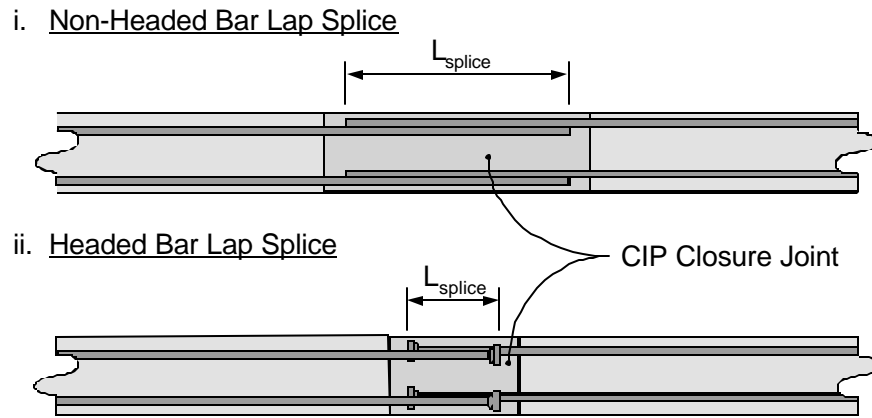


Figure 1-2: Reduction of closure strip width using headed bars

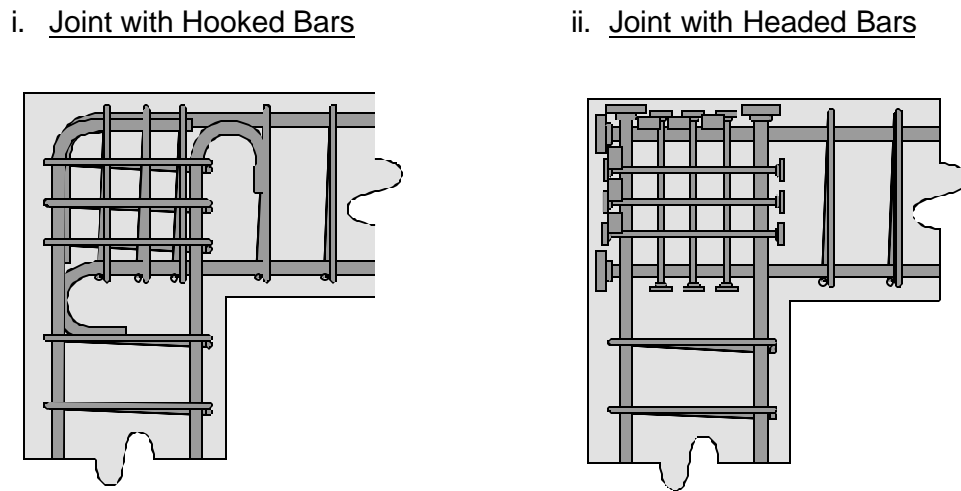


Figure 1-3: Reduction of congestion in a knee joint using headed bars

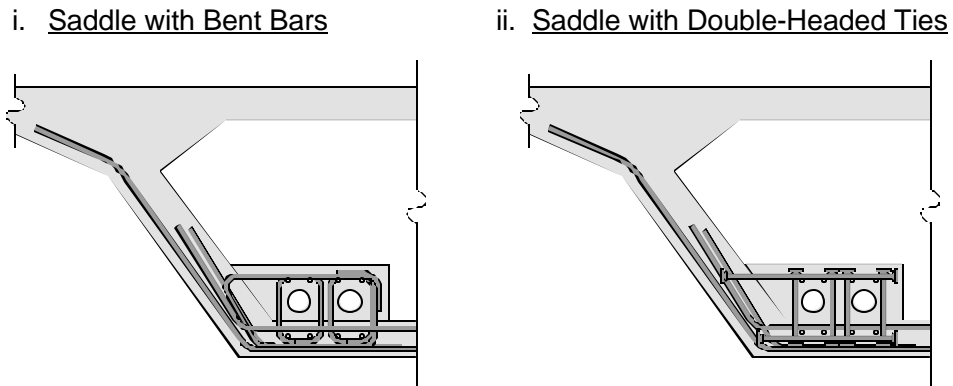


Figure 1-4: Simplification of bar details in a deviation saddle using headed bars

1.2 PROJECT DIRECTION AND SCOPE

After several meetings between the research team and TxDOT bridge design engineers to identify bridge details for which headed bars showed the most promise, two experimental directions were decided upon. TxDOT representatives expressed the most interest in the use of headed bars to reduce lap lengths and to replace hooked bars in congested discontinuity regions. Two specimen types were selected: lap splices and compression-compression-tension (CCT) nodes. These specimens were designed to be as general as possible so that the behavior of the headed bars in these details could be extrapolated to a variety of specific applications in which lap splices and CCT nodes occur.

A CCT node specimen was developed to test the anchorage of a single headed bar in a CCT node. Companion specimens with non-headed bars and hooked bars were also tested. Other variables of the test program included the angle of the compression strut, head size and shape, bar size, and the presence of confinement in the nodal zone. A total of 64 CCT node specimens were tested. In addition to studying the anchorage performance of headed bars, these specimens were

used to determine the behavior of CCT nodes and the current provisions related to strut-and-tie modeling (STM) were evaluated against the results.

A lap splice specimen was developed to test the anchorage of multiple headed bars anchored within a single layer lap splice. Companion specimens with non-headed bars were also tested. Other variables of the lap splice test program included the lap length, the head size and shape, the bar spacing, contact versus non-contact laps, and the presence of confinement in the lap zone. A total of 27 lap splices were tested.

A comprehensive literature review was compiled (Chapters 2, 3, and 4). The behavior of the test specimens is described in detail (Chapters 5, 6, 8, and 9). The data from the current study were compared to results from previous studies (Chapters 7 and 10). Data from the experimental tests were analyzed and used to determine guidelines for the design of headed bar anchorages (Chapter 10). Recommendations for changes to the ACI 318 [2] and AASHTO LRFD [1] specifications are provided (Chapter 10). Design examples are developed to illustrate the use and applicability of the design guidelines (Chapter 11). A summary and recommendations for future research are also provided (Chapter 12).

Chapter 2: Bond and Development Length of Deformed Bars

2.1 INTRODUCTION

Before discussing the state-of-the-art of headed reinforcement, a brief overview of conventional anchorage of reinforcing bars will be presented emphasizing bond of straight reinforcement and standard hook details. In this chapter, the nature of bond stress and how it is utilized to achieve development of reinforcement will be discussed. The behavior of hooked bar anchorages is also discussed. Review of design provisions focuses on the two American codes that are pertinent to the project sponsors: ACI 318 [2] and the AASHTO LRFD Specifications [1]. ASTM Standards will also be referenced for some topics.

2.2 THE MECHANICS OF BOND

2.2.1 What is bond?

Bond refers to the interaction between reinforcing steel and the surrounding concrete that allows for transfer of tensile stress from the steel into the concrete. Bond is the mechanism that allows for anchorage of straight reinforcing bars and influences many other important features of structural concrete such as crack control and section stiffness. Figure 2-1 shows a straight bar embedded into a block of concrete. When the bond stress is sufficient to resist design tensile loads in the bar, then the bar is “developed” and the embedment length necessary for anchorage of the fully stressed reinforcing bar is referred to as its development length.

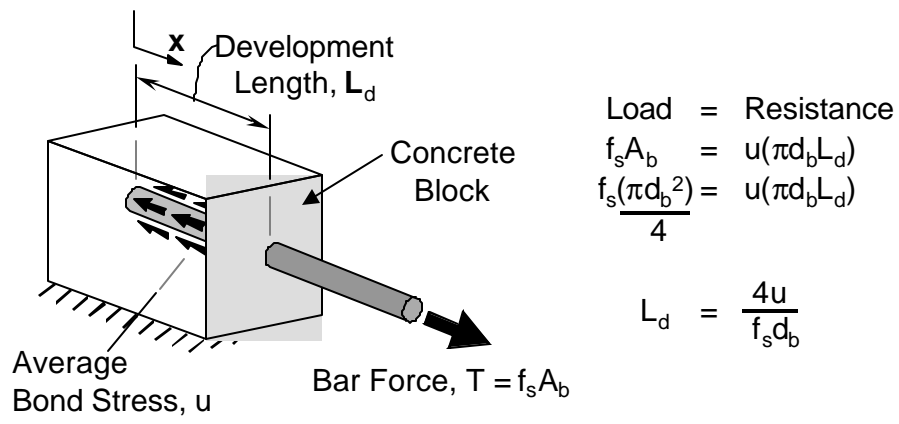


Figure 2-1: Simple concept of bond stresses

Deformed reinforcing bars develop bond stresses by means of transverse ribs that bear directly on the concrete. As tensile forces develop in a reinforcing bar, transverse cracks propagate from the edges of the ribs. This was experimentally shown by Goto [54] and is reproduced in Figure 2-2. The bond stress produced by the bearing of the ribs is not uniform. Mains [74] showed experimentally that local bond stress can be more than twice the average bond stress. Figure 2-2 also shows the distribution of tensile and bond stresses for the bar shown. Bond stress peaks near cracks and tapers off as the concrete carries more of the tensile load. The bond stress then reverses sign as another crack is approached. The process by which concrete around reinforcing bars shares tensile loads is called “tension stiffening.” It is important to note that a bar does not uniformly yield in cracked concrete when it is properly bonded. Yielding occurs only locally near cracks.

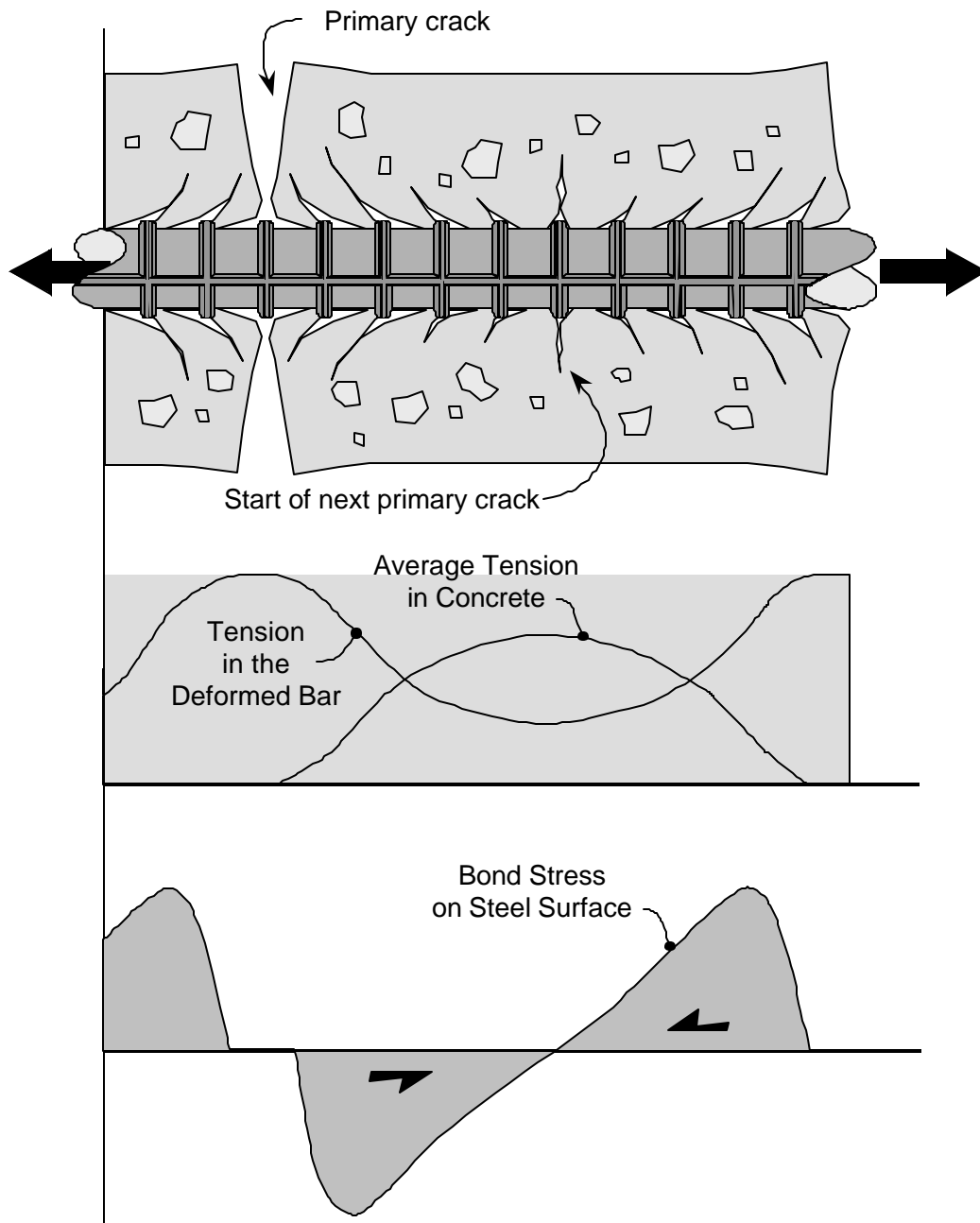


Figure 2-2: Transverse cracking at deformations

The transverse cracking shown in Figure 2-2 causes the bearing stresses on the ribs to act along a direction parallel to the transverse crack angle and not parallel with the axis of the bar. Figure 2-3, part i shows bearing stresses acting at an angle, θ_{bond} , relative to the bar axis. These bearing forces can be split into parallel and perpendicular components (Figure 2-3, part ii). The components parallel to the bar constitute the bond responsible for resisting the tensile force in the reinforcement. The components perpendicular to the bar act outward from the bar surface as splitting stresses on the concrete. These radial splitting stresses must be counteracted by ring tension stresses in the concrete surrounding the reinforcing bar, section A-A of Figure 2-3, part iii. Ultimately, the radial splitting stresses exceed the tensile capacity of the surrounding concrete and splitting cracks begin to propagate from the bar surface.

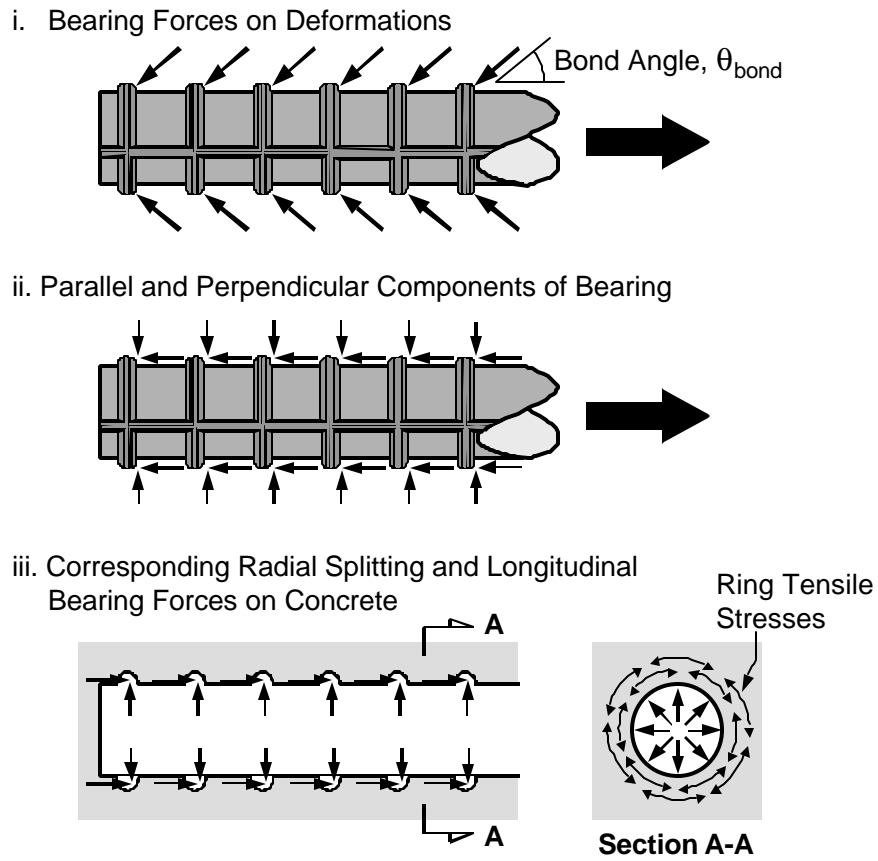


Figure 2-3: Bond and splitting components of rib bearing stresses

Bond can fail in multiple ways. The longitudinal bond stresses can exceed the shear strength of the concrete keys between ribs and the bar can pull free. This is referred to as a “pullout” failure (It is also sometimes termed a “shear-out” failure, but this report will use the more common term of pullout.). More commonly though, splitting cracks will propagate from the bar to the surface of the concrete and the cover will spall off. Figure 2-4 shows some of the many splitting cracks that can occur. The type of splitting failure that occurs in unconfined concrete is governed by bar spacing and cover dimensions. Limitless cover does not provide limitless bond. Beyond a certain level of splitting resistance, pullout failure will govern. Typically though,

splitting resistance governs the level of bond stress that concrete can sustain. The rest of the discussion in this section will deal with bond and splitting.

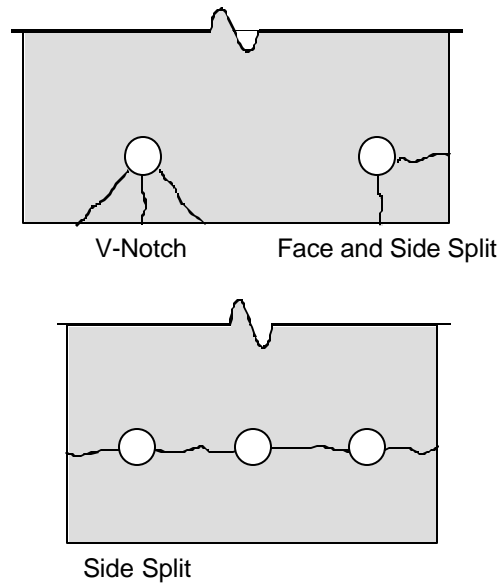
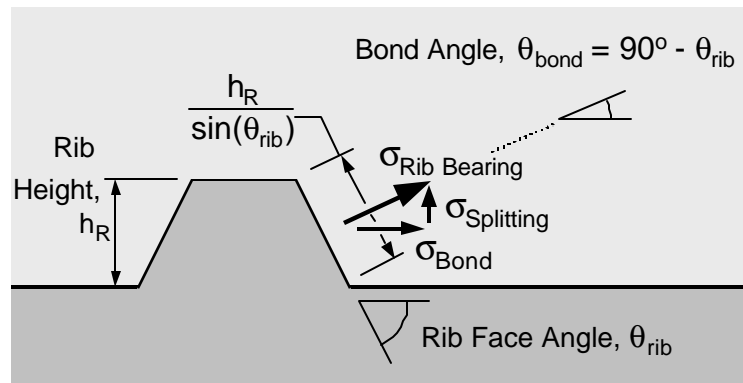


Figure 2-4: Possible splitting crack failures

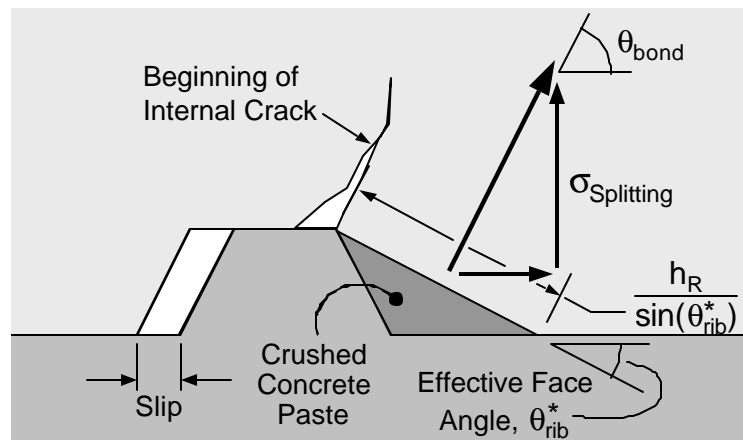
As a rib begins to bear on the concrete a wedge of crushed paste is formed in front of the rib. This wedge acts to change the effective face angle of the rib (Figure 2-5). Thus, the bond angle, θ_{bond} , tends to change as a reinforcing bar acquires load. The effect of this is that radial splitting stresses tend to increase at a rate greater than the longitudinal bond stresses as tensile load in the reinforcing bar rises. Furthermore, efforts to reduce splitting stresses in reinforcing bar by fabricating a steep rib angle into the bars tend to be unsuccessful because the formation of the concrete wedges neutralizes the effect of the different rib angles. Lutz [72] performed experimental studies of single rib specimens. He observed that at failure the angle of the concrete

wedge was between 30° and 45° and that ribs with face angles less than 30° showed poor bond-slip performance in tests.

While rib face angle does not significantly affect bond strength within certain limits, rib bearing area has been shown to be important. Rib bearing area can be increased by manipulating one or both of two geometric parameters: the height of the ribs or the spacing of the ribs. Rib bearing area is generally referred to by the ratio of rib bearing area to shearing area of the concrete keys between successive ribs. This ratio is referred to as the relative rib area, R_r . The effect of the relative rib area has been studied since the earliest research on bond. Abrams [17] was the first to recognize that bond was enhanced by increases in relative rib area. Later studies by Clark [36, 37] supported Abrams' conclusions. Clark's studies were used to establish the modern ASTM standards for deformation requirements on reinforcing bars [3]. Both Abrams and Clark recommended deformation criteria that translate to relative rib areas around 0.2 for optimum bond performance. However, the current ASTM requirements only provide for relative rib areas less than 0.1 for reinforcing bars. Most recently, studies by Darwin et al. [40, 41] and Hamad [55] have led to a reconsideration of the issue of rib geometry and bond performance. Darwin and Hamad have also recommended a relative rib area of 0.2 for optimal bond performance of reinforcing bars with the limitation that ribs not be spaced too closely.



i. Initial Bearing of Rib on Concrete



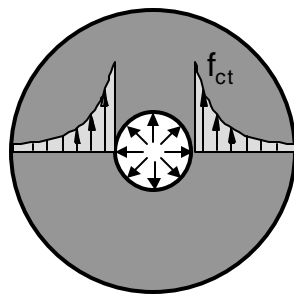
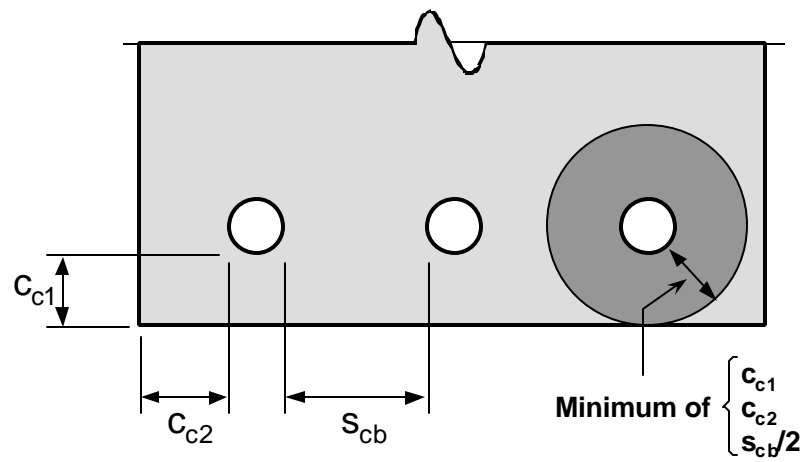
ii. Final Bearing of Rib on Concrete

Figure 2-5: Mechanics of rib bearing on concrete

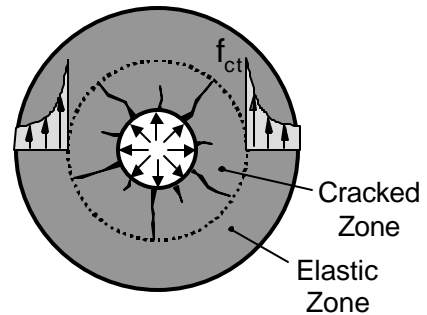
Based on the experimental evidence on the mechanics of rib bearing, several models have been developed to calculate bond as a function of ring-tension stresses in the surrounding concrete. All of the models are based on various stress-strain relationships for concrete tensile strength. Figure 2-6 illustrates the basic models. The elastic-uncracked model assumes that once the tensile strength of the concrete is reached and splitting cracks begin, bond failure is imminent. In this case, the bond capacity is limited by purely elastic material behavior. The elastic-cracked

model achieves a slightly greater bond capacity by allowing a cracked zone around the reinforcing bar with elastic behavior outside of that zone. No tensile stress is allowed within the cracked zone. The elastic-cracked model has a higher capacity than the purely elastic model by allowing the region of maximum tensile stress to move away from the bar surface to a distance where the stresses act over a larger circumference. The elastic-cohesive model allows for tensile stresses within the cracked zone based on cohesive material theory that derives from concrete fracture mechanics. The plastic model allows for a perfectly plastic distribution of tensile stress and gives the highest capacity. The first, second and fourth models were first analyzed by Tepfers [110]. The third model was developed by Rosati and Schumm [53, 103].

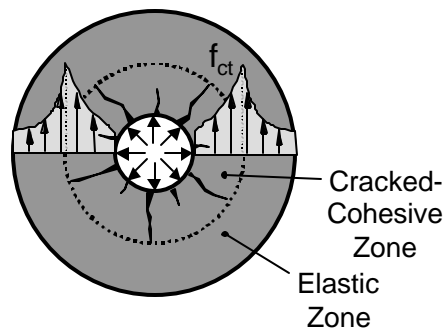
The elastic-cohesive model of concrete tensile behavior was derived to adapt principles of fracture mechanics to analysis of concrete materials [12]. Ordinary linear elastic fracture mechanics does not properly describe concrete cracking. In order to apply fracture mechanics theory, a zone of material softening is included in the crack model. This zone is called the “fracture process zone” (Figure 2-7). Within the fracture process zone, micro-cracked concrete carries some tensile resistance. At the tail of this zone, the “true crack” grows by spreading from micro-crack to micro-crack. At the head of the zone, micro-cracks begin to form as strains in the concrete exceed a certain tensile limit. The truly cracked concrete does not carry any tensile resistance. The elastic-cohesive model of bond stress thus assumes that the cracked-cohesive zone around the reinforcing bar is still within the process of crack development and has exceeded the threshold of elastic behavior where optimal tensile resistance occurs.



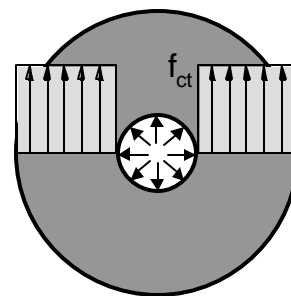
(i) Elastic-Uncracked Model



(ii) Elastic-Cracked Model



(iii) Elastic-Cohesive Model



(iv) Plastic Model

Figure 2-6: Models for ring-tension behavior

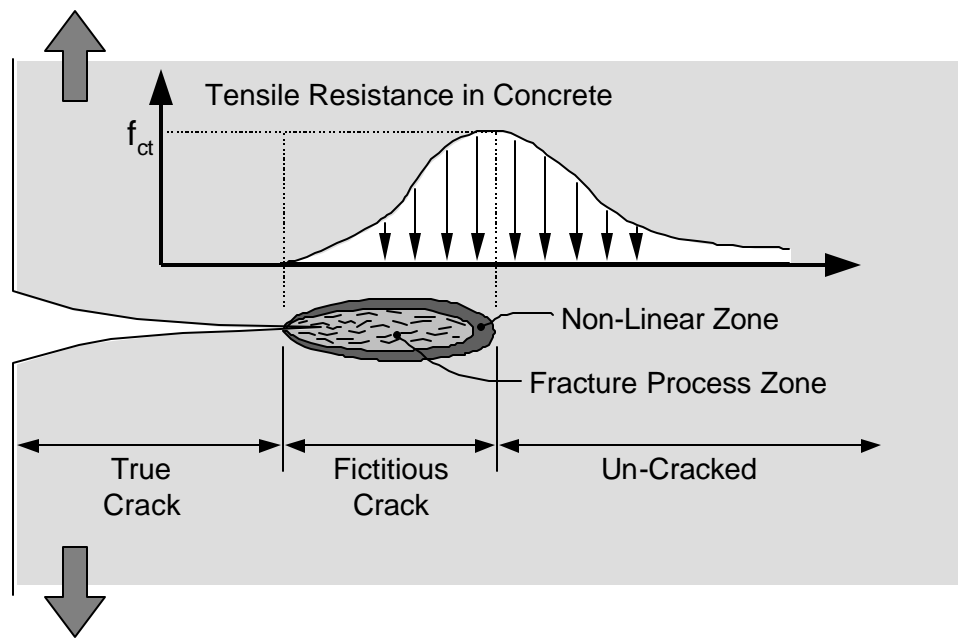


Figure 2-7: Cohesive crack growth (after Bažant [12])

Tepfers compared his models of bond resistance to experimental results from pullout tests and beam tests of lapped specimens [110]. Rosati and Schumm later added their model to Tepfer's analysis [53]. Figure 2-8 shows the predictions of the four different models on a plot of bond capacity versus cover dimension (the parameters are normalized with respect to bar diameter and concrete tensile strength, f_{ct}). Tepfer's experimental data are included in the plot. There is much scatter in the experimental data, but it is obvious that the elastic-cracked model forms a good lower bound and the plastic model a good upper bound for ultimate bond capacity governed by splitting. Only, the elastic-cohesive model cuts through the data. As a description of behavior it is probably the best, but there is too much scatter in the actual data for any model to accurately predict capacity.

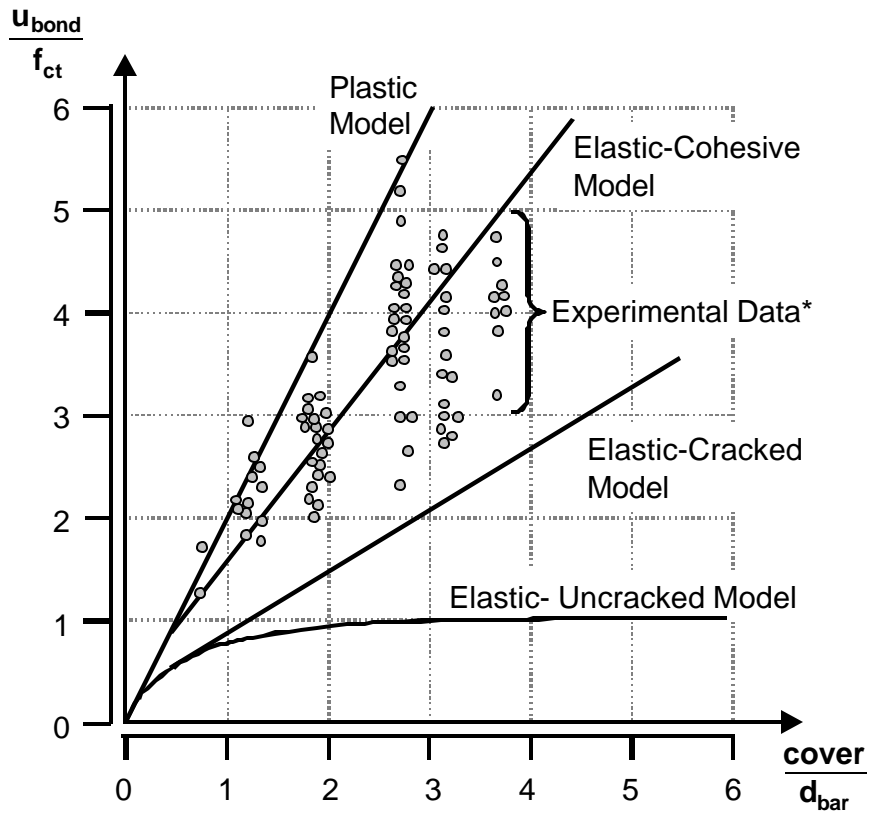


Figure 2-8: Comparison of various bond model predictions with experimental data (after Tepfers [110] and Gambarova [53])
 *Data credited to Tepfers

2.2.2 Lap Splices

When bars are lap spliced, they are typically laid adjacent to one another. The interaction of ring-tension stresses around the bars creates an oval shaped tensile zone, but otherwise, the bond developed by the bars is comparable to that of single bars in tension. Figure 2-9 shows the zone of ring tension stresses and the common splitting crack patterns.

Older research by Chamberlin [33] and Chinn, Ferguson, and Thompson [35] demonstrated that there is no significant change in bond strength for increasing clear space

between spliced bars. Their studies showed that adjacent deformed bars which are tied together can achieve greater than normal bond strengths due to interlocking of the ribs on each bar. More recent research by Hamad and Mansour [56] showed an optimal lap spacing of $5d_b$ where a 7 - 10% increase in bond strength over contact splices was observed. Beyond $5d_b$ the bond strength dropped off below the contact splice bond strength. Their tests were for lap lengths of 17 to $20d_b$. Altogether, the research suggests that lapped bar data can be compared to non-lapped bar data for analysis of anchorage and bond.

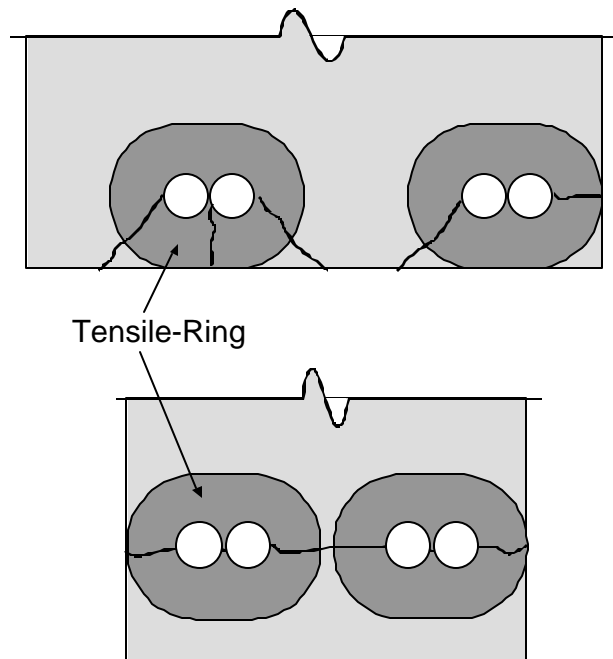


Figure 2-9: Splitting around lapped bars

2.2.3 Confinement of Splitting Stresses

The splitting strength of concrete can be enhanced if compressive stresses are superimposed onto the tensile-ring stresses around the reinforcing bar. The concrete is said to be

“confined” when compressive forces are used to counteract internal splitting forces. Confinement can be classified as two types: active and passive. Active confinement will refer to stress fields that are created by the actions of superimposed structural loads such as dead and live loads and prestress forces. Passive confinement will refer to stress fields that are created by forces in the mild reinforcement placed around anchorage zones such as stirrups or spiral rings.

Figure 2-10 shows the state of stress that occurs at a beam end where the longitudinal reinforcement terminates. This is an example of active confinement. Over the bearing pad a vertical compression field is created by the balance of the bearing reaction and the beam shear. This vertical compression field is superimposed onto the ring-tension field caused by bond of the reinforcing bars. The vertical components of the ring tension field are partially counteracted. As a result, the beam end has an enhanced resistance to horizontal splitting cracks and the anchorage of the longitudinal reinforcing bars is improved.

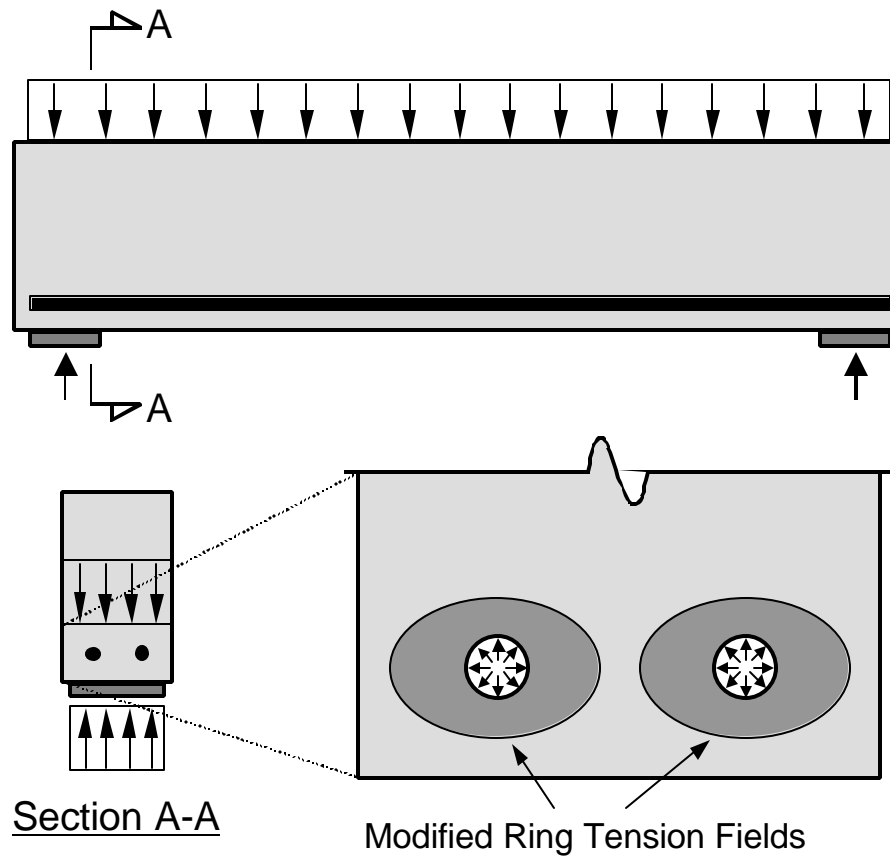


Figure 2-10: Active confinement in a beam end bearing

Spirals, transverse ties, and stirrups in anchorage zones are examples of passive confinement. These systems are distinguished from active confinement because they are dependent on crack propagation to become effective. Such confinement systems do not begin to counteract splitting forces until radial cracks emanating from the bar surface cross the axis of the confining steel (Figure 2-11). Because confining steel does not play any part in resisting tensile splitting stresses until the splitting cracks intersect the steel, they are termed a passive system.

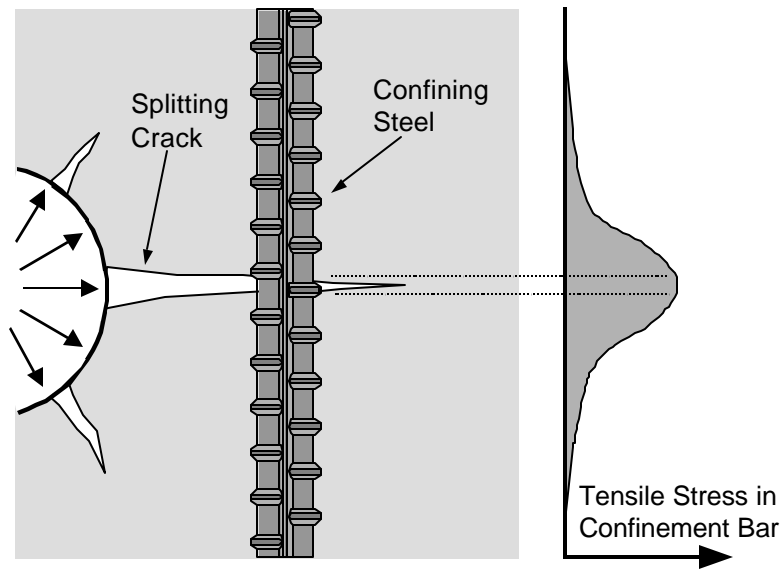


Figure 2-11: Confinement steel in the vicinity of a splitting crack

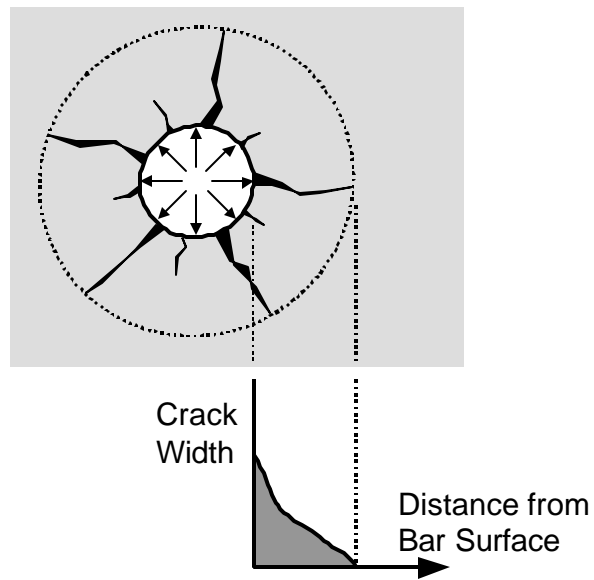


Figure 2-12: Crack widths of splitting cracks

Many experimental studies have been performed on passive confinement. The results of those studies have been incorporated into the development length modification factors found in the ACI 318 code [2], the AASHTO Bridge Design Specifications [1], and in many other structural concrete design codes found around the world. In general, mild reinforcement, placed so that it intersects splitting crack planes, helps to improve bond capacity if splitting failure modes control. Beyond a certain level, pullout failure modes begin to determine the bond capacity and additional confining steel fails to improve bond capacity.

Three references have been found regarding the effects of active confinement on bond:

Untrauer and Henry [112] studied the effects of lateral pressure on 6" sided cube pullout specimens with #6 and #9 bar sizes. Their lateral pressures ranged from 0 % to 50 % of f'_c , or 0 psi to around 2500 psi. They found that there was a slight increase in bond strength related to the square root of the lateral pressure. They also concluded that the effect of the lateral pressure was more pronounced for smaller embedment lengths.

Lormanometee [70] studied specimens modeled after the Untrauer and Henry tests but with the addition of studying the effect of the proximity of the lateral load application. Lormanometee found slightly higher bond capacities than Untrauer and Henry had with less dependence on the magnitude of the lateral pressure. This may have been due to the method of load application or differences in the deformation pattern of the reinforcing bars or the mix parameters of the concrete. Lormanometee determined that the lateral pressure was more effective when applied close to the surface of the reinforcing bar and diminished with increasing concrete cover between the bar and the applied lateral load.

Thrö [111] performed pullout tests with similar lateral pressures, but with bars anchored over much shorter development lengths ($\sim 3d_b$). Thrö maintained a constant ratio between the

lateral pressure and the steel stress as the test was being performed. He found increases in bond stress for increasing lateral pressures. He recommended a reduction factor for development length that is linearly proportional to the active lateral pressure with a cutoff at 1,160 psi. The reduction factor reduces the development length by half at that value. Thrö's results showed a much greater impact on bond from lateral compression than the previous tests, but it should be noted that his specimens used a short bar embedment length which may not be translatable to longer development lengths.

The effect of lateral active confinement is an important issue for the anchorage performance of deformed bars in nodal zones which is discussed in Chapter 4. So far, the research has been limited and the results inconsistent. Furthermore, the effects of platen restraint (additional restraint provided by load plates which provides biaxial lateral compression – see Figure 2-13) have not always been clearly separated from the effects of lateral compression in the available studies. Thus, the topic remains a gray area in the knowledge of bond and development of reinforcement. However, in practice, when lateral confinement forces are provided by design loads, no enhancement to bond should be taken into account due to the unpredictability of actual loading conditions.

- i. No Platen Restraint
(uniaxial lateral compression where transverse deformation is unrestrained)
- ii. Platen Restraint
(rigid load plates prevent transverse deformation and cause biaxial lateral compression near the plates)

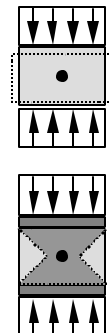


Figure 2-13: Platen restraint in lateral compression studies

2.2.4 Effect of Concrete Properties

The splitting failure mode of bond is dependent on the tensile strength of concrete. Thus, the mechanical properties of concrete are important for good deformed bar development. Two other concrete related parameters can also have significant affects on bond capacity: lightweight concrete and top cast bars.

Lightweight concretes are produced by using special porous lightweight aggregates or by aerating the cement paste. In both cases, the pore spaces introduced into the hardened mix make lightweight concretes weaker in tension and shear than normal weight concretes with equivalent compression strengths. Because of their weaker tensile properties, lightweight concretes generally give lower bond capacities than normal concretes. In some cases, the shear strengths are low enough that deformed bars will pullout rather than split the concrete in pullout tests. Because of their weaker bond capacities, lightweight concretes are penalized in design code development length equations. Generally a factor of 1.3 is applied to the development length when lightweight concrete is used (this equates to a 23% reduction in predicted bond capacity).

When concrete is placed and vibrated, lighter components of the mix will rise as heavier components settle to the bottom. When this occurs near reinforcing bars, air pockets and bleed water tend to collect on the undersides of the bars in place of coarse aggregates (Figure 2-14). When the concrete sets, the bond around the bar is weaker on its underside because of the inferior quality of the concrete there. This effect is more pronounced for bars that have greater quantities of concrete placed under them than bars that are positioned close to the bottom surface of forms. Design code equations for development length distinguish this effect by requiring a “top-cast bar” factor for reinforcement with more than 12” of concrete placed beneath them. No top-cast bars were included in this research project, but the understanding that bond on the underside of

deformed bars is weaker than bond on the top of deformed bars helped to determine the placement of strain gages when reinforcing bars were instrumented in this project.

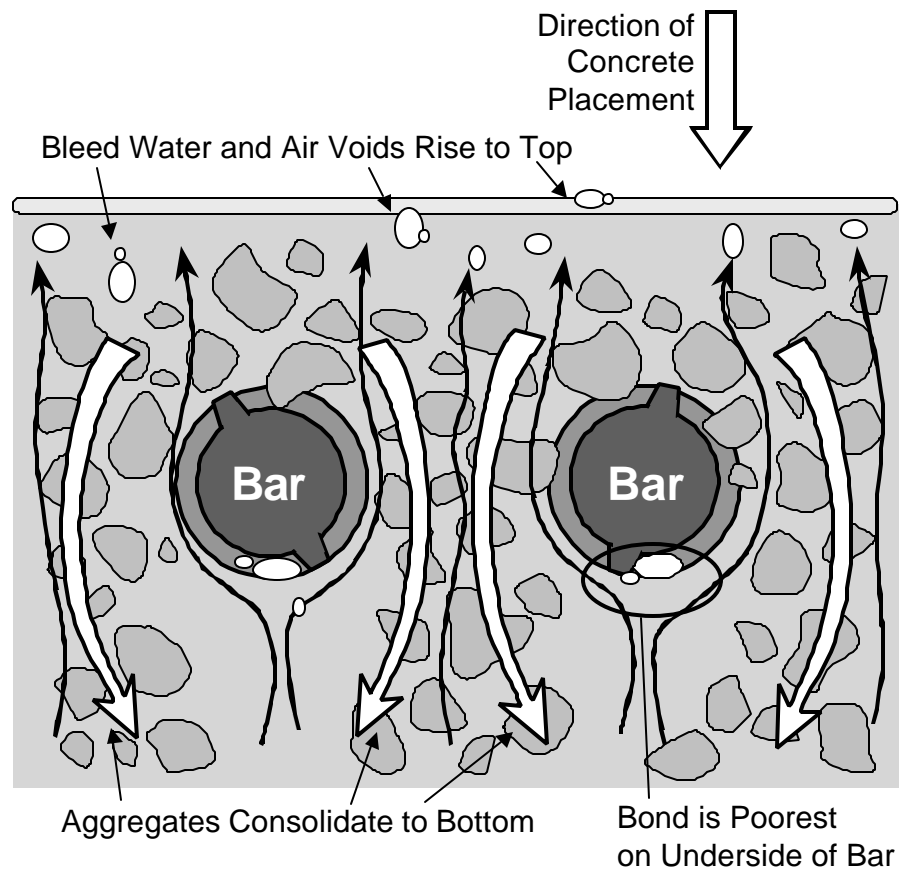


Figure 2-14: Top cast bar effect

2.2.5 Epoxy-Coated Reinforcement

Epoxy-coatings are placed on reinforcing bars to provide corrosion protection. However, the presence of the epoxy coating inhibits the ability of the reinforcing bar deformations to bear on the concrete by acting as a friction reducer and by partially concealing the height of the

deformations. Epoxy-coated bars have substantially reduced bond from uncoated bars. Research on high relative rib area reinforcing bars (Darwin et al. [40] and Hamad [55]) has shown that the loss of bond from epoxy-coating is less when rib deformations are large indicating that epoxy-coating has a lessened effect when anchorage relies more on direct bearing. However, in practice high relative rib area reinforcing bars are typically harder to coat than normal reinforcing bars.

2.2.6 Measurement of Bond Stress

Theoretical understanding of bond provides a framework for design methodologies, but data are needed to calibrate theoretical derivations into design equations. Such data can only be obtained through experimental studies. Because the experimental data for bond stress has been critical for the empirical calibration of design equations, it is important to understand the ways in which bond has been traditionally measured. Several different types of experimental tests have been reviewed in the literature on bond. Five categories of bond specimens have been categorized from the literature: single bar pullout specimens, beam specimens, beam-end specimens, lap splice tensile specimens and lap splice beam specimens. Though several experimental studies may be said to use the same category of specimen, the particular details of specimens used in different studies may vary. There is little standardization of the different types of bond specimens and the categories discussed herein are broad generalizations based on certain similarities of mechanics.

Figure 2-15 presents the classic pullout specimen. A single bar is cast into a block or cylinder of concrete. Confining reinforcement may or may not be placed around the embedded bar. Failure generally occurs by splitting to the closest cover surface unless confinement is very heavy in which case a pullout failure can be forced. These specimens were used extensively by Abrams for his acclaimed study of bond though he also used beam specimens [17]. Bar force can be measured directly as well as slip at the loaded and free ends of the bar. Pullout specimens have

the disadvantage that the load ram bears directly on the concrete surface and provides lateral restraint near the loaded end of the bar. Such compression is not always present when bars are developed in practice and the results of pullout tests can tend to over-estimate bond stresses.

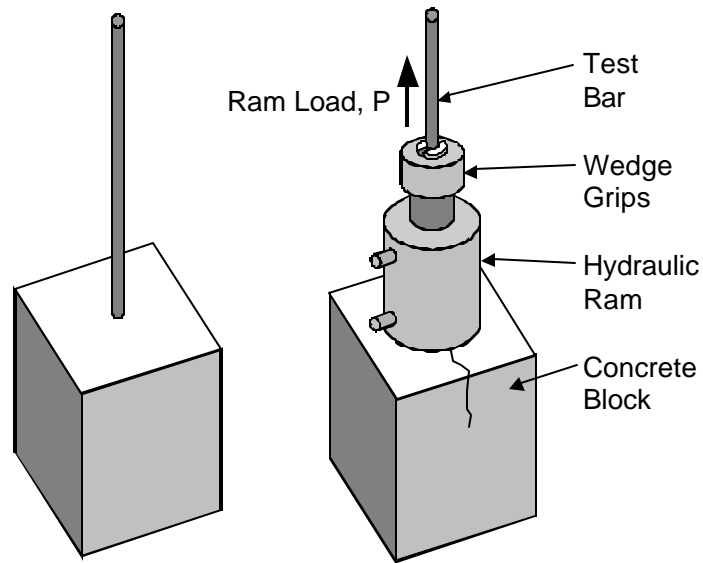


Figure 2-15: Typical pullout specimen

Beam specimens are more accurate representations of bar anchorage than pullout specimens. The test bars are cast into a concrete beam that is then loaded in flexure. The termination point of the bars is placed away from load points where local compression can enhance the bond and restrain splitting cracks. Figure 2-16 shows a typical specimen. Because the bars are placed in flexure as well as tension, prying forces in the bars tend to exacerbate bond failure. The direction and placement of reaction loads in beam specimen can be manipulated to create constant moment or moment with shear along the bar development length. Beam specimens are more realistic than pullout specimens, but are much more costly in material, space, and labor to fabricate and test. It is also harder to determine the bar forces in beam tests. Bar forces must be

calculated from beam moments or from strain gage readings. Thus test data from beams are much less common than from other forms of bond tests.

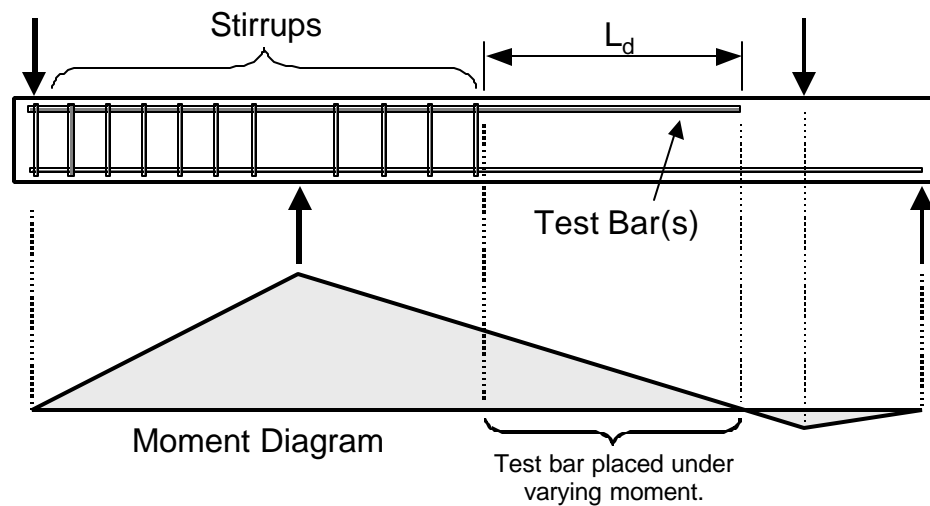


Figure 2-16: Typical beam specimen for bond tests

A compromise specimen somewhat between a pullout test and a beam test is the stub-beam or beam-end specimen. Figure 217 shows a typical beam-end specimen. Only the end region of the beam is fabricated for such a test. Less material is necessary than for a full beam test and the exposure of the bar for loading makes determination of the bar force simple. Direct compression of the concrete near the loaded end of the bar is avoided by separating the load ram from the surface of the specimen. The free end of the bar is either terminated outside of the rear reaction point or debonded over its length in that zone. Access to the bar's free and loaded ends is available for slip measurements. The test bar is placed in direct tension, which may or may not be representative of actual bond situations. The beam-end specimen was recently standardized in ASTM Specification A944-99 "Standard Test Method for Comparing Bond Strength of Steel

Reinforcing Bars to Concrete Using Beam-End Specimens [4] and is the only standardized bond specimen at this time. The main disadvantage of the beam-end test is the complex load arrangement required to test the specimen.

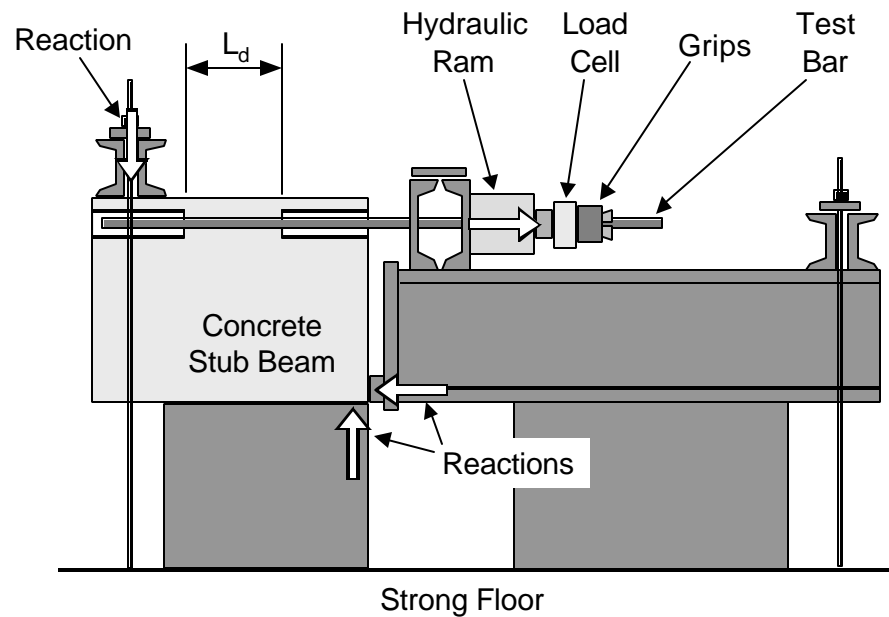


Figure 2-17: Typical beam-end test

The remaining two categories of bond tests utilize lap splices. Tensile lap splice specimens resemble the basic pullout test, but no direct compression of the concrete is caused by the loading of the specimen. Figure 2-18 shows some typical specimens. The test is essentially a modified form of the pullout specimen. The last type of bond test, the lap splice beam test is shown in Figure 2-19. The lap zone can be placed in constant moment or a varying moment zone with shear depending on the arrangement of external loads.

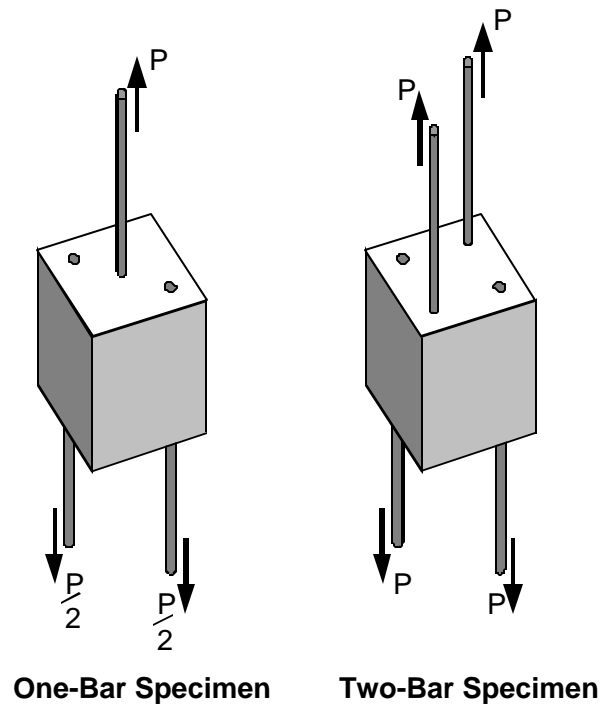


Figure 2-18: Typical tensile lap splice specimens

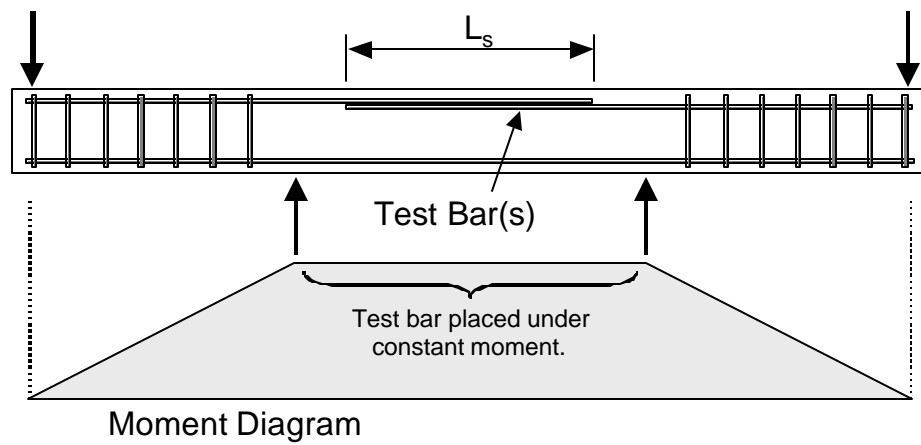


Figure 2-19: Typical beam specimen for lap tests

2.3 CODE PROVISIONS FOR DEFORMED BARS

2.3.1 Quality of Reinforcing Bars: ASTM A615

Quality of deformed reinforcing bars is controlled by ASTM A615 “*Standard Specification for Deformed and Plain Billet-Steel Bars for Concrete Reinforcement*” [3]. This document contains standards for chemical composition, deformation geometry, tensile strength, bending strength, and weight of deformed reinforcing bars. With respect to deformation geometry, four parameters are controlled: rib spacing, included rib angle (not to be confused with the rib face angle), rib height, and the gap caused in the transverse ribs by the main (longitudinal) rib of the bar. Figure 2-20 graphically presents these parameters.

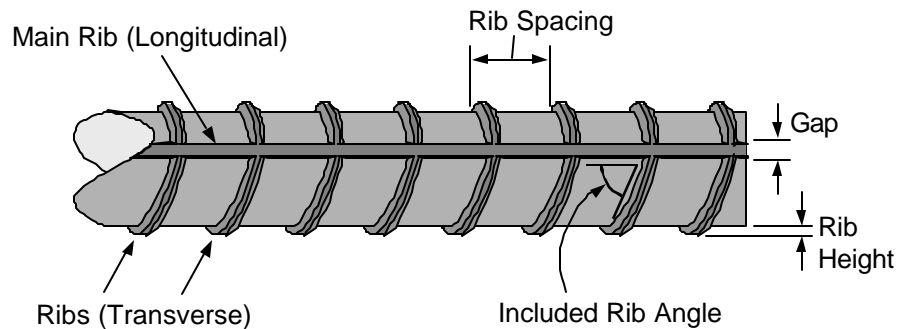


Figure 2-20: Important dimensions for reinforcing bar specifications

The spacing of ribs shall not exceed 0.7 bar diameters and shall be uniform along the bar length. The included rib angle relative to the axis of the bar shall not be less than 45° . No gap shall be more than 12.5% of the perimeter of the rib and the sum of all gaps within the path of a rib shall not total more than 25% of the perimeter of the rib. The average minimum height of the ribs is required to be between 0.04 - 0.05 bar diameters. Specific values for each bar size are tabulated in the ASTM specification. The ASTM requirements for deformations are listed in Table 2-1.

| Bar Size | Maximum Avg. Spacing (in) | Minimum Avg. Height (in) | Maximum Gap (in) |
|----------|---------------------------|--------------------------|------------------|
| # 3 | 0.262 | 0.015 | 0.143 |
| # 4 | 0.350 | 0.020 | 0.191 |
| # 5 | 0.437 | 0.028 | 0.239 |
| # 6 | 0.525 | 0.038 | 0.286 |
| # 7 | 0.612 | 0.044 | 0.334 |
| # 8 | 0.700 | 0.050 | 0.383 |
| # 9 | 0.790 | 0.056 | 0.431 |
| # 10 | 0.889 | 0.064 | 0.487 |
| # 11 | 0.987 | 0.071 | 0.540 |
| # 14 | 1.185 | 0.085 | 0.648 |
| # 18 | 1.580 | 0.102 | 0.864 |

Table 2-1: ASTM A615 requirements for reinforcing bar deformations

2.3.2 Code Equations for Development Length

Design equations for the anchorage of reinforcing bars do not present results in terms of predicted bond stresses, rather they provide a required development length necessary to achieve the full yield strength of a bar. Two code provisions are discussed in this section: the ACI 318 code and the AASHTO Bridge Design Specifications.

2.3.2.1 ACI 318-02

The ACI 318-02 *Building Code Requirements for Structural Concrete* [2] contains provisions for straight bar development in Section 12.2 “Development of deformed bars and deformed wire in tension.” Two methods for calculating a development length are allowed. A table is provided in sub-section 12.2.2 that contains simplified and conservative equations for development length given certain conditions of cover, spacing, etc. for the bars being anchored.

Sub-section 12.2.3 contains a more accurate and involved equation for development length. This equation (12-1 in the ACI code) is shown below:

$$\frac{L_d}{d_b} = \frac{3}{40} \frac{f_y}{\sqrt{f'_c}} \frac{\alpha\beta\gamma\lambda}{\left(\frac{c + K_{tr}}{d_b}\right)} \quad (2-1)$$

with
$$\frac{c + K_{tr}}{d_b} \leq 2.5$$

and
$$K_{tr} = \frac{A_{tr} f_{yt}}{1500 s n} \quad (2-2)$$

L_d = development length of bar (same units as d_b , typically inches)

d_b = nominal bar diameter (inches)

f_y = yield stress of reinforcing steel being developed (psi)

f'_c = cylinder compressive stress of concrete (psi, limited to 10,000 psi maximum in section 12.1.2)

α = reinforcement location factor (1.3 if 12" of concrete cast below bar)

β = coating factor (1.5 for epoxy-coated bars with minimum clear dimension $\leq 3d_b$, 1.2 for all other epoxy-coated bars)

γ = reinforcement size factor (0.8 for # 6 bars and smaller)

λ = lightweight aggregate factor (1.3 when lightweight aggregates are used)

c = minimum spacing or cover dimension (in, reference Figure 2-6)

K_{tr} = transverse reinforcement index

s = maximum spacing of transverse reinforcement within L_d , center-to-center (in)

- n = number of bars or wires being developed along the plane of splitting
- A_{tr} = total area of transverse reinforcement within the spacing, s , that crosses the plane of splitting through the reinforcement being developed (in²)
- f_{yt} = yield stress of transverse reinforcement (psi)

Development length is limited to a minimum of 12”.

The ACI development length equation is based on work performed by Orangun, Jirsa, and Breen [93, 94]. They evaluated the results of several well-documented studies on lap lengths and development lengths from the United States and Europe and used data from those studies to fit an equation via regression analysis. The choice of terms and positioning of variables within the equation was based on theoretical considerations, but the final selection of constants was based on regression analysis. The equation they developed is not quite the same as the ACI code equation, but is very close. They recommended the factors used in the ACI equation plus an additional factor for widely spaced bars that would shorten the necessary development length. They recommended a ϕ factor of 0.8 for their equation. The ACI equation has a ϕ of 0.9 built into it.

Though Orangun, Jirsa, and Breen reported that they found no difference in the development length required for single bars and lapped bars and many other researchers have noted the same results, the ACI Code, Section 12.15 requires multipliers for lapped bars in most situations. Splices are categorized according to the ratio of steel provided to that required and the amount of steel being spliced at a given location. Table 2-2 summarizes the categories and the required splice lengths, L_s . The multipliers are used as a penalty (by increasing the lap length) to dissuade designers from needlessly or unwisely using lap splices in a structural design and

particularly to prevent the Class B splice situation in which all tensile bearing bars in a section are spliced at a single location.

| $\frac{A_s \text{ provided}}{A_s \text{ required}}$ | Maximum % of A_s Spliced Within the Required Lap Length | |
|---|---|----------------------------------|
| | 50% | 100% |
| ≥ 2 | Class A Splice $L_s = 1.0L_d$ | Class B Splice $L_s = 1.3L_d$ |
| < 2 | Class B Splice $L_s = 1.3L_d$ | Class B Splice $L_s = 1.3L_d$ |

Table 2-2: ACI 318-02 multipliers for development length of lap splices

2.3.2.2 AASHTO LRFD Bridge Design Specifications (2nd Ed., 1998)

The AASHTO LRFD *Bridge Design Specifications* [1] contain equations for reinforcing bar development length in Section 5.11.2 “Development of Reinforcement.” Three equations for development length are provided in sub-section 5.11.2.1.1 and multipliers for these equations are provided in the subsequent sub-sections 5.11.2.1.2 and 5.11.2.1.3. One development length equation is for # 11 bars and smaller, one for # 14 bars, and one for # 18 bars. The first of these equations (for # 11’s and smaller) is presented below:

$$L_d = \frac{1.25 A_b f_y}{\sqrt{f'_c}} \geq 0.4 d_b f_y \quad (2-3)$$

L_d = development length (inches)

A_b = area of bar or wire (in²)

f_y = yield stress of bar being developed (ksi)

f'_c = compressive strength of concrete (ksi)

d_b = diameter of bar being developed (inches)

Note that the units of stress used in the equation are in ksi rather than psi as in the ACI equation.

Modification factors are provided for many of the same conditions as the ACI equation. The factors are listed below:

- Top cast concrete (12" of concrete below bar): 1.4
- Clear dimension (cover or ½ spacing) $\leq d_b$: 2.0
- Lightweight aggregates used: 1.3
- Sand lightweight concrete used: 1.2
- Epoxy-coated bars with clear dimension $\leq 3d_b$: 1.5
- All other epoxy-coated bars: 1.2
- Clear cover ≥ 3 " and center-to-center bar spacing ≥ 6 " : 0.8
- Reinforcement confined within a # 2 or greater
bar size spiral with pitch ≤ 4 " : 0.75

AASHTO limits development length to a minimum of 12".

The AASHTO equation is based on the ACI 318-71 development length equation. That equation was in turn based on ultimate bond stresses specified in ACI 318-63. The derivation of the equation is as follows:

Ultimate bond stress:
$$u_{\text{bond}} = \frac{9.5\sqrt{f'_c}}{d_b} \leq 800 \text{ psi} \quad (2-4)$$

The value of f'_c used in equation (2-4) is in psi. Subsequent variables with units of stress will be in psi until a conversion is specified to ksi. The bar force at 125% of yield (a safety factor to insure ductile development of the bar) is equated to the resultant of bond resistance:

Resultant of Bond Stresses = Tensile Force in Bar

$$L_d \pi d_b u_{\text{bond}} = A_b (1.25 \cdot f_y) \quad (2-5)$$

Equation (2-5) is rearranged to solve for L_d and equation (2-4) for the ultimate bond stress is substituted for u_{bond} :

$$L_d = \frac{A_b (1.25 \cdot f_y)}{\pi d_b u_{\text{bond}}} \quad (2-6)$$

$$L_d = \frac{A_b (1.25 \cdot f_y)}{\pi d_b \left(\frac{9.5 \sqrt{f'_c}}{d_b} \right)} \quad (2-7)$$

$$L_d \cong \frac{0.04 \cdot A_b f_y}{\sqrt{f'_c}} \quad (2-8)$$

Equation (2-8) is made to look like the AASHTO equation (2-3) with a unit conversion from psi to ksi:

$$\frac{0.04 \cdot A_b f_y [\text{psi}]}{\sqrt{f'_c} [\text{psi}]} \cdot \left(\frac{1000}{\sqrt{1000}} \right) \cong \frac{1.25 \cdot A_b f_y [\text{ksi}]}{\sqrt{f'_c} [\text{ksi}]} \quad (2-9)$$

The development of the original equation for bond stress (Equation 2-4) is undocumented. It is believed to have been developed by ACI Committee 408 based on the test data available in the early 1960's, but no published report has been identified that provides an explanation for its development. The majority of the test data available at that time would have been from pullout tests, which tend to over-estimate bond stress. No ϕ factor is included in the AASHTO equation because flexural equations used to determine the area of steel required already include a $\phi = 0.9$. Additionally, the equation is already based on a steel stress that is 125% of the

specified steel yield stress. The 1.25 factor that first appears in equation (2-5) can be considered equivalent to a built-in ϕ of 0.8.

The AASHTO LRFD Specifications also require additional development length multipliers when bars are spliced. The multipliers are given in Section 5.11.5.3. Like ACI, AASHTO categorizes splices into classes based on the amount of reinforcement being spliced and the ratio of steel area provided to that required, however, they have more classes of splices and more stringent requirements for some splice categories. Table 2-3 summarizes the splice multipliers.

| $\frac{A_s \text{ provided}}{A_s \text{ required}}$ | Maximum % of A_s Spliced Within the Required Lap Length | | |
|---|--|----------------------------------|----------------------------------|
| | 50% | 75% | 100% |
| ≥ 2 | Class A Splice $L_s = 1.0L_d$ | Class A Splice $L_s = 1.0L_d$ | Class B Splice $L_s = 1.3L_d$ |
| < 2 | Class B Splice $L_s = 1.3L_d$ | Class C Splice $L_s = 1.7L_d$ | Class C Splice $L_s = 1.7L_d$ |

Table 2-3: AASHTO LRFD multipliers for development length of lap splices

Both the ACI and AASHTO code equations for development length are based on deformed bars conforming to ASTM A615. Darwin et al. [41] studied bars with deformations exceeding the minimal requirements of ASTM A615, and recommended development length equations for bars with high relative rib area.

2.4 STANDARD HOOKS

When anchorage by bond requires too long a straight bar development, a viable option is the use of a hooked bar. Hooked bars achieve their anchorage by a combination of bond and direct bearing of the hook on concrete.

Both ACI and AASHTO provide standard dimensions for hooks with 90° and 180° bends. These standard dimensions are the same for both codes. Throughout this report a hook which fits the dimensions specified in those codes will simply be called a “standard hook.” The ACI 318-95 code contains information for detailing and designing standard hooks in Section 12.5. The AASHTO LRFD Specifications deal with standard hooks in Section 5.11.2.4. Figure 2-21 shows the dimensions of the two standard hooks. The bend radius dimensions are based on safe flexural strains that can be imposed on reinforcement without fracture of the steel.

Both the ACI and AASHTO codes provide a development length equation applicable for the 90° or 180° hooks. The equation is the same in both codes but appears in different forms because the units used for stress are different in each code specification. The form of the equation presented below uses units of ksi for the concrete and steel stresses.

$$L_{hb} = \frac{38 \cdot d_b f_y}{60 \cdot \sqrt{f'_c}} \quad (2-10)$$

L_{hb} = basic development length of hooked bar (inches)

The development length of the hook, L_{dh} , is determined by the product of the basic hooked bar development length, L_{hb} , and any applicable multipliers listed below:

- Side cover $\geq 2.5''$ and cover over 90° hook extension $\geq 2.0''$: 0.7

- Hook enclosed within stirrups or ties all along L_{dh} at spacing $\leq 3d_b$: 0.8
- Lightweight aggregate factor: 1.3
- Epoxy-coated bar factor: 1.2

There is no factor for top-cast bars because hooks develop most of their anchorage by direct bearing, and not by bond along the surface area of the bar. Hooked bars can be developed over significantly shorter lengths than straight bars, particularly at low concrete strengths. Figure 2-22 demonstrates this by plotting the code development lengths for hooked and straight bars as a function of concrete compressive strength. Lap splice lengths are also included. The plots are for #8 bars with the maximum benefits from confinement and cover multipliers.

The mechanism of stress transfer in hooked bars is shown in Figure 2-23. The concrete in front of the hook, where it just begins to bend away from the straight portion of bar, is typically crushed at full development of the bar. 90° hooks tend to be pulled straight around the bend of the bar as load is applied. Thus it is important that the hook extension be well confined on 90° bends or the extension may cause spalling of concrete cover behind the hook. 180° bends tend to pull forward as a unit without slipping around the bend of the hook. Hooked bars tend to fail by side spalling of concrete cover (Figure 2-24).

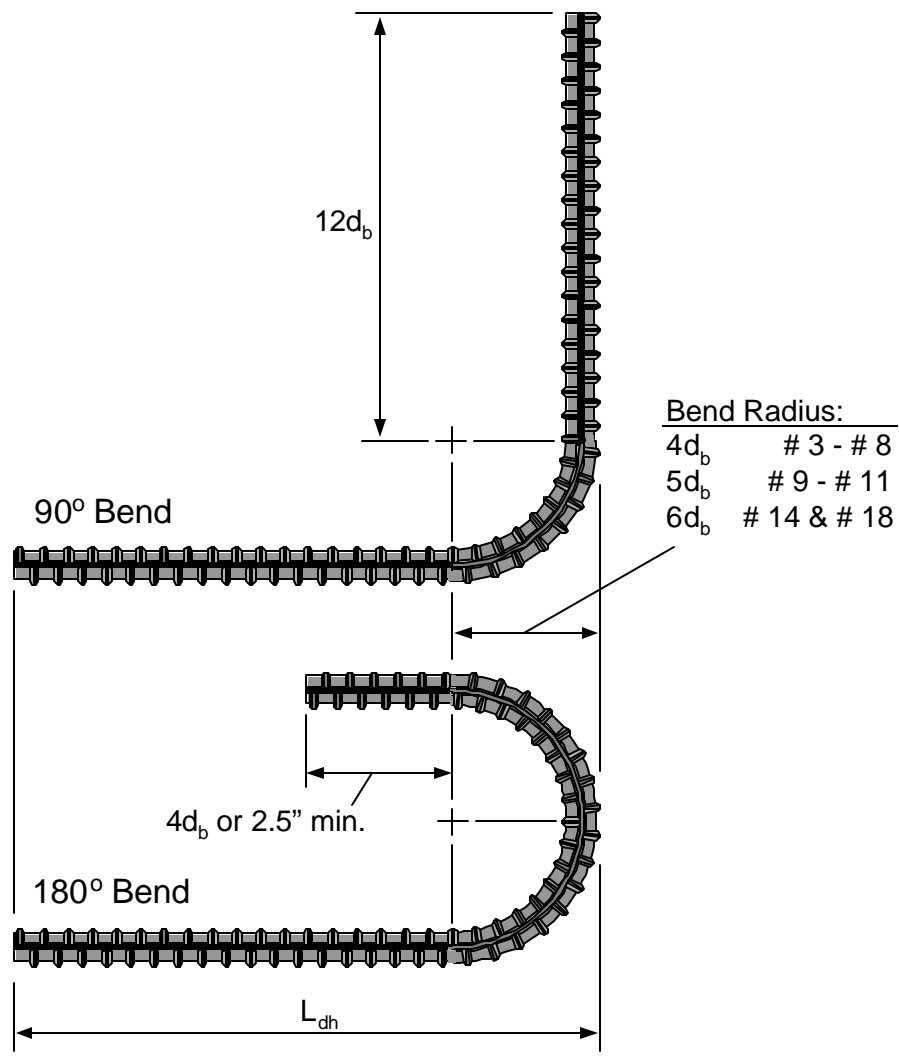


Figure 2-21: Standard hook dimensions

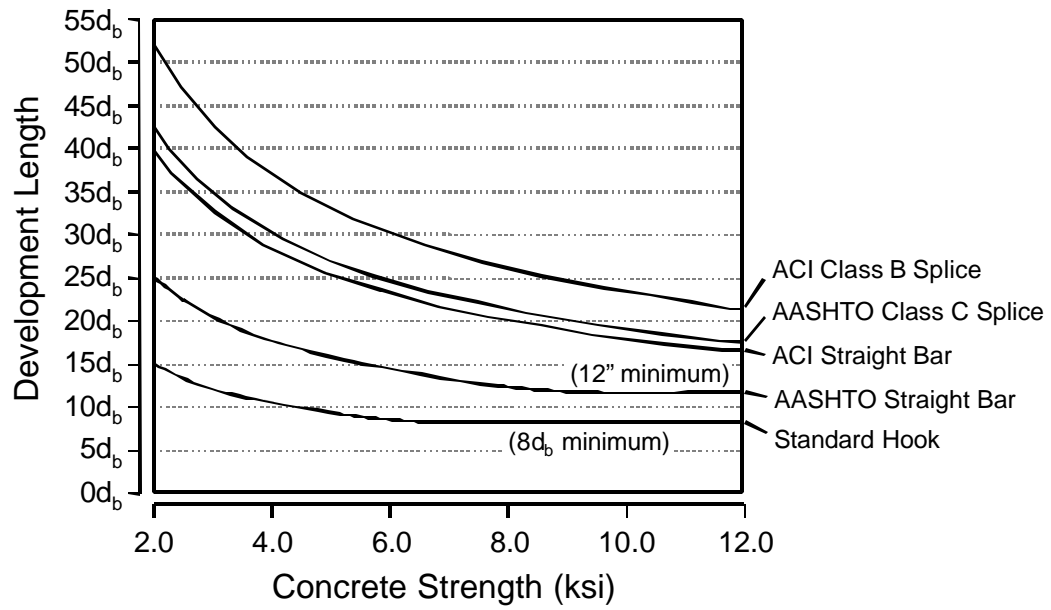


Figure 2-22: Development lengths of standard hooks and straight bars

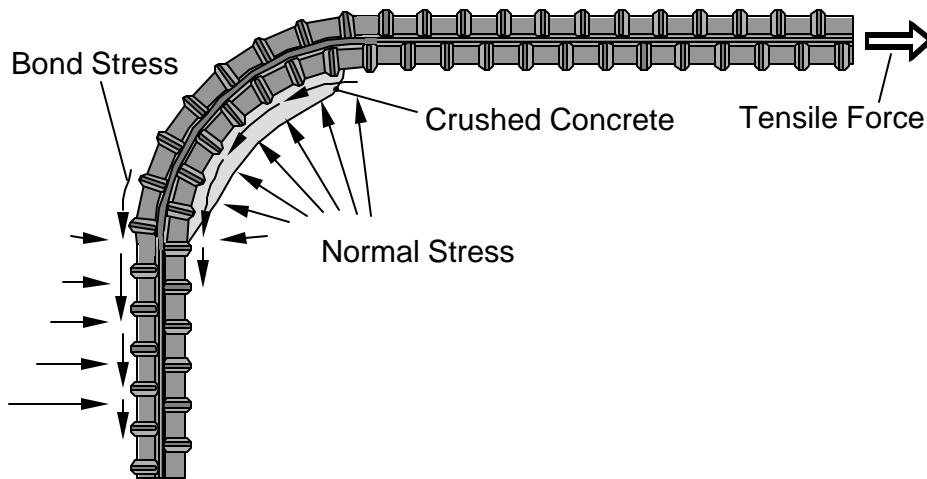


Figure 2-23: Stress transfer in a hooked bar

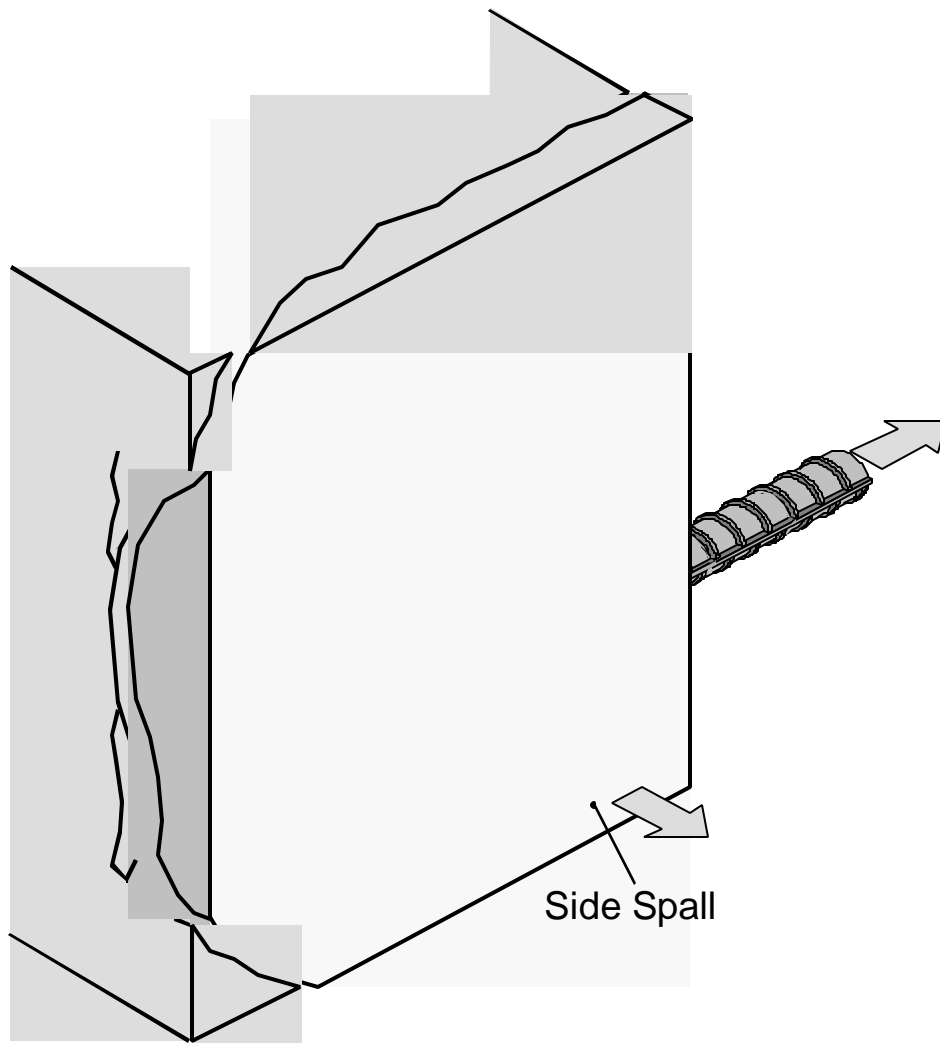


Figure 2-24: Side spall failure of a hooked bar

Studies by Minor [84] have shown that 180° hooks experience more slip than 90° hooks and both of these hooks exhibit more slip than straight bars as load is applied. Follow-up studies by Marques [75] have demonstrated that compressive pressure within the plane of the bend does not significantly enhance the anchorage capacity of the hook. Thrö [111] studied U-bent bars with lateral pressure applied perpendicularly to the plane of the bend. Thrö found increasing anchorage

strength as lateral pressure was increased. He recommended a reduction factor for development length that cut the length by half at a pressure of 1160 psi, the same as his recommended reduction factor for straight bars (see Section 2.2.3). Mattock [80] also studied U-bent bars with applied lateral pressure. Mattock found increasing anchorage capacity with lateral pressure for bars with the minimum allowable bend diameter ($6d_b$). He recommended a capacity formula that was proportional to $(f_n/f_{ct})^{0.7}$ where f_n is the applied lateral pressure and f_{ct} is the tensile strength of the concrete.

Chapter 3: Background on Headed Bars

3.1 INTRODUCTION

Headed bars are created by the attachment of a plate or nut to the end of a reinforcing bar to provide a large bearing area that can help anchor the tensile force in the bar. Figure 3-1 shows an example of a headed bar. The tensile force in the bar can be anchored by a combination of bearing on the ribs and on the head. This chapter discusses the current state-of-the-art of headed bar technology. The current products available on the market are discussed; the available research is reviewed; and pertinent code provisions are discussed.

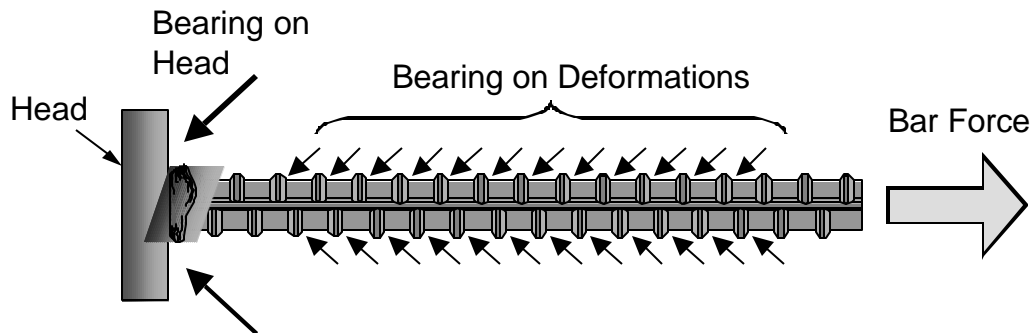


Figure 3-1: Anchorage of a headed bar

Throughout this chapter and through most of this report, the central parameter used for comparing different heads will be the area of the heads. In order to normalize results with respect to different bar sizes the ratio of head area to nominal bar area is repeatedly used. Specifically, this ratio, termed the relative head area, is defined as the net head area divided by the nominal bar area; the net head area being the gross head area (defined by the outer dimensions and shape of the head) minus the nominal bar area:

$$\text{Relative Head Area} = \frac{A_{nh}}{A_b} = \frac{A_{gh} - A_b}{A_b} \quad (3-1)$$

A_{nh} = the net head area (in²)

A_{gh} = the gross head area (in²)

A_b = the nominal bar area defined by ASTM A615 [3.1] (in²)

3.2 HISTORICAL DEVELOPMENT OF HEADED BARS

Headed reinforcing bars have evolved from headed stud anchors. Extensive studies on stud anchors first began in the 1960's. Most of this work was conducted by the Nelson Stud Welding Company and researchers at Lehigh University [82]. Their research established the pullout cone design method for anchors under combined shear and tension. Headed studs are commonly used only as shallow anchorage devices or to provide composite action between steel girders and overlying concrete deck slabs. The behavioral understanding of headed studs was limited to these applications and there was little similarity to the anchorage problems associated with deformed reinforcing bars.

Subsequently shear studs were adapted for use as punching shear reinforcement in flat slabs. This work was conducted by Dilger and Ghali at the University of Calgary [44, 86] in the late 1970's. They found the current methods of slab shear reinforcement, which used small closed stirrups, to be structurally deficient and difficult to construct. They began to examine alternative methods of shear reinforcement and looked to double-headed shear studs as a possible solution. Initially, these headed studs were created by cutting thin sections out of steel I-beams, by fusion welding existing shear stud connectors to flat plates creating a prototype studrail, or by welding square plates to both ends of short deformed bar lengths to create double-headed ties (Figure 3-2).

The first method (I-sections) was found to be economically unfeasible and the second failed because the head sizes of the existing shear stud products were too small to properly anchor the heads into the top of the slab. The third method proved very effective. Eventually, the second and third methods were combined to create an improved studrail with larger head areas. This product was patented and is now produced commercially by Decon (founded in 1989). An important aspect of the Calgary research was the recommendation that a head size of 10 times the bar area was necessary for proper anchorage of the studs.

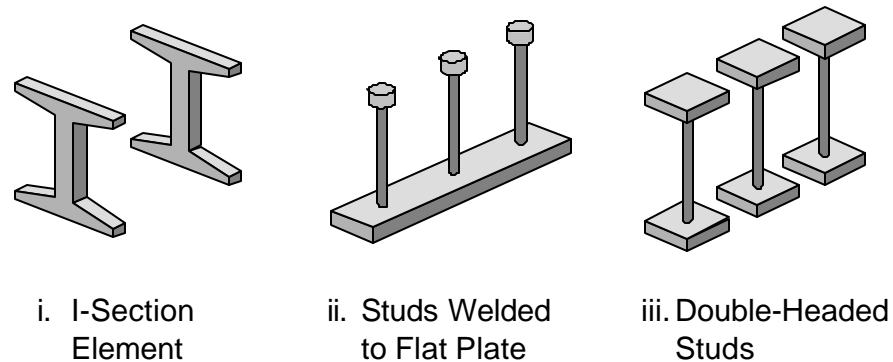


Figure 3-2: Shear reinforcement tested at University of Calgary

Caltrans also performed a small study of headed reinforcement in the 1970's [108]. Their interest was in determining a method of anchoring large diameter bars used in monolithic connections between bridge piers and box-girder superstructures. They wanted to shorten the development length of the bars without resorting to congestion prone hooks. They tested three methods of attaching the head to the end of the bar: allowing the bar to pass through a hole in the head plate and fillet welding on the back side of the head, a tapered-threaded connection, and a cylindrical metal sleeve with a filler metal material connecting the sleeve to the bar (also referred to as a "cad-weld"). These bars were supplied by ERICO who already had experience producing

headed studs in the stud anchor industry. ERICO did not find much interest in these headed bars at the time and never developed the welded or cad-welded headed bars into a commercial product [122].

After the Dilger and Ghali studies demonstrated the potential benefits of double-headed ties for use as shear reinforcement, the Alaska Oil and Gas Association (AOGA) began to study the technology in the early 1980's. They were interested in the possible use of double-headed bars as shear reinforcement in heavily reinforced concrete offshore oil platforms. They were also interested in using headed bars to alleviate high congestion created by the use of hooked bars. Additionally, they believed the headed bars could supply superior anchorage to conventional hooks. Several series of tests were conducted by AOGA. Most of the results of these tests are proprietary, but some findings have been reported by Berner, Gerwick, and Hoff [29].

Following their research, AOGA recommended the use of headed bars to Norwegian Contractors, a firm specializing in the design and construction of offshore oil platforms [29]. Norwegian Contractors began a program to design a headed bar product that could be mass produced economically but with a consistent level of high-grade quality. They teamed up with Metalock, a British supplier of industrial services for structural contractors. These two companies contracted the services of the SINTEF Group, a private research organization linked to the Foundation for Scientific and Industrial Research at the Norwegian Institute of Technology [124]. Based on the work performed by Norwegian Contractors, Metalock and SINTEF, a friction-welded headed bar was conceived. This bar design has since been used extensively in several offshore and coastal structures including: Oseburg Platform A, Gullfaks Platform C, the Ekofisk Barrier Wall, Sleipner Platform A (both the original and revised designs), the Snorre Foundation, Draugen Platform, Troll East Platform, and the Hibernia Platform (all of which are located in the

North Sea) [30]. Metalock patented the friction-welding technology and eventually formed a North American subsidiary to produce and sell friction-welded headed bars. This subsidiary became the Headed Reinforcement Corporation (HRC), the primary supplier of headed bars in the United States and the sponsor of much of the research that has been conducted on the new technology.

At the same time that Metalock was developing the friction-welded headed bar in the 1980's, ERICO developed a threaded headed bar. They first marketed the bar in Europe on a limited basis during the 1980's [122]. In the 1990's, after the use of headed bars in the offshore industry created greater interest in headed bars, ERICO began to sell their product under the trademark Lenton Terminator in the U.S. Their headed bars utilize a smaller head than the products of HRC and Decon. The Lenton heads are only 4 times the bar area rather than 10. This head size was derived from accepted head sizes used in the stud anchor industry [122]. ERICO and HRC are currently the only suppliers of headed bars. HRC has been a main supporter of headed bar research though ERICO has recently helped to sponsor some studies. Although the early work aimed at applications within the offshore industry, recent headed bar research has become focused primarily on bridge and seismic related applications.

3.3 HEADED BAR FABRICATORS

This section discusses the products of the two main companies that provide headed bars in North America: Headed Reinforcement Corporation (HRC) and ERICO. Decon, the manufacturer of the Studrail is excluded because their product does not have the versatility of HRC's and ERICO's products and is solely intended for use in flat slabs.

3.3.1 Headed Reinforcement Corporation

The Headed Reinforcement Corporation (HRC) is currently centered in Fountain Valley, California. HRC manufactures only two products, both of which can qualify as headed bars: a friction welded head that comes in four varieties and a forged head product that is intended for a mechanical coupler system. The forged head is very small but it is easy to fabricate, particularly in field conditions and shows promise for some applications in which only a small enhancement to reinforcement anchorage is required.

3.3.1.1 Friction-Welded Heads

The friction-welded or Theaded bar is HRC's main consumer product. The friction-welded heads are manufactured by pressing the end of a deformed reinforcing bar onto a plate spinning at very high speed. The heat produced by the friction between the deformed bar and plate causes the bar material to melt and form a weld between the two. The machinery required for this process is quite large and the headed bars can only be created in factory conditions. The headed bars come in four shapes: square, rectangular, circular, and oval. The circular and oval shaped heads are fatigue rated. All of the headed bars manufactured by HRC provide relative head areas between 8.6-11.9. Table 31 lists the head dimensions, head areas, and relative head areas for HRC's square and rectangular Theaded bars. Figure 33 shows a typical HRC friction-welded head.

| Bar Size | Square Head Size | Gross Area, A_{gh} (in ²) | $\frac{A_{nh}}{A_b}$ | Rectangular Head Size | Gross Area, A_{gh} (in ²) | $\frac{A_{nh}}{A_b}$ |
|----------|---|---|----------------------|---|---|----------------------|
| # 5 | 2" x 2" | 4.00 | 11.90 | 1 ¹ / ₄ " x 2 ¹ / ₂ " | 3.13 | 9.08 |
| # 6 | 2 ¹ / ₄ " x 2 ¹ / ₄ " | 5.06 | 10.51 | 1 ¹ / ₂ " x 3" | 4.50 | 9.23 |
| # 7 | 2 ¹ / ₂ " x 2 ¹ / ₂ " | 6.25 | 9.42 | 1 ¹ / ₂ " x 4" | 6.00 | 9.00 |
| # 8 | 3" x 3" | 9.00 | 10.39 | 2" x 4" | 8.00 | 9.13 |
| # 9 | 3 ¹ / ₄ " x 3 ¹ / ₄ " | 10.56 | 9.56 | 2" x 5" | 10.00 | 9.00 |
| # 10 | 3 ¹ / ₂ " x 3 ¹ / ₂ " | 12.25 | 8.65 | 2 ¹ / ₂ " x 5" | 12.50 | 8.84 |
| # 11 | 4" x 4" | 16.00 | 9.26 | 2 ¹ / ₂ " x 6" | 15.00 | 8.62 |
| # 14 | 5" x 5" | 25.00 | 10.11 | 3" x 7 ¹ / ₂ " | 22.50 | 9.00 |

Table 3-1: HRC head sizes (friction-welded heads)

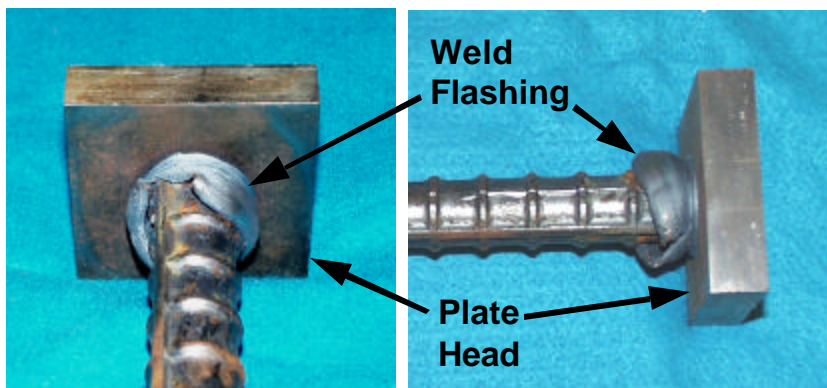


Figure 3-3: HRC friction-welded head

3.3.1.2 Forged Heads

The forged head system developed by HRC is part of a mechanical coupling system called the Xtender. The system is shown in Figure 3-4. Threaded mechanical sleeves are slipped over the ends of the bars, then upset ends are forged onto the bar ends. When the mechanical sleeves are coupled together, they bear on the forged heads and hold the separate bars together.

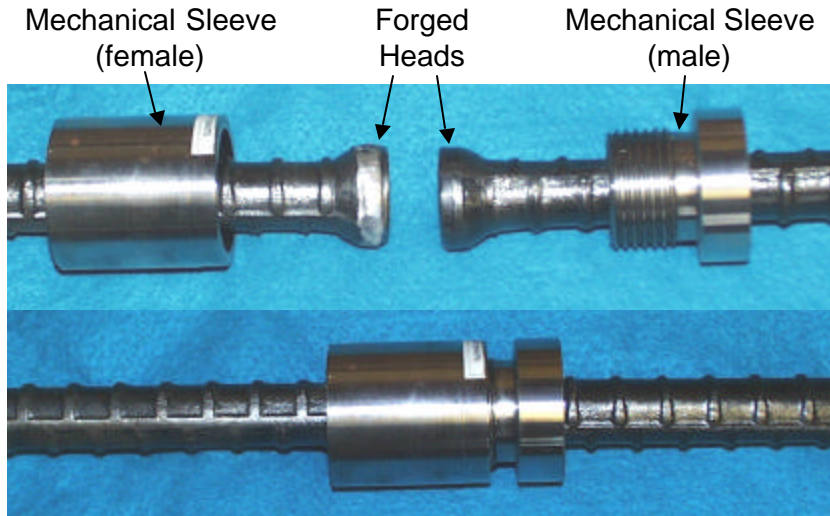


Figure 3-4: The Xtender coupler system

The Xtender forged heads can be created in the field. First the bar end is preheated with a blowtorch, then a special hydraulic vise is used to forge the head out of the material of the bar. An ICBO (International Conference of Building Code Officials) evaluation report [13] supplied by HRC lists minimum acceptance standards for Xtender head dimensions. The minimum head diameters specified by HRC are typically about 1.3 times the bar diameter providing a relative head area of about 0.7. In practice however, the final heads are slightly bigger. Measurements made of the Xtender headed bars supplied to this project by HRC showed that the forged head diameters were generally 1.5 times the bar diameter providing a relative head area of 1.3. These measurements are summarized in Chapter 6, section 6.6.3.

3.3.2 ERICO

ERICO (short for the Electric Railway Improvement Company) was founded in 1903 and manufactures products for a variety of marketplaces including construction, electrical,

railway, utilities, and communications. Their Lenton subsidiary produces products for reinforcement applications mostly consisting of mechanical splicing devices. Their Lenton Terminator utilizes a tapered thread connection between the reinforcing bar and a special nut that is screwed onto the bar to provide a head. Currently, this is their only headed bar product. Figure 3-5 shows the Lenton Terminator.



Figure 3-5: ERICO's Lenton Terminator head

The tapered thread of the Terminator head allows a more efficient stress transfer than conventional straight thread connections. ERICO's product literature claims that the tapered thread connection can support 125% of yield for a grade 60 reinforcing bar. Terminator heads are circular and generally have a relative head area around 3 or 4. Table 3-2 lists the available Terminator head sizes. ERICO also provides information on the development lengths of the terminator bars and these values are supplied in Table 3-2 as well.

| Bar Size | Head Diameter (in) | Gross Area, A_{gh} (in ²) | $\frac{A_{nh}}{A_b}$ | Terminator Development Length (in) |
|----------|-------------------------------|---|----------------------|------------------------------------|
| # 4 | 1 ³ / ₈ | 1.48 | 6.40 | 3.6 |
| # 5 | 1 ³ / ₈ | 1.48 | 3.77 | 4.6 |
| # 6 | 1 ¹ / ₂ | 1.77 | 3.02 | 5.5 |
| # 7 | 1 ³ / ₄ | 2.41 | 3.02 | 6.5 |
| # 8 | 2 ¹ / ₄ | 3.98 | 4.04 | 7.3 |
| # 9 | 2 ¹ / ₄ | 3.98 | 2.98 | 8.4 |
| # 10 | 3 | 7.07 | 4.57 | 9.3 |
| # 11 | 3 | 7.07 | 3.53 | 10.4 |
| # 14 | 3 ³ / ₄ | 11.04 | 3.91 | 12.4 |
| # 18 | 4 ¹ / ₂ | 15.90 | 2.98 | 16.8 |

Table 3-2: Lenton Terminator head sizes and development lengths

Terminator heads can be applied in the field provided the bar ends are pre-threaded. Threading may be accomplished in the field. Reinforcing bars may even be tied in place before the head is attached. To attach the head, all that is needed is the Terminator nut and a torque wrench. Table 3-3 lists the manufacturer's required torque values for installation of the Terminator heads.

| Bar Sizes | Setting Torque |
|------------|----------------|
| # 4 | 30 ft-lbs |
| #5 | 90 ft-lbs |
| #6 | 130 ft-lbs |
| #7 | 160 ft-lbs |
| # 8 - # 18 | 200 ft-lbs |

Table 3-3: Setting torques for Lenton Terminator heads

3.4 PREVIOUS RESEARCH ON HEADED BARS

The available research on headed bars can be separated into two categories: application studies and general behavior studies. The distinction between the two categories derives from the scope of the research. The research grouped under application studies tends to focus on particular structural uses of headed bars and utilizes test specimens whose behavior cannot be extrapolated beyond the specific application that is being modeled in the study. General behavior studies are those research programs aimed at determining mode of behavior that can be extrapolated to many different types of structural situations. For the most part these studies entail research on development length or anchorage capacity. This research program is intended to fall under the latter category of general behavioral research. Only the research that was deemed to study general behavioral trends is reviewed in detail within this section. The remaining literature is described briefly at the end of this section.

3.4.1 Caltrans Study

Nineteen pullout tests of headed bars were conducted at the Transportation Laboratory of the California Department of Transportation (Caltrans) in the early 1970's [108]. Their test specimens used large diameter reinforcing bars with #11, #14, and #18 sizes. The purpose of the tests was to determine if headed bars could represent a viable alternative to hooks in monolithic bridge pier/superstructure connections. The scope of the study also involved testing of several different head-bar connections. The various connections are shown in Figure 3-6. With only two exceptions, the headed bars tested used very large head sizes: relative head areas of 15.0 for the #11 and #14 bars tested and 13.1 for the #18 bars tested. The two exceptions included one non-headed #18 bar and one small headed #18 bar using only a cad-weld coupler sleeve as anchorage (the sleeve provided a relative head area of 1.8).

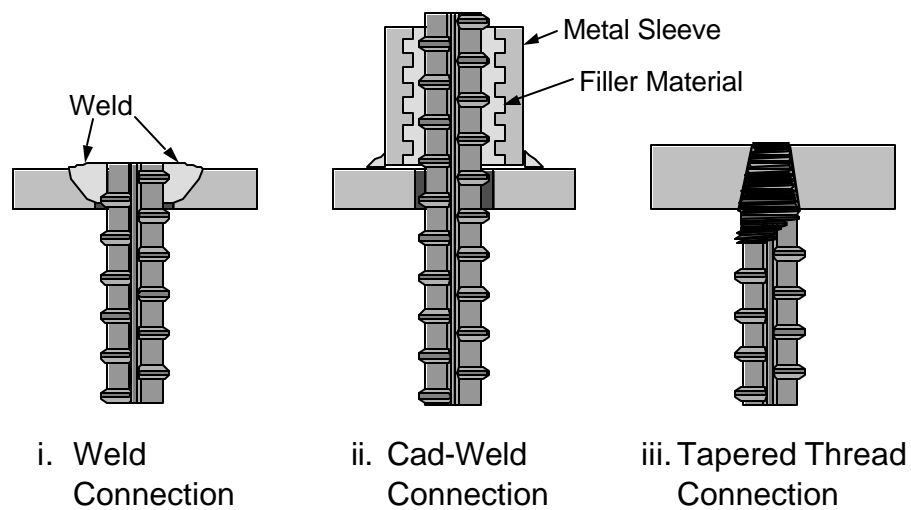


Figure 3-6: Head-bar connections tested by Caltrans

The test specimens consisted of tensile pullout specimens similar to those shown in Figure 2-17. Large embedment lengths were provided for the bars. Additionally, supplementary transverse reinforcement was used around the perimeter of the specimen blocks. The variables tested included: bar size (#11, #14, or #18), single versus group action (four bar groups of #11's), concrete cover ($7\frac{1}{2}$ " or 19"), embedment depth ($h_d/d_b = 8$ to 32), method of head attachment (see Figure 3-6), and head size ($A_{nh}/A_b = 0.0, 1.8, \text{ or } 13.0$). Most test specimens used fully bonded bars so that anchorage occurred by a combination of bond and bearing of the head.

The Caltrans researchers discovered that the bonded lengths of their bars were too long to allow much anchorage capacity of the bars to be carried by the heads. In most tests the test bar yielded in tension or the load to failure exceeded the capacity of the test frame. The research provided the following conclusions:

- The head sizes selected for testing were more than adequate for the development lengths tested in the research program.

- One test of a much smaller head size ($A_{nh}/A_b = 1.8$) provided comparable results to similar tests of larger head sizes ($A_{nh}/A_b = 13$) indicating that smaller head sizes could achieve yield. The Caltrans researchers recommended that smaller heads should be investigated in any forthcoming research.
- More load was carried by the head as the bonded length of the bar was reduced. When compared to stress results measured from the non-headed test specimen in which anchorage was carried completely by bond, the measured load carried by the heads compared favorably to the forces that would be predicted assuming that the remainder of the load would be carried by normal bond stresses along a fully bonded bar. Figure 3-7 shows data from the Caltrans study. In the figure, the percent of load carried by the heads aligns well with the load distribution curves measured from the fully bonded test bar. The data indicate that the portion of the load carried by bond in a headed bar follows a similar load distribution as the case in which no head is present. One data point suggests that the head may carry a greater percentage of the load for smaller development lengths at greater stress levels and that bond resistance breaks down in favor of transferring the load to the head under such conditions.
- Load-slip measurements of the test bars indicated that more slip is experienced for bars acting in groups than single headed bars.

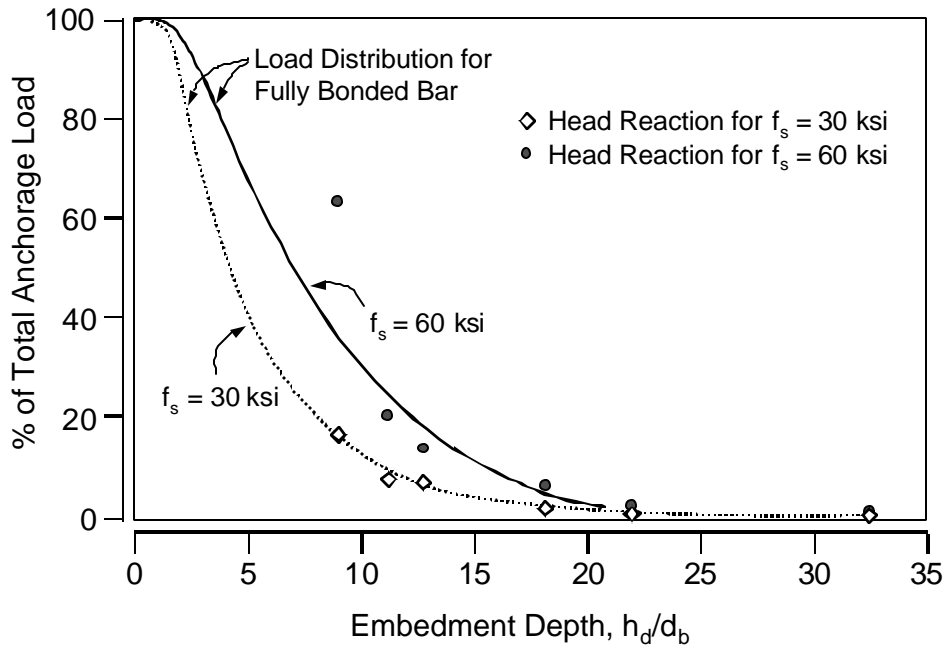


Figure 3-7: Head reaction versus embedment depth compared to fully bonded load profiles (after Caltrans data [108])

The Caltrans researchers made several recommendations for the use of headed bars including specifications for acceptable head-bar connections (any of the three connection types tested was found to be acceptable for the given embedment depths) and staggering arrangements for headed bars in groups (staggered termination points were recommended to avoid overlap of the heads). The recommendations were restricted to grade 60, #18 bars with at least four feet of embedment depth.

3.4.2 SINTEF Studies

Most of the literature regarding the SINTEF studies [45, 50, 51, 52, 95, 96] is proprietary and unavailable for review. The information presented here comes from a summary paper written by two engineers from Norwegian Contractors: Dyken and Kepp [46].

SINTEF performed a number of studies primarily intended to demonstrate the strength and ductility of the friction-welded head-bar connection. These studies included static tension, static bending, and fatigue tension tests on the headed bars in air. Three groups of tests studied the performance of the headed bars embedded in concrete: static pullout bond tests, fatigue pullout bond tests, and beam shear tests.

Figure 3-6 shows a typical static pullout specimen. The Dyken and Kepp report suggests that only headed bars with the head size shown in Figure 3-8 were studied ($A_{nh}/A_b = 6.0$) and that studies of the effects of head area were not a parameter of the study. Specimens were tested with normal weight concrete with 8,700 psi compressive strength and light-weight aggregate concrete of compressive strength 10,400 psi. Bond between the concrete and the deformed portion of the bar was prevented by use of a plastic sleeve. All specimens tested failed by yielding of the bars ($f_y = 80$ ksi). Minimal slip of the heads was observed in all tests. Comparison tests with hooked bars were also studied. All that is reported in the available literature is that the headed bars had a better load-slip response than the hooked bars.

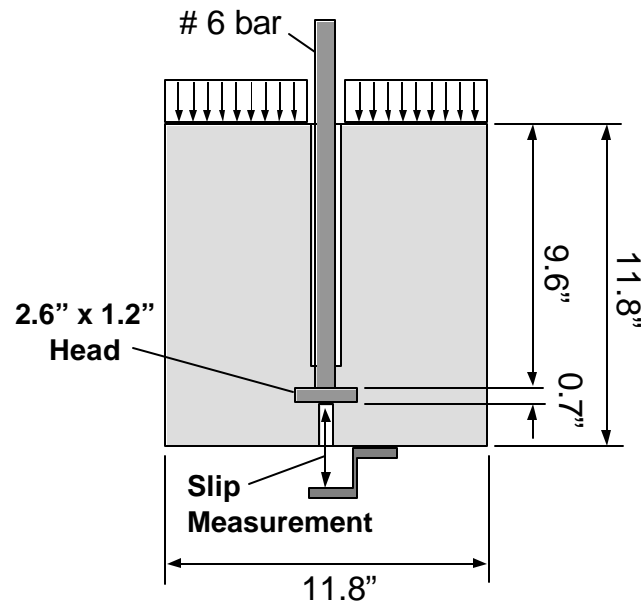


Figure 3-8: Static pullout test performed by SINTEF

The fatigue pullout test used identical specimens as the static tests, but specimens were tested with #6 and #8 size bars. The tests were intended only for a fatigue test of the head-bar connection. The bars were embedded in concrete only to provide a realistic support condition for the head. In order to prevent premature failure of the concrete, deliberately high compressive strengths of 12,000 psi were used. All specimens failed by fatigue fracture of the friction-welded head-bar connection.

Three shear beam specimens were tested. Two specimens used headed bars for the shear reinforcement and the third used a standard stirrup detail. All three beams failed at nearly identical loads thus demonstrating that the headed bars were an adequate substitute for standard stirrups.

It is known that the SINTEF research was related to the development of HRC's headed bars. They developed tests to show the quality of the friction-welded head-bar connection and influenced the choice of the head sizes adopted. However, the HRC head sizes may also derive

from the recommendations for studrail heads that were derived at the University of Calgary [44, 86]. The SINTEF study serves as the basis for many of the standards required in ASTM A970 “*Standard Specification for Welded Headed Bars for Concrete Reinforcement*” [5] which is discussed later in this chapter.

3.4.3 University of Kansas Study

Beam-end bond tests of headed bars were conducted at the University of Kansas [119]. The research was sponsored by HRC and all headed test bars were supplied by them. The test specimens were modeled after specifications contained in ASTM A944 “*Standard Test Method for Comparing Bond Strength of Steel Reinforcing Bars to Concrete Using Beam-End Specimens*” [4] (see Figure 2-17 for an example of this specimen type). Seventy specimens were tested. Test bars were non-headed, hooked with 180° bends, or friction-welded headed bars. The goal of these tests was to determine a development length formula for headed bars. Parameters studied in the research were:

- **Concrete cover** – cover was 2 or $3d_b$ measured to the surface of the bar (not the head).
- **Bar exposure** – in some specimens, plastic sheathing was placed over the deformed bar in order to test the strength of the head by itself.
- **Transverse reinforcement** – four arrangements of stirrup bars were tested as confining reinforcement for the pullout tests and compared against unconfined test results. Figure 3-9 shows the four stirrup arrangements.

Parameters that were kept constant throughout the study were bar size (#8), embedment length (12”), concrete strength (4,500 – 5,000 psi), and the size and shape of the friction-welded heads (HRC’s standard #8 square head size: 3” x 3”). Additionally, all bars were bottom-cast and only single bar groups were tested.

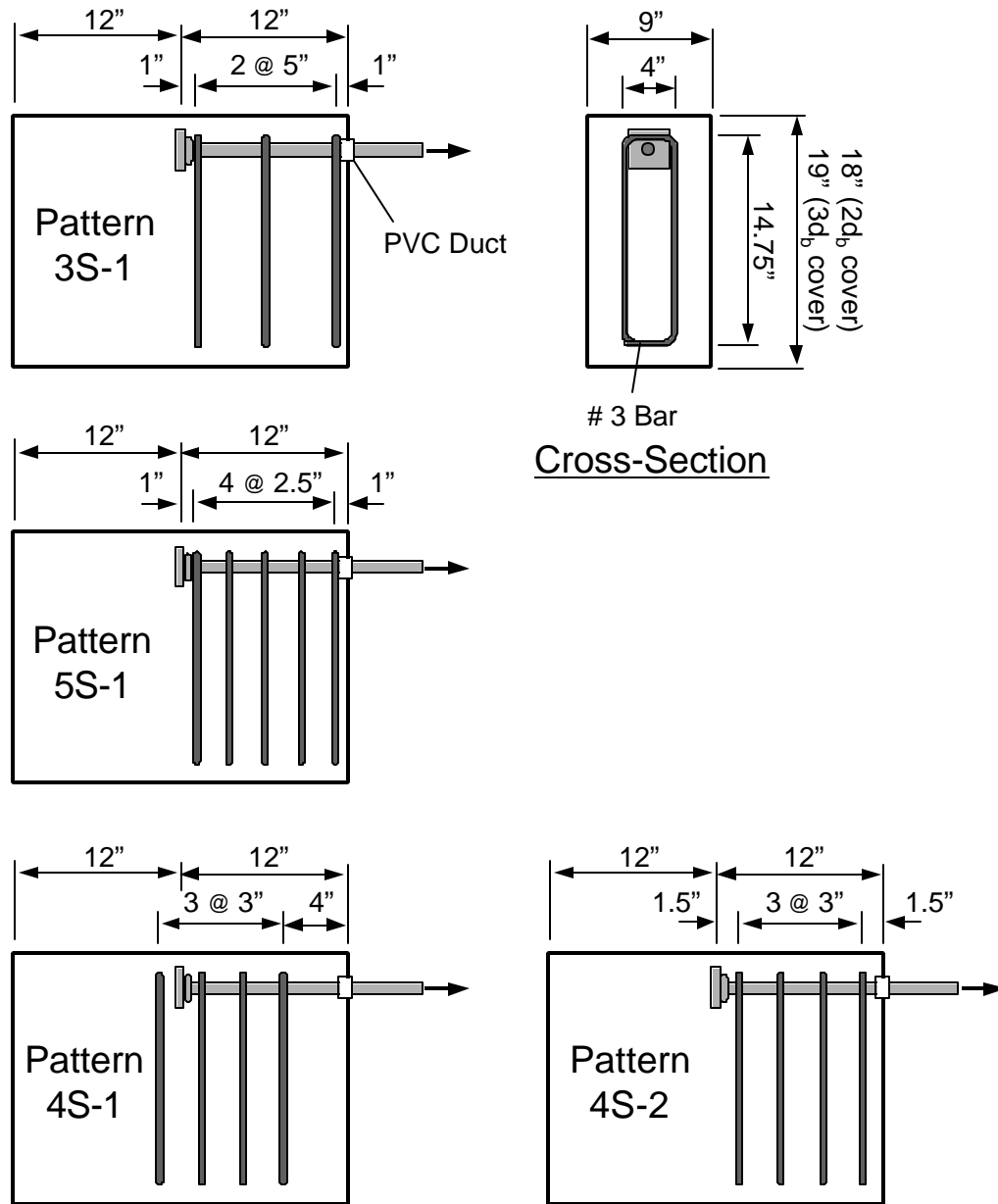


Figure 3-9: Transverse reinforcement patterns studied at Kansas [119]

Results of the Kansas study indicated the following:

- Headed bars failed at equal or higher loads than hooked bars. Both types of bar anchorages exhibited similar load-slip and failure behavior. In addition, the response of hooked and headed bars to transverse reinforcement and increases in cover were similar.
- The benefit from increases in cover was diminished when increasing amounts of transverse confinement were provided.
- Capacity was increased by 50% by the addition of transverse reinforcement. Thereafter, additional transverse reinforcement provided diminishing returns in capacity.
- PVC sheathing over the straight bar length of the headed bars increased the capacity of the headed bar. Additionally, PVC sheathing also lessened the degree of surface cracking exhibited before failure of the anchorage. This occurred because splitting forces and cracking associated with bond of the deformed bar were eliminated and the ability of the concrete to carry forces from the head was increased.
- The optimal anchorage performance from the headed bar was achieved by sheathing the straight bar deformations over the embedment length and providing $3d_b$ clear cover over the bar if no transverse reinforcement was used or providing transverse reinforcement if only $2d_b$ clear cover was provided. There was minimal advantage to providing both large amounts of cover and transverse reinforcement.

Following the experimental testing, a regression analysis was performed to provide a best-fit equation for development length of the headed bars tested. Many forms of design

equations were used, most of them based on straight bar development length. However, none of the straight bar based equations was found to be adequate as a design expression. Eventually, an equation based on the ACI 318 [2] expression for hooked bars was used. The following were recommended in a proposal [119] for an addition to ACI 318 Building Code:

1. The headed bar development length, L_{dt} , shall be calculated as the following:

$$L_{dt} = \frac{22d_b f_y}{60\sqrt{f'_c}} \left(\frac{3d_b}{c + K_{tr}} \right) (\alpha\beta\lambda\psi) \quad (3-2)$$

2. The basic development length, L_{dt} , shall not be less than $6d_b$ or 6".
3. Concrete cover shall not be less than $3d_b$.
4. A minimum of three transverse stirrups shall be positioned within the development length, L_{dt} .
5. The amount of transverse reinforcement within the development length, L_{dt} , required is $A_{tr}f_{ytr}/s \geq 2000$ lb/in or no less than $5d_b$ of clear cover must be provided.

d_b = bar diameter (in)

f_y = bar yield strength (ksi)

f'_c = concrete compressive strength (ksi)

c = minimum cover dimension to the surface of the bar (in)

K_{tr} = transverse reinforcement index (as defined in Equation 2-2)

α = casting position factor (*to be determined by future research*)

λ = lightweight aggregate factor (*to be determined by future research*)

β = epoxy-coated reinforcement factor (*to be determined by future research*)

ψ = excess reinforcement factor (*to be determined by future research*)

The Kansas recommendation for headed bars is essentially 7/12 of the existing ACI Building Code formula for hooked bars. However, the formula limited to the type of headed bar tested in the Kansas program, the standard HRC friction-welded head ($A_{nh}/A_b \cong 9$ for most bar sizes). Ideally, the nature of the connection of the head to the bar should not have any impact on development length provided that the connection is strong enough, so it should not matter that the bars tested were friction-welded. However, the size and geometry of the head is important. By testing only one head size and basing proposed code text on that head size, the Kansas study presents the danger of standardizing that head size. Since all head geometry parameters were kept constant throughout the test series and the development length proposals are based only on those parameters, the proposed anchorage requirements depend on the head size used. As a result, this “standard” head then becomes the only choice for designers and contractors, and all other products or head geometries can not be considered. This problem is discussed later in regard to certain headed bar provisions that have already been included in standards.

3.4.4 University of Texas Study

An extensive study sponsored by the Headed Reinforcement Corporation was conducted at the Phil M. Ferguson Engineering Research Laboratory of the University of Texas at Austin. This research was conducted by two PhD students, Richard DeVries and Tarek Bashandy, and is documented in their dissertations [42, 26]. In the first phase of the study, over 160 pullout tests were conducted studying a variety of variables. Tests in that phase of the study can be further subdivided into shallow and deep embedment tests. In the second phase of the study, 32 large-scale specimens simulating exterior beam-column joints were tested, then one full exterior beam-

column sub-assembly was constructed and tested under cyclic loading. Once again, design equations were fit to the data and recommendations proposed for code implementation.

Figure 3-10 shows some geometric parameters that must be defined to discuss the Texas study. The embedment depth, h_d , is the length measured from the critical section where the full load of the bar must be carried to the inside face of the head. This is distinguished from bond length, L_{bond} , which is the length over which bond of the bar can occur and might not be the full length of the embedment depth. In test specimens, the bonded length (L_{bond}) of the straight deformed bar was controlled by PVC sheathing placed over the bar surface. Perpendicular to the bar axis are the two axes of clear cover, 1 and 2. Axis 1 is oriented in the direction parallel to the minimum clear cover to the bar axis; axis 2 is perpendicular to axis 1. Consequently, clear distances contain subscripts related to the axis along which they are measured: c_1 , the minimum cover distance to the center line of the bar; c_{c1} , the clear cover distance measured to the bar surface along axis 1; and c_{h1} , the minimum clear cover distance measured to the head surface along axis 1. The variables c_2 , c_{c2} , and c_{h2} are the analogous cover distances measured along axis 2. The variables h_1 and h_2 are the edge lengths of rectangular heads measured along axes 1 and 2.

Most pullout tests were of single bars in tension. Bars were generally cast in the vertical position unless otherwise noted. Bar sizes were #6, #8 and #11.

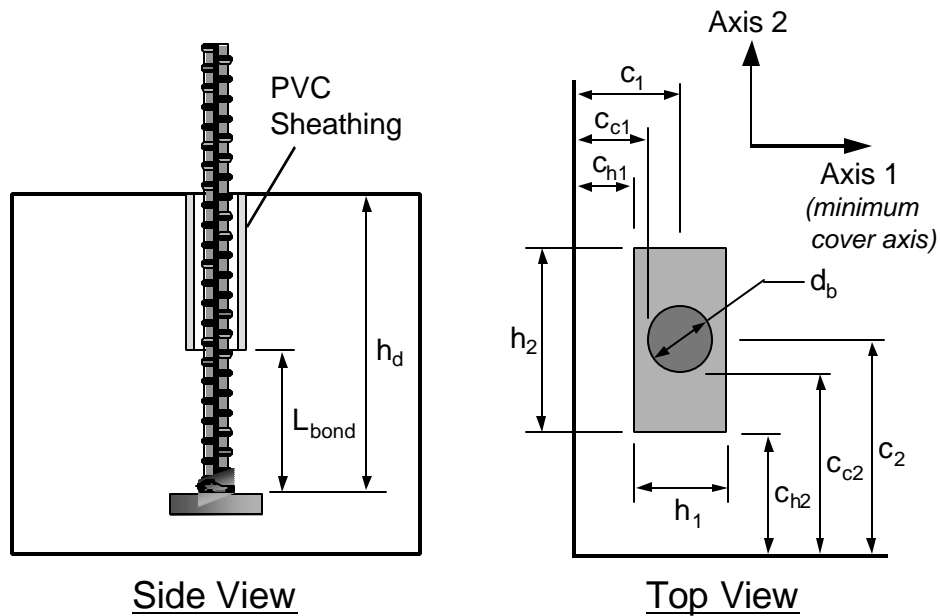


Figure 3-10: Definition of geometric parameters for University of Texas study

3.4.4.1 Shallow Embedment Pullout Tests

Twenty-one shallow embedment pullout tests were conducted by DeVries [42]. Shallow embedment tests were somewhat arbitrarily distinguished from deep embedment tests by having a ratio of embedment depth, h_d , to bar clear cover, c_{c1} , less than 5. Among these tests, the primary variables were concrete strength (4 to 11 ksi), embedment depth and edge distances. Also studied were the effects of transverse reinforcement, development length, and head size. Figure 3-11 shows the basic shallow embedment test specimen.

DeVries determined that transverse reinforcement did not significantly affect the ultimate pullout strength of the headed bar but did add post-peak residual strength to the anchorage. Bonded development length added some contribution to ultimate capacity primarily when transverse reinforcement was used and helped to reduce head slip. Tests studying head size were

limited (only one pair of comparable tests both with rather large heads: $A_{nh}/A_b = 5.7$ and 7.4) but showed no effect due to head size. This conclusion may not be true for smaller head sizes.

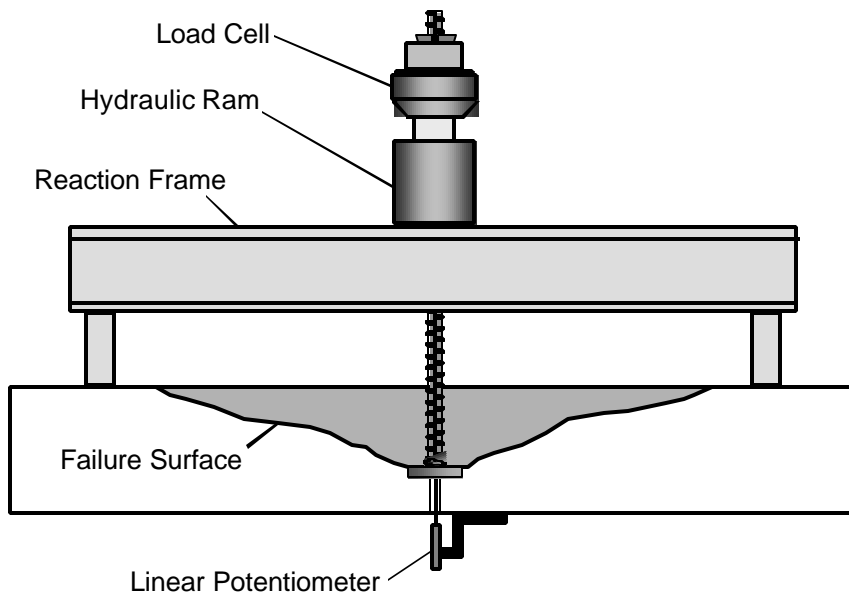


Figure 3-11: Shallow embedment pullout specimen used by DeVries

All but three tests failed by pullout of a large concrete cone initiating at the head (see Figure 3-11). The three exceptions failed by fracturing of the bar steel. DeVries compared his pullout capacities to several models of anchorage and found that the Concrete Capacity Design (CCD) method for breakout of anchor bolts best fit his data. In the CCD method, a cone failure surface is projected from the head of the anchor bolt or headed bar and the area of this surface is used in capacity calculations [48]. DeVries modified the coefficient of the equation slightly to account for lower head bearing stresses in headed bars than are typical of anchor bolts. He also proposed basing the projected failure surface on the head perimeter rather than the center of the

bar, as is typical of anchor bolts (Figure 3-12). The following equations for concrete breakout capacity were proposed:

$$\text{Concrete Breakout Capacity, } N_n = \frac{A_N}{A_{N_0}} \Psi_1 N_b \quad (3-3)$$

$$N_b = 22.5(h_d)^{1.5} \sqrt{f'_c} \quad (3-4)$$

$$\Psi_1 = 0.7 + 0.3 \frac{c_{\min}}{1.5h_d} \leq 1 \quad (3-5)$$

N_b = the basic concrete breakout capacity (lbs)

Ψ_1 = modification factor for stress disturbance caused by proximity to an edge

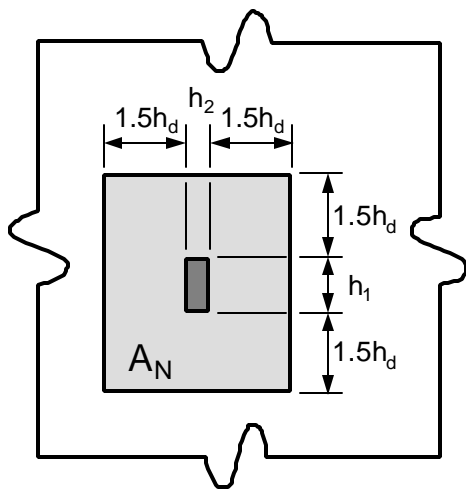
A_{N_0} = basic projected area of a single anchored bar, $9(h_d)^2$ (in²)

A_N = projected area of concrete breakout failure as defined in Figure 3-12 (in²)

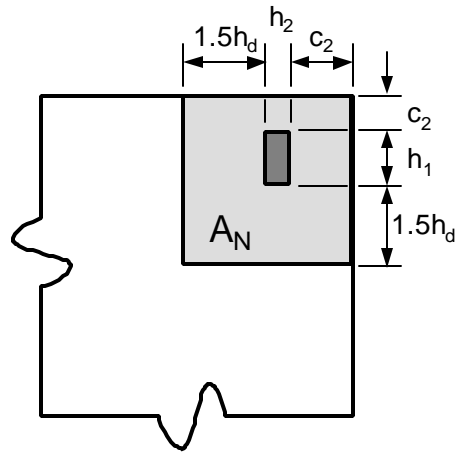
h_d = the embedment depth as defined in Figure 3-10 (in)

c_{\min} = the minimum edge distance equivalent to c_1 in Figure 3-10 (in)

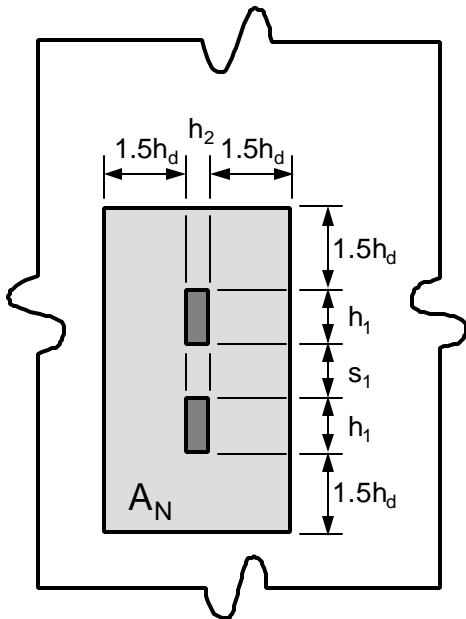
f'_c = concrete compressive strength (psi)



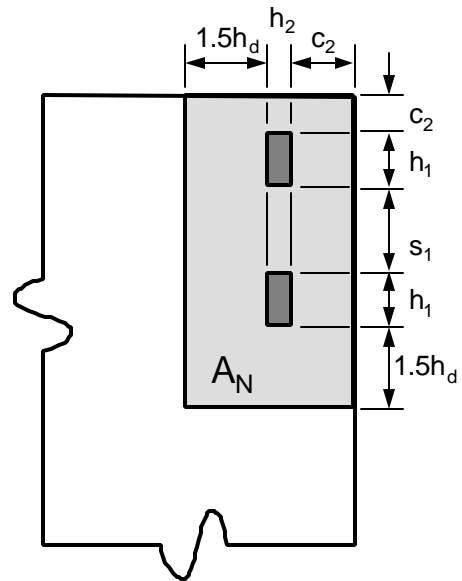
i. Single Bar Centered within Mass Concrete



ii. Single Bar Near Corner or Edge



iii. Multiple Bars Centered within Mass Concrete



iv. Multiple Bars Near Corner or Edge

Figure 3-12: Projected concrete breakout areas for different situations

3.4.4.2 Deep Embedment Pullout Tests

A total of 123 deep embedment tests were performed by DeVries [42]. Bashandy also performed 25 follow-up tests [26]. Deep embedment tests were distinguished from shallow embedment tests by having a ratio of embedment depth, h_d , to bar clear cover, c_{c1} , greater than 5. The primary variables of DeVries' tests were embedment depth, development length, head orientation, head geometry (including head area, aspect ratio, shape, and thickness), transverse reinforcement, concrete strength, cover, corner versus edge bars, and closely spaced bars. Bashandy's follow-up tests studied the effects of cyclic loading and anchorage of the head behind a crossing bar or against another head. Figure 3-13 shows the basic test set-up.

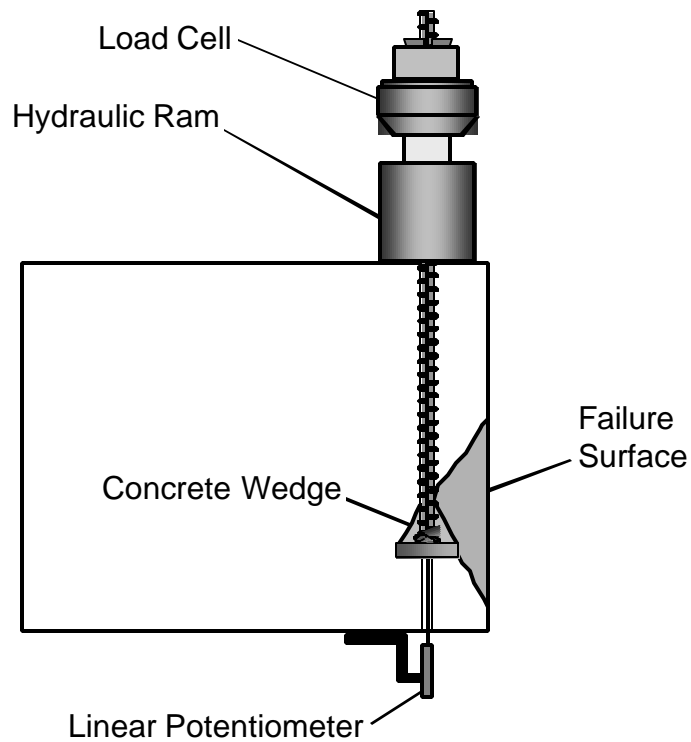


Figure 3-13: Deep embedment pullout specimen used by DeVries and Bashandy

Among the conclusions from the deep embedment studies were:

- The primary mechanism of failure was side blow-out.
- Provided that the embedment depth was sufficient to classify the bar as deeply embedded, further embedment depth did not enhance the ultimate capacity.
- Bonded length did enhance the slip performance of the bar, and provided a small increase in ultimate capacity. The increase in anchorage load due to bond could be reasonably estimated by existing bond equations (here DeVries referred particularly to the Orangun equation used as the basis of the ACI provisions [94]).
- The orientation of rectangular heads had no effect on the ultimate capacity.
- The aspect ratio (width:length) of rectangular heads had no noticeable effect on ultimate capacity.
- The shape of the head (circular versus square) had no visible effect on ultimate capacity.
- Ultimate side blow-out capacity increased with increasing head size and the relationship tended to be linear. DeVries' data were reformulated in terms of bar stress versus relative head area and are shown in Figure 3-14. Many of the bar stresses exceed yield levels because DeVries loaded the bar into the strain hardening range. All the data points presented in Figure 3-14 represent side blow-out failures.
- Ultimate capacity was unaffected by the head thickness even when the head yielded. It should be noted that DeVries' range of head thickness was limited (0.5" – 0.75").

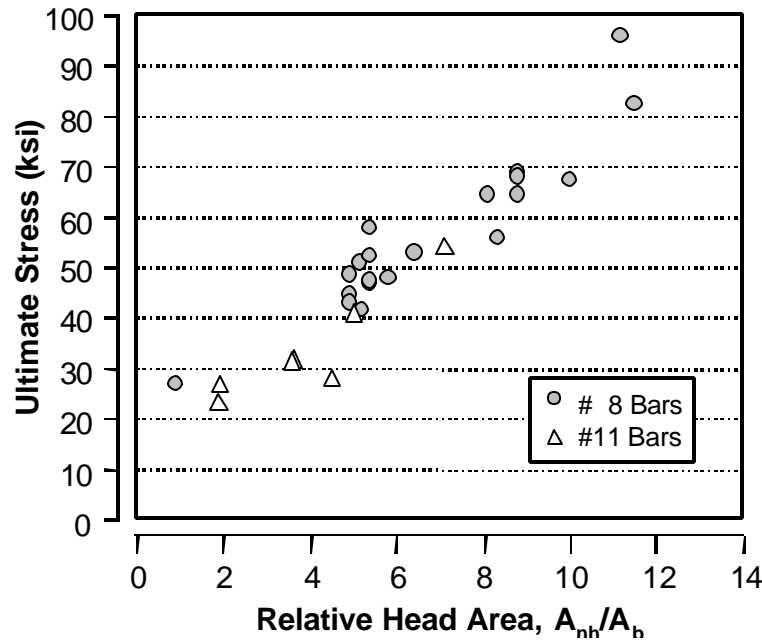


Figure 3-14: DeVries' data on side blow-out capacity versus relative head area

- DeVries studied transverse reinforcement in the form of tie-backs or transverse bars crossing in front of the head. His maximum levels of transverse reinforcement were approximately half the area of the headed bars being anchored. Within those steel limits he found that there was only a small increase in the side blow-out capacity of the headed bar and that the primary benefit of the transverse reinforcement was the residual post-failure capacity provided. Bashandy studied transverse reinforcement in the form of crossing bars and loaded headed bars (ie. a CTT node situation which is discussed further in the next chapter). His transverse levels of steel varied from half to equal amounts of the headed bar area. He found that capacity was improved 10 – 25% by the transverse steel.

- Ultimate capacity improved with increasing concrete compressive strength, and was roughly proportional to $(f_c')^{0.67}$ with much scatter.
- Ultimate capacity improved with increasing edge distance, c_1 , and was roughly proportional to $(c_1)^{0.55}$ with much scatter.
- Corner bars had less capacity than bars along only one edge. DeVries recommended that the headed bar should be treated as a corner bar when the maximum edge distance, c_2 , was less than 3 times the minimum edge distance, c_1 .
- Close bar spacing resulted in a reduction of anchorage capacity similar to edge bars.
- Side blow-out capacity was unaffected by cyclic loading up to a maximum of 15 load cycles.

DeVries determined that the primary variables upon which a design should be based were edge distance, c_1 , net head bearing area, A_{nh} , and the concrete compressive strength, f_c' . DeVries compared his data to several models of bearing or side blow-out capacity. He also performed a regression analysis to determine a best-fit equation for capacity. Many existing models of bearing capacity and side blow-out capacity fit the data reasonably well. DeVries' final model of capacity was based on the method recommended in CEB documents [10, 11] for side blow-out of deeply embedded anchor bolts. The CEB formulation is in turn based on research conducted by Furche and Eligehausen at the University of Stuttgart [49]. DeVries recommended the following:

$$\text{Side Blow-Out Capacity, } N_n = \frac{A_{Nsb}}{A_{Nsbo}} \Psi_2 N_{sb} \quad (3-6)$$

$$N_{sb} = 144 c_1 \sqrt{A_{nh} f_c'} \quad (3-7)$$

$$\Psi_2 = 0.7 + 0.3 \frac{c_2}{3c_1} \leq 1 \quad (3-8)$$

- N_{sb} = the basic side blow-out capacity (lbs)
- Ψ_2 = modification factor for stress disturbance caused corner affects
- A_{Nsbo} = basic projected side blow-out area of a single anchored bar, $36(c_1)^2$ (in²)
- A_{Nsb} = projected area of side blow-out failure as defined in Figure 3-15 (in²)
- A_{nh} = the net bearing area of the head (in²)
- c_1, c_2 = the minimum and maximum edge distances (see Figure 3-10) (in)
- f'_c = concrete compressive strength (psi)

Additionally, DeVries also recommended that the head be thick enough to prevent yielding of the head steel at ultimate anchorage capacity.

3.4.4.3 Beam-Column Joint Tests

Bashandy tested 32 simulated exterior beam-column joints and one exterior beam-column sub-assembly [26]. The exterior beam-column joint was designed to be similar to tests performed by Jirsa et al. on hooked bar anchorages in beam-column joints [75, 84]. Figure 3-16 shows the basic configuration. In some tests column ties were included within the joint region to enhance the anchorage confinement of the headed bar or to improve the shear capacity of the joint. Specimens failed by one of two modes: “side blow-out” failure of the headed bar anchorage or shear related failure of the joint region. Bashandy’s “side blow-out” failures are placed in quotes because, while they superficially resembled the side blow-out failures in the deep embedment pullout tests, there were some indications of more complex behavior. Similarly, the specimens that

failed by a shear related mode could not be easily categorized by either of the distinct modes observed in the shallow and deep embedment pullout studies. Many of the variables studied in the previous headed bar tests were studied here: bar diameter, head geometry (area, aspect ratio, and orientation), embedment depth, side cover, and transverse steel.

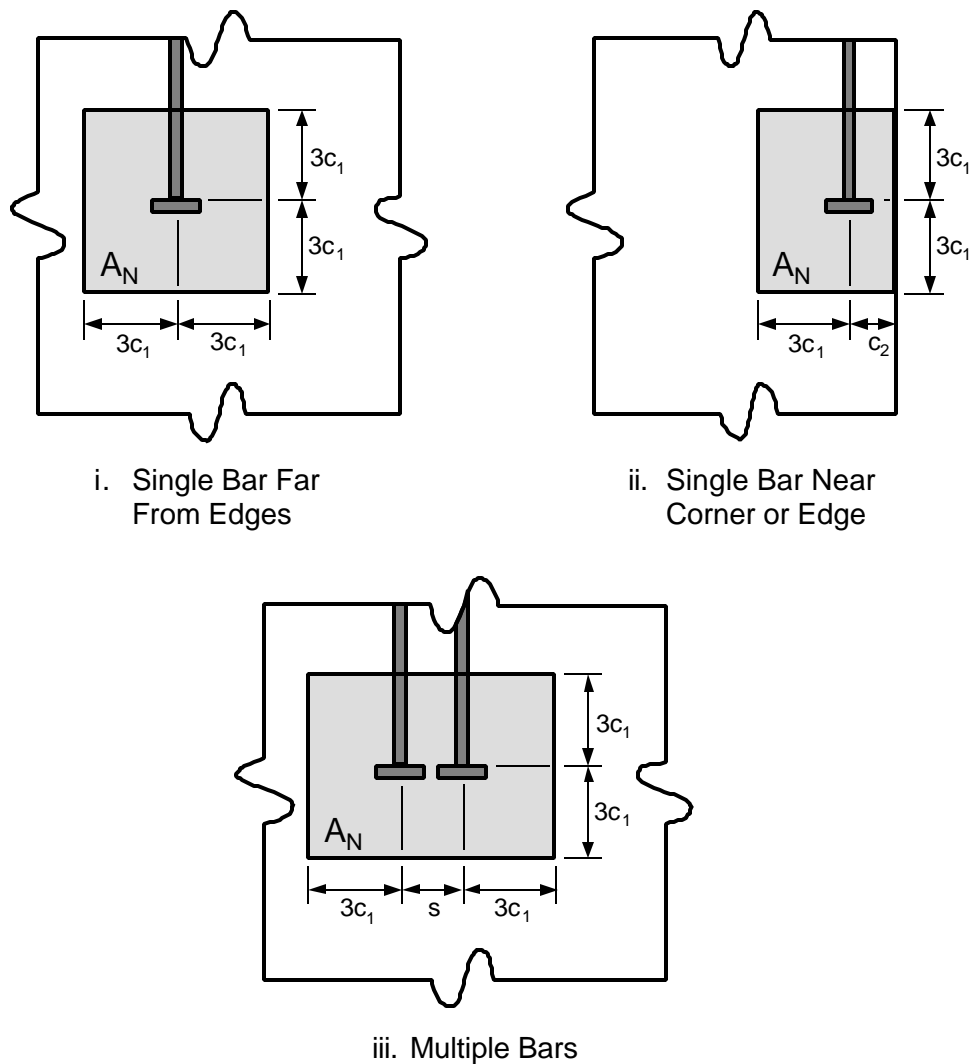


Figure 3-15: Projected concrete side blow-out areas for different situations

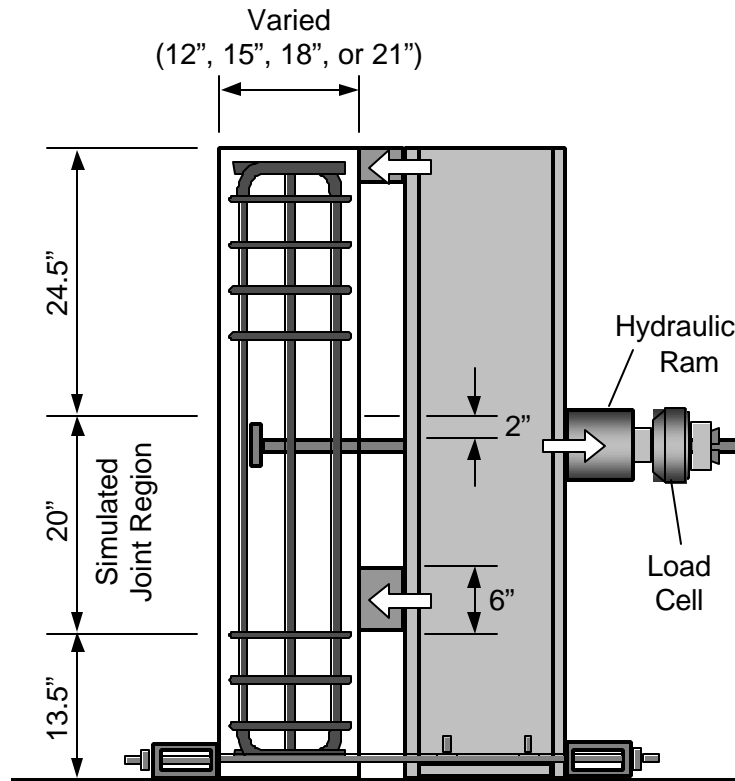


Figure 3-16: Typical exterior beam-column joint studied by Bashandy

Eighteen of the 32 beam-column tests failed by “side blow-out.” The following conclusions were drawn from those tests:

- Among test pairs in which the gross head area and the embedment depth were constant, the bar diameter had no effect on ultimate capacity.
- The results of three companion tests showed that ultimate capacity was improved by increasing the head area of the bar.
- Head aspect ratio and orientation had insignificant effects on ultimate capacity.
- Ultimate capacity increased linearly with embedment depth (measured from the face of the column to the head of the bar). Strain gages indicated that less of the total

capacity was carried by the head as embedment depth was increased (Bashandy left the deformed bar unsheathed in these tests). Past a certain embedment length (12”), load in the head did not increase but rather increases in the capacity of the bar were due to bond along the straight lead length.

- Side cover improved the ultimate capacity of the bars.
- Transverse steel confinement was studied in the form of #3 column ties placed parallel to the axis of the headed bars (a typical joint detail). Ultimate capacity was improved with increasing transverse steel which enhanced the anchorage by restraining the side cover from lateral blow-out and by confining the concrete underneath the heads to improve bearing capacity.
- The anchorage performance of headed bars was at least equivalent to and frequently better than analogous hooked bars.

Bashandy compared his test data to data from similar test conditions in DeVries' pullout study. Bashandy found that the capacity of headed bars in joints was 14 – 44% less than analogous bars tested in deep embedment pullout studies. Bashandy concluded that the capacity of the bars was influenced by the shear in the joint region that affected the failure mode of the bars.

Only one full exterior joint sub-assembly was tested by Bashandy. Cyclic testing was performed on the sub-assembly. Bashandy found that the headed bars provided superior performance to hooked bars tested in an equivalent specimen and that capacity degradation and anchorage loss was minimal.

3.4.5 Application Studies

Application studies involving headed bars fall into three categories: tests on joints utilizing headed bars, tests of double-headed bars as shear and confining reinforcement, and studies on the use of headed reinforcement to retrofit and rehabilitate walls and piers for seismic performance.

3.4.5.1 Joint Tests

Five roof corner joint specimens and two exterior beam-column joint specimens were tested at Clarkson University [115]. The research was sponsored by the National Science Foundation with materials supplied by HRC and ERICO. The corner joints utilized HRC friction-welded heads and hooked bars for comparison. The exterior joint specimens used ERICO's Lenton Terminator heads. The tests were intended to test if headed reinforcement could conform to the ACI 352 recommendations for seismic joints in buildings. The researchers found that the headed bars provided greater member stiffness than hooks because there was less slip of the anchorage during cyclic testing. When subjected to cyclic loading eventually all bond was lost and anchorage of the bar was carried solely by the head. At large deformations this caused pushout of the concrete behind the heads when reversed loading placed bottom headed bars in compression. However, this did not occur until unrealistically large deformations had been imposed on the joints.

One bridge column/cap-beam knee joint specimen was tested at the University of California, San Diego [62] with reinforcement provided almost completely by headed reinforcing bars (with the exception of spiral column reinforcement). The research was sponsored by HRC and all of the heads were friction-welded. The specimen was designed to mimic earlier tests using conventional hooked bar anchorage details. The purpose of the test was merely to prove the

acceptability of headed bar details for seismic bridge knee joints. The headed bar anchorage was sufficient to carry the anchorage forces and the specimen failed by plastic hinging at the top of the column member. However, the close spacing of the horizontal bars in the cap beam required staggering of the headed anchorages in order to prevent overlapping of head plates. The staggering of the bars within the anchorage zone necessitated a stub extension of the cap beam length beyond the joint region (Figure 3-17).

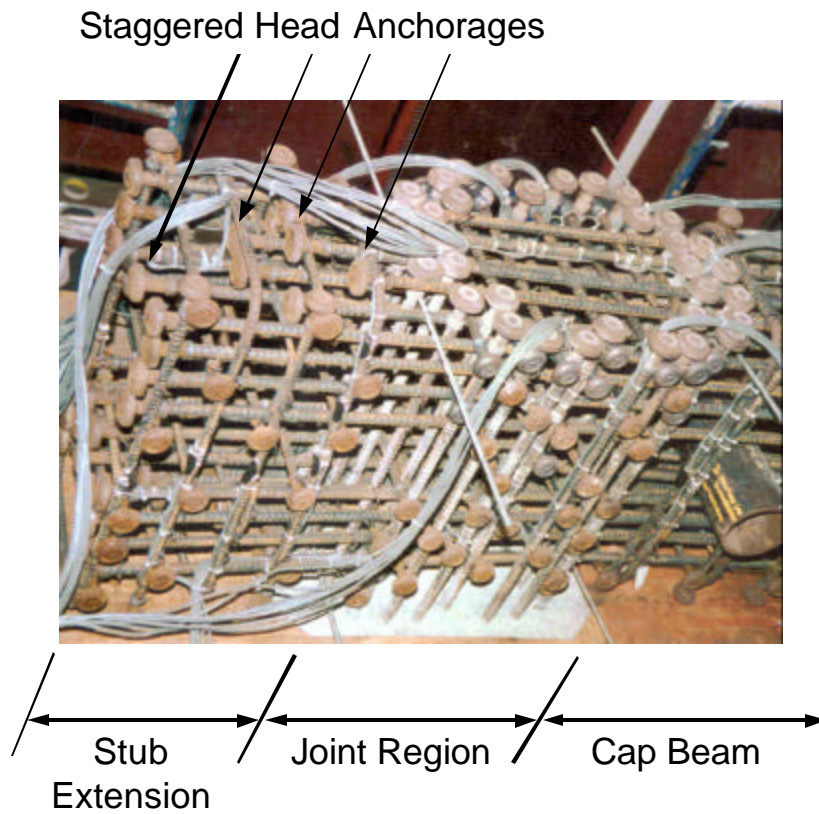


Figure 3-17: Photo of cap-beam/column joint reinforcement from U.C. San Diego study [62]

A follow-up headed bar test at the University of California, San Diego studied the effectiveness of headed reinforcement in a seismic pile/foundation connection [107]. Once again, the research was funded by HRC. They supplied all headed bars used in the specimen. This test was interesting in the fact that Xtender heads were used as anchoring elements for lapped bars. Figure 3-18 shows the basic detail. Short bond bars with large friction-welded heads at one end and Xtender bulb heads at the other were used as bond bars to enhance the anchorage of the pile dowel bars to the foundation slab. This test represents the only known lap splice test of headed bars described in the background literature. Once again, the headed bars were sufficient to provide anchorage and the specimen failed by plastic hinging of the pile element next to the foundation.

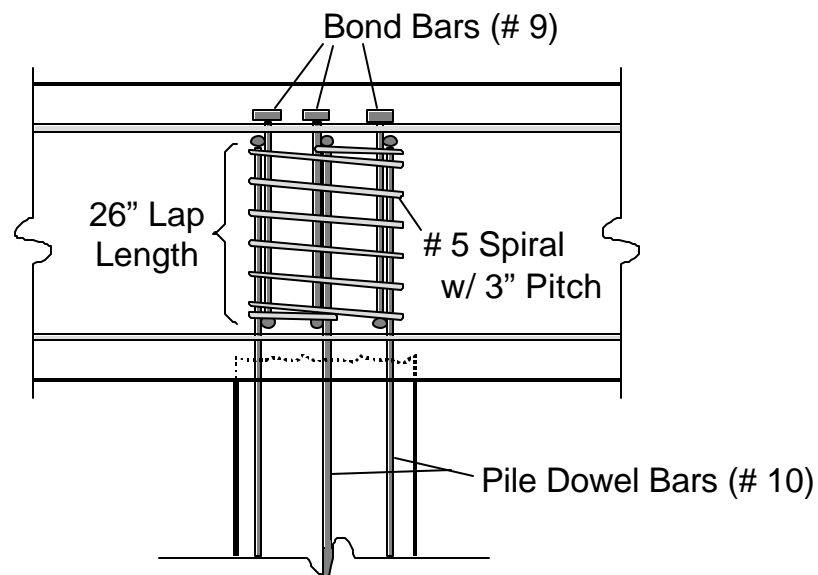


Figure 3-18: Pile/foundation connection studied at University of California, San Diego

Xtender headed bars were studied at the University of Texas at Austin as tie bars for connecting precast bent caps to cast-in-place bridge columns [79]. In the first phase of the study,

which was aimed at developing viable pier-cap connection details for precast bent caps, 18 pullout tests were performed on epoxy-coated headed and non-headed bars embedded into grout-filled pockets. The variables of the pullout tests included bar anchorage (Xtender forged heads or non-headed), bar size (#6, #8, and #11), embedment depth ($5 - 18d_b$), grout pockets versus grouted ducts, confining reinforcement around the outside of the grout pocket, and grout parameters including the brand and the inclusion of pea gravel. Headed bar anchorage underwent four stages: (1) anchorage entirely by bond, (2) formation of splitting cracks in the grout and transfer of bar force from bond to the head, (3) the extension of splitting cracks into the surrounding concrete and the propagation of cracks from the corners of the grout pocket, and (4) failure by yield or concrete breakout. Concrete breakout capacities were compared to the modified CCD equations developed by DeVries [42]. The breakout capacities of the headed bars in the grout pockets were proportional to embedment depth and were about 20% less than the capacities predicted by the modified CCD equations. The reduction in strength was attributed to the influence of cracks propagating from the corners of the grout-filled pockets.

Headed bars were used in several cantilever bridge pier tests at the University of Texas at Austin [23, 118]. The headed bars were tested as anchorage in the CCT and CTT nodes that form at the end of the cantilevered bent and the connection of the bent and the column (Figure 3-19). All of the test specimens were reduced scale, so the headed bars were specially manufactured at the lab. #2 - #5 bar sizes were used with square or rectangular plates fillet-welded to the end of the bar. The relative head areas of the bars varied between 6.5 - 8.8. The researchers found that the headed bars reduced congestion and improved constructability of the cages. The anchorage ability of the headed bars was found to be comparable to hooked bars. Comparisons were made on the

basis of crack width measurements that showed that the performance of the headed bars was comparable to that of hooked bars.

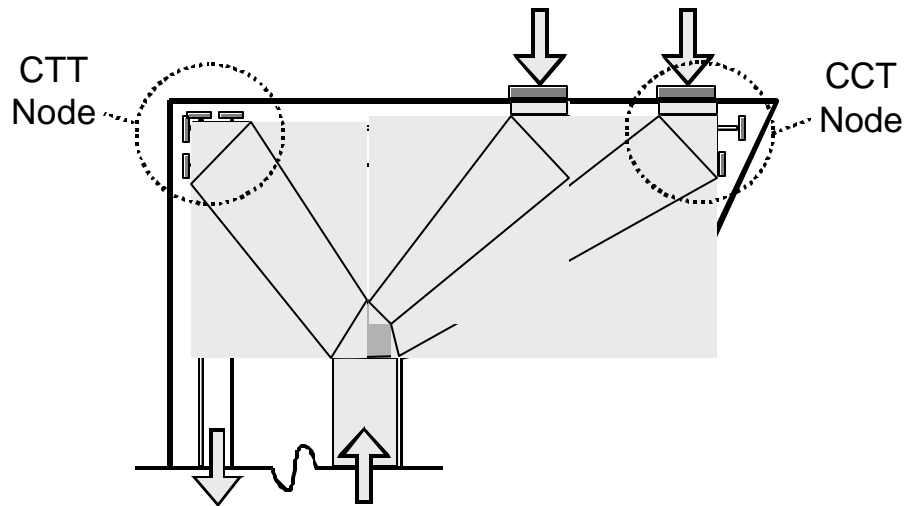


Figure 3-19: Cantilever bridge pier tested at the University of Texas

Following the collapse of the gravity base structure (GBS) of the Sleipner A offshore oil platform on August 23, 1991, a series of full-scale tests were conducted on tri-cell wall joints to verify hypotheses of the collapse causes and to assist in the redesign of the platform. The original and revised plans of the tri-wall cell joint utilized headed bars at a critical juncture and the collapse of the structure was linked to improper anchorage of these headed bars. 10 tri-cell joint specimens were tested by SINTEF in 1992 [38, 63]. Figure 320 shows the basic specimen. Failure was attributed to the short anchorage length provided for the double headed bars and the absence of shear reinforcement within the joint zone. Experimental and analytical results indicated that had the headed bar been lengthened 10" on both ends, the failure mode of the tri-wall cell unit would have shifted to the flexure related mode it was designed for rather than the shear-related

failure that occurred. This experiment does not indicate that the headed bar did not develop within the provided length. Rather it showed that the as-detailed anchorage point of the headed bar did not correspond to the required location for the tension tie based on strut-and-tie modeling and the flow of forces in the tri-cell wall. The failure crack propagated around the head of the bar. The Sleipner A collapse and corresponding structural tests vividly emphasize that good anchorage should not be confused with good detailing.

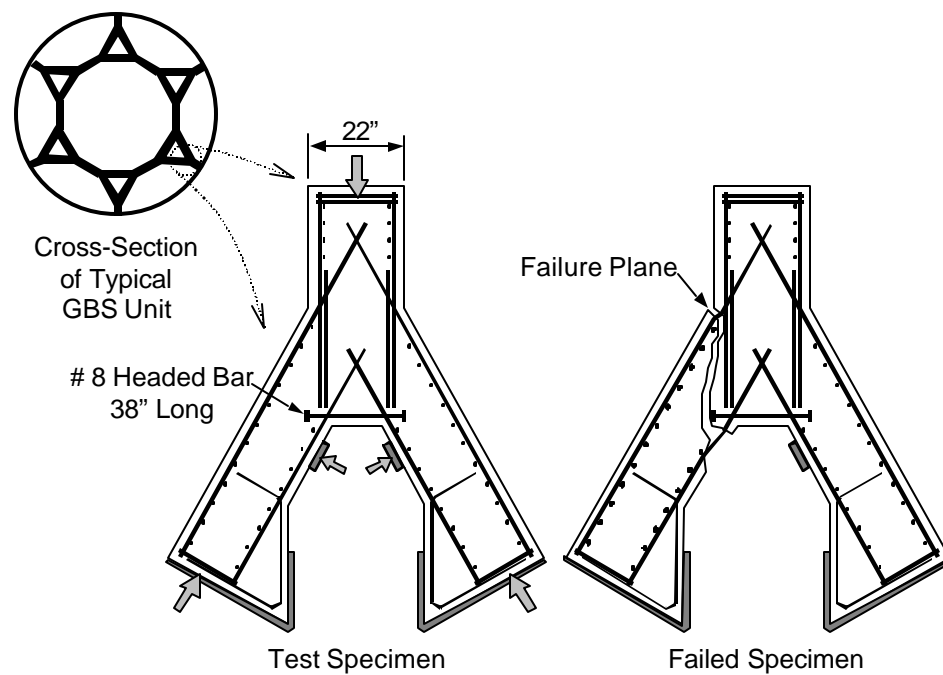


Figure 3-20: Test specimen for Sleipner A collapse investigation

3.4.5.2 Shear and Confining Reinforcement Tests

During the early AOGA (Alaska Oil and Gas) tests on headed bars, a beam test utilizing double-headed stirrups cut from plate steel was tested [29]. The short, deep beam achieved a

substantial capacity and sustained that capacity for a ductility factor greater than 40 (due largely to catenary action). A few years later, the consulting firm hired to perform the AOGA tests (Ben C. Gerwick Inc.), was employed by HRC to test three large scale deep beams utilizing HRC manufactured double-headed stirrups [30]. The primary variable was the transverse reinforcing ratio. The beams were supported so that continuous beam conditions were modeled. All three specimens achieved peak ultimate loads that more than doubled the design loads predicted by ACI code equations. After sustained loading, the capacity of the specimens dropped in a ductile manner to the capacity predicted by the ACI code and that capacity was sustained until the tests were halted.

Following their work on studrails for punching shear reinforcement in flat slabs, Dilger and Ghali began to exam usage of double-headed studs as confining reinforcement for wall and shell elements [43]. Five wall specimens were tested at the University of Calgary. One wall contained no transverse confinement and served as a baseline for experimental results. Two walls were confined with conventional bent cross-ties with a 180° bend at one end and a 135° bend at the other. The remaining two walls utilized double-headed ties provided by Decon. The double headed ties utilized heads with the 10 bar area size used in Decon's Studrail design. Dilger and Ghali found that the double-headed ties provided superior performance to conventional cross-ties. The enhanced performance was due to the fact that the cross-ties did not achieve their full yield capacity before anchorage failure of the bent ends occurred. In contrast, the double-headed ties achieved yield. They also found that the headed ends did not need to engage vertical and horizontal crossing bars in order to achieve yield.

Sixteen large-scale wall elements were tested in the University of Toronto's Shell Element Tester by Kuchma and Collins [64]. Eight of these wall elements contained double-

headed ties as transverse confining reinforcement. The other eight specimens contained no transverse confining reinforcement. Kuchma and Collins found that the capacity and ductility of confined wall elements was superior to that of the analogous unconfined walls. Results of the testing were used to provide transverse confinement modifiers to analytical formulations for use in non-linear finite element computer programs developed at the University of Toronto for design of offshore oil structures.

3.4.5.3 Rehabilitation and Retrofit Studies

The use of double-headed ties to repair earthquake damaged pier walls was studied at the University of California, Irvine [57]. Walls built to 1971 design standards were tested cyclically to failure then repaired using cross-ties or double-headed ties and re-tested. One out of six wall tests utilized double-headed ties manufactured by HRC. The remaining five tests utilized conventional bent-up cross-ties. The wall repaired with double-headed ties was found to perform better than analogous walls repaired with the cross-ties due to the fact that the cross-ties tended to spall the wall side cover as they acquired load and the bent ends of the ties straightened. The double-headed ties were also found to be far easier to install than the cross-ties. It was determined that the heads did not need to engage buckled longitudinal reinforcement in order to provide confinement.

Four earthquake damaged bridge columns were tested the University of California, Berkeley [69]. Three of the columns had severe damage and different repair schemes utilizing HRC double-headed ties or Xtender mechanical couplers were tried on each column. The first column used the Xtender coupling scheme to replace buckled and fractured longitudinal bars. The remaining two columns used double-headed ties placed longitudinally within an external jacket at the base of the columns. The ties were confined transversely by spiral reinforcement and embedded into the footing member of the bridge column specimens. The three repair schemes

were sufficient to rehabilitate the columns to equal or greater capacity than they originally possessed though in some cases the original ductility could not be achieved. The repair schemes were considered successful and the tests proved the potential of the HRC products to be used for seismic rehabilitation of bridge columns.

In addition to the various application studies listed in the proceeding sections, Lenton Terminators were recently used as anchorage for the primary reinforcement in two of four deep beam specimens tested at Purdue University [21]. However, the test specimens were intended to test aspects of structural performance other than anchorage (namely, the performance of diagonal compression struts). Nothing of significance concerning headed bars was noted in the tests other than that the heads provided enough anchorage to sustain yielding of the primary tension steel. Hooked anchorages were used in the remaining two specimens and were also shown to be sufficient.

3.5 RELATED BEHAVIORAL TOPICS

Two phenomena have very similar behavior to the anchorage of headed bars: bearing of rigid plates and anchorage of deeply embedded anchor bolts. These two topics are discussed briefly in this section.

3.5.1 Background on Bearing Capacity

The bearing action of heads very much resembles the bearing action of rigid plates on concrete with the difference that the bond related splitting stresses caused by deformations on the bar disrupt the bearing zone in front of the head (Figure 3-21). Because of the similarities in behavior, it thus seems pertinent to review some of the research on bearing capacity. Only three investigations are summarized herein: the work by Hawkins at the University of Sidney [60, 61],

the work by Niyogi at the Indian Institute of Technology [90, 91, 92], and the work by Williams [116]. These studies contain the most extensive research on concrete in bearing and will suffice for an overview of the subject.

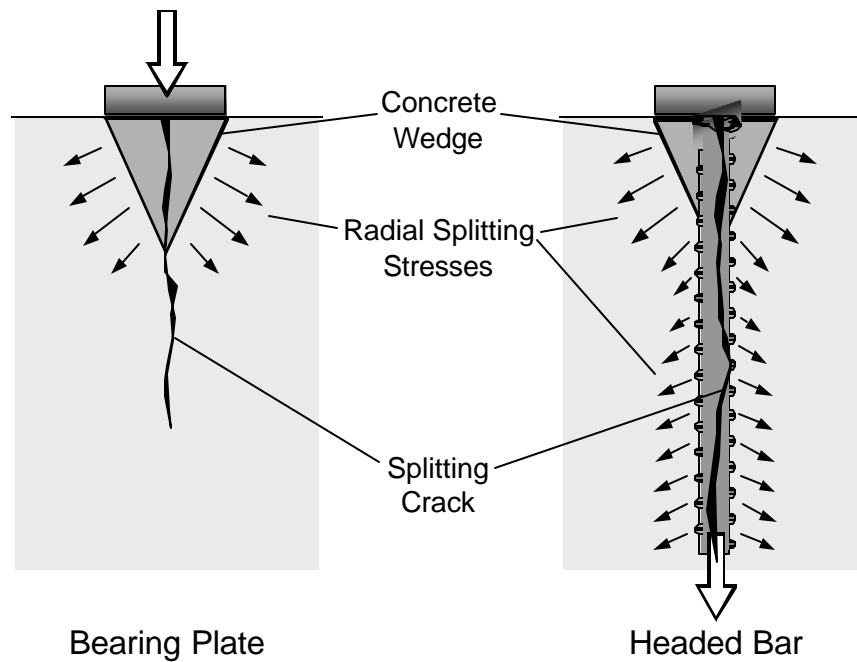


Figure 3-21: Bearing of a rigid plate versus bearing of a headed bar

3.5.1.1 *Hawkins*

In a two part study on the bearing strength of concrete, Hawkins performed 300 tests on concrete cube specimens loaded under 113 different test conditions [60, 61]. Hawkins studied such variables as specimen size, specimen shape, plate size, plate shape, plate stiffness, eccentricity of load, edge loading, concrete strength, maximum aggregate size, and aggregate density (lightweight versus normal). He used a theoretical model of failure to develop an equation for the bearing capacity of concrete which he then compared to his test data. Hawkins modeled bearing as a

mechanism through which a wedge of concrete forms underneath the bearing plate that subsequently splits the surrounding concrete mass apart as it is pushed downward. Movement of the wedge is resisted by shear friction along the wedge surface and tensile stresses in the surrounding concrete. The resulting model contains components that are added to one another which are proportional to f'_c and $\sqrt{f'_c}$ respectively. The equation that Hawkins derived for concentric loading by a rigid plate is presented below:

$$P_n = f'_c A_1 \left[1 + \frac{K}{\sqrt{f'_c}} \left(\sqrt{\frac{A_2}{A_1}} - 1 \right) \right] \quad (3-9)$$

P_n = the bearing load supported by the plate (lbs)

f'_c = the concrete cylinder strength (psi)

A_1 = the area of the load plate (in²)

A_2 = the effective unloaded area of concrete (in²)

K = a constant derived from concrete properties of tensile strength and the angle of internal friction which varied from 50 – 65. Hawkins recommended a value of 50 for design purposes.

Additionally, Hawkins recommended that the effective unloaded area should be concentric with and geometrically similar to the load plate. Furthermore, the area of the effective loading area may be as much as 40 times the area of the load plate before a limit must be imposed. Hawkins also suggested alternative formulations for strip loading and edge loading of concrete surfaces and proposed a criteria by which a load plate could be considered rigid.

3.5.1.2 Niyogi

Niyogi tested 858 unreinforced concrete specimens under 327 different test conditions [90, 91] and 106 reinforced concrete specimens under 69 different test conditions [92]. He studied variables such as the shape and size of the specimen, the shape and size of the load plate, the position of the load plate, the rigidity of the support conditions for the specimen, the effect of concentrated loading from both ends of the specimen, the concrete strength, and the amount and form of reinforcement under the load plate. Niyogi determined empirical expressions for bearing strength for concentric and eccentric load conditions. His expression for bearing strength under concentric conditions is listed below:

$$P_n = A_1 f_{cc}' \left[0.42 \left(\frac{h_1}{2c_2} + \frac{h_2}{2c_1} + 1 \right) - 0.29 \sqrt{\left(\frac{h_1}{2c_2} - \frac{h_2}{2c_1} \right)^2 + 5.06} \right] \quad (3-10)$$

P_n = the bearing load supported by the plate (lbs)

f_{cc}' = the concrete cube strength (psi)

A_1 = the area of the load plate (in²)

h_1 = the width of the load plate (in)

h_2 = the breadth of the load plate (in)

$2c_2$ = the width of the specimen (in)

$2c_1$ = the breadth of the specimen (in)

Niyogi's notation was different than the notation listed above. The notation has been altered to resemble the notation used by DeVries for headed bars (see Figure 3-10). Also note that Niyogi's formula is related to the compression strength of concrete cube tests, not the typical cylindrical

compression strength. Cube tests generally provide compressive strength values 15-20% higher than cylinder tests of the same concrete. The conversions $f_c' = \frac{5}{6} f_{cc}'$ or $\frac{6}{7} f_{cc}'$ are typically used.

Niyogi made several observations from his study:

- The bearing capacity of eccentrically loaded blocks was greater than the capacity predicted using a concentric reduced area to calculate load capacity.
- The bearing capacity was affected by the height of the specimens when the breadth and width were greater than the height. Beyond that point, the capacities leveled off. Specimens with smaller ratios of unloaded area to load plate area ($A_2/A_1 < 16$) showed decreasing capacity with increasing specimen height. Specimens with larger ratios ($A_2/A_1 > 16$) showed increasing capacity with increasing specimen height.
- The support medium of the specimen (see Figure 3-22) affected its capacity when the specimen blocks were shallow (height/width < 2). The more compressible the support medium, the less the capacity of the blocks.
- Simultaneous concentrated loading on both ends of the specimen (Figure 3-22, ii.) resulted in reduced bearing capacity. The reduction in bearing capacity was diminished as the specimen height was increased but did not disappear even when the height was increased to twice the width dimension.

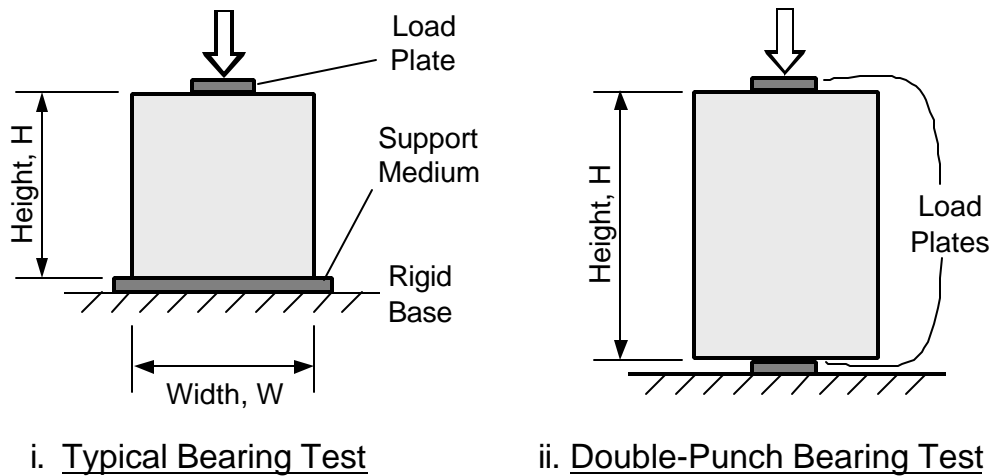


Figure 3-22: Bearing tests on concrete blocks

- At low ratios of unloaded to loaded area ($A_2/A_1 < 4$), the bearing strength was directly proportional the concrete strength, but as the A_2/A_1 ratio was increased, the bearing capacity was proportional to a lesser power of concrete strength.
- A size effect was observed for geometrically proportional specimens of varying sizes. Bearing capacity diminished as the dimensions of the specimen and load plate increased (Figure 3-23).
- Large diameter spirals provided the most effective reinforcement for bearing capacity. The spiral steel closest to the load plate was the most effective portion of the spiral.

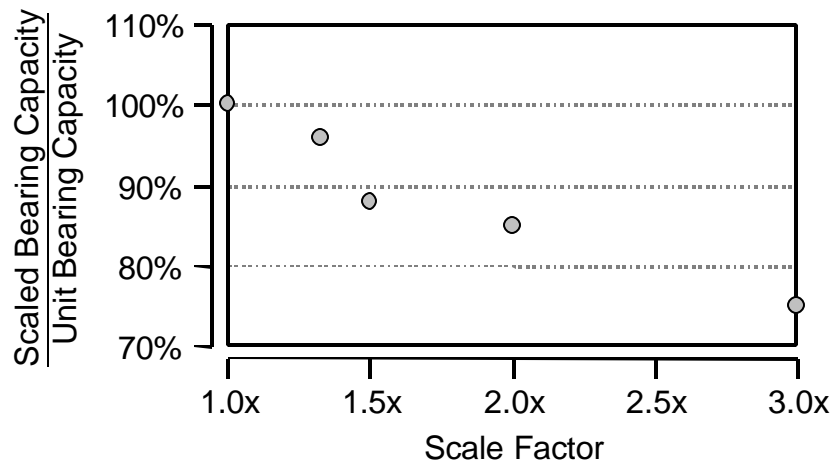


Figure 3-23: Niyogi's size effect data

3.5.1.3 Williams

Williams performed more than 1500 tests under 382 different test conditions [116]. In addition, Williams collected a database of test results from the array of literature on bearing capacity or related behavior such as post-tensioned anchorage plates. His experimental work was aimed at filling in the gaps left in the experimental database. He studied such variables as specimen height, the effect of a softening medium placed between the load plate and the concrete surface, the effect of the concrete surface condition (trowelled or cast flat), eccentric loading, the effect of the secondary width dimension, the effect of support friction, the size effect produced by using a micro-concrete with a very small maximum aggregate size, and the effect of a lateral shearing component of load on capacity. After performing a regression analysis of the combined database of his work and previous investigations he determined that the following equation best predicted the bearing capacity of concrete:

$$P_n = 6.92 \cdot A_1 f_{ct} \left(\frac{A_2}{A_1} \right)^{0.47} \quad (3-11)$$

P_n = The bearing load supported by the plate (lbs)

f_{ct} = The concrete tensile strength (determined from split cylinder tests) (psi)

A_1 = The area of the load plate (in²)

A_2 = The effective unloaded area of concrete (in²)

For simplicity, Williams recommended that an exponent of 0.5 be used rather than 0.47 for the A_2/A_1 ratio.

In addition, Williams observed the following:

- Specimens with height/width ratios greater than 1.5 were unaffected by the supporting medium on which they reacted.
- Bearing capacity was affected by the placement of a softening medium between the load plate and the concrete surface. In general, the softer the load medium, the lesser the bearing capacity.
- Bearing capacity was affected by the friction and rigidity of the support medium. In general, the softer the support medium and the less friction provided by the support medium, the lesser the bearing capacity.
- Bearing capacity was reduced when the contact surface between the load plate and the concrete surface was not uniform (ie. when the concrete bearing surface was trowelled rather than cast flat).
- The bearing capacity was determined by the resistance of the specimens to splitting, therefore the tensile strength, not the compressive strength, of the concrete is the governing factor for bearing resistance.

- Because capacity was governed by lateral splitting, the affect of lateral tensile loads on capacity can severely reduce the bearing capacity. He did not examine the effect of lateral compression loads.
- For edge loading, increases in the secondary cover dimension (see Figure 3-24) can enhance the bearing capacity. This increase in capacity diminished once the secondary cover dimension exceeds four times the width of the load plate.

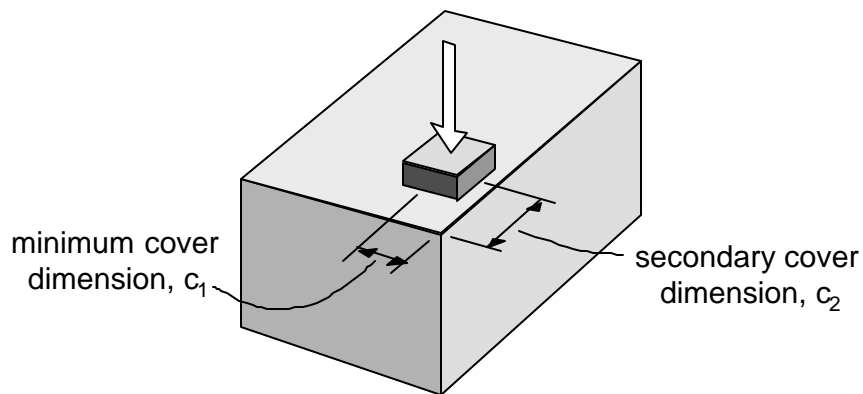


Figure 3-24: Minimum and secondary cover dimensions

3.5.2 Deeply Embedded Headed Anchor Bolts

Deeply embedded headed anchor bolts are frequently used to connect steel columns to concrete support blocks or drilled piers. Deeply embedded headed anchor bolts differ from shallow embedment anchors by the nature of their failure mechanism. Shallow embedment headed anchors fail by the formation of a breakout cone which pulls out of the face of the concrete (see Figure 3-11). Deeply embedded anchors fail by side spalling of the concrete cover near the anchor head which is referred to as side blow-out (see Figure 3-13). DeVries' [42] pullout tests reproduced these two failure modes for headed bars. However, prior to DeVries' research, several

studies on the anchorage behavior of deeply embedded headed anchor bolts were performed at The University of Texas in Austin and the University of Stuttgart. The behavior of headed anchor bolts is very similar to the behavior of the headed bars. This section summarizes the research on deeply embedded headed anchor bolts and the similarities and differences in anchorage behavior of headed bars and headed anchor bolts. Emphasis is placed on deep embedment tests because their side blow-out behavior resembles the failure modes which occur in this investigation much more than the concrete breakout failure of shallow embedment tests. Due to the importance of the model for prediction of side blow-out capacity, some in depth background into the development of the model is necessary.

3.5.2.1 *Lee and Breen*

In the 60's Breen [31] and Lee [68] studied the development length of anchor bolts cast into square footings. Breen performed 36 bolt tests using the test setup shown in Figure 3-25. He studied variables such as bolt diameter ($1\frac{1}{4}$ " to 3"), embedment depth ($10d_b$ or $15d_b$), and the presence of a nut or a washer and nut at the end anchorage of the bolt. His concrete strengths ranged from 3.2 to 5.3 ksi. Lee performed a follow-up study on 26 anchor bolts using the same type of specimen. In some tests, he modified the load arrangement slightly so that the maximum footing moment occurred at the level of the bolt end anchorages. Lee studied variables such as the clear cover ($1d_b$ to $4d_b$), cyclic loading, the shape of the footing (square or circular), concrete strength (2.5 to 6.0 ksi), and the use of 90° bend end anchorages. Because many of Breen's bolt specimens yielded before failure of the concrete occurred, Lee used higher strength bolts in his tests.

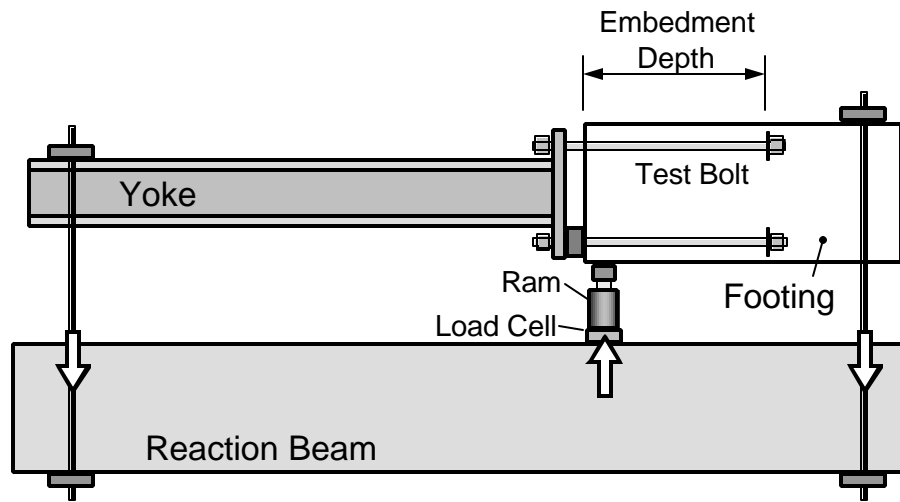


Figure 3-25: Test specimen used by Lee and Breen

Lee and Breen observed the following:

- Bolts failed by one of three mechanisms: longitudinal splitting of the concrete cover similar to the failure of a deformed bar, side blow-out of the cover over the head, or fracture of the bolt steel.
- Initially, adhesion of the bolt shaft to the concrete provided bond anchorage. However, as the bolt load was increased, the bond of the bolt shaft deteriorated until full anchorage was provided by the head only. This behavior was determined by analysis of the loaded end slip.
- The method of loading (varied by Lee) affected the loaded end slip but not the ultimate strength of the bolt.
- The shape of the drilled shaft footing did not affect the slip or ultimate strength behavior of the bolt.
- The primary variables affecting bolt anchorage were cover and concrete strength.

3.5.2.2 *Hasselwander and Lo*

In the 70's Hasselwander and Lo [58, 59] conducted 35 full-scale and 29 model bolt tests using specimens similar to those used by Lee and Breen. The primary purpose of their study was to develop design equations for the use of deeply embedded high strength anchor bolts. The variables studied in their test program were: bolt diameter ($1/2''$, $1''$, or $1\ 3/4''$), embedment depth ($10d_b$, $15d_b$, or $20d_b$), clear cover ($1d_b$ to $4.5d_b$), bearing area ($A_{nh}/A_b = 1.9$ to 19.3), cyclic loading, lateral shear loading of the bolt, bolts in groups of two (center spacing = $5''$, $10''$, or $15''$), and transverse reinforcement in the form of hairpins (1 or 2 #4 bars placed close to the head).

Hasselwander and Lo observed the following:

- Bolts failed by the three mechanisms previously observed by Lee and Breen. Splitting or spalling of the concrete cover was preceded by the formation of a wedge of concrete at the anchor head that produced lateral splitting forces.
- The primary variables affecting bolt capacity were concrete strength, clear cover, and the bearing area of the head.
- Cyclic loading at or below the service level did not significantly affect the strength or behavior of the anchor bolt.
- Transverse reinforcement significantly increased the strength and ductility of anchor bolts with shallow cover.
- Lateral shear loading significantly reduced the tensile capacity of the bolt.
- The capacity of individual bolts in groups was lower than the capacity of individual bolts in tension. At the spacings studied, the two bolt groups had total capacities approximately equal to the capacity of individual bolts.

Hasselwander performed a regression analysis of the data from bolts that failed by wedge splitting (longitudinal splitting of the cover over the bolt) and developed an equation for the capacity of anchor bolts loaded in tension:

$$T = 140 A_{nh} \sqrt{f'_c} \left[0.7 + \ln \left(\frac{2c'}{d_w - d_b} \right) \right] \quad (3-12)$$

T = ultimate capacity of a single anchor bolt (lbs)

A_{nh} = net bearing area of the anchor head which is limited to $4d_b^2$ (in²)

d_b = bolt diameter (in)

d_w = washer (head) diameter (in)

c' = clear cover to bolt (in)

Equation 3-10 is limited to anchor bolts with embedment depths greater than $12(d_w - d_b)$.

3.5.2.3 *Furche and Eligehausen*

In the 80's, Furche and Eligehausen [49] conducted 35 tests of single headed anchors in specimens similar to DeVries'. The variables in their study included embedment depth ($h_d = 4''$ to $20''$), cover dimension ($c_1 = 1.6''$ to $3.1''$), head area ($A_{nh} = 0.41$ to 1.71 in²), and the head angle ($\theta_{head} = 5^\circ, 20^\circ, \text{ or } 90^\circ$). Figure 3-26 describes the head angle. Their concrete strength was kept constant at 3.8 ksi as was their bolt diameter at 1''.

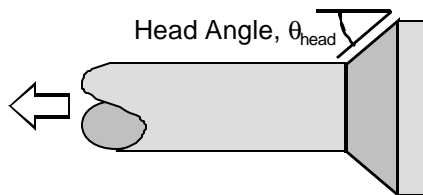


Figure 3-26: Definition of head angle

Furche and Eligehausen's specimens failed by one of two modes: concrete breakout or side blow-out. The transition from concrete breakout failure to side blow-out was dependent on the ratio of cover dimension to embedment depth and the ratio of embedment depth to head bearing area. They determined an equation to define the critical cover/embedment ratio as a function of embedment/bearing area ratio:

$$\frac{c_1}{h_d} = \frac{0.06}{\left(\sqrt{A_{nh}/h_d} - 0.1\right)} \quad (3-13)$$

c_1 = cover dimension (in)

h_d = embedment depth (in)

A_{nh} = net bearing area (in²)

Figure 3-27 plots equation 3-11. Cover/embedment values that plot above the transition line fall in the region where concrete breakout failure should occur. Values below the transition line fall in the region of side blow-out failure.

Furche and Eligehausen developed an equation to define the side blow-out capacity of headed anchors:

$$T = 6.4c_1\sqrt{A_{nh}f'_c} \quad (3-14)$$

T = ultimate capacity of a single anchor bolt (lbs)

f'_c = concrete cylinder strength (ksi)

The variables c_1 and A_{nh} are as defined for equation 3-11. Equation 3-14 was produced from a regression analysis of Furche and Eligehausen's data as well as the published data of

Hasselwander and Lo [58]. Furche and Eligehausen recommended an additional factor of 0.8 to produce a 5% fractile capacity.

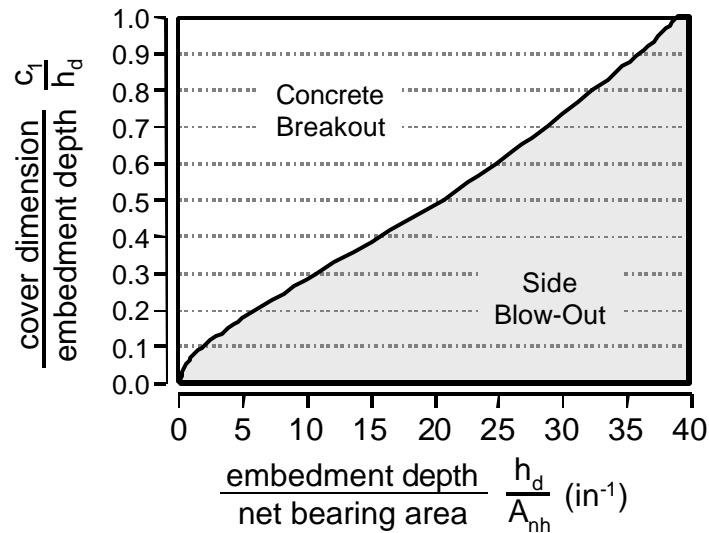


Figure 3-27: Furche and Eligehausen's transition of failure modes for headed anchors

Additionally, Furche and Eligehausen observed the following:

- Of the bolts which failed by side blow-out, the diameter of the blow-out cone was between 6 to 8 times the cover dimension, c_1 .
- Measurements of lateral concrete deformations indicated that lateral bulging of the concrete cover did not begin until the peak capacity of the bolt was achieved.
- Shallower head angles resulted in significantly reduced anchorage capacities. For the shallow angles tested by Furche and Eligehausen (5° and 20°), the capacity of the bolts was reduced by as much as 50% from the capacity of bolts with head angles of 90° .

3.6 CODE PROVISIONS

There are no code provisions that provide direct guidance for the detailing of headed reinforcing bars. Both Wright and McCabe [119] and DeVries [42] have proposed anchorage provisions for headed bars which have already been presented. However, neither of the proposed guidelines has been included in the 2002 ACI 318 Building Code. The few guidelines that do exist among the design codes are discussed in this section. The ACI and AASHTO codes are discussed as well some provisions from the Canadian design and a controversial ASTM specification. Guidelines for bearing plates will also be discussed since they closely resemble the theoretical anchorage behavior of headed bar heads.

3.6.1 U.S. Mechanical Anchorage Provisions

Both the ACI 318 code [2] and the AASHTO Bridge Design Specifications [1] use nearly identical language for their mechanical anchorage provisions. Currently, designers using headed bars would probably take their guidance from the provisions for mechanical anchorage. Section 12.6 of the ACI code and Section 5.11.3 of the AASHTO code provide provisions for mechanical anchorage. Both provisions state the following:

- Any mechanical device capable of developing the strength of a reinforcing bar without damaging the concrete is allowed.
- Such devices may consist of a combination of the mechanical anchorage and bond of the additional embedment length of reinforcement between the point of maximum bar stress and the mechanical anchoring device. The commentary of both provisions specifically states that the yield strength of the bar does not need to be entirely supported by the mechanical anchorage provided that the combination of bond and mechanical anchorage can support the yield strength.

- Documentation of the sufficiency of the mechanical anchoring device shall be provided in contract drawings or presented to the pertinent building official.

Otherwise, no guidelines for design and use of mechanical anchoring devices is provided.

3.6.2 Canadian Shear Provisions

The Canadian Code, CSA A23.3-94 for Design of Concrete Structures [9] allows for the use of headed shear reinforcement in Clause 13.4.8 of the code. Sub-clauses 13.4.8.1-3 of this code requires the following:

- The headed anchorage shall be capable of developing the full yield strength of the bar.
- The head area of the bar shall be at least 10 times the area of the bar unless experimental evidence justifies a smaller size.
- The factored total shear stress resistance (in SI units) shall be no greater than $0.8\lambda\phi_c\sqrt{f'_c}$ which is 1.33 times greater than the total allowed for members with conventional shear reinforcement.
- The factored shear stress contribution from concrete (in SI units) shall be no greater than $0.3\lambda\phi_c\sqrt{f'_c}$ which is 1.5 times greater than that allowed for members with conventional reinforcement.

The second statement undoubtedly derives from the headed stud research performed by Dilger and Ghali [44, 86] at the University of Calgary. The increases in concrete shear capacity result from the enhanced confinement effect that headed bars should presumably provide.

3.6.3 ASTM Specification for Weld Connected Heads

The ASTM A970 Specification for Welded Headed Bars [5] applies to headed bars in which the head is connected to the bar by means of any welded connection. The specification deals primarily with quality control standards for the head-bar weld connection, but also contains requirements for head sizes. Specification 7 deals with the quality control of the weld connection and mandates procedures for several performance tests including static tension and bend tests of the head-bar connection. Additionally, Appendix X2 includes non-mandatory recommendations for metallurgical and hardness tests of the head and welded zone. The appendixes (in X3.6-7) also recommend extensive record keeping of automated production process parameters specifically citing force, temperature, and revolutions, all of which are parameters associated particularly with friction-welded heads.

Specification 5 “Materials and Manufacture” is the most significant for structural designers. This is the specification that mandates head sizes for welded headed bars. Table 1 lists gross head area requirements that correspond to 10 bar areas for each bar size (or $A_{nh}/A_b = 9$). Note 2 of the table states that such head sizes are to ensure that concrete crushing failure does not occur underneath the head based on a concrete compressive strength of 30 MPa (4.4 ksi) and a bar yield strength of 420 MPa (61 ksi). Note 4 states that the specified head sizes are necessary for anchorage of the bar by the head only. Heads with smaller sizes are permissible provided that the headed bar manufacturer provide documentation that confirm the suitability of the head for the intended application (Specification 5.3).

This ASTM Specification is controversial because of the head size specifications. Some designers and manufactures feel that it is inappropriate for the ASTM document to specify head size and that that decision should rest with the structural engineer. In a correspondence between

this author and Steven McCabe of the University of Kansas who was the author of the standard [123], Mr. McCabe stated that the head size recommendations were developed out of a collective work including the SINTEF tests performed for Metalock as well as “hundreds of studies of these [headed bars] in various locations on both sides of the Atlantic.” The size recommendations were also influenced by the inclusion within the Canadian CSA Code of a 10 bar area requirement for head size.

The quality control measures specified in the document also bear striking resemblance to those practiced by HRC. The language in parts of the code suggests a bias towards friction-welded headed bars over other potential forms of welded headed bars. Mr. McCabe stated that he worked with representatives from HRC during the formation of the ASTM specifications. Given the fact that HRC is the only manufacturer of friction welded headed bars at the current time and thus have the only documented methods for the quality control of welded headed bars, their standards of production may have overly influenced the writing of the code.

As a result of the head size requirements and the language of the quality control standards, the ASTM specification has been viewed as biased towards HRC’s headed bars and biased against their competitor, ERICO’s Lenton Terminator. Due to these controversies over the first draft of the ASTM specification, new drafts of the A970 Specification are currently under development. Within the newer drafts, inclusion of quality control standards for other forms of head-bar connections such as the tapered thread used by ERICO may also be included and the minimum head size standards may also be modified or dropped [123].

3.6.4 U.S. Bearing Strength Provisions

Both the ACI and AASHTO code contain similar provisions regarding the bearing strength of concrete. Bearing strength is covered in Section 10.17 of the ACI code and Section 5.7.5 of the AASHTO code. Both codes give the following equation:

$$P_n = 0.85f'_c A_1 \sqrt{\frac{A_2}{A_1}} \quad (3-15)$$

P_n = concrete bearing strength (lbs)

f'_c = concrete compressive stress (psi)

A_1 = loaded area (in²)

A_2 = notional area defined by a frustum projected beneath the loaded surface, as defined in Figure 3-28 (in²)

Because there is a limit imposed on the maximum size of A_2 (see Figure 3-28), the maximum bearing strength provided by Equation 3-13 is $1.7f'_c A_1$.

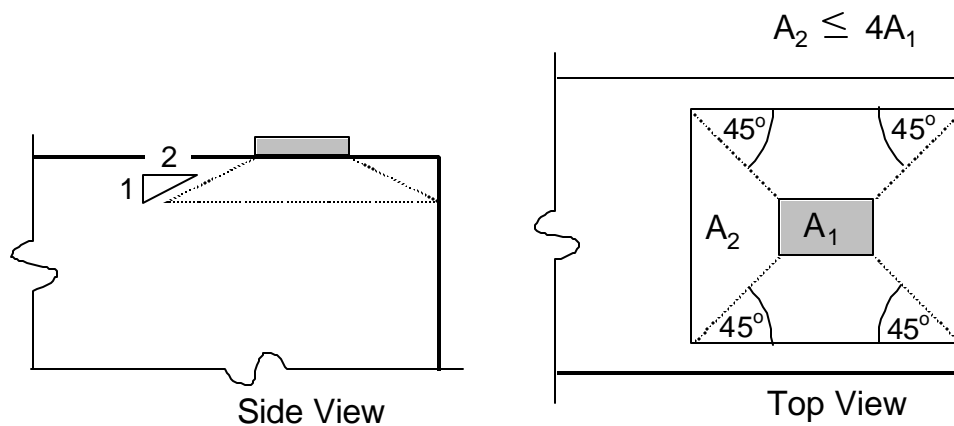


Figure 3-28: Definition of notional area

3.7 FINAL COMMENTS

There are many details from the collection of reviewed literature in this chapter that warrant reflection.

First, among the research that has been performed on headed bars, a disproportionate amount of the work has used only one type of headed bar, HRC's friction welded head. Of the 15 research projects on headed bars that were reviewed, only one project has represented both HRC's and ERICO's head types in the research (the Clarkson study), and even then, the experiments with the friction-welded heads and the threaded heads were not directly comparable to one another. The early Caltrans study was also comprehensive in its representation of a variety of head types, and the pullout tests by DeVries and Bashandy at the University of Texas represented a variety of head sizes. However, despite these exceptions, the predominance of the research has used only one head type: a friction-welded head of a size of about 10 bar areas. This is a major shortcoming of the available research and should be addressed in future studies.

The studies by Caltrans (1974) and the University of Texas (DeVries) have both demonstrated that bond can be a significant component of headed bar anchorage and that the current development length equations can be used to reasonably estimate the contribution of bond stress. Data from Caltrans, the University of Texas, and Clarkson have also indicated that, because of the contribution of bond, head sizes smaller than 10 bar areas can work for certain situations particularly when the embedment length of the bar is large.

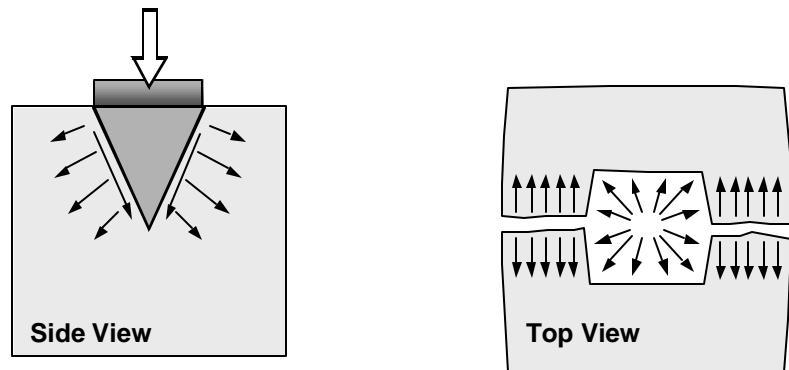
The bearing capacity study by Williams has shown that capacity is proportional to the square root of the plate area times the effective unloaded area. If the effective unloaded area is considered to be four times the minimum cover dimension squared, $4c_1^2$ (essentially the largest square which can be inscribed underneath the load plate), then the following results:

$$P_n \propto A_1 \sqrt{\frac{A_2}{A_1}} = \sqrt{A_1 A_2} = \sqrt{A_1 (4c_1)^2} = 2c_1 \sqrt{A_1} \quad (3-16)$$

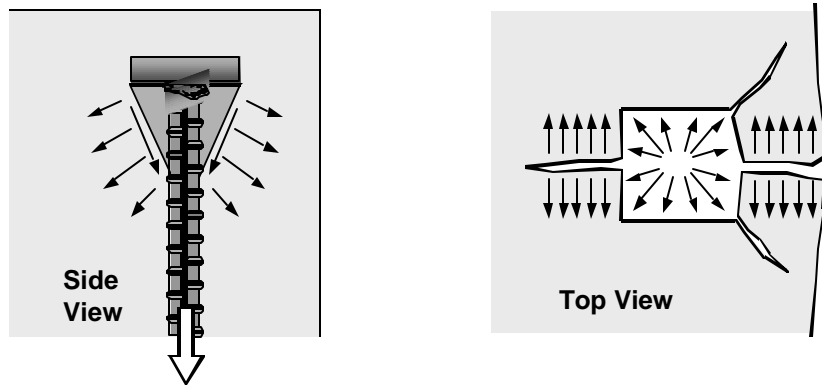
The final product shown above is very similar to the basic side blow-out formula which DeVries used to model the behavior of the deeply embedded headed bars and Furche and Eligehausen used for deeply embedded anchor bolts:

$$N_{sb} = 144c_1 \sqrt{A_{nh}} f'_c \propto c_1 \sqrt{A_{nh}} \quad (3-17)$$

The similarity between the two equations tends to suggest a similarity in behavior. Side blow-out failure and bearing failure both involve the formation of a compressed wedge of concrete at the head or bearing plate. Forward movement of this wedge is resisted by friction parallel to the surface of the wedge and lateral tension stresses in the surrounding concrete. In the case of a bearing plate test, lateral tension results in through splitting of the concrete block specimen (Figure 3-29, part i.). In the case of a headed bar or anchor bolt which is close to an edge, the lateral tension results in splitting and spalling of the concrete surface that provides the least cover (Figure 3-29, part ii). The three types of tests demonstrate similar behavior and their capacities show a dependency on the same variables. Thus, it is reasonable that the collected data from bearing tests, deeply embedded anchor bolt tests, and deeply embedded headed bar tests could be assimilated into one database representing a class of behavior which could be used to calibrate a formula for the bearing capacity in all three types of applications.



i. Bearing Failure



ii. Side Blow-Out

Figure 3-29: Splitting mechanism in bearing and side blow-out failures

Another similarity in behavior between bearing studies, anchor bolt studies, and headed bar studies appears in the term for the modification factor for radial stress disturbances, Ψ_1 . While such a term does not appear in any of the bearing capacity formulas, experimental evidence has suggested that such a term might be appropriate. The Ψ_1 term recognizes an improvement in capacity for headed bars in which the secondary cover dimension, c_2 , is greater than the minimum cover dimension, c_1 (see Figure 3-30). Williams noted that the capacity of an edge plate was enhanced when additional width was added to the sides of his specimens. Niyogi also noted that

capacity calculations based solely on the projection of the load plate in defining the effective unloaded area tended to under-predict the measured capacities of uni-axial eccentric specimens. Williams' and Niyogi's experimental observations suggest that bearing capacity improves as the ratio c_2/c_1 increases and a Ψ_1 type term would be appropriate for bearing capacity formulations.

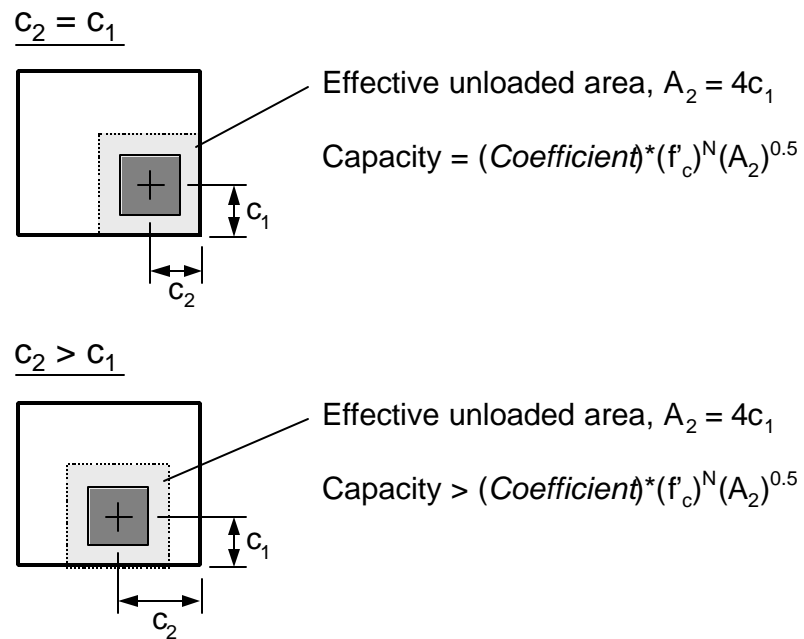


Figure 3-30: Effect of the secondary cover dimension, c_2

Chapter 4: Background on Strut-and-Tie Modeling

4.1 INTRODUCTION

Strut-and-Tie Modeling (STM) is a detailing and ultimate strength calculation procedure for discontinuity regions within structures. When point loads are introduced onto structural members or abrupt changes in cross-section are introduced, conventional methods of plane section analysis are no longer sufficient. Such locations (termed disturbed regions) are generally detailed using rules of experience or empirical guidelines based on limited research data. Such methods are not based in structural mechanics for ultimate strength determination. Empirical methods are limited to the experience base from which the method derives. It is possible to analyze disturbed regions using complex analysis procedures such as finite elements. However, the computer software necessary for such computation is not readily available to many designers. Furthermore, the cost and time of such analysis, which might constitute a large percentage of the designer's effort, does not always reflect the material and construction cost of the disturbed regions, which may represent only a minor part of the cost of a complete construction project. Strut-and-tie modeling represents an in-between design method for complex structural details that has a basis in mechanics but is simple enough to be readily applied in design.

STM is a method involving the idealization of a complex structural member into a simple collection of struts, ties, and nodes representing, in a general manner, the flow of stress paths within the member. Figure 4-1 shows some typical structural components for which STM could be applied. STM is ideal for deep members, joints, supporting brackets or corbels, dapped beam ends, anchorage zones for post-tensioning, and many other complex structural components.

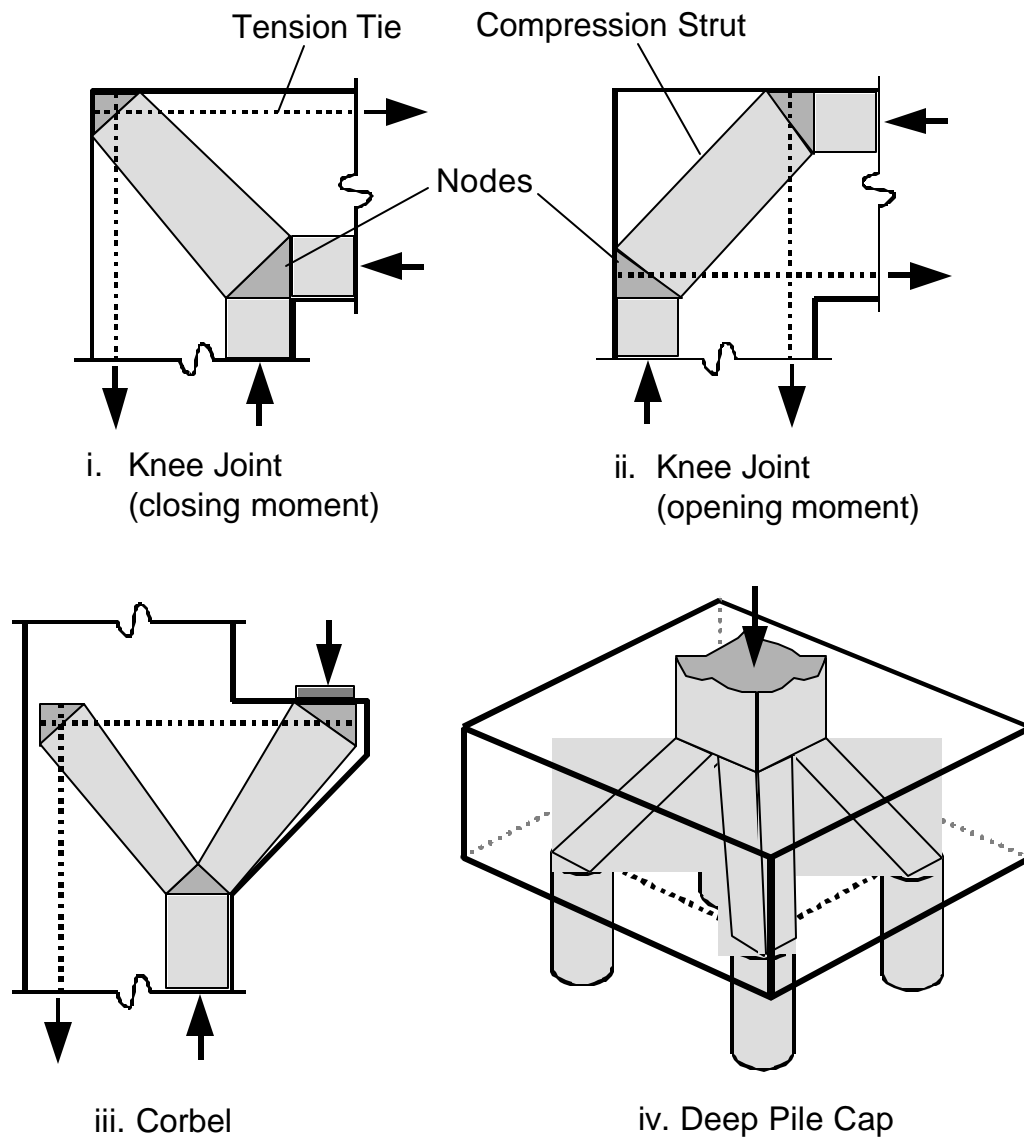


Figure 4-1: Examples of strut-and-tie modeling

STM is derived from plasticity theory. STM is a lower bound solution method. According to the theory of plasticity, any statically admissible stress field that is in equilibrium with the applied loads and in which stress levels are on or within the material yield surface

constitutes a lower bound solution [89]. Plastic material behavior is a primary assumption of plasticity theory. Strain capacity of the materials is a fundamental requirement to fully satisfy that a lower bound solution occurs. Though plain concrete lacks considerable plastic stress-strain behavior, properly detailed, confined concrete can sustain ductile compressive strains (Figure 4-2). Plasticity theory has been applied to the design of reinforced concrete but only with the proviso that strain limits within the concrete are limited or adequate detailing is provided to enhance the ultimate strain limits of the material.

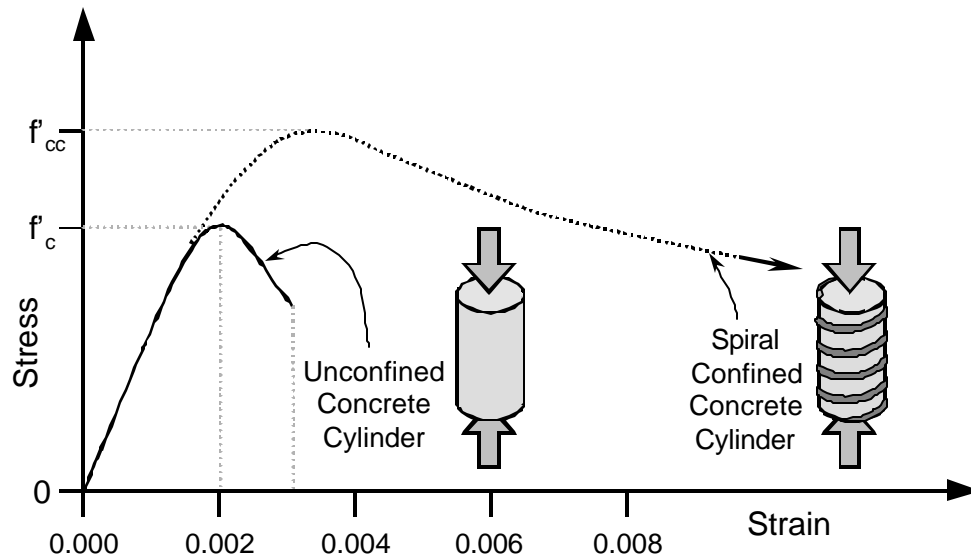


Figure 4-2: Deformation response of plain and confined concrete

STM involves the construction of a truss mechanism contained within the boundaries of the member being analyzed. The truss mechanism is composed of struts that model concrete compression fields, ties that model tensile steel reinforcement, and nodes that represent the localized zones in which the tensile steel is anchored into the concrete and strut forces are transferred into the ties. The struts and ties carry only uniaxial stresses. This truss mechanism must

be stable and properly balance the applied loads. Failure of the truss mechanism is dictated by yielding of one or more ties or by excessive stresses within the struts or nodes or by an anchorage failure of the reinforcement at one of the nodes. When used properly to detail a structural member, only the first of the aforementioned failure modes should occur. The choice of acceptable concrete stress levels for struts and nodes is an empirical add-on to conventional plastic theory designed to allow for the use of concrete. Allowable stress levels are chosen to prevent local crushing or splitting of struts and nodes and are generally based on the degree of confinement available to the concrete.

In order to apply STM to structural concrete members, it is convenient to delineate disturbed regions from the other parts of the structure that will follow plane section material behavior and which can be analyzed using conventional beam analysis (Figure 4-3). Such regions of the structure are typically termed bending or B-regions. Likewise, the disturbed regions are termed D-regions. The selection of the D-region boundary is based on St. Venant's Theorem and the transition of local stress fields into full section stress fields. Typically, a boundary line is drawn at a distance of 1-1.5 times the depth of the member from the point of applied load or the edge of the abrupt change in section. A static solution is found for the member as a whole to determine all reaction forces, moment diagrams, and the like. Then cracked section analysis (Figure 43, ii.) is conducted within the B-regions to determine boundary stresses for the D-regions. Following this step, the D-region can be isolated and treated as a separate entity with all reaction forces and boundary stresses treated as externally applied loads. Consideration must also be given to the placement of reinforcement within the B-regions and the continuity of that reinforcement into the D-region. Figure 4-4 shows the separation of a dapped beam into D- and B-regions.

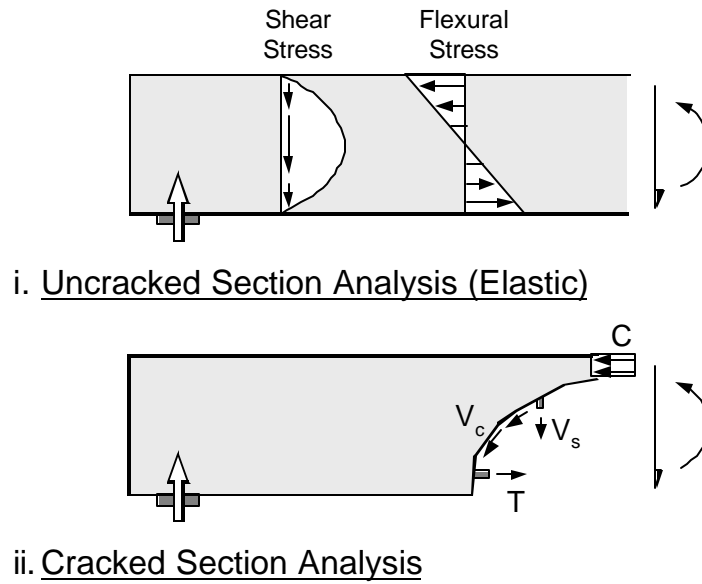


Figure 4-3: Beam analysis methods

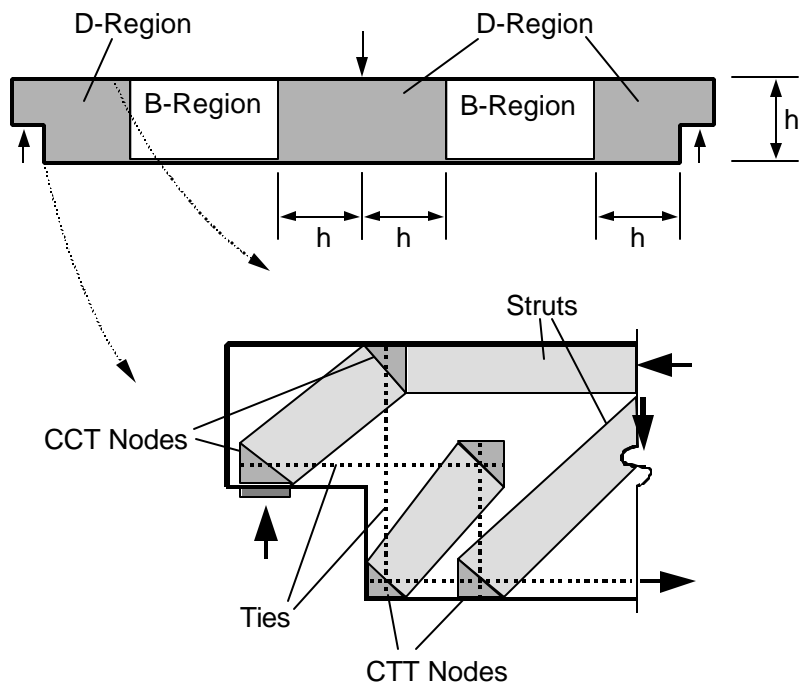


Figure 4-4: Division of dapped beam into B- and D-regions

Once the D-region is isolated, a truss mechanism is constructed based on a probable flow path for the internal stresses. As stated before, the truss mechanism consists of struts, ties, and nodes. Figure 44 shows some of these components for a dapped beam end. STM allows for several different types of struts and nodes. Figure 4-5 shows some possible strut types. The most likely strut type is the prism strut with a constant cross-sectional shape all along its length. A fan type strut is likely to occur at a deep beam end where the diagonal shear struts converge to a single node. The bottle-shaped strut is likely to occur where large amounts of surrounding concrete allow the compression stresses to bulge outward in the middle of the strut. The spreading within a bottle-shaped strut produces tension stresses that may require transverse reinforcement. A bottle shaped strut may be reduced to an equivalent truss for a better understanding of the flow of forces.

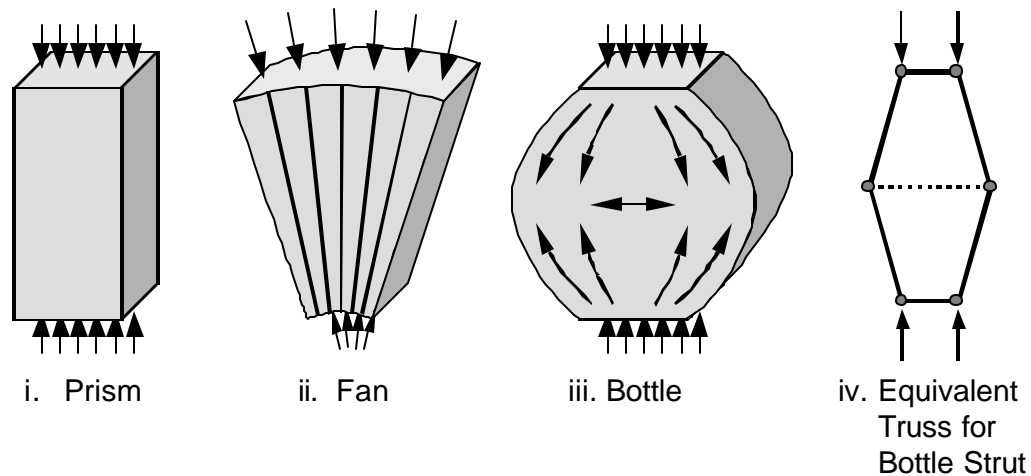


Figure 4-5: Strut types

Figure 4-6 shows the three basic node types. A Compression-Compression-Compression (CCC) node is the intersection of three compression struts. A Compression-Compression-Tension (CCT) node is the intersection of two struts and a tension tie. A Compression-Tension-Tension

(CTT) node represents the intersection of one compression strut with two tension ties. CCT and CTT nodes generally have lower effective strengths than CCC nodes due to the disruption effect created by the splitting associated with bond anchorage of the reinforcing bars. Theoretically Tension-Tension-Tension (TTT) nodes are possible, but they are not likely in practice. There are, of course, other possible node combinations involving the intersection of four or more struts and ties. In 3-dimensional truss models these are quite possible (see Figure 4-1, iv. Deep Pile Cap).

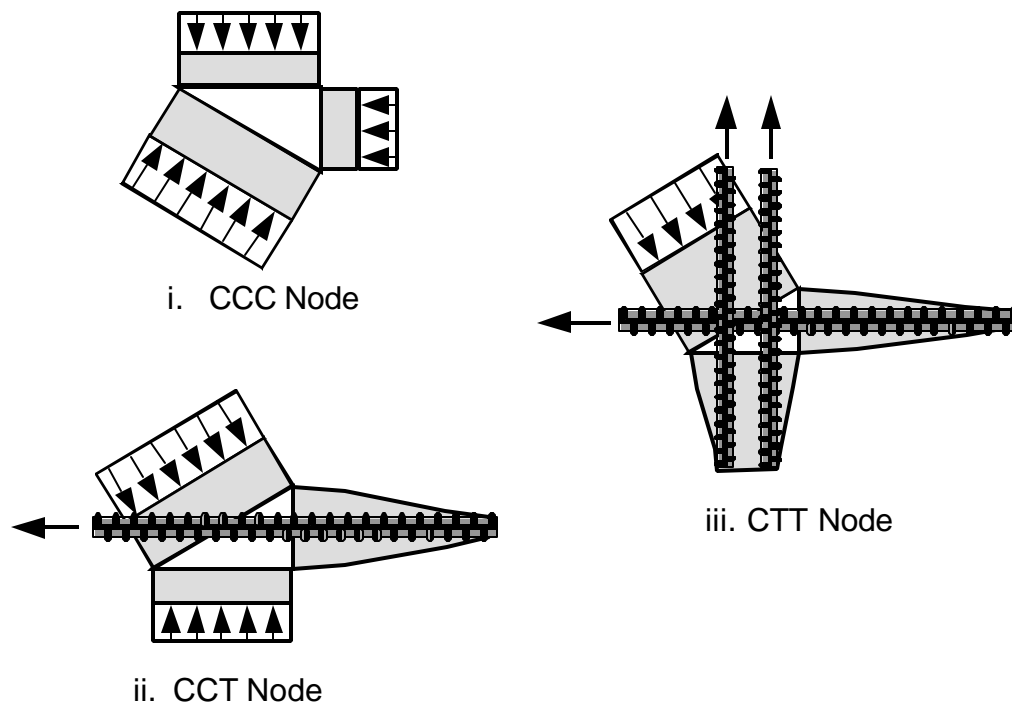


Figure 4-6: Basic node types

4.2 HISTORICAL DEVELOPMENT

The use of truss models to describe behavior of structural concrete members began slightly over 100 years ago when Ritter developed a truss model (Figure 4-7) to analyze the action

of shear in reinforced concrete beams [102]. In the following years (from 1900 – 1920's), the shear truss model was refined by Mörsch [87], Withey [117] (who introduced the concept to the United States), and Talbot [109] (who compared truss model analysis to data from experimental beam tests). Experimental testing indicated that the truss models provided very conservative estimates of shear capacity. The truss models simply did not account for shear contributions that came from the tensile capacity of the concrete and other miscellaneous factors. Eventually a more empirical method was developed to calculate shear strength in which the capacity was determined by the summation of a concrete contribution, V_c , and a stirrup contribution, V_s . This practice was first introduced by Richart in 1927 [101], and the truss models for shear soon fell out of fashion. Though truss models were sometimes utilized to explain certain phenomena in simple terms such as the model Mörsch [88] developed for distribution of a concentrated load into a cross-section (Figure 4-8), emphasis on the truss modeling waned in English speaking countries.

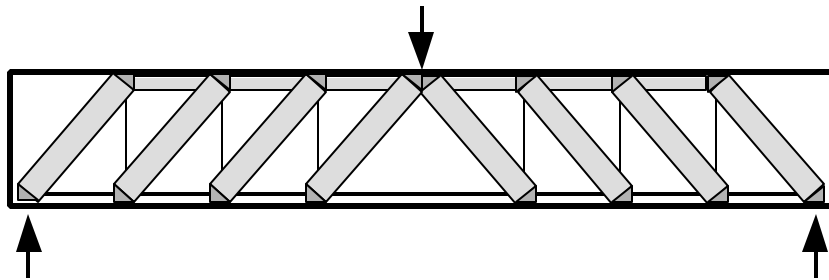


Figure 4-7: The Ritter truss model for shear

The truss model was eventually revisited in the English speaking countries in the late 1960's and early 1970's as a means of calculating the ultimate capacity of beams subjected to combined shear and torsion. Lampert and Thürlimann [66] developed a model for torsion based on the theory of plasticity (Figure 4-9). The torsion model was refined by Lüchinger [71], Mitchell

and Collins [85], and Ramirez and Breen [97] so that the space truss could account for all actions of shear, torsion, bending, and axial load in combination.

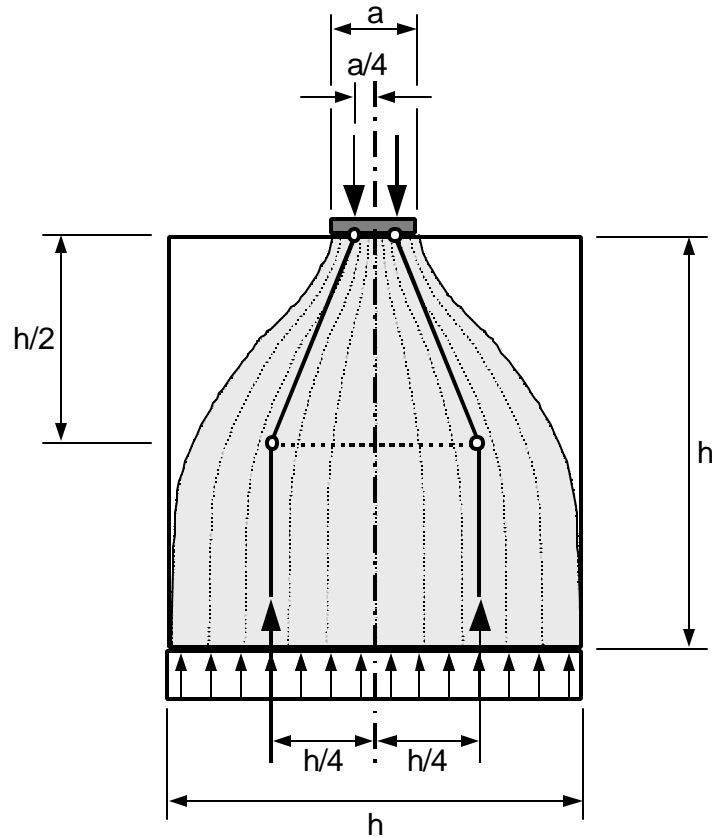


Figure 4-8: Morsch's truss model for concentric, concentrated load

Following the resurgence of the truss model in the 1970's for shear, torsion, and bending, a general method of truss modeling began to emerge for all structural situations. The strut-and-tie modeling approach for discontinuity regions was developed and endorsed by Marti [76, 78] and Schlaich [105] in the 1980's. In 1984, the Canadian CSA Standard [9] introduced STM into code draft. STM provisions have been introduced into the AASHTO Bridge Design Specifications [1] and ACI recently included provisions in the ACI 318 Code, 2002 Edition [2].

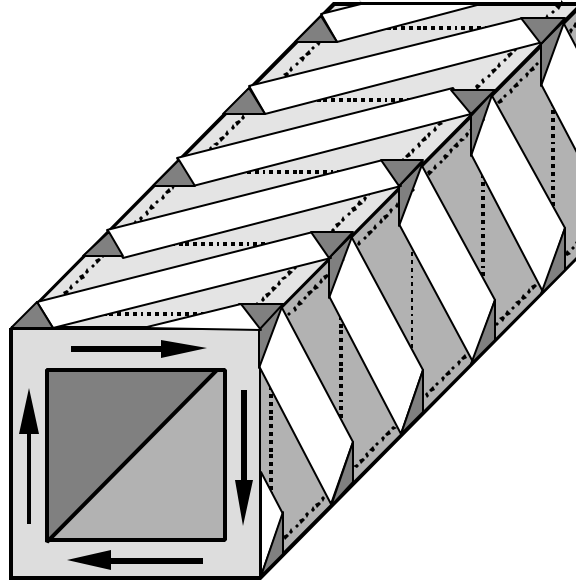


Figure 4-9: Truss model for torsion

4.3 STM DESIGN PROVISIONS

4.3.1 Procedure for STM Design

STM is only a small part within the design of a structure, and usually one of the later steps. Figure 4-10 shows the flowchart for structural design and the place of STM within the complete process. STM is a tool that may facilitate detailing disturbed regions. Other methods (empirical or mechanical) may also be available to the designer to guide the detailing of D-Regions. If STM is to be utilized, the primary structural analysis must be performed beforehand. Because compatibility between D- and B-regions must be maintained, STM can only be performed after the primary structural analysis and the determination of the forces at the boundaries of the D-regions and the selection of the primary (B-Region) reinforcing steel that will be continued into and anchored within the D-regions.

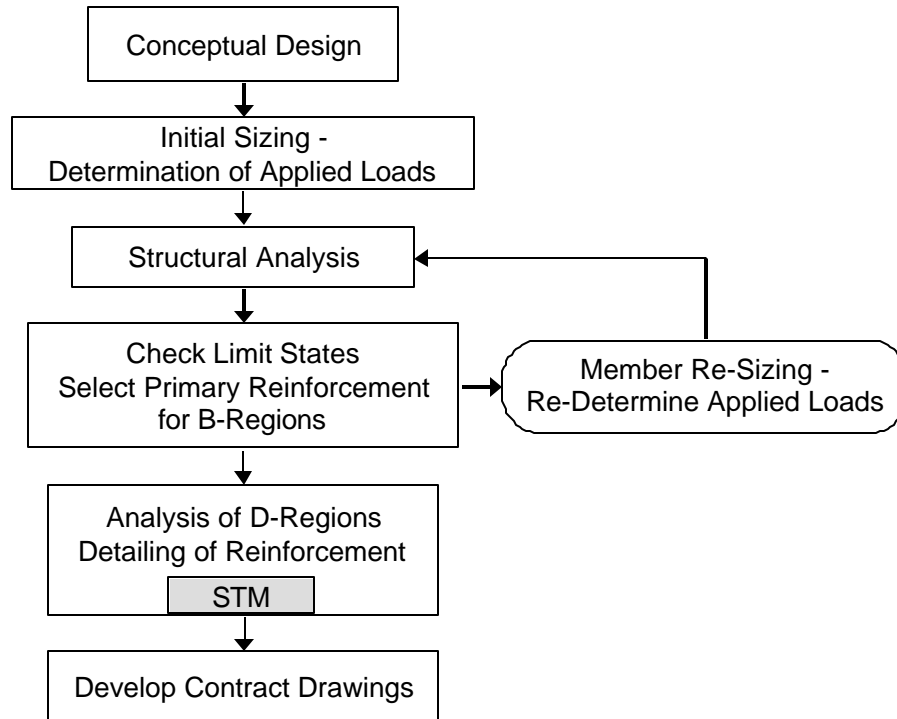


Figure 4-10: Flowchart for structural design

Figure 4-11 outlines the procedure for STM. STM begins with the determination of D-region boundaries and the calculation of boundary forces on the D-region (steps 1 and 2 in the flowchart). Once the geometry of the D-region and the applied loads are known, a truss model can be chosen (step 3). If several load cases exist for the structural member, then different boundary forces may exist for each load case. One truss model may not be sufficient for the different configurations of applied loads and separate truss models may be developed for each load case. Truss models should be determinate if possible. Indeterminate truss models for STM are somewhat questionable since they require elastic properties for the truss members to carry out the analysis of forces. It is difficult to determine reasonable elastic properties for struts and ties

because the actual structure will not be a truss, but a complex bulk member with non-uniform stress fields. Since the method is approximate in any case, it makes much more sense to maintain simplicity by keeping the truss determinate and avoiding the additional work required for an indeterminate analysis. An alternative when stress flow paths are complex is to develop multiple truss arrangements and arbitrarily divide the applied loads among the different trusses (This approach has been recommended by Schliach [105] and experimentally confirmed by Maxwell [81] for a wall with an opening). It is important for the designer to keep the approximate nature of STM in mind when performing the process. Exaggerated complexity in the analysis is not likely to enhance the STM design outcome to any significant degree and will only consume time and energy.

Once a basic truss model is chosen, the geometry of the truss must be established. The geometry of the final truss will depend on the depth of nodes, struts, and tie steel. However, these parameters may not be known at the beginning of the STM process and an iterative process must be used. Some geometric parameters may be set because of boundary conditions such as bearing plate dimensions or the centroids of reinforcing steel layers and struts that continue from the B-regions into the D-regions. Such information can be utilized to bring the geometry of the initial truss model close to its final form (step 4). For this reason, it is necessary to have performed an analysis and design of the adjacent B-regions before proceeding with STM. When the geometry of the truss model is determined, then the truss can be analyzed and the forces in the struts, ties, and nodes calculated (step 5).

Following the calculation of the strut and tie forces, the required area of steel for the ties is generally calculated (step 6). Thus bar sizes can be selected and the layout of steel detailed. The layout of the tie steel must be checked to see if it fits within the geometry of the concrete member

and must be detailed so that its centroid aligns with the assumed centroid of the tie in the truss model. If the tie steel does not fit, then the designer must redraw the truss model to suit a geometry in which the tie steel will fit and re-calculate the truss forces (step 6a). The designer must then determine if the selected tie steel will still work or if a new bar selection must be made. Once the tie steel has been selected, then the layout of the tie bars can be used to help determine the geometry of the nodes and struts.

The next part of the process (step 7) is the checking of strut and node stresses. The designer must determine some dimensions of depth and width for the nodes and struts, so that the node and struts forces can be converted into stresses and compared to the allowable stress limits imposed by the code provisions. Some designers prefer to work backwards for this step, by using the allowable stress limits to determine what face areas are necessary for the struts and nodes to accommodate the known strut and tie forces. Once the necessary face areas are known, they can be compared against the geometry of the concrete member to see if the truss model would actually fit. If the nodes and struts cannot be made to fit within the concrete dimensions, then the truss model must be redrawn to allow the nodes and struts to fit and the forces in the model must be re-calculated (step 7a). If the forces change significantly, then the struts and nodes must be rechecked and the process repeated as necessary until all of the truss components meet acceptable stress limits and fit within the confines of the overall member dimensions. This process can be quite tedious. The biggest disadvantage of the STM is the necessity to iterate repeatedly until the components of the model meet the restraints of geometry and stress. The process of STM needs to be streamlined as much as possible to prevent unnecessary iteration.

After the locations of the struts, ties, and nodes have been finalized and meet the acceptable stress limits, the last detail to be attended to is anchorage of the primary reinforcement.

Development of reinforcement follows the conventional provisions for straight and hooked bars that were discussed in Chapter 2. The critical section where development must occur is generally where the bar intersects the strut(s) that it anchors. Anchorage in strut-and-tie models is a major issue in applying the STM method. Frequently, nodes are not large enough to accommodate the full development length necessary for a straight or hooked bar. In many cases it is necessary to extend the development of the bar past the back face of the node. This may require the extension of the concrete dimensions of the structural member that is being designed. Mechanical anchorage has become an inviting alternative for many anchorage problems in STM because of this.

Throughout the STM process, much iteration may be required before a final detailing solution for the D-region is achieved. This iteration should not require changes in overall structural dimensions or the layout of reinforcement that continues into B-regions. The design process of the D-regions should flow smoothly from the design of the B-regions and should never require the designer to proceed backward in the process outlined in Figure 4-10.

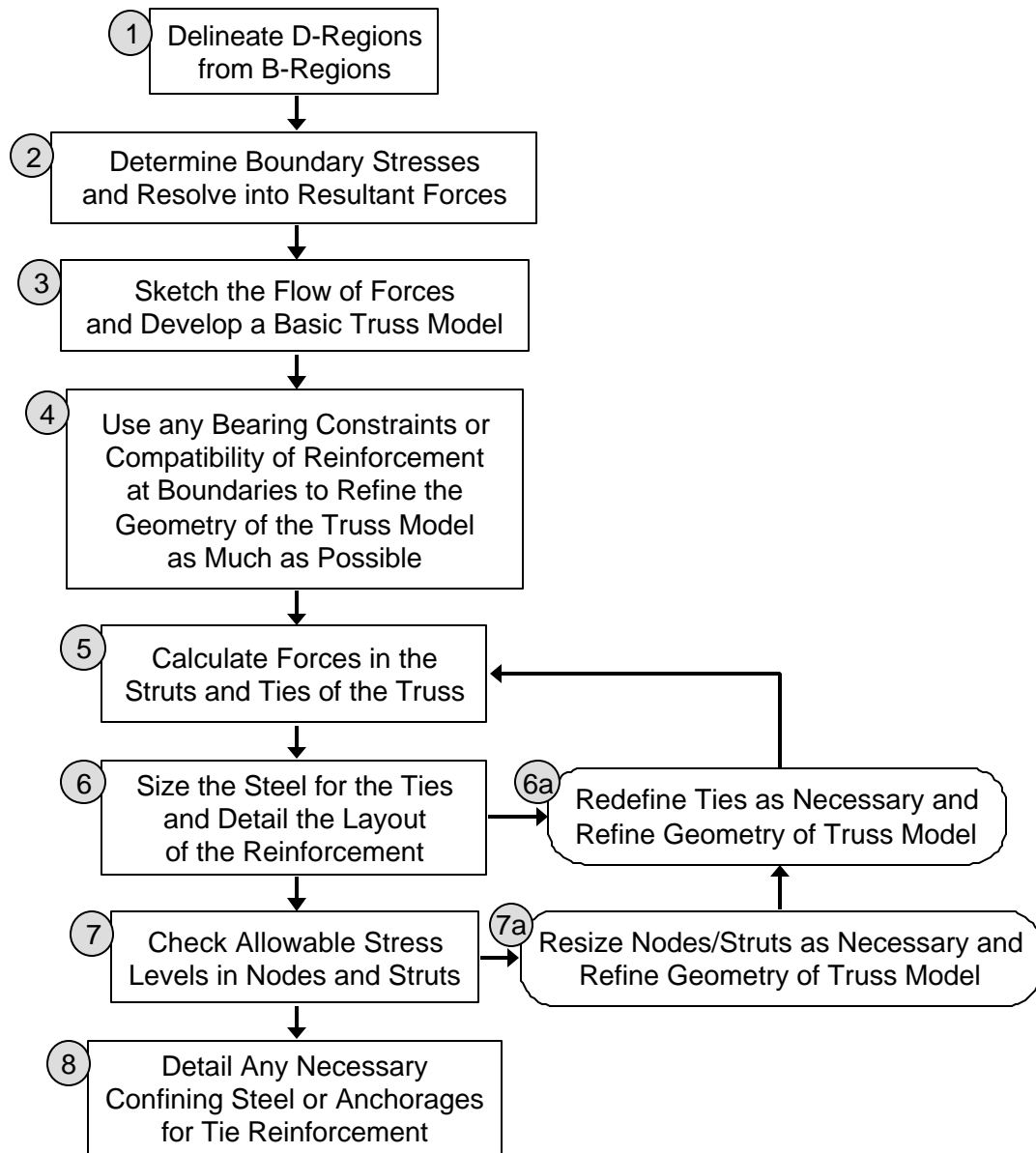


Figure 4-11: Flowchart for the STM process

4.3.2 Dimensioning of Nodes, Struts, and Ties

Dimensioning of nodes, struts, and ties is based on compatibility with boundary conditions when possible. Code guidelines sometimes provide guidance as well. Dimensioning of struts is typically based on the dimensions of the nodes at either end of the strut. Dimensioning of a node is in turn typically based on the detailing of steel tie bars that anchor at the node, bearing plate dimensions that define one or two edges of the node, or compatibility with struts that propagate from the B-regions into the D-regions. Dimensioning of ties is based on compatibility with reinforcing bars that continue from the B-regions into the D-region, detailing requirements such as minimum clear spacing or development length provisions, or recommendations contained with the code literature.

Several factors may govern the selection of tie bars. Limited space available for development length may prompt a designer to choose a large number of smaller bars to provide a tie because smaller bars require less length to develop. Furthermore, most code provisions recommend a wide spacing of tie reinforcement in order to better distribute anchorage stresses at nodes. On the other hand, it is frequently preferable to closely space tie reinforcement and consolidate the tie steel area into larger bars so that the tie force can be positioned close to the concrete surface. This improves crack control and makes more efficient use of tie steel by increasing the lever arm over which it acts (Figure 4-12). Many times, the layout of tie steel is governed by the continuation of reinforcement from the B-region. However, when continuity is not a concern, the engineer must weigh the conflicting considerations listed above when detailing the layout of tie bars.

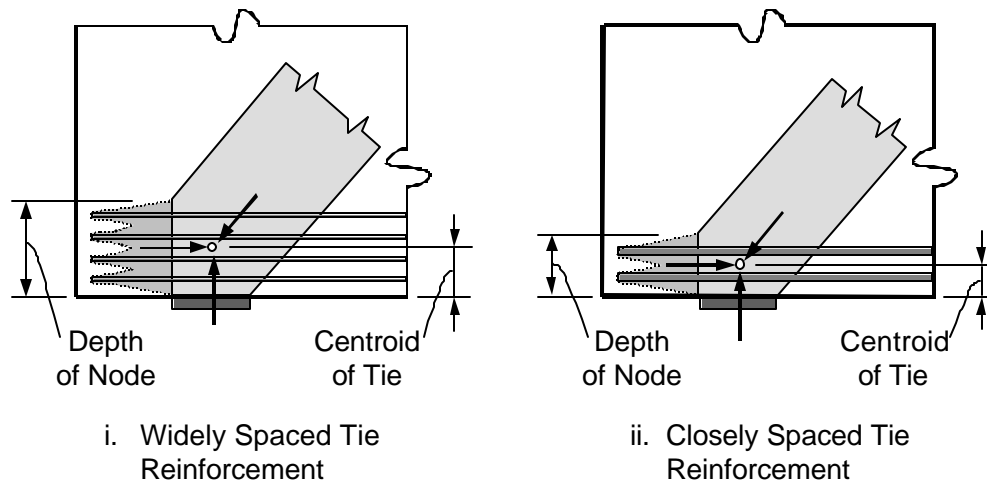


Figure 4-12: Distribution of tie reinforcement

Nodes are generally dimensioned after ties. Most codes specify limits to which nodal boundaries can be assumed to extend beyond the dimensions of the tie reinforcement for CCT and CTT node situations. FIB recommendations [16] allows for the node to extend to the limit of the clear cover or $\frac{1}{2}$ the clear spacing between layers of bars (Figure 4-13). FIB does require that reinforcement be extended at least a distance equal to the clear cover or $\frac{1}{2}$ the clear spacing beyond the face of the node before these limits can be assumed for the node dimensions. The AASHTO Code [1], the Ontario Bridge Code [14], and the CSA Canadian Concrete Building Code [9] all allow the node boundary to be drawn up to six bar diameters ($6d_b$) from the surface of the tie reinforcement (Figure 4-14). Most literature refers to the use of STM within two-dimensional members wherein the model is assumed to act across the full member width. However, if the detailing provides for a very large side cover or if the truss model acts within a three-dimensional body, then the above limits can also be applied to define the transverse limits of the node. The ACI code [2] recommends dimensioning of nodes based on hydrostatic principles.

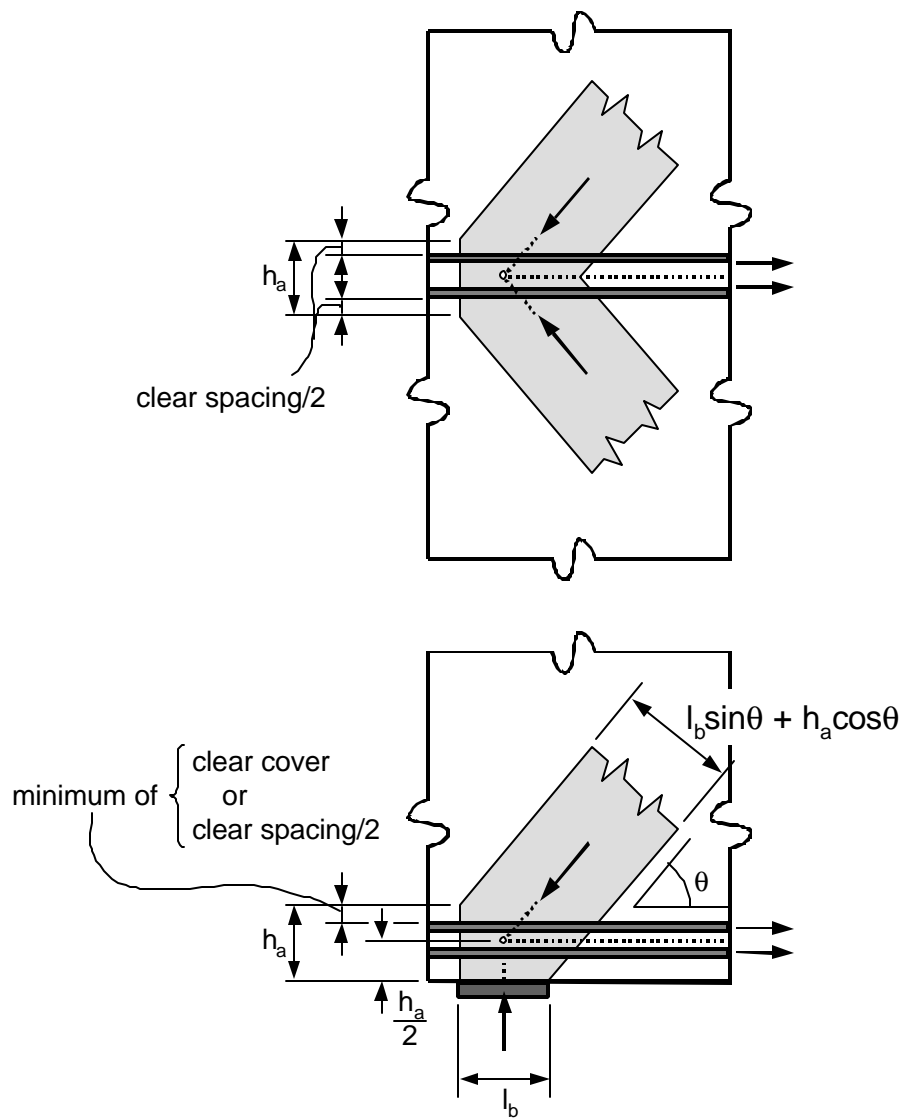
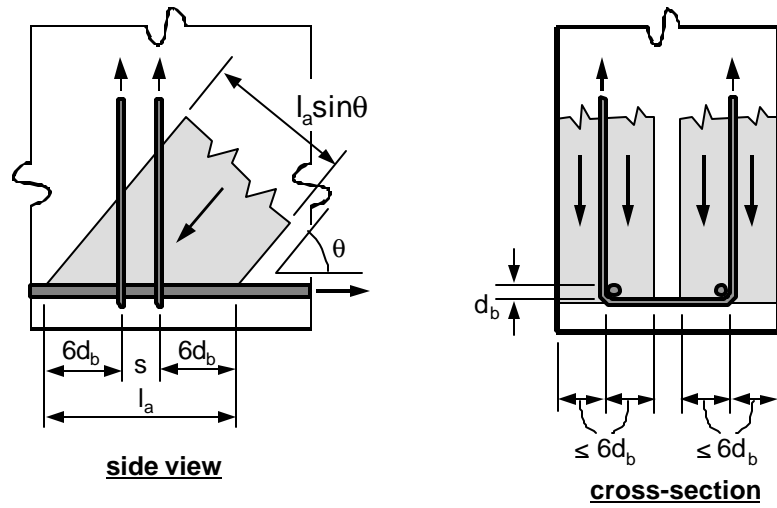
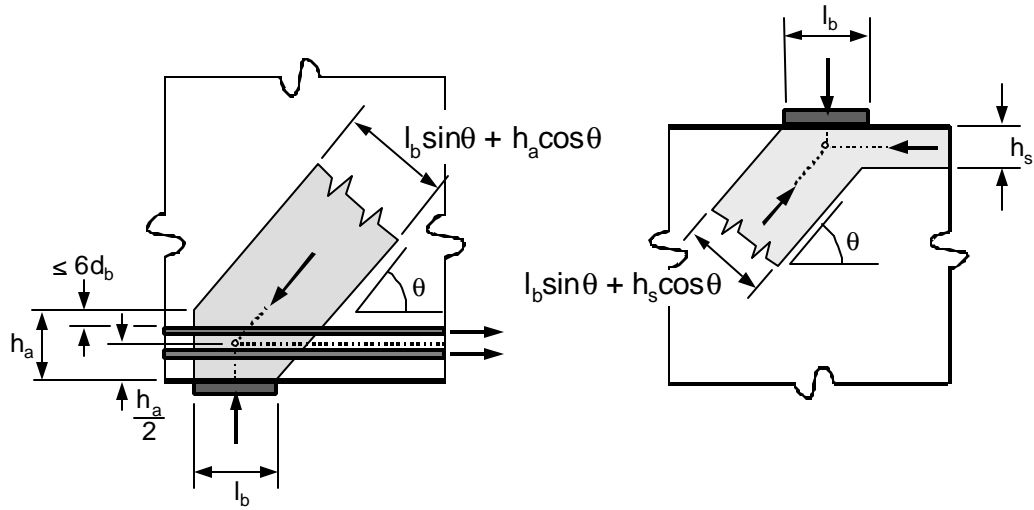


Figure 4-13: FIB recommendations for dimensioning of nodes



i. Strut anchored by reinforcement (CTT node)



ii. Strut anchored by bearing and reinforcement (CCT node)

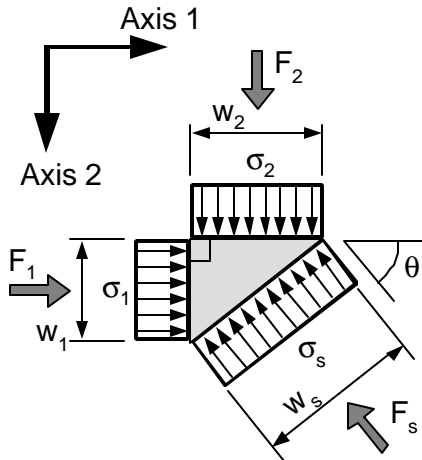
iii. Strut anchored by bearing and strut (CCC node)

Figure 4-14: AASHTO recommendations for dimensioning of nodes (after Figure 5.6.3.3.2-1 [1])

In addition to the recommended limits, all of the above mentioned codes recommend proportioning of nodes based on “hydrostatic” stress distributions when the face geometry is not governed by the dimensions of tie reinforcement or bearing pads. The term “hydrostatic” implies equal normal stresses along all three axes of the material stress block. In the convention of STM terminology, however, a node is termed “hydrostatic” when the stresses balance along only the two axes defining the plane of the truss. The state of stress along the transverse axis is generally ignored or treated with a separate truss model. When a node is hydrostatic, the dimensions of the faces are in proportion to the forces acting on those faces and the normal stresses are equal on all faces (Figure 4-15). Because the stresses are equal on all three faces, there is presumably no shear stress within the region defined by the node. It is not necessary that a node be hydrostatic. Concrete can bear shear stress to a certain extent and nodes need not be proportioned according to hydrostatic principles. Schlaich [105] recommended that the ratio of the maximum to minimum stress (σ_1/σ_2) in a non-hydrostatic node not exceed a value of two.

Generally nodes are defined by the intersection of three struts and/or ties. However, in some complex truss models, four or more struts or ties may intersect at a single node (termed a “macro-node” for lack of a better term). In such cases, nodes may be subdivided into more basic struts and nodes for easier analysis. Schlaich [105] first provided such an example in which five struts intersected at a single node. Schlaich demonstrated that it was possible to combine some of the struts before they intersected the node, thus cleaning up the node region and simplifying the problem (Figure 4-16, part i.). Sometimes it is preferable to partition a node so that stress at an interior section can be checked (Figure 4-16, part ii.). The geometry of nodes can be subdivided and treated in such manners as long as equilibrium is satisfied and the material stress limits are not violated.

i. Hydrostatic Node



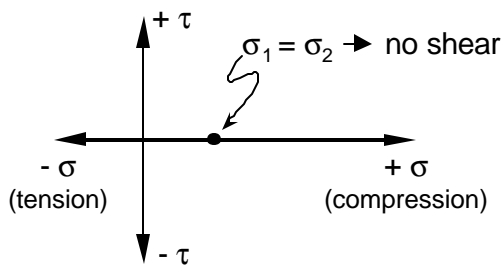
$$\sigma_1 = \sigma_2 = \sigma_s$$

$$F_s = \sqrt{(F_1)^2 + (F_2)^2}$$

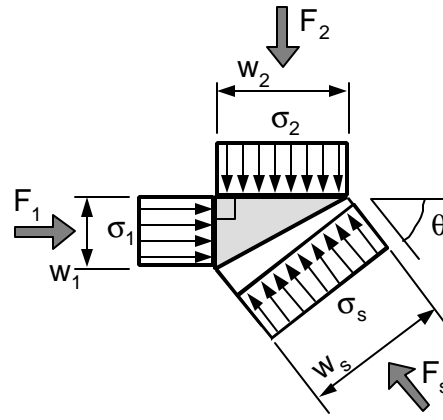
$$w_s = w_1 \sin\theta + w_2 \cos\theta$$

$$= \sqrt{(w_1)^2 + (w_2)^2}$$

Mohr's Circle



ii. Non-Hydrostatic Node



$$\sigma_1 > \sigma_s > \sigma_2$$

$$F_s = \sqrt{(F_1)^2 + (F_2)^2}$$

$$w_s = w_1 \sin\theta + w_2 \cos\theta$$

$$> \sqrt{(w_1)^2 + (w_2)^2}$$

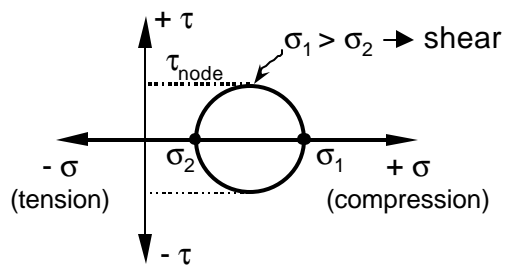
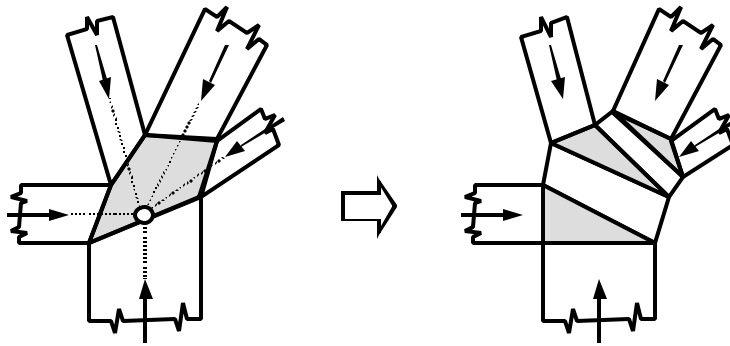
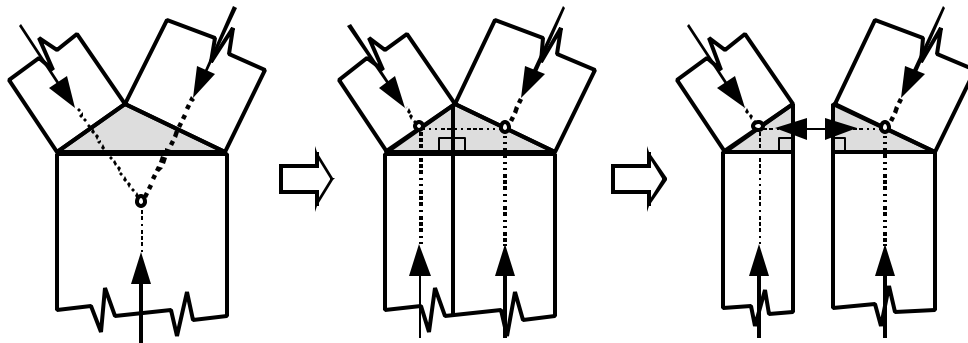


Figure 4-15: Hydrostatic and non-hydrostatic nodes



i. Subdivision of Macro-Node into Smaller Units (after Schlaich [105])



ii. Subdivision of Node at an Interior Section

Figure 4-16: Subdivision and simplification of nodes

Once the geometry of the nodes has been set, the struts are drawn. Struts are defined by the face geometry of the nodes that they intersect. Thus, all of the geometric considerations of struts are solved when the nodes are defined. When struts taper from a large node face to a smaller node face, they are generally analyzed at their smaller end where the stress will be greater.

The last consideration in dimensioning is the development length of the tie reinforcement. Most codes allow for the development length of the reinforcement to be measured from the point where the tie steel intersects the struts that they anchor (Figure 4-17). This point is a good approximation of the location of the critical crack in many CCT node situations. When

multiple layers of bars are used in the tie, the point where the centroid of the steel intersects the strut is used as the beginning of the development length.

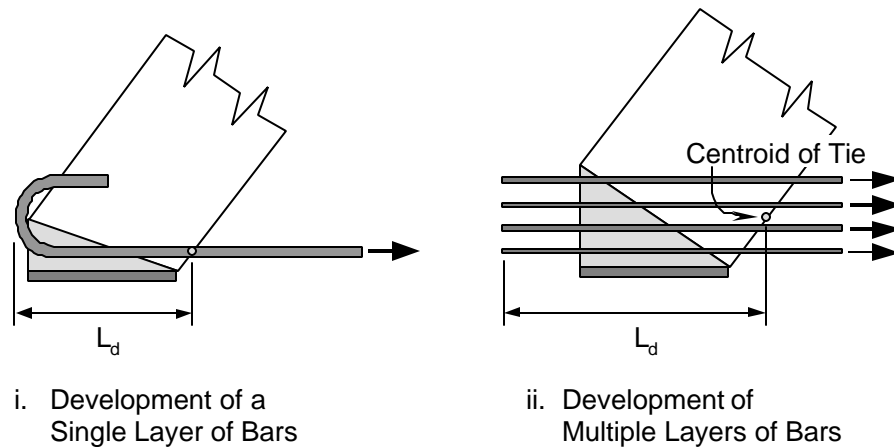


Figure 4-17: Development of tie reinforcement in nodes

4.3.3 Limitations on Strut-Tie Angle

Various sources (Lampert and Thürlimann [66], Ramirez and Breen [97], and Mitchell and Collins [85]) have proposed limitations on the angle that can be subscribed between a compression strut and a tie that anchors within that strut. Limits on strut angle have been proposed between 15° to 65° from various studies. These limits derive from studies of one-way members (beams) in shear and are specifically intended for the application of truss models and compression field theory for shear and torsion. Rational strut angle limits for truss models in less regular conditions have not been studied. Strut angle limits exist as an indirect method of controlling strain in the tie. At low angles, the cracks that develop as the truss mechanism forms become too wide to be acceptable. The AASHTO code [1] bases the capacity of struts on strut-tie angle (see

discussion in Section 4.3.5) and allows less capacity when the angle is low. The ACI code [2] places a lower limit of 25° on the strut-tie angle in Section A.2.5.

4.3.4 Strength of Nodes

Once the dimensions of the nodes are determined, then the stresses at the faces of the nodes can be checked. The stress limits for nodes are generally some fraction, v_e , of the concrete compressive strength, f_c' , times a reduction factor, ϕ for safety. The factor v_e is frequently referred to as an efficiency factor. The efficiency factors for CCC, CCT, and CTT nodes are usually different. CCT and CTT nodes are generally assigned smaller efficiency factors than CCC nodes because the tensile stresses produced by bond of the tie reinforcement are presumed to have a weakening effect on the strength of those nodes. Table 4-1 lists the efficiency (v_e) and strength reduction (ϕ) factors from various design codes. Note that while many of the codes have different safety reduction factors, they also use different load factors in the design process. Thus the ϕ factors are not always comparable. The Canadian CAN3-A23.3-M94 [9], Ontario Bridge Code [14], and AASHTO LRFD Bridge Design Specifications [1] were all authored by the same person and hence use the same efficiency factors. Notes on the FIB [16] allowable stresses are provided with the table. The units of stress are ksi for all formulations listed in Table 4-1.

| Node Type | Design Code | Limiting Concrete Stress | Strength Reduction Factor, ϕ_c |
|-----------|---------------------|-----------------------------|-------------------------------------|
| CCC | ACI 318-02 | $1.00\phi_c f_c'$ | 0.75 |
| | CAN3-A23.3-M94 | $0.85\phi_c f_c'$ | 0.60 |
| | Ontario Bridge Code | $0.85\phi_c f_c'$ | 0.75 |
| | AASHTO LRFD | $0.85\phi_c f_c'$ | 0.70 |
| | FIB* | $0.85(1-f_c/36)\phi_c f_c'$ | 0.57 |
| CCT | ACI 318-02 | $0.80\phi_c f_c'$ | 0.75 |
| | CAN3-A23.3-M94 | $0.75\phi_c f_c'$ | 0.60 |
| | Ontario Bridge Code | $0.75\phi_c f_c'$ | 0.75 |
| | AASHTO LRFD | $0.75\phi_c f_c'$ | 0.70 |
| | FIB* | $0.70(1-f_c/36)\phi_c f_c'$ | 0.57 |
| CTT | ACI 318-02 | $0.60\phi_c f_c'$ | 0.75 |
| | CAN3-A23.3-M94 | $0.60\phi_c f_c'$ | 0.60 |
| | Ontario Bridge Code | $0.60\phi_c f_c'$ | 0.75 |
| | AASHTO LRFD | $0.60\phi_c f_c'$ | 0.70 |
| | FIB* | $0.60(1-f_c/36)\phi_c f_c'$ | 0.57 |

* The FIB Recommendations use α/γ_c rather than ϕ . At ultimate loads, α , a reduction factor, is equal to 0.85 and γ_c , a partial safety factor, is equal to 1.5. The term $(1-f_c/36)$ is a reduction factor for higher characteristic concrete strengths, f_c , to recognize the more brittle nature of high strength concrete failure.

Table 4-1: Allowable stresses for nodes

Most of the codes listed in Table 4-1 require node stress checks only at the faces that abut struts or bearing plates. The faces at which tensile reinforcement is anchored are considered acceptable if the anchorage requirements of the tensile reinforcement are met (ie. if the development length is acceptable). However, the ACI provisions require that allowable stresses not be exceeded on “any face of the nodal zone or on any section through the nodal zone” (section RA.5.2) [2]. This is a rather stringent and possibly unnecessary requirement.

4.3.5 Strength of Struts

Struts are checked at both node faces that define their ends. The allowable stress in the strut can depend on several factors: the orientation of confining reinforcement across the strut (if any), the extent of cracking along the strut at the ultimate limit state, tensile or compression stresses perpendicular to the axis of the strut, and the slenderness of the beam web if shear compression struts are being modeled. The Canadian Code [9], the Ontario Bridge Code [14], and the AASHTO LRFD Bridge Design Specifications [1] all use a stress limit recommended by Collins [85] that accounts for the orientation of the strut with respect to ties (strut angle) and the principle tensile strain perpendicular to the axis of the strut. The FIB uses a simple stress limit similar to those used for nodes. The ACI code recommends various efficiency factors based on the condition of the concrete through which the strut passes.

The formulation used in the Canadian Code, the Ontario Bridge Code, and the AASHTO Bridge Code is given below:

$$f_{cu} = \frac{f'_c}{0.8 + 170\varepsilon_1} \leq 0.85f'_c \quad (4-1)$$

$$\varepsilon_1 = \varepsilon_s + (\varepsilon_s + 0.002)\cot^2 \theta_s \quad (4-2)$$

f_{cu} = ultimate stress of the strut (ksi)

f'_c = concrete compression strength (ksi)

ε_1 = principal tension strain perpendicular to the axis of the strut (in/in)

ε_s = tension strain in tie steel crossing the axis of the strut (in/in)

θ_s = angle between the axis of the strut and the axis of the tie that it anchors

It is permissible to assume a design value of 0.002 for ε_s in order to simplify the calculation. The strength of the strut is then determined solely by its inclination to the axis of the tie that it anchors.

In Figure 4-18 the ultimate strut stress is plotted as a function of the inclination assuming ϵ_s equal to 0.002. Additionally, safety factors, ϕ equivalent to the ones shown in Table 4-1 are used.

Equation 4-1 was developed based on deep beam and shell element tests. The original definitions of θ_s and ϵ_s were developed for ties composed of stirrups crossing the paths of shear struts within deep beams at well distributed intervals, not bars that anchor the ends of the struts. The adaptation of equation 4-1 to the general STM case has not been verified by tests, nor has it been demonstrated that the equation is even suitable for such situations as stout, compact elements like corbels or three-dimensional strut-and-tie models such as in pile caps and post-tensioned deviation saddles to name but a few examples.

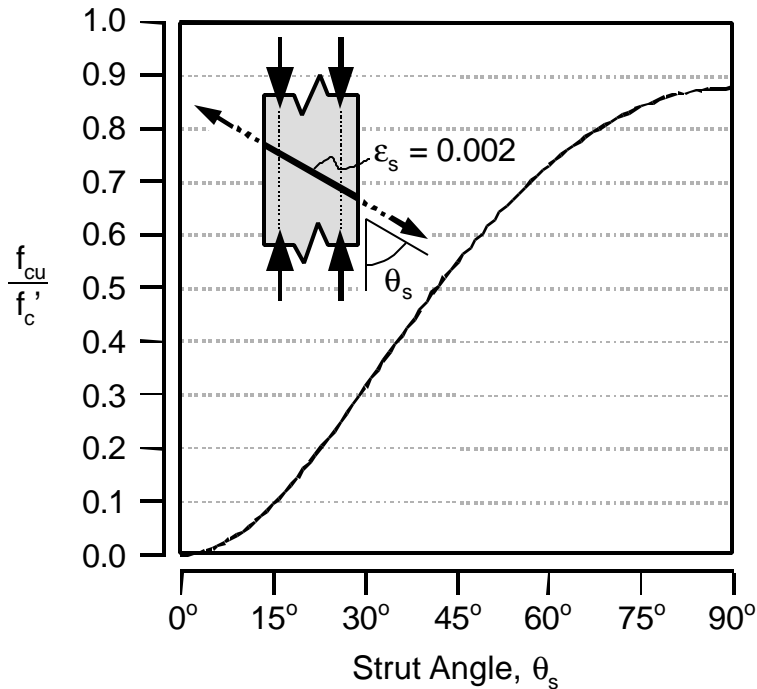


Figure 4-18: Change in strut efficiency factor versus strut angle (AASHTO specifications)

The ACI specifications use a more basic design assumption. Strut-tie angle is limited to 25° , which corresponds approximately to a shear span to depth ratio of 2, the limit that defines a deep beam from a slender beam. Strut ultimate stress is determined by:

$$f_{cu} = 0.85\beta_s f'_c \quad (4-3)$$

where β_2 is chosen from the following conditions:

- struts passing through uncracked concrete in a uniaxial fashion (such as in the compression zone of a beam): $\beta_s = 1.00$
- struts passing through concrete in tension: $\beta_s = 0.40$
- bottle shaped struts with appropriate reinforcement: $\beta_s = 0.75$
- bottle shaped struts with no reinforcement: $\beta_s = 0.60$
- all other cases: $\beta_s = 0.60$

Appropriate reinforcement for bottle shaped struts must satisfy the following:

$$\sum \frac{A_{s_i}}{bs_i} \sin \gamma_i \geq 0.003 \quad (4-4)$$

A_{s_i} = area of steel in spacing, s_i , that crosses the path of the strut (in^2)

s_i = spacing of reinforcement crossing the path of the strut (in)

b = the width of the strut perpendicular to the axis of the crossing reinforcement (in)

γ_i = the angle between the axis of the strut and the axis of the crossing reinforcement; γ must be greater than 40° if only one layer of reinforcement crosses the strut

Subscript i refers to the i^{th} layer of reinforcement. Typically there would be two layers of reinforcement: horizontal and vertical. Additionally, the concrete stress is reduced by a strength reduction factor, ϕ of 0.75.

The FIB uses only one formulation:

$$f_{cu} = 0.6 \left[1 - \frac{f_c}{36} \right] f_c' \quad (4-5)$$

f_{cu} = ultimate concrete stress (ksi)

f_c = characteristic concrete stress (a statistical formulation of the concrete strength based on cylinder tests; it is reasonable to substitute $f_c' - 1.1$ ksi) (ksi)

f_c' = concrete compression strength (ksi)

Equation 45 provides the same stress limit for struts that is used for CTT nodes and conservatively assumes that the concrete in the struts will probably be cracked at the ultimate limit state. The same reduction factors applied to nodes are applied to struts.

4.4 EXPERIMENTAL STUDIES

Numerous experimental studies have been performed to refine truss models for shear in deep beams and prestressed beams (Ramirez and Breen [97], Rogowsky and MacGregor [99, 100], Vecchio and Collins [114, 115], and Alshegeir and Ramirez [22]). These studies have focused primarily on the shear strength provided by struts in plane stress situations. The results of these studies have formed the basis for the compression field theory and various truss models for shear in one-dimensional members (These theories are subsets of STM that have been specialized for the modeling of shear in beams and shell structures). Few experimental studies have examined the

application of STM in complex discontinuity regions using the most general application of the method. Fewer still have attempted to perform tests of isolated struts or nodal zones. Summarized herein is a brief overview of the literature of such tests that has been found.

4.4.1 Cook and Mitchell (Disturbed Regions)

Cook and Mitchell studied the use of STM to predict failure loads for four scaled-down specimens at McGill University [39]. They studied a double-sided corbel, a rectangular dapped beam, an inclined dapped beam, and a beam with a rectangular opening in its web. They also compared the experimental results with non-linear finite element analysis. The purpose of the research was to verify the validity of the strut-and-tie method which Cook and Mitchell found acceptable for design purposes but not as accurate for predicting ultimate strength and failure modes as the non-linear finite element analysis. They recommended that the effective bearing area of struts and nodes should ignore cover concrete because this concrete tends to spall away at the ultimate limit state. STM under-predicted the ultimate capacity of all four experimental specimens as expected for a lower bound method.

4.4.2 Beaupre (Deviation Saddles)

Beaupre applied STM to the analysis of 10 tests of $1/3$ and $1/5$ scale deviation saddles for external post-tensioned tendons [27]. A deviation saddle for an external bridge tendon redirects the path of a tendon through a sharp angle break. Due to the abrupt change in tendon angle, a large vertical shear force must be transmitted through the deviation saddle into the bridge cross-section. Figure 4-19 shows the cross-section of a typical saddle tested by Beaupre. Beaupre tested 10 such saddles as part of a large scale research program sponsored by TxDOT to study the design and

behavior of post-tensioned box-girder bridges with external tendons. STM was examined as a potential method for deviation saddle design.

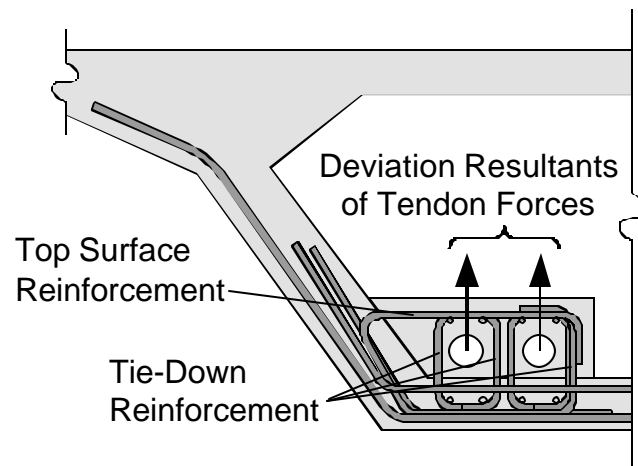


Figure 4-19: Typical deviation saddle tested by Beaupre

STM for the deviation saddle was conducted in two parts: an analysis of the contribution of the tie-down reinforcement and an analysis of the contribution of the top surface reinforcement. Beaupre's test results averaged 98% of his STM predictions with a standard deviation of 10%. Some test results were only 85% of his predicted STM values. STM should provide a lower bound solution and a calculated strength not less than the actual capacity of the specimen. Some of Beaupre's over-predictions may have been due to an over-estimation of the contribution from the top surface reinforcement to hold down the tendons. The pullout force of the tendons acts almost perpendicularly to the axis of the top surface reinforcement. In order for the top surface reinforcement to act effectively against the pullout force of the tendons, it must deform substantially out of its plane until it can act at an angle to the applied load. This does not occur until the tie-down reinforcement has yielded substantially. It is very difficult for the two types of

reinforcement to act in conjunction with one another and certainly difficult for the top surface reinforcement to contribute significantly to the capacity of the model without substantial distress to the deviation saddle. Omission of the contribution of the top surface reinforcement made Beaupre's STM predictions conservative for six of the ten specimens. The remaining four specimens had potentially significant horizontal deviation forces that were neglected during STM analysis and almost certainly affected the ability of his simple STM model to predict test capacities.

The behavior of the deviation saddles was dominated by tie action of the reinforcing steel. Compressive strength of the struts and nodes and anchorage of the ties was not critical for the capacity of the specimens. Failure of the specimens occurred by violent rupture of the top concrete and fracture of the tie-down steel.

4.4.3 Barton, Anderson, and Bouadi (Dapped Beams and Nodes)

Dapped beams and nodes were studied at the University of Texas as a means of experimentally evaluating the use of STM and providing data for the design of the various components of strut-tie models particularly nodes [25].

The first phase of the research (conducted by Barton) consisted of tests of 4 dapped-end details. Two of the specimens were designed using STM, one using a method suggested by PCI [15], and a third using a method previously used by TxDOT that was suggested by Menon and Furlong [83]. All specimens had the same dimensions and were designed for the same external load. Barton found that all specimens performed adequately. In both cases in which STM was used for design, the capacity of the beam was 27-42% higher than predicted. The Menon and Furlong approach gave the best estimate of strength while requiring the least horizontal and vertical steel reinforcement in the main tension ties (However, a difficult strap reinforcement detail was

required.). Failure of specimen ST1 designed with STM occurred through yielding of the primary reinforcement, then crushing of the compression zone within the beam at large deflections. Failure of specimen ST2 designed with STM occurred at a lower load than ST1 by non-ductile crushing of the compression zone within the beam. In both ST specimens, the STM method was applied successfully. Yielding of the primary tension reinforcement was achieved before crushing of the concrete within struts or nodal zones occurred.

Following the tests of the dapped beam ends, isolated node tests were conducted by Anderson and Bouardi as the second phase of the project.

Anderson tested nine isolated CTT nodes modeled after the anchorage point of the primary vertical tensile tie and the longitudinal beam reinforcement within the dapped beam ends from ST1 and ST2 (see Figure 4-20). Anderson tested such parameters as concrete strength (high: 5800 psi or low: 3700 psi), longitudinal bar anchorage (hooked or straight), confining reinforcement, strut width (a full bearing plate, 8", or half width, 4"), and strut angle (45° versus 30°). He found that cracking patterns of the isolated nodes were similar to cracking patterns observed in CCT nodes of the dapped beams. Of the nine specimens tested, three achieved the maximum capacity of the test set-up. All three of those specimens were made with high strength concrete and used the same reinforcement details as the ST1 dapped beam design. The following observations were noted for the remaining specimens:

- When the vertical reinforcement detail was altered from looped U-bars to 90° hooks placed parallel to the longitudinal bars, the node failed by spalling of side cover and anchorage failure of the vertical reinforcement.
- When the strut bearing plate was reduced to half its width, the high concrete strength node still achieved the maximum capacity of the test set-up. However, the low

concrete strength node failed by crushing under the load plate at a bearing stress of 3800 psi (approximately the compressive strength of the concrete).

- Replacement with straight bar development of the hooked anchorage of the top layer of longitudinal reinforcement resulted in a bar slip failure.
- Alteration of the strut angle from 45° to 30° resulted in higher forces in the longitudinal steel and failure of the straight bar anchorage for the lower layer of bars.
- Cracking within the nodes extended from the bearing plate to the far corner of the node resulting in a severely reduced development length for the lower layer of the longitudinal reinforcement.
- Cracking patterns also indicated that hooked bar anchorages tended to allow deeper struts at the face of the node than when straight bar anchorage was used.

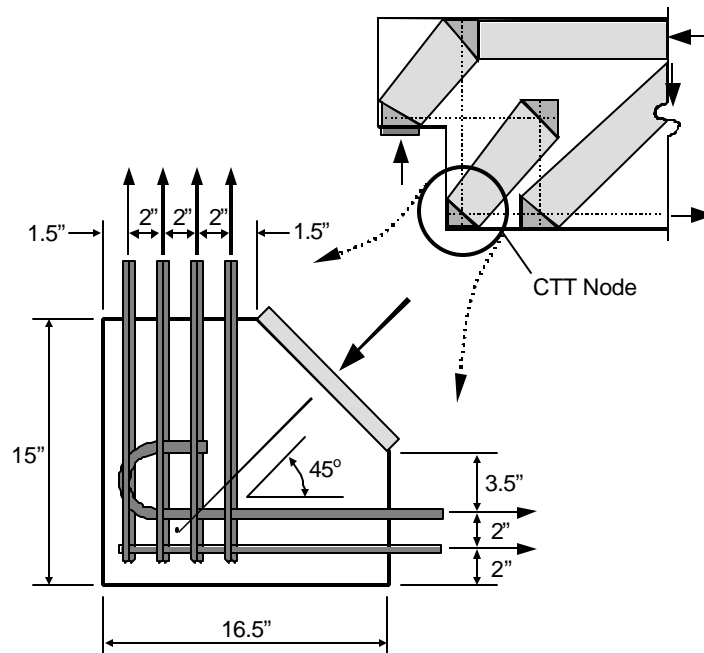


Figure 4-20: Isolated CTT node tested by Anderson

Bouardi tested ten isolated CCT nodes modeled after the intersection of the bearing plate force and the primary horizontal tensile reinforcement (see Figure 4-21). Bouardi tested parameters such as concrete strength (high: 5000 psi or low: 2500 psi), the width of the bottom bearing plate (full, 12", or half width, 6"), confining reinforcement (none or # 3 hoops at 4"), anchorage of the tie reinforcement (hooked or straight), and bottom concrete cover (small: 1.25" or large: 3.75"). Four out of the ten specimens failed by compression failure. The tie bars began to yield in one specimen, but then an anchorage failure occurred. The remaining five specimens all failed by anchorage failures characterized by spalling of the side cover. Bouardi noted that it was very difficult to perform the isolated CCT node tests. The tests suffered from uneven bearing of the top load plate, horizontal friction at the bottom bearing, and uneven distribution of strain and bending among the tie bars. Despite these problems, Bouardi noted the following:

- Only the low concrete strength specimens failed in compression.
- One low strength concrete specimen failed in anchorage because no confining reinforcement was provided for the tie bars.
- Increased bottom cover increased the capacity of the specimens by 20%.
- Replacing the straight bar anchorage of the bottom layer of tie bars with hooked bars decreased the capacity by a slight amount, 4%.
- Calculation of effective bearing stresses for the four specimens that failed in compression indicated that the efficiency factor of the concrete in bearing was approximately 1.0.

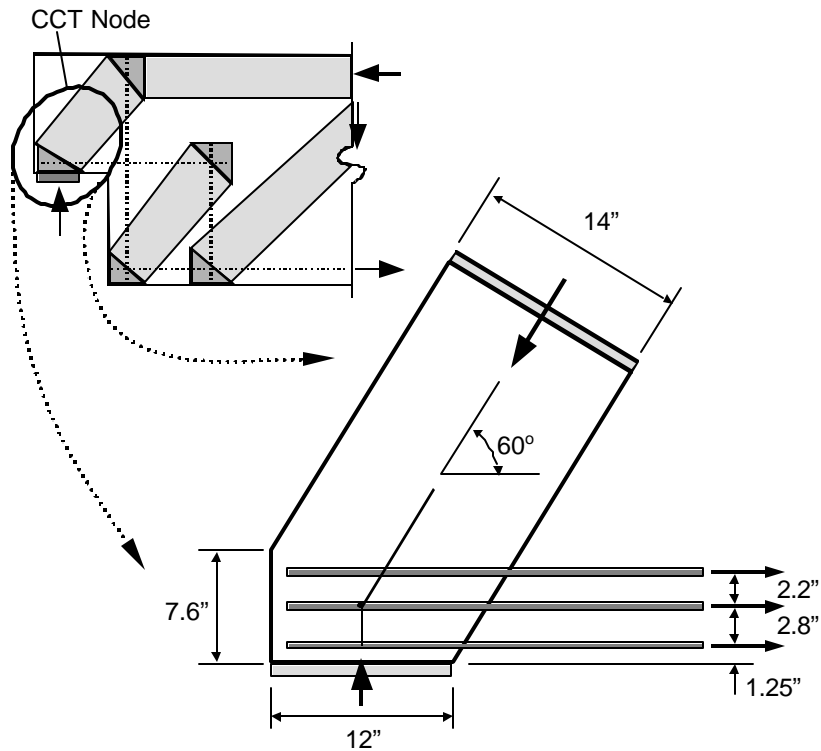


Figure 4-21: Isolated CCT node tested by Bouardi

4.4.4 Roberts, Sanders, Burdet, and Wollmann (Anchorage Zones)

As part of an extensive study sponsored by the National Cooperative Highway Research Program (NCHRP) [32], Roberts performed experimental tests on local anchorage zones and Sanders and Wollmann performed half-scale tests on a number of typical post-tensioned general zone configurations. The local zone essentially constitutes the enlarged CCC node in front of a post-tensioned anchorage plate. The general zone constitutes the remainder of the D-region surrounding the anchorage as shown in Figure 4-22. Note that the distinction between the general and local zone for post-tensioned anchorages has more to do with construction practice and design liability than with structural behavior. The general and local zones represent partitions of design

responsibility of the total disturbed region. Roberts studied local zones in order to develop design guidelines for anchor plates and confining steel of the local zone node. Sanders and Wollmann performed experimental tests on general zones for the purpose of verifying the acceptability and accuracy of STM as a method of designing the secondary tie steel required for spreading of the local zone stress into a full cross-section. Burdet performed numerous linear elastic finite element analyses that contributed to the design of test specimens and interpretation of results.

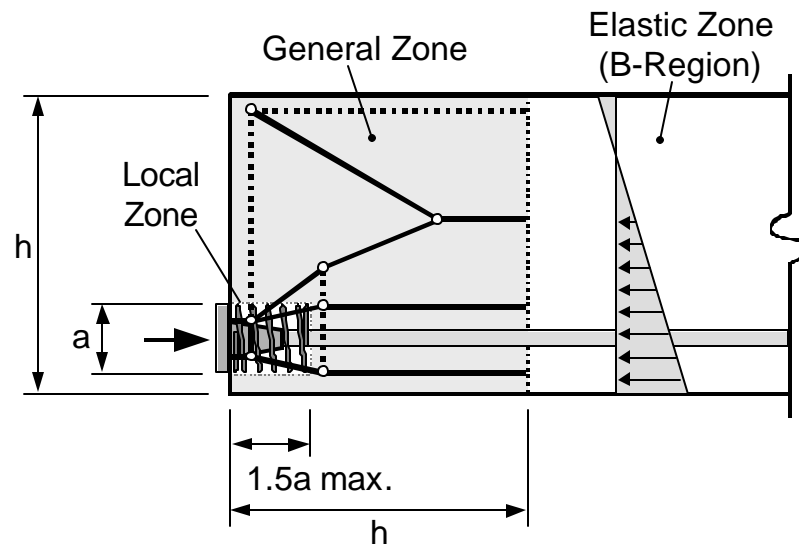


Figure 4-22: Local and general zones of post-tensioned structures

Roberts [98] performed 28 tests of isolated local zones and 3 tests of non-isolated local zones. The purpose of the tests was to rate the quality of the existing acceptance tests for anchorage devices and to develop an improved test method. She studied such parameters as anchor plate type (multi-plane or flat plate), load history (monotonic, cyclic, or sustained loading), cover distance, spiral confinement parameters (pitch and diameter), auxiliary reinforcement in the local

zone specimen, and the interaction between the local and general zones. Two interesting results were determined from these tests: the comparison of the local zone capacity to a variety of bearing formulas including a node strength formula developed by Schlaich and Schäfer [104] and the comparison of the results of isolated local zone tests to analogous tests of non-isolated local zones which were a parts of larger general zone elements.

Roberts compared the results of her isolated local zone tests to seven models of bearing capacity. The focus of her analysis was to determine the best model that would account for the impact of the two primary variables of her study: the ratio of the unloaded concrete area to the bearing plate area of the anchorage plate, A_2/A_1 (see the discussion on bearing strength in sections 3.5.1 and 3.6.4 for more discussion on the A_2/A_1 ratio) and the amount of lateral confining steel. Roberts found that the following formula, based on work by Schliach and Schäfer, provided the best fit for her data:

$$f_{\text{bearing}} = 0.8f'_c \sqrt{\frac{A_2}{A_1}} + 4.1f_{\text{lat}} A_{\text{core}} \left(1 - \frac{s}{D}\right)^2 \quad (4-6)$$

$$\text{in which } 0.8f'_c \sqrt{\frac{A_2}{A_1}} \leq 3.0f'_c \quad (4-7)$$

f_{bearing} = bearing stress of supported by the anchorage device (ksi)

f'_c = concrete cylinder strength (ksi)

A_2 = the unloaded concrete area (refer to Figure 3-28) (in^2)

A_1 = the bearing area of the anchorage device (in^2)

A_{core} = the area of concrete confined by spirals or ties (in^2)

f_{lat} = the lateral confining stress provided by spirals or ties (ksi):

$$\frac{2A_s f_y}{Ds} \text{ for spirals}$$

$$\frac{A_s f_y}{Ss} \text{ for ties}$$

- A_s = the bar area of the spiral or tie confining steel (in²)
 s = the pitch of spiral steel or the spacing of tie steel (in)
 D = the diameter of spiral confinement (in)
 S = the width tie reinforcement (in)

Robert's recommended formula for the allowable bearing stress of local zones once again shows the reliance of the bearing pressure on the A_2/A_1 ratio which was seen with many other anchorage situations. Furthermore, the formula indicates that even unconfined local zones can sustain a bearing stress as large as $3f_c'$. Since the local zone test was basically a node test, Robert's work implies that the limitations on allowable bearing stresses that were reviewed in section 4.3.4 are very conservative.

Robert's also studied the influence of the general zone configuration on the capacity of the local zone. In a series of five tests, Roberts demonstrated that cracking and ultimate load data from isolated tests of local zones could suffice as lower bound estimates of the behavior of the local zone within a whole disturbed region. This conclusion has significant impact on the determination of node service and ultimate limit states. Robert's work indicates that isolated tests of node zones can be used to conservatively determine limits for the performance of nodes.

Sanders performed 36 tests of end bearing anchorages. He tested such parameters as anchorage eccentricity, multiple anchorages, curved and inclined tendon paths, the distribution of tie reinforcement, the confinement provided by lateral post-tensioning, and concrete strength. Wollmann performed 3 beam tests in which the general zone was influenced by reaction forces, 8

intermediate anchorage tests, and 3 anchorage diaphragm tests. Wollmann's tests represented complex yet commonly occurring instances of post-tensioned anchorages. Sanders' and Wollmann's test results were compared to STM predictions of capacity. Compression struts and nodes were limited by an allowable concrete compressive stress of $0.7f'_c$. The average measured/calculated capacity ratio of all specimens was 1.40 (with a range from 0.95 to 3.33) and the standard deviation was 0.44. The data suggest that STM is an acceptable and often very conservative design method for the post-tensioned anchorage zones.

STM was poor in predicting of the mode of failure of all specimens. Where STM analysis determined that yielding of tie reinforcement would determine failure for most of the specimens, almost all specimens failed by compression in front of the local zone or bursting in the same location. These failure modes occurred because the general zones exceeded their yield capacities. The unanticipated high capacities of the general zones allowed the local (anchorage) zones to reach much higher stress levels than their design values, which resulted in brittle failures.

The goal of much of the research on post-tensioned anchorages was to determine the specific rules that would make STM applicable to design of the anchorages. Thus much of the research interest was in the configuration of truss models and not on the strength of struts and nodes. Among the results of the post-tensioned anchorage zone studies that can be extrapolated to the broad realm of STM application are:

- Serviceability (ie. crack control) within the D-region can best be accounted for if truss models are aligned closely with elastic stress distributions. The centroids of compression struts and tensile ties must match with centroids of compressive and tensile stress field in the elastic solution. An elastic solution must be available to properly implement a strut-and-tie model. For complex geometries in which designer

intuition of stress fields will not suffice, elastic FEM analysis is preferred prior to the STM process.

- Compression stresses from the anchor plate spread laterally at a slope of 1:3.
- A simple compression stress limitation of $0.7f_c'$ for struts and nodes provided acceptable predictive results for the experimental tests.
- Roberts' tests imply that a conservative lower bound estimate of local nodal strength can be obtained from isolated tests of the nodal zones.

4.4.5 Zeller (Corbels)

Zeller [47, 121] studied four corbel specimens at the University of Karlsruhe in Germany. He studied the behavior of diagonal spitting in the primary compression strut. The variables were the orientation and amount of splitting reinforcement provided for the corbel struts and the length/depth ration of the corbels. Zeller measured the distribution of strain across the struts in his specimens. He determined that the compression stress was distributed non-uniformly and peaked at the re-entrant corner where the corbel and the support column joined one another (Figure 4-23). The extreme state of stress produced at the re-entrant corner caused all corbel struts to fail in compression at that location, but only after yielding of the tie reinforcement had occurred.

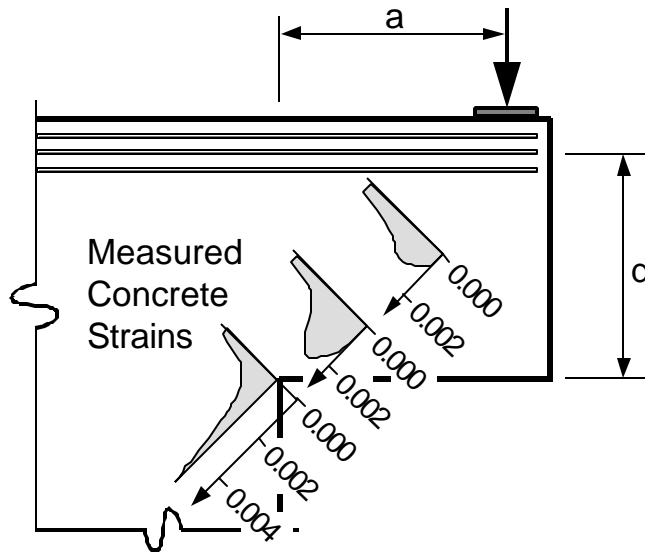


Figure 4-23: Concrete strains in corbels tested by Zeller

4.4.6 Armstrong, Salas, and Wood (Cantilever Bridge Piers)

STM was examined experimentally as an alternative design method for cantilever bridge piers at the University of Texas [23, 118]. Specimens in the study resembled the corbels studied by Zeller [47, 121]. Figure 3-19 of the last chapter presented a schematic of a cantilever bridge pier typical of those studied at University of Texas.

In tests of scaled down pier overhangs [23], researchers found the STM method provided conservative results comparable to conventional design methods. Overhangs designed using the STM method failed in flexure as they were designed to while some specimens designed using ACI provisions for corbels failed in shear when a flexural failure had been designed for. The re-entrant corner of the overhang was found to be the critical design region. Analysis of the CCC node at that region demonstrated that the node had a much higher capacity than predicted using allowable stress criteria recommended by Bergmeister [28]:

Concrete efficiency factor,
$$v_e = 0.9 - \frac{0.25f'_c}{10,000\text{psi}} \quad (4-8)$$

$$4,000 \text{ psi} \leq f'_c \leq 10,000 \text{ psi}$$

Additional tests were later performed to examine design procedures for the CCT node that occurs in the joint at the connection of the overhang to the support column [118]. The researchers found that the STM method was the only suitable method that correctly modeled the actions of the forces in the joint.

4.4.7 Adebar and Zhou (Deep Pile Caps)

Adebar and Zhou have examined the use of STM for design of deep pile caps [18, 19, 20]. They found that the current design practices recommended by ACI for deep pile caps based on punching shear and one-way flexure are unconservative. They proposed a design procedure based on STM (see illustration iv. in Figure 4-1).

As part of their study on deep pile caps, Adebar and Zhou conducted analytical and experimental studies of isolated struts [19]. The isolated strut tests resembled double punch tests of concrete cylinders [34, 77] and they compared their strut results to existing data from double punch studies. Figure 4-24 shows a typical double punch strut specimen. The purpose of the strut studies was to determine the maximum allowable compressive stress before transverse cracking would occur in the strut. In deep pile caps, it is not convenient to place confining reinforcement within the struts, therefore, the compressive stress in the struts must be limited to prevent splitting cracks. Based on the results of 40 experimental tests and their analytical work, Adebar and Zhou derived the following expression for the allowable compressive strength of struts:

$$\text{Allowable Bearing Stress, } f_b \leq 0.6f'_c(1 + 2\alpha\beta) \quad (4-9)$$

$$\alpha = 0.33 \left(\sqrt{\frac{A_2}{A_1}} - 1 \right) \leq 1.0 \quad (4-10)$$

$$\beta = 0.33 \left(\frac{h}{b} - 1 \right) \leq 1.0 \quad (4-11)$$

α = factor for confinement of surrounding concrete

β = factor for aspect ratio of strut

h = length of the strut from node face to node face (in)

b = width of strut, measured at the node faces (in)

A_1 = area of strut at node faces (in²)

A_2 = area of strut at point of maximum spreading (in²)

Average values of b and A_1 should be used when the two end node faces of the strut have different geometries. The equation gives an absolute maximum bearing pressure of $1.8f'_c$.

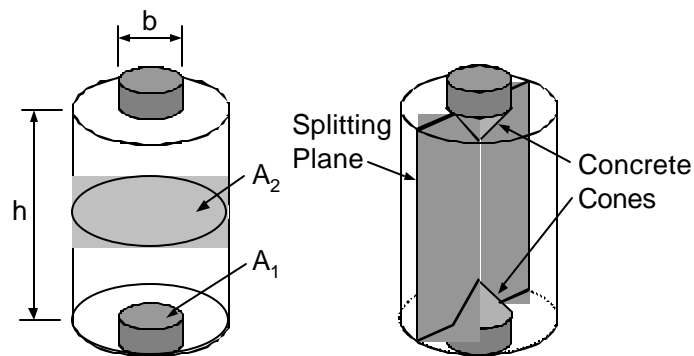


Figure 4-24: Double punch strut test used by Adebar and Zhou

Following their study of struts, Adebar and Zhou used their bearing stress formula in conjunction with strut-and-tie models to predict the strength of 48 experimental tests of fifth-scale to full-scale size pile caps [18, 20]. The experimental data came from a variety of published studies on experimental tests of pile caps. They found that their STM method provided better results than the current ACI and CRSI methods of pile cap design. The range of measured/calculated capacity ratios using STM was 0.99 – 2.88 with a mean of 1.55. The ACI and CRSI methods frequently over-estimated the capacity of the specimens. Despite that success, the ability of STM to predict the failure mode of the pile caps was very poor with only 21 out of 48 failure mode predictions correct. Of the 27 tests in which STM did not predict the correct mode of failure, all specimens were reported to have failed in shear although flexural failure (yielding of the tie steel) was predicted. It is possible that many of the reported shear failures may have actually been of mixed shear and flexural modes and were difficult to properly categorize.

4.4.8 Maxwell (Wall with Opening)

Maxwell [81] studied four small-scale wall specimens modeled after a hypothetical design example provided by Schlaich [105]. The purpose of the experiment was to provide service limit state and ultimate limit state data for a well-known design example using STM. Schlaich developed two independent strut-and-tie models for the flow of forces through a discontinuous wall with an opening. Schlaich then used both models in combination by splitting the wall loads 50-50 among the two trusses. His detailing recommendations were based upon the combined analysis.

Maxwell tested four specimens: two specimens based on the two independent truss models developed by Schlaich, a third based upon combining the two trusses in the manner that Schlaich recommended, and a fourth that represented a slight modification of the combined truss

analysis of the third specimen. All specimens achieved higher capacities than the design load, thus demonstrating that numerous truss models could be developed for the design of the wall structure and still supply a lower bound estimation of capacity. The combined truss analysis of specimen 3 proved more successful than the independent truss analyses of specimens 1 and 2 providing both a higher capacity and stiffer response to load. Specimen 2 was designed with a truss based most closely on the elastic flow of stresses within the wall. It utilized the least weight of steel for its detailing requirements and achieved a higher capacity per pound of reinforcement than the other three specimens.

4.4.9 Aguilar, Matamoros, and Parra-Montesinos (Deep Beams)

Four deep beams were tested at Purdue University [21]. The study was similar to the Maxwell study in that the main purpose was to examine the effect of various design approaches to the performance of a structural element (in this case a simple deep beam). This type of approach is different from a strictly behavioral study in which only a single parameter is changed from specimen to specimen in order to examine the significance of that parameter without any interfering factors. In a design comparison, the various design approaches may lead to many differences in details from specimen to specimen. It is then much harder to discern the effect of single parameters on the behavior of the specimens. The purpose of the Purdue study was to compare the current ACI design approach for deep beam shear with proposed STM guidelines that are applicable to deep beams. Four deep beams were designed for a given loading and geometry (shown in Figure 4-25). The first beam was designed according to provisions from ACI 319-99, Section 11.8 for deep beam shear members. The remaining three specimens were designed according to various STM approaches all conforming to the new ACI 318 code provisions [2]. The first two specimens used Lenton Terminators for anchorage of the primary reinforcement (The

Purdue research was mentioned briefly in Section 3.4.5 of the last chapter because of this). The remaining two specimens used 90° hooked anchorages.

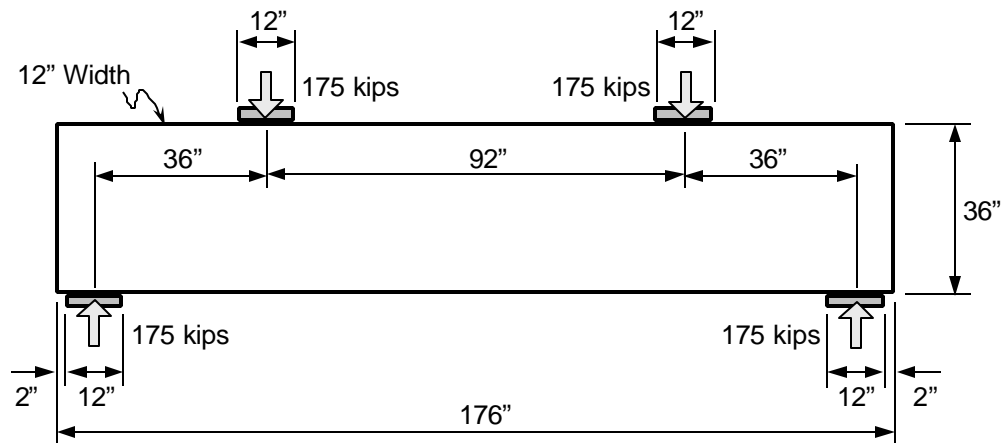


Figure 4-25: Design specimen for the Purdue study

The researchers were primarily interested in the horizontal and vertical splitting steel necessary for confinement of the diagonal shear struts. All specimens exceeded their estimated capacities whether those capacities were calculated using the current ACI shear provisions or the new STM provisions. The STM calculations were shown to be more accurate than the ACI deep beam calculations, though neither gave a close estimate of strength. The STM design approach generally required less splitting steel than the ACI deep beam approach. Two specimens failed in shear and two failed in flexure though both design approaches predicted shear failures for all four specimens. Measured strains indicated that development of primary tension steel occurred over a very short length within the nodal zone located over the reaction bearing pads.

Detailing procedures were different for all four specimens. Only the two specimens that utilized hooked anchorages are directly comparable. Only the amount and placement of splitting

steel were different for these two specimens. The lever arm of the primary tension steel was varied in the other two specimens thus precluding a direct comparison of behavior. The behavior of the two comparable specimens showed that there was no significant change in capacity though nearly 80% of the confining vertical and horizontal steel was omitted from the end shear panel regions in one of the specimens. The more heavily reinforced specimen had a somewhat better distribution of cracking in the end regions. Both of these specimens failed by splitting of the diagonal compression struts (shear).

4.5 FINAL COMMENTS

The survey of experimental work and recommended design procedures for STM leads to the following observations and overall trends.

The procedures for strut-and-tie modeling require additional refinement. Particularly, the topics of node stress limits and anchorage at nodes require attention. The code guidelines for dimensioning of nodes are not based on rational models for the flow of forces at the intersections of struts or the anchorages of ties. For example, at the anchorage of a tie bar in a CCT node, it is unlikely that strut stresses would uniformly extend up to 6 bar diameters to either side of the tie (see Figure 4-14). Geometric compatibility requires that the strut stresses must concentrate and flow into the tie bar. Consequently, the stresses in a CCT node must be much greater than would be calculated based on the dimensioning guidelines put forth by the codes and also much greater than the stress limits allowed by the codes. The dimensioning guidelines require experimental study. Realistic dimensioning guidelines for nodes are necessary in order to properly reflect the flow of forces and would allow for larger and more realistic stress limits to be specified in the codes. Experimental studies of the bearing strength of concrete have shown that in many situations bearing stresses can be much larger than the cylinder compressive strength, f'_c . Similar large

bearing strength capacities should also be expected for many node cases. However, the current provisions allow a maximum bearing strength of $1.0\phi_c f_c'$ for the best node case. The stress limits seem to be much too conservative. However, the dimensioning guidelines allow for unrealistically large node boundaries to be assumed.

The issues with node dimensioning and stress limits are exacerbated by the lack of guidelines for addressing those nodes that do not meet the current requirements. How is a node improved when the stresses acting on it are greater than the code limits? Only two alternatives are available: the D-region must be re-detailed to increase the size of the node and thus reduce the stresses or the concrete strength must be re-specified to meet the stress demands. Neither alternative is appealing. Re-detailing of the D-region requires that tie steel must be redistributed and spread out in order to increase the size of CCT and CTT nodes or that the dimensions of the structure must be enlarged to increase the size of CCC nodes (in many cases CCC can be simply improved by enlarging a bearing plate). Once the D-region is re-detailed, the truss model must be re-drawn and the STM process proceeds through another iteration. This requires additional design time and can lead to detailing compatibility problems at the boundaries between D- and B-regions. The second alternative, increasing the concrete strength, is a radical and expensive solution to accommodate the stress limits of a single node. Currently, though all of the codes allow for improvement of the nodes using confining steel, their procedures do not provide any guidelines for improving the confinement or anchorage details at nodes in order to make them meet stress limits.

Anchorage at nodes also presents similar problems. Space limits at nodes are frequently too small to fully develop straight reinforcing bars and hooked bars may create congestion problems. Designers have previously had few alternatives to address anchorage problems at nodes, but new developments in headed bars offer a promising direction for solving this problem.

These issues regarding design of nodes represent the largest obstacle to the implementation of strut-and-tie modeling in common design practice. Research and re-evaluation of node behavior must be performed and incorporated into STM design procedures. Fortunately, the studies by Anderson (CTT nodes), Bouardi (CCT nodes), and Roberts (local anchorage zones) have confirmed that isolated node tests will provide lower bound results compared to similar nodes in non-isolated situations. Similarly, the research by Adebar and Zhou (pile caps) has confirmed this for isolated tests of struts. This result could be put to good use in determining limits on nodal zone stresses and anchorage requirements. While the application of STM might be limitless, the number and types of node situations that occur may be a much smaller number. Since it seems possible to isolate nodes for experimental testing, it should be reasonable to derive experimentally based design limits for the detailing of nodal zones in STM applications much as Adebar and Zhou were able to do for the analysis of struts.

Finally, in many experimental studies, STM has been shown to be a conservative design approach because it typically provides a lower-bound estimate of capacity. However despite this success it is somewhat discouraging to look back over the extent of the research and recall how often STM fails to properly predict the failure mode of specimens. Sanders and Wollmann noted that tie yielding was predicted for many of their specimens and crushing at the boundary of the local zone actually resulted. Adebar and Zhou also predicted flexural yielding for many of the pile cap tests that they reviewed, but most of the caps failed in shear. Ideally, tie yielding should result in a plastic limit of the specimen capacity and no other failure should occur until material strain limits are exceeded by excessive deformations. However, in tests, post-yielding capacity very often resulted in a brittle failure for specimens as other components of the model reached their limit states. In design practice, it is unlikely that a Dregion would be loaded near its design

capacity before the capacity of a neighboring B-region was reached, thus limiting the ultimate load that would be placed on the D-region. Therefore, post-yield capacity is probably not an issue. However, it is still a flaw of the STM method that it cannot be relied on to accurately predict the nature of failure for many structural situations.

Chapter 5: CCT Nodes: Specimen Fabrication and Testing Procedures

5.1 INTRODUCTION

This chapter briefly discusses the details of the CCT node specimens and of the test setup and procedures used in the testing of the CCT nodes. A total of 64 CCT node specimens were tested in the course of the project. Figure 5-1 shows a photo of a test specimen and the test frame. The basic test was essentially as shown in Figure 5-1, however, many small details of the test specimens and the testing procedure evolved over the course of the project.

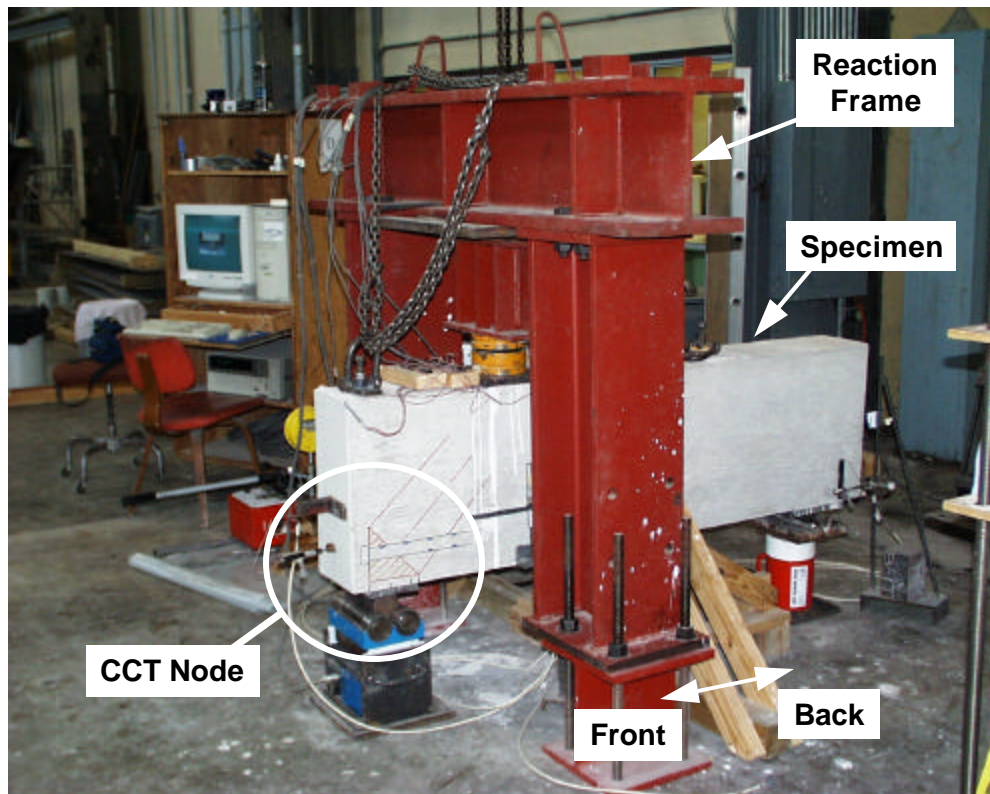


Figure 5-1: A typical CCT node test

5.2 SPECIMEN DETAILS

Both unconfined and confined CCT node specimens were tested. Confined specimens contained stirrup reinforcement through the nodal zone while unconfined specimens contained nothing but the tensile tie steel in the nodal zone region. Figure 5-2 shows the basic reinforcement layout for the unconfined specimens. No stirrups were placed in the region through which the nodal zone and the primary diagonal strut pass. In the unconfined specimen series, three strut angles were tested: 30° , 45° , and 55° . Changes in strut angle were accomplished by moving the location of the top reaction frame. All CCT node specimens were 20" deep and 72" long. The width of the specimens was changed depending on the size bar used in the primary tension tie. The width was generally $6d_b$, where d_b was the diameter of the tension tie bar. #8 and #11 size bars were tested with corresponding specimen widths of 6" and 8.5" respectively (Figure 5-4). The tension tie was always centered at 4" from the bottom of the specimen. The yield strength (f_y) of the ties was between 61 - 68 ksi (refer to Table A-1 in Appendix A for further details).

The first 8 specimens of the CCT node test program differed from the final layout described above. The first four specimens were cast with 5500 psi concrete, $8d_b$ width (#8 bars with 8" width), and no stirrup reinforcement. Originally it was thought that node failure would occur before shear dominated the capacity of the specimen, thus stirrups were omitted as an unnecessary detail. However, the nodes achieved higher capacities than expected and shear failure occurred in the back section of the specimens ("Front" and "back" are labeled in Figure 4-2(a)). The "front" of the specimen refers to the end containing the CCT node region. The "back" refers to the other end of the specimen.). Thereafter, stirrups were placed in the back portions of all specimens. Stirrups were either #3 or #4 closed hoops. Additionally, the concrete mix used in the CCT node specimens was changed to reduce the strength of the concrete to make node failure

more likely. The second group of CCT node specimens was cast with 3000-4000 psi concrete that was used throughout the rest of the test program. Seven specimens were cast in that batch: 4 with an $8d_b$ specimen width and 3 with a $6d_b$ width. Following the test of those specimens, the $6d_b$ width was used throughout the rest of the testing to allow more specimens to be cast in a single batch while still producing the failure modes of interest.

The reinforcement layout for the confined specimens is shown in Figure 5-3. Five confined CCT node specimens were tested. Confinement was provided by extending the stirrup reinforcement across the full length of the specimen. #3 hoop stirrups ($f_y = 63$ ksi) were used. Spacing was at 3" and 6" within the nodal zone and 6" along the rest of the specimen. Figure 5-5 shows the geometry of the stirrups used in the confined specimens.

The tensile tie reinforcement of the CCT nodes was generally anchored by a mechanical head. The tensile bars were always placed so that the bearing face of the head aligned with the front edge of the CCT node bearing plate (Figure 5-6). Non-headed bars were aligned such that the end of the bar lined up with the edge of the bearing plate. Xtender headed bars were aligned such that the point where the maximum head diameter began lined up with the front edge of the bearing plate. Stirrups in confined specimens began 1" from the front edge of the bearing plate. Two details were used for hooked bar specimens: either the point of horizontal tangency of the bend was aligned with the front edge of the bearing plate (detail 1) or the inside bend of the hook was aligned with the front edge of the bearing plate (detail 2). The details of the hooked bar specimens are shown in Figure 5-10.

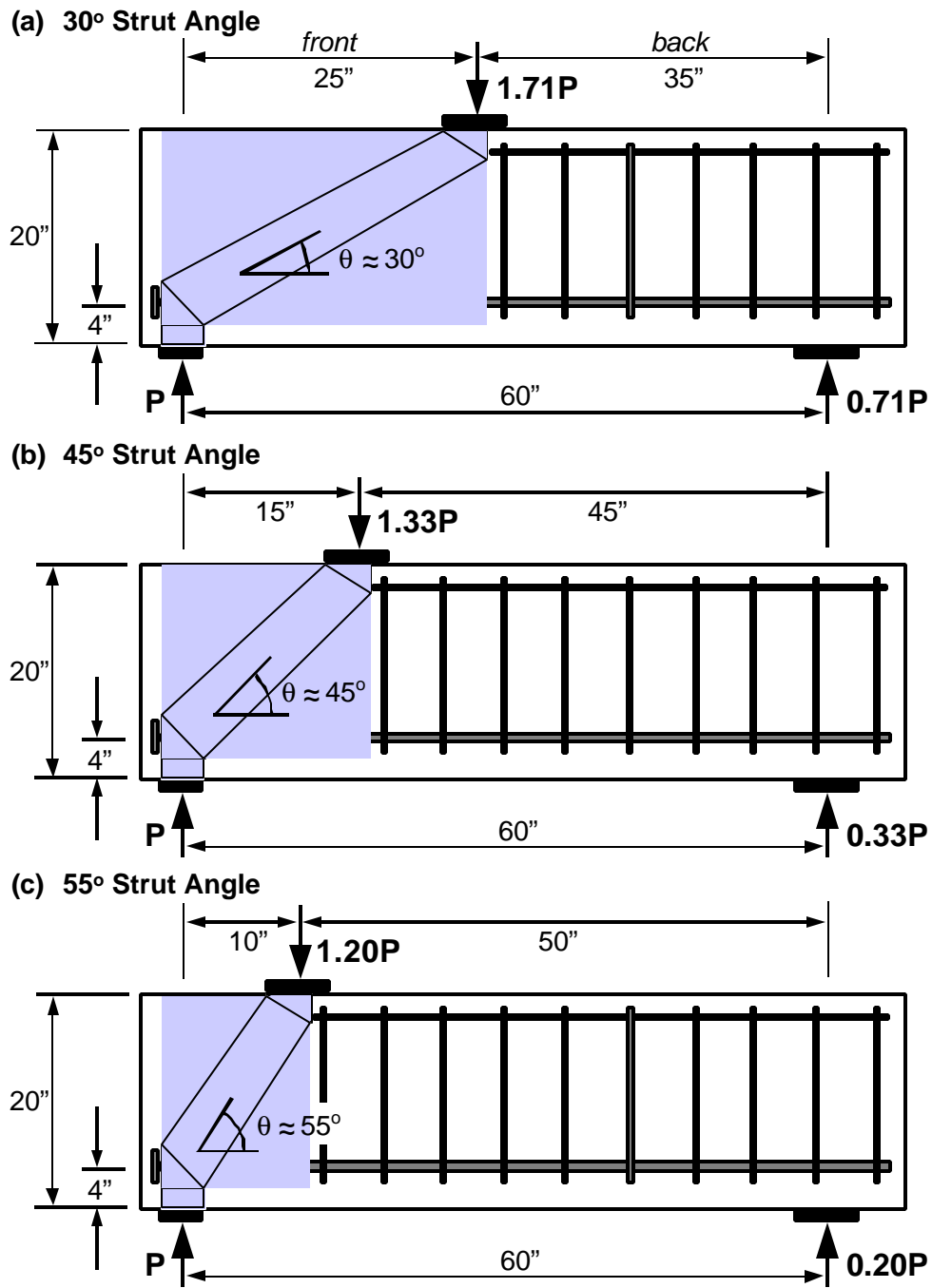
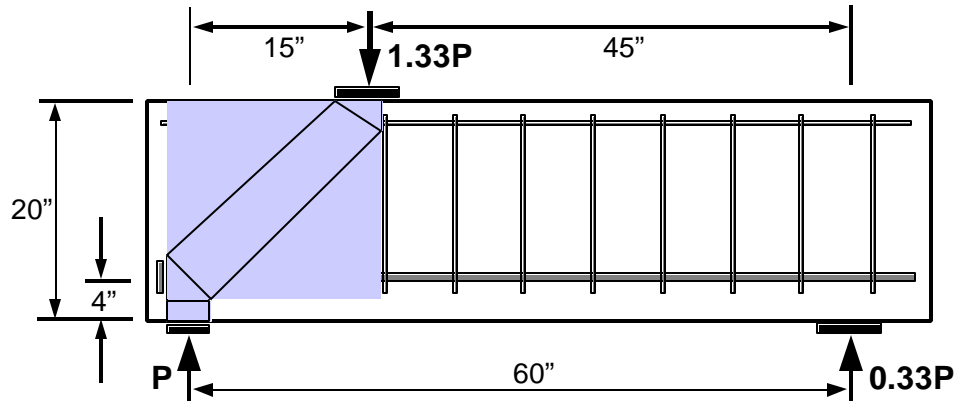


Figure 5-2: Reinforcement layouts for unconfined specimens

(a) #3 stirrups at 6" in nodal zone



(b) #3 stirrups at 3" in nodal zone

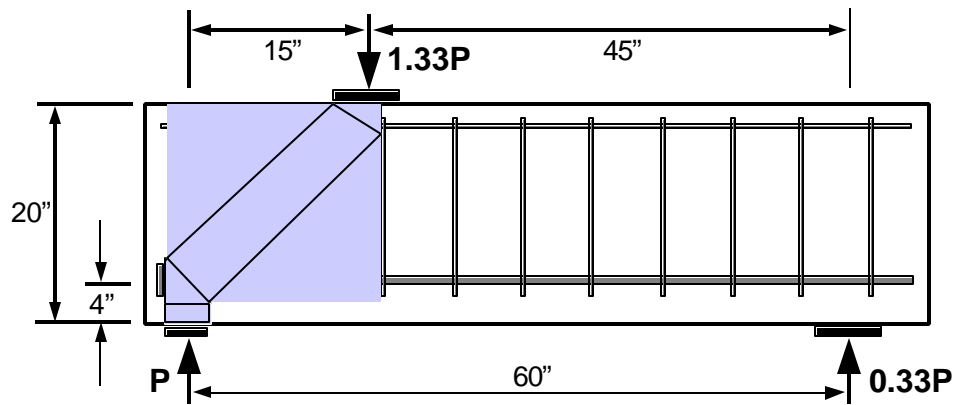


Figure 5-3: Reinforcement layouts for confined specimens

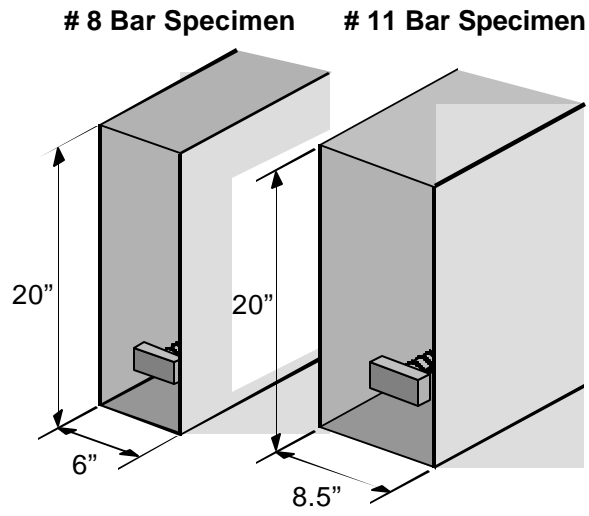


Figure 5-4: Widths of unconfined specimens

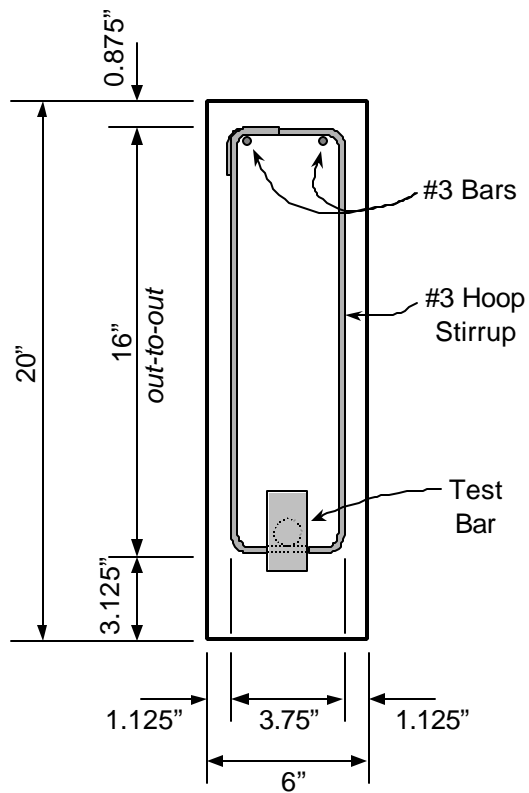


Figure 5-5: Cross-section of confined specimen and stirrup geometry

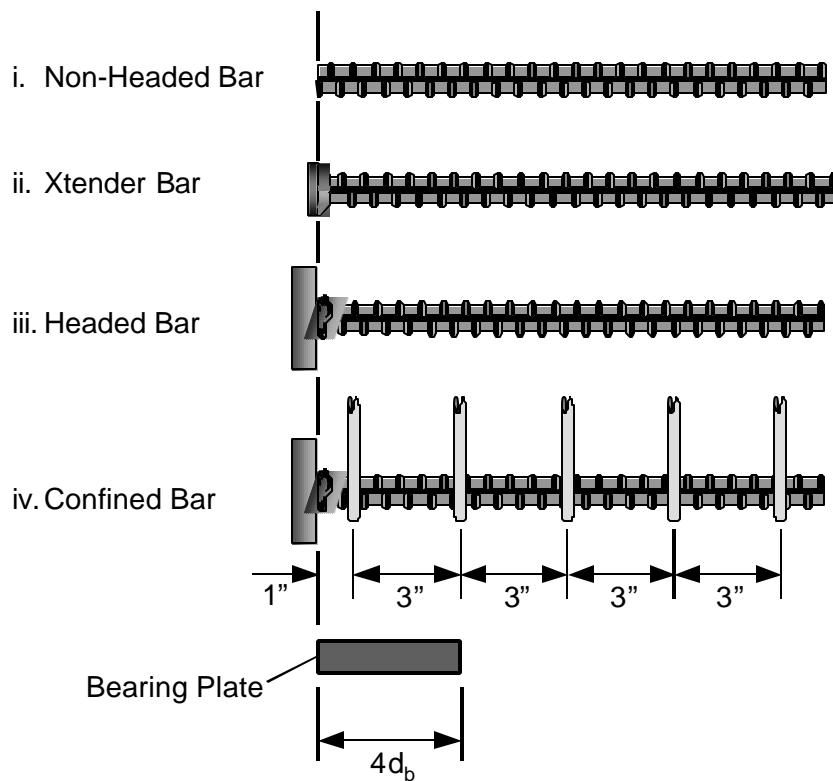


Figure 5-6: Alignment of heads with bearing plate

All but two specimens were cast upright. Concrete was placed from above and vibrated into position. Formwork was constructed of standard lumber ($\frac{3}{4}$ " plywood and 2 x 4 lumber). The formwork for the CCT nodes could accommodate up to eight specimens in one cast. The formwork was reused several times. Two unconfined hooked bar specimens were cast on their sides.

Three concrete mixes (A, B, and C) were used in CCT node specimen casting. The concrete was supplied by a local company. Table 51 lists the concrete mix proportions. A nominal maximum aggregate size of 0.75" was specified. Mechanical properties of the hardened concrete were determined using standard 6" diameter cylinders. Compression strength, splitting

tensile strength, and modulus of elasticity were measured just prior to and just following tests of a group of specimens with the same concrete. Initially, only compression strength was measured. Tests were performed according to ASTM standards C39 (compressive strength), C496 (splitting tensile strength), and C469 (modulus of elasticity) [6, 7, 8]. Table 5-2 lists the measured properties from each cast.

| Mix | Mix Proportions by Weight | | | | | w/c Ratio |
|-----|---------------------------|-------|-------|-----------------|--------|-----------|
| | Coarse Aggregate | Sand | Water | Portland Cement | Flyash | |
| A | 45.7% | 37.2% | 6.4% | 7.7% | 3.0% | 0.60 |
| B | 48.0% | 36.6% | 6.8% | 6.7% | 2.0% | 0.78 |
| C | 47.5% | 36.3% | 6.8% | 7.3% | 2.2% | 0.72 |

Table 5-1: Concrete mix proportions

| Concrete Batch | Cast Date | Age (days) | f'_c (psi) | f_{ct} (psi) | E_c (ksi) |
|----------------|-----------|------------|--------------|----------------|-------------|
| A1 | 7/12/99 | 42 | 5700 | - | - |
| B1 | 9/23/99 | 39 | 3000 | - | - |
| B2 | 1/21/00 | 28 | 4000 | - | - |
| B3 | 5/16/00 | 55 | 3900 | - | - |
| B4 | 10/6/00 | 63 | 4100 | 460 | 4300 |
| B5 | 11/16/00 | 33 | 4000 | 430 | 3700 |
| B6 | 1/25/01 | 41 | 3100 | 350 | 3300 |
| B7 | 2/8/01 | 35 | 4100 | 420 | 4000 |
| C6 | 5/17/01 | 35 | 3800 | 360 | 4000 |

Table 5-2: Hardened concrete properties

All specimens included miscellaneous details such as lifting inserts and bar chair spacers. Placement of these details was avoided in the critical nodal zone and surrounding concrete. Figure 5-7 shows the typical placement of these extra details within an unconfined specimen. Individual chair spacers were used on the bottom and sides of the primary tension tie to maintain its position during the cast. The same details were included in confined specimens in the same locations.

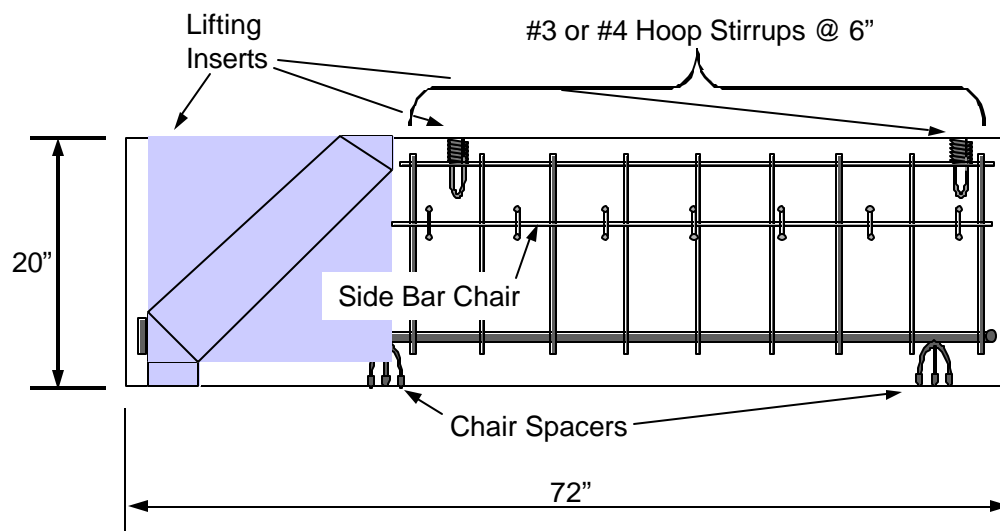


Figure 5-7: Placement of miscellaneous details in the CCT node specimens

In addition to the specimens listed above, three specimens with special details were tested. These specimens were not typical and were fabricated to study some special aspects of CCT node behavior and are discussed in section 6.1.7.

5.3 SPECIMEN INSTRUMENTATION

Three types of instrumentation were used during the testing. Below is a list of the different instrumentation types and their purpose in the testing:

- **Strain gages** were used on the tie bar surface to provide information on the development of force in the tie bar in the nodal zone and in the confining reinforcement. Use of the strain gages is discussed in detail in Appendix A.
- **Linear potentiometers** were used to measured horizontal slip of the head relative to the outside face of the concrete and to measure deflection of the specimen under the top load point.
- A **load transducer (load cell)** was used to measure the load directly underneath the CCT node bearing pad.

The placement of this instrumentation is shown in Figure 5-8. Figure 5-9 shows a close-up of the node region and the details of the strain gage placement for the standard specimens. A hollow tube was cast into every specimen to allow access to the head for slip measurements. The linear potentiometers were spring-loaded and required no special attachment to the head. Slip potentiometers were connected to hooked bars through a small diameter hollow tube to determine slip at the point of bend tangency. However, the particular slip potentiometers used for those tests provided very unreliable data. A later test of a confined hooked bar specimen was performed with a linear potentiometer connected to the point at which the hook bend is vertical, treating that portion of the hook in the same manner as the head was treated for all of the other tests. Slip measurements of non-headed bars were simply made against the termination point of the bar. Strain gage layouts for the hooked bars are shown in Figure 5-10. Strain gage layouts on the confined specimen stirrups are shown in Figure 5-11.

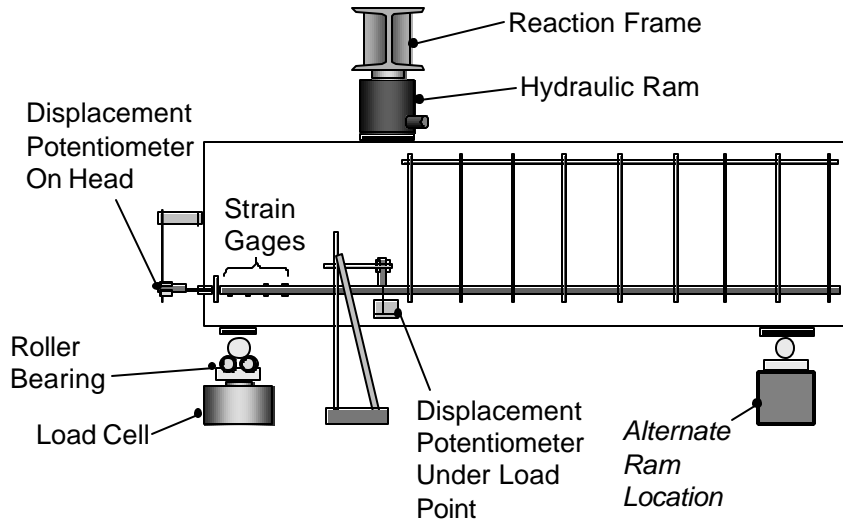


Figure 5-8: Placement of instrumentation for a typical specimen

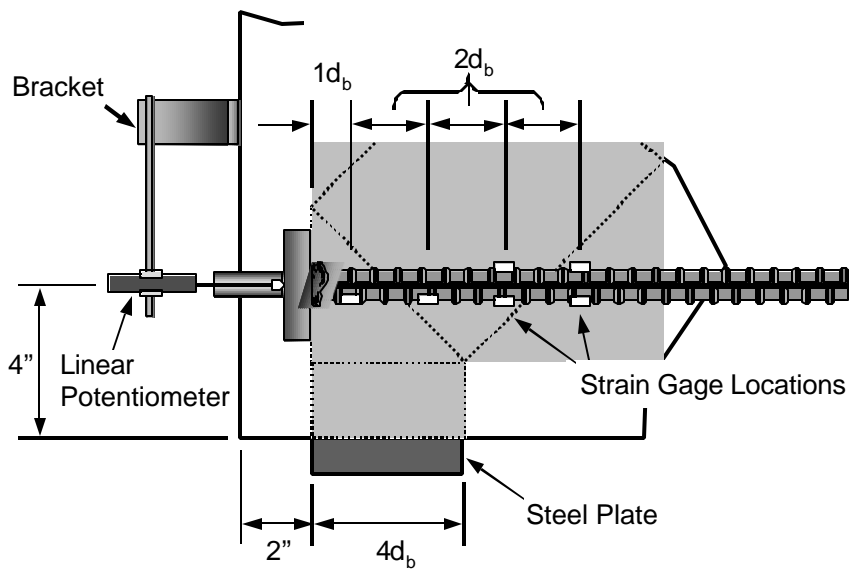
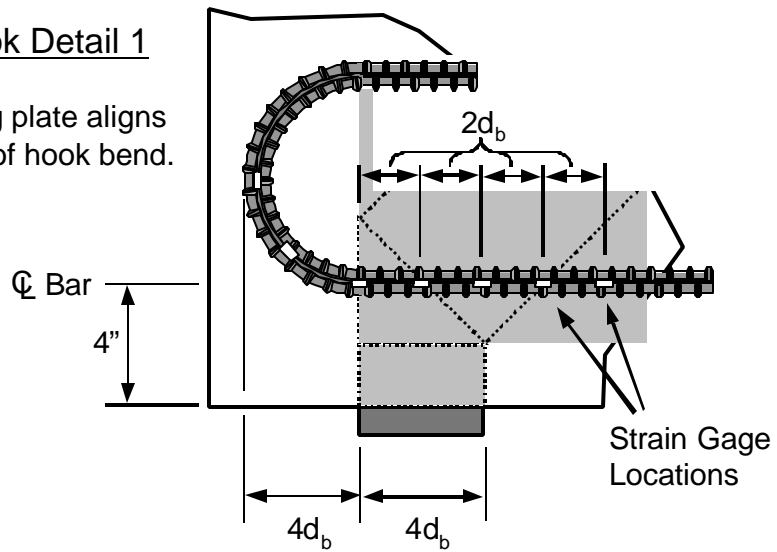


Figure 5-9: Placement of instrumentation in the nodal region of a typical specimen

Standard Hook Detail 1

Edge of bearing plate aligns with beginning of hook bend.



Standard Hook Detail 2

Edge of bearing plate aligns with inside of hook bend.

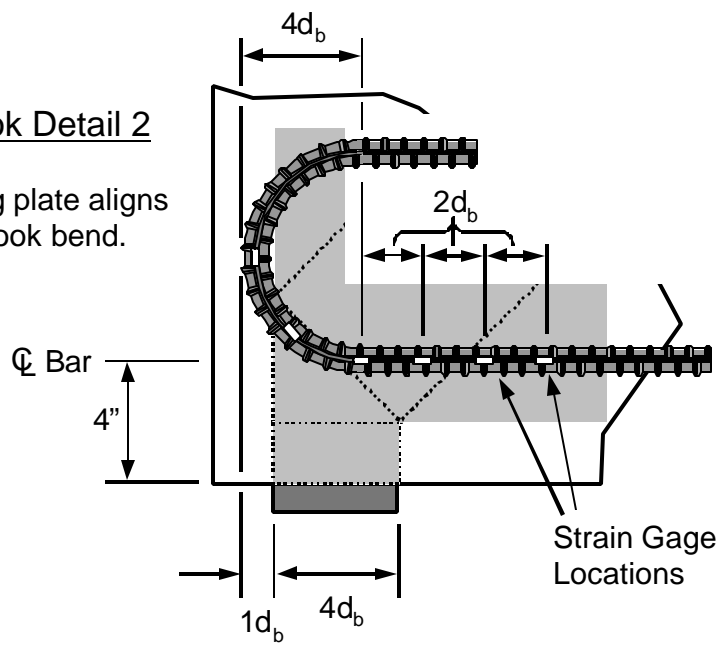


Figure 5-10: Details of the reinforcement and instrumentation for hooked bar specimens

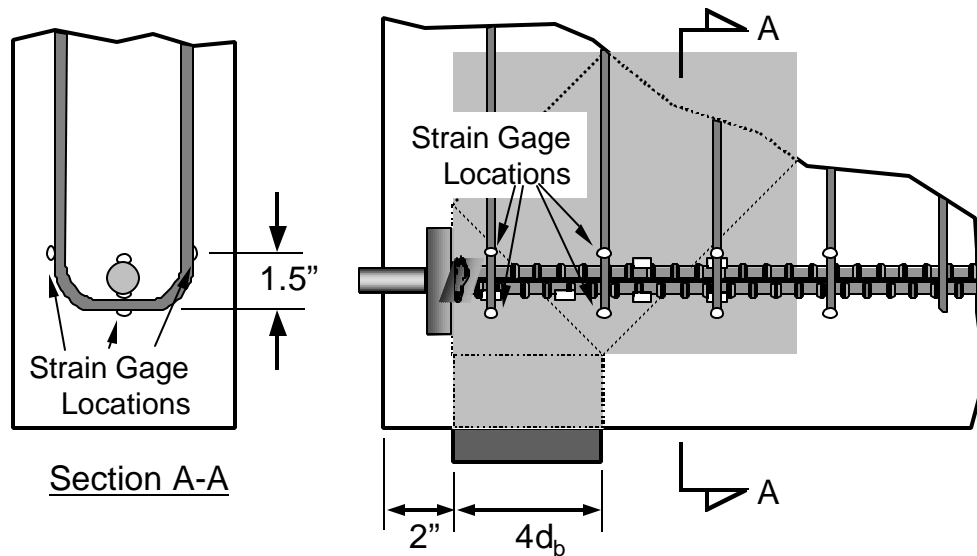


Figure 5-11: Placement of instrumentation on stirrups of confined specimens

The arrangement of strain gages shown in Figure 5-9 was not the initial layout used for the first sets of CCT tests. As with the reinforcement detailing, the placement of strain gages evolved as the testing progressed. The first two groups of CCT node specimens contained strain gages on only the bottom side of the tie bar. Furthermore, the spacing of the gages was at $4d_b$ rather than $2d_b$ as used in the later specimens. Data from these first two casts of CCT node specimens was problematic for many reasons, and those specimens are not included in any of the data presentation. In the third group of CCT node specimens, a layout very similar to the one shown in Figure 5-9 was used, except that the top gage that is placed at a distance of $7d_b$ from the face of the head was placed on the bottom of the bar at $9d_b$. Following the tests of those specimens, it was realized that little of interest was occurring at that location and the gage was moved up to the top to give redundancy to the other top gage. The layout of the strain gages was then finalized for the remaining casts of specimens with the exception of one specimen. One

unconfined specimen was cast with 22 strain gages placed at $2d_b$ on the top and bottom of the tie bar so that the complete strain profile of a bar at a CCT node could be determined.

As mentioned in the last section three specimens with special reinforcing details were cast. Each of these three specimens contained strain gage instrumentation on the special reinforcing details. The details of the instrumentation of these specimens will be with the test results.

5.4 LOAD SETUP

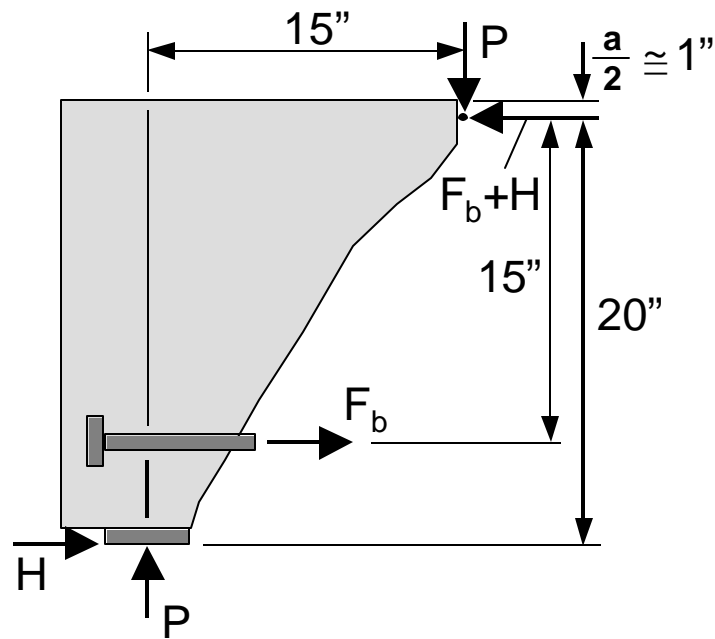
The basic load setup for the CCT node specimens is pictured in Figures 5-1 and 5-8. Essentially, the CCT node specimen was a deep beam that rested on two bearing supports. A hydraulic ram exerted load through a top bearing plate. The ram reacted against a steel cross-frame that was tied into the floor. The reaction frame was composed of heavy steel W-sections and exhibited no discernible deformation during the loading of any of the test specimens. A hemispherical head was placed in series with the load ram to ensure that load was exerted uniformly from the ram into the specimen.

For the CCT node specimens with #11 bars, the capacity of the specimen exceeded the capacity of the ram. In order to load these specimens, the ram was moved to the back bearing plate and a rigid steel piece was placed between the specimen and the reaction frame (the hemispherical head was left in place). Figure 5-1 shows a photograph of this arrangement. The alternate location of the ram is indicated in Figure 5-8. The placement of the ram at the back bearing plate provided more leverage for the application of load and required less ram force. The disadvantage of this arrangement was that more stroke was required in order to load the specimen and an additional linear potentiometer had to be placed at that location in order account for deflection at that point. This change in the load arrangement did not affect the behavior of the specimens in any way.

Changes in the strut angle required changes in the loading geometry. The reaction frame remained stationary, but the supports and the specimen had to be moved either forward or backward in order to change the placement of the load.

As with the reinforcement layout and the strain gage instrumentation, the configuration of the load setup went through several steps before it was finalized. For the testing of the first two groups of CCT node specimens, the load cell was placed in line with the hydraulic ram at the top of the specimen and the magnitude of the reaction at the node was calculated. Initially, neoprene pads were used to support the beam. However, the distribution of load through the bearing plate was uneven under this configuration. A fixed pin roller was added to the front bearing. However, analysis of subsequent test results indicated that a horizontal reaction might occur due to friction. The presence of a horizontal reaction in the CCT node region can seriously affect the equilibrium of the assumed truss (Figure 5-12). The force in the bar, F_b , should be related to the force in the bearing pad, P , by equilibrium of the CCT node and the geometry of the strut angle. If a horizontal reaction, H , is introduced at the bearing plate, the truss mechanism becomes indeterminate. For a 45° strut, the horizontal reaction also makes the vertical reaction, P , larger than the bar force, F_b . Normally the capacity of the specimen, P , should be limited by the force that can develop in the tie bar, but if a horizontal force, H , is introduced, the specimen can reach higher than expected capacities and, unless it can be measured, loads calculated for the bar are not correct. The higher bearing plate reaction causes greater compression in the CCT node region which may affect the CCT anchorage capacity. For the third cast of specimens, a free roller bearing was placed under the CCT node. The free roller was designed to eliminate any horizontal force development at the bearing plate. Additionally, the load cell was moved underneath the CCT node in order to have an exact measure of the reaction there. Figure 5-13 shows the final support arrangement. The

development of this support arrangement at the CCT node was an important advance in the accuracy and consistency of the CCT testing process.



$$\sum \text{Moments} = P(15'') - F_b(15'') - H(20'') = 0$$

$$P = F_b + 1.33H$$

Figure 5-12: Equilibrium of CCT node panel with a horizontal reaction at the bearing plate (45° strut angle)

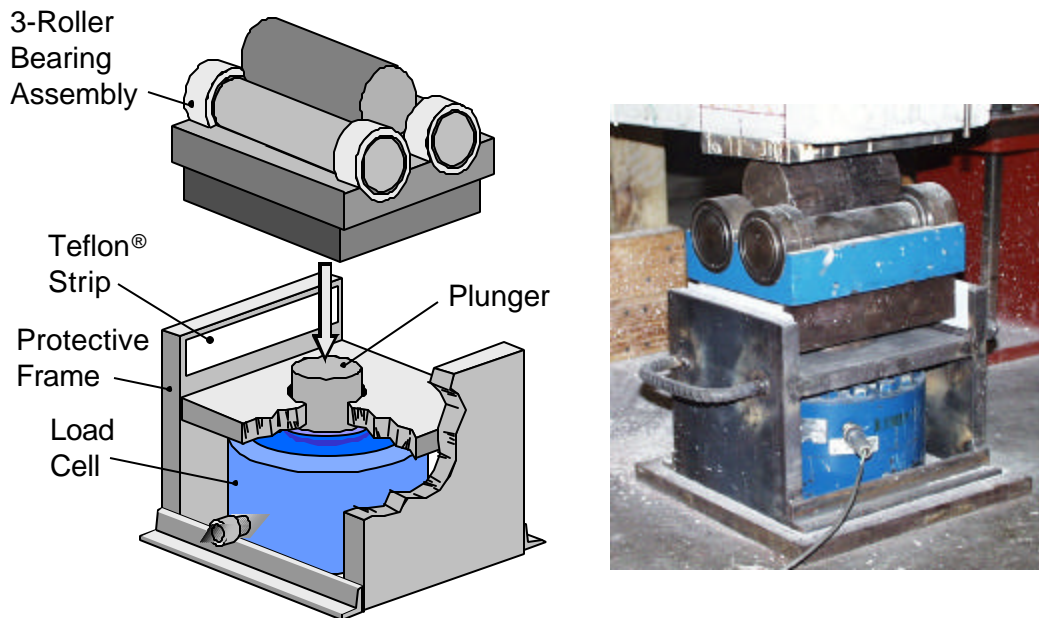


Figure 5-13: Free roller detail used for the final CCT node test setup

Young [120] reported on the first CCT node tests. Her thesis contains a more detailed discussion of the evolution of the CCT fabrication and testing process. By the fourth group of CCT node specimens, all of the reinforcement, instrumentation, and loading details of the CCT node specimens had been finalized (There were 9 groups of CCT node specimens which were separated by casts.).

5.5 TESTING PROCEDURE

Preparation of the specimen for testing involved the attachment of the top and bottom bearing plates, the front bracket used to hold the linear potentiometer for slip measurements of the head, the attachment of the side bracket used for deflection measurements, and drawing of the reinforcement layout and node geometry on the sides of the specimen (The drawing of those details facilitated in understanding the cracking patterns and provided a reference for picture

taking.). $\frac{3}{4}$ " to 1" thick steel bearing plates were used. The plates were the full width of the specimen. The top and rear-bottom plates were each $6d_b$ long for all tests. The front-bottom plate (the critical CCT node plate) was either $4d_b$ or $6d_b$ in length for all tests. Initially the $6d_b$ length was used, but, by the third group of specimens, most tests were carried out with the $4d_b$ length. The smaller bearing area made the node region more likely to fail and thus provided insight into the failure modes. The bearing plates were attached to the specimen with Hydrostone® plaster. The plaster provided a uniform bearing between the plate and the concrete surface allowing for an even transfer of stress. The slip and deflection potentiometer brackets were simply epoxied to the concrete surface.

After the pre-test preparation, the specimen was placed into position within the load frame (the top cross-piece was removable for this purpose) and the load ram and hemispherical head were placed into position on the top of the specimen. Next, all instrumentation was connected to the data acquisition equipment and a computerized check of the circuits was conducted. Once the instrumentation was deemed to be working properly, the test was begun.

Load was controlled in the specimen via a hand-controlled pump. The data acquisition equipment allowed for instantaneous reading of the load cell data. A hydraulic dial gage was also used as an alternative check on the specimen load. Load was generally applied in 3-5 kips increments up to the cracking point of the specimen. Thereafter, load was applied in 1-2 kip increments with data acquisition after each load increment. Load increments were generally once every 15-30 seconds. Loading was halted at intervals of 5-10 kips to check the specimen for cracking and take pictures if necessary. On some specimens crack widths were measured. These breaks in loading usually took around 5 minutes or less. Once the ultimate load of the specimen was approached, the load increment was reduced to about 0.2-0.5 kips until failure. Failure was

generally sudden and brittle (frequently explosive). Photographs were then taken of the failed specimen and the load setup was cleaned up for the next test.

The complete testing process generally took 3-4 hours with loading taking only one hour or less of that time. Two CCT node tests could easily be performed in a day. At the peak of testing activity, three tests were performed on some days. The specimen fabrication process was much longer. Usually, three workweeks were required to build and cast 8 CCT node specimens. The testing of these 8 specimens could be performed in one week.

5.6 CCT NODE VARIABLES

As stated at the beginning of this chapter, 64 CCT node test specimens were fabricated and tested. The first 11 of these tests (from the first two specimen casts) must be discounted in the final analysis because the reinforcement layout and/or load setup were flawed. These tests were valuable in the information they provided on construction and testing procedures. However, the data can not be compared with other test results. Two other specimens in the later casts were also flawed due to poor concrete consolidation and the results were omitted in the final analysis. The study is based on 51 specimens that provided reliable test data. This section outlines the variables tested in the CCT node series and finally provides a master list of all the CCT node specimens.

Four basic variables were tested in the CCT node tests: the bar size, the strut angle, the head size and type, and the amount of confining steel.

5.6.1 Bar Size

Two bar sizes were tested: #8 bars and #11 bars. These sizes were chosen as being of the most interest to the project sponsors, TxDOT. #8's and #11's are at the larger end of the bar size spectrum (though not at the extreme end with #14's and #18's). Anchorage of smaller size bars in

nodal zones is not of much concern because the smaller development lengths required for those bars are usually easier to fit into the tight nodal zone space restrictions. Larger bars are frequently more difficult to incorporate into disturbed regions because of their correspondingly larger development lengths. Typical Texas bridge projects typically do not use bars larger than #11 size. #8's were chosen to represent the smaller end of the spectrum and because their area is almost exactly $1/2$ that of the #11's.

5.6.2 Strut Angle

Three strut angles were tested in the CCT test series: 30°, 45°, and 55°. The 45° strut angle was chosen as the baseline for testing because it provided a convenient equilibrium solution and represented a median strut angle that is believed to be very realistic for strut-and-tie modeling. The 30° angle was chosen as an extreme lower bound for possible strut angles. The debate over reasonable strut angles in ACI code committee work has surfaced the question of whether or not the 30° angle is a realistic limit. Specimens with 30° angles were included in the test series in order to answer questions regarding the lower bounds of strut angle limits. A 60° degree strut angle as been considered as an upper limit for strut-and-tie modeling. Specimens with a 55° strut angle were tested as an upper limit. The geometry of the 60° strut configuration placed the top load plate too close to the front of the specimen, so a slightly shallower angle was used for the upper limit of the test program.

5.6.3 Head Size/Type

Several different head types were tested in the program as well as standard hooks. Though the different head types frequently had different geometric shapes (square, rectangular, circular) they can usually be distinguished by their size alone. The hooks have no reasonable

geometry to define as a head area. Head/anchorage types consisted of non-headed bars, standard 180° hooked bars, Xtender headed bars, Lenton Terminator headed bars, and HRC headed bars. The HRC headed bars were frequently cut down in size to provide a variety of head sizes and proportions. For most of the discussion in this report, heads will be distinguished by their relative head area alone. Only in sections that discuss the effect of head shape will the type and shape of the head be distinguished. The relative head areas of the various head types ranged from 0.00 to 10.39. Most of the heads had very consistent dimensions except the Xtender heads supplied by HRC. This head type is created by a forging process that is not very precise. Micrometer measurements were made of the Xtender heads supplied by HRC and the relative head areas of the bars were calculated. These results are summarized in Table 5-3. The mean head sizes from these measurements were used for all data reduction related to the Xtender headed bar tests. Headed bars that were made by cutting down HRC heads were accomplished by first torch cutting the head to slightly over-size dimensions, then by grinding the excess material off until the head had reasonable proportions. Cut-down heads were rejected if either side dimension was off by more than 0.1” or if the total head area was off by more than 5%.

| | | Bar Size | | |
|--|----------------|--------------------|--------------------|--------------------|
| | | # 5 | # 8 | # 11 |
| Number of Bars Measured | | 11 | 35 | 20 |
| Head Diameter, d_h (in) | Minimum | 0.916 | 1.447 | 2.019 |
| | Maximum | 1.016 | 1.512 | 2.107 |
| | Average | 0.970 | 1.479 | 2.041 |
| | Std. Deviation | 0.034 | 0.016 | 0.021 |
| Gross Head Area, A_{gh} (in²) | Minimum | 0.66 | 1.64 | 3.20 |
| | Maximum | 0.81 | 1.80 | 3.49 |
| | Average | 0.74 | 1.72 | 3.27 |
| | Std. Deviation | 0.05 | 0.04 | 0.07 |
| Relative Head Area, $\frac{A_{nh}}{A_b}$ | Range | 1.13 - 1.61 | 1.08 - 1.28 | 1.05 - 1.24 |
| | Average | 1.39 | 1.18 | 1.10 |
| | Std. Deviation | 0.17 | 0.05 | 0.04 |

Table 5-3: Measured head dimensions for Xtender bars

5.6.4 Confinement

Only a few confined CCT node specimens were tested. Confinement consisted of #3 hoops stirrups. The only variable with respect to confinement was the spacing of the stirrups. Stirrups spacing was 3" or 6". It is also reasonable to define the analogous unconfined CCT node specimens as confined specimens with a very large spacing of ties. Confinement was referred to by the confinement ratio: A_s/b_s (the stirrup steel area divided by the specimen width and the stirrup spacing). The three confinement ratios are then 0.000 (unconfined), 0.006 (#3 stirrups at 6"), and 0.012 (#3 stirrups at 3").

5.7 NOMENCLATURE AND LIST OF SPECIMENS

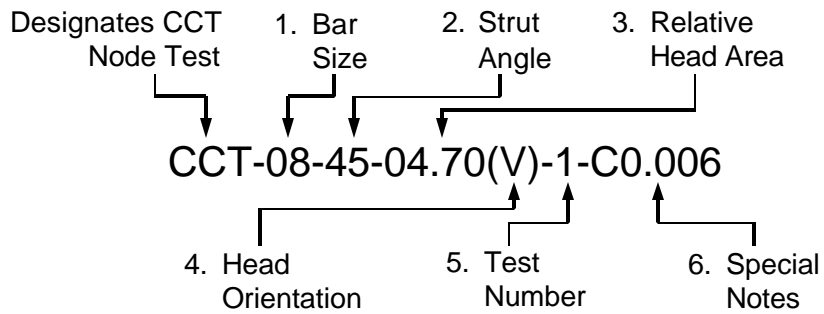
In this section, a standard nomenclature for CCT node specimen identification is presented. Young [120] developed a standard nomenclature in her report on the early CCT node testing that included bar size, head area and shape, specimen width, base plate length, single or multiple bars, confined or unconfined bars, and first or repeat tests. Her nomenclature was extended to include strut angle but symbols for multiple bars were omitted (no multiple bar tests were ever performed). Table 5-4 provides an example of the nomenclature and descriptions of the different identifiers.

The example given in Table 54 is for a CCT node specimen with a #8 bar, 45° strut angle, a head with 4.70 relative head area (this happens to be a 1.5” x 3” rectangular head) oriented with the long side parallel to the vertical axis. It is the first test of its kind and has confinement with a stirrup ratio of 0.006 (#3 closed hoops at 6” spacing within a 6” wide specimen). Special notes are included with the id’s only when necessary. Some other examples are given below:

- | | |
|--------------------------|---|
| CCT-11-45-02.85(H)-1: | #11 bar size, 45° strut angle, relative head area of 2.85; the head is rectangular and oriented horizontally. |
| CCT-08-45-Hook1-1: | #8 bar size, 45° strut angle, bar anchored by a standard hook with positioning conforming to detail 1 shown in Figure 6-10. |
| CCT-08-45-00.00-1-E2,W8: | #8 bar size, 45° strut angle, relative head area equal to zero (non-headed); the specimen was an early test from the 2 nd cast with 8d _b width. |

CCT-08-45-04.70(V)-1-C0.000: #8 bar size, 45° strut angle, relative head area equal to 4.7, a rectangular head with vertical orientation; the special note is optional and only included when the specimen is listed next to confined specimens; it indicates that zero confinement was provided

Table 5-5 is a list of all the CCT node specimens. Every specimen that was fabricated and tested is listed in Table 5-5 whether the test was successful or not. The table lists the specimen id's, the head type used, the concrete used in the test (refer to Table 5-2), the date of the test, and special notes not indicated by the id. Square and rectangular heads are referred to by their outer dimensions. Circular heads are referred to by their diameter, d_h . Standard hooks are referred to by name.



| Identifier | Description | Choices |
|------------|--|--|
| 1. | Bar Size - the size of the tie bar in standard ASTM sizes. | 08..... #8 11..... #11 |
| 2. | Strut Angle - given in degrees. | 30, 45, or 55 |
| 3. | Relative Head Area -given to four significant digits. <i>or alternatively</i> a designation for a standard hook detail. | 00.00 - 10.39 <i>or</i> Hook1 or Hook2 |
| 4. | Head Orientation - either vertical or horizontal; used only for rectangular head tests. | (H)...Horizontal (V).....Vertical |
| 5. | Test Number - gives the number for repeated tests | 1.....1 st Test 2.....2 nd Test |
| 6. | Special Notes - Information for non-standard tests (<i>optional</i>): | |
| | C - Confined Test; followed by the stirrup reinforcement ratio A_s/bs | C0.000-C0.012 |
| | W - Nonstandard specimen width; followed by the width/ d_b | W8..... $8d_b$ wide W6..... $6d_b$ wide |
| | B - Nonstandard bearing plate length; followed by the length/ d_b | B6..... $6d_b$ long B4..... $4d_b$ long |
| | E - Early tests with no stirrups in back region (1 st cast) or without a free roller bearing (2 nd cast) | E1.....1 st cast E2.....2 nd cast |
| | S - Special reinforcement detail (<i>discussed in next chapter</i>) | S1, S2, or S3 |

Table 5-4: Nomenclature of CCT node test identifiers

| Specimen Identification | Head Type | Concrete | Test Date | Notes |
|--------------------------------|---------------|----------|-----------|-----------------------------------|
| CCT-08-45-00.00-1-E1,W8 | no head | A1 | 08-12-99 | 1 st Trial Group |
| CCT-08-45-01.18-1-E1,W8 | $d_h = 1.48"$ | A1 | 08-13-99 | |
| CCT-08-45-04.70(H)-1-E1,W8 | 1.5" x 3.0" | A1 | 08-14-99 | |
| CCT-08-45-10.39-1-E1,W8 | 3.0" x 3.0" | A1 | 08-15-99 | |
| CCT-08-45-00.00-1-E2,W8 | no head | B1 | 10-26-99 | 2 nd Trial Group |
| CCT-08-45-01.18-1-E2,W8 | $d_h = 1.48"$ | B1 | 10-28-99 | |
| CCT-08-45-04.70(H)-1-E2,W8 | 1.5" x 3.0" | B1 | 11-01-99 | |
| CCT-08-45-10.39-1-E2,W8 | 3.0" x 3.0" | B1 | 11-03-99 | |
| CCT-08-45-00.00-1-E2,W6 | no head | B1 | 11-05-99 | |
| CCT-08-45-04.70(H)-1-E2,W6 | 1.5" x 3.0" | B1 | 11-07-99 | |
| CCT-08-45-10.39-1-E2,W6 | 3.0" x 3.0" | B1 | 11-09-99 | |
| CCT-08-45-00.00-1-B6 | no head | B2 | 02-21-00 | |
| CCT-08-45-00.00-1 | no head | B2 | 02-22-00 | #8 Bars |
| CCT-08-45-01.18-1 | $d_h = 1.48"$ | B2 | 02-23-00 | |
| CCT-08-45-01.85-1 | 1.5" x 1.5" | B2 | 02-23-00 | |
| CCT-08-45-01.85-2 | 1.5" x 1.5" | B6 | 03-06-01 | |
| CCT-08-45-02.80(H)-1 | 1.5" x 2.0" | B2 | 02-24-00 | |
| CCT-08-45-02.80(H)-2 | 1.5" x 2.0" | B6 | 03-07-01 | |
| CCT-08-45-02.80(V)-1 | 1.5" x 2.0" | B3 | 07-10-00 | |
| CCT-08-45-04.04-1 | $d_h = 2.25"$ | B2 | 02-25-00 | |
| CCT-08-45-04.06-1 | 2.0" x 2.0" | B6 | 03-05-01 | |
| CCT-08-45-04.70(H)-1 | 1.5" x 3.0" | B6 | 03-06-01 | |
| CCT-08-45-04.70(V)-1 | 1.5" x 3.0" | B3 | 07-10-00 | |
| CCT-08-45-10.39-1* | 3.0" x 3.0" | B6 | 03-05-01 | |
| CCT-08-45-10.39-2 [†] | 3.0" x 3.0" | C6 | 06-18-01 | |
| CCT-08-45-Hook1-1 [‡] | Hook Detail 1 | B2 | 02-28-00 | |
| CCT-08-45-Hook2-1 [‡] | Hook Detail 2 | B2 | 02-28-00 | |
| CCT-08-30-00.00-1 | no head | B7 | 03-12-01 | #8 Bars |
| CCT-08-30-01.18-1 | $d_h = 1.48"$ | B7 | 03-12-01 | |
| CCT-08-30-01.85-1 | 1.5" x 1.5" | B7 | 03-14-01 | |
| CCT-08-30-04.04-1 | $d_h = 2.25"$ | B7 | 03-13-01 | |
| CCT-08-30-04.06-1 | 2.0" x 2.0" | B7 | 03-13-01 | |
| CCT-08-30-10.39-1 | 3.0" x 3.0" | B7 | 03-14-01 | |
| | | | | 30° Strut Angle |

Table 5-5a: List of all CCT node tests

| Specimen Identification | Head Type | Concrete | Test Date | Notes |
|-----------------------------|----------------|----------|-----------|--|
| CCT-08-55-00.00-1 | no head | B3 | 07-11-00 | #8 Bar 55° Strut Angle |
| CCT-08-55-01.18-1 | $d_h = 1.48''$ | B3 | 07-11-00 | |
| CCT-08-55-01.85-1 | 1.5" x 1.5" | B3 | 07-12-00 | |
| CCT-08-55-02.80(H)-1 | 1.5" x 2.0" | B3 | 07-13-00 | |
| CCT-08-55-02.80(V)-1 | 1.5" x 2.0" | B3 | 07-13-00 | |
| CCT-08-55-04.04-1 | $d_h = 2.25''$ | B6 | 03-01-01 | |
| CCT-08-55-04.06-1 | 2.0" x 2.0" | B6 | 03-01-01 | |
| CCT-08-55-04.70(H)-1 | 1.5" x 3.0" | B2 | 03-07-00 | |
| CCT-08-55-04.70(H)-2 | 1.5" x 3.0" | B6 | 03-02-01 | |
| CCT-08-55-04.70(V)-1 | 1.5" x 3.0" | B3 | 07-14-00 | |
| CCT-08-55-10.39-1 | 3.0" x 3.0" | B2 | 03-08-00 | |
| CCT-08-45-00.00-1-C0.006 | no head | C6 | 06-19-01 | Confined Specimens |
| CCT-08-45-00.00-1-C0.012 | no head | C6 | 06-20-01 | |
| CCT-08-45-04.70(V)-1-C0.006 | 1.5" x 3.0" | C6 | 06-19-01 | |
| CCT-08-45-04.70(V)-1-C0.012 | 1.5" x 3.0" | C6 | 06-20-01 | |
| CCT-08-45-Hook2-1-C0.012 | Hook Detail 2 | C6 | 06-19-01 | |
| CCT-08-45-04.70(V)-1-S1* | 1.5" x 3.0" | B7 | 03-08-01 | Special Details |
| CCT-08-45-04.70(V)-1-S2 | 1.5" x 3.0" | B7 | 03-09-01 | |
| CCT-08-45-04.70(H)-1-S3 | 1.5" x 3.0" | C6 | 06-18-01 | |
| CCT-11-45-00.00-1 | no head | B4 | 12-05-00 | #11 Bars 45° Strut Angle |
| CCT-11-45-01.10-1 | $d_h = 2.04''$ | B4 | 12-05-00 | |
| CCT-11-45-01.56-1 | 2.0" x 2.0" | B4 | 12-06-00 | |
| CCT-11-45-02.85(H)-1 | 2.0" x 3.0" | B4 | 12-07-00 | |
| CCT-11-45-02.85(V)-1 | 2.0" x 3.0" | B4 | 12-07-00 | |
| CCT-11-45-03.53-1 | $d_h = 3.00''$ | B5 | 12-15-00 | |
| CCT-11-45-04.13(H)-1 | 2.0" x 4.0" | B4 | 12-08-00 | |
| CCT-11-45-04.13(V)-1 | 2.0" x 4.0" | B5 | 12-14-00 | |
| CCT-11-45-04.77-1 | 3.0" x 3.0" | B5 | 12-18-00 | |
| CCT-11-45-06.69(H)-1 | 3.0" x 4.0" | B5 | 12-17-00 | |
| CCT-11-45-06.69(V)-1 | 3.0" x 4.0" | B5 | 12-15-00 | |
| CCT-11-45-09.26-1 | 4.0" x 4.0" | B5 | 12-19-00 | |

* Unsuccessful testing due to poor concrete consolidation.

† Specimen specially outfitted with extensive strain gaging.

‡ Specimen was side-cast.

Table 5-5b: List of all CCT node tests (continued)

Chapter 6: CCT Nodes: Behavior During Testing

The behavior of the CCT node test specimens as observed during the testing process are discussed in terms of: cracking development, deformation and stress, and failure modes. Results of unconfined CCT node specimens that constitute the majority of the testing are discussed first.

6.1 UNCONFINED SPECIMEN BEHAVIOR

6.1.1 Cracking Behavior

Specimen CCT-08-45-10.39-2 represents a typical CCT node test. A large number of strain gages were placed along the length of the bar in this test; 22 as opposed to 6 used in other tests. The additional data are helpful in explaining stress gradients along the length of the headed tie bar. This specimen had a 45° strut angle and used a #8 bar with a standard HRC square head (3" x 3") at its anchorage. The measured concrete compressive strength was 3800 psi and the measured split cylinder tensile strength was 360 psi. Figures 6-1a and 6-1b outline the development of cracking in the specimen during testing.

Every CCT node specimen began cracking in the same manner as the representative test (CCT-08-45-10.39-2). A vertical crack initiated at the bottom of the specimen at the maximum moment point somewhere directly underneath the top bearing plate, the point of load application (Figure 6-1, part i). Following the development of the first crack, the pattern of crack growth then followed one of two distinct patterns. The representative test followed a pattern of crack development in which secondary diagonal cracks formed successively at regular intervals along the headed bar, starting from the initial vertical crack forming underneath the point of load application and forming closer and closer to the node (parts ii, iii, iv). In this pattern of crack development, the closer the crack was to the nodal zone, the higher the load that precipitated its

formation. Next, as the headed bar reached peak force in the strut-tie mechanism, bond tended to break down along the length of the bar and horizontal cracks appeared between the vertical/diagonal cracks (part v). It was also not unusual for a longitudinal crack to form along the bar on the bottom of the specimen. Longitudinal cracks along the tie bar usually started away from the node and grew towards the head. Crack development generally stopped well before the capacity of the CCT node was reached (part vi). Failure of the specimen could occur in several ways, but generally involved the explosive cleaving of the triangular portion of concrete above the diagonal compression strut (Figure 6-2).

Figure 6-3 illustrates the pattern of crack widening that was observed in specimen CCT-08-45-10.39-2. Initially the first crack widened until the formation of the second crack closer to the node. Then widening of the first crack ceased and the second crack grew wider than the first. Eventually a third crack formed even closer to the node. After the formation of the third crack, the widening of the second crack halted and the third crack widened to an even greater extent. The crack closest to the node always demonstrated the greatest crack widths and the most rapid growth of crack width.

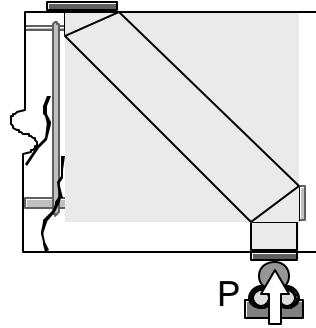
Specimen CCT-08-45-01.85-2 demonstrated a different pattern of crack development that was typical of a different group of the CCT node specimens. This specimen had a 45° strut angle and a #8 tie bar anchored by an HRC head that was cut down to 1.5" x 1.5" dimensions. This test is representative of the CCT tests with small head sizes. The measured concrete compressive strength was 3100 psi and the tensile strength was 350 psi. Figure 6-4 illustrates the pattern of crack development.

After the initial development of a crack underneath the load point (part i), no new cracks formed until the sudden appearance of a splitting crack along the length of the diagonal

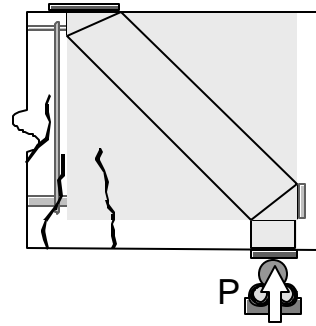
compression strut (part ii). The appearance of the splitting crack along the diagonal strut alleviated strain build-up in the concrete adjacent to the nodal zone and very few cracks formed after the development of the splitting crack. A small vertical crack next to the node was common (part iii) in this cracking behavior. No additional cracks formed prior to failure (part iv).

The pattern of crack development in Figure 6-4 differs from the first one described in Figures 6-1a and 6-1b by the occurrence of the large splitting crack along the length of the strut. This type of crack development was more common in specimens that had tie bars anchored by small heads. The bars anchored by small heads experienced more slip at the anchorage point than bars with large heads (see Section 6.1.5) and the cracking behavior may have been influenced by that difference.

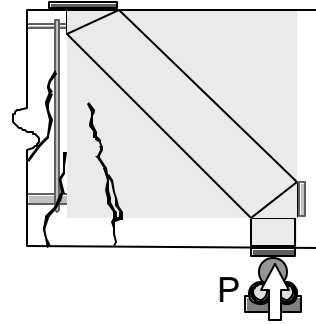
- i. $P = 14.5$ kips
First cracking just under load point initiated by presence of front-most stirrup.



- ii. $P = 26.1$ kips
A second crack forms closer to the nodal zone.



- iii. $P = 29.8$ kips
Growth of the first and second cracks towards the top bearing plate.



- iv. $P = 31.6$ kips
Sudden appearance of a third crack even closer to the nodal zone. The third crack grows at an angle parallel to the diagonal strut.

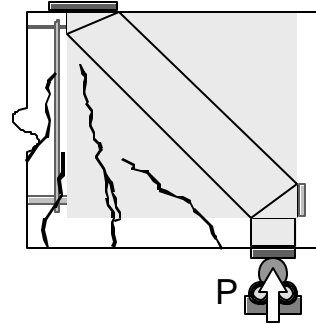


Figure 6-1a: Development of cracks in a representative test with a large head (CCT-08-45-10.39-2)

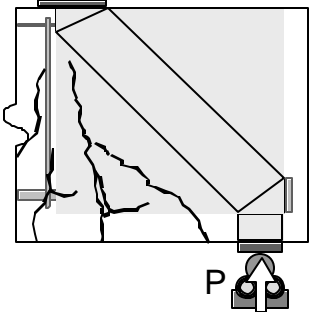
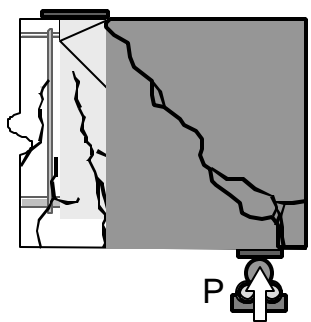
- v. P = 35.3 kips
A horizontal crack grows from the second to the third crack.
- 
- vi. P = 59.5 kips
No significant growth of the existing cracks until sudden and brittle failure of the specimen. The front portion of the specimen (shaded gray) is split away from the main body.
- 

Figure 6-1b: Development of cracks in a representative test with a large head (CCT-08-45-10.39-2) (continued)



Figure 6-2: Failure of specimen CCT-08-45-10.39-2

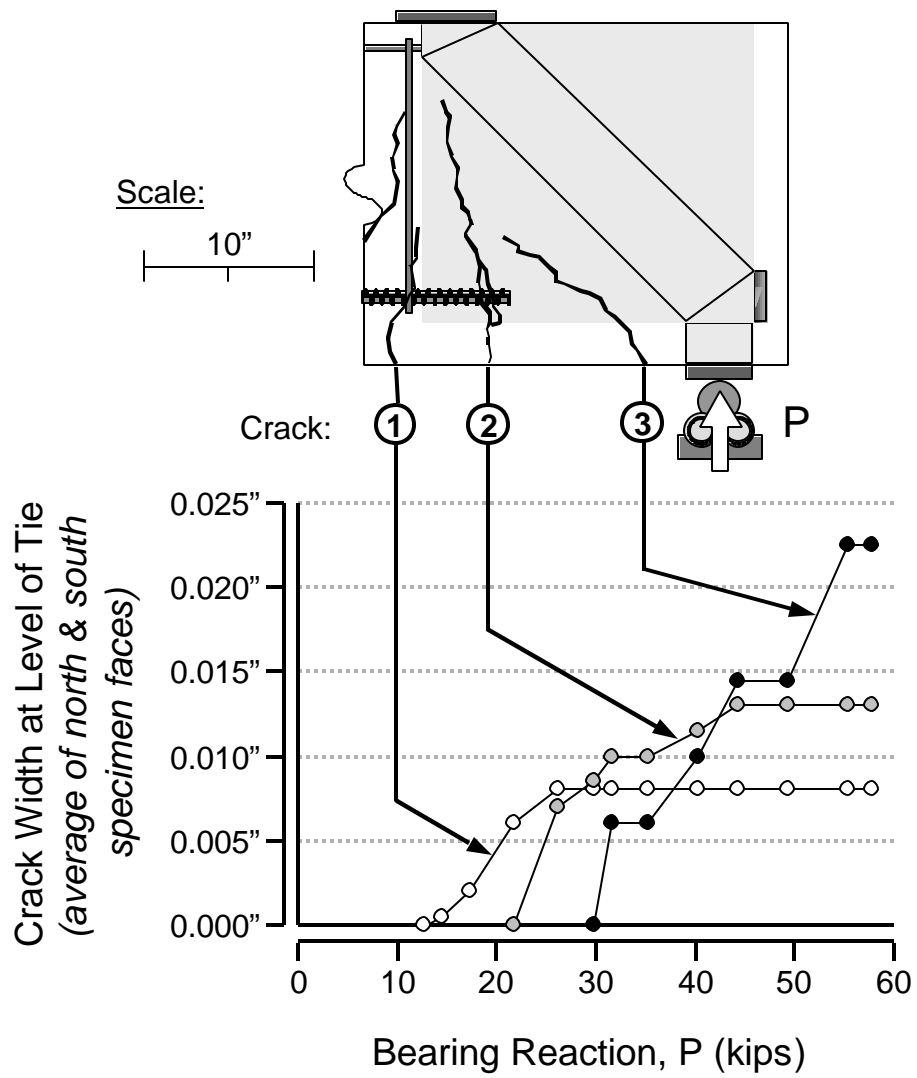


Figure 6-3: Crack width measurements from specimen CCT-08-45-10.39-2

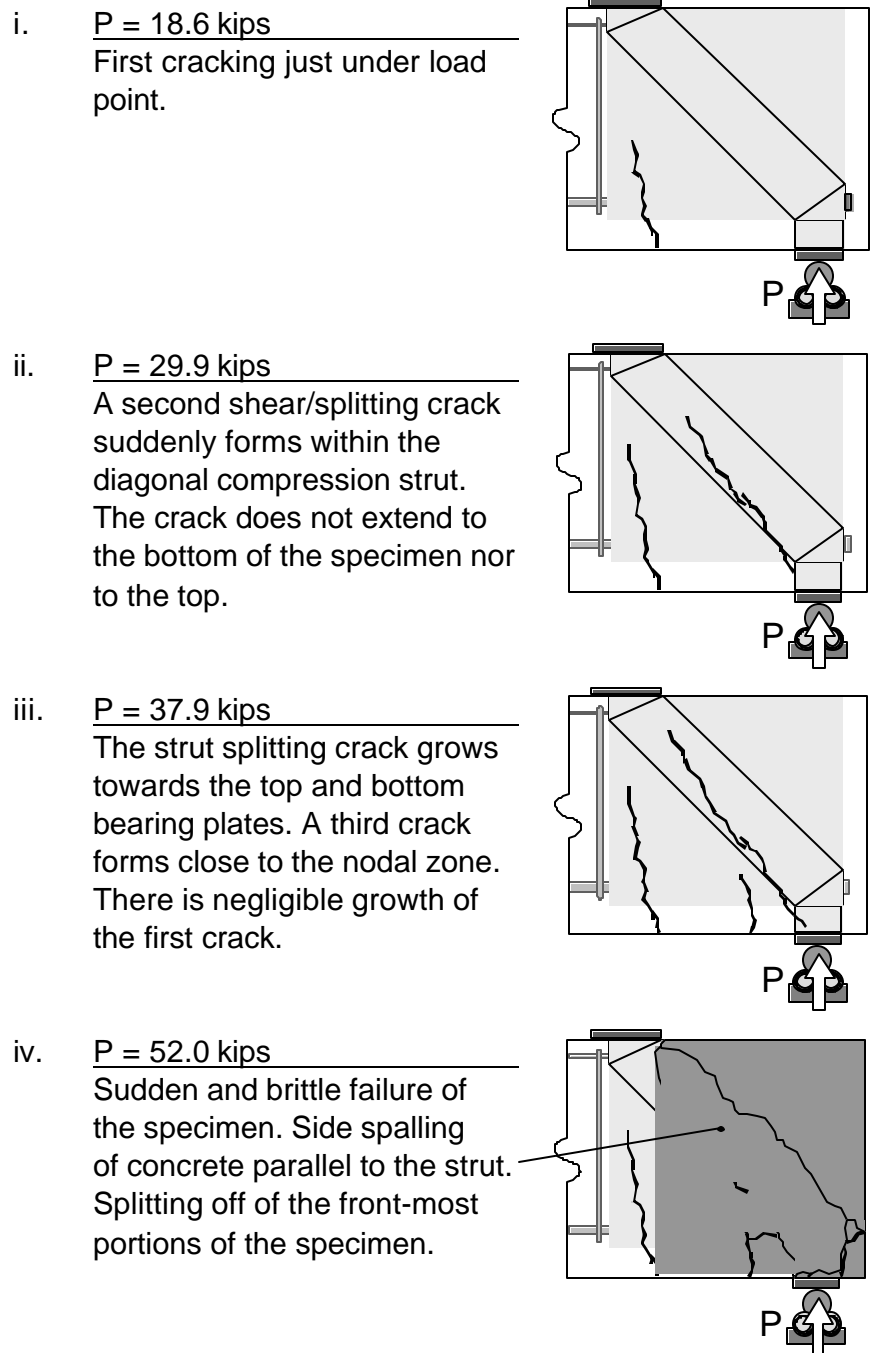


Figure 6-4: Development of cracks in a representative test with a small head (CCT-08-45-01.85-2)

The crack patterns from the previous two specimens are compared to a similar specimen with a tie bar anchored by a standard hook: CCT-08-45-Hook2-1. The measured concrete compressive strength of this specimen was 4000 psi (the tensile strength was not determined by tests, but can be estimated at 400 psi). Figure 6-5 illustrates the development of cracks in the hooked bar test.

Cracking in the hooked bar test was similar to the cracking pattern in specimens with bars that had large heads. Cracking began with a vertical crack just under the load point (part i). A second crack formed between the first crack and the node. A horizontal crack due to bond failure along the tie bar began shortly after that (part ii). By the time the specimen was near its peak load, a diagonal crack formed in the direction of the strut and several small cracks formed between it and the second crack (part iii). Failure was sudden and brittle. The tail of the hook prevented the concrete above the strut from splitting off. The concrete bulged outward along the diagonal compression strut particularly near the bend of the hook. A crack passed horizontally at this location diverting upward along the bend of the hook. Cracking tended to indicate that the depth of the diagonal compression strut exceeded the presumed dimensions which were more applicable to the headed bar tests (part iv). The increased depth of the diagonal compression strut results because the hooked bar allows a taller CCT node to form (Figure 6-6).

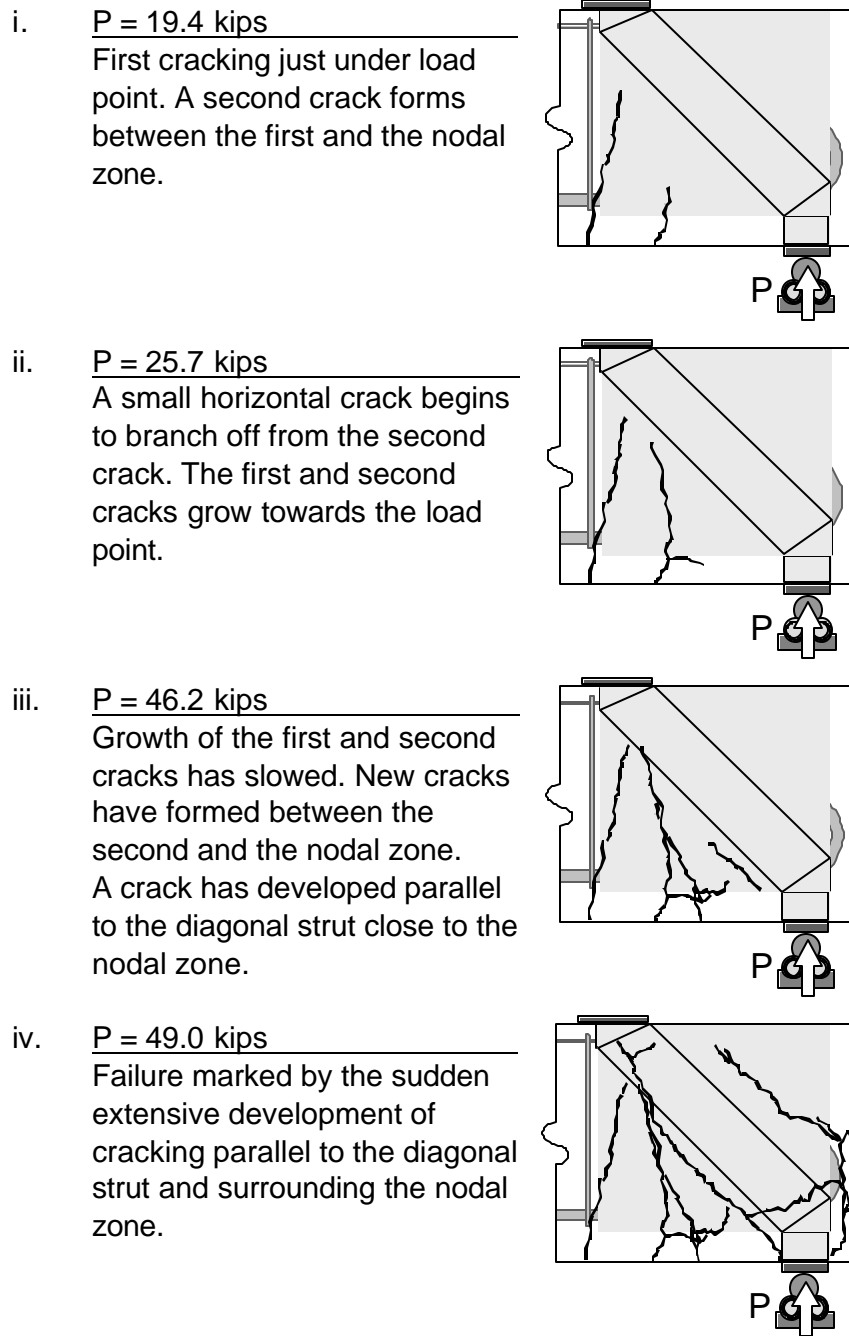


Figure 6-5: Development of cracks in the hooked bar test (CCT-08-45-Hook2-1)

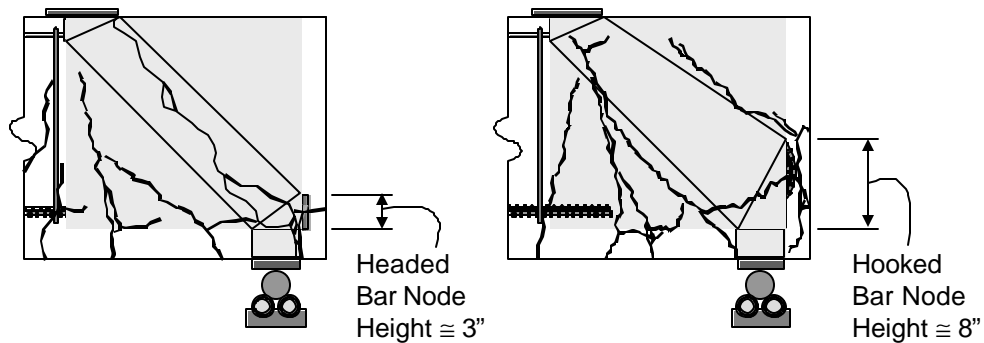


Figure 6-6: CCT node height in headed bar and hooked bar tests

The cracking patterns described in Figures 61(a and b), 64, and 65 were all for specimens with 45° strut angles. Analogous specimens with 30° and 55° struts are examined next.

Figure 67 shows the cracking pattern for CCT-08-55-10.39-1. This specimen had a 55° strut angle and a #8 tie bar anchored with a standard square HRC head (3" x 3"). The measured concrete compressive strength was 4000 psi (the tensile strength was not measured, but can be estimated at 400 psi). This specimen was directly comparable to the representative test with a large head size (CCT-08-45-10.39-2); the only difference was the strut angle.

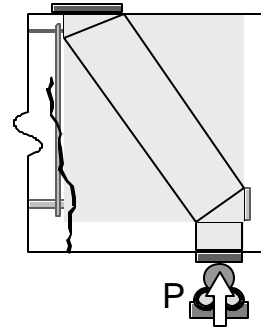
As with its 45° counterpart, cracking initiated with a vertical crack just under the load point (part i). A small horizontal crack began to branch off of the first crack and grow towards the node (part ii). Then, like the 45° strut specimen, a second crack formed between the first crack and the node (part iii). A horizontal crack also branched off from the back of the first crack and began to grow away from the node. The horizontal cracks were most likely associated with bond failure of the bar. No new cracking occurred until the load increased by 50% from the load at which the previous cracking had been observed. A long crack occurred along the edge of the strut (part iv). The maximum bearing reaction reached was over 91 kips. Based on presumed equilibrium of the truss mechanism, that load indicated a force that exceeded yield in the tie by almost 12%. The test

was halted shortly afterwards due to the fact that the load ram was near ultimate capacity. Unfortunately, the halt in the testing made it impossible to determine the potential ductility of the specimen and its ability to sustain further load. The observed cracking of CCT-08-55-10.39-1 was typical of other specimens with 55° struts.

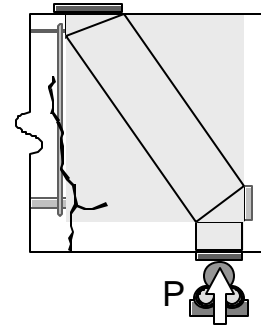
Figures 68a and 68b illustrate the cracking pattern for specimen CCT-08-30-10.39-1. This specimen had a 30° strut angle and a #8 tie bar anchored with a standard square HRC head (3" x 3"). The measured concrete compressive strength was 4100 psi and the tensile strength was 420 psi. This specimen was also directly comparable to the representative test with the large head size (CCT-08-45-10.39-2); the only difference being the strut angle.

Cracking in the 30° strut test began with a vertical crack under the load point (part i). This crack was primarily flexural. As bond stresses increased in the tie bar next to this crack, horizontal cracks appeared that grew towards the node (part ii). A diagonal crack eventually connected the horizontal crack to the vertical one (part iii). As more load was applied, second and third diagonal shear cracks appeared between the first crack and the diagonal strut (part iv). The front-most crack eventually grew to the full depth between the bottom fibers and the top of the compression strut as the truss mechanism of the specimen was developed (part v). The top diagonal crack became the primary tensile crack and experienced the most widening. The critical stress location of the tensile tie was at the point where it crossed this crack. The tie began to yield at this point, and after extensive plastic deformation, a fourth diagonal crack began to form next to the node (part vi). The behavior of CCT-08-30-10.39-1 was typical of the 30° strut angle specimens.

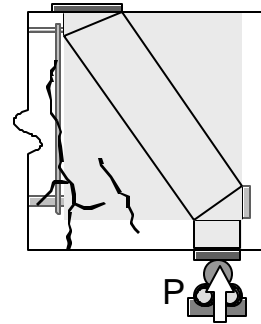
- i. P = 33.7 kips
 By this load, there is still only one vertical flexural crack. The path of the crack follows closely to the location of the front-most stirrup.



- ii. P = 44.4 kips
 A small horizontal crack begins to branch off of the vertical crack and grows along the depth of the tie bar towards the nodal zone.



- iii. P = 51.1 kips
 The first diagonal crack appears halfway between the vertical crack and the path of the diagonal compression strut.



- iv. P = 76.2 kips
 Sudden appearance of a second diagonal crack that grows along the edge of the diagonal strut. There is no new crack growth before the test is terminated at a load of 91.9 kips.

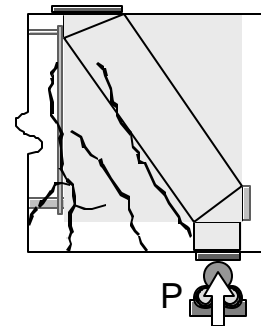
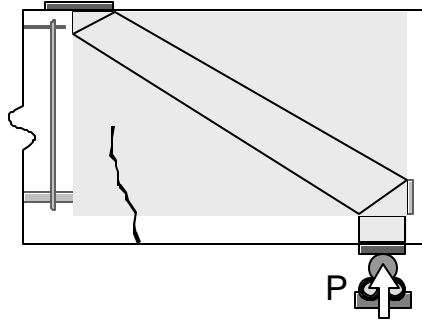
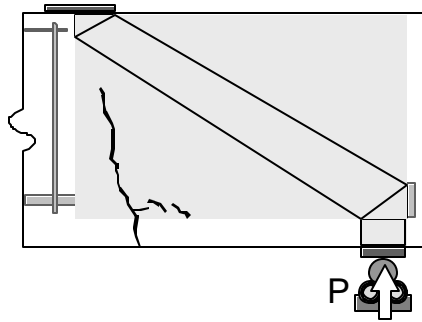


Figure 6-7: Development of cracks in a steep strut angle test (CCT-08-55-10.39-1)

- i. P = 12.2 kips
First cracking due to flexure underneath the load point.



- ii. P = 20.5 kips
A small horizontal crack begins to branch off from the first crack.



- iii. P = 25.7 kips
Development of the first diagonal crack. It branches downward from the flexural crack and connects to the horizontal crack.

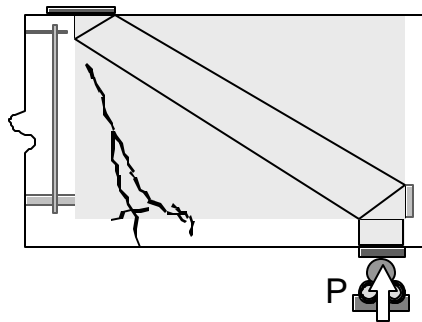
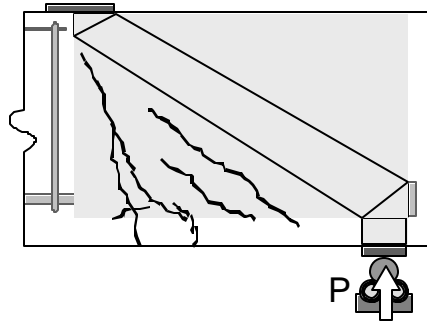


Figure 6-8a: Development of cracks in a shallow strut angle test (CCT-08-30-10.39-1)

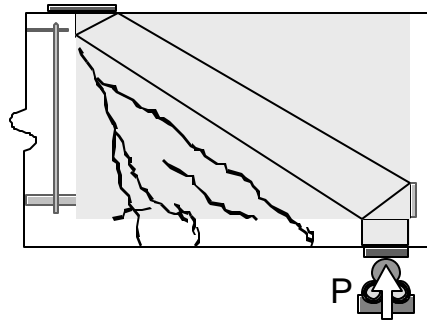
iv. $P = 28.0$ kips

The second and third diagonal cracks appear between the flexural crack and the diagonal compression strut.



v. $P = 38.3$ kips

Specimen begins yielding. The front-most diagonal crack connects with the bottom fibers and the first flexural crack.



vi. $P = 38.9$ kips

After extensive plastic deformation, a fourth diagonal crack appears next to the diagonal compression strut. There is extensive cracking along the bottom of the specimen.

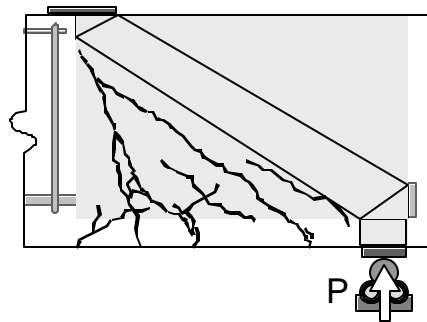


Figure 6-8b: Development of cracks in a shallow strut angle test (CCT-08-30-10.39-1) (continued)

It is apparent from the cracking behaviors of 30°, 45°, and 55° tests that decreases in the strut angle of the specimen increased the anchorage length of the tie bar. For the shallowest angle, 30°, the primary tensile crack was further away from the node boundary than in the cases of the 45° and 55° strut angles. This allowed more development length for the tie bar at the node. In the 55° strut test, a diagonal crack formed right at the edge of the CCT node and diagonal strut boundary thus reducing the development length of the tie bar to a minimum. As a result, the shallower strut angle specimens tended to show better tie anchorage than specimens with the steeper strut angle.

Cracking in the #11 bar specimens resembled the cracking of #8 bar specimens with the same 45° strut angles. In many cases the large bar diameter of the #11 bar resulted in the earlier formation of horizontal cracking along the tie bar. Otherwise, the cracking behaviors shown in Figures 6-1 (a and b) and 6-4 can be regarded as typical for the #11 bar specimens.

6.1.2 Stress/Strain Development in the Bar

The representative test specimen (CCT-08-45-10.39-2) was specially instrumented to fully measure the development of stress in the bar along its length in the CCT node panel region. Strain gages were placed at 2" on the top and bottom of the bar in this specimen. The gages started at 1" from the face of the head and extended for 20". Twenty-two strain gages were used in total. Figure 6-9 is a plot of the measured strains. The distribution of strain along the top and bottom fibers of the bar is plotted for four different load levels (the front reaction is generally used as the indicator of load level for most results presented in this report). Positive strain corresponds to tension. A diagram of the north face of the specimen is drawn to scale at the top of the figure for reference.

No large strains were recorded along the bar until first cracking occurred around a load of 14.5 kips (refer to Figure 6-1 for the progression of cracking in specimen CCT-08-45-10.39-2). The strain distribution indicated for a load of 19.4 kips shows that the largest strains in the bar correlate to the position of crack 1. The bottom fiber strains were only slightly greater than the top fiber strains at that load level. The next crack in the specimen, crack 2, occurred around a load of 26.1 kips. The strain distribution at 29.8 kips shows that the zone of large tensile strains in the bar had extended to the location of crack 2. The difference between the top and bottom fiber strains has also grown. This indicates that the bar was in positive curvature (positive curvature equating to larger tensile strains along the bottom of the bar) through the region of maximum tension. The third and last major crack in the specimen appeared at a load of 31.6 kips. The strain distribution at 59.3 kips shows that the bar was strained beyond yield along nearly the entire gaged length. The strain distribution at this load also shows that a situation of reverse curvature had developed in the bar near the location of the third crack (between 6" and 8"). The strain profile indicates that the bar was "kinked" in a manner consistent with dowel action across shear cracks (Figure 6-10). The final strain distribution at a load of 59.3 kips shows that the bar had begun yielding, however, yielding was more pronounced along the bottom fibers of the tie bar. Full yielding of the bar was observed when the load reached 59.8 kips. Large increases in top and bottom strains at a distance of 13" from the head indicated that plastic deformation was concentrated at one location on the tie bar.

Bar stresses are shown in Figure 6-11. The stresses were calculated from the measured strains in accordance with procedures outlined in Appendix A. At a load of 19.4 kips, the maximum stress in the bar was measured at 19" from the face of the head. At a load of 29.8, the maximum stress was reached at 13". At a loads of 39.4 kips and higher, the maximum stress level

in the bar was nearly uniform from a point of 7" away from the head. The shortening of the development length corresponded with the formation of cracks closer and closer to the node as the truss mechanism became fully active. Final anchorage of the bar clearly occurred within the first 7", the length roughly from the face of the head to the point where the bar passed out of the diagonal strut. The stresses at 1" in from the head provide an indication of the bar force carried by the head while the stresses at 7" give an indication of the total force in the bar.

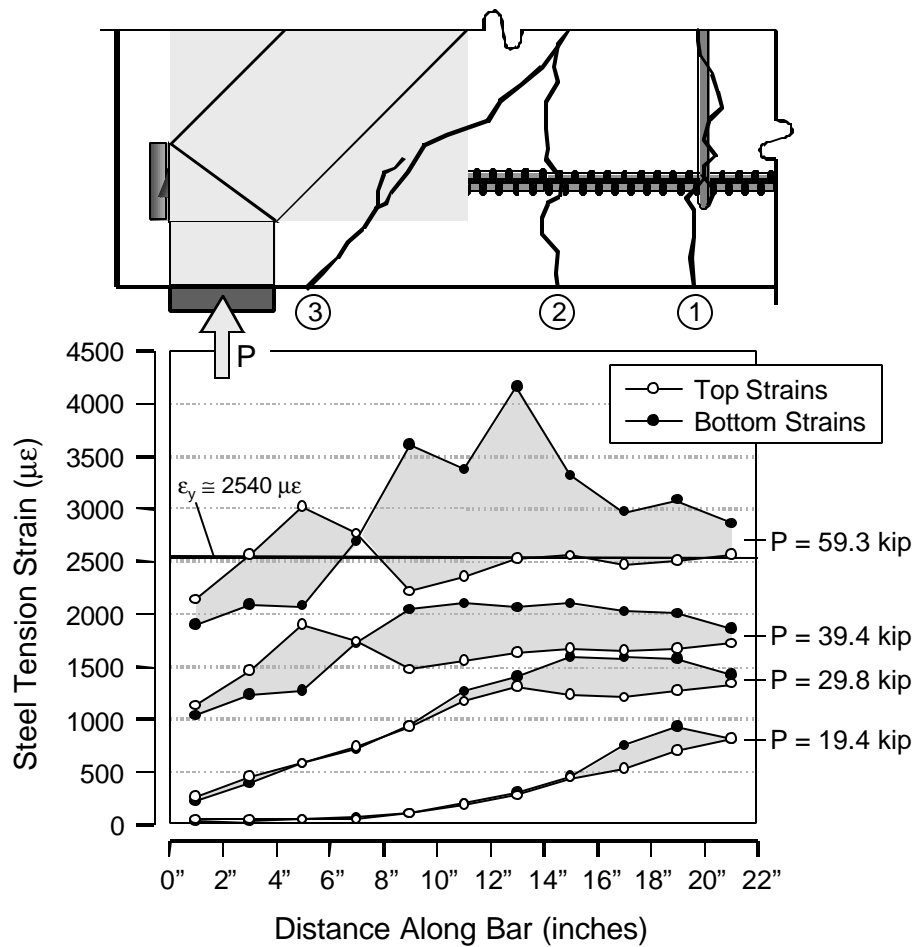


Figure 6-9: Top and bottom fiber strains of the tie bar in specimen CCT-08-45-10.39-2

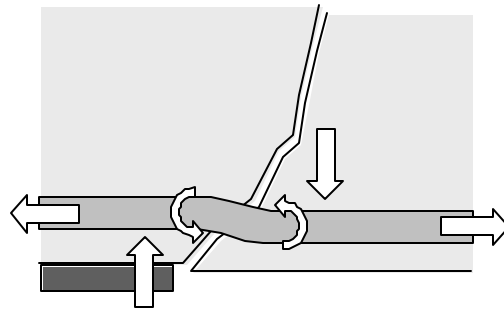


Figure 6-10: “Kinking” of reinforcement caused by dowel action across diagonal shear cracks

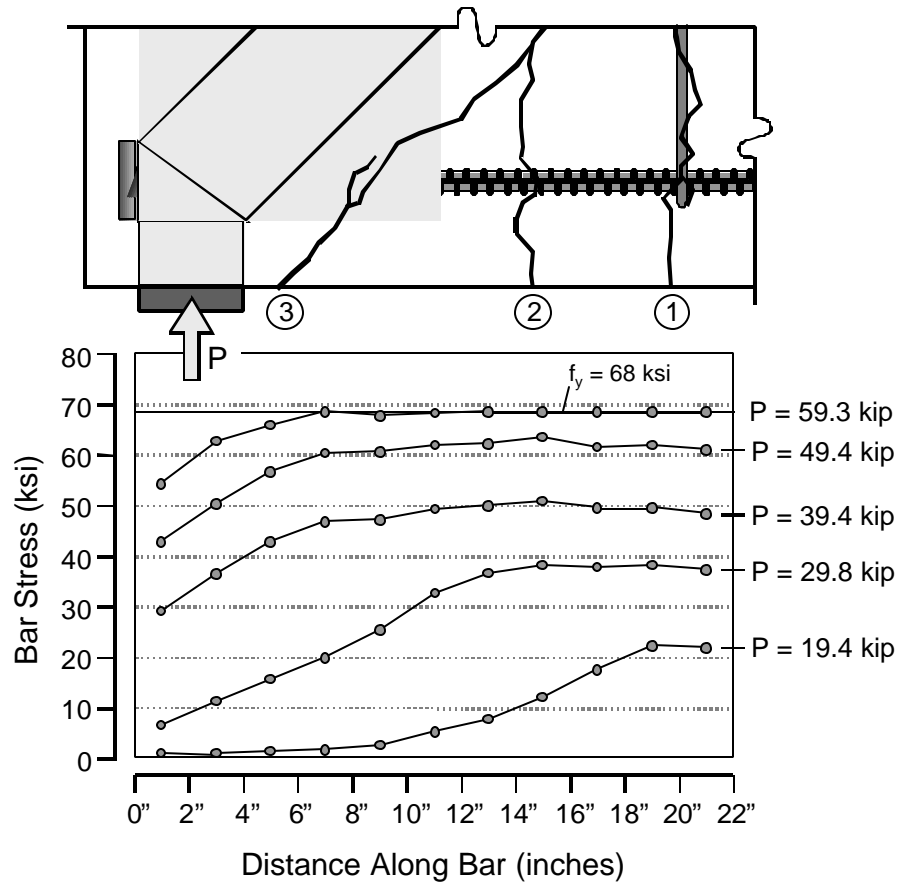


Figure 6-11: Development of bar stress in specimen CCT-08-45-10.39-2

The stress data from Figure 6-11 were used to determine bond stress along the bar in specimen CCT-08-45-10.39-2 as shown in Figure 6-12. At 25.6 kips, the point of maximum bond occurred away from the head, close to the first crack. When the next crack formed at a load of 26.1 kips, the maximum bond shifted to 10" from the head. When the third crack formed, the location of maximum bond moved next to the head. Peak bond stresses increased as the point of maximum bond approached the head. This could be due to the increased vertical compression or platen restraint in the node region next to the head. The bond stress calculated using the ACI development length equations is plotted in the Figure. The implied understrength factor of 0.9 was removed from the ACI equation. The measured local bond exceeded the ACI value. However, because the ACI equation represents average bond stresses, this is expected.

The development of a non-headed bar is compared to the development of a bar with a small head in Figure 6-13. The strain and stress development at peak capacity for two specimens with 55° struts (CCT-08-55-00.00-1 and CCT-08-55-01.85-1) is plotted. Data from the non-headed bar show that the stress tapered to zero at the end of the bar. Data from the headed bar, on the other hand, show that the stress at the end of the bar was somewhere between 35-40 ksi. The head, even though it is very small, provided a significant boost to the development of the bar. Figure 6-13 also shows that the development of the headed bar was composed of a combination of bond plus a contribution from head bearing. Figure 6-14 shows the contributions to total bar stress provided by bond and head bearing in specimen CCT-11-45-02.85(V)-1. The stress from bond was measured over the bar length from $1d_b$ to $7d_b$. Figure 6-14 shows that the contribution from bond peaked and then began to decrease before the contribution from head bearing reached its maximum capacity. This behavior was common for many of the CCT node tests with larger head sizes. The bond component of anchorage frequently could not be sustained to the load necessary to

achieve full capacity from the larger heads. Thus, anchorage of the headed bars consisted of a two step process, in which bar force was at first carried by bond, then as the bond reached its maximum level and began to fail, anchorage shifted towards the head. The final development of the bar was comprised of the peak bearing capacity of the head plus a diminished bond contribution.

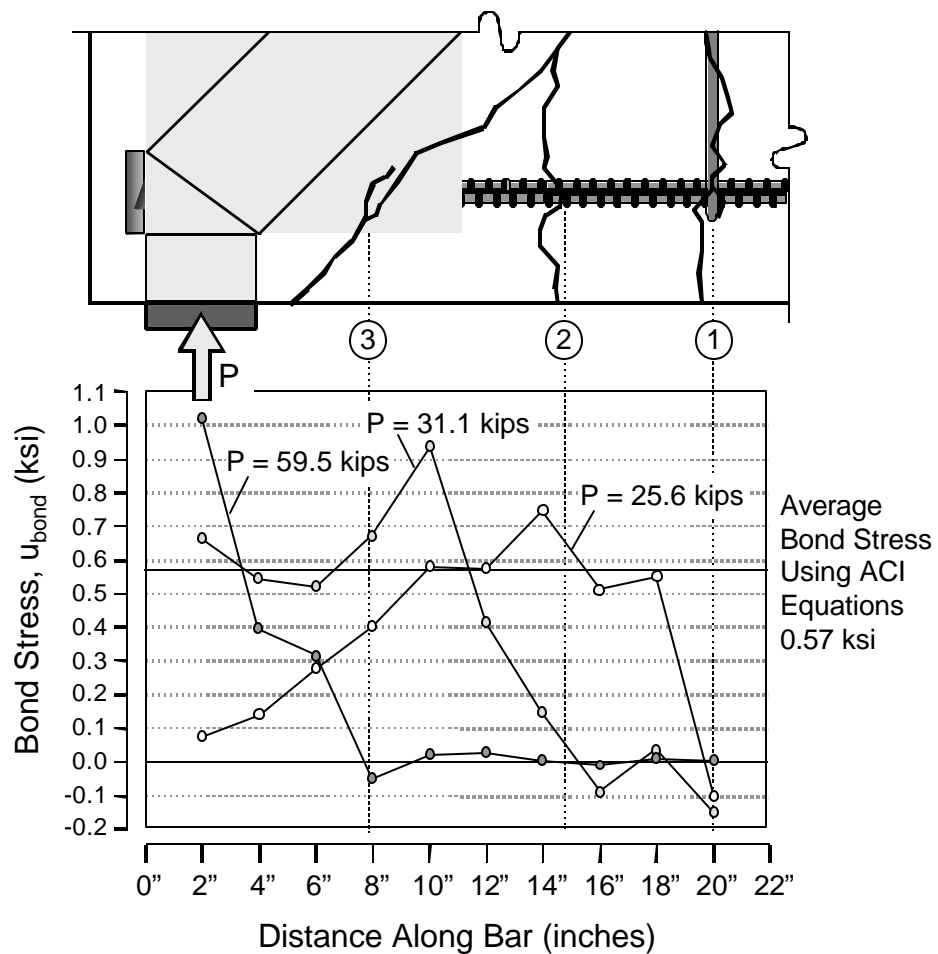


Figure 6-12: Measured bond stresses in CCT-08-45-10.39-2

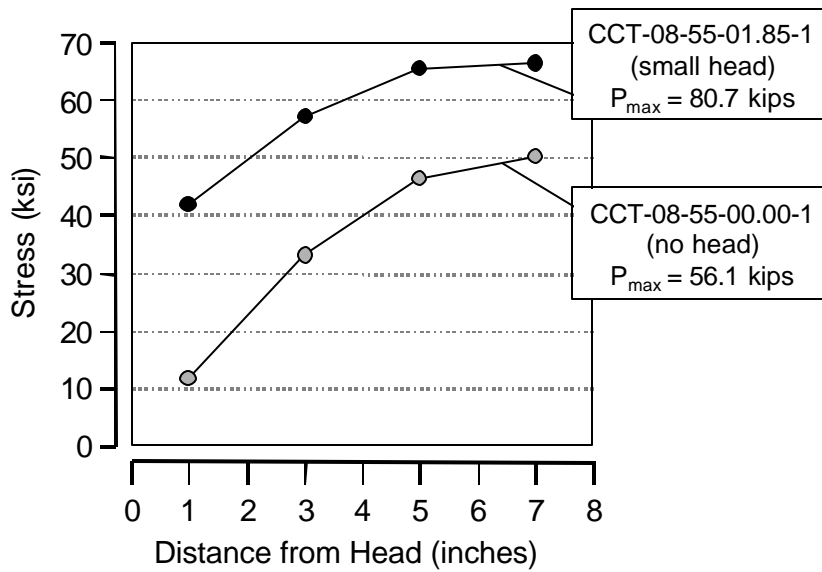


Figure 6-13: Development of stress for headed and non-headed bars

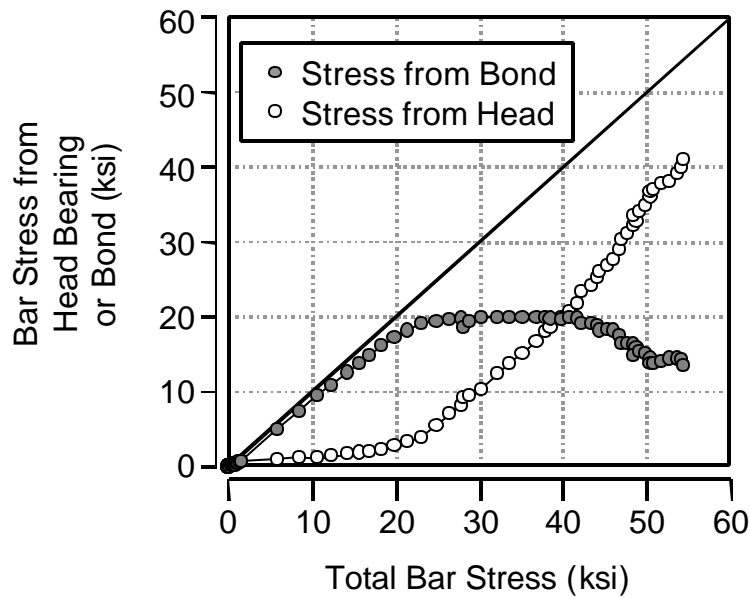


Figure 6-14: Components of bar stress provided by bond and head bearing in CCT-11-45-02.85(V)-1

6.1.3 Equilibrium of the Truss Mechanism

As a check to verify that no horizontal restraint was acting in the load setup and that the strain data for the tie bar were correct, equilibrium of the CCT node was always checked. Figure 6-15 shows a schematic of a CCT node region and the assumed equilibrium solution. When analyzed, the depth of the upper compression block for most of the CCT nodes was between 2.5" - 3.5". Thus the approximate lever arm over which the horizontal forces act was about 14.5" on average. The lever arm over which the vertical forces acted changed for the different strut angles. The appropriate values are listed in Figure 6-15.

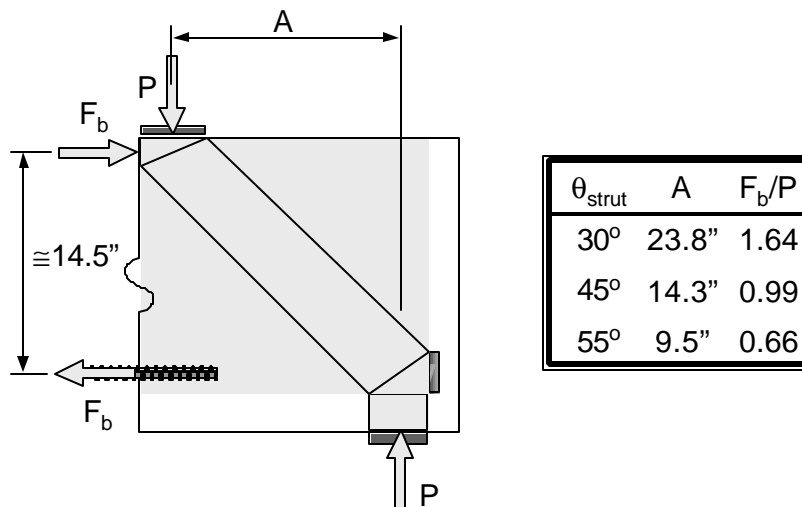


Figure 6-15: Equilibrium of CCT node

Figure 6-16 shows a plot of bar force versus bearing reaction for specimen CCT-08-45-10.39-2. The bar force was calculated from the strain gage readings at a location 7" from the bearing face of the head. For CCT-08-45-10.39-2, a 45° strut specimen, the equilibrium solution approximates to $F_b = P$. A straight line is plotted in Figure 6-16 that represents the theoretical

relationship. Because the bar force was not initially fully developed at 7", the force in the bar does not equal the bearing reaction at low levels of load. However, after the specimen had undergone significant cracking (the formations of the 2nd and 3rd cracks in CCT-08-45-10.39.2 are labeled in the plot), the bar force approached the theoretical value and closely paralleled the expected behavior. The only thing that is surprising about the behavior is the development of load beyond the yield level of the bar. The plot shows that after bar force reached yield of the bar (54 kips) additional load developed at the reaction. The yield level of the reinforcing bar was determined from tensile tests of bar samples. There is no doubt that the bar force was limited to 54 kips for this particular specimen. The reasons for capacity beyond the yield level of the bar are discussed in section 6.1.5.

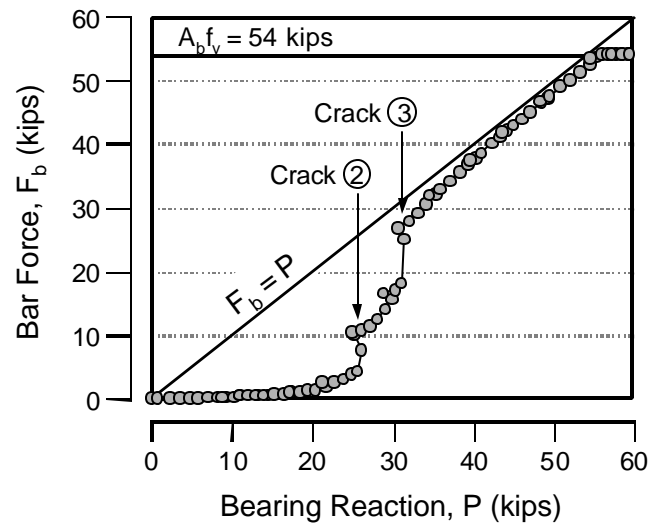


Figure 6-16: Equilibrium plot of bar force versus bearing reaction in specimen CCT-08-45-10.39-2

6.1.4 Head Slip

Head slip was measured for all of the CCT node tests. In general the results showed that the larger head sizes slipped less. Results for the smaller head sizes tended to be mixed. Some bars began to slip immediately and others did not slip at all until failure was imminent. The most consistent slip results came from the #11 bar tests. Figure 6-17 shows the head slip data for four #11 bar CCT node tests. Information for the four specimens is listed in Table 6-1. The stress at the head is based on data from the strain gage placed a distance d_b from the bearing face of the head.

The characteristics of the stress-slip plots were similar. No measurable slip occurred up to some load level. From that point on, there was little slip resistance until failure was reached especially for small head sizes. The data from the #11 bar tests in Figure 6-17 clearly show that slip resistance improved with increasing head size. As the relative head area increased from 0.00 to 4.77, the bar stress when slip initiated rose from 10 to 30 ksi. An additional increase in relative head area to 9.26 did not increase the stress at initiation of slip. However, there was improved stiffness of the anchorage beyond that point. The initiation of slip did not seem to be simply related to the level of compression stress applied to the concrete by the bearing face of the head. Larger head sizes began to slip at lower bearing stresses than the smaller head sizes.

| Specimen | Head Dimensions | $\frac{A_{nh}}{A_b}$ | f'_c (ksi) | E_c (ksi) |
|-------------------|-----------------|----------------------|--------------|-------------|
| CCT-11-45-00.00-1 | no head | 0.00 | 4.1 | 4300 |
| CCT-11-45-01.56-1 | 2" x 2" | 1.56 | 4.1 | 4300 |
| CCT-11-45-04.77-1 | 3" x 3" | 4.77 | 4.0 | 3700 |
| CCT-11-45-09.26-1 | 4" x 4" | 9.26 | 4.0 | 3700 |

Table 6-1: Specimen information for data plotted in Figure 6-17

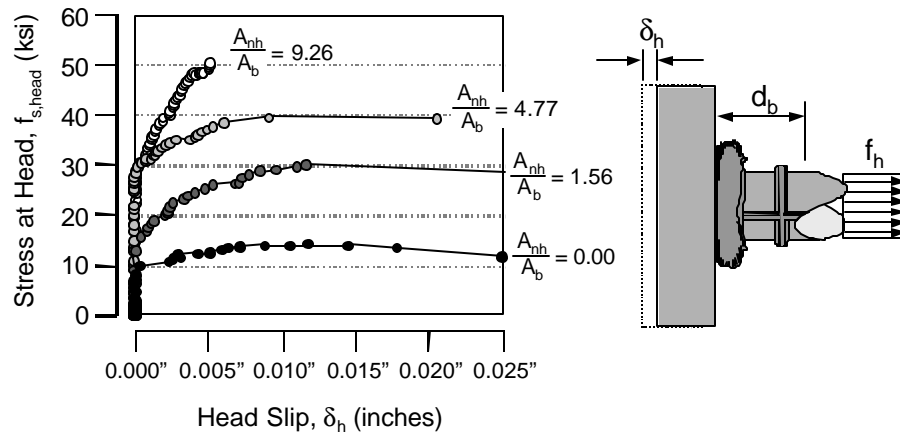


Figure 6-17: Bar stress versus head slip for CCT node specimens with #11 bars

Figure 6-18 shows stress-slip data for analogous #8 bar size tests. Data from 30°, 45°, and 55° strut angle tests are presented. Table 6-2 lists details of the specimens included in Figure 6-18. Slip data from specimens CCT-08-30-01.85-1 and CCT-08-55-01.85-1 were flawed. The results follow a regular pattern of improved slip resistance with increasing relative head area.

| θ_{strut} | Specimen | Head Dimensions | $\frac{A_{nh}}{A_b}$ | f'_c (ksi) | E_c (ksi) |
|-------------------------|-------------------|-----------------|----------------------|--------------|-------------|
| 30° | CCT-08-30-00.00-1 | no head | 0.00 | 4.1 | 4000 |
| | CCT-08-30-01.85-1 | 1.5" x 1.5" | No slip data | | |
| | CCT-08-30-04.06-1 | 2" x 2" | 4.06 | 4.1 | 4000 |
| | CCT-08-30-10.39-1 | 3" x 3" | 10.39 | 4.1 | 4000 |
| 45° | CCT-08-45-00.00-1 | no head | 0.00 | 4.0 | 4000* |
| | CCT-08-45-01.85-2 | 1.5" x 1.5" | 1.85 | 3.1 | 3300 |
| | CCT-08-45-04.06-1 | 2" x 2" | 4.06 | 3.1 | 3300 |
| | CCT-08-45-10.39-2 | 3" x 3" | 10.39 | 3.8 | 4000 |
| 55° | CCT-08-55-00.00-1 | no head | 0.00 | 3.9 | 4000* |
| | CCT-08-55-01.85-1 | 1.5" x 1.5" | No slip data | | |
| | CCT-08-55-04.06-1 | 2" x 2" | 4.06 | 3.1 | 3300 |
| | CCT-08-55-10.39-1 | 3" x 3" | 10.39 | 4.0 | 4000* |

* Estimated modulus of elasticity

Table 6-2: Specimen information for data plotted in Figure 6-18

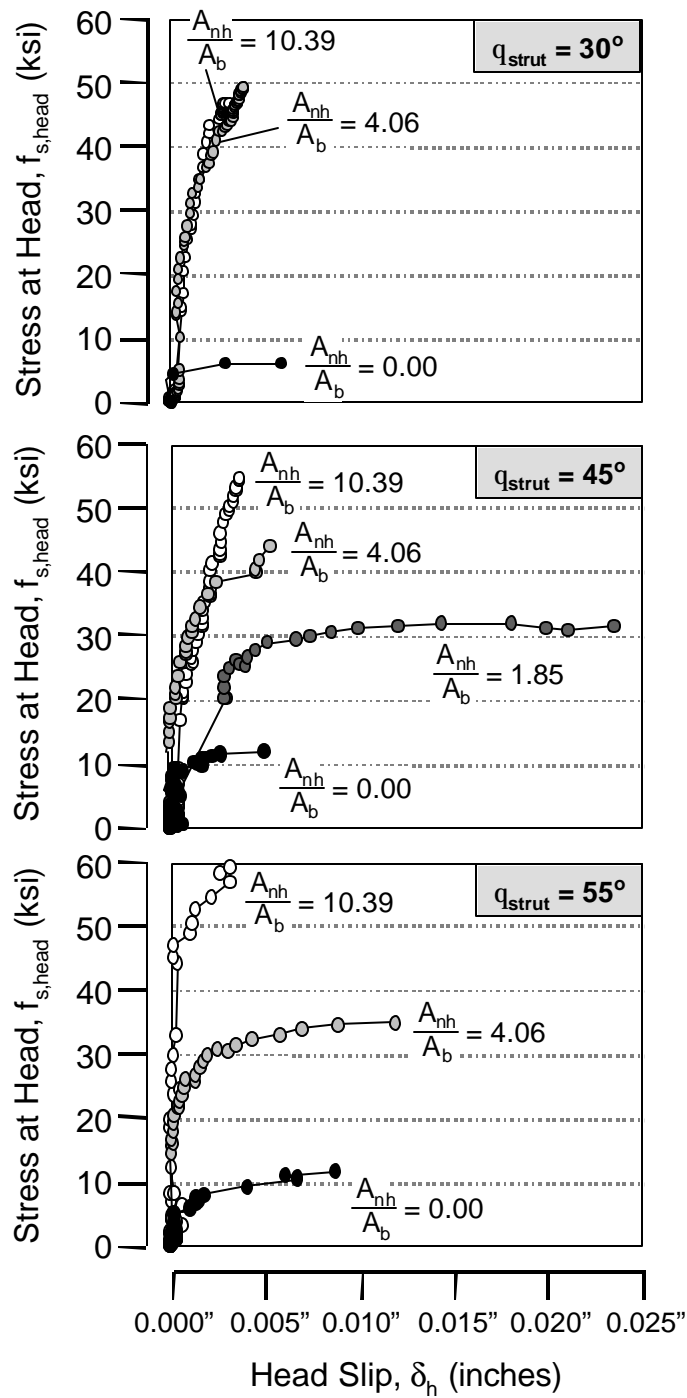


Figure 6-18: Bar stress versus head slip for CCT node specimens with #8 bars

6.1.5 Load-Deflection Response

The deflection of the CCT node specimens was measured underneath the load point for all tests. The deflection data helped to identify key features in the specimen behavior such as changes in stiffness due to head slip or the effects of horizontal restraint at the supports. Figure 6-19 shows the load-deflection response for two 30° strut angle specimens with small and large head sizes: CCT-08-30-01.18-1 and CCT-08-30-04.06-1. Both specimens had the same concrete with $f'_c = 4.1$ ksi and $E_c = 4,000$ ksi. The steel properties of the tie bars were also the same with $f_y = 68$ ksi and $E_s = 27,000$ ksi. Head slip data for the two specimens are presented adjacent to the deflection data. The measured bearing reaction is used as an indication of the load on the specimen.

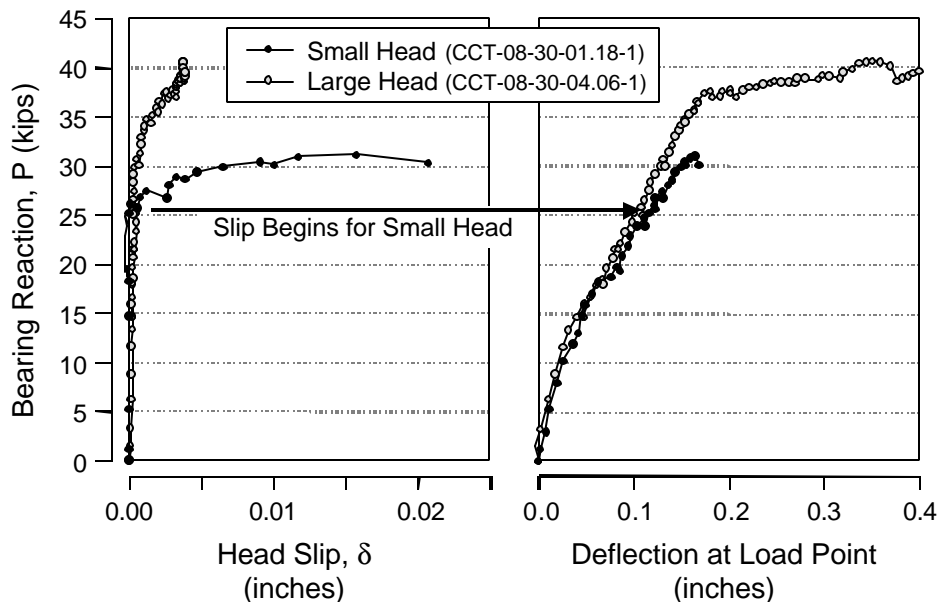


Figure 6-19: Load-deflection and load-slip data for specimens with small and large heads

Head slip data are presented next to the deflection data in Figure 6-19 in order to illustrate the effect of the head slip on the stiffness of the specimen. Initially both specimens had no head slip until a load of about 25 kips was reached. Then, the specimen with the small head began to slip. In the deflection data, a reduction in the stiffness of this specimen can be seen when compared with the specimen that had a larger head. The two load-deflection curves began to diverge around 25 kips. The specimen with a small head failed shortly thereafter at about 31 kips. The specimen with a large head continued to gain load and yielded at about 37 kips. There was a slight gain in strength even after the bar yielded.

The load at which yielding occurs in Figure 6-19 does not coincide with the expected yield load of the specimen. Given the geometry of the specimen, the placement of the loads, and the known yield strength of the tie bar, the yield capacity of the specimen should occur at a load of about 33 kips. However, the specimen with the large head clearly began yielding at a load of 37 kips. This unexpected increase in capacity is difficult to explain. Figure 6-19 shows the expected equilibrium state of the CCT node panel at the front of the specimen. Equilibrium of the moment forces dictates the expected yield capacity, P_y . The yield load of the tie bar, F_y , is known from tensile measurements of bar samples (see Appendix A). Only two other factors could account for an increase in the yield capacity of the specimen: an increase in the vertical lever arm between the horizontal forces or a decrease in the horizontal lever arm between the vertical forces. These two distances could change with changes in the dimensions of the top CCC node (as shown in Figure 6-20, part ii).

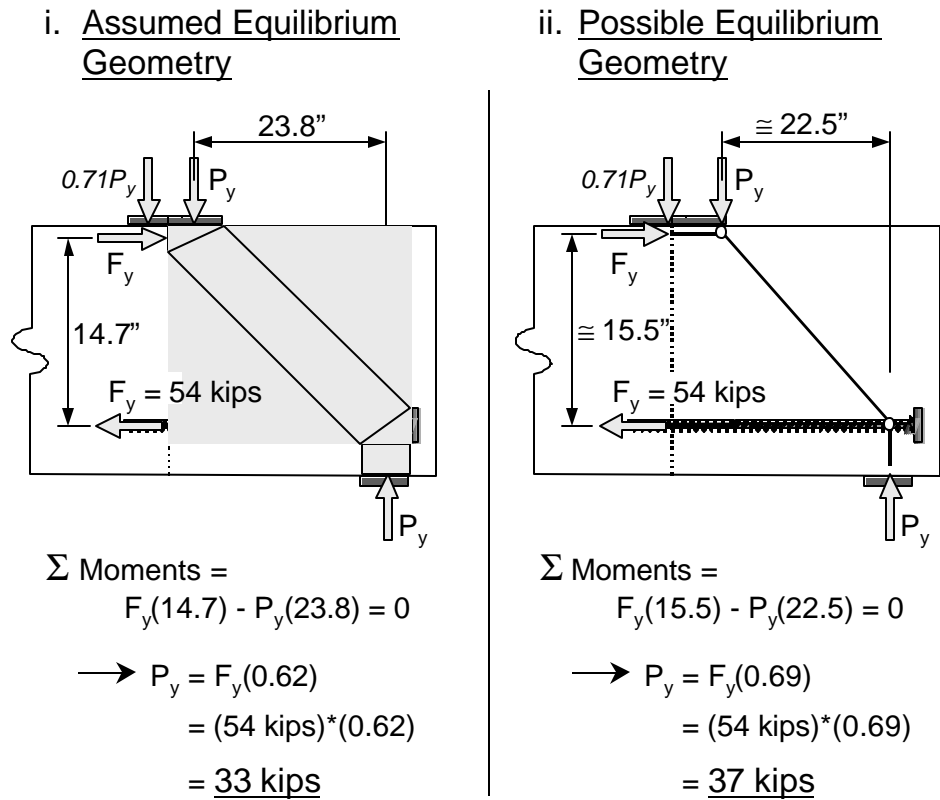


Figure 6-20: Assumed and possible equilibrium geometries for 30° CCT node specimens

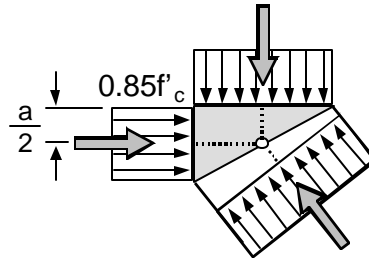
The assumed dimensions of the top CCC node are dictated by the depth of the concrete compression block at the top of the specimen, a , and a proportional distribution of the load plate length based on the applied load distribution between the front and back reactions of the specimen. The assumed dimensions of the CCC node are also based on assumed uniform stress distributions on all three faces of the node and on a $0.85f_c'$ upper limit on concrete stress. Neither of these two assumptions is necessarily correct. Zeller's tests on corbels, which were reviewed in Section 4.4.5, showed that the strain distribution of the concrete along the diagonal compression strut is extremely non-uniform near the re-entrant corner of the corbel [47, 121]. Zeller's corbel tests are

essentially the same type of test as conducted in this study but oriented differently. The re-entrant corner of his specimens coincides with the location of a CCC node. If non-uniform stress distributions were occurring at the top CCC node in the specimens of this study it would be entirely consistent with Zeller's earlier observations. The latter of the two assumptions that dictate the CCC node dimensions is a stress limit state that is based on an assumption of uniaxial compression behavior in the concrete. However, the state of stress of the top CCC node is biaxial. Experimental studies by Kupfer, Hilsdorf, and Rusch [65] have shown that the biaxial strength of concrete can be as high as $1.2f_c'$ when non-restraining bearing platens (brush type platens) were used to compress the material. When restraining load platens were used (solid steel plates), the strength could reach up to $1.5f_c'$. Since the bearing plates of the CCT node specimens were all solid steel, it is reasonable to propose that the concrete strength at the top CCC node may have reached $1.5f_c'$. Figure 6-21 shows the assumed node condition and the possible node conditions next to one another.

Though the current node dimensioning assumptions of STM would suggest that large CCC nodes should occur in the test specimens, there is reasonable experimental data to suggest that the actual nodes are much smaller with much higher stresses than have been previously assumed. Smaller node dimensions would allow for changes in the lever arms over which the horizontal and vertical forces act in the CCT node specimens and thus allow the specimens to reach higher than expected capacities. This seems to be the most rational explanation for the results that are demonstrated in Figure 6-19 and earlier in 6-16.

i. Assumed Node Condition

- uniform stress state
- concrete stress limited to $0.85f'_c$



ii. Possible Node Condition

- non-uniform stress state
- concrete stress limit as high as $1.5f'_c$

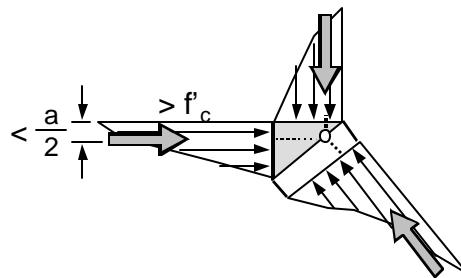


Figure 6-21: Assumed and possible stress states of CCC nodes

6.1.6 Modes of Failure

CCT node specimens failed in three basic ways: pullout of the tie bar from the CCT node, rupture of the concrete strut, or ductile yielding of the tie bar. Most of the discussion in this chapter will deal with the second mode of failure.

Pullout failure was always foreshadowed by extensive slip of the head before the capacity of the anchorage was achieved. It was the mode of failure for all of the non-headed bar specimens. Pullout failure resulted in a loss of load capacity and unrestrained opening of the cracks closest to the node. Generally, extensive slip of the bar resulted in very poor crack distribution with only one primary crack propagating at failure. Pullout is shown in Figure 6-22. Horizontal splitting cracks were sometimes visible in the node region at failure, but typically not beforehand.

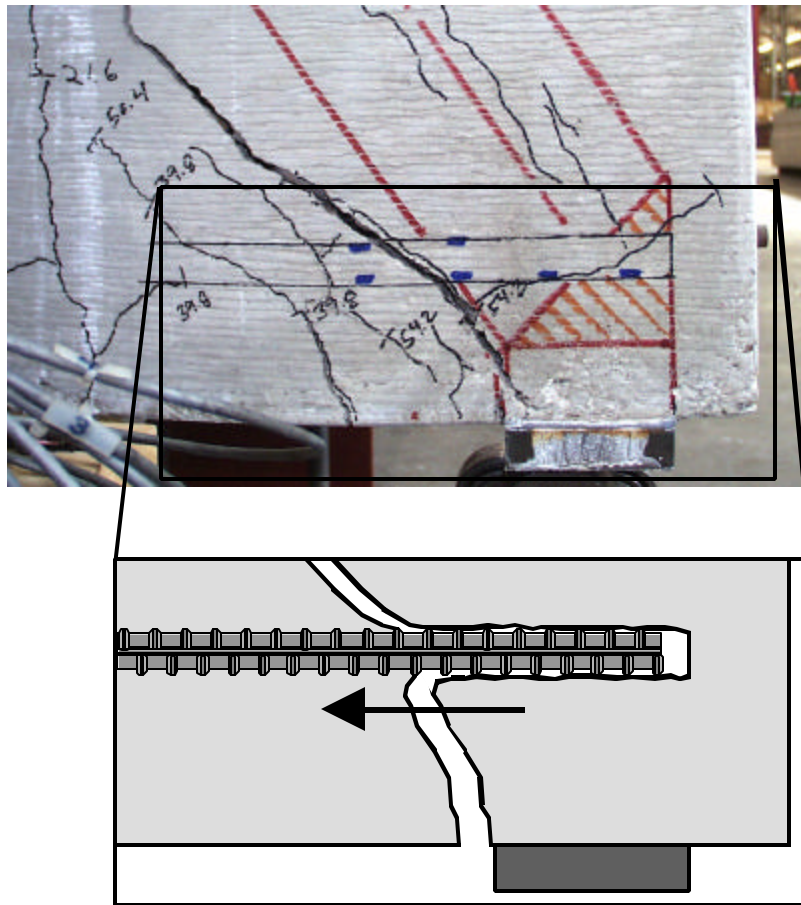


Figure 6-22: Pullout failure of a non-headed bar (specimen CCT-08-55-00.00-1)

All of the headed bar specimens that did not yield experienced rupture of the strut and node region during failure. For smaller heads and vertically oriented rectangular heads, rupture was usually characterized by splitting of the diagonal compression strut along a transverse plane. Larger heads and rectangular heads with horizontal orientations caused a lesser degree of splitting near the node region. A characteristic of the larger head sizes that failed by rupture was extensive crushing of the concrete near the bottom face of the diagonal compression strut. Figure 6-23 shows the two basic failure modes.

i. Strut Rupture with Splitting
(vertical head orientation)

ii. Strut Rupture with Crushing
(horizontal head orientation)

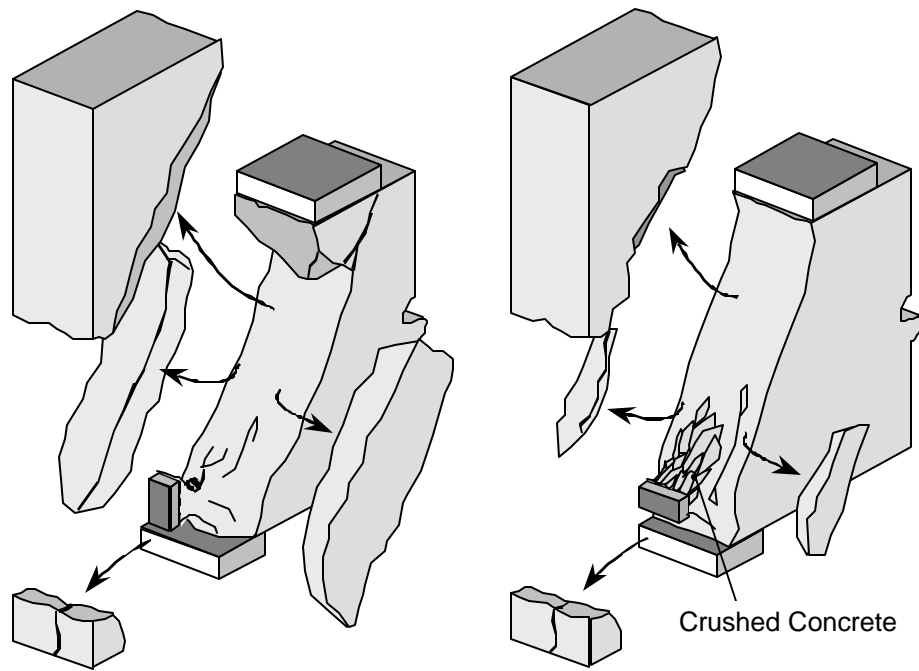


Figure 6-23: Patterns of strut/node rupture

Figures 6-24 and 6-25 show post-test photographs of specimen with a vertically oriented head (CCT-08-55-02.80(V)-1) which provide an excellent example of strut rupture with transverse splitting. Figure 6-24 shows a side view of the failed specimen in which the individual pieces of the shattered specimen can be distinguished. Two very clear strips along the path of the diagonal compression strut were blown out laterally from the specimen. The zone between the bottom bearing plate and the headed bar anchorage disintegrated. A very clear cone of concrete was visible on the underside of the headed bar sweeping from the lower head face to the back edge of the bottom bearing plate. On the upper portion of the head face, was a partial wedge of concrete.

Figure 6-25 shows a front view of the same specimen. A vertical splitting crack can be seen along the length of the diagonal compression strut. Beneath the head, the zone of disintegrated concrete resembled a pyramid rising up from the lower bearing plate to meet the head.

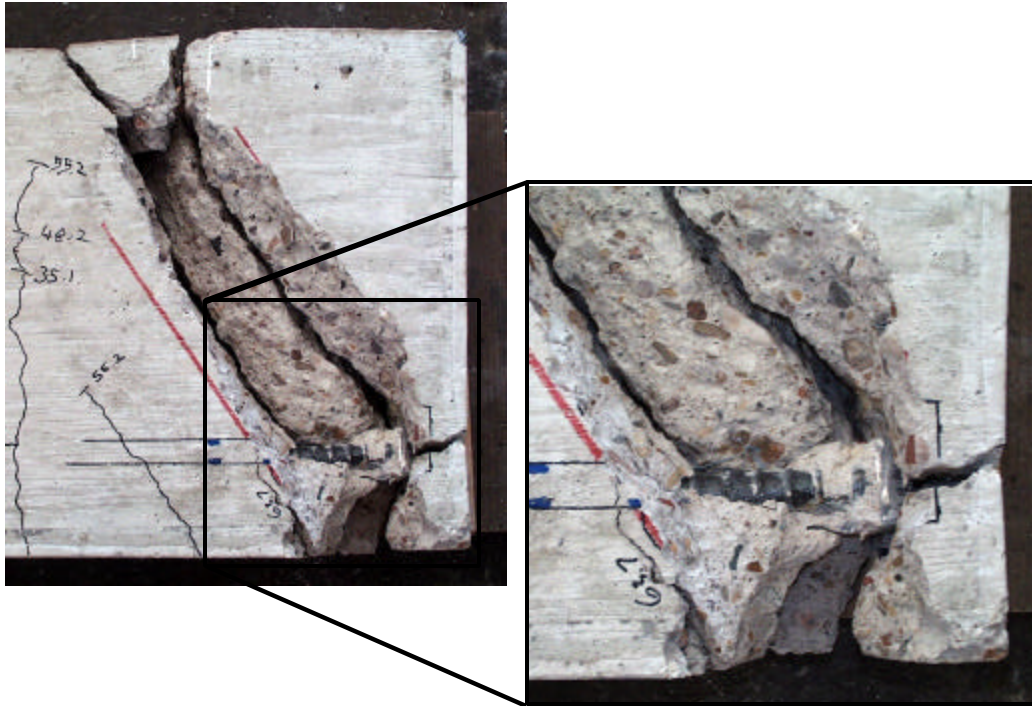


Figure 6-24: Side view of a failed specimen with a vertically oriented head (CCT-08-55-02.80(V)-1) demonstrating splitting of the diagonal compression strut

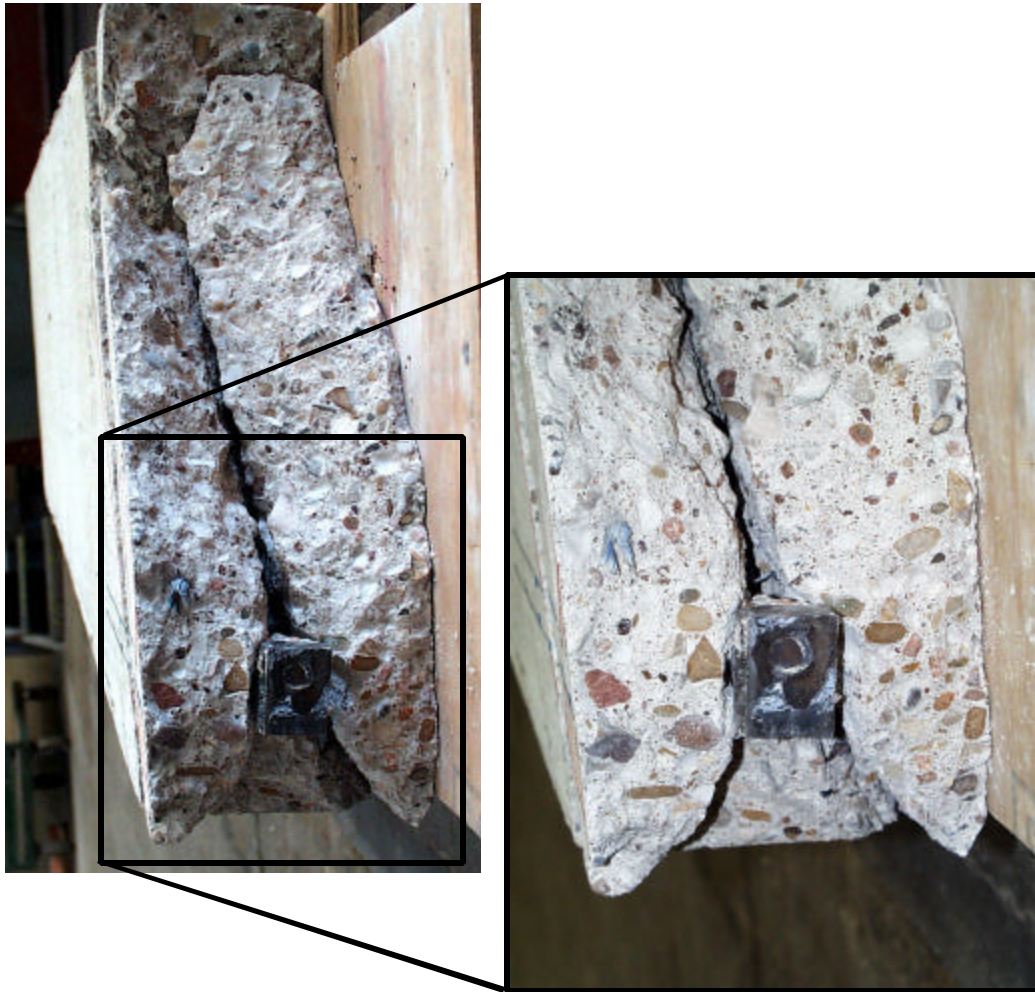


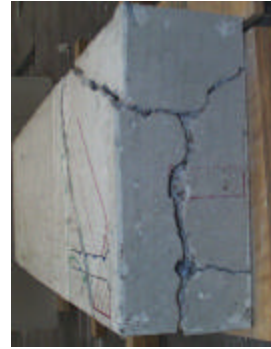
Figure 6-25: Front view of a failed specimen with a vertically oriented head (CCT-08-55-02.80(V)-1) demonstrating splitting of diagonal compression strut

Figure 626 shows the splitting failure of a specimen with a small head (CCT-11-45-01.10-1) which was somewhat different from the splitting failure of the previous specimen (CCT-08-55-02.80(H)-1). Side and front views clearly indicate a splitting failure with much cleaner edges of cleavage than was seen in the example of the specimen with a larger vertically oriented

head. There is much less distress of the concrete between the bottom bearing plate and the head (an Xtender head in this specimen). The differences can be attributed to the much smaller relative head area. More slip of the head occurred in this specimen (CCT-11-45-01.10-1) than in the previous one (CCT-08-55-02.80(H)-1) before failure. Less strain energy was stored in the CCT node region and along the strut before rupture occurred. The result was that there was less distress along the failure surfaces at failure. Thus the final appearance of the specimen was much cleaner with well-defined crack planes.



i. Side View - Exterior Cracking



ii. Front View - Exterior Cracking



iii. Side View - Internal Cracking



iv. Front View - Internal Cracking

Figure 6-26: Splitting failure of a specimen with a small head (CCT-11-55-01.10-1)

Transverse splitting at the node tended to occur to some degree in all specimens that did not reach yield or fail by pullout of the tie bar. Splitting was least pronounced in specimens with large head sizes. Also particular to the specimens with larger, horizontally oriented heads was the presence of a distinct zone of crushed concrete progressing from the top of the head up a short distance along the length of the strut. Figures 6-27 and 6-28 show photographs taken of two specimens with horizontally oriented heads (CCT-08-45-04.70(H)-1 and CCT-11-45-04.13(H)-1) after failure. Both photographs show good examples of the type of crushing witnessed during the CCT node testing. Crushing was apparent from the numerous small fragments of destroyed concrete. When the fragments were brushed away, a voided area was apparent at the base of the diagonal strut. Figure 6-29 depicting specimen CCT-08-55-02.80(H)-1 shows this as well as the general appearance of the larger concrete fragments cleaved from the specimen at failure.

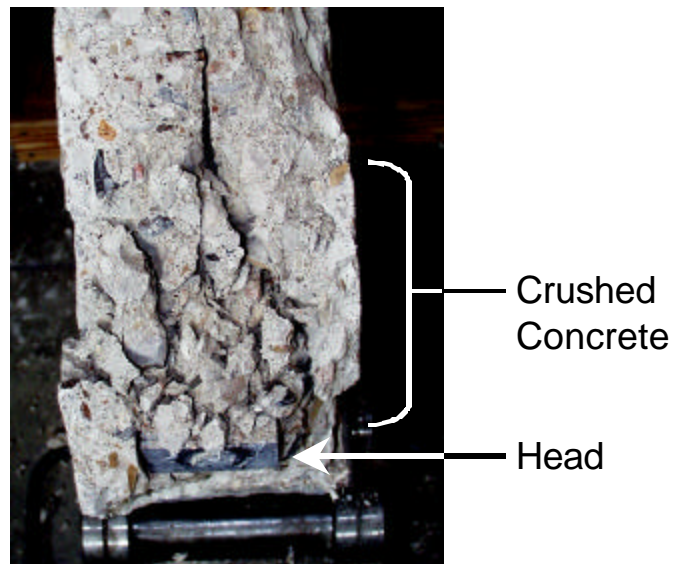


Figure 6-27: Zone of crushed concrete in a specimen with a horizontally oriented head (CCT-08-45-04.70(H)-1) after failure (top view)

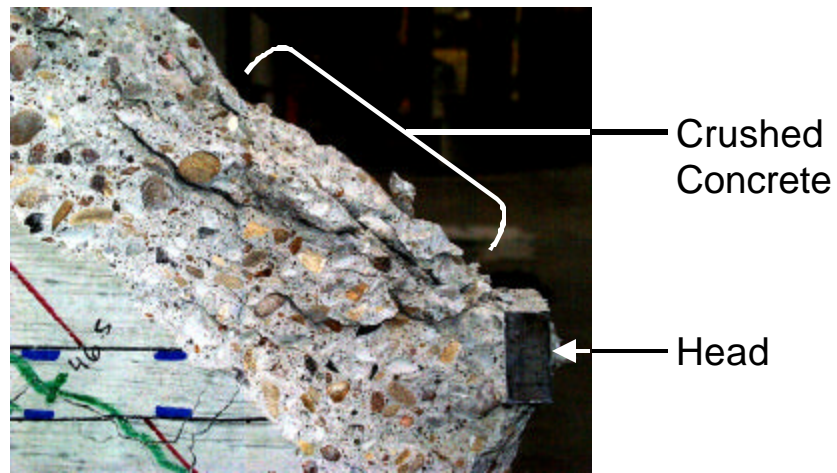
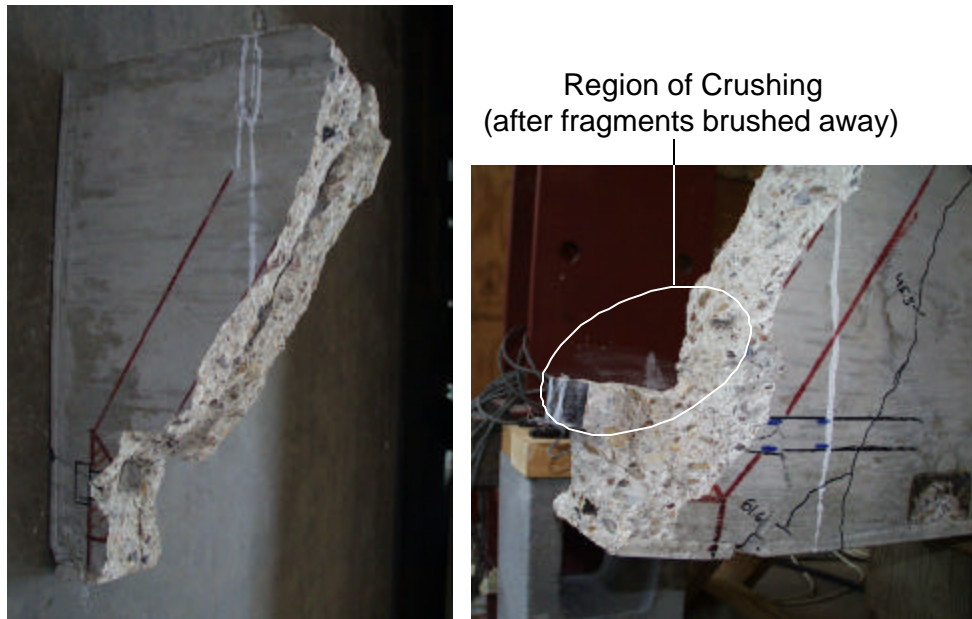


Figure 6-28: Zone of crushed concrete in a specimen with a horizontally oriented head (CCT-11-45-04.13(H)-1) after failure (side view)



i. Fragmented Portion of Concrete

ii. Close-Up of CCT Node Region

Figure 6-29: Specimen CCT-08-55-02.80(H)-1 after failure

Though the hooked bar specimens did not suffer the same explosive rupture as the examples listed above, bulging of the concrete along the strut and vertical cracking along the front face of the specimen suggested a splitting failure also occurred in the hooked bar tests. This would be consistent with the behavior of the headed bar specimens that had vertical head orientation. Such heads provided a tall and narrow bearing profile for the anchorage of the tie bar similar to the profile provided by the hooked bars.

The final mode of failure, yielding, was achieved with many of the largest head sizes that were studied. When testing first began, yielding was judged by strain gage readings taken during the test. Later, it was realized that strain gage readings might indicate yielding, yet the specimen would continue to gain capacity, as was discussed in the proceeding section. In some cases this could result in a failure at or just past the yield point. Once this was realized, testing was continued past the yield point until deflection data indicated a satisfactory yield plateau had occurred in the behavior. Some of the earlier tests unfortunately have an ambiguous yield failure because the tests were prematurely stopped at a point in which strain data indicated yielding, but the deflection data had not yet done so. Tables 6-1a and 6-1b list the failure modes of all of the unconfined CCT node tests excluding those from the first and second casts (the early trial specimens). Failure modes are categorized as pullout, splitting (rupture), crushing (rupture), or yield. Additional notes are provided for some specimens. A more complete list of failure modes and ultimate capacities is provided in Appendix C.

| Specimen Identification | f_c' | Failure Mode - Notes |
|-------------------------|--------|--|
| CCT-08-45-00.00-1-B6 | 4000 | Pullout |
| CCT-08-45-00.00-1 | 4000 | Pullout |
| CCT-08-45-01.18-1 | 4000 | Splitting |
| CCT-08-45-01.85-1 | 4000 | Splitting |
| CCT-08-45-01.85-2 | 3100 | Splitting |
| CCT-08-45-02.80(H)-1 | 4000 | Yield - Unconfirmed; test stopped early |
| CCT-08-45-02.80(H)-2 | 3100 | Splitting |
| CCT-08-45-02.80(V)-1 | 3900 | Splitting |
| CCT-08-45-04.04-1 | 4000 | Yield - Bar $f_y = 61$ ksi; lower than most bars |
| CCT-08-45-04.06-1 | 3100 | Crushing |
| CCT-08-45-04.70(H)-1 | 3100 | Crushing |
| CCT-08-45-04.70(V)-1 | 3900 | Splitting |
| CCT-08-45-10.39-1 | 3100 | Crushing - Very poor concrete quality |
| CCT-08-45-10.39-2 | 3800 | Crushing |
| CCT-08-45-Hook1-1 | 4000 | Splitting |
| CCT-08-45-Hook2-1 | 4000 | Splitting |
| CCT-08-30-00.00-1 | 4100 | Pullout |
| CCT-08-30-01.18-1 | 4100 | Splitting |
| CCT-08-30-01.85-1 | 4100 | Yield |
| CCT-08-30-04.04-1 | 4100 | Yield |
| CCT-08-30-04.06-1 | 4100 | Yield |
| CCT-08-30-10.39-1 | 4100 | Yield |
| CCT-08-55-00.00-1 | 3900 | Pullout |
| CCT-08-55-01.18-1 | 3900 | Splitting |
| CCT-08-55-01.85-1 | 3900 | Splitting |
| CCT-08-55-02.80(H)-1 | 3900 | Splitting |
| CCT-08-55-02.80(V)-1 | 3900 | Splitting |
| CCT-08-55-04.04-1 | 3100 | Crushing |
| CCT-08-55-04.06-1 | 3100 | Crushing |
| CCT-08-55-04.70(H)-1 | 4000 | Yield - Unconfirmed; test stopped early |
| CCT-08-55-04.70(H)-2 | 3100 | Crushing |
| CCT-08-55-04.70(V)-1 | 3900 | Splitting |
| CCT-08-55-10.39-1 | 4000 | Yield |

Table 6-3a: Failure modes of unconfined CCT node specimens

| Specimen Identification | f'_c | Failure Mode - Notes |
|-------------------------|--------|----------------------|
| CCT-11-45-00.00-1 | 4100 | Pullout |
| CCT-11-45-01.10-1 | 4100 | Splitting |
| CCT-11-45-01.56-1 | 4100 | Splitting |
| CCT-11-45-02.85(H)-1 | 4100 | Splitting |
| CCT-11-45-02.85(V)-1 | 4100 | Crushing |
| CCT-11-45-03.53-1 | 4000 | Crushing |
| CCT-11-45-04.13(H)-1 | 4100 | Crushing |
| CCT-11-45-04.13(V)-1 | 4000 | Splitting |
| CCT-11-45-04.77-1 | 4000 | Crushing |
| CCT-11-45-06.69(H)-1 | 4000 | Yield |
| CCT-11-45-06.69(V)-1 | 4000 | Yield |
| CCT-11-45-09.26-1 | 4000 | Yield |

Table 6-3b: Failure modes of unconfined CCT node specimens (continued)

6.1.7 Special Test Results

Though analysis of the rupture patterns of failed specimens provided some interesting insight into the behavior, one question still persisted: Does splitting initiate at the bottom of the strut, the middle, or the top? In order to answer this question, two special specimens were fabricated. Each of these specimens was built with special instrumented details aligned along the axis of the diagonal strut. The strain gages along the special details provided insight about the behavior of tensile strains within the struts.

6.1.7.1 Specimen CCT-08-45-04.70(V)-1-S2 (Transverse Splitting)

Specimen CCT-08-45-04.70(V)-1-S2 was detailed with gages oriented transversely along the length of the strut. A reinforcing detail resembling a ladder was built out of $3/16$ " diameter plain wire. Gages were placed along each rung of the ladder. This detail was then tied into the specimen reinforcing cage such that the gages on the rungs of the ladder would measure transverse splitting strains at every 2" up the length of the diagonal strut. Figure 6-30 illustrates the layout of this

ladder detail. A vertically oriented rectangular head was chosen specifically to create a transverse splitting situation along the strut. The measured concrete compressive strength of the specimen was 4100 psi and the tensile strength was 420 psi.

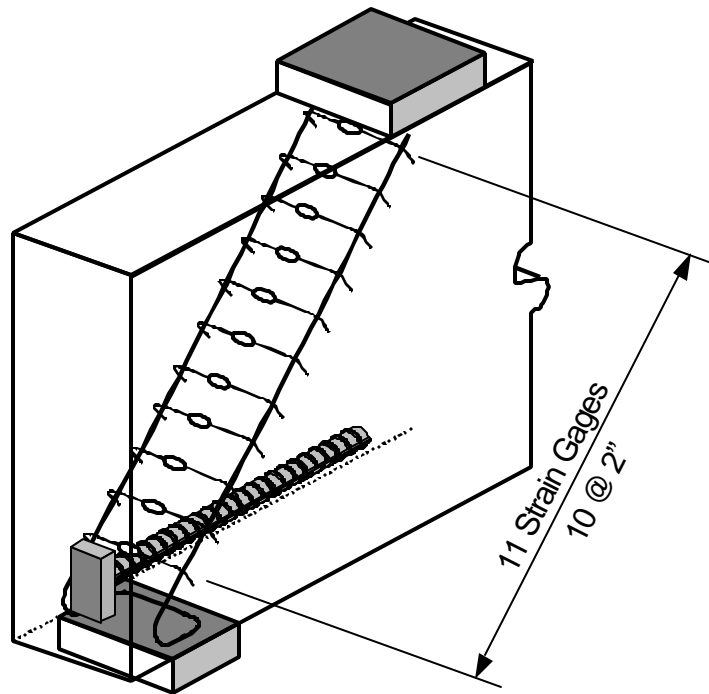


Figure 6-30: Special instrumentation in Specimen CCT-08-45-04.70(V)-1-S2

Data from the ladder detail in specimen CCT-08-45-04.70(V)-1-S2 are shown in Figure 6-31. The gage on the lower-most rung of the ladder was damaged during the casting process. Transverse tensile strain developed very slowly in the strut. At a load of 40 kips, the maximum measured strain was just over $200\mu\epsilon$ (0.0002 in/in), less than the cracking strain of concrete which can be estimated at $300\mu\epsilon$. The maximum strain occurred at the top of the strut next to the CCC node. Some tensile strains were developed at the bottom of the strut as well. From load levels of 40 kips to 55 kips, strain increased rapidly at the top and bottom of the strut. The length from 8”–

14" (directly in the middle of the strut) developed very little tensile strain even up to failure. Maximum tensile strain at the top of the strut occurred slightly outside of the CCC node. These results do not indicate if transverse splitting begins at the top or bottom of the strut, only that it does not occur in the middle. Beyond a load of 50 kips, tensile strains at the top and bottom of the strut exceeded $300\mu\epsilon$ indicating that the concrete had begun to split. At that point, the rungs of the ladder detail had begun to act as transverse reinforcement for the strut. The specimen reached a maximum capacity of 54.8 kips, then split along a plane parallel to the rungs of the ladder detail and perpendicular to the transverse splitting plane.

Transverse strains measured along the strut in specimen CCT-08-45-04.70(V)-1-S2 match a shape similar to concrete cylinders subjected to a double-punch tensile test. The head at the lower end of the strut formed a concrete wedge that subjected the immediate concrete to large tensile stress. A similar event occurred at the top of the strut where it met the CCC node and the load plate. Based on these test results, transverse splitting can be characterized as the cleaving of the strut laterally by naturally forming wedges at one or both ends of the strut. It does not conform to the expected stress distribution envisioned for bottle shaped struts in which splitting is caused by spreading of the compression forces such that maximum tension results in the middle of the strut.

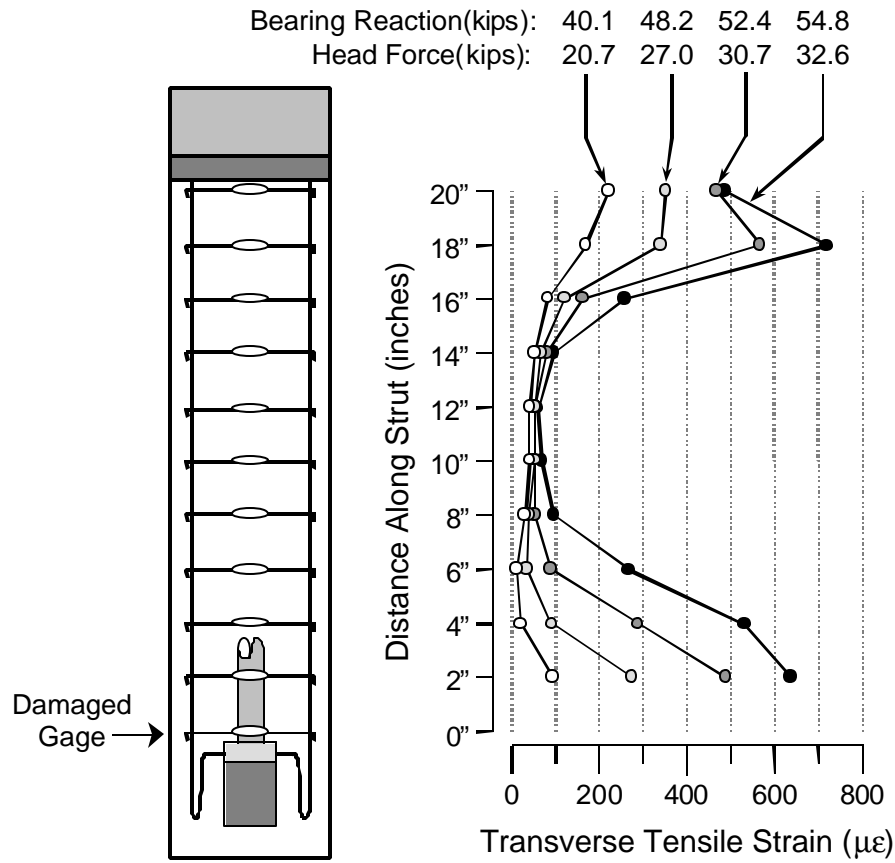


Figure 6-31: Transverse splitting strains in specimen CCT-08-45-04.70(V)-1-S2

6.1.7.2 Specimen CCT-08-45-04.70(H)-1-S3 (In-Plane Splitting)

Specimen CCT-08-45-04.70(H)-1-S3 was detailed with gages perpendicular to the plane instrumented in the ladder detail test. Figure 6-32 shows the detailing of specimen CCT-08-45-04.70(H)-1-S3. The strut detail consisted of $\frac{3}{16}$ " diameter plain wire pieces bent up to form the pattern shown in Figure 6-32. The wires were in a single plane centered along the strut transversely. Because the special detail did not fit correctly into the formwork when tied (due to fabrication errors), a 1.5" plinth was added to the top of specimen. Strain gages were placed on the

rungs of the detail, perpendicular to the axis of the strut, but within the plane of the specimen. Ten strain gages were placed at 2" spacing. The lower-most gage and the 6th one from the bottom were damaged during the casting process (the electrical connections of the gages were severed). In order to help initiate splitting perpendicular to the axis of the strut gages, a horizontally oriented head was used. The measured concrete compressive strength was 3800 psi and the split cylinder tensile strength was 360 psi.

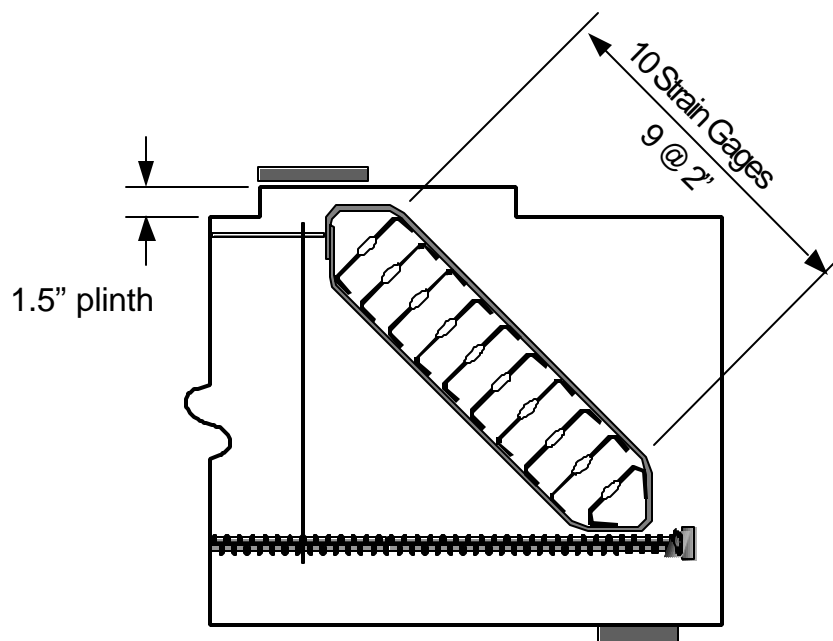


Figure 6-32: Special instrumentation in Specimen CCT-08-45-04.70(H)-1-S3

Figure 6-33 is a plot of the data collected from specimen CCT-08-45-04.70(H)-1-S3. Data from two load levels is presented. At a bearing reaction of 58.8 kips, the maximum load measured for the specimen, very little tensile stress had developed along the strut. The maximum measured strain was just over $300\mu\epsilon$ indicating that the concrete in the strut was close to splitting

or had just begun to split along a short length. Tensile stress was higher at the bottom of the strut, next to the head. There was a small amount of compression at the top of the strut close to the CCC node. During the process of applying the next increment of load, a splitting crack formed along the length of the strut right along the path of the strain gages (see photo in Figure 6-33). Though the load capacity remained high, capacity was lost and never again reached the prior level. Once the splitting crack formed, larger tensile strains were measured in the middle of the strut. This is the conventional strain distribution expected for strut splitting. However, it only occurred once cracking had initiated and capacity was lost. Before the maximum capacity had been reached, tensile stresses were greatest next to the anchorage of the tie bar, at the head. The measured strains tend to indicate that the splitting crack initiated at the CCT node and spread upward. The special detail restrained complete failure of the strut after the splitting crack had formed, however, the splitting crack continued to open and the capacity decreased once the crack had formed.

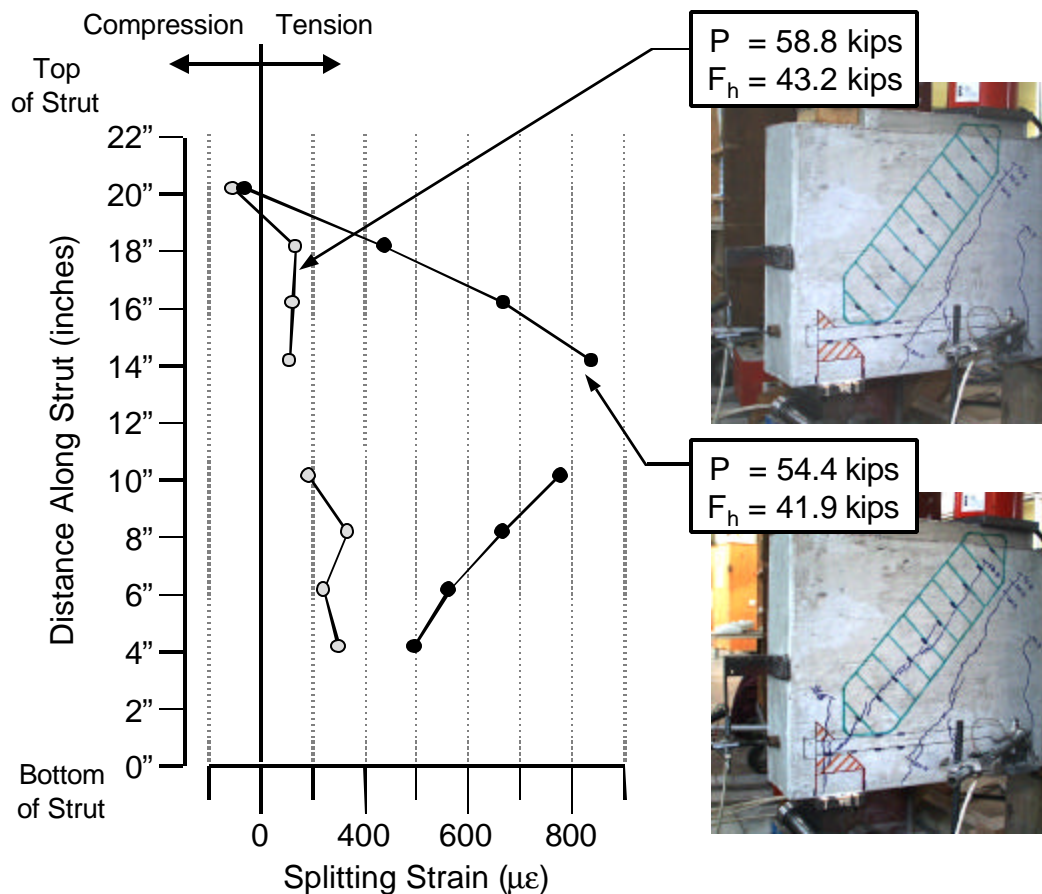


Figure 6-33: In-plane splitting strains in specimen CCT-08-45-04.70(H)-1-S3

6.2 CONFINED SPECIMEN BEHAVIOR

Confining reinforcement was provided for the CCT node in the form of vertical stirrups. Five specimens with vertical stirrups were cast. One other confining detail was attempted prior to the use of stirrups. Specimen CCT-08-45-04.70(V)-1-S1 was cast with a spiral made of $\frac{3}{16}$ " diameter plain wire around the end of the bar in the CCT node region (Figure 6-34). The spiral idea was conceived because of the resemblance of the headed bars to post-tensioned anchors and the evidence that failure of the strut initiates at the headed anchor. A spiral was envisioned as the

ideal method of reinforcing the anchor region of the CCT node. However, while theoretically an ideal placement of tensile reinforcement, in practice the spiral prevented concrete from properly consolidating around the head. A large void was trapped inside of the spiral. Thus, specimen CCT-08-45-04.70(V)-1-S1 failed prematurely due to poor concrete consolidation and the spiral detail proved to be a hindrance to the performance of the node rather than an enhancement. This section thus deals only with the performance of the specimens with stirrups.

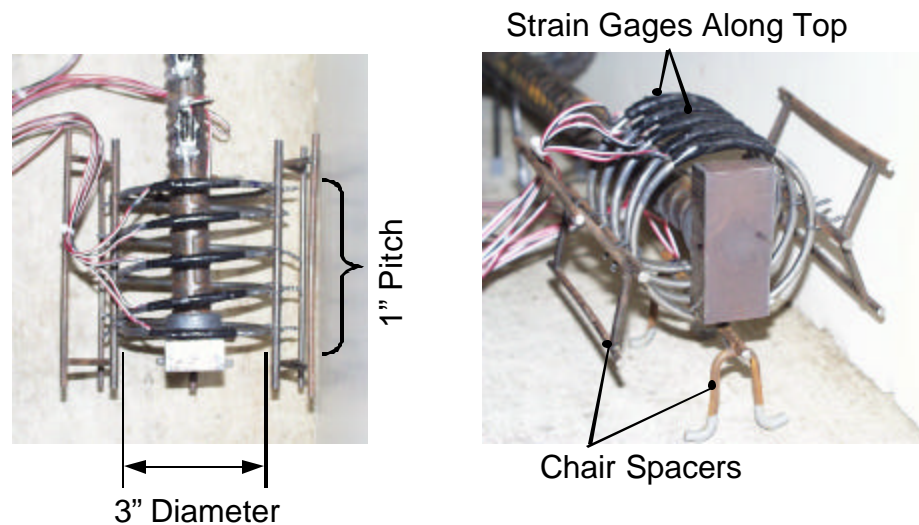


Figure 6-34: Spiral confinement detail attempted in specimen CCT-08-45-04.70(V)-1-S1

6.2.1 Cracking Behavior

Cracking behavior for the confined specimens differed from that of the unconfined ones. Figure 635a and 635b show the progression of crack development for specimen CCT-08-45-04.70(V)-1-C0.012, a heavily confined headed bar specimen. The north face of the specimen is shown in these figures unlike the south face that was used in all previous crack development

figures because the cracking was more interesting on the north face. This specimen contained #3 hoop stirrups at 3" spacing in the node and strut region. The measured concrete compression strength was 3800 psi and the measured tensile strength was 360 psi. A vertically oriented rectangular head was used to anchor the tie bar in order to encourage a transverse splitting failure of the strut.

First cracking in the heavily confined headed bar specimen occurred in the same manner as most unconfined specimens with vertical cracking underneath the top load plate when the bearing reaction reached 18 kips (part i). The formation of the first diagonal crack was consistent with the behavior of the unconfined specimens. A diagonal crack formed midway between the load point and the CCT node at a reaction of 22 kips (part ii). After the formation of that diagonal crack, no additional cracking occurred for some time. Between a bearing reaction of 22 kips and 57 kips, there was only modest growth of the two existing cracks. At 57 kips, a third crack formed parallel to the second one, propagating upwards from the nodal zone towards the top CCC region (part iii). Following the formation of that crack, deterioration of the specimen was rapid. At 61 kips, a fourth crack formed along the top of the primary strut path (part iv). As load was increased, these cracks grew quickly along the strut path (part v). At 66.8 kips, a fifth crack formed next to the first, along a path from the CCC node to the base of the fifth stirrup (part vi). Maximum capacity was reached at 68.2 kips. At this load level, a small vertical crack appeared next to the head of the tie bar (part vii). The appearance of the crack gave the impression of a breakout cone projecting from the head to the surface of the concrete. The specimen then began to lose capacity. Extensive cracking occurred across a broad area from the CCT node to the CCC node (part viii).

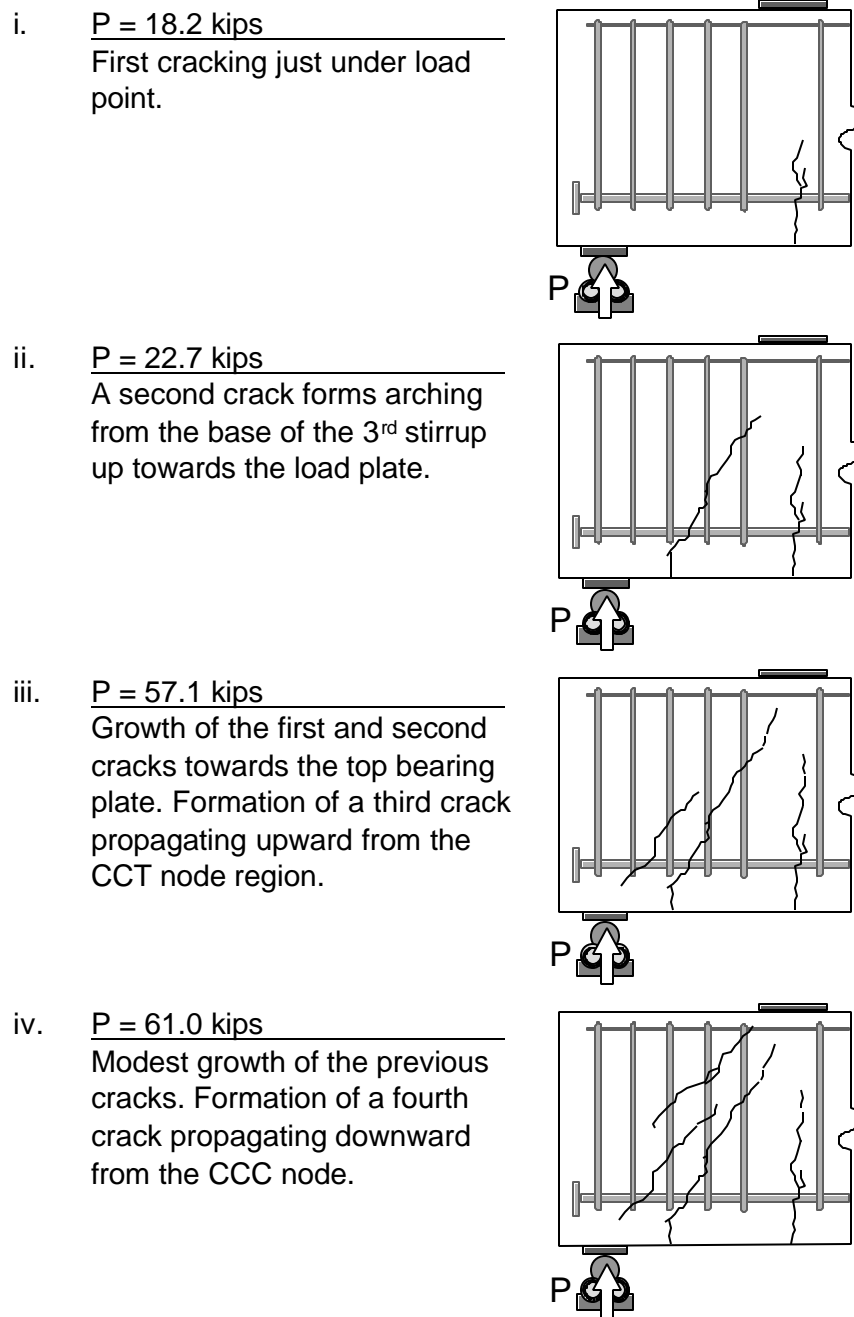


Figure 6-35a: Development of cracks in a heavily confined, headed bar specimen (CCT-08-45-04.70(V)-1-C0.012)

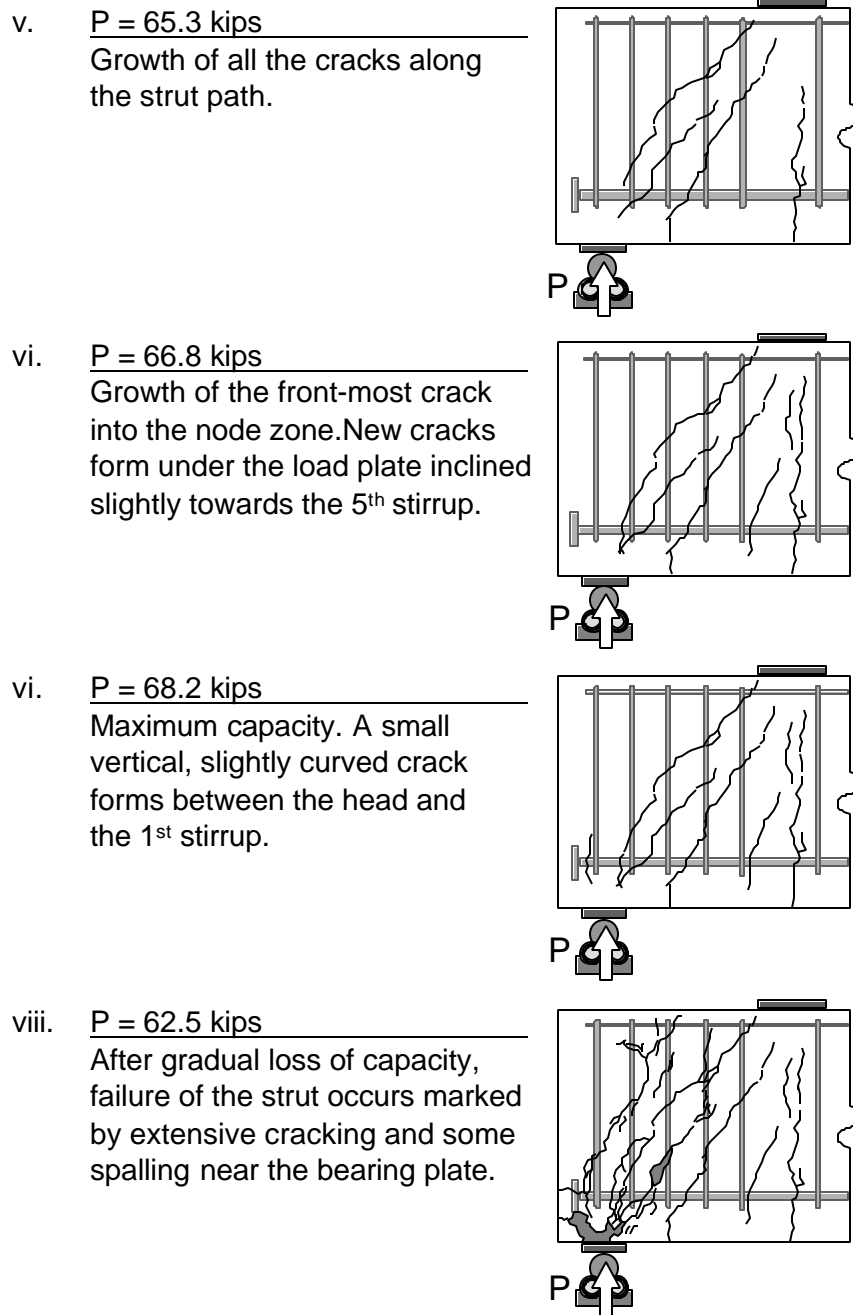


Figure 6-35b: Development of cracks in a heavily confined, headed bar specimen (CCT-08-45-04.70(V)-1-C0.012) (continued)

Prior to reaching maximum load, cracking of the heavily confined, headed bar specimen was similar to that seen in the unconfined specimens with cracking limited to the strut region or below the strut. After the peak capacity was reached, the specimen underwent extensive cracking and continued to hold 90% of its peak load. The nature of the cracking suggested that the specimen initially developed a truss behavior similar to the unconfined specimens, then shifted to a truss mechanism that utilized the stirrups in the transfer of the strut force (Figure 6-36).

Measurements of the crack widths also indicated differences in behavior between specimens with and without stirrups; with stirrups, cracking tended to follow the pattern shown in Figure 6-37. After the formation of the first diagonal crack, no further diagonal cracks formed during a large increase in load. Thus, the first diagonal crack to form showed the greatest widening rather than the latter diagonal cracks (see Figure 6-3 and related discussion).

Specimen CCT-08-45-04.70(V)-1-C0.006 had half the transverse steel as the previous specimen, but was the same in all other aspects. Figure 6-38 shows the development of cracks in this lightly confined, headed bar specimen. Cracking in this specimen showed tendencies between that similar to specimens without stirrups and that of the more heavily reinforced one discussed earlier. Cracking followed the common patterns discussed earlier with vertical cracking under the load point (part i) and the development and growth of cracks along the diagonal strut (parts ii and iii). At failure, there was extensive cracking along and next to the primary strut path (part iv). The cracking was less extensive than the more heavily reinforced specimen, but more extensive than the unreinforced case.

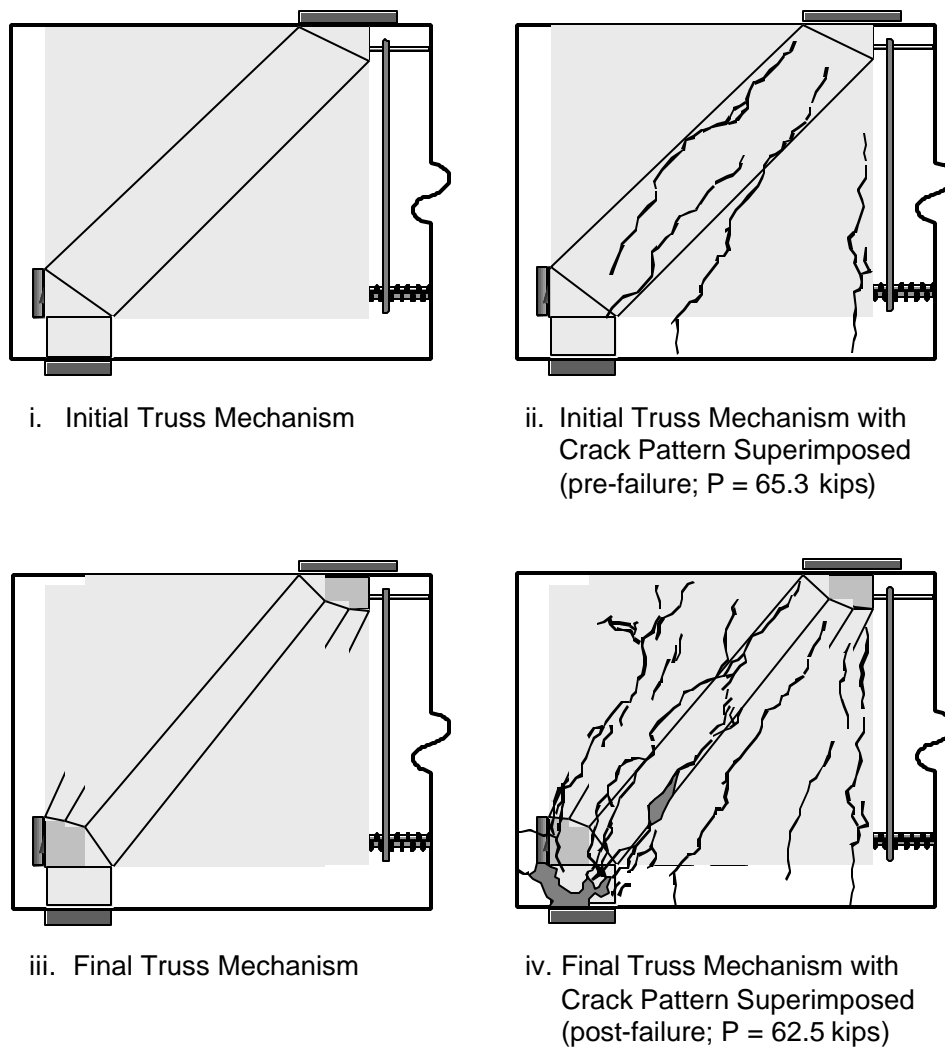


Figure 6-36: Crack patterns overlaid onto probable truss mechanisms for the heavily confined, headed bar specimen (CCT-08-45-04.70(V)-1-C0.012)

Figure 639 shows the development of cracks in specimen CCT-08-45-Hook2-1-C0.012. This specimen is similar to the heavily confined, headed bar specimen except that a hooked bar was used as a tie rather than a headed bar. This specimen can also be compared to the unconfined hooked bar specimen shown in Figure 6-5. Diagonal cracking in the heavily confined, hooked bar

specimen developed much closer to the CCT node and tended to occur through the center of the primary diagonal strut. The specimen had a lower ultimate capacity than the companion unreinforced specimen, though the differences can probably be attributed to differences in concrete material properties. At failure, there was extensive cracking along the strut path (in the unreinforced case, cracking occurred only along the top and bottom edges of the diagonal strut). Bulging of the concrete along the strut path indicated a splitting failure.

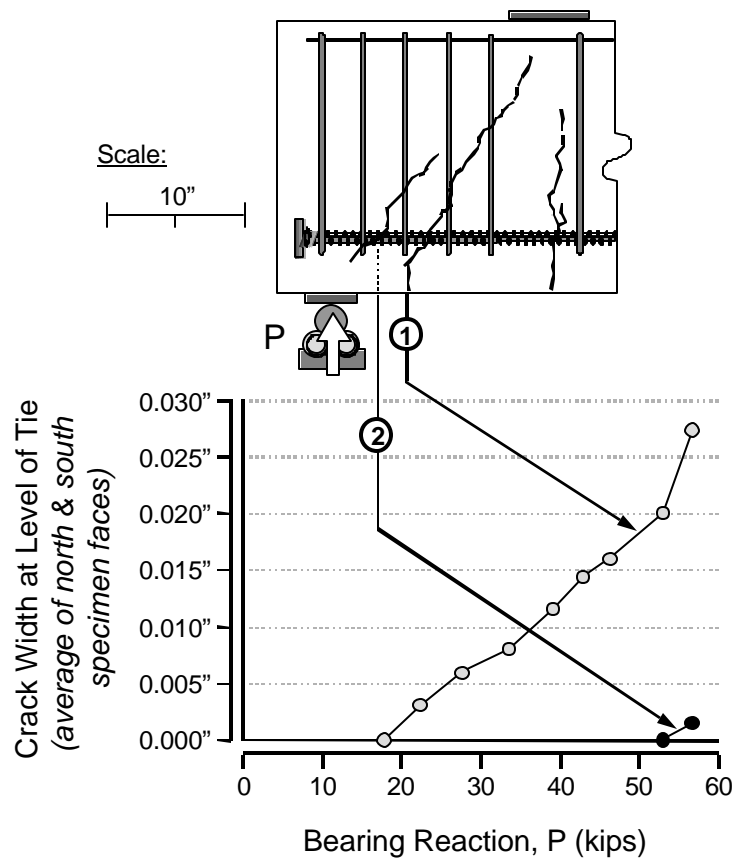


Figure 6-37: Crack width measurements from the heavily confined, headed bar specimen (CCT-08-45-04.70(V)-1-C0.012)

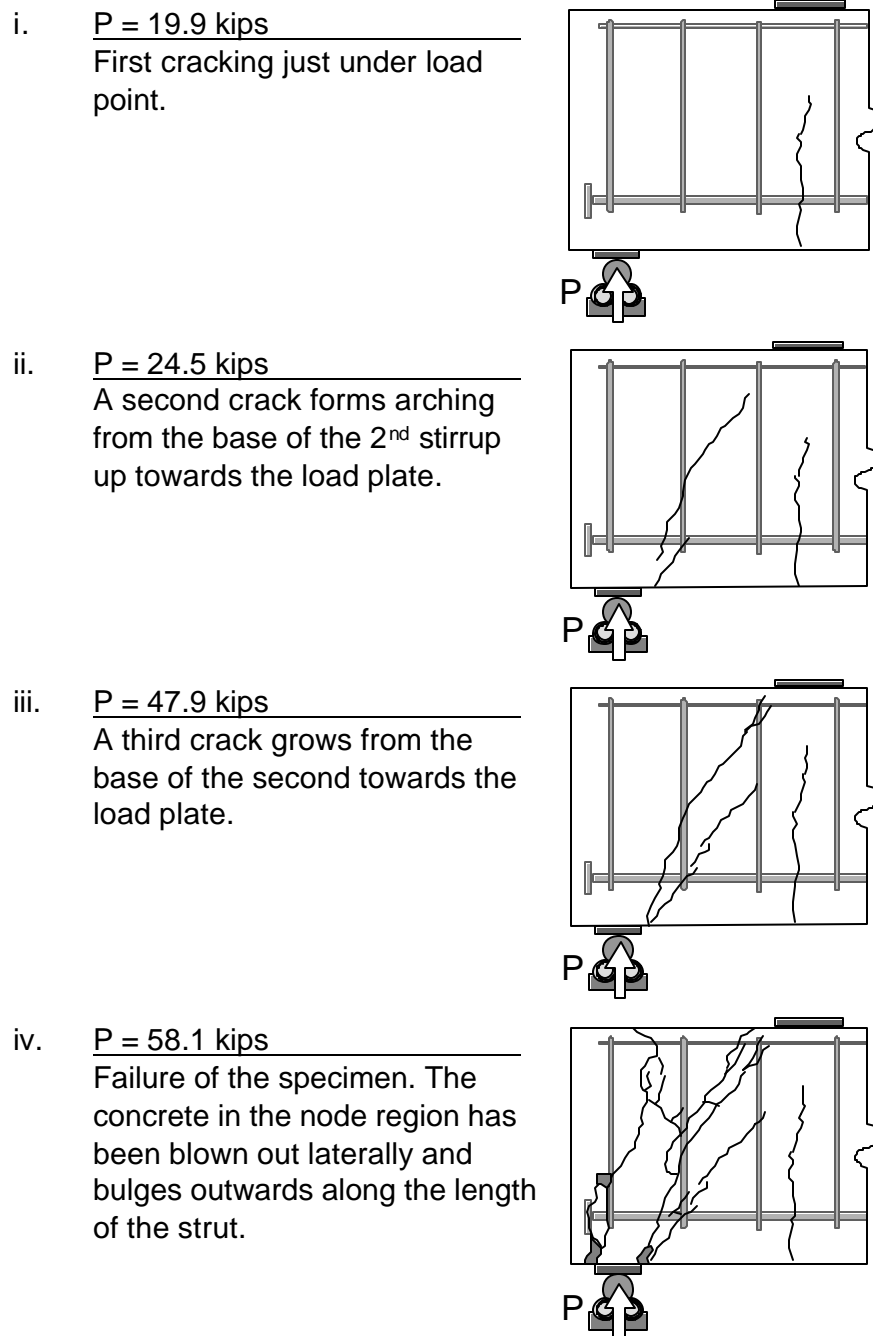
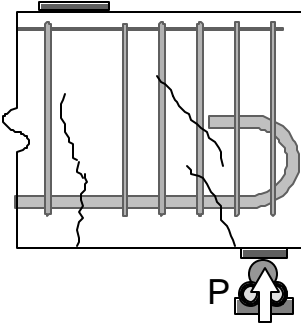
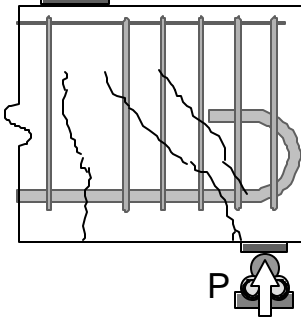
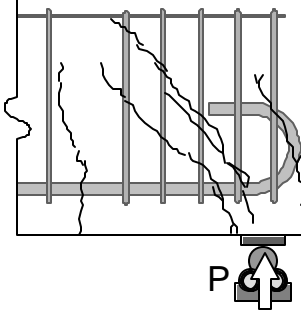


Figure 6-38: Development of cracks in a lightly confined, headed bar specimen (CCT-08-45-04.70(V)-1-C0.006)

- i. P = 29.6 kips
 Diagonal cracks form along the primary strut path.


- ii. P = 42.7 kips
 All three cracks have grown towards the load plate.


- iii. P = 42.5 kips
 Maximum capacity. Cracks form along the top of the hook bend.


- iv. P = 39.2 kips
 After gradual loss of capacity, the strut completely fails. Failure is marked by extensive cracking and bulging of the concrete along the length of the strut.

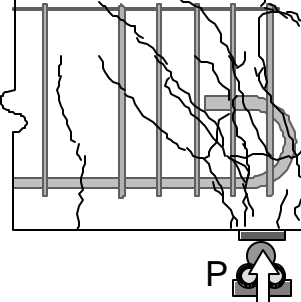


Figure 6-39: Development of cracks in a heavily confined, hooked bar specimen (CCT-08-45-Hook2-1-C0.012)

6.2.2 Stress/Strain Development in the Bar

Measurements of strain along the tie bar indicated that there was a lower strain gradient in the confined condition over the unconfined condition. In Figure 6-40, strain development in unconfined and heavily confined specimens (CCT-08-45-04.70(H)-1-C0.000 and CCT-08-45-04.70(H)-1-C0.012 with concrete compressive strengths of 3900 psi and 3800 psi respectively) is shown by plotting the bar strains at 5" from the head against bearing load, P. The slopes of the plots show that with stirrups, the strain at 5" increased at a slower rate than in the unconfined specimen. This indicates that development of the bar occurred closer to the head in the unconfined specimen than in the confined specimen. In the confined specimen, fan-like strut behavior (as in the strut mechanism depicted in Figure 6-36 part iii) was made possible by stirrups in the nodal zone. This strut behavior allowed for transfer of diagonal forces by multiple paths that extended away from the nodal zone, thus reducing the strain gradient along the bar.

Examination of the difference between the top and bottom fiber bar strains showed that kinking of the tie bar across diagonal cracks was reduced in the confined specimen. There was much less separation between the magnitudes of the top and bottom strain gage measurements in the confined specimen, than in the unconfined case. As expected, the stirrups reduced shear deformation after cracking. As a result, dowel action of the tie bar was also reduced.

Figure 6-41 shows the relative components of bar stress that were provided by bond and head bearing in specimen CCT-08-45-04.70(V)-1-C0.012. This specimen displayed behavior similar to the unconfined specimen shown in Figure 6-14. The presence of heavy confinement did not improve the peak bond capacity, however the confinement did maintain the level of the bond stress until failure of the head occurred.

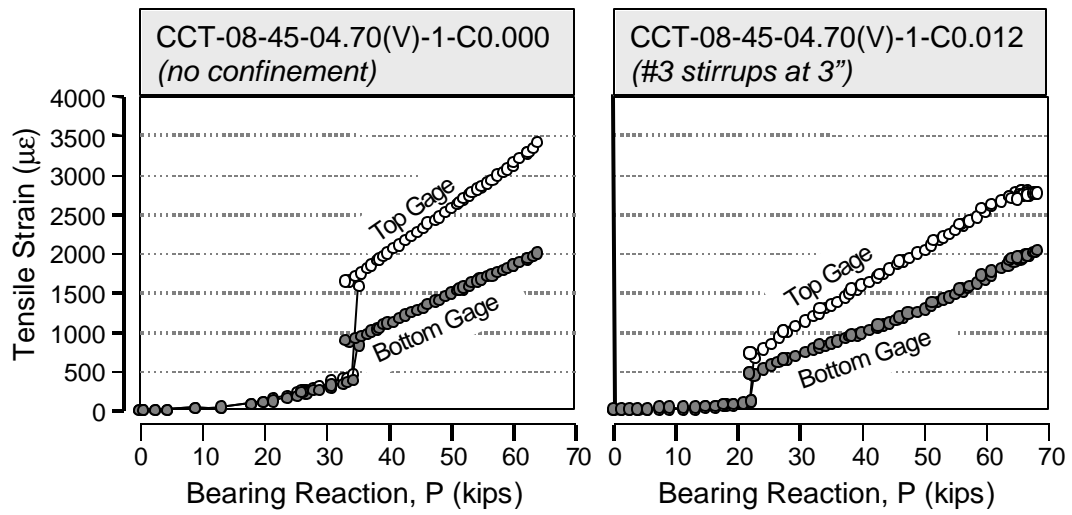


Figure 6-40: Strain at 5" vs. bearing reaction in unconfined and confined specimens

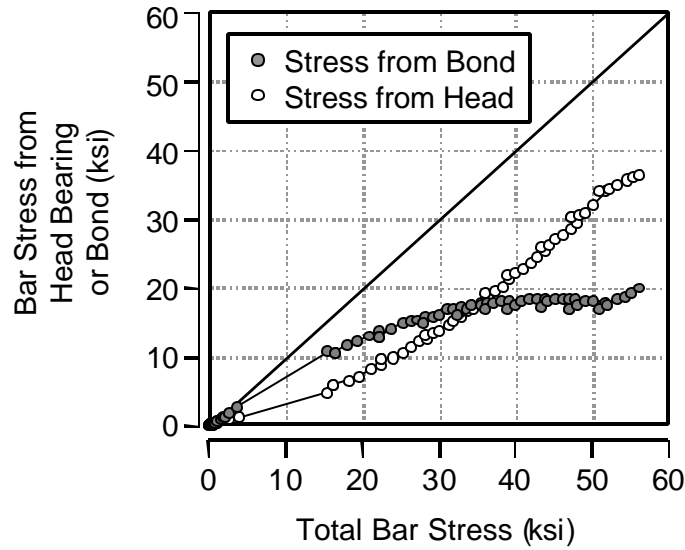


Figure 6-41: Components of bar stress provided by bond and head bearing in CCT-08-45-04.70(V)-1-C0.012

6.2.3 Stress/Strain Development in the Stirrups

Strain gages were placed on the vertical legs of each nodal zone stirrup and on the horizontal leg underneath the tie bar.

6.2.3.1 Vertical Splitting Strains Along the Tie Bar

Vertical strains were measured at a point just above the tie bar to determine the role of the stirrups as: (1) shear cracking developed in the member and (2) bond splitting occurred along the bar and bearing on the head increased. Figure 6-42 shows the development of tensile strain in the stirrups of the heavily confined, headed bar specimen (CCT-08-45-04.70(V)-1-C0.012). Strain increased most rapidly in stirrup 4, located furthest from the CCT node, when the first crack formed. Stirrup 1 was in compression through most of the test. Initially, the diagonal strut and reaction forces placed stirrup 1 in compression. As tie force was transferred from the bar to the head, a concrete wedge formed in front of the head. This wedge created splitting stresses near the head. Near peak capacity splitting forces from the head began to counteract vertical compression in the node region. Once splitting from the head initiated, tensile strain in stirrup 1 quickly exceeded that of the other stirrups and peak capacity of the specimen was reached. Figure 6-43 shows the development of vertical tensile strains in the stirrups of the lightly confined, headed bar specimen (CCT-08-45-04.70(V)-1-C0.006) in which the stirrup spacing was doubled. The plot shows much higher strains in stirrup 2 because fewer bars crossed the diagonal crack. Strain in stirrup 2 reached the yield at peak capacity of the specimen.

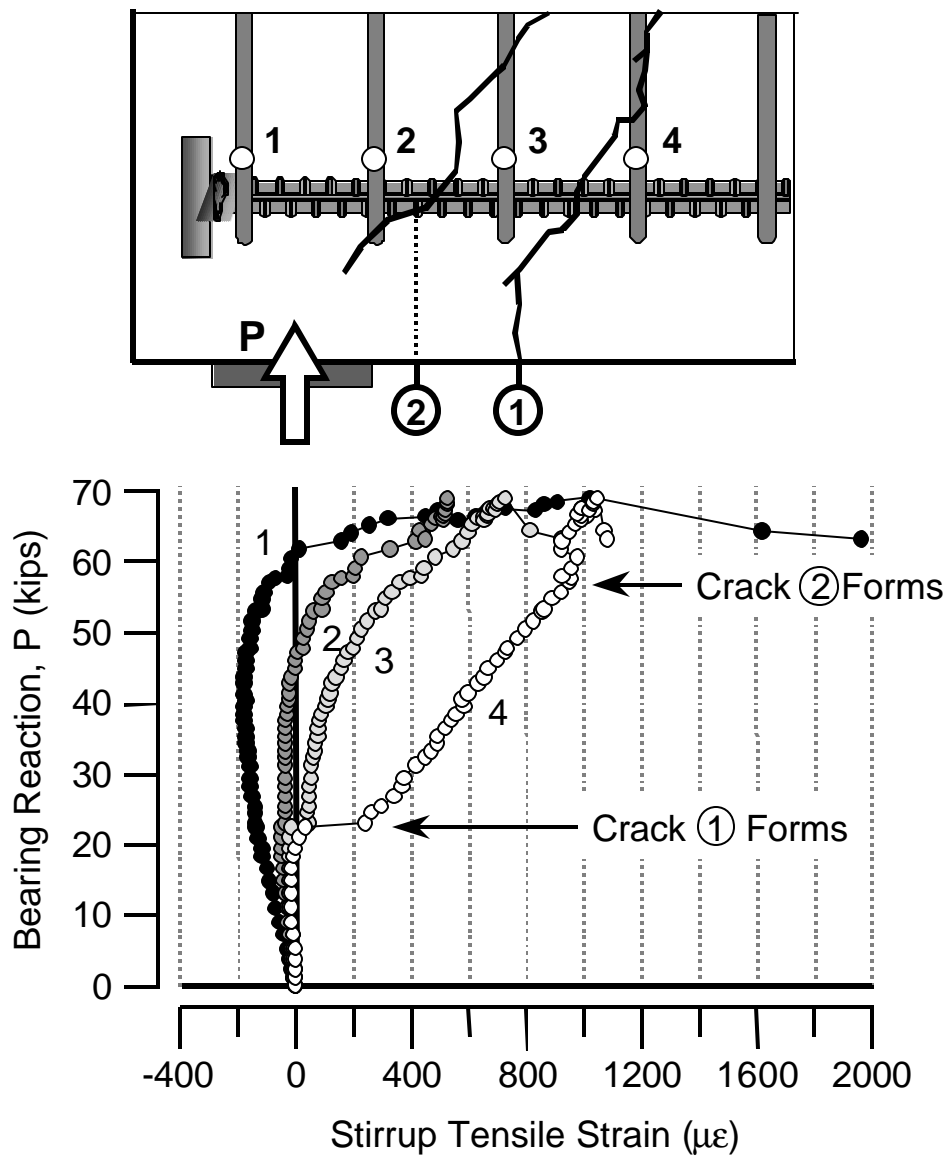


Figure 6-42: Development of vertical tensile strain in the stirrup confinement of the heavily confined, headed bar specimen (CCT-08-45-04.70(V)-1-C0.012)

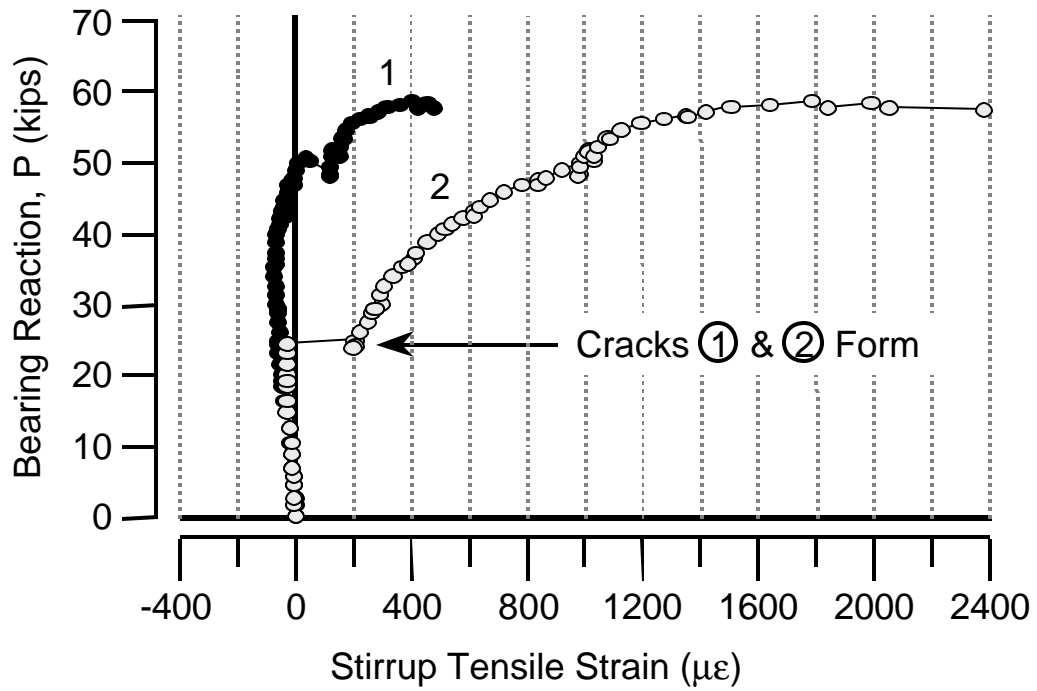
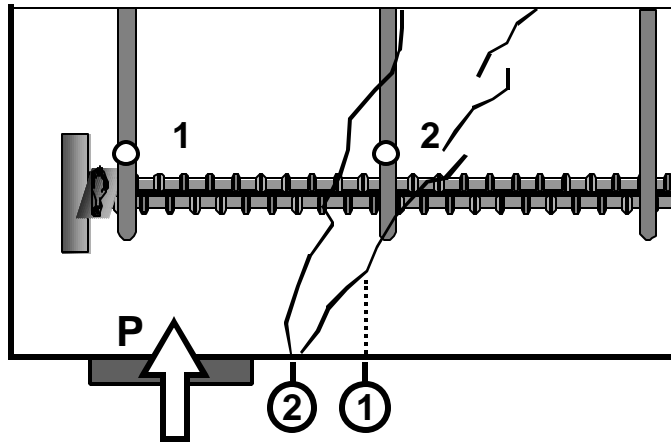


Figure 6-43: Development of vertical tensile strain in the stirrup confinement of the lightly confined, headed bar specimen (CCT-08-45-04.70(V)-1-C0.006)

The vertical stirrup strain along the length of the tie bar for the heavily confined, headed, non-headed, and hooked bar specimens (CCT-08-45-04.70(V)-1-C0.012, CCT-08-45-00.00-1-C0.012, and CCT-08-45-Hook2-1-C0.012) is shown in Figures 6-44 through 6-46. All three specimens had the same confinement, strut angle, and concrete properties and differed only in anchorage detail.

The headed bar specimen (Figure 6-44) showed a linear distribution of strain until the peak capacity was approached. Then large splitting strains began to develop at the head. At 61 kips, the third crack had just formed along the upper part of the diagonal strut. By 66.4 kips, that crack had propagated down to the bottom of the strut. At both of these load stages, the vertical tensile strains were nearly linear along the tie bar. At the final load stage, 68.2 kips, crack 4 formed near the head, and large vertical tensile strains appeared in stirrup 1.

The non-headed specimen (Figure 6-45) also showed a linear profile of vertical tensile strains at low load levels. At 35.8 kips, only the first and second diagonal cracks had formed. By 41.6 kips, the maximum capacity, a third crack had branched off of the second. During post failure loading, this crack turned horizontally and propagated to the front face of the specimen. The corresponding vertical tension plots show that considerable strain developed in the first stirrup as this occurred. However, the strains were higher further along the bar.

The hooked bar specimen (Figure 6-46) again showed a non-linear though generally increasing profile of vertical tensile strain. At a load of 42.7 kips, cracks 1 and 2 had formed and stirrups 2-4 were in tension. No new cracks had formed by a load of 52.4 kips. At 52.5 kips, cracks 3 and 4 formed and the maximum capacity of the specimen was reached. The profile of the vertical tensile strains did not change significantly throughout the cracking process. The gages on

stirrup 4 were lost at the peak load. Stirrup 1 never developed significant tension indicating that, unlike headed bars, the hook does not create vertical splitting in the bend region.

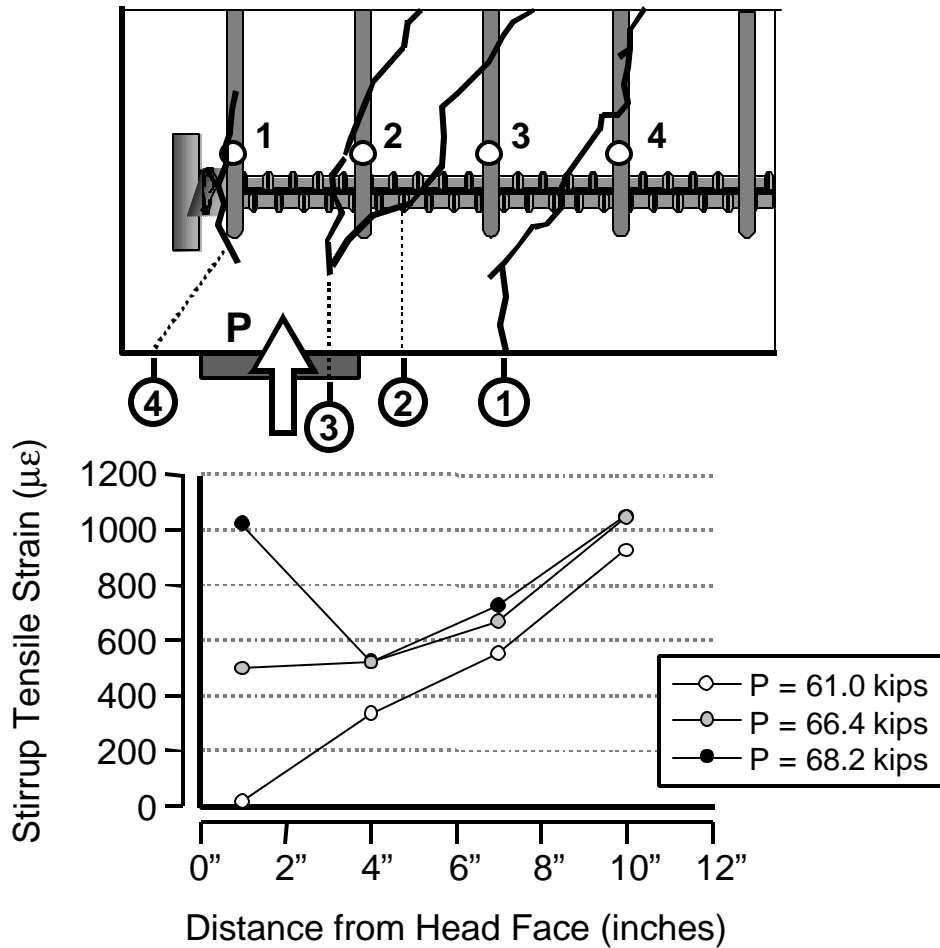


Figure 6-44: Vertical tensile strains along the tie in the heavily confined, headed bar specimen (CCT-08-45-04.70(V)-1-C0.012)

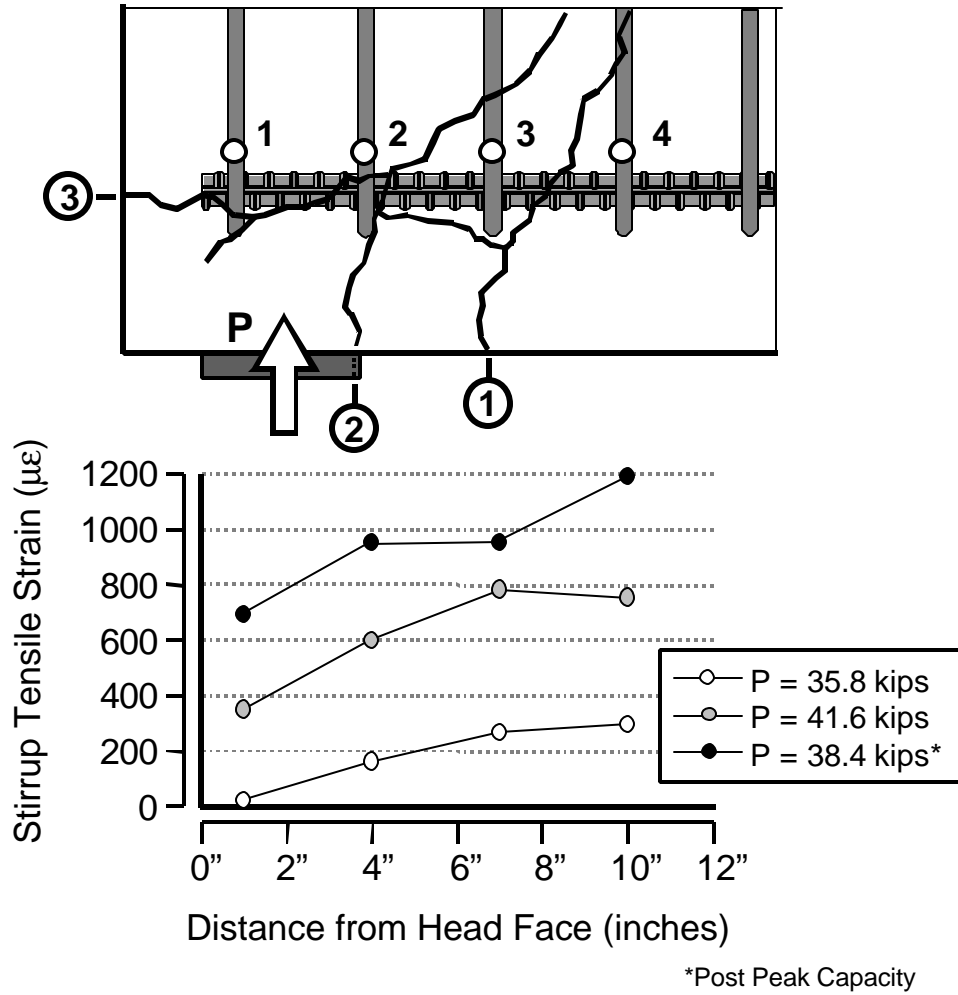


Figure 6-45: Vertical tensile strains along the tie in the heavily confined, non-headed bar specimen (CCT-08-45-00.00-1-C0.012)

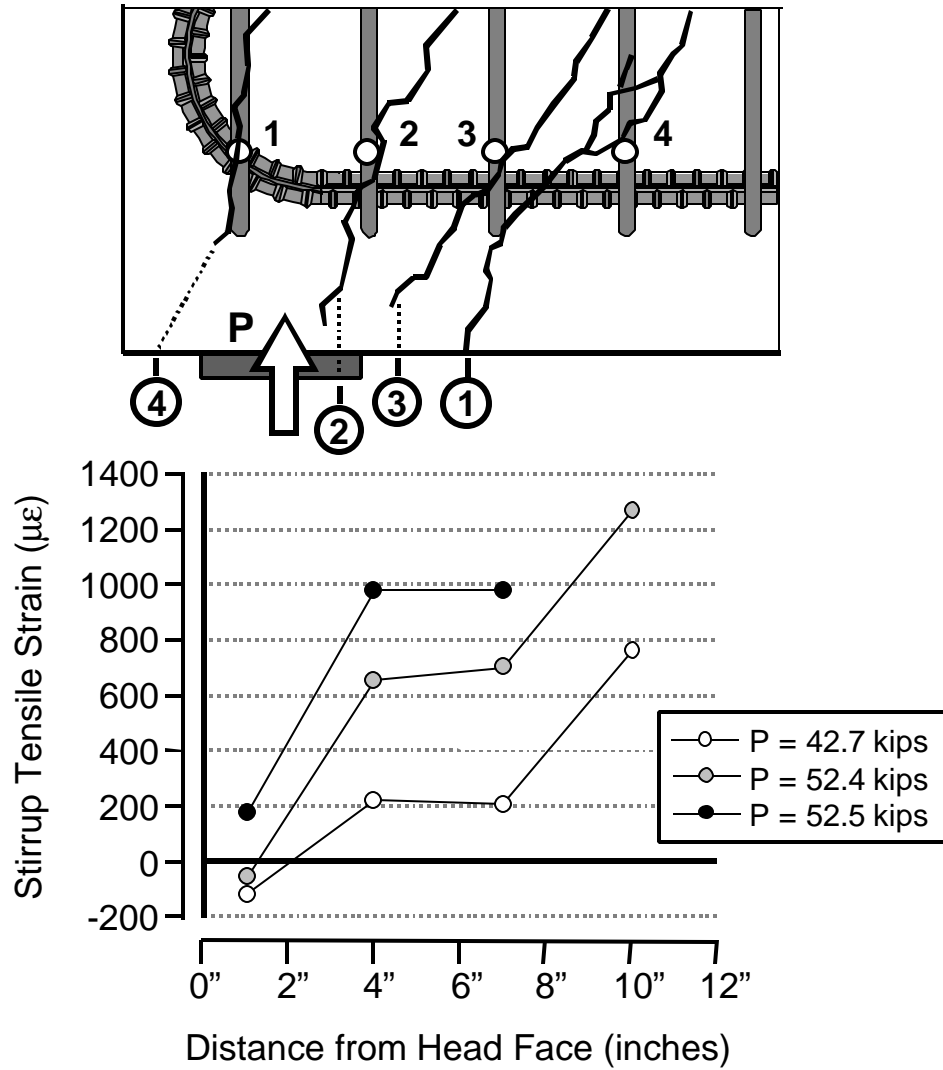


Figure 6-46: Vertical tensile strains along the tie in the heavily confined, hooked bar specimen (CCT-08-45-Hook2-1-C0.012)

6.2.3.2 Transverse Splitting Strains Underneath the Tie Bar

Gages on the bottom of the hoop stirrups provided data on the transverse tensile strains along the underside of the tie bars. Transverse tensile strain was caused by bond splitting along the bar and wedging action at the head. Tensile strain was counteracted by compression between the bottom bearing plate and the head in the CCT node region. The full width of the beam at the CCT node was subject to compression by the bottom bearing plate. At the CCT node, these compression stresses must neck inward to equilibrate with the compression stresses at the head of the tie bar. This creates transverse compression on the underside of the CCT node. This effect is illustrated in Figure 6-47. The transverse strain is plotted as a function of bearing load for the four instrumented stirrups of the heavily confined, headed bar specimen (CCT-08-45-04.70(V)-1-C0.012). From the earliest stages of load to the final stages, stirrups 1 and 2 remain in compression and stirrups 3 and 4 remain in tension. The two sets of stirrups are divided by their placement inside (stirrups 1 and 2) or outside (stirrups 3 and 4) of the CCT node/strut compression region. Outside of the node/strut zone, bond along the tie bar creates radial splitting stress and produces tension in the stirrups. Inside the node/strut zone, the radial tension stress is counteracted by the transverse compression within the CCT node. Similar behavior is seen in the lightly confined, headed bar specimen (CCT-08-45-04.70(V)-1-C0.006). Figure 648 shows the behavior of this specimen. Near peak capacity, the radial tension stress from bond splitting forced stirrup 2 to yield.

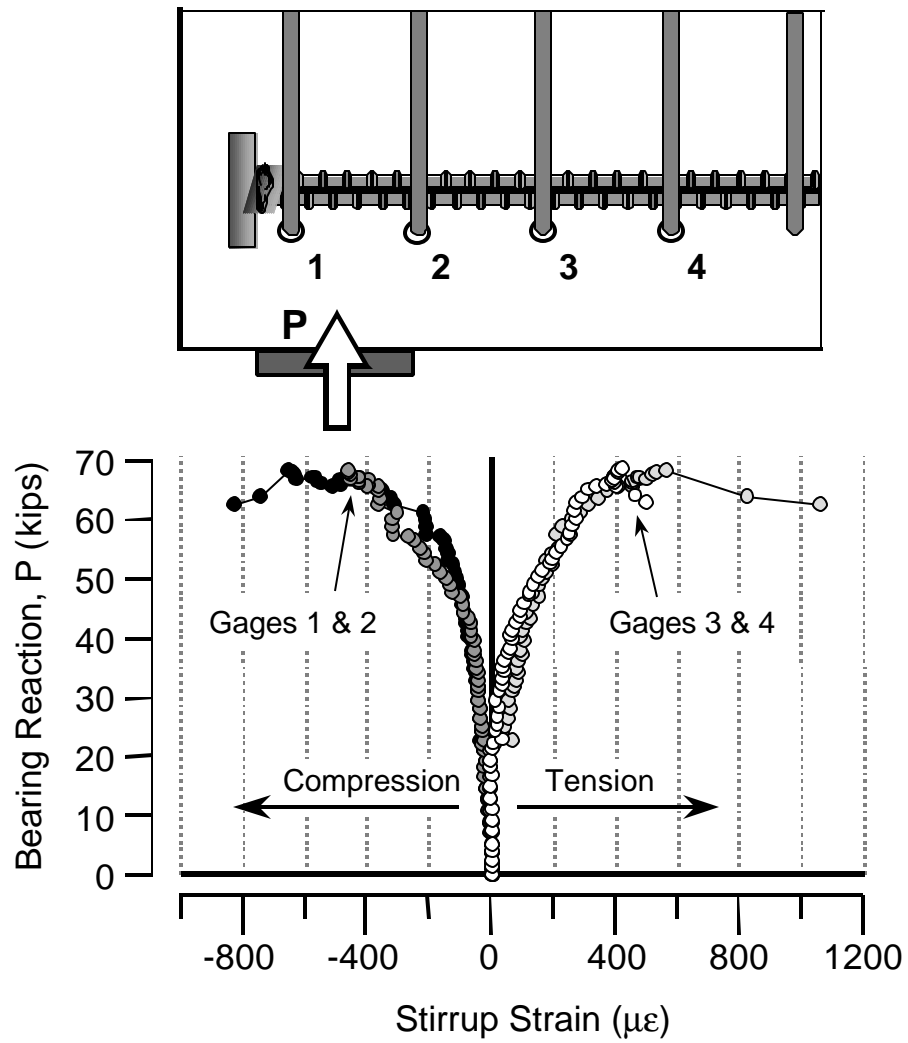


Figure 6-47: Development of transverse tensile strain in the stirrup confinement of the heavily confined, headed bar specimen (CCT-08-45-04.70(V)-1-C0.012)

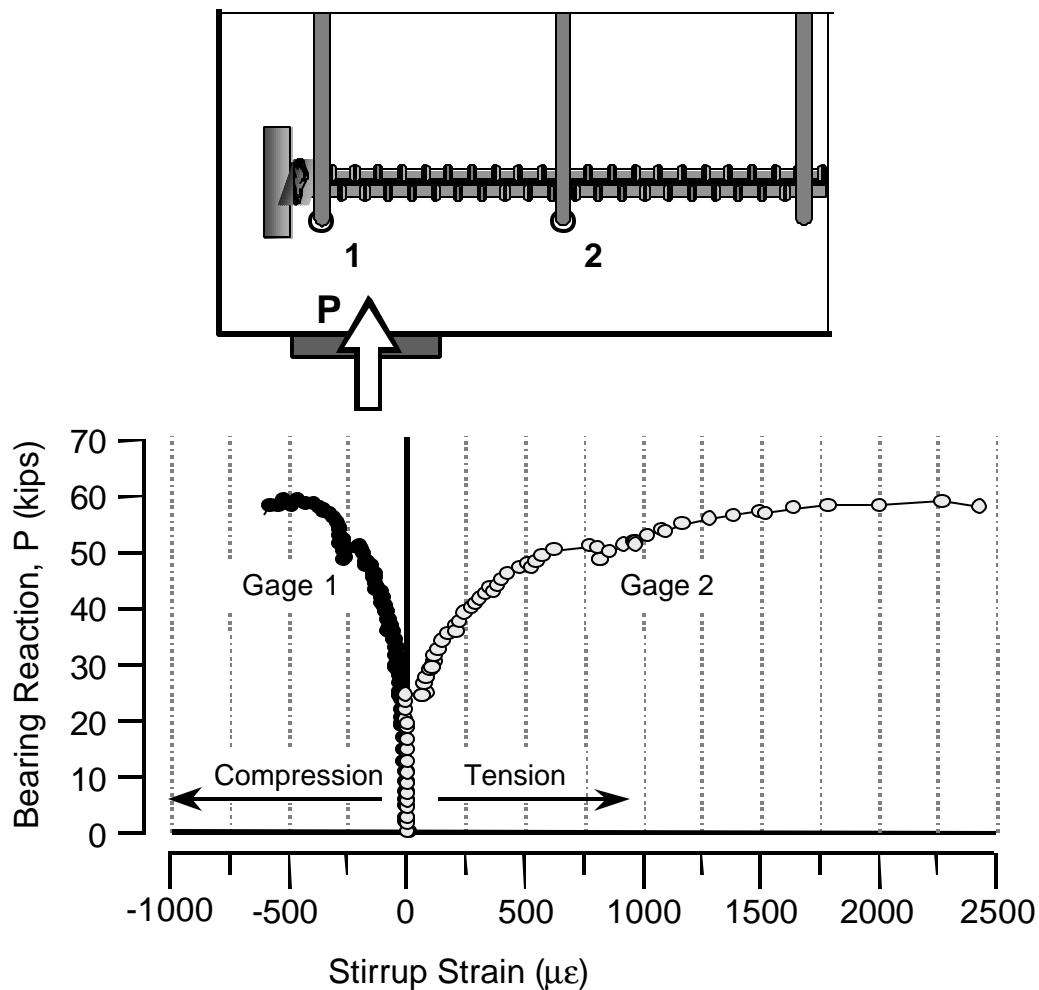


Figure 6-48: Development of transverse tensile strain in the stirrup confinement of the lightly confined, headed bar specimen (CCT-08-45-04.70(V)-1-C0.006)

In Figure 649 through 651, the transverse strain profiles for specimens the heavily confined, headed, non-headed, and hooked bar specimens (CCT-08-45-04.70(V)-1-C0.012, CCT-08-45-00.00-1-C0.012, and CCT-08-45-Hook2-1-C0.012) are presented. All three of these specimens contained similar concrete properties, confinement, and load geometry. They differed only the anchorage condition of the tie bar in the CCT node.

The headed bar specimen (Figure 6-49) demonstrated a transverse strain profile with very distinct regions of compression and tension strain. Inside of the node region, the stirrup gages were in compression. Outside of the node region, the stirrup gages were in tension. At the peak load, 68.2 kips, the measured tension strain exceeded $300\mu\epsilon$ indicating that the concrete was probably cracked. Longitudinal cracking along the underside of the specimen was witnessed in many tests and is consistent with the results from these stirrup gages.

The non-headed specimen (Figure 6-50) demonstrated a more linear distribution of transverse splitting strain. While the first stirrup gage went into compression, the 2nd and 3rd stirrup gages were in tension. The 4th gage was damaged during the casting process. This transverse strain profile differed from the profile for the headed bar in the readings from the 2nd and 3rd gages. Not only was the 2nd gage in tension rather than compression, but the 3rd gage exceeded the level of tensile strain that was seen for the headed bar specimen at the same location. The reason that the non-headed bar exhibited much more transverse tension than the headed bar is most likely due to higher bond stresses along the non-headed bar. Because the bar had no head, it relied more on bond for anchorage. This greater reliance on bond resulted in greater radial splitting stresses and thus a greater reliance on the stirrups to resist those splitting stresses. Hence, the higher tensile strains.

The hooked bar specimen (Figure 6-51) demonstrated similar transverse strains outside of the CCT node region. The tensile strain levels in the 3rd and 4th stirrups were slightly higher at lower load levels than the headed bar case indicating that the hooked bar was slightly more reliant on bond at that location similar to the behavior of the headed bar test. Within the CCT node however (stirrups 1 and 2), the results of the hooked bar vary from the headed bar. Transverse strain in stirrup 1 was initially in compression and eventually shifted into tension. However, the

strains were low indicating that virtually no stress transfer was occurring within the node at that location. At stirrup 2, the compression strain was much greater than was the case for the headed bar. The bend of the hook shifts the point of bearing back and upward from the location at which the headed bar bears on the concrete. Thus stirrup 1 was less effective and more demand was placed on the stirrup 2. These results, coupled with the vertical strain data from the previous section (Figure 6-46), show that the optimum location for stirrup confinement of a hooked bar is closer to the start of the bend than the end of the bend. Stirrup 1 was ineffective and merely hampered the ability to place concrete around the hook.

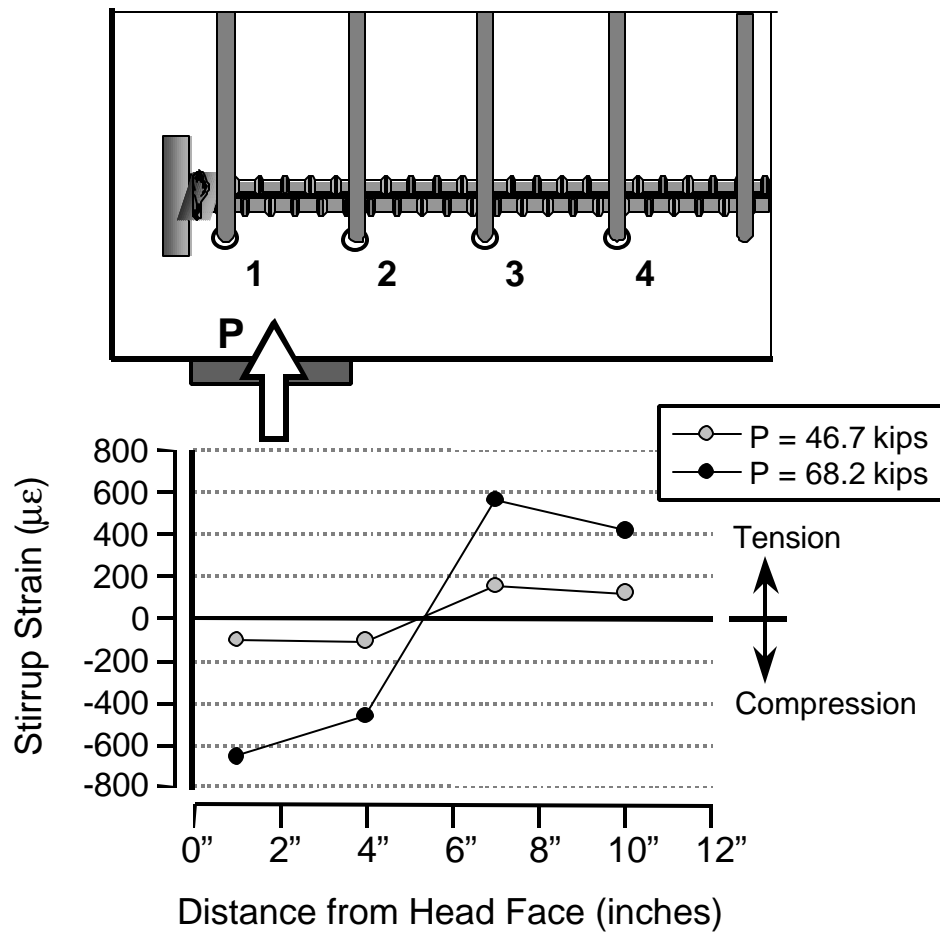


Figure 6-49: Transverse strains along the underside of the tie in the heavily confined, headed bar specimen (CCT-08-45-04.70(V)-1-C0.012)

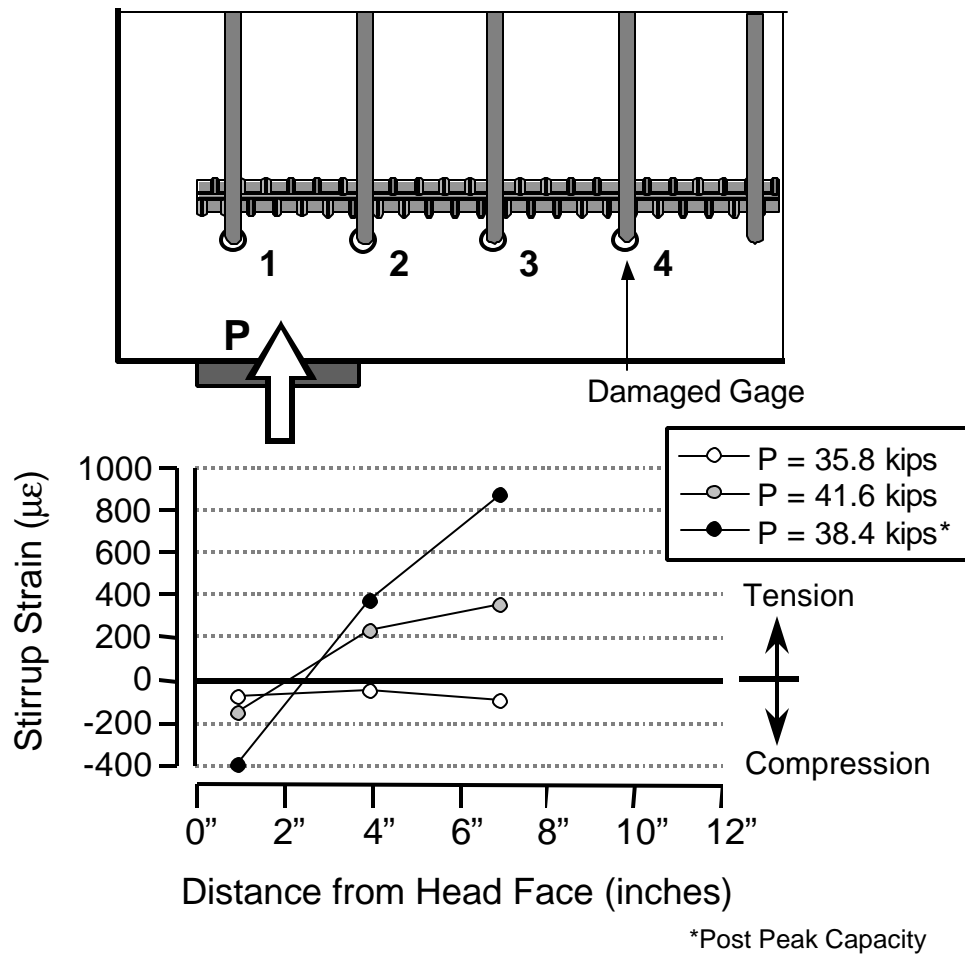


Figure 6-50: Transverse strains along the underside of the tie in the heavily confined, non-headed bar specimen (CCT-08-45-00.00-1-C0.012)

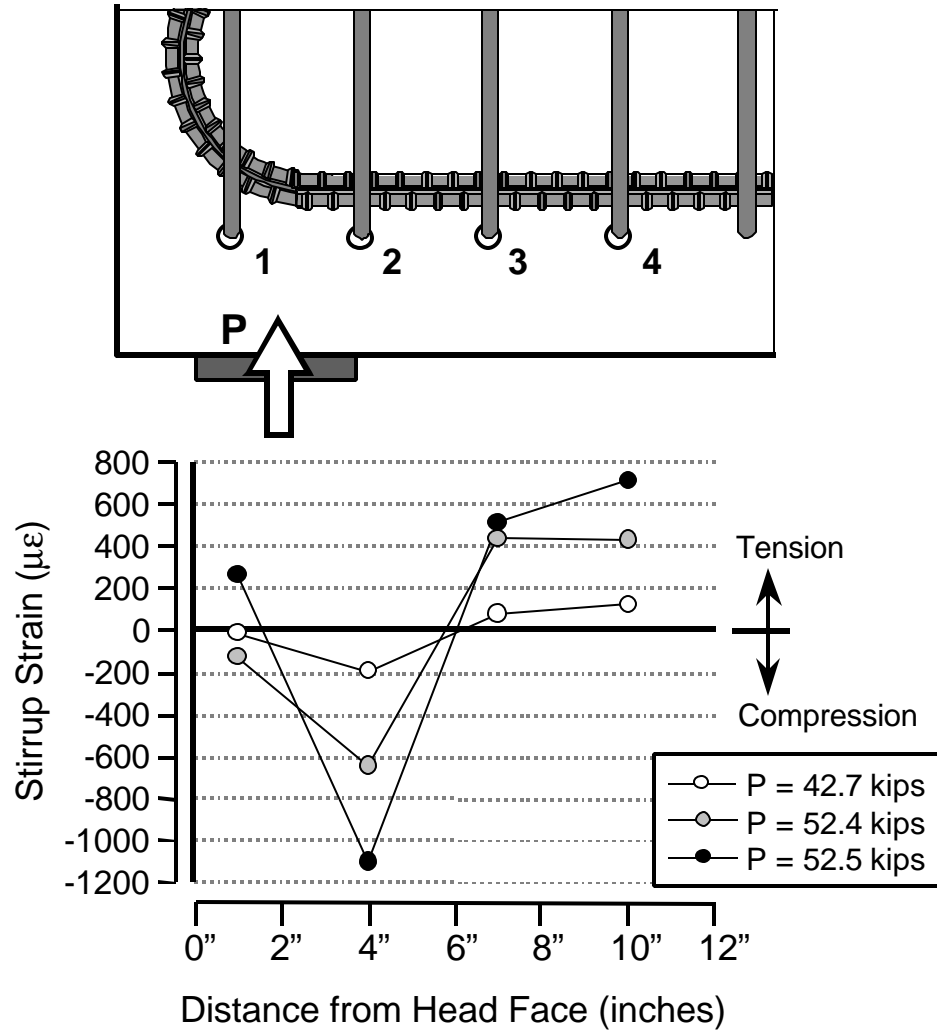


Figure 6-51: Transverse strains along the underside of the tie in the heavily confined, hooked bar specimen (CCT-08-45-Hook2-1-C0.012)

6.2.4 Head Slip

Head slip in the confined specimens is presented in Figure 6-52. Data from the unconfined companion specimen were not available due to instrumentation errors during that test. The behavior of the two confined specimens followed expected behavior. The specimen with more confinement demonstrated a stiffer slip resistance than the specimen with less confinement. The slip response of the two specimens is generally less stiff than that of similar head sizes of unconfined specimens shown in Figure 6-18, however, the test results come from specimens with different concrete properties and the stiffness responses may not be directly comparable.

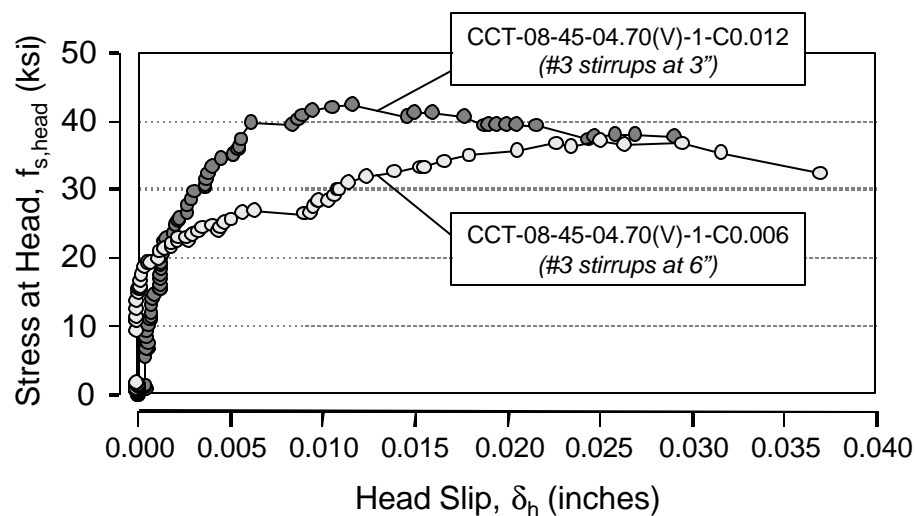


Figure 6-52: Bar stress versus head slip for unconfined and confined specimens

6.2.5 Load-Deflection Response

Load-deflection data for an unconfined and a confined specimen (CCT-08-45-04.70(V)-1-C0.000 and CCT-08-45-04.70(V)-1-C0.012) are shown in Figure 6-53. The load-deflection responses of these two specimens were very similar. The two plots align on top of one another up

until a load of 64 kips when the unconfined specimen failed. The similarity of the data also suggest that there must have been little difference in the head slip behavior of the two specimens which would have affected the overall stiffness of the specimens. For the confined specimen, a definite yield plateau was achieved. Never-the-less, the confined specimen could not sustain the ductility demand placed on it and eventually failed at the node.

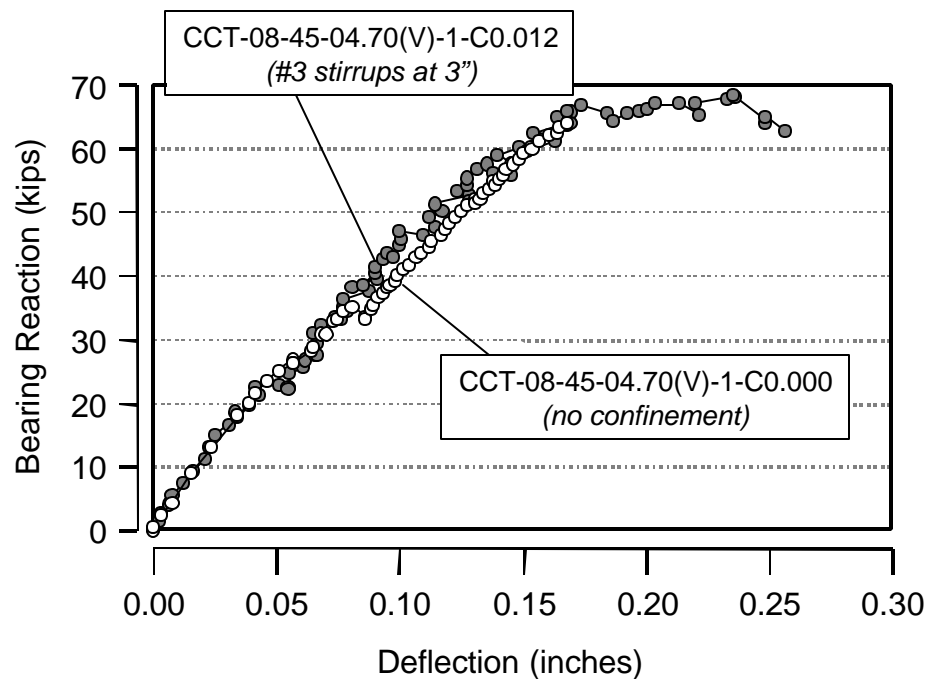


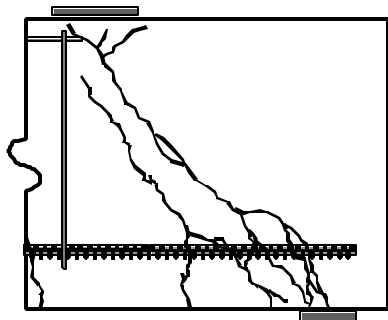
Figure 6-53: Load-deflection data for specimens unconfined and confined specimens

6.2.6 Modes of Failure

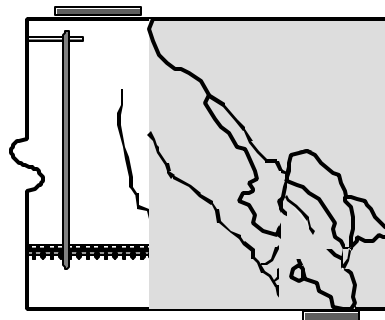
The failure modes of the five confined specimens resembled those of the unconfined specimens. The non-headed bars failed by pullout. The headed bars and the hooked bar failures involved strut rupture and transverse splitting. The one exception was the heavily confined,

headed bar specimen (CCT-08-45-04.70(V)-1-C0.012), the most successful of the confined tests with the highest capacity. The specimen exhibited some ductility prior to failure, which did not occur in any of the previous specimens. Post-yield failure occurred because the node could no longer sustain the degree of deformation placed on it or because of continued development of the confined strut-and-tie mechanism. The confined mechanism (shown in Figure 6-36) involved the utilization of not just the bottom horizontal bar, but also the vertical stirrup bars as ties. This type of truss mechanism reaches its ultimate capacity when all the ties have yielded or until a strut or node fails. In the heavily confined, headed bar specimen, though the main horizontal tie may have begun to yield, redistribution of forces to alternative strut paths continued until one of the struts or nodes failed.

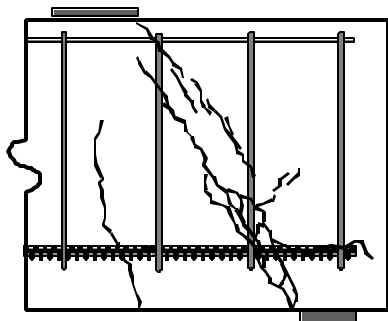
Figure 6-54 shows the cracking patterns at failure for non-headed and headed bar specimens with varying degrees of confinement. The cracking at failure of the non-headed bar specimens did not change significantly with the addition of confinement. The headed bar specimens did show some changes in behavior at failure. When unconfined, the specimen failed by splitting at the bottom of the strut and cleaving off of the top-front corner of the specimen. In the confined specimens, this dramatic cleaving off of large portions of the concrete was restrained. However, after failure, the confined specimens were left with large chunks of concrete bulging out from the sides along the length of the primary strut. This behavior tended to indicate that transverse splitting was significant.



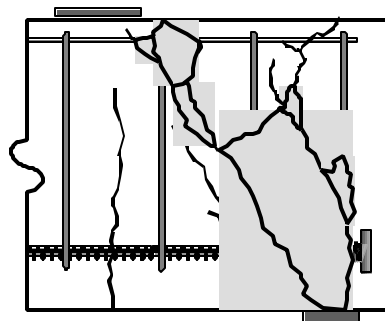
i. CCT-08-45-00.00-1-C0.000
(no head, no confinement)



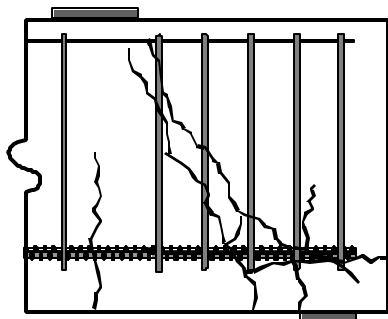
ii. CCT-08-45-04.70(V)-1-C0.000
(headed, no confinement)



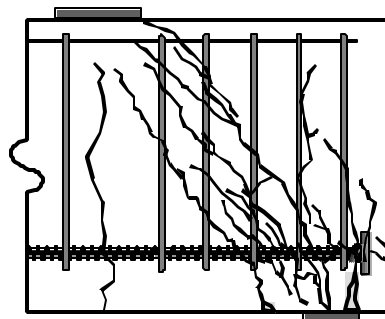
iii. CCT-08-45-00.00-1-C0.006
(no head, stirrups at 6")



iv. CCT-08-45-04.70(V)-1-C0.006
(headed, stirrups at 6")



v. CCT-08-45-00.00-1-C0.012
(no head, stirrups at 3")



vi. CCT-08-45-04.70(V)-1-C0.012
(headed, stirrups at 3")

Figure 6-54: Failure cracking patterns for non-headed and headed specimens with varying degrees of confinement

Table 6-4 summarizes the failure modes for the confined specimens. Failure modes conform to the categories discussed in section 6.1.6.

| Specimen Identification | f'_c | Failure Mode - Notes |
|-----------------------------|--------|----------------------|
| CCT-08-45-00.00-1-C0.006 | 3800 | Pullout |
| CCT-08-45-00.00-1-C0.012 | 3800 | Pullout |
| CCT-08-45-04.70(V)-1-C0.006 | 3800 | Splitting |
| CCT-08-45-04.70(V)-1-C0.012 | 3800 | Yield then Splitting |
| CCT-08-45-Hook2-1-C0.012 | 3800 | Splitting |

Table 6-4: Failure modes of confined CCT node specimens

6.3 SUMMARY OF BEHAVIORAL OBSERVATIONS

The various observations from the confined and unconfined specimens add together like pieces of a jigsaw puzzle to form a picture of the whole mechanism of force transfer in the CCT node specimens. Strain gage data from the confined, unconfined and special detail specimens provided information on the development of the tie bar and the locations of compression and tension regions within the CCT node panel. Combined strain data with the observations of cracking and failure modes provides an overall picture of the CCT node behavior.

Data from the special detail tests have shown that splitting tension along the diagonal strut begins at the ends of the strut. The behavior of the strut resembles the behavior of a concrete cylinder subjected to a double punch test. A wedge of concrete forms in front of the bearing face of the head and acts to cleave the strut in two. Splitting may occur in the plane of the truss model or transverse to the plane of the truss model depending on the orientation and size of the head. Failure most likely initiates at the CCT node.

Anchorage of the headed bars consists of two stages: the first in which load is primarily anchored by bond. This stage continues until maximum bond is reached, past which the bond stress gradually declines. This point begins the start of the second stage in which anchorage force is transferred to the head. This stage continues until the head reaches its maximum capacity or bar yield occurs. Final anchorage capacity is the sum of the maximum head capacity plus the residual bond left after the decline in bond begins.

Strain readings from gages on the tie bar indicate that the critical section at which the tie bar must fully develop occurs at the front-most diagonal crack. This crack forms along the lower edge of the diagonal compression strut and propagates downward to the edge of the bearing plate. The critical section can thus be estimated as the location at which the tie bar passes out of the path of the diagonal compression strut. Shear deformation across this crack can cause severe kinking of the tie bar.

Strain readings from stirrups in the confined specimen indicate that beneath the CCT node, compression stresses from the lower bearing plate must neck inward to equilibrate spatially with the bearing face of the head. This creates a region of vertical and transverse compression. This region begins at the bearing face of the head and extends to the surface of the critical diagonal crack. On the other side of the crack, radial splitting stresses created by bond of the reinforcing bar cause the reverse stress state.

Load-deflection data suggest that the top CCC node undergoes severe contraction during loading of the specimen. The CCC node is under a state of biaxial compression and can potentially sustain compression stresses up to 1.5 times the uniaxial concrete compression strength, f_c' . As the CCC node becomes highly stressed, the top of the strut can also become a critical location for the initiation of failure.

The truss mechanism forms after a succession of cracks develop. Cracks form first underneath the load point (the CCC node), then closer and closer to the CCT node. The cracks closest to the CCT node propagate diagonally and follow the lower edge of the diagonal strut path. Even in confined specimens, the initial truss mechanism to form begins with a single diagonal strut connecting the CCT node directly to the CCC node. This is the stiffest and most direct path for force transfer. As this strut begins to weaken due to cracking, secondary strut paths may form to mobilize the stirrups.

Crack width measurements indicate that the primary diagonal crack, closest to the strut and the CCT node, undergoes the most opening during loading.

Finally, head slip measurements demonstrate the enhanced resistance provided with increased head size. Head slip was shown to have a detrimental affect on the overall stiffness of the specimen. Slip was very often a precursor to failure. However, the amount of slip was also related to the amount of total bar stress transferred to the head. For longer development lengths, less bar stress would be transferred to the head before yielding and smaller heads could be used without concern for slip.

Chapter 7: CCT Nodes: Comparison to Failure Models and Formulation of Design Methodology

7.1 INTRODUCTION

In this chapter the CCT node data are examined for trends then compared to existing theories of head capacity. This analysis leads towards the development of a design formula for headed bar anchorage. The existing theories to which the CCT node data are compared include: the ACI STM design procedures for nodes and struts [2], the modified CCD methods developed by DeVries [42] for headed bars, the ACI bearing capacity equations [2], and the ACI development length equations [2].

7.2 TRENDS IN THE DATA

The variables studied in the CCT node study included relative head area, strut angle, head shape and orientation, bar size, and confinement. The effects of these variables on the trends in the data are examined in this section.

7.2.1 Effect of Relative Head Area

Figure 7-1 shows the effect of increases in relative head area on the ultimate bar stress carried by the head. Values of ultimate bar stress have been adjusted by a ratio of $4\text{ksi}/f_c'$ to normalize the effects of differences in concrete strength. Only data from specimens that did not yield are plotted. Figure 7-1 shows that the ultimate capacity of the head generally increased with increasing relative head area but the relationship did not appear to be linear.

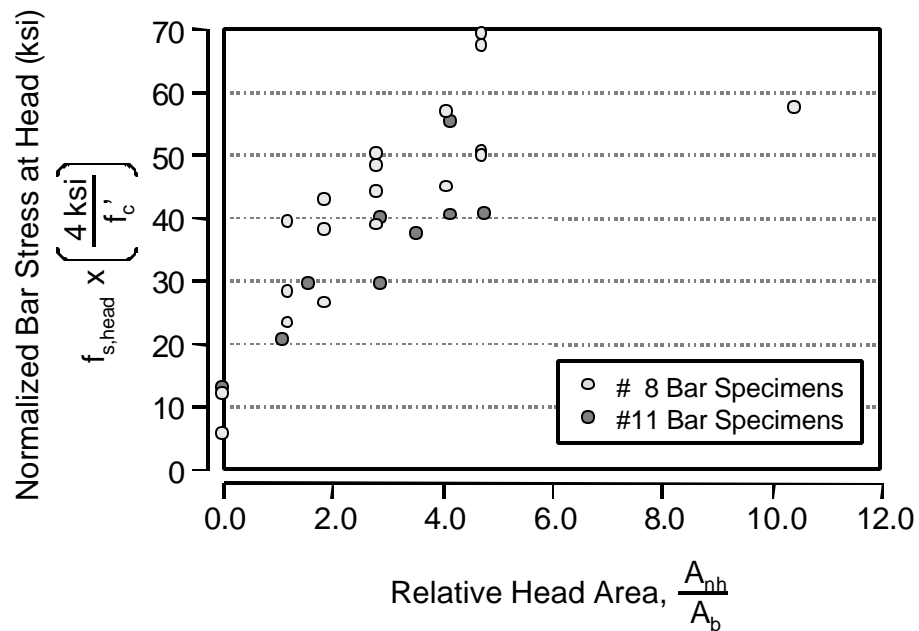


Figure 7-1: Effect of relative head area on head capacity

7.2.2 Effect of Strut Angle

Figure 7-1 included data from specimens with different strut angles. The head capacity was not influenced by the strut angle. However, the strut angle did affect the bond component of the anchorage. As the strut angle was decreased, more of the length of the tie bar was included in the path of the strut as shown in Figure 7-2. As a result, the development length of the tie bar was increased and bond became a larger component of the anchorage. Thus smaller head sizes were able to achieve full development of the tie bar. In Figure 7-3, the minimum head sizes that achieved yield of the tie bar are plotted for the three different strut angles studied. The plot shows that decreases in the strut angle allowed smaller head sizes to successfully anchor the tie bar.

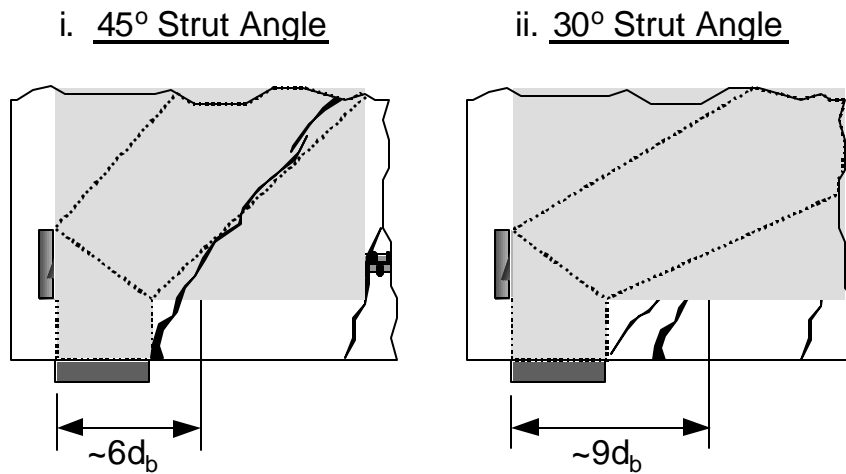


Figure 7-2: Approximate development lengths for 45° and 30° strut angles

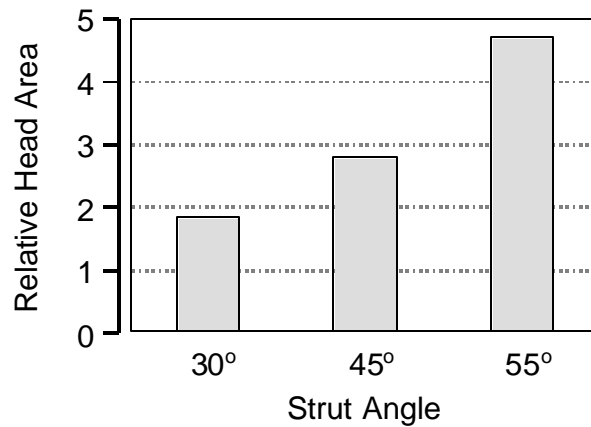


Figure 7-3: Minimum head size necessary to achieve yield of the tie bar

7.2.3 Effect of Head Shape and Orientation

Three basic head shapes were studied in the research: circular, square, and rectangular. For the rectangular head shapes, the affect of the orientation of the head was also studied. Three pairs of specimens used circular and square heads of almost exactly the same relative head area

(Table 7-1). Of these three pairs, however, only one provided two specimens that both failed to yield and thus provided data that could be used to study the effects of head shape. Head slip plots for specimens CCT-08-55-04.04-1 and CCT-08-55-04.06-1 are presented in Figure 7-4. The data show that the square head performed slightly better than the circular one, but not significantly. DeVries [42] also studied head shape. He concluded that it was not a significant variable and excluded it from his design equations.

| Specimen Pair | Head Shape | f'_c (ksi) | $f_{s,head}$ (ksi) | Failure Mode |
|-------------------|------------|--------------|--------------------|--------------|
| CCT-08-30-04.04-1 | Circular | 4.2 | 27.5 | Yield |
| CCT-08-30-04.06-1 | Square | 4.2 | 33.5 | Yield |
| CCT-08-45-04.04-1 | Circular | 4.0 | 32.7 | Yield |
| CCT-08-45-04.06-1 | Square | 3.1 | 34.8 | Crushing |
| CCT-08-55-04.04-1 | Circular | 3.1 | 25.1 | Crushing |
| CCT-08-55-04.04-1 | Square | 3.1 | 27.5 | Crushing |

Table 7-1: Companion specimens for effect of head shape

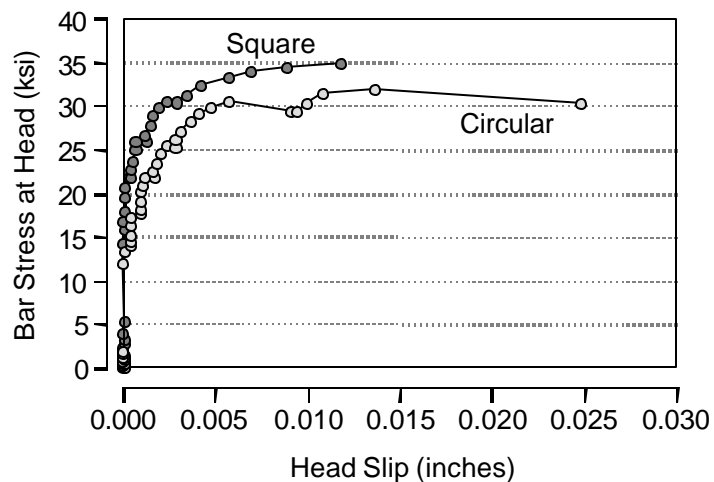


Figure 7-4: Head slip plots for circular and square heads

Seven pairs of specimens provided information on the effect of rectangular head orientation (Table 72). One pair of specimens (CCT-11-45-06.69(H)-1 and CCT-11-45-06.69(V)-1) both yielded. Thus, the bar stress sustained by the heads at a slip of 0.005" was used instead of ultimate stress data. Ratios of the horizontal head capacity to vertical head capacity were then calculated for each pair of specimens and plotted against the aspect ratio (long dimension / short dimension) of the head (Figure 7-5). This plot shows that the head orientation did have an effect on the capacity for heads with larger aspect ratios. The data for slightly rectangular heads (long/short \approx 1.3-1.5) were inconsistent. Some head capacities were greater with a horizontal orientation and some greater with a vertical orientation. However when the aspect ratio of the head approached 2, the horizontal orientation of the head consistently provided a capacity 30-40% greater than the vertical orientation.

The effect of head orientation can be explained by examining the angles of the forces produced by the head. As a concrete wedge forms in front of a rectangular head, the orthogonal faces of the wedge form at steep and shallow angles relative to the axis of the bar (Figure 7-6). As this wedge bears against the concrete, the shallow faces of the wedge produce greater transverse splitting stresses than the steep faces (Figure 7-7). Thus for a rectangular head, transverse splitting stresses are greater along the axis perpendicular to the long head dimension. In a CCT node, the larger transverse splitting stress are counteracted by vertical compression stresses when a head is oriented horizontally (Figure 7-8, part i). Thus, a head with a horizontal orientation should have a greater capacity than a head with a vertical capacity as the data in Figure 7-5 suggest. From a practical point of view, however, it is unrealistic to dictate what the orientation of the heads should be when a reinforcement cage is assembled. It is likely that heads will be oriented randomly. For

design, limits should be placed on the aspect ratio of head shapes to prevent undue influence from head orientation. Thus head orientation can be dropped as a factor in capacity equations.

| Specimen Pair | Head Dimensions | Aspect Ratio | Horizontal Test | | Vertical Test | | $\frac{(f_s/f_c)_{\text{Horiz.}}}{(f_s/f_c)_{\text{Vert.}}}$ |
|--|-----------------|--------------|---------------------------|--------------|---------------------------|--------------|--|
| | | | $f_{s,\text{head}}$ (ksi) | f_c' (ksi) | $f_{s,\text{head}}$ (ksi) | f_c' (ksi) | |
| CCT-08-45-02.80(H)-2 CCT-08-45-02.80(V)-1 | 1.5" x 2.0" | 1.33 | 37.6 | 3.1 | 49.1 | 3.9 | 0.96 |
| CCT-08-45-04.70(H)-1 CCT-08-45-04.70(V)-1 | 1.5" x 3.0" | 2.00 | 53.7 | 3.1 | 48.7 | 3.9 | 1.39 |
| CCT-08-55-02.80(H)-1 CCT-08-55-02.80(V)-1 | 1.5" x 2.0" | 1.33 | 38.0 | 3.9 | 43.2 | 3.9 | 0.88 |
| CCT-08-55-04.70(H)-2 CCT-08-55-04.70(V)-1 | 1.5" x 3.0" | 2.00 | 52.2 | 3.1 | 49.2 | 3.9 | 1.33 |
| CCT-11-45-02.85(H)-1 CCT-11-45-02.85(V)-1 | 2.0" x 3.0" | 1.50 | 30.3 | 4.1 | 40.9 | 4.1 | 0.74 |
| CCT-11-45-04.13(H)-1 CCT-11-45-04.13(V)-1 | 2.0" x 4.0" | 2.00 | 56.5 | 4.1 | 39.6 | 3.9 | 1.36 |
| CCT-11-45-06.69(H)-1 CCT-11-45-06.69(V)-1 | 3.0" x 4.0" | 1.33 | 42.6* | 3.9 | 39.3* | 3.9 | 1.08 |

* Stress at 0.005" slip.

Table 7-2: Companion specimens for effect of head orientation

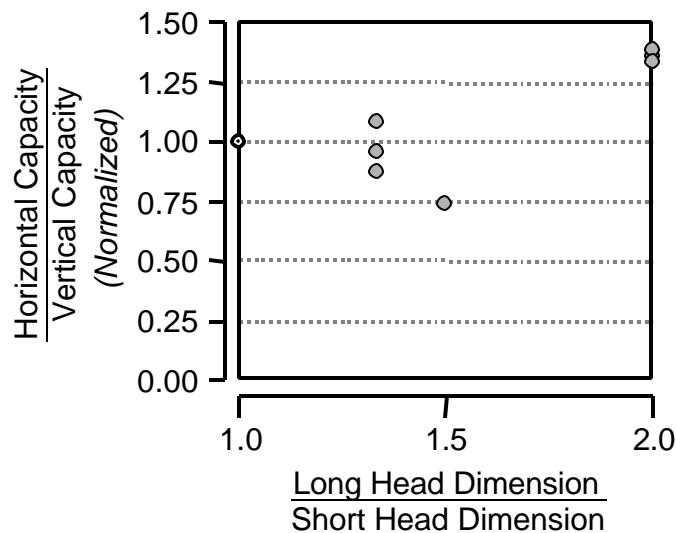


Figure 7-5: Effect of head orientation and aspect ratio on head capacity

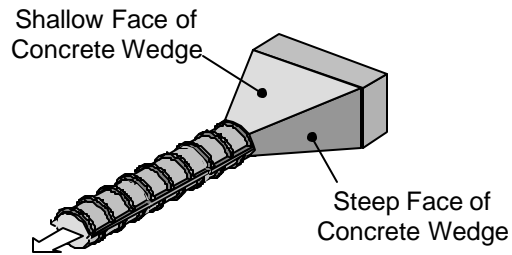


Figure 7-6: Shallow and steep faces of the wedge for a rectangular head

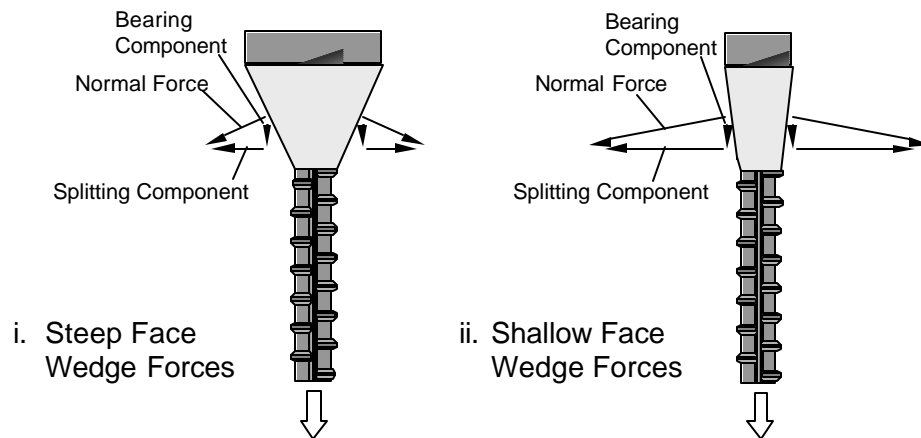


Figure 7-7: Transverse splitting components of shallow and steep wedge face bearing

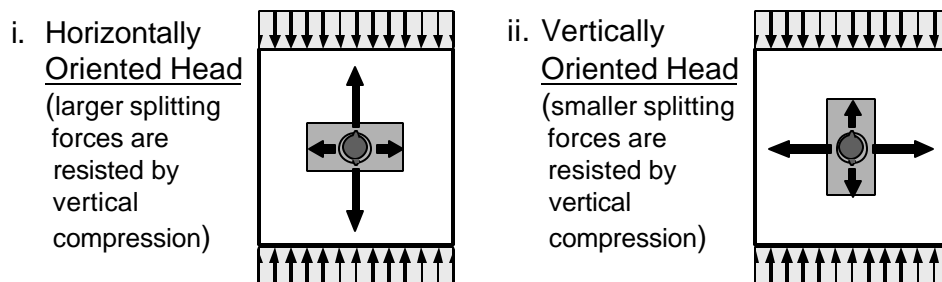


Figure 7-8: Horizontal versus vertical head orientation in a CCT node

7.2.4 Effect of Bar Size

Two bar sizes were tested in the CCT node study: #8's and #11's. The side cover and bottom bearing plate length were scaled to the bar diameter to maintain the proportionality of the CCT node. However, bottom cover remained constant. The data from the #8 and #11 tests with 45° strut angles are plotted in Figure 7-9. The #11 bar data points generally lay below the #8 bar data points. The decreased capacity of the #11's may be due to the smaller relative bottom cover in those specimens.

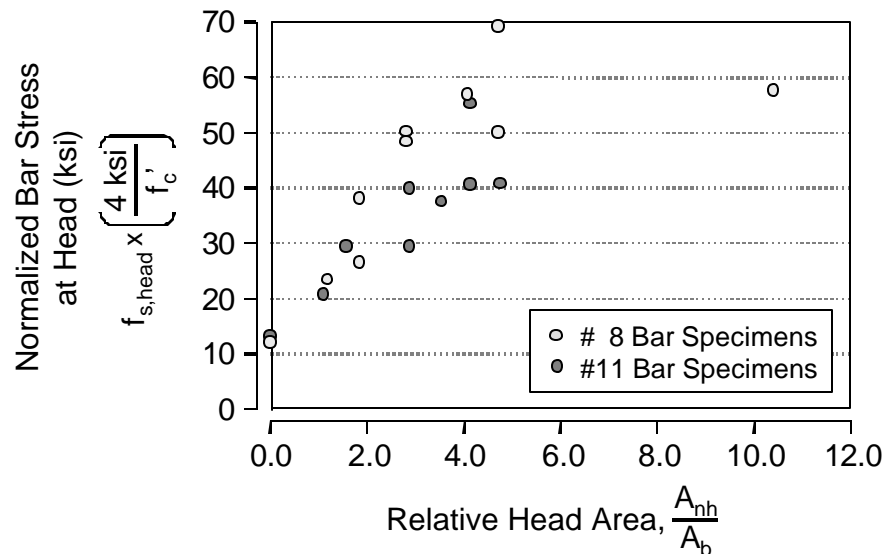


Figure 7-9: Effect of bar size on head capacity

7.2.5 Effect of Confinement

Tests were performed on non-headed, headed, and hooked bars with transverse reinforcement (stirrups) in the anchorage region. Confinement enhances the bond when the cover provided over the bar is small. However, in the CCT node specimen configuration, the tie bar always had large cover. Analysis of the effect of confinement on bond showed that the

confinement provided no discernible improvement in bond stress. However, confinement had an effect similar to that of strut angle. The presence of the stirrups changed the manner in which the diagonal strut intersected the tie bar. The result was that the development length of the bar was increased. This allowed for a greater contribution of bond to anchorage capacity.

The effect of confinement on the head capacity is shown in Figure 7-10. The plot shows that the head anchorage carried about 20% less capacity when confinement steel was added. This could have been due to two factors. First, the unconfined specimen was cast separately from the confined specimens. The drop off in capacity might be an effect of variations in the concrete mixes and curing conditions. The compressive strengths of the concrete batches were not greatly different, though the tensile strength was lower in the batch used for the confined specimens. Secondly, the presence of the confining steel may have affected the ability of the fresh concrete to consolidate properly around the head. This would have resulted in the drop in capacity. It should also be noted that the configuration of the confining steel was not ideal for restraining the critical splitting stresses produced by the anchorage of the head. As the results of the specially detailed specimens showed, the critical location of tensile splitting stresses occurs at the upper portion of the head. The stirrup confining steel passed along the sides and bottom of the head, but not along the top of the head through the critical section where maximum tensile stresses developed. Though consistent with typical detailing, the confinement that was studied was not ideal for enhancing the capacity of the head anchorage. Furthermore, whatever the cause of the decreased capacity in the confined specimens, the results come from only three tests which is not enough to provide compelling evidence that a trend exists. This issue requires further study.

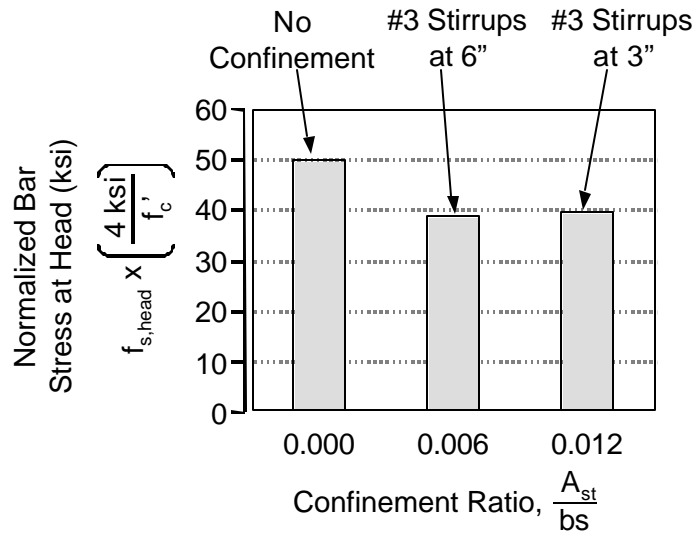


Figure 7-10: Effect of confinement on head capacity

7.2.6 Comparison to Hooked Bars

Results of the two unconfined hook tests are compared to the headed bar results in Figure 7-11. Hook 1 refers to standard hook detail 1 and hook 2 refers to standard hook detail 2 (see Figure 5-10). All of the data are for #8 bar tests. The figure shows that both hooks and headed bars are substantial improvements over straight, non-headed bars ($A_{nh}/A_b = 0$). The plot also shows that the for relative head areas greater than 2, all but two of the headed bars had greater than or equal anchorage capacities than comparable hooked bars. The data show the feasibility of using headed bars in place of hooks.

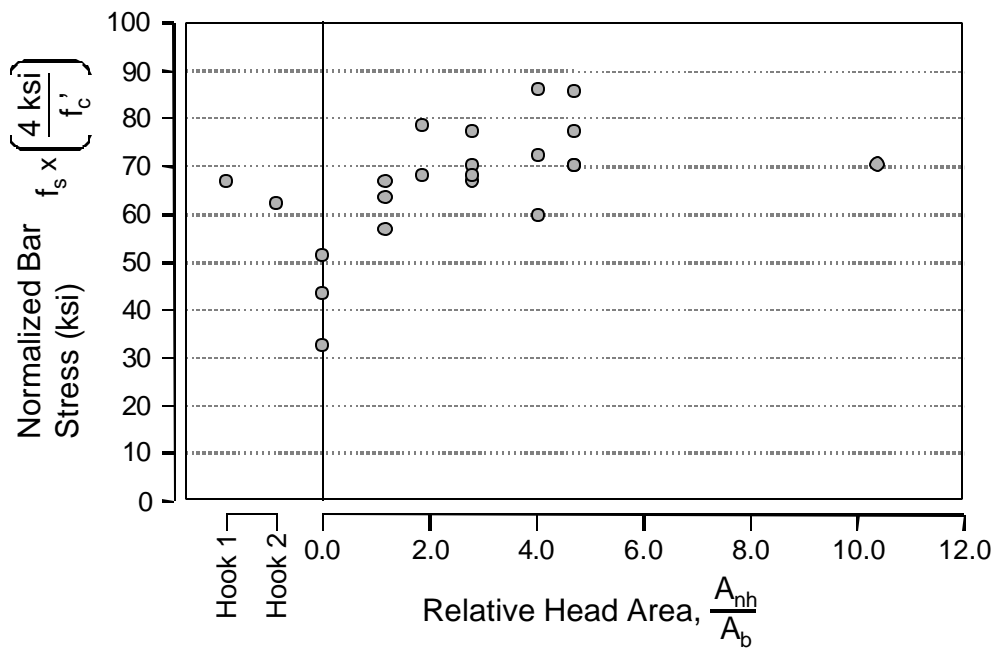


Figure 7-11: Bar stress from hooked bars compared with headed bars (#8 sizes)

7.3 COMPARISON OF HEAD CAPACITY TO THEORETICAL MODELS

7.3.1 Comparison to ACI STM Procedures

The ACI STM procedures [2], like the other existing STM procedures, base the capacity of nodes and struts on allowable stresses limits at the faces of the nodes and struts (see Section 4.3). In this section, the ACI stress limits are compared with the data from the CCT node specimens. The strength of the node was checked at the forward face of the node, where it abuts against the bearing face of the head and the strength of the strut was checked at the face that adjoins against the CCT node (Figure 7-12).

Bearing of the CCT node was most critical at the face that contacted the bearing area of the head. At that face, the geometry of the node was rigidly defined by the boundaries of the head and the face area was equivalent to the net bearing area of the head. The force at the head was

determined from strain gage measurements close to the head. Bearing stresses at failure were calculated for all specimens that failed by rupture of the strut and node region. Efficiency factors for each test were then determined as a fraction of f'_c . Figure 7-13 shows these values plotted against the relative head area for the 26 CCT node specimens that failed by rupture.

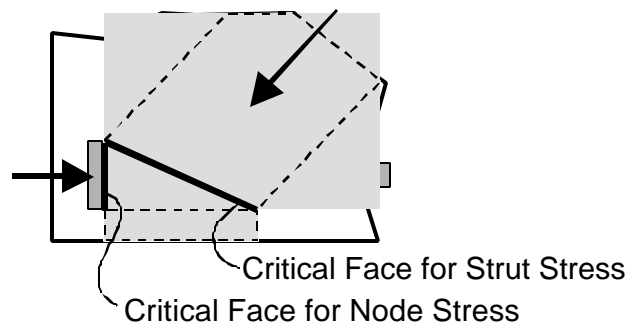


Figure 7-12: Critical node faces for STM stresses

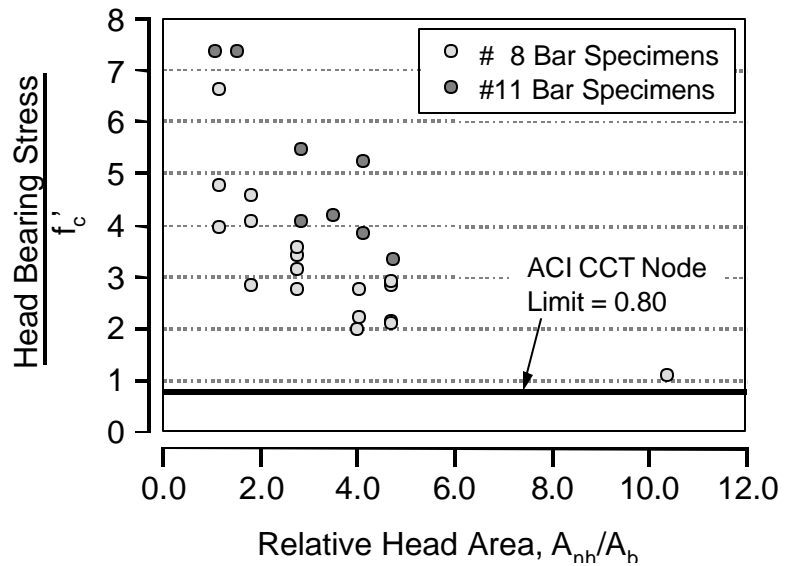


Figure 7-13: Efficiency factors for node bearing at the face adjacent to the head

Figure 7-13 shows that the bearing capacity of the concrete at the head was much greater than the uniaxial compression strength of the concrete. There was a trend of decreasing bearing strength with increasing relative head area. For the smallest heads, the efficiency factor of the concrete was between 4.0 and 7.5. The efficiency factor dropped off with increasing head size. A single data point at the far right indicates that the efficiency factor dropped off to 1.0 at a relative head area of 10.4. There was no apparent difference between the data points from #8 bar tests with different strut angles. However, there was a significant difference between the data from #8 bar tests and #11 bar tests. The data for the #11 bar tests were greater than analogous data from #8 bar tests. All of the calculated efficiency factors were greater than the maximum ACI limit of $0.80f'_c$ for CCT nodes.

Figure 7-14 shows the distribution of the efficiency factors for the 26 specimens. The distribution had an average value of 3.8 with a standard deviation of 1.6. The distribution shape was not normal.

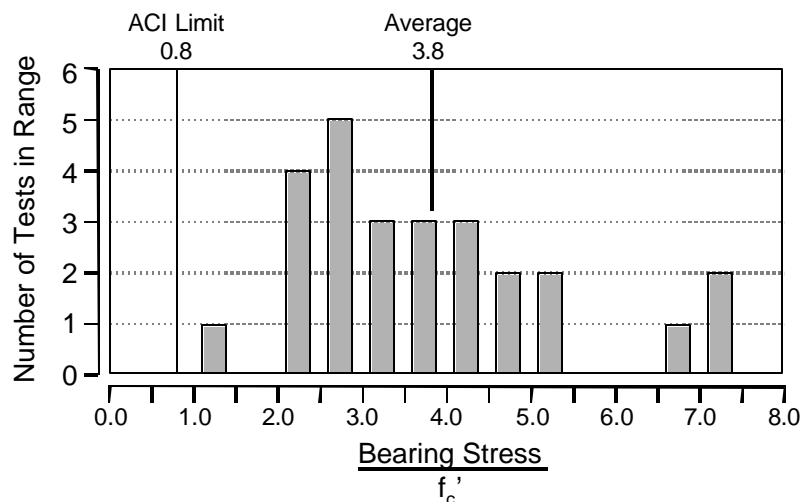
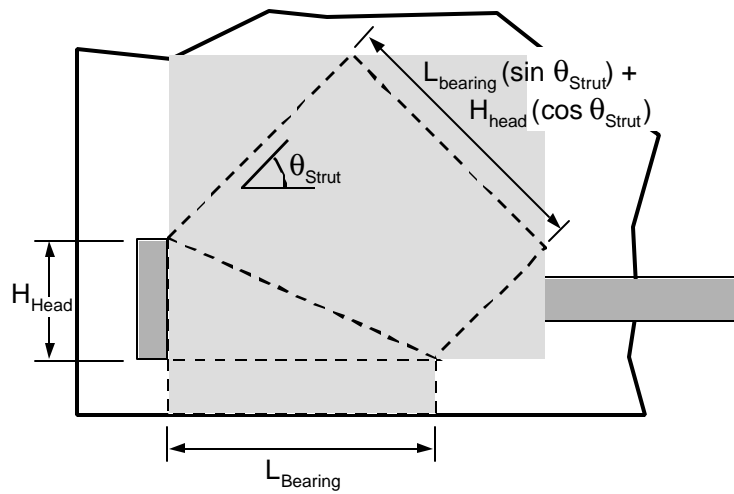


Figure 7-14: Distribution of efficiency factors for CCT node bearing results

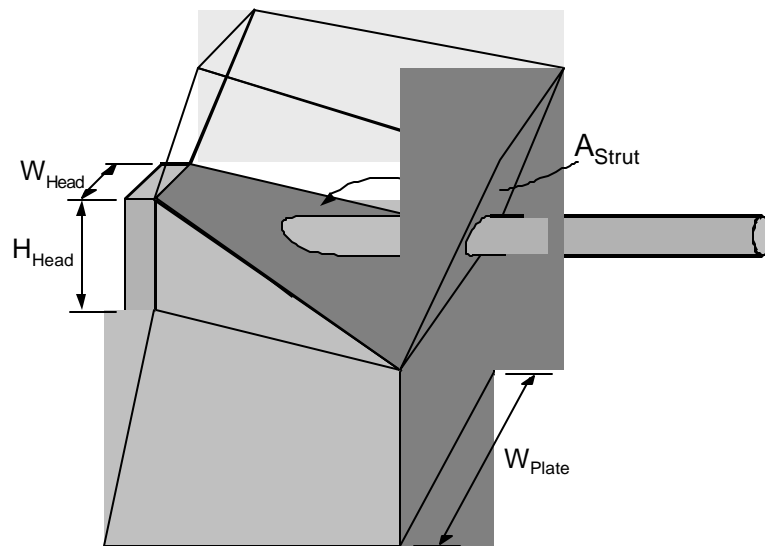
The bearing capacity of the strut was analyzed. The face area of the strut was determined by the boundary conditions at the CCT node. The bottom bearing plate and the geometry of the head define the shape and dimensions of the lower strut face. Figure 7-15 illustrates the geometry that can be reasonably assumed for the node/strut intersection. The assumed shape was trapezoidal. The depth of the trapezoid was dictated by the height of the head, H_{head} , and the length of the bearing plate, L_{bearing} . The top width of the trapezoid was assumed to match the width of the head, W_{head} , and the bottom width to match the width of the bearing plate, W_{plate} . The actual cross-sectional shape of the strut may have been different, but given the geometry of the conditions that defined the node, the bearing plate and head plate, the trapezoidal assumption was reasonable within the dictates of STM analysis.

The area of the strut, A_{strut} , was calculated as described above and the force in the strut was determined from the measured bar force and the measured bearing reaction. Using this data, bearing stresses at failure were calculated for 25 CCT specimens that failed by rupture. One specimen, CCT-08-45-01.18-1 was omitted because data for the bar force were lacking. This specimen had a damaged strain gage at a critical location and the total bar force could not be calculated properly. The calculated strut bearing stresses were divided by f'_c to determine efficiency factors. The distribution of these efficiency factors is plotted in Figure 7-16. Figure 7-16 shows that there were distinct differences between the #11 bar tests and the #8 bar tests. The lowest efficiency factor was 0.87. All of the data were greater than the ACI maximum strut limit of $0.85f'_c$ for uniaxial struts. The struts in the CCT node specimens would most likely be assumed to be bottle shaped in an analysis and subject to a maximum efficiency factor of 0.51 because they were unreinforced. The distribution of all specimens was non-normal because of the distinct differences between the #8 and #11 bar results. The average efficiency factor for the #11 bar tests

was 0.95 and the average efficiency factor of the #8 bar tests was 1.37. The overall average was 1.24.



i. Side view of strut and node geometry



ii. Oblique view of strut and node geometry

Figure 7-15: Geometry of the strut/node intersection at the CCT node

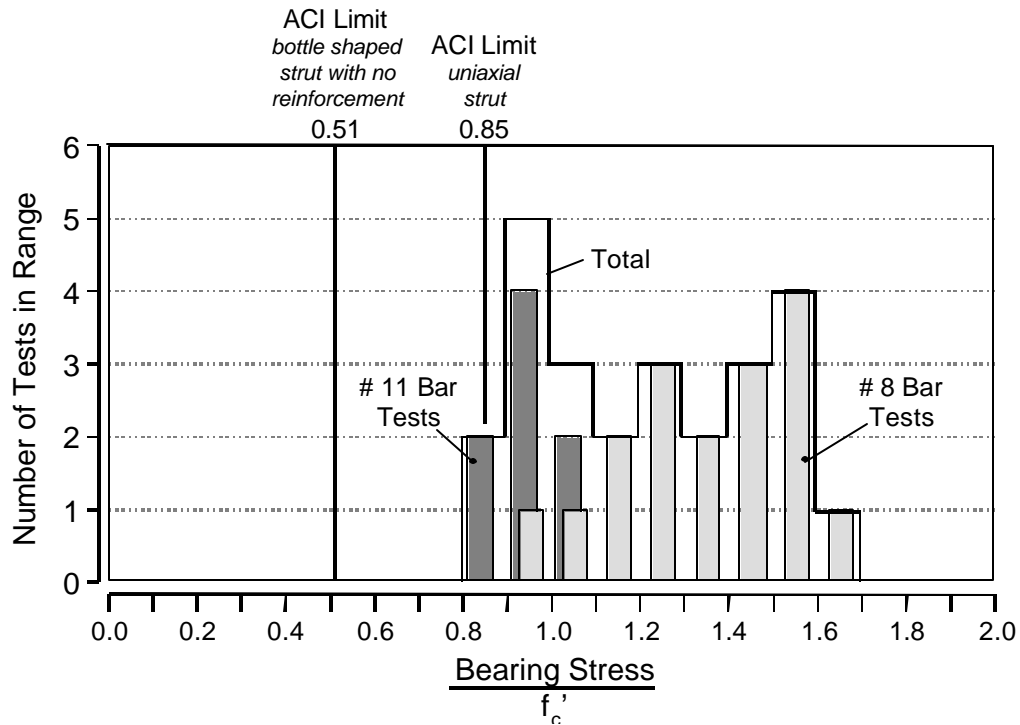


Figure 7-16: Distribution of efficiency factors for strut bearing at the face adjacent to the CCT node

The proceeding analyses suggest that a single efficiency factor cannot be applied to the design of the CCT nodes. The bearing stress that can be supported by the head was not constant but seemed to vary inversely with relative head area (Figure 7-13). The bearing stress that could be supported by the strut seemed to be affected by bar size or the geometric variations between the larger and smaller bar size tests. In both analyses, the estimated bearing stresses were always greater than the ACI allowable. The ACI STM procedure provided an extremely conservative estimate of capacity.

7.3.2 Comparison to Modified CCD Approach

DeVries [42] developed modified Concrete Capacity Design (CCD) formulas for calculating the anchorage capacity of headed bars in mass concrete. In Section 3.4.4, the work performed by DeVries was reviewed and summarized. Data from the CCT nodes were compared to the two models recommended by DeVries: concrete breakout and side blow-out.

7.3.2.1 Comparison to Concrete Breakout Model

The concrete breakout failure mode applies to headed bars with very shallow embedment lengths. The anchorage lengths of the headed bars tested in the CCT nodes (measured from the head to the critical crack location) were generally in the $5-9d_b$ range which should normally qualify as shallow embedment. The model neglects contributions from bond of the bar. The concrete breakout model is most dependent on the embedment depth, the concrete strength, and the cover conditions which affect the projected breakout area, A_N . Figure 7-17 shows how the embedment depth and projected breakout area were defined for capacity calculations. The definition of the projected breakout area was modified to accommodate the slanted failure surface of the CCT node specimens.

Calculated concrete breakout capacities were very low and did not vary with increases in relative head area. The model does not recognize changes in capacity with increased head area except in the manner in which head dimensions affect the breakout surface, which is a very slight effect. In Figure 7-18, measured bar stress at the head is plotted against the calculated values. There was no correlation between the concrete breakout model and the measured results. The failure behavior of the CCT node specimens did not resemble the failure behavior that the breakout model is based on, so the lack of correlation is unsurprising.

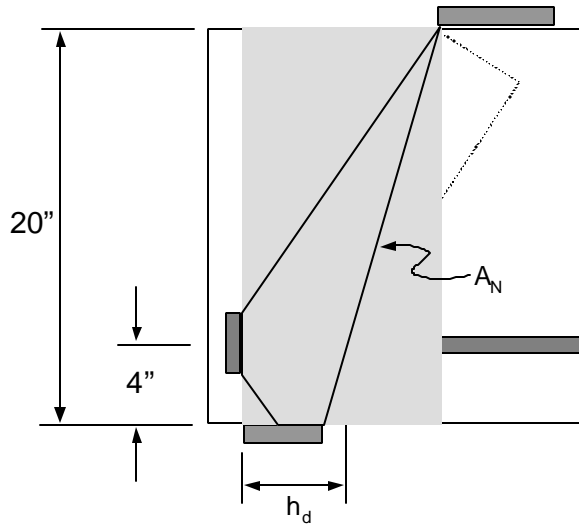


Figure 7-17: Definition of embedment depth and project breakout area for application of concrete breakout model

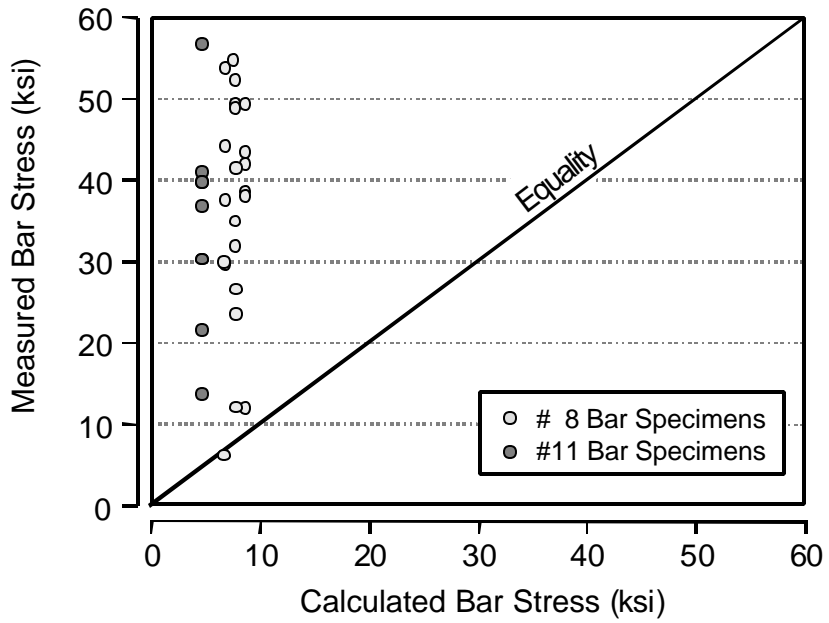


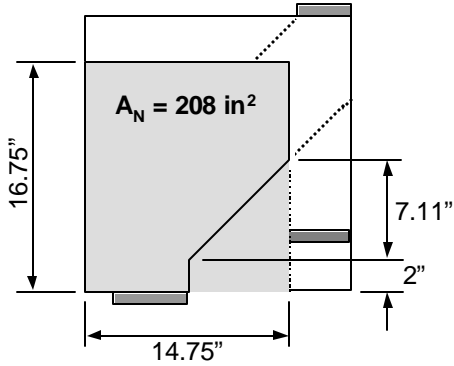
Figure 7-18: Correlation of measured and calculated values for concrete breakout model

7.3.2.2 *Comparison to Side Blow-Out Model*

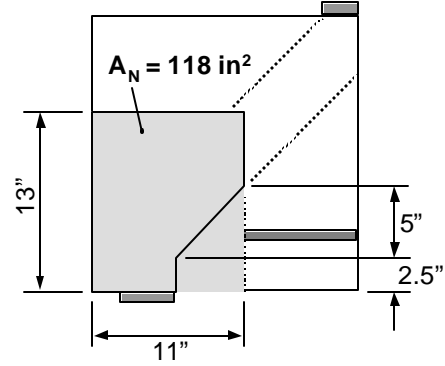
Many of the CCT node specimens failed by splitting the strut transversely. The lateral rupture of the concrete caused by the splitting was similar to the side blow-out blowout failures observed by DeVries for deeply embedded bars. DeVries' side blow-out model is primarily dependent on concrete strength, head area, concrete cover, and the projected side blow-out area, A_{Nsb} . Figure 7-19 shows the projected side blow-out areas used for the different specimen series. The portion of the projected side blow-out area that crossed beyond the critical crack location (assumed at the lower-back boundary of the diagonal compression strut) was subtracted from the area. The side blow-out capacity was calculated for all of the CCT specimens that failed by rupture. In Figure 7-20, measured bar stresses at the heads are plotted against the calculated stresses.

Figure 7-20 shows that the side blow-out model appreciably underestimated the results of the CCT nodes. Mean and standard deviation were calculated for the ranges of measured/calculated ratios for the side blow-out model (Table 7-3). The mean values of the #8's and #11's were close showing that the model accounted for the differences between bar sizes that was observed in the raw data (Figure 7-9). The overall coefficient of variation was 19% which compares favorably to the coefficient of variation of 30% reported by DeVries for his data [42]. However, the method provided a very poor overall average of 2.6. The form of the side blow-out equation is promising and could be adapted for design purposes by manipulating the coefficients of the equation.

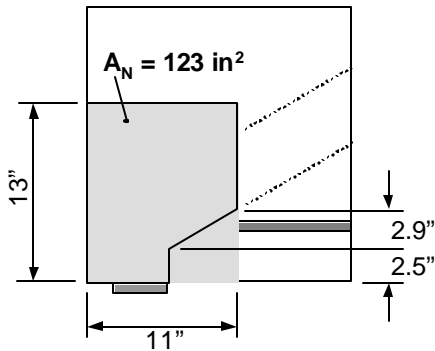
i. #11 Bar, 45° Strut Angle



ii. #8 Bar, 45° Strut Angle



iii. #8 Bar, 30° Strut Angle



iv. #8 Bar, 55° Strut Angle

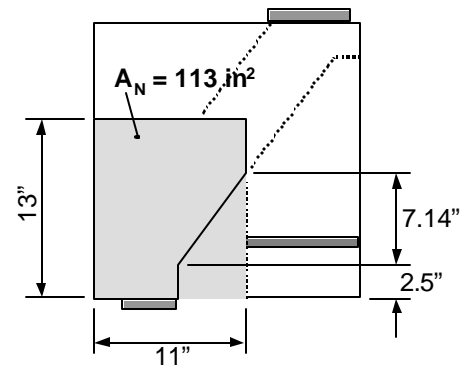


Figure 7-19: Projected side blow-out areas for various CCT specimen series

| Bar Size | Number of Specimens | Measured/Calculated Values | | |
|----------|---------------------|----------------------------|------|--------------------|
| | | Range | Mean | Standard Deviation |
| #8 | 8 | 1.87 - 4.02 | 2.67 | 0.53 |
| #11 | 19 | 2.08 - 3.24 | 2.52 | 0.40 |
| All | 27 | 1.87 - 4.02 | 2.63 | 0.49 |

Table 7-3: Statistical data for accuracy of side blow-out model

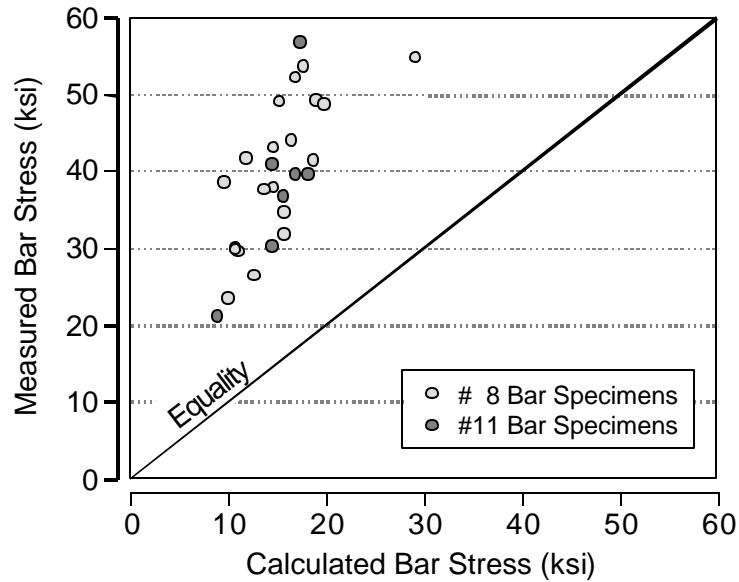


Figure 7-20: Correlation of measured and calculated values for side blow-out model

7.3.3 Comparison to ACI Bearing Capacity Model

The ACI bearing capacity model was used to calculate the contribution of the head to the tie bar anchorage. The bearing capacity equation depends on three main variables: the net head area, A_{nh} , the concrete compressive strength, f'_c , and the notional area projected beneath the surface of the loaded plate, A_2 . The notional area is primarily dependent on the cover conditions and is limited to four times the bearing area by the ACI provisions. As discussed in Section 3.5.4, this limitation is very severe. Research by Niyogi [90] and Hawkins [60] has shown that the limit should be much higher, around 40 times the bearing area. For the following analysis, the effect of a limitation on notional area was examined, and the bearing model was found to fit the measured data much better without it. Furthermore, the notional area was simply defined as the largest square that fit within the cover limitations provided by the CCT node specimen even for

rectangular heads. Vertically oriented heads would typically project a larger notional area than other heads because their proportions fit the shape of the CCT specimen better. However, in keeping with the assumption that head orientation will likely be random in actual construction, it is recommended that the notional area should generally be assumed to be square for single heads attached to single bars. This removed many complications associated with head shape in the analysis of the CCT nodes and from foreseeable design approaches using bearing as a failure model for headed bars. Figure 7-21 shows the notional areas that were used.

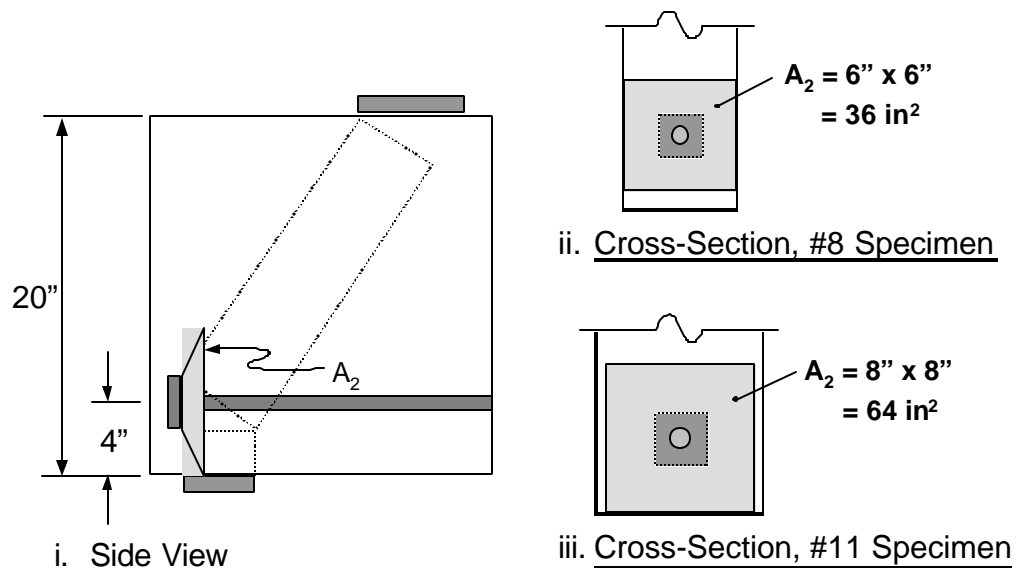


Figure 7-21: Notional areas for bearing analysis of CCT nodes

Figure 7-22 presents the measured and calculated values for the heads using the bearing model and shows that the model performed better than the previous models. Except for one point, the data are well distributed around the equality line.

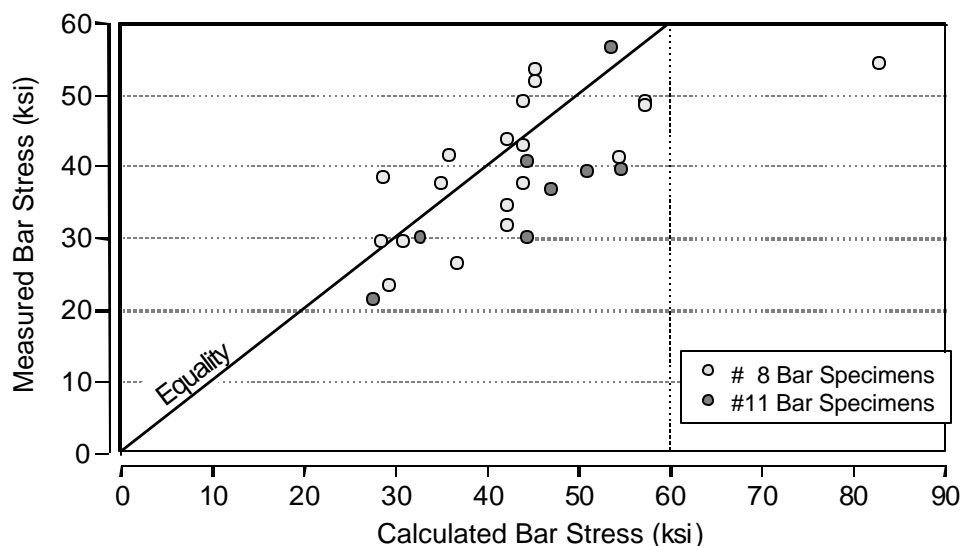


Figure 7-22: Correlation of measured and calculated values for bearing model

Mean and standard deviation were calculated for the range of measured/calculated ratios for the bearing model (Table 7-4). The mean was 0.92 and the standard deviation was 0.18 giving a coefficient of variation of 20% similar to the side blow-out model. Figure 7-23 shows the distribution of the measured/calculated ratios. The distribution was slightly skewed towards low values.

| Bar Size | Number of Specimens | Measured/Calculated Values | | |
|----------|---------------------|----------------------------|------|--------------------|
| | | Range | Mean | Standard Deviation |
| #8 | 8 | 0.66 - 1.35 | 0.96 | 0.19 |
| #11 | 19 | 0.68 - 1.06 | 0.83 | 0.13 |
| All | 27 | 0.64 - 1.35 | 0.92 | 0.18 |

Table 7-4: Statistical data for accuracy of ACI bearing model

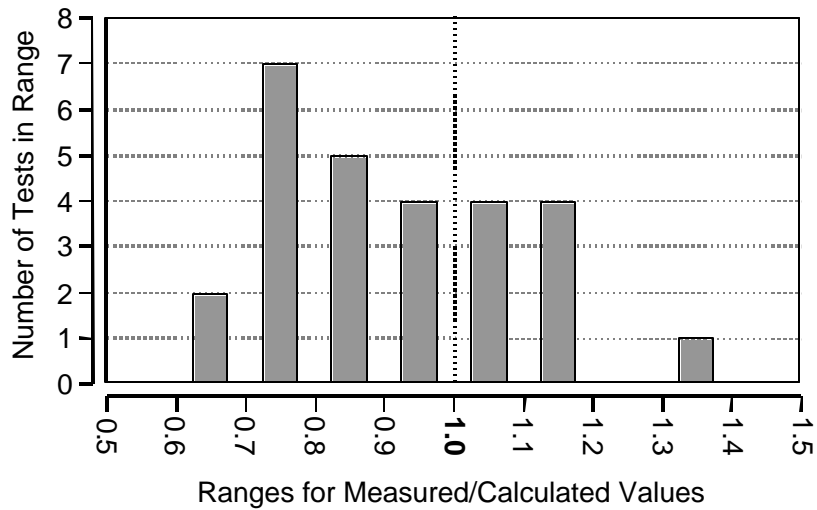


Figure 7-23: Distribution plot of measured/calculated ratios for bearing model

7.4 DEVELOPMENT OF A CAPACITY MODEL FOR HEAD BEARING

Both the side blow-out and the bearing models discussed in the previous section provided reasonable models for the anchorage capacity provided by the head. However, an investigation was performed to determine if a better model could be developed. Throughout Chapter 3 the similarities between the behavior of headed bars, anchor bolts, and bearing plates was emphasized. The side blow-out model developed from research performed on anchor bolts and headed bars. The bearing model developed from studies of bearing plates on concrete blocks. Though developed to describe different phenomena, these models depend on a number of the same variables: bearing area (A_{nh}), concrete cover (c_1 or $\sqrt{A_2}$), and the concrete strength (f'_c). The primary differences between the models are the exponent applied to the concrete strength and the radial stress disturbance factor (Ψ_1) which is applied to anchor bolts and headed bars, but not bearing plates. In this section, the collected data base of headed bar tests, deeply embedded anchor

bolt tests, and bearing plate tests are analyzed to produce one model that adequately predicts the capacity in all three situations.

A variety of literature sources was reviewed to collect a sizable database of test data that could be used in a regression analysis. Table 7-5 lists the sources that were collected. The following criteria were used to select appropriate test results for the database:

- Headed bar tests in which the capacity provided solely by the head could be determined. Thus only the deep embedment tests from the University of Texas in which the deformed bar portion was sheathed with PVC were used because the published capacity data reflected anchorage provided by the head alone without any contribution from bond. The CCT test data of this study could also be used because strain gage instrumentation allowed for the head capacity to be separated from the total bar capacity.
- Anchor bolt tests in which the embedment depth to side cover ratio was greater than or equal to five. This criteria was used in the University of Texas headed bar pullout tests to separate deeply embedded bars from shallow embedded bars.
- Bearing block tests in which the side cover to block depth ratio was at least two. This included all concentrically loaded cube tests. This ratio was selected because it represented the majority of the available data. Furthermore, only tests in which the bottom surface of the block was fully supported by a rigid medium were included.
- Tests in which the aspect ratio of the head or bearing plate was less than 2.1. This restriction is examined in section 7.4.4.
- Tests in which no confinement was provided near the head or bearing plate.

Within the restrictions imposed by the above criteria, 544 test results were selected for the database. This number included 100 results from headed bar tests (18.4% of the total), 69 results from anchor bolt tests (12.7% of the total), and 375 results from bearing plate tests on concrete (68.9% of the total). Though the database was heavily loaded with bearing capacity tests on concrete blocks, the results presented in this section show that the headed bar and anchor bolt tests are well calculated by the proposed models, and the behavior of those tests can be treated in the same fashion as the behavior of the bearing tests.

| Source | Type of Test | Number of Data Values | Ranges for Variables | | |
|-----------------------------------|---------------|-----------------------|----------------------|------------------------------|-------------------|
| | | | f'_c (ksi)* | $\frac{2c_1}{\sqrt{A_{nh}}}$ | $\frac{c_2}{c_1}$ |
| UT Deep Embedment [42] | Headed Bar | 73 | 2.8 - 6.4 | 1.0 - 3.8 | 1.0 - 15.2 |
| UT CCT Node Tests (present study) | " | 27 | 3.1 - 4.2 | 2.1 - 6.2 | 1.1 - 1.3 |
| Breen [31] | Anchor Bolt | 17 | 3.2 - 5.5 | 2.0 - 3.7 | 3.1 - 4.0 |
| Lee & Breen [68] | " | 7 | 2.2 - 5.4 | 2.6 - 3.5 | 4.0 - 6.4 |
| Lo [58] | " | 16 | 3.0 - 5.5 | 1.3 - 3.6 | 3.0 - 6.0 |
| Hasselwander [58] | " | 9 | 2.6 - 5.5 | 1.5 - 4.1 | 3.4 - 12.0 |
| Furche & Eligehausen [49] | " | 20 | 3.8 | 2.9 - 7.4 | 3.8 - 7.5 |
| Shelson [106] | Bearing Block | 12 | 5.6 - 6.7 | 2.8 - 8.0 | 1.0 |
| Au & Baird [24] | " | 12 | 4.5 - 8.1 | 1.4 - 4.0 | 1.0 |
| Hawkins [60] | " | 73 | 1.7 - 7.6 | 1.0 - 6.8 | 1.0 - 6.0 |
| Niyogi [90, 91] | " | 119 | 1.4 - 7.3 | 1.0 - 8.0 | 1.0 - 4.0 |
| Williams [116] | " | 159 | 2.6 - 9.8 | 1.0 - 10.2 | 1.0 - 9.4 |
| All Headed Bar Tests | | 100 | 2.8 - 6.4 | 1.0 - 6.2 | 1.0 - 15.2 |
| All Anchor Bolt Tests | | 69 | 2.2 - 5.5 | 1.3 - 7.4 | 3.0 - 12.0 |
| All Bearing Block Tests | | 375 | 1.4 - 9.8 | 1.0 - 10.2 | 1.0 - 9.4 |
| All Tests | | 544 | 1.4 - 9.8 | 1.0 - 10.2 | 1.0 - 15.2 |

*Equivalent Cylinder Strength Values

Table 7-5: Summary of sources for collected database of headed bar, anchor bolt, and bearing tests

Table 7-6 lists the dependency of the bearing and side blow-out models to the primary variables that have been shown to be the most significant factors affecting capacity. Both models are proportional to side cover, c_1 , and the square root of bearing area, $(A_{nh})^{0.5}$. They are also related to concrete strength, but differ in the power assigned to the concrete strength. Bearing is directly proportional to compression strength, f'_c , while the side blow-out model is directly proportional to concrete tensile strength represented by the square root of compression strength, $(f'_c)^{0.5}$. Furthermore, the side blow-out model allows for an increase in capacity due to the influence of the secondary side cover, c_2 . In developing a new model for head capacity, these variables (f'_c , A_{nh} , c_1 , and c_2) were selected as the most important factors influencing capacity. The form of the new model was selected to be a product of three factors:

- A factor for bearing area and side cover, $A_{nh}(2c_1/\sqrt{A_{nh}})$. This factor is expressed in a form similar to that of the bearing model, as a product of bearing area and the square root of the ratio of supporting area to bearing area, $\sqrt{A_2/A_1}$. If the supporting area is taken as square in shape, then A_2 is equal to $4c_1^2$. The bearing area notation is changed from A_1 to A_{nh} . Thus the term $\sqrt{A_2/A_1}$ translates to $2c_1/\sqrt{A_{nh}}$, the form used in the proposed model.
- A factor for concrete strength. Two possible forms were examined: one in which the power of the concrete strength was constant and one in which the power of concrete strength varied based on the $2c_1/\sqrt{A_{nh}}$ ratio. Niyogi [91] noted that the dependency of bearing strength on concrete strength changed as the bearing plate size shrunk relative to the bearing block size. As the bearing plate size was decreased, the capacity was no longer directly proportional to f'_c , but some lesser power of f'_c .

Hawkin's [60] formula for bearing capacity was related to terms that contained both f'_c and $\sqrt{f'_c}$. The relative contributions of these terms in Hawkin's formula are dependant on values of A_1 and $\sqrt{A_2/A_1}$. Thus the contribution from concrete strength was related to the relative sizes of the bearing area and the supporting area. These two previous investigations noted a dependency of the concrete strength contribution on geometric considerations. This dependency is explained in Figure 7-24. When the ratio of bearing area to supporting area is near 1.0, loading is primarily uniaxial (like a cylinder test) and capacity is proportional to compression strength. As the ratio of bearing area to supporting area shrinks, failure of the bearing plate is governed by resistance in the surrounding concrete to the splitting caused by wedging action of the plate. Thus capacity is proportional to tensile strength or $\sqrt{f'_c}$.

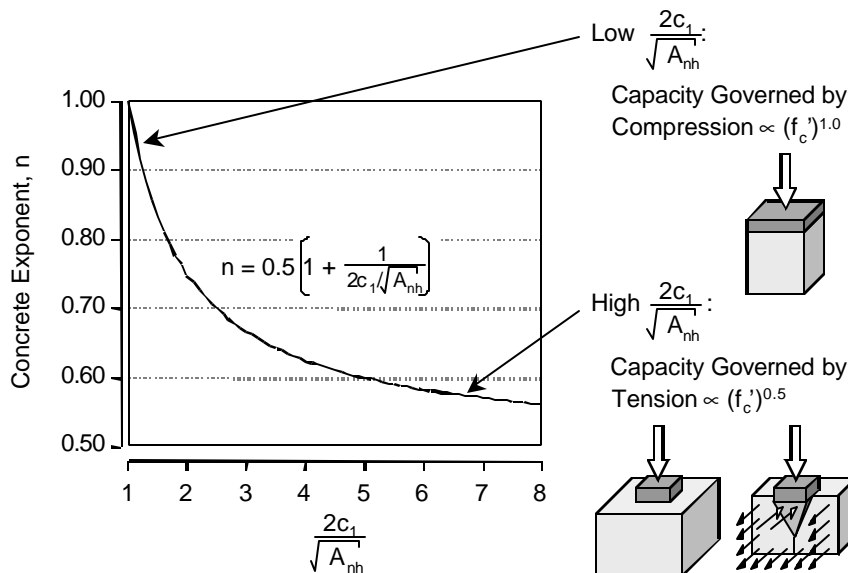


Figure 7-24: Relation of concrete power to $2c_1/\sqrt{A_{nh}}$ ratio

- A factor recognizing the contribution provided by the secondary cover dimension, c_2 .
A form similar to that used in the side blow-out model was examined in which this factor is linearly dependent on the ratio of secondary cover to minimum cover. The factor equals 1.0 when the c_2/c_1 ratio equals 1.0 and rises as the c_2/c_1 ratio increases. Upper limits were examined for this factor as well.

These factors were examined in regression analyses to develop best-fit models that calculated bearing capacity for the collected database listed in Table 75. After an extensive investigation, which is not detailed in this report, two potential models were developed. These models are listed below and justified by the discussion contained in the subsequent subsections. Table 7-6 lists the relation of these models to the significant variables discussed previously.

Model #1:

$$\text{Bearing Capacity, } P = A_{nh} \left(2.6 \Psi \left(\frac{2c_1}{\sqrt{A_{nh}}} \right) \left(\frac{f'_c}{2.4} \right)^{0.5 \left(1 + \frac{\sqrt{A_{nh}}}{2c_1} \right)} \right) \quad (7-1)$$

$$\text{with } \Psi = 0.7 + 0.3 \frac{c_2}{c_1} \leq 1.8 \quad (7-2)$$

Model #2:

$$\text{Bearing Capacity, } P = A_{nh} \left(0.9 \Psi \left(\frac{2c_1}{\sqrt{A_{nh}}} \right) (f'_c) \right) \quad (7-3)$$

$$\text{with } \Psi = 0.6 + 0.4 \frac{c_2}{c_1} \leq 2.0 \quad (7-4)$$

P = head capacity (kips)

Ψ = radial disturbance factor

A_{nh} = net head area (in²)

c_1 = minimum cover dimension (in)

c_2 = secondary cover dimension (the smallest cover dimension measured perpendicular to the minimum cover) (in)

f'_c = concrete cylinder strength (ksi)

| Failure Model | Relation to Significant Variables: | | | |
|---------------|------------------------------------|-------------------|---------------------------|----------------------|
| | Concrete Strength | Head Bearing Area | Minimum Side Cover | Secondary Side Cover |
| Bearing | f'_c | $(A_{nh})^{0.5}$ | $(A_2)^{0.5} \propto c_1$ | - |
| Side Blow-Out | $(f'_c)^{0.5}$ | $(A_{nh})^{0.5}$ | c_1 | $0.7+0.1(c_2/c_1)$ |
| Proposed # 1 | $(f'_c)^{0.5(1+\sqrt{A_1/A_2})}$ | $(A_{nh})^{0.5}$ | c_1 | $0.7+0.3(c_2/c_1)$ |
| Proposed # 2 | f'_c | $(A_{nh})^{0.5}$ | c_1 | $0.6+0.4(c_2/c_1)$ |

Table 7-6: Various models for head capacity

7.4.1 Effect of Cover/Head Bearing Area Ratio

Normalized bearing capacity is plotted against the ratio $2c_1/\sqrt{A_{nh}}$ in Figure 7-25 for the collected database. Bearing capacities were normalized against f'_c , Ψ , and A_{nh} . The plot shows that a linear relationship exists between the normalized capacities and the $2c_1/\sqrt{A_{nh}}$ ratio. The plot also shows that this relationship is unlimited up to values of $2c_1/\sqrt{A_{nh}} = 10$, the upper limit within the database. This trend justifies the inclusion of the $2c_1/\sqrt{A_{nh}}$ term in equations 7-1 and

7-3. Furthermore, no limits were placed on the contribution to capacity provided by $2c_1/\sqrt{A_{nh}}$ as is the case in the bearing capacity equation provided in the ACI code [2].

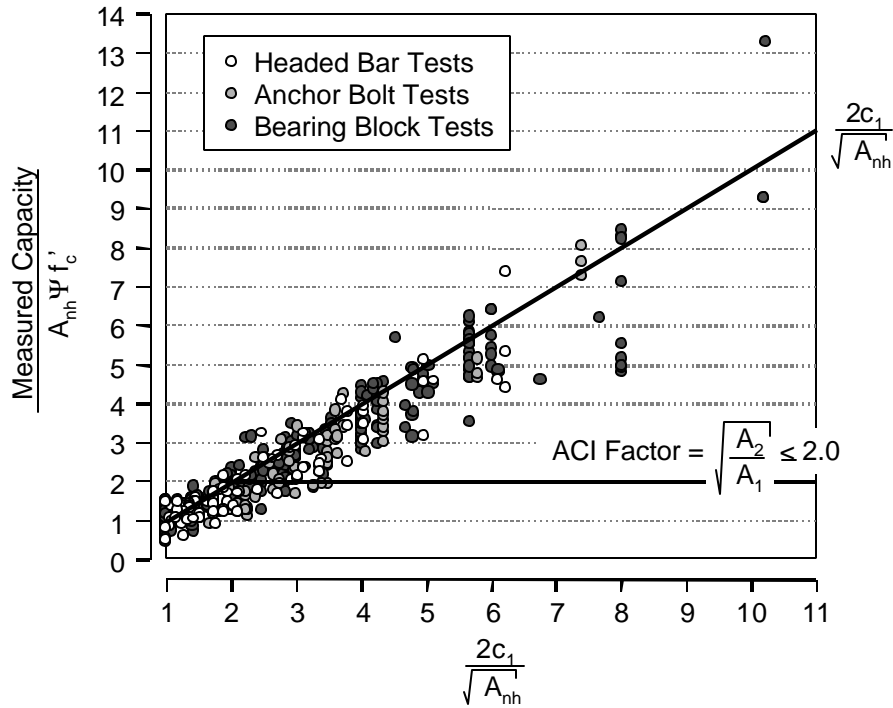


Figure 7-25: Normalized bearing capacity versus $2c_1/\sqrt{A_{nh}}$ ratio

7.4.2 Effect of the Secondary Cover

DeVries [42] accounted for the effect of second cover dimension in the form of a radial disturbance factor, Ψ . Similar factors were included in the proposed models, however, the proposed factors allow for greater increases to capacity from the secondary cover. DeVries' Ψ factor was designed to equal 1.0 when a headed bar was close to only one edge and to decrease to 0.8 as a corner condition was approached. The proposed Ψ factors were designed to do the opposite. They equal 1.0 under the corner condition and increase as the headed bar is moved away

from the corner. In order to compare the two equations for Ψ , they must both be normalized to reflect the same boundary limits. Normalized bearing capacity is plotted against the c_2/c_1 ratio in Figure 7-26. The three equations for Ψ have been plotted against the data in order to compare their predictive capacities. DeVries' Ψ factor has been normalized to equal 1.0 when the c_2/c_1 ratio is equal to 1.0. Equations 7-2 and 7-4 have also been adjusted to normalize the differences between coefficients in Equations 7-1 and 7-3. The plot demonstrates there is a clear increase in capacity as the secondary cover dimension is increased. This increase ceases after the non-critical cover dimension begins to exceed about 4 times the minimum cover dimension ($c_2/c_1 = 4$). The increase to capacity is significant and is underestimated by DeVries' Ψ factor.

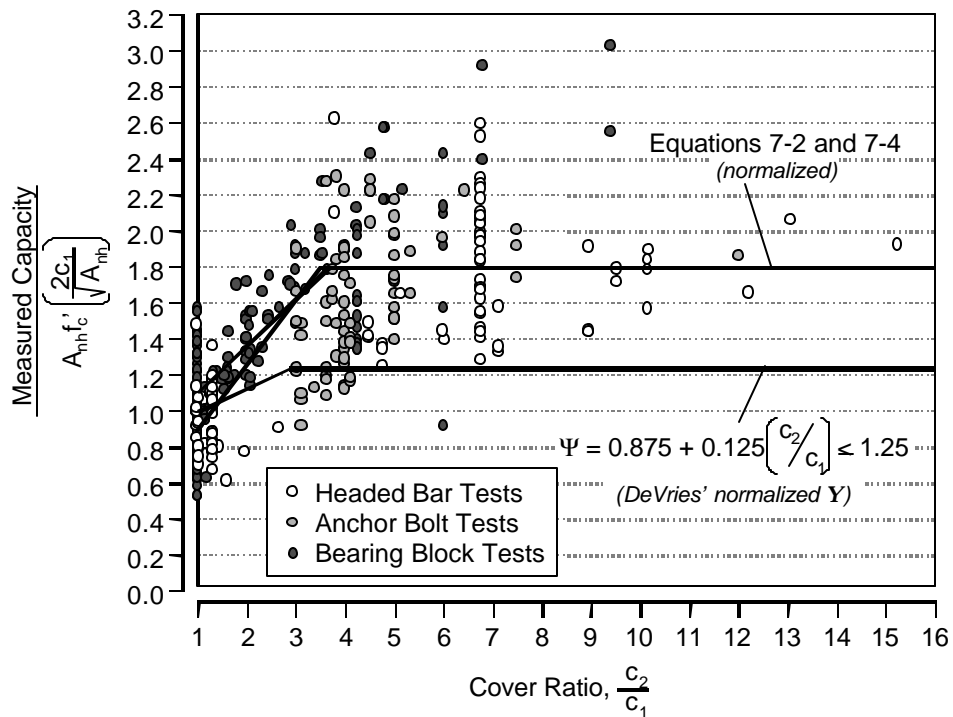


Figure 7-26: Normalized bearing capacity versus cover ratio, c_2/c_1

7.4.3 Effect of Concrete Strength

Normalized bearing capacity is plotted against concrete strength in Figure 7-27. Best-fit trend lines based on linear relationships to f_c' and $\sqrt{f_c'}$ are plotted against the data. Figure 7-27 shows that, between the two fixed powers of concrete strength, the capacity is best predicted with an exponent of 1.0. The bearing data are divided into two groups: data with $2c_1/\sqrt{A_{nh}}$ ratios less than or equal to 2.0 and data with $2c_1/\sqrt{A_{nh}}$ ratios greater than 2.0. At low concrete strengths (less than 6 ksi), the data from these two groups are fairly well intermixed. However, at higher concrete strengths, there is some indication of divergence between the two groups. The data with lower $2c_1/\sqrt{A_{nh}}$ ratios are generally higher than the data with $2c_1/\sqrt{A_{nh}}$ ratios greater than 2.0, but the trend is slight.

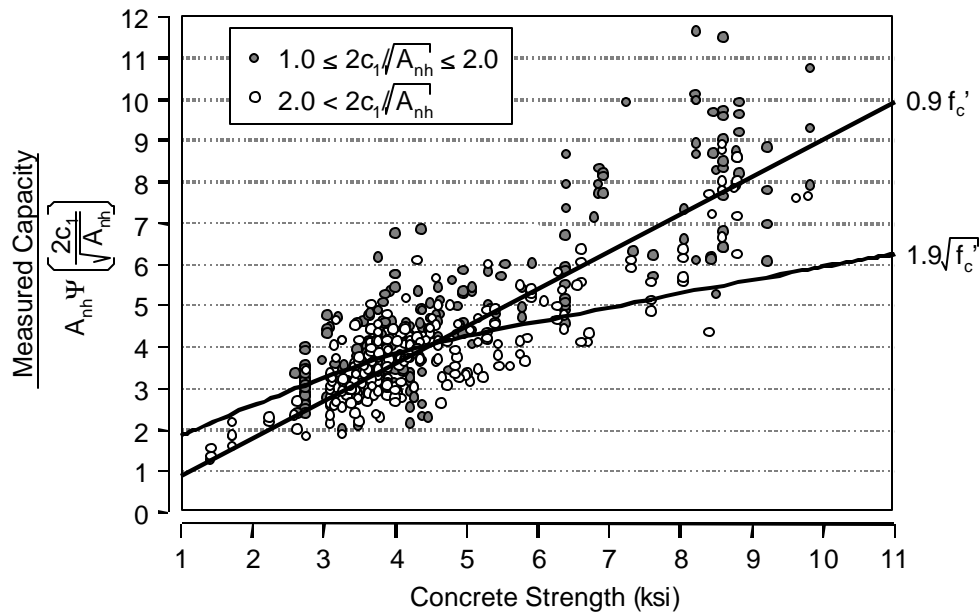


Figure 7-27: Normalized bearing capacity versus concrete strength, f_c' , with trend lines for relationships to f_c' and $\sqrt{f_c'}$

The data are plotted against the proposed model with the variable concrete exponent in Figure 728. The data are divided into two plots for clarity. The top plot presents data with $2c_1/\sqrt{A_{nh}}$ ratios between 1.0 and 2.0. The bottom plot presents data with $2c_1/\sqrt{A_{nh}}$ ratios greater than 2.0. The proposed model does not have a single trend line within a given range of $2c_1/\sqrt{A_{nh}}$ values, therefore, the bounds of the proposed model are presented in each plot for the appropriate ranges. The best fit of the proposed model was provided by:

$$\text{Concrete Factor} = 2.6 \left(\frac{f'_c}{2.4} \right)^{0.5(1+\sqrt{A_{nh}}/2c_1)} \quad (7-5)$$

with variables as defined previously.

The proposed model fits the data slightly better than the relationship provided by f'_c with an exponent of 1.0. However, the improvement may not be significant enough to justify the use of the complex concrete exponent. A simple, single exponent of 1.0 would be preferable for design purposes. The best fit provided by a concrete strength factor with an exponent of 1.0 provides a maximum bearing pressure of $0.9f'_c$ when $2c_1/\sqrt{A_{nh}}$ is equal to 1.0. The variable exponent provides a maximum bearing pressure of $1.1f'_c$ when $2c_1/\sqrt{A_{nh}}$ is equal to 1.0. Which model makes more sense? For the most part, the experimental data were provided by cube tests. The concrete strength used in the model is based on cylinder strengths however. When $2c_1/\sqrt{A_{nh}}$ is equal to 1.0, the model is providing a conversion from cylinder strength to cube strength which should equal about $1.1f'_c$ to $1.2f'_c$. The other extreme of $2c_1/\sqrt{A_{nh}}$ values corresponds with the bearing of a deformed bar lug which has a very small dimensions compared with the surrounding concrete. This situation corresponds to bond stress, which is related to $\sqrt{f'_c}$. Thus, at the extremes of $2c_1/\sqrt{A_{nh}}$, the variable exponent model fits the considerations of mechanics better than the simple model based on f'_c with a constant exponent of 1.0.

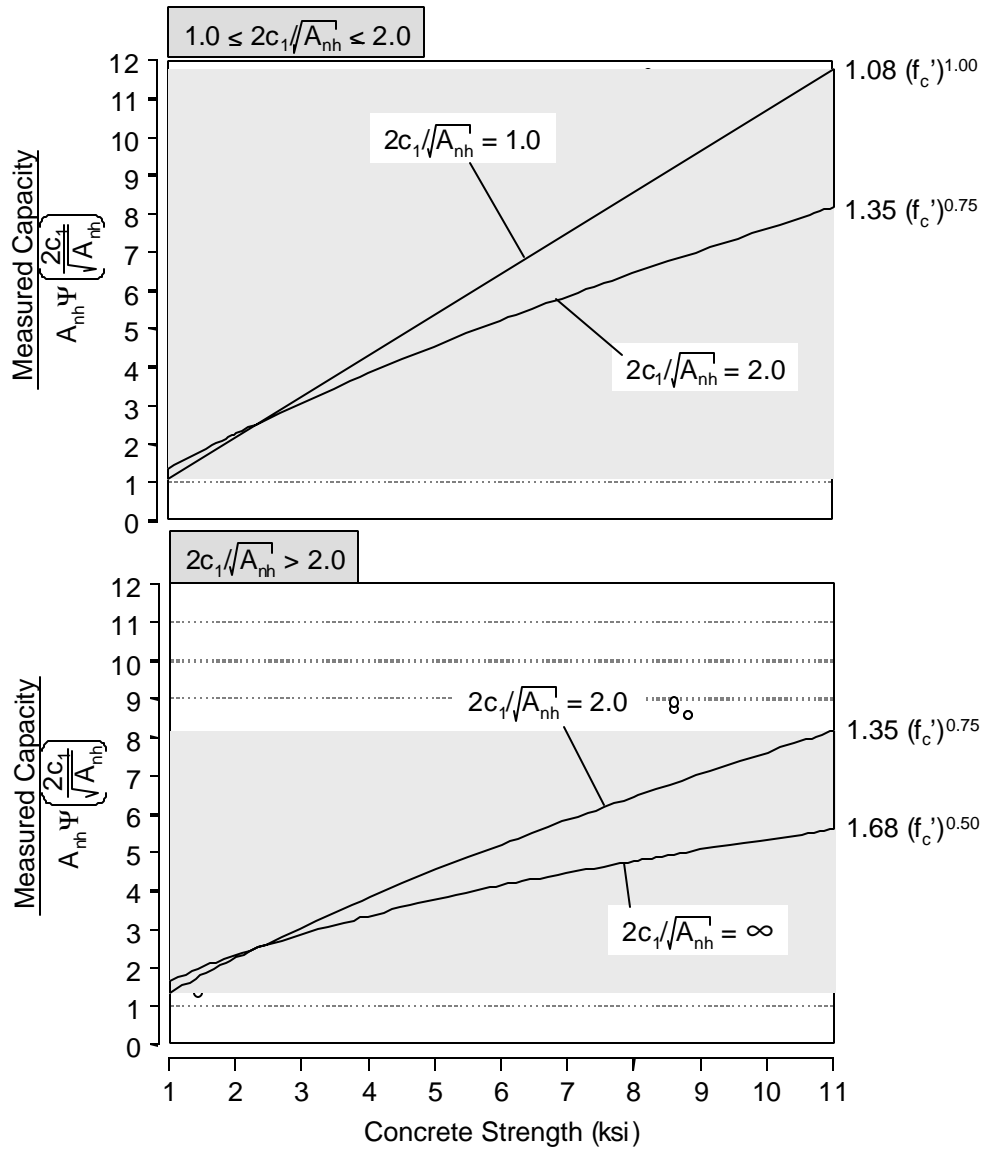


Figure 7-28: Normalized bearing capacity versus concrete strength, f_c' , with trend lines for the proposed concrete exponent term

7.4.4 Effect of Aspect Ratio

Though the aspect ratio of the bearing plates and heads was restricted for the data used in the database, a number of additional tests from outside of the database were accessed in order to examine the effect of aspect ratio. 82 additional tests from among the sources listed in Table 7-5 fit the criteria used to select the database, yet had aspect ratios greater than 2.1. Almost all of these tests were bearing block tests. The data points with large aspect ratios were from strip load tests on concrete blocks. Figure 7-29 plots the measured/calculated values against aspect ratio. Model 1 (Equation 71) was used to calculate capacity values. A similar analysis using model 2 was conducted and produced similar results.

Figure 7-29 shows that much scatter exists in the data. However, there is a slight trend of decreasing capacity with increasing aspect ratio. This reduction in capacity is most likely due to the neglect of head shape in the proposed models. Both models treat the unloaded area, A_2 , as being square and equal to $4c_1^2$ rather than using an area geometrically similar to the loading area, A_1 . For larger aspect ratios this simplification becomes unrealistic and results in lower capacities. A trend of the data suggests an adjustment to capacity equal to:

$$\text{Aspect Ratio Factor} = (45 - \text{Aspect Ratio})/44 \quad (7-6)$$

This reduction is only 2.5% for the largest aspect ratio used in the database, 2.1. This difference is smaller than the scatter seen in the data indicating the models are reasonable for large aspect ratios and that a limit larger than 2 could be recommended for the model. A limit of 4 would result in an average reduction of only 7% according to the trend line.

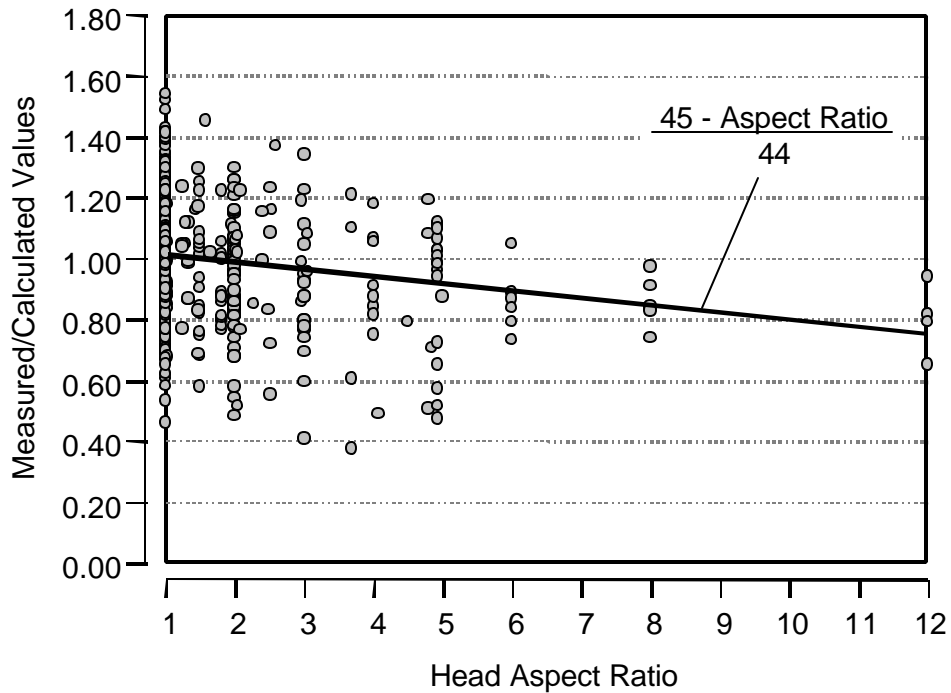


Figure 7-29: Effect of head aspect ratio on capacity

7.4.5 Aggregate Size Effect

No consideration was given to differences in aggregate size among the tests included in the database. Differences in the relative size of the specimen dimensions to the maximum aggregate size have been shown to affect the capacity of tests when all other variables are similar [12]. In general, a decrease in capacity is expected as the maximum aggregate size becomes smaller relative to the specimen dimensions. The cover/aggregate size ratio was determined for 524 of the 544 tests included in the database. Aggregate size was not reported in the study by Furche and Eligehausen [49]. The measured/calculated ratios of the specimens are plotted against the cover/aggregate size ratio in Figure 7-30. Calculated capacities were determined using model 1

(Equation 7-1), however, the trends were the same when calculations were performed using model

2.

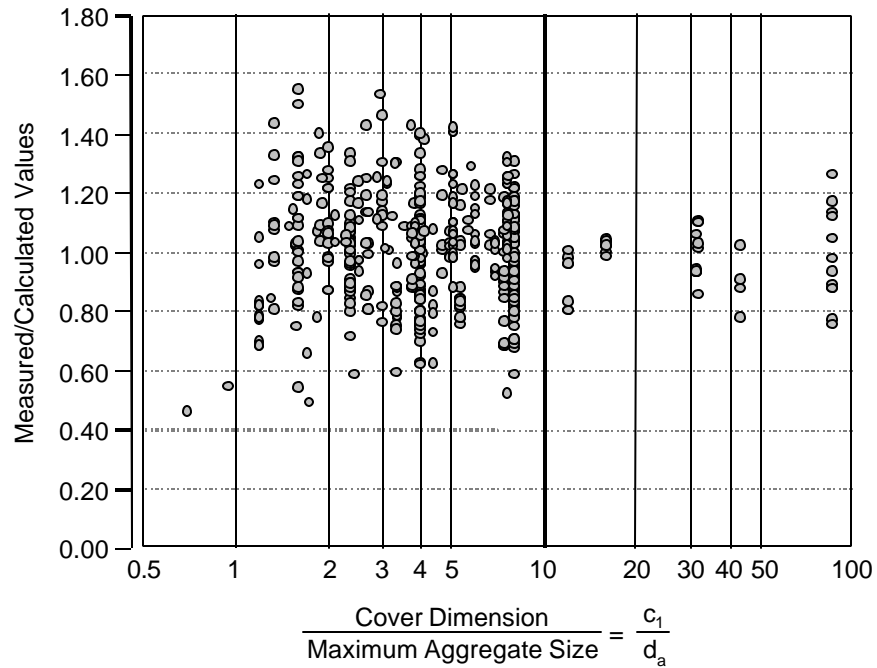


Figure 7-30: Size effect on capacity

Figure 7-30 shows that reductions in the aggregate size had no significant effect on capacity. The analysis plotted in Figure 7-30 used the cover as the critical dimension for analysis of size effect. The data were also analyzed using bearing plate dimensions (estimated by $\sqrt{A_{nh}}$) as the critical dimension. Again, no trend was found related to relative aggregate size. Niyogi [91] noted a size effect in his study, however, over the collected database, which includes test specimens cast and cured under a variety of environmental conditions, the scatter in the data is more significant than any trend that may exist related to size effect.

7.4.6 Regression Analysis of Proposed Models

The proceeding sections have been presented to justify the selection of variables chosen for the proposed models. Two models were proposed: Equation 7-1 and Equation 7-3. The first model contains a variable exponent for concrete strength. The second model uses a constant exponent of 1.0 for the concrete strength. Both models fit the data well, but the second was much simpler. Statistical analysis was performed for each model. The results of those analyses are presented in this section.

Table 7-7 presents the statistical information for the two models of bearing. The first model (Equation 7-1) performed better than the second (Equation 7-3) among each subgroup of the data (headed bars, anchor bolts, and bearing tests) and over the entire database. However, the difference was not great. Model 1 had an overall coefficient of variation of 17.5% and model 2 had an overall coefficient of variation of 19.6%. Model 1 provided a closer agreement between the mean values of the three test types than model 2 (0.95 – 1.03 versus 0.90 – 1.04). This indicates that model 1 does a slightly better job of representing each test type equally than model 2 does.

| Model | Measured/Calculated Values | | | |
|---------------------------|----------------------------|-------------|--------------------|--------------------------|
| | Range | Mean | Standard Deviation | Coefficient of Variation |
| # 1 (Equation 8-1) | | | | |
| Headed Bars | 0.49 - 1.46 | 0.95 | 0.17 | 18.1% |
| Anchor Bolts | 0.59 - 1.40 | 0.98 | 0.20 | 20.2% |
| Bearing Blocks | 0.46 - 1.55 | 1.03 | 0.17 | 16.5% |
| All Tests | 0.46 - 1.55 | 1.00 | 0.18 | 17.5% |
| # 2 (Equation 8-3) | | | | |
| Headed Bars | 0.53 - 1.63 | 0.97 | 0.20 | 20.7% |
| Anchor Bolts | 0.55 - 1.27 | 0.90 | 0.19 | 21.3% |
| Bearing Blocks | 0.50 - 1.73 | 1.04 | 0.19 | 18.2% |
| All Tests | 0.50 - 1.73 | 1.01 | 0.20 | 19.6% |

Table 7-7: Statistical data for proposed models of bearing capacity

Figures 7-31 and 7-32 present the distributions of measured/calculated values for both models. Model 1 has a more normal distribution than model 2, which is slightly skewed towards low values. The plots also show that the distributions of the headed bars and anchor bolts line up better with the total distribution for model 1. It is evident that model 1 works better than model 2, however, model 2 uses a much simpler equation. A final recommendation must consider the performance of the model and the ease by which it can be used. Model 2 works reasonably and is much more simple than model 1 and is thus recommended.

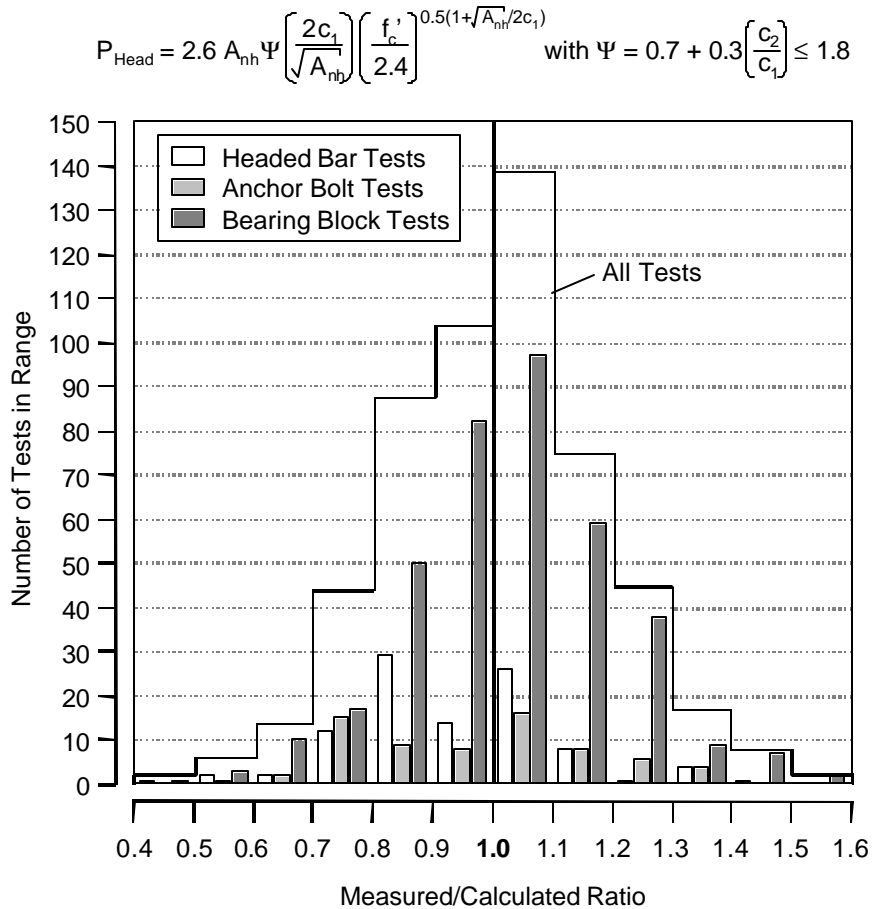


Figure 7-31: Distribution of measured/calculated values for bearing model 1

$$P_{\text{Head}} = 0.9 A_{\text{nh}} \Psi \left(\frac{2C_1}{A_{\text{nb}}} \right) f_c' \quad \text{with } \Psi = 0.6 + 0.4 \left(\frac{C_2}{C_1} \right) \leq 2.0$$

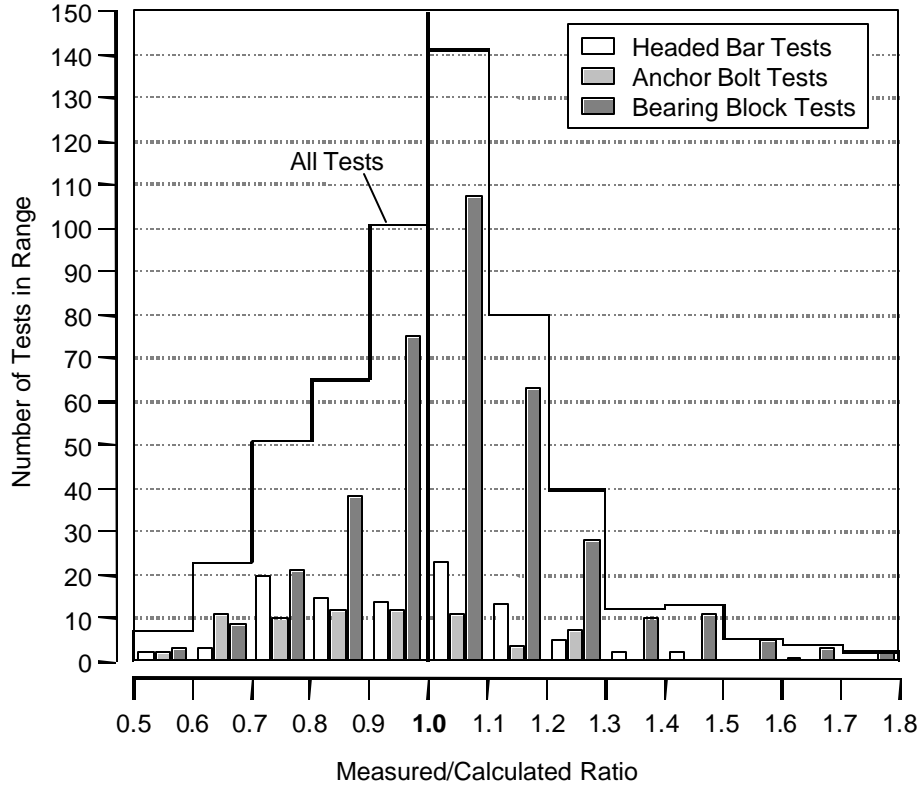


Figure 7-32: Distribution of measured/calculated values for bearing model 2

The preceding analysis has been based on mean capacity. An exclusion factor must be applied to provide a lower bound to the test results. A 5% exclusion was chosen as an acceptable lower bound. The probability of an unsafe test outcome is plotted against exclusion factor in Figure 7-33. The probability that an unsafe test would occur was determined by integrating the distribution plots in Figures 7-31 and 7-32 and plotting those results against the measured/calculated ratio. To produce a 5% exclusion of test results, models 1 and 2 require factors, $n_{5\%}$, of 0.72 and 0.68 respectively. A 5% exclusion factor of 0.7 would be appropriate for

both models. In addition to the 5% exclusion factor, a strength reduction (ϕ) factor that accounts for potential understrength of materials and deviations from tolerable dimensions should also be applied. The recommendation of an acceptable ϕ factor is not made at this time.

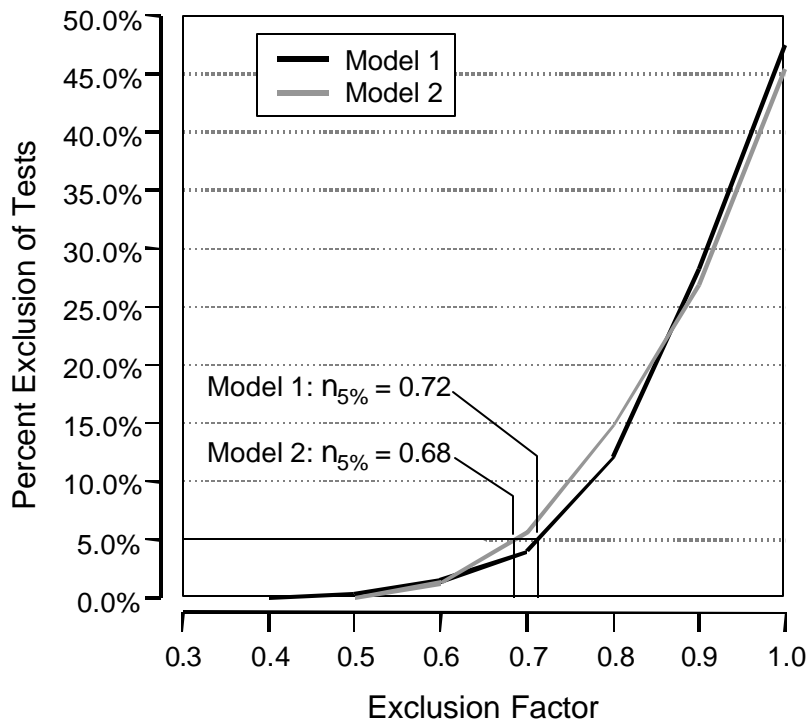


Figure 7-33: Probability of unsafe test outcome as a function of exclusion factor

Table 7-8 lists the ranges, averages, and standard deviations of the CCT node data under proposed model 1. The distribution of measured/calculated ratios for model 1 is plotted in Figure 7-34. The data show that the new model predicts capacity much better than the side blow-out and bearing models did. The average measured/calculated ratios are closer to 1.0 with less variation. The distribution of the data was more normal than the distribution was for the ACI bearing model.

Table 7-9 lists the ranges, averages, and standard deviations of the CCT node data under proposed model 2. The distribution of measured/calculated ratios for model 2 is plotted in 7-35. The data show that models 1 and 2 produced very similar results to one another. The mean of measured/calculated ratios was the same under each model. Model 2 had a slightly better coefficient of variation than model 1 for the CCT node data: 18.2% versus 18.6%. The distributions of the two models were similar in shape. Appendix B summarizes the statistical data for proposed models 1 and 2 for all of the test series listed in Table 7-5.

| | | Measured/Calculated Values | | |
|----------|---------------------|----------------------------|------|--------------------|
| Bar Size | Number of Specimens | Range | Mean | Standard Deviation |
| #8 | 8 | 0.63 - 1.39 | 0.93 | 0.19 |
| #11 | 19 | 0.75 - 1.15 | 0.91 | 0.14 |
| All | 27 | 0.63 - 1.39 | 0.93 | 0.17 |

Figure 7-8: Statistical data for accuracy of model 1 (CCT node tests)

| | | Measured/Calculated Values | | |
|----------|---------------------|----------------------------|------|--------------------|
| Bar Size | Number of Specimens | Range | Mean | Standard Deviation |
| #8 | 8 | 0.65 - 1.32 | 0.94 | 0.18 |
| #11 | 19 | 0.74 - 1.15 | 0.90 | 0.14 |
| All | 27 | 0.65 - 1.32 | 0.93 | 0.17 |

Figure 7-9: Statistical data for accuracy of model 2 (CCT node tests)

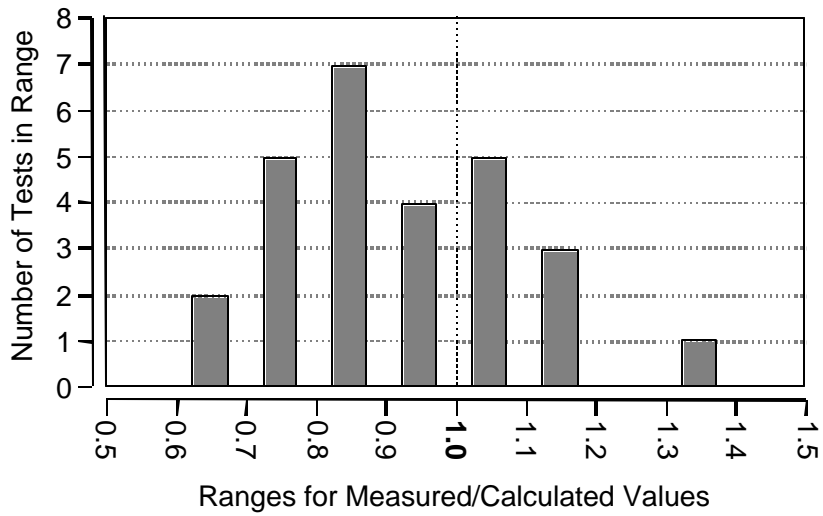


Figure 7-34: Distribution plot of measured/calculated ratios for model 1 (CCT node tests)

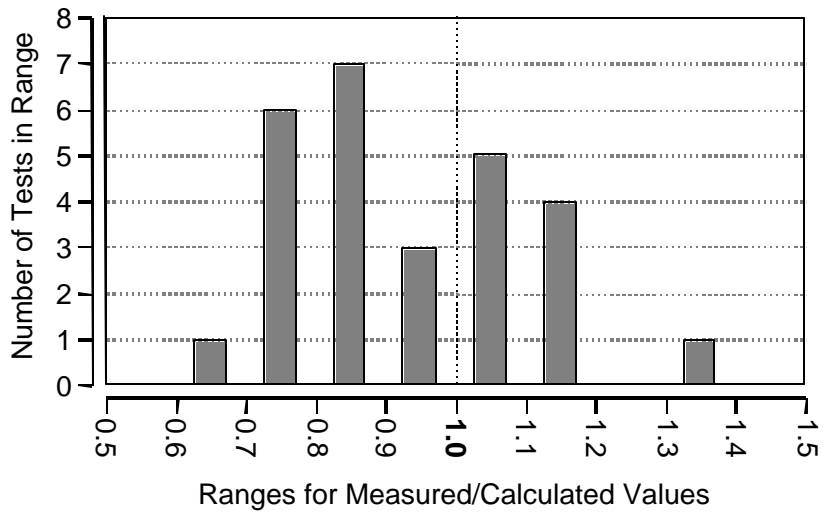


Figure 7-35: Distribution plot of measured/predicted ratios for model 2 (CCT node tests)

7.5 CONTRIBUTION FROM BOND

The development length equation from ACI 12.2.3 (equation 2-1 in Chapter 2 of this report) was used to calculate the contribution to anchorage from bond that would occur over the deformed bar length. Calculated bar stresses were then compared to the measured stress data collected from strain gages on the headed bars. The contribution to bar stress from bond was determined by the difference in strain readings between the strain gages at $1d_b$ (immediately behind the head) and $7d_b$ (approximately the location of maximum development for most of the CCT node test bars) along the length of the bar. The difference in bar stress over the $6d_b$ length was then used to determine average bond stress over that length. A total of 30 tests were used in the CCT node database for bond analysis.

Measured bond stress (normalized to a concrete strength of 4 ksi) at failure is plotted against relative head area in Figure 7-36. It is clear from the plot that the bond stress at failure decreased as the relative head area was increased. As discussed in the last chapter (section 6.1.2), development of the headed bars was a two stage process: bar force was first resisted by bond which would then break down allowing the head to carry a greater component of the bar force. Final capacity tended to consist of head bearing plus some residual bond resistance. Peak bond stresses occurred and then began to decrease before the maximum capacity of the tie bar was reached. The degree to which bond stress declined before failure of the specimen depended on the size of the head. A non-headed bar failed once bond stress reached its peak capacity. A bar with a small head would experience only a slight loss in bond before the head reached its ultimate capacity and failure occurred. A bar with a large head experienced a large loss of bond before the head achieved its peak capacity and failure occurred. This trend is demonstrated by the data in Figure 7-36. Bond stresses at failure decreased as the head size increased.

The bond stress determined by the ACI development length equation is also plotted in Figure 7-36. The calculated bond stress was determined by rearranging the ACI development length equation to determine bar stress, then converting that bar stress into bond stress:

$$u_{\text{bond}} = \frac{f_s A_b}{\pi d_b L_d} = \frac{40}{3} \cdot \frac{L_d}{d_b} \cdot \sqrt{f'_c} \cdot \left(\frac{c + K_{tr}}{d_b} \right) \cdot \frac{A_b}{\pi d_b L_d} \quad (7-7)$$

$$u_{\text{bond}} = \frac{10}{3} \cdot \sqrt{f'_c} \cdot \left(\frac{c + K_{tr}}{d_b} \right) \quad (7-8)$$

For the bond analysis of the CCT node specimens, $(c + K_{tr})/d_b$ was equal to its maximum limit, 2.5. Concrete strength was normalized to 4 ksi. Additionally, the calculated bond stress was divided by 0.9 to remove the built-in safety reduction factor from the ACI equation.

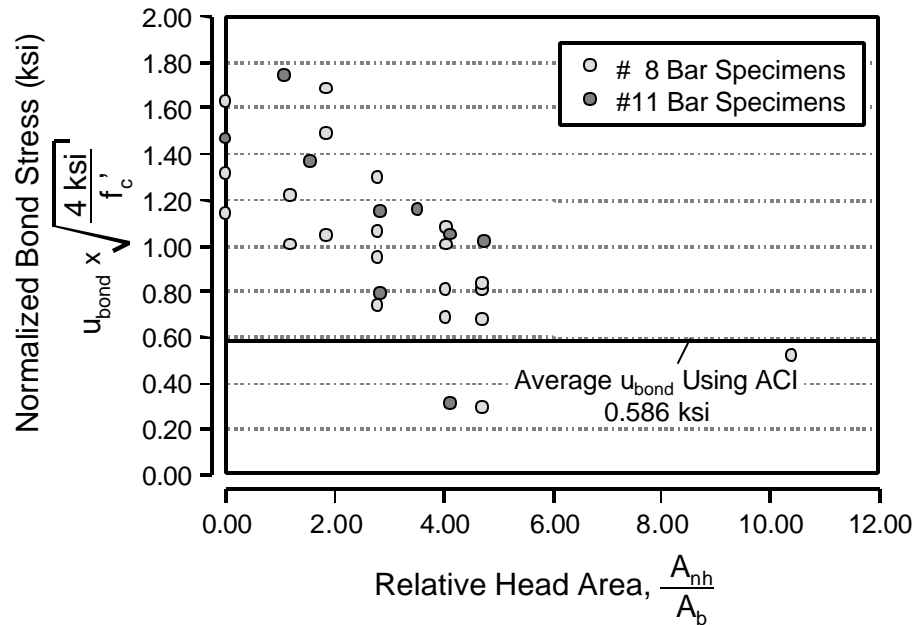


Figure 7-36: Measured failure bond stress versus relative head area

Figure 7-36 shows that most of the measured bond stresses were greater than the ACI calculated bond stress. The four non-headed bars had an average bond stress of about 1.4 ksi which is more than twice the calculated value. The high bond stresses may be due to the confinement provided by the vertical compression at the CCT node or platen restraint provided by the rigid bearing plate. If the compression stress played a role in enhancing bond, then differences should be seen between the specimens with different strut angles. The magnitude of the vertical compression stress was a function of the strut angle of the CCT node configuration. Such a trend would be hard to discern from Figure 7-36 because the data in that figure are also affected by head size. In order to determine if vertical compression played a role in enhancing the bond stress, peak bond stresses were determined from each CCT node test. Rather than using the bond stress measured when the specimen achieved its ultimate capacity, the peak bond stress that occurred during the loading sequence of the node specimen was used to examine the influence of compression stress.

In Figure 7-37, peak measured bond stress is plotted against the vertical compression stress that was present at the time of the peak bond. Vertical compression stress was determined by the load cell measurement of the bearing reaction at the CCT node. The bearing reaction was simply divided by the area of the bearing plate to determine vertical compression stress at the node. Between lateral compression stresses of $0.1f_c'$ and $0.7f_c'$, no clear trend is apparent in the data, and there is much scatter. All of the measured bond stresses were greater than the bond stress calculated using the ACI equation. However, the lack of a clear trend in the relationship between bond stress and lateral compression stress suggests that lateral compression stress may not be the cause of the enhanced bond stress. Rather, the platen restraint provided by the rigid bearing support may have a more significant effect on bond.

Two studies have proposed models for increases in bond stress with increasing lateral compression: Untraeur and Henry [112] and Thrö [111]. These models were applied to the ACI calculated bond stress to determine if they fit the data measured from the CCT node tests. They are plotted in Figure 7-37. The Thrö model fits the data better than the Untraeur and Henry model, however, the data are so scattered, that no definite conclusion of behavior can be asserted.

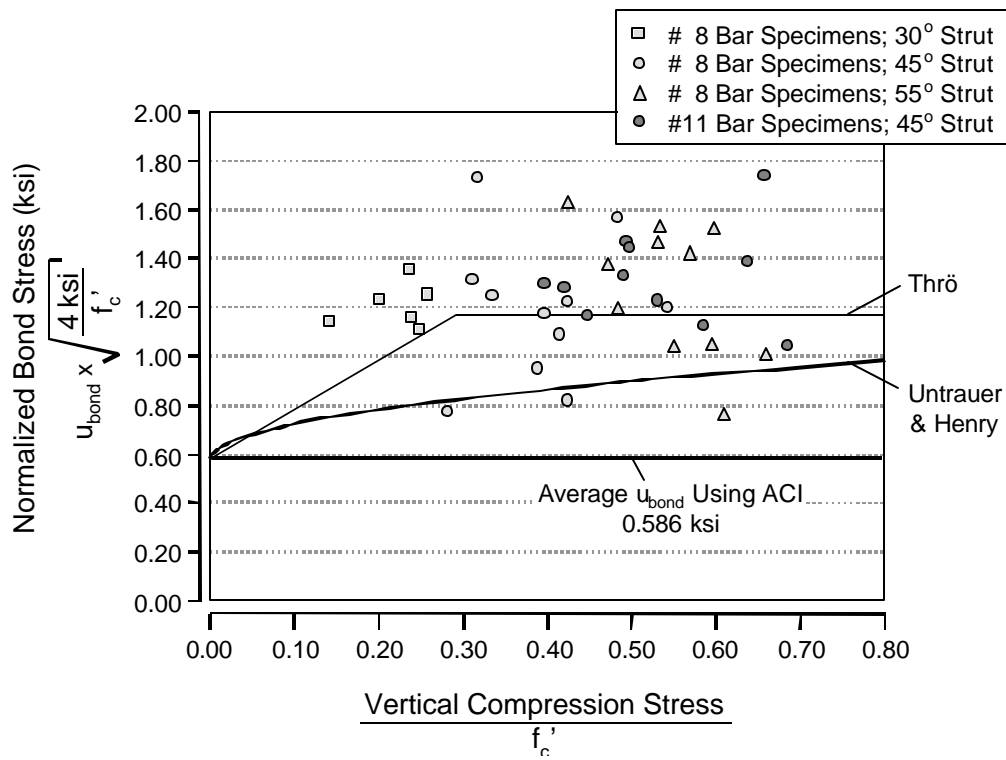


Figure 7-37: Measured peak bond stress versus vertical compression stress

In Figure 7-38, peak bond stress is plotted against relative head area. The peak bond stresses are much more constant than the failure bond stresses, but there still seemed to be a trend of decreasing capacity with increasing head size. This trend may be due to changes in the relative anchorage stiffness between the head and the deformed bar as the head size become larger. Larger

head sizes experienced less slip than did the smaller head sizes. This increase in the stiffness of the end anchorage of the bar may have prevented optimum bond from occurring. As the head became larger, it becomes a stiffer component of the bar anchorage, thus attracting more of the anchorage force, possibly away from the bond. This would account for the decrease in peak bond stress as the relative head area was increased.

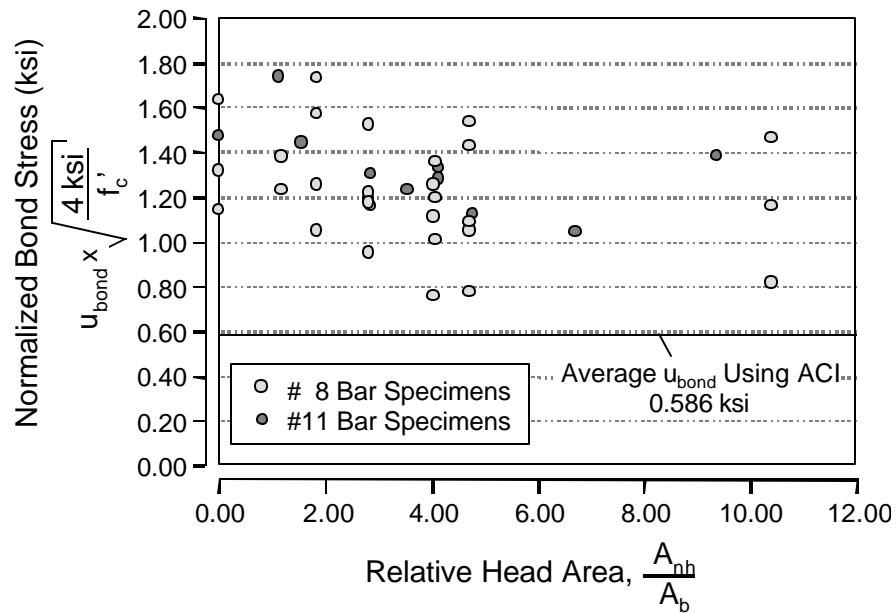


Figure 7-38: Measured peak bond stress versus relative head area

Statistical analysis was performed of the failure bond and the peak bond stresses. Tables 7-10 and 7-11 present the statistical data for the sets of peak and failure data. Figures 7-39 and 7-40 present the distributions of measured/calculated values. The ACI bond stress equation was very poor for calculating the failure bond stress, though it was conservative for most tests. The ACI equation was even more conservative for peak bond. The average peak bond was nearly twice the

predicted bond stress. The lateral compression model proposed by Thrö would account for the high peak bond values. However, the effect could also be due to platen restraint. Furthermore, it is the bond at failure that matters, not the peak bond. The bond at failure is the product of two effects. First, it is increased by the lateral compression stresses and/or platen restraint in the CCT node. Second, it is diminished by the nature of the anchorage failure, which necessitates that bond deteriorates before bar force can be transferred to the head. These two actions counter each other and the final bond that results does not fit the existing models of bond stress.

| | | Measured/Calculated Values | | |
|----------|---------------------|----------------------------|------|--------------------|
| Bar Size | Number of Specimens | Range | Mean | Standard Deviation |
| #8 | 9 | 0.50 - 2.86 | 1.72 | 0.55 |
| #11 | 21 | 0.38 - 2.11 | 1.35 | 0.47 |
| All | 30 | 0.38 - 2.86 | 1.61 | 0.58 |

Table 7-10: Statistical data for accuracy of ACI bond equation in predicting the failure bond

| | | Measured/Calculated Values | | |
|----------|---------------------|----------------------------|------|--------------------|
| Bar Size | Number of Specimens | Range | Mean | Standard Deviation |
| #8 | 11 | 1.27 - 2.11 | 1.60 | 0.23 |
| #11 | 28 | 1.30 - 2.94 | 2.08 | 0.43 |
| All | 39 | 1.27 - 2.94 | 1.95 | 0.44 |

Table 7-11: Statistical data for accuracy of ACI bond equation in predicting the peak bond

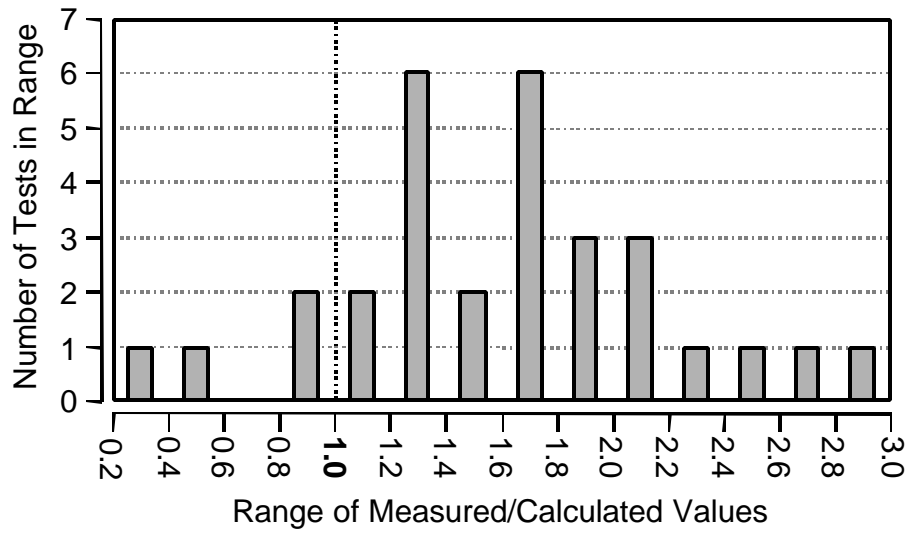


Figure 7-39: Distribution plot of measured/calculated ratios for failure bond

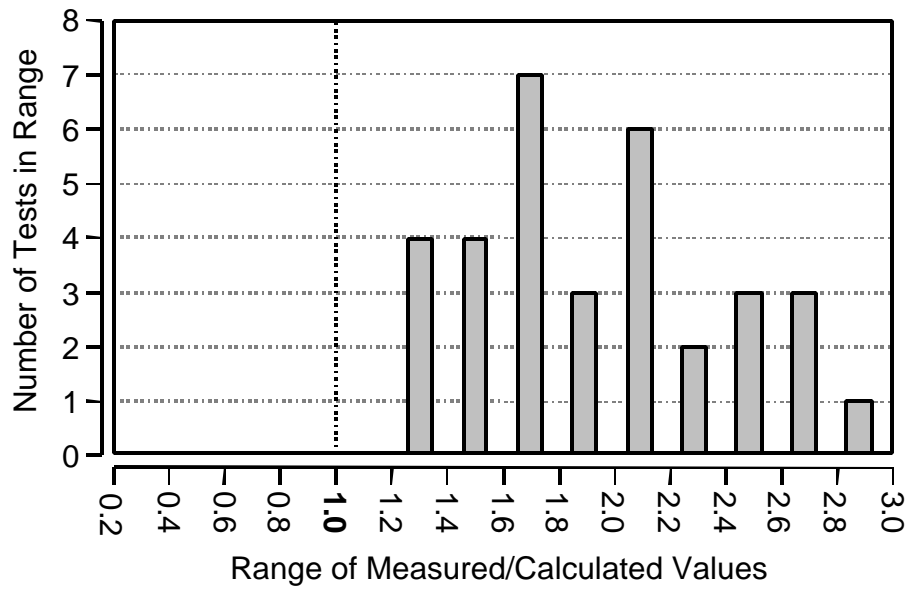


Figure 7-40: Distribution plot of measured/calculated ratios for peak bond

7.6 SUMMARY

Headed bar anchorage is achieved through contributions from bond and bearing on the head. These behavior of these two components are not independent of each other (head capacity affects the magnitude of bond stress at failure). However, the capacities provided by each can be determined separately and added to find the total anchorage capacity. The data for these two components from the CCT node tests were analyzed separately in this chapter. The combination of these two components is dealt with in Chapter 10.

Two models for the capacity of head bearing were recommended. These models were shown to adequately model the behavior of the measured head capacities from the CCT node tests as well a variety of additional headed bar tests, anchor bolt tests, and bearing plate tests on concrete blocks. The following model was recommended:

$$\text{Bearing Capacity, } P = A_{\text{nh}} \left(0.9 \Psi \left(\frac{2c_1}{\sqrt{A_{\text{nh}}}} \right) (f'_c) \right) \quad (7-9)$$

$$\text{with } \Psi = 0.6 + 0.4 \frac{c_2}{c_1} \leq 2.0 \quad (7-10)$$

P = head capacity (kips)

Ψ = radial disturbance factor

A_{nh} = net head area (in²)

c_1 = minimum cover dimension (in)

c_2 = secondary cover dimension (the smallest cover dimension measured perpendicular to the minimum cover) (in)

f'_c = concrete cylinder strength (ksi)

The ACI model for bond stress was examined as a possible candidate for the bond data measured from the CCT node tests. This model was found to provide very poor, though conservative results. Bond stress at failure was influenced by lateral compression and/or platen restraint in the CCT node and the breakdown in bond that occurs as bar stress is transferred to the head. These two influences greatly affected the bond behavior and prevented the ACI model from working. This model must be modified in order to work under the conditions of CCT node confinement and the effect of head bearing.

Additionally, the following observations were noted:

- Head capacity increased linearly with increases in the ratio $2c_1/\sqrt{A_{nh}}$. There was no limit to the increase in head capacity up to $2c_1/\sqrt{A_{nh}} = 10$, the upper limit of available test data. This limit is 5 times the current ACI limit of 2.
- Head capacity increased linearly with increases in the ratio c_2/c_1 with an upper limit on the c_2/c_1 ratio between 3 and 4.
- Head capacity increased with increasing concrete strength. The order of the relationship seemed to be variable with exponents between 0.5 and 1.0. The value of this exponent was inversely proportional to the $2c_1/\sqrt{A_{nh}}$ ratio. The exponent was 1.0 when $2c_1/\sqrt{A_{nh}}$ equaled 1.0 and dropped off to 0.5 as $2c_1/\sqrt{A_{nh}}$ approached infinity. However, a reasonable model of head capacity could be achieved using a single exponent of 1.0 for the concrete strength.
- The peak bond stress achieved by the headed bars averaged twice the ACI predicted bond stress most likely due to the active confinement provided by vertical compression and/or platen restraint in the CCT node. This increase was best modeled

by the recommendations of Thrö [111]. However, the peak bond stress was not as important to capacity as the bond stress at failure.

- There was some indication that peak bond stress was affected by the head size and decreased slightly as the relative head area became larger.
- The bond stress at failure was less than or equal to the peak bond stress. The failure bond stress was equal to peak bond stress for non-headed bars but decreased as the head size became larger.
- Final anchorage was achieved by a combination of peak head capacity and diminished bond capacity.
- In the CCT nodes, head orientation had a small effect on capacity. Optimal head performance was provided when the head was oriented such that the long axis was perpendicular to the vertical splitting plane. For all other tests, the head capacity was not significantly affected up to an aspect ratio of 3. Within this limit, the decrease in capacity fell within the limits of scatter.
- Decreases in strut angle resulted in a longer development length for the bar. The longer development length provided a greater contribution from bond and allowed for smaller head sizes to achieve yield.
- Limited test data showed that confinement in the form of stirrups did not improve the capacity of the head. However, stirrup confinement did change the behavior of the strut-and-tie model allowing for a longer development length, thus enhancing the total anchorage capacity of the bar.

A summary of all CCT node test results is provided in Appendix C.

Chapter 8: Lap Splices: Specimen Fabrication and Testing Procedures

8.1 INTRODUCTION

In this chapter, the details of the fabrication and testing of 27 lap splices are discussed. Figure 8-1 shows a photo of the lap splice test setup. The lap splice specimens consisted of 10" thick, 13' long slabs. The primary tensile reinforcement was spliced at the midspan of these specimens. Loading of the specimens was designed to place this middle portion under constant moment creating tension on the top surface so that cracks could be observed and recorded. Load was applied until the splice failed or the lapped bars yielded.

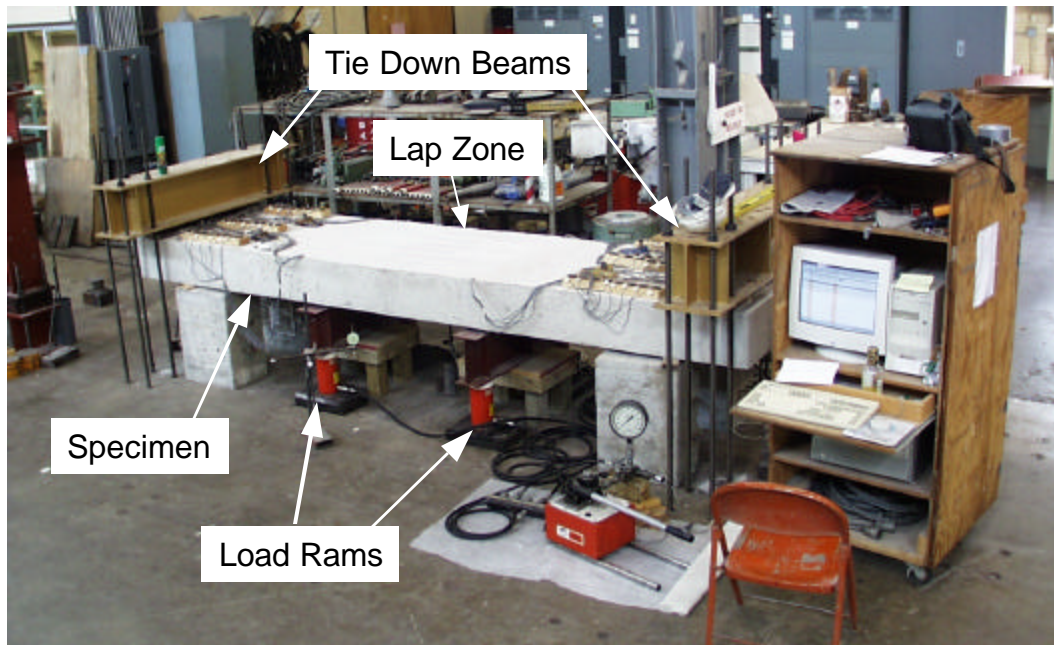


Figure 8-1: A typical lap splice test

8.2 SPECIMEN DETAILS

As with the CCT node specimens, both confined and unconfined lap splices were tested. In unconfined specimens, no transverse reinforcement was placed within the lap zone and for one foot on either side of the lap zone. Figure 82 shows the basic reinforcement layout for an unconfined specimen. Three #8 bars were lapped in the top layer of reinforcement of the specimen. Four #5 continuous bars were placed in the bottom of the beam. The #5 bars provided moment capacity for lifting and moving the specimen after failure and for positioning the transverse reinforcement. #3 closed hoop stirrups were tied around the two layers of longitudinal bars starting at a distance 12" from the end of the lap length. The stirrups provided a stable reinforcing cage for ensuring that the headed bars retained their position during casting. All reinforcement chairs, spacers, and lifting inserts were placed outside of the lap splice zone. Center-to-center bar spacing of the lapped bars was either 6" or 10" ($6d_b$ or $10d_b$). The width of the specimen was altered to accommodate the bar spacing: 25" for 6" spacing and 36" for 10" spacing. Two inch clear cover was provided over the lapped bars so that the lever arm, d , of the #8 top reinforcement was about 7.5". Clear cover over the heads was at least 1.375".

The initial four lap splice tests used different details. The basic dimensions of the specimens were the same. However, #5 headed bars were tested and placed in both the top and bottom layers of the specimen. First the specimen was loaded in one direction to test one layer of bars, then flipped to place load in the reverse direction and test the other layer of bars. Thus the first four tests were conducted with just two specimens. This test practice was begun as a convenience in order to produce more tests from each specimen. But after the first set of tests, this practice was found to be unsatisfactory because the first layer of reinforcement could not be

properly tested without unduly damaging the opposite layer before its test. Ledesma's MS thesis [67] can be referenced for more information on the initial lap splice tests.

Two confinement details were studied. The first detail consisted of hairpin tie-downs at either end of the bars in the lap zone. In the second detail, transverse bars were placed over the lapped bars in the middle of the lap zone and connected to bars in the bottom of the beam using U-shaped ties with 90° hooks. Figure 8-3 shows the basic configuration and Figure 8-4 shows photos of the two details.

The hairpin confinement detail was envisioned to cross the failure crack that formed in the lap zone and tended to split the cover concrete. It appeared that the best confinement for the bars would come from a detail that intercepted horizontal splitting cracks through the plane of the lap. Thus the hairpins, which encircled the lap bars and tied back directly into the underlying concrete, seemed like an ideal detail. The hairpins were designed to be easily dropped down over the individual lap bars and tied off against the bottom layer of reinforcement. Figure 8-5 shows the dimensions of the hairpin bars. The hairpins were usually tied into the reinforcement cage so that they were not in direct contact with the surface of the lap bars. Confined lap tests were performed with #2, #3, and #4 hairpins.

The transverse tie-down detail was used once. This detail was developed to confine the compression struts that were idealized as forming between the heads of the lap bars using a strut-and-tie model. The Ushaped ties were envisioned to confine the struts both transversely and vertically. The ties and transverse bars were fabricated from #3 bars. Figure 85 shows the dimensions of the transverse and tie-down bars.

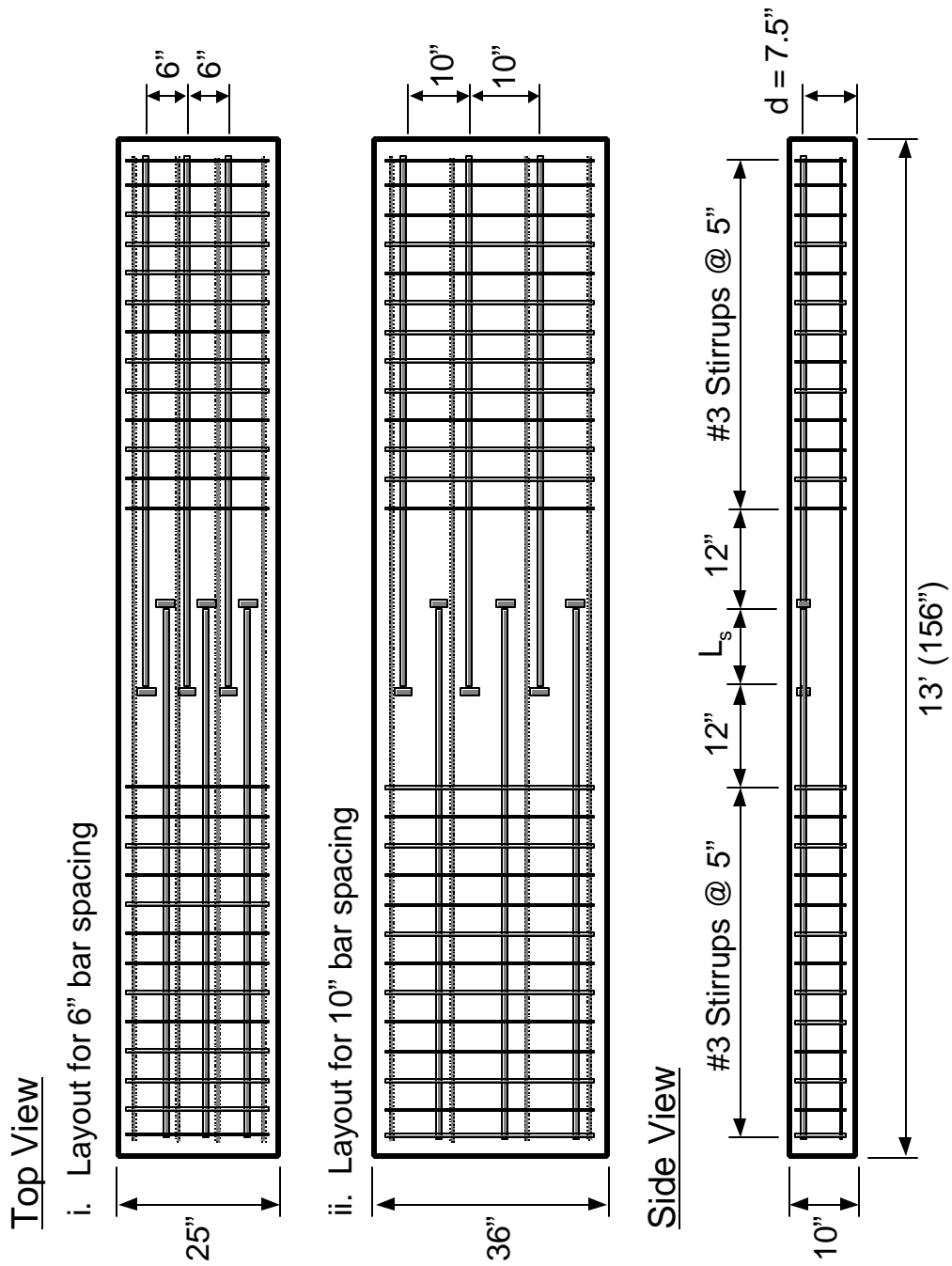
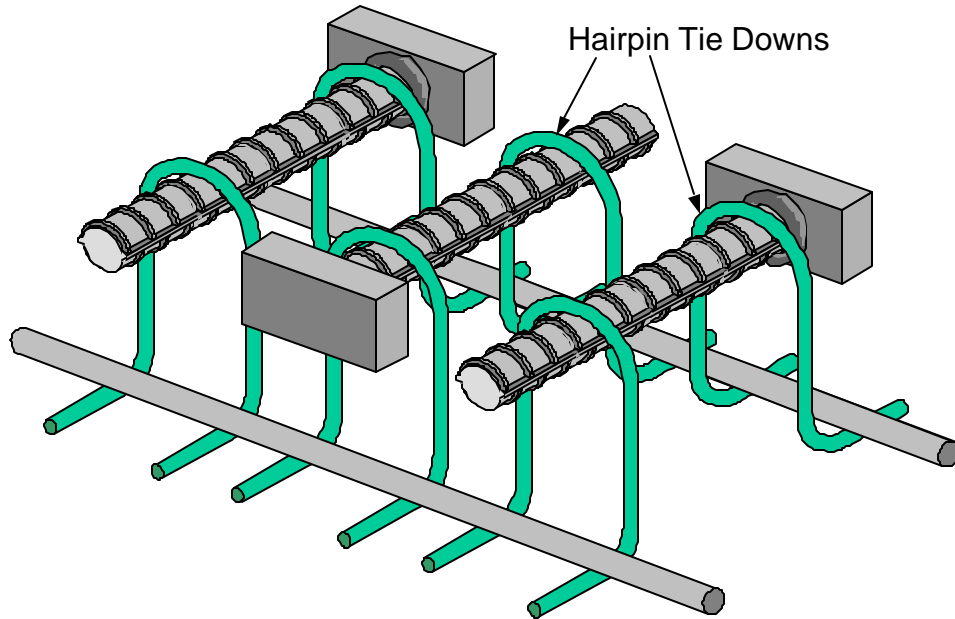


Figure 8-2: Reinforcement details of unconfined lap splice specimens

i. Hairpin Confinement Detail



ii. Transverse Tie-Down Detail

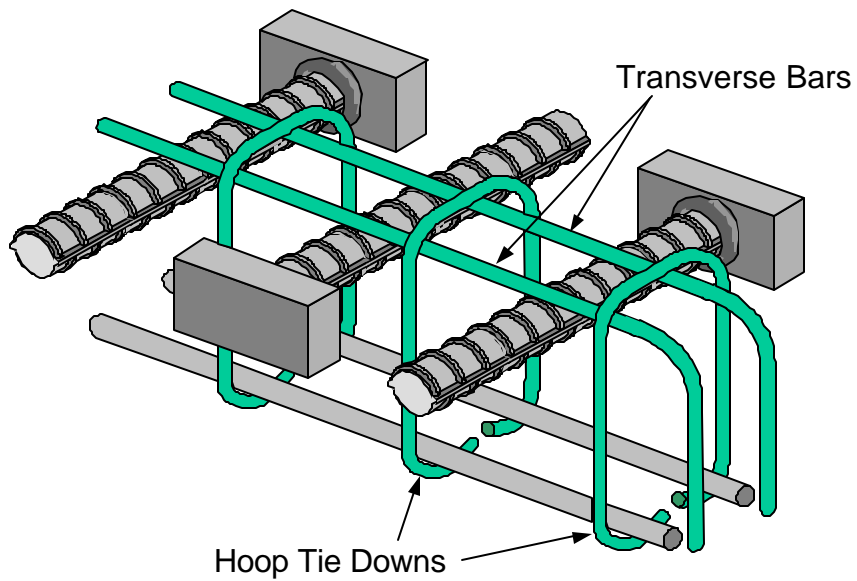


Figure 8-3: The two types of lap splice confinement details tested



i. Hairpin Confinement Detail



ii. Transverse Tie-Down Detail

Figure 8-4: Photos of the two lap splice confinement details

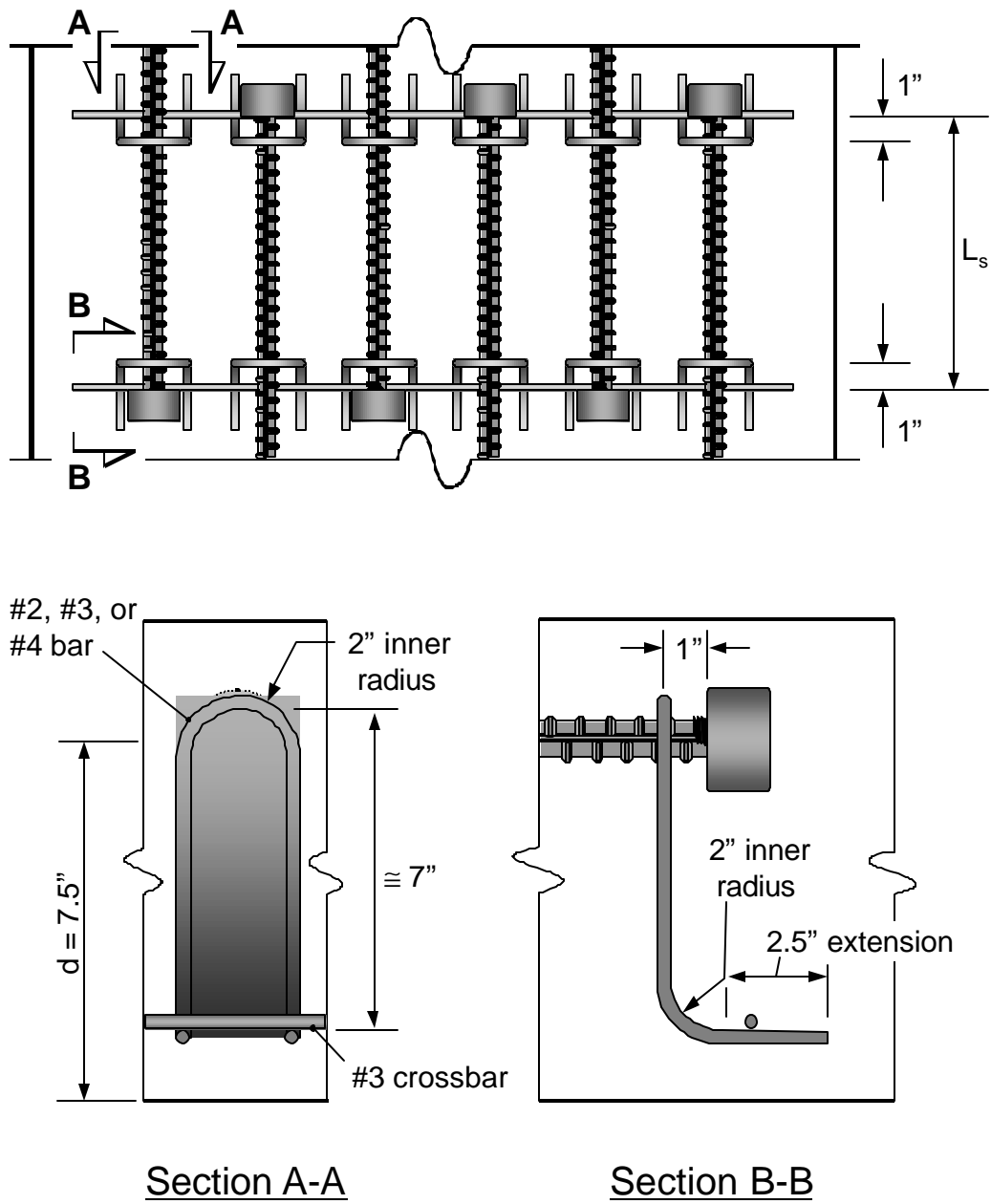
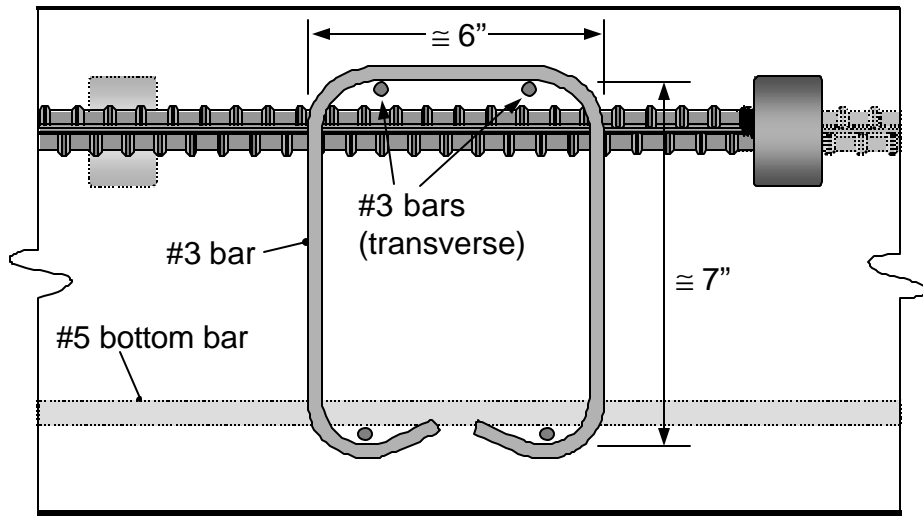
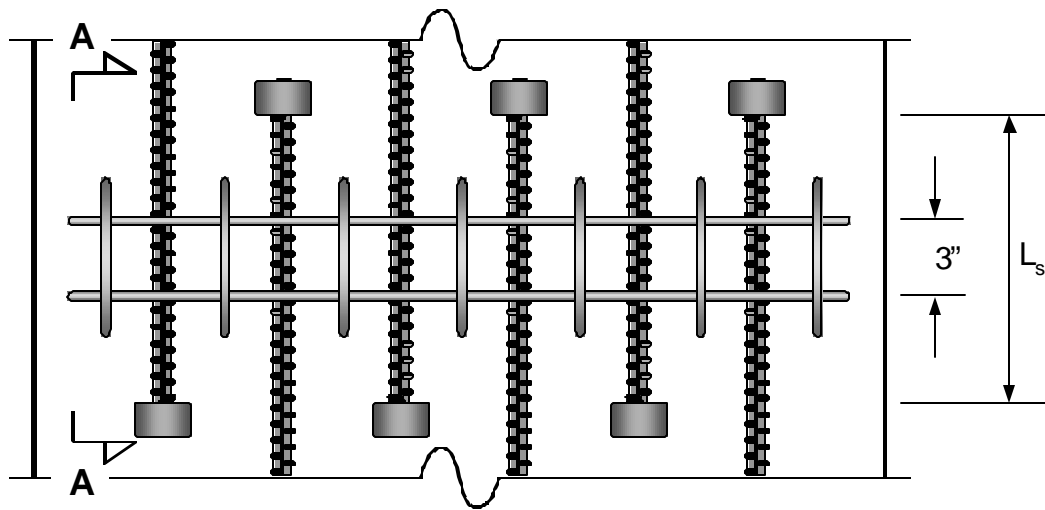


Figure 8-5: Dimensions of the hairpin confinement detail



Section A-A

Figure 8-6: Dimensions of the transverse tie-down confinement detail

Two concrete mixes were used. Concrete was supplied by a local company. Table 8-1 lists the concrete mix proportions. A nominal maximum aggregate size of 0.75" was specified.

Mechanical properties of the hardened concrete were determined using standard 6” diameter cylinders. Compression strength, splitting tensile strength, and modulus of elasticity were measured just prior to and just following tests of a group of specimens with the same concrete. Initially, only compression strength was measured. Tests were performed according to ASTM standards C39 (compressive strength), C496 (splitting tensile strength), and C469 (modulus of elasticity) [6, 7, 8]. Table 8-2 lists the measured properties from each cast.

| Mix Proportions by Weight | | | | | | |
|----------------------------------|------------------|-------|-------|-----------------|--------|-----------|
| Mix | Coarse Aggregate | Sand | Water | Portland Cement | Flyash | w/c Ratio |
| A | 45.7% | 37.2% | 6.4% | 7.7% | 3.0% | 0.60 |
| C | 47.5% | 36.3% | 6.8% | 7.3% | 2.2% | 0.72 |

Table 8-1: Concrete mix proportions

| Concrete Batch | Cast Date | Age (days) | f'_c (psi) | f_{ct} (psi) | E_c (ksi) |
|----------------|-----------|------------|--------------|----------------|-------------|
| A1 | 7/12/99 | 42 | 5700 | - | - |
| C1 | 10/8/99 | 42 | 3200 | - | - |
| C2 | 10/29/99 | 31 | 3700 | - | - |
| C3 | 1/20/00 | 28 | 4000 | 440 | 3800 |
| C4 | 5/2/00 | 45 | 4200 | - | 3800 |
| C5 | 9/26/00 | 69 | 3500 | 400 | 4000 |
| C6 | 5/17/01 | 35 | 3800 | 360 | 4000 |

Table 8-2: Hardened concrete properties

The concrete strength was 5700 psi for the first four specimens. For the remainder of the tests, the concrete strength ranged between 3000-4000 psi. The concrete strength was reduced to increase the likelihood of splice failure rather than bar yielding. Specimens were cast four at a time in the test position. Concrete was placed using a bucket and vibrated into position. The specimens were covered with plastic after casting and left for one full week before removal of the formwork. Formwork was fabricated from standard lumber and plywood and reused several times.

8.3 SPECIMEN INSTRUMENTATION

Three types of instrumentation were used during the testing:

- **Strain gages** were placed on the lapped bars so that the strain gradient along the bars in the lap zone could be determined and on the confining bars to provide information on effectiveness of the ties in resisting splitting.
- **Linear potentiometers** were used to measure end and midspan deflection of the specimen.
- A **pressure transducer** was used to monitor the load placed on the specimen.

Figure 8-7 shows the placement of strain gages in the lap zone. Strain gages were placed at regular intervals along the lap length on of each of the lap bars. Gage placement typically extended until slightly beyond the lap length. For the longer lap lengths, an additional gage was placed on the top of each lap bar to provide an indication of any strain differential across the depth of the bar due to local bending. In one specimen, the headed bars were debonded along the lap length. Gages were placed underneath the debonding wrap at two locations: next to the head and at the end of the lap length.

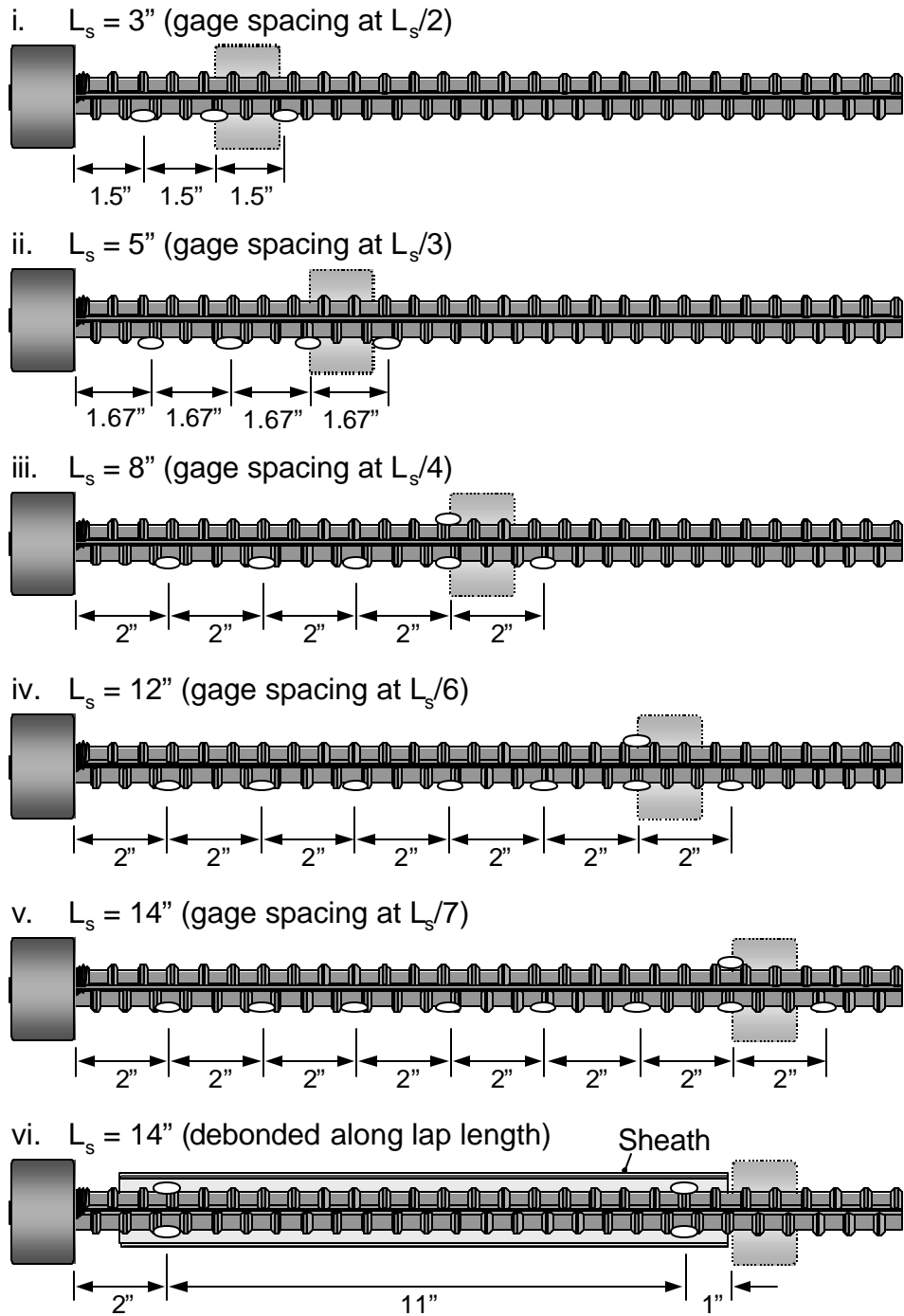


Figure 8-7: Spacing of strain gages for various lap lengths

Figure 8-8 shows the placement of strain gages on the hairpins. Because the bond of the hairpins was not an issue (they were positively anchored by 90° bends), the gages on the hairpins were wrapped with a debonding tape for a length of 2.5" to increase the "active length" of the gage. This was to insure that the gage reading would reflect the effects of any splitting cracks propagating from the surface of the lap bars even if those cracks did not intersect the exact location of the strain gage and also permitted placing of the strain gage further from the 90° bend. In the first tests with hairpins, gages were placed on only one leg of the hairpins and they were wrapped with aluminum foil tape. On the last hairpin specimen tested, two gages were used for each hairpin (one on the outside of each leg) and electrical tape was used. The elastic tape was easier to apply and worked as well as the foil tape provided several layers were applied.

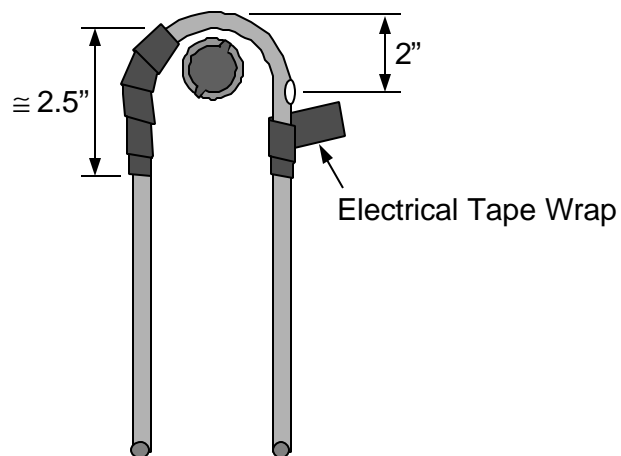
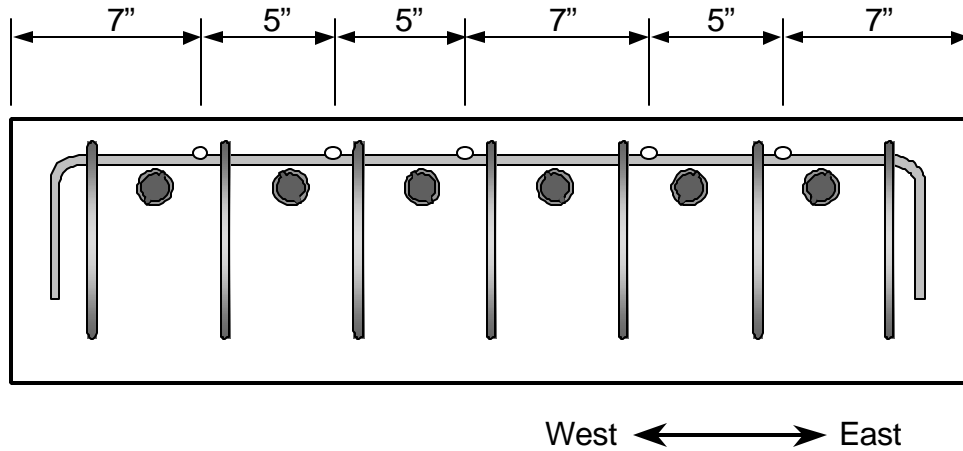


Figure 8-8: Instrumentation of hairpin bars

Gages were placed on both the transverse and tie-down bars of the transverse tie-down confinement. Figure 8-9 shows the placement of strain gages on the transverse and tie-down bars. Strain gages on the transverse bars were placed within 1" of adjacent tie-down locations. It was

assumed that the transverse bars would be most effective near the center of the compression struts that form between the heads of the lap bars. The gages on the transverse bars were wrapped in electrical tape to extend their active length across the space crossed by the tie down bars. Gages were placed on both legs of the tie down hoops. Like the hairpin bars, they were wrapped in electrical tape to extend their active length.

i. Transverse Bar Instrumentation



ii. Tie-Down Instrumentation

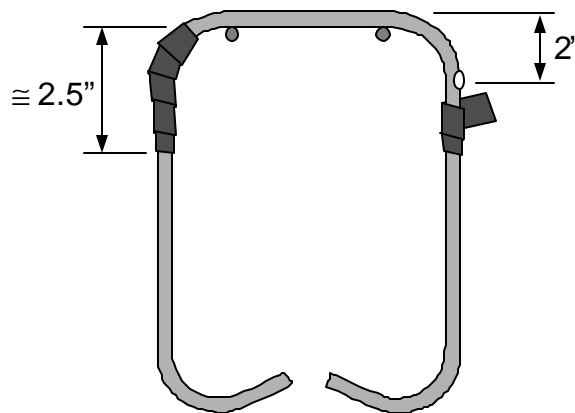


Figure 8-9: Instrumentation of transverse tie-down confinement

8.4 LOAD SETUP

The basic setup for the lap splice specimens is shown in Figure 8-10. A photo of the test setup was also provided in Figure 8-1. The specimen was pushed upward in the middle by four hydraulic rams (2 on either side of the lap zone). The ends of the specimen were restrained downward by reaction beams tied to the strong floor of the lab. This load configuration placed the center of the specimen under negative moment (the top of the specimen in tension). Loading through negative moment provided the advantage of putting the test zone on the top of the specimen. This made the surface of the lap zone visible so that cracks could be easily mapped and pictures taken.

The force from the load rams was distributed into the specimen through 6" wide and 10" deep steel I-beams that extended the full width of the specimen. The hydraulic rams were connected in parallel through the hydraulic lines so that each ram would carry the same pressure. The tie down reaction forces at the ends of the specimen were distributed through pinned rollers so that uneven loading of the specimen would not occur. These rollers were added after the first four tests that used #5 headed bars. Prior to the addition of the rollers, the flanges of the reaction beams rested directly on the concrete surface. Support pedestals were placed underneath the specimen to support it prior to loading and to catch the ends of the specimen should failure result in complete loss of capacity.

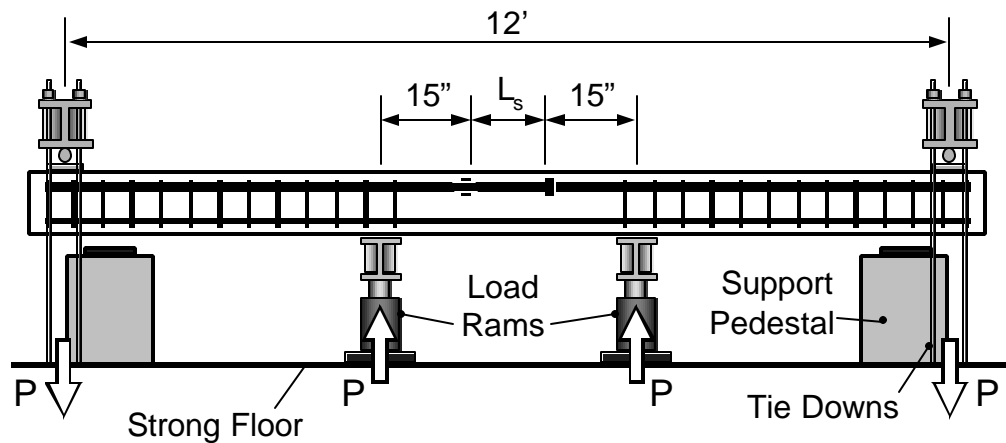


Figure 8-10: Load setup for lap splice specimens

8.5 TESTING PROCEDURE

The specimen was moved from the casting bed into position and placed on the support pedestals shown in Figure 8-10. The strain gage wires were then connected to the data acquisition system and the linear potentiometers were placed at midspan and at the tie down locations underneath the specimen. The reinforcement layout within the lap zone was drawn on the surface of the specimen to facilitate the interpretation of the cracking behavior and for recording the position of cracks.

A hand pump provided hydraulic pressure which was monitored by the data acquisition system and by a pressure dial gage. During the test, the beam was lifted from the support to engage the tie rods that transferred the load reaction into the strong floor. Load was applied in 1-2 kip increments until first cracking generally at about 6 or 7 kips of load. Thereafter load was applied in 0.5-1 kips increments until failure appeared imminent (indicated by excessive cracking or a softening of the stiffness of the specimen). Thereafter, load was applied in increments of about 0.2 kips. Failure was generally marked by a sudden loss in load capacity and appreciable

deflection. The failures were brittle when the splice failed, but the bottom layer of continuous bars provided residual capacity and prevented complete release of the load in the specimen. Cracks were marked and pictures were taken of the top surface of the specimen at 3-5 kip intervals. Crack recording generally took about 5 minutes to complete.

Fabrication of four specimens required about 10 to 12 weeks. The most time consuming task was installation of the large number of strain gages on the lap bars and confining steel. However, once fabricated, four specimens could be tested in a week. Preparation of a specimen before testing required about 6-8 hours and the actual testing took 45 minutes to 1 hour.

8.6 LAP SPLICE VARIABLES

Twenty-seven lap splice tests were performed. The first four tests provided useful information in defining the test procedure. However, the usable data acquired from those tests was minimal. For the remaining tests, the concrete strength was lower, the relative lap lengths (L_s/d_b) were shortened, the bar size was increased to #8 bars, and the amount of instrumentation placed on the bars was significantly increased. Five basic variables were studied: head size and shape, lap length, lap configuration, bar spacing, and confining steel.

8.6.1 Head Size/Shape

Three basic head sizes were tested: no heads, small heads, and large heads. Non-headed bars were tested to provide a reference for the headed bar results. Small headed bar results were provided by tests using HRC's Xtender product (relative head area equal to 1.18, see Table 5-3). Large headed bars included ERICO's Lenton Terminator and a reduced size HRC friction-welded head. HRC provided friction-welded headed bars with half-size rectangular heads (1.5" x 3.0"). These two head types were tested against one another with all other variables unchanged and

found to behave in a very similar manner. Thus the two large head types were treated interchangeably in the data analysis though they provided slightly different relative head areas (Lenton's 4.04 versus HRC's 4.70) and different head shapes (Lenton's circular versus HRC's rectangular). Though these heads were called "large," this designation was arbitrary. There are larger possible head sizes (HRC makes heads with relative head areas up to 10). However, the head sizes that were chosen corresponded to the larger head sizes that are currently manufactured and can potentially be retrofit to existing bars under field conditions (ERICO's Lenton Terminator which can be threaded onto an existing bar). Retrofit applications in which headed bars could be spliced with existing bars were of particular interest to TxDOT, the project sponsor. Thus the designation of "large," taken within the context of the lap splice tests, is not intended as a general qualification for a relative head area of 4.

8.6.2 Lap Length

Lap lengths ranged from 3" to 14". Lap lengths are referred to by the relative lap length, L_s/d_b (lap length divided by the bar diameter). Lap length was measured between the bearing faces of the heads of opposing lapped bars. Practical lap length would also incorporate the thickness of the heads on the bars (an out-to-out lap length). However, from a performance standpoint, the bonded lap length of headed bars (the length of deformed bar inside of the head faces) is probably a more important parameter than out-to-out lap length.

8.6.3 Lap Configuration

An important application for lapped headed bars appears to be closure strips in precast construction. In such a situation, it is desirable that the headed bar ends protruding from two adjoining precast segments be offset from one another as much as possible so that overlapping is

avoided and placement of the segments is facilitated. Thus, for placement, the optimum lap configuration results when opposing headed bars are non-contact to produce equal spacing between opposing bars. The optimum configuration for force transfer through the development of compression struts would be to place opposing bars in direct contact with one another. Pairs of specimens using both lap configurations were tested to examine the effect of contact versus non-contact placement of lapped bars. Figure 8-11 illustrates the two possibilities.

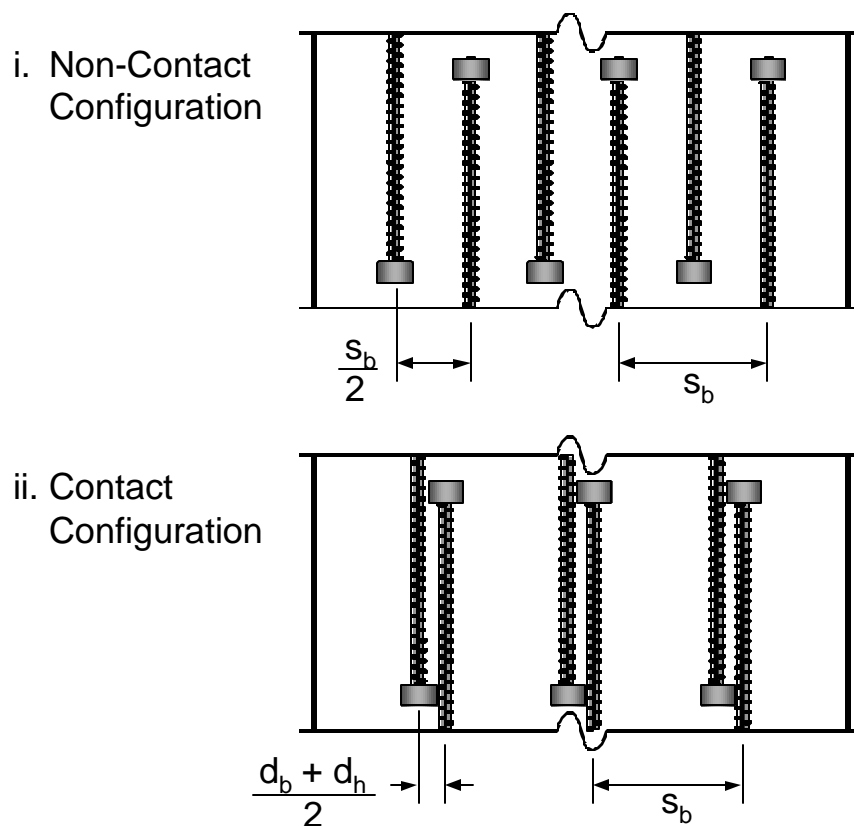


Figure 8-11: Non-contact and contact lap configurations

8.6.4 Bar Spacing

Bar spacing refers to the center-to-center separation of bars outside of the lap zone. Within the lap zone, the center-to-center separation is shortened because the opposing lap bars double the number of bars within the given width of the specimen. However, the bar spacing outside of the lap zone affects the spacing within the lap zone. A smaller bar spacing would usually weaken the capacity of the lap because the splitting stresses from bond would be more closely concentrated. However, a smaller bar spacing might improve the effectiveness of a headed bar lap because the compression struts forming between the heads are steeper and shorter. Bar spacing is referred to by the relative bar spacing, s_b/d_b (the center-to-center bar spacing divided by the bar diameter).

8.6.5 Confinement

Two confinement details were studied: hairpin and transverse tie-down details. The hairpin tests were easily defined by a parameter termed the tie-down ratio, A_{td}/A_b . This ratio defined the amount of confinement by the area of tie-down steel crossing the potential splitting crack divided by the area of the lapped bar. For the hairpin detail, two hairpins were provided for each lapped bar. Thus 4 legs are tying down each lapped bar. The tie-down ratio is then 4x the area of the hairpin bar divided by the area of the lapped bar. For a specimen with #3 size hairpins and #8 lap bars, the tie-down ratio is then $4*(0.11 \text{ in}^2)/(0.79 \text{ in}^2) = 0.56$. All confined tests were performed with #8 size lap bars. Thus, four tie-down ratios define the hairpin tests: 0.00 (no hairpins), 0.20 (#2 hairpins), 0.56 (#3 hairpins), and 1.01 (#4 hairpins).

A tie-down ratio can also be defined for the single transverse tie-down test. This detail had seven #3 tie-down hoops with two legs each. Thus 14 legs were tying down 6 lap bars. The tie-down ratio was then $14*(0.11 \text{ in}^2)/6*(0.79 \text{ in}^2) = 0.32$.

8.7 NOMENCLATURE AND LIST OF SPECIMENS

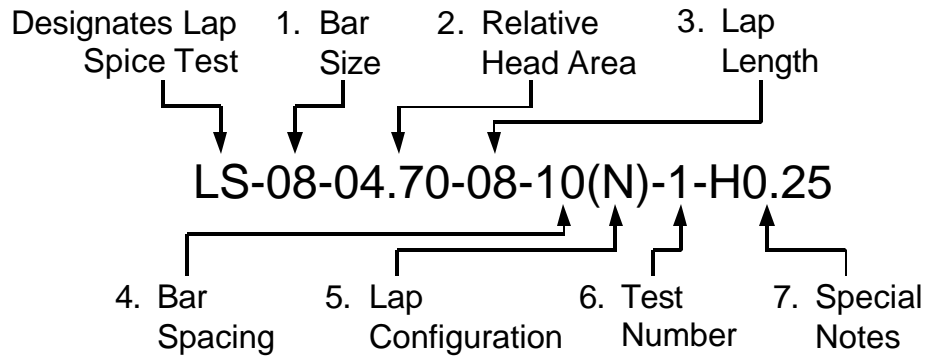
In this section, a standard nomenclature for identifying lap splice specimens is presented. Ledesma [67] developed a standard nomenclature in his report on the early lap splice tests. However, his nomenclature has been altered slightly when used in this report. The identifying terms within his nomenclature have been re-arranged to reflect the importance of the various parameters. Table 8-3 provides an example of the nomenclature that will be used in this report and descriptions of the different identifiers.

The example given in Table 8-3 is for a lap splice that had #8 bars with half-size HRC heads. It had an $8d_b$ lap length and $10d_b$ bar spacing with a staggered lap. The specimen was confined with #2 hairpins. Some further examples are provided below:

LS-05-01.39-12-10(C)-1: #5 bar size with small Xtender heads; $12d_b$ lap length (7.5") and $10d_b$ bar spacing (6"), lap bars were positioned in contact with one another.

LS-08-04.04-14-10(N)-1-DB: #8 bar size with large Terminator heads; $14d_b$ lap length (14") and $10d_b$ bar spacing (10"); lap bars were non-contact; the bars were debonded along the lap length.

Table 8-4 is a list of all lap splice tests, including the early #5 bar tests. The table lists the specimen, the head type (the shape: circular or rectangular, can be distinguished from the dimensions given; d_h refers to head diameter), the concrete batch used to cast the specimen, the date the specimen was tested and special notes regarding the test.



| Identifier | Description | Choices |
|------------|--|--|
| 1. | Bar Size - the size of the tie bar in standard ASTM sizes. | 05..... #5 08.....#8 |
| 2. | Relative Head Area -given to four significant digits. | 00.00 - 11.90 |
| 3. | Lap Length -divided by d_b . | 03 - 14 |
| 4. | Bar Spacing -divided by d_b . | 06 - 16 |
| 5. | Lap Configuration -refer to Figure 9-11. | (C).....Contact (N)..Non-Contact |
| 6. | Test Number - gives the number for repeated tests | 1....1 st Test 2....2 nd Test |
| 7. | Special Notes - Information for non-standard tests (<i>optional</i>): | |
| | H - Hairpin Confinement; followed by the tie-down ratio, A_{td}/A_b | H0.00 - H1.01 |
| | TTD - Transverse Tie-Down Detail Confinement | |
| | DB - Debonded along lap length | |

Table 8-3: Nomenclature of the lap splice test identifiers

| Specimen Identification | Head Type | Concrete | Test Date | Notes |
|------------------------------|----------------|----------|-----------|------------------|
| LS-05-01.39-12-16(C)-1 | $d_h = 0.97''$ | A1 | 08-18-99 | Trial Tests |
| LS-05-01.39-12-16(C)-2 | $d_h = 0.97''$ | A1 | 08-19-99 | |
| LS-05-01.39-12-10(C)-1 | $d_h = 0.97''$ | A1 | 08-23-99 | |
| LS-05-11.90-11-10(C)-1 | 2.0" x 2.0" | A1 | 08-20-99 | |
| LS-08-00.00-05-10(N)-1 | no head | C1 | 11-19-99 | Non-Headed Tests |
| LS-08-00.00-08-10(N)-1 | no head | C3 | 02-15-00 | |
| LS-08-00.00-12-10(N)-1 | no head | C4 | 06-07-00 | |
| LS-08-01.18-03-06(N)-1* | $d_h = 1.48''$ | C2 | 12-03-99 | Small Head Tests |
| LS-08-01.18-05-10(N)-1 | $d_h = 1.48''$ | C2 | 11-29-99 | |
| LS-08-01.18-05-10(C)-1 | $d_h = 1.48''$ | C2 | 12-02-99 | |
| LS-08-01.18-08-10(N)-1 | $d_h = 1.48''$ | C3 | 02-16-00 | |
| LS-08-04.70-03-06(N)-1 | 1.5" x 3.0" | C1 | 11-12-99 | Large Head Tests |
| LS-08-04.70-05-06(N)-1 | 1.5" x 3.0" | C2 | 12-07-99 | |
| LS-08-04.70-05-10(N)-1 | 1.5" x 3.0" | C1 | 11-18-99 | |
| LS-08-04.70-05-10(C)-1 | 1.5" x 3.0" | C1 | 11-17-99 | |
| LS-08-04.70-08-10(N)-1 | 1.5" x 3.0" | C3 | 02-18-00 | |
| LS-08-04.04-08-10(N)-1 | $d_h = 2.25''$ | C3 | 02-17-00 | |
| LS-08-04.70-12-10(N)-1 | 1.5" x 3.0" | C4 | 06-09-00 | |
| LS-08-04.04-12-10(N)-1 | $d_h = 2.25''$ | C6 | 06-25-01 | |
| LS-08-04.04-14-10(N)-1 | $d_h = 2.25''$ | C5 | 11-27-00 | |
| LS-08-04.04-14-10(N)-1-DB | $d_h = 2.25''$ | C5 | 11-28-00 | |
| LS-08-00.00-08-10(N)-1-H0.25 | no head | C4 | 06-12-00 | Confined Tests |
| LS-08-04.70-08-10(N)-1-H0.25 | 1.5" x 3.0" | C4 | 06-14-00 | |
| LS-08-04.04-08-10(N)-1-H0.56 | $d_h = 2.25''$ | C5 | 11-29-00 | |
| LS-08-04.04-08-10(N)-1-H1.01 | $d_h = 2.25''$ | C5 | 11-30-00 | |
| LS-08-04.04-12-10(N)-1-H0.56 | $d_h = 2.25''$ | C6 | 06-27-01 | |
| LS-08-04.04-12-10(N)-1-TTD | $d_h = 2.25''$ | C6 | 06-28-01 | |

* instrumentation spacing of 5" lap length

Table 8-4: List of all lap splice tests

Chapter 9: Lap Splices: Behavior During Testing and Data Trends

The behavior of the lap splice test specimens is discussed in terms of: cracking development, stress and strain, load-deflection response, failure modes, and overall trend behavior.

9.1 CRACKING BEHAVIOR AND FAILURE MODES

Specimen LS-08-04.04-12-10(N)-1 represents a typical lap splice test. This specimen had lapped #8 bars with large heads ($A_{nh}/A_b = 4.04$), a 12" lap length with bars in a non-contact lap configuration, and 10" center-to-center bar spacing outside of the lap zone. This specimen was unconfined. The concrete compressive strength was 3800 psi and the splitting tensile strength was 360 psi. The development of cracking in this specimen is outlined in Figures 9-1a through 9-1c.

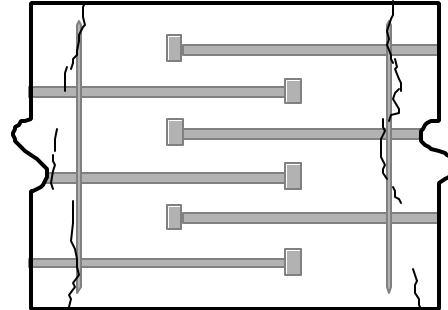
Cracking initiated outside of the lap zone at the location of the closest stirrups (Figure 9-1a, part i). This behavior was observed in all lap splice tests; first cracking always occurred at the same locations. First cracking within the lap zone occurred along the line of heads at each end of the lap (part ii) at a slightly higher load. As additional load was applied, these cracks propagated across the width of the specimen and new transverse cracks occurred at regular intervals along the length of the specimen. Transverse cracks frequently cut across the width of the specimen at a slight diagonal (part iii) and could indicate that some twisting was caused by the load arrangement or possibly by the non-symmetric arrangement of the lap bars in the beam.

The first longitudinal crack occurred along one of the lap bars at a load of 12.6 kips (Figure 9-1b, part iv). Longitudinal bond splitting cracks were common in the headed bar tests and occurred as bond along the deformed bars deteriorated and stress was transferred to the heads. As this process continued and the heads began to carry most of the bar force, diagonal cracks began to

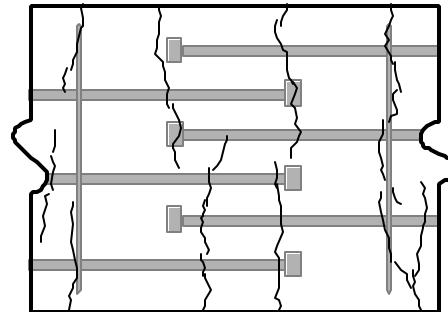
appear within the lap zone (part v). Diagonal cracks occurred along strut paths between opposing heads of the lap and indicated the formation of a strut-and-tie mechanism of force transfer in the lap zone. Once the formation of diagonal cracks along the strut paths initiated, crack development within the lap zone became extensive (part vi). Failure occurred soon afterwards (Figure 9-1c, part vii). Failure typically was sudden with nearly no moment capacity remaining.

Following failure of the specimen, additional deformation was imposed on the specimen until the cover over the lap zone spalled from the bars. This allowed viewing of internal crack patterns (Figure 9-2). Spalling of the concrete cover was caused by two mechanisms: (1) bond and wedge splitting caused by tension in the lap bars and (2) prying caused by the curvature of the specimen and bending moments in the lap bars at large deformations beyond the point at which the splice failed (Figure 9-3).

- i. P = 4.8 kips
First cracking occurs along the stirrups closest to the lap zone.



- ii. P = 6.2 kips
First cracking in the lap zone occurs close to the heads.



- iii. P = 7.6 kips
Full width transverse cracks extend through the lap zone at a slight diagonal.

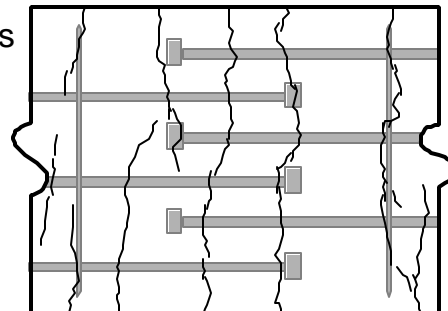


Figure 9-1a: Crack development in a typical unconfined lap splice test (specimen LS-08-04.04-12-10(N)-1)

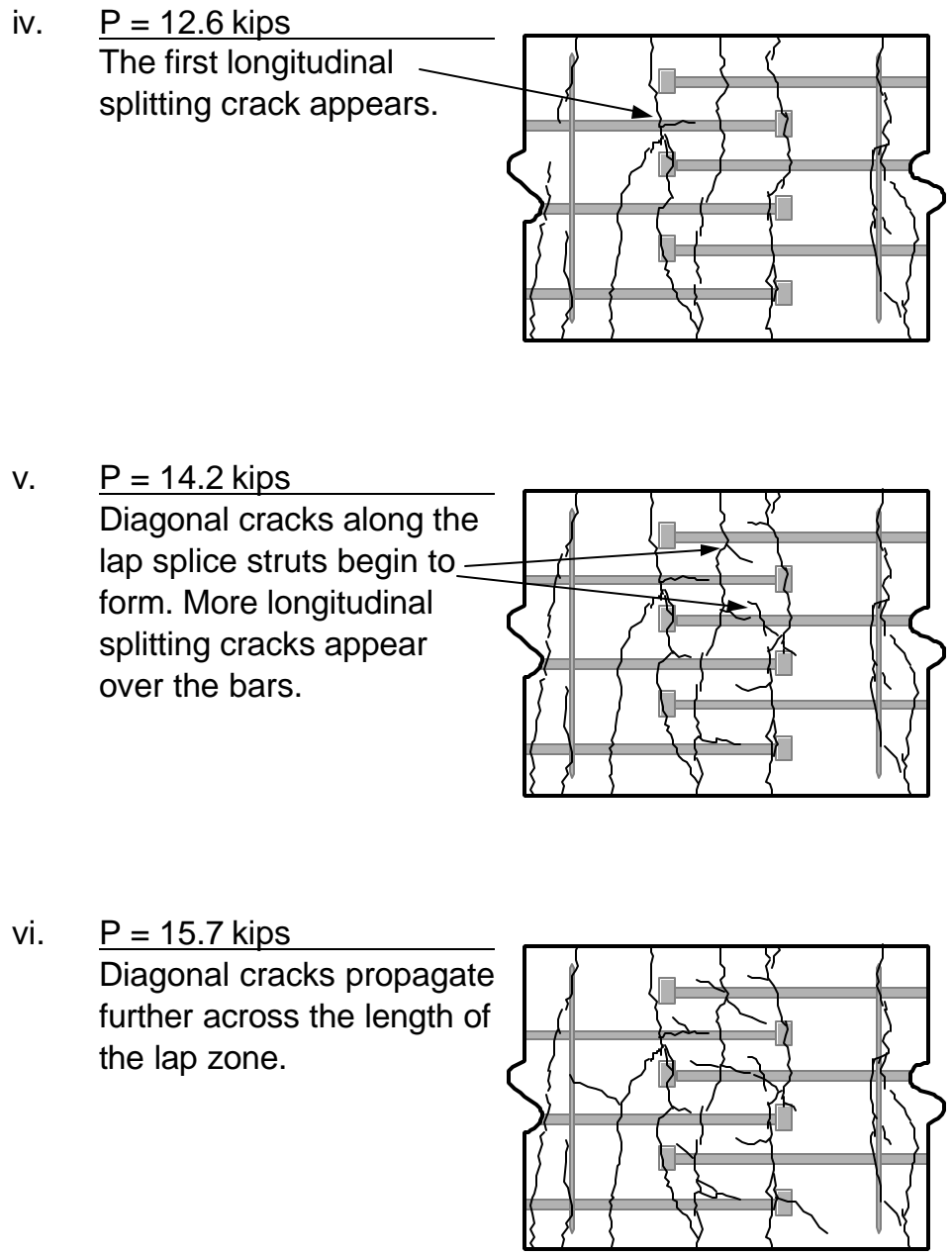


Figure 9-1b: Crack development in a typical unconfined lap splice test (specimen LS-08-04.04-12-10(N)-1) (continued)

- vi. P = 16.6 kips
Failure. Diagonal cracks extend the full length of the lap zone. Extensive cracking occurs over many of the heads.

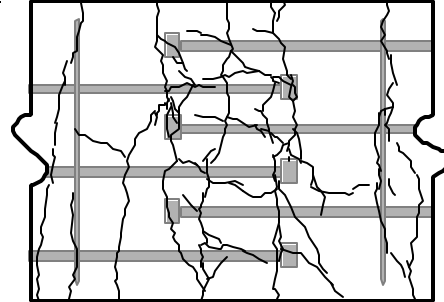
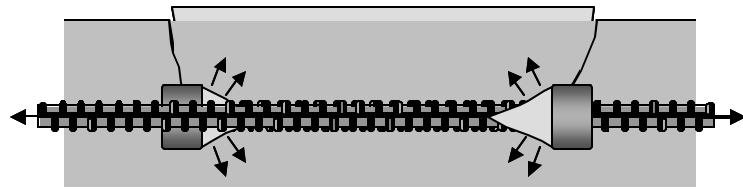


Figure 9-1c: Crack development in a typical unconfined lap splice test (specimen LS-08-04.04-12-10(N)-1) (continued)

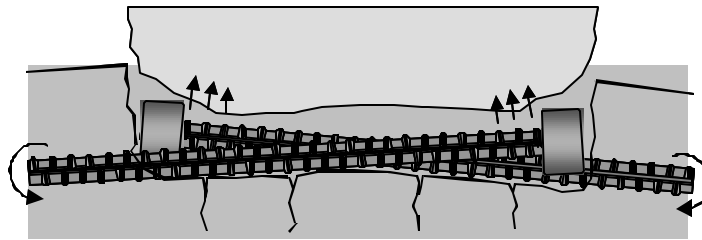


Figure 9-2: Photograph of failed lap splice specimen with cover removed from lap zone (specimen LS-08-04.04-12-10(N)-1)

Inspection of the internal crack patterns is important for understanding the mechanism of force transfer. A photograph of another large headed specimen (LS-08-04.70-10(N)-1) is shown in Figure 9-4. The internal cracking pattern reveals wedges at the heads and diagonal cracks propagating from edges of the heads to opposing lap bars. The diagonal cracks indicate that force transfer from the head occurred along struts projected at diagonals. Because force transfer between opposing bars occurred along diagonal strut lines, the full lap length was not utilized for anchorage of the bars. The anchorage point of a lap bar begins where the projected struts from opposing bars intersect that bar (Figure 9-5). The angles of these struts were measured in several specimens and were typically at about 55° from the axis of the bar. Furthermore, the full anchorage length of headed bars was not active in bond. A short length next to the head was taken up by the formation of a concrete wedge. The typical wedge length was approximately equal to the side dimension of the head. For rectangular heads, the wedge length was approximately equal to the geometric average of the sides. Figure 9-6 shows close up photos of concrete wedges for circular and rectangular head shapes. The wedges of the lap splice specimens were flattened along the horizontal plane of the lap and projected along the sides of the head into the paths of the struts. Projection of the concrete wedge into the path of the strut occurred in many CCT node tests as discussed previously.



i. Wedge and Bond Splitting (caused by bar tension)



ii. Prying (caused by beam curvature)

Figure 9-3: Causes of cover spalling in lap zone

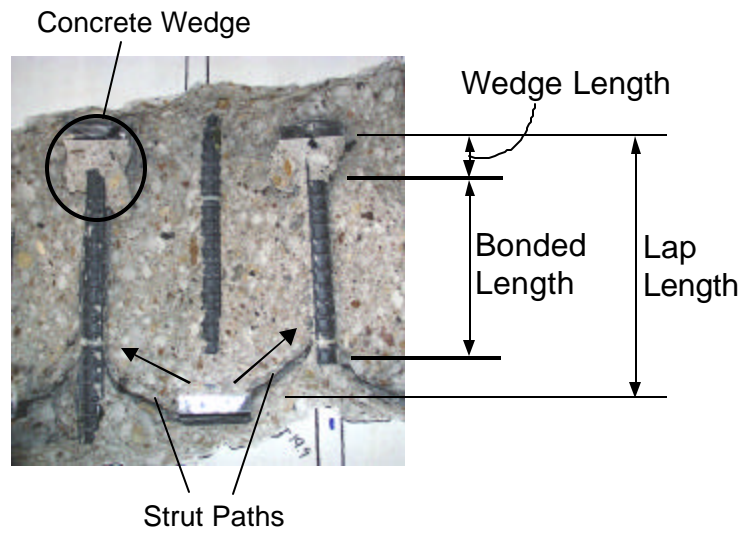


Figure 9-4: Features of force transfer in lap zone (photo of specimen LS-08-04.70-12-10(N)-1)

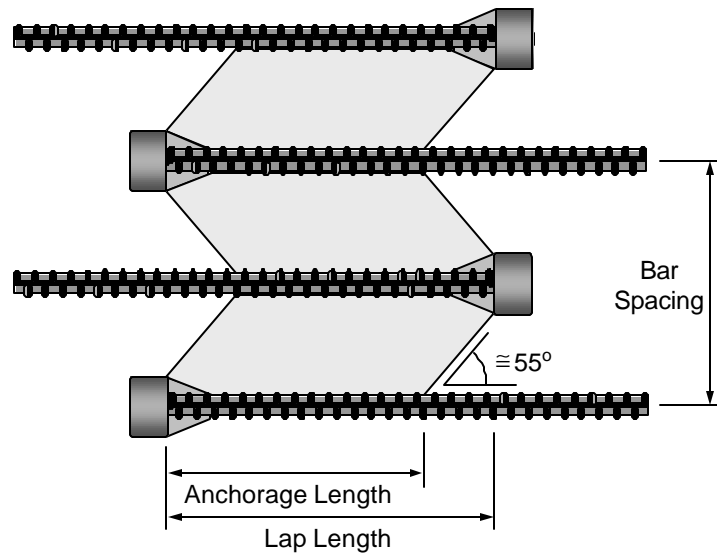


Figure 9-5: Strut model for lap splices



i. Round Head
(LS-08-04.04-12-10(N)-1)



ii. Rectangular Head
(LS-08-04.70-08-10(N)-1)

Figure 9-6: Photos of concrete wedges in lap splice specimens

9.1.1 Effect of Lap Length

The effect of lap length on cracking behavior is demonstrated by four large-headed specimens with varying lap lengths. Crack patterns at failure are shown for specimens with lap splice lengths of 5, 8, 12, and 14 bar diameters in Figure 9-7.

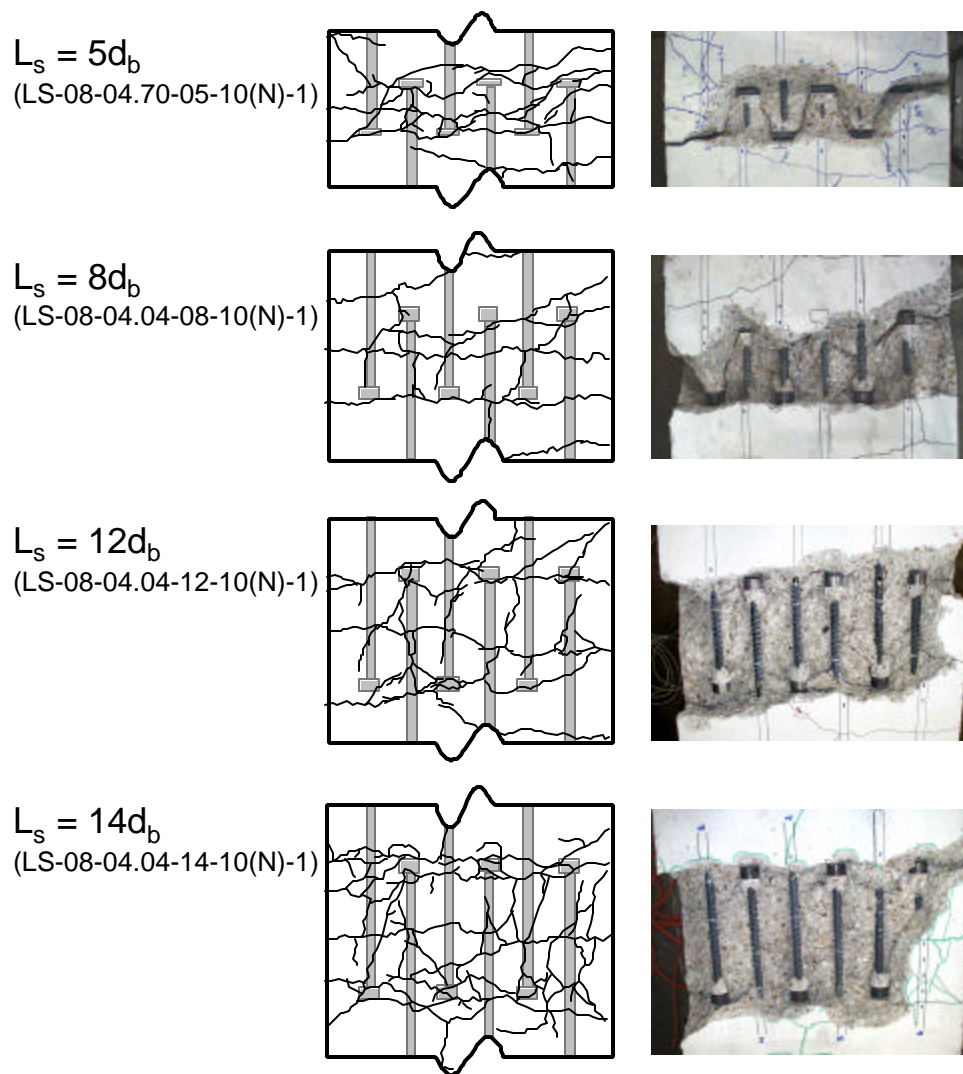


Figure 9-7: Crack patterns for large headed specimens with different lap lengths

At a lap length of $5d_b$, the internal crack pattern (photos on the right in Figure 9-7) shows that the failure surface propagated along direct paths between opposing heads. This crack pattern suggests that the lap length was so short that force transfer occurred directly between the heads with no contribution from bond. As the lap length was increased to $8d_b$, the failure surface

propagated from the heads to points on the opposing bars in front of the heads. This crack pattern indicates that the anchorage length of the bars included a portion of the deformed bar length over which bond was active. Subsequent increases in lap length did not change the internal crack pattern significantly. However, the external crack pattern of the $14d_b$ lap specimen was much more extensive than the companion specimens with shorter laps. This occurred because this specimen nearly reached yield before it failed. The increase in moment capacity allowed the specimen to reach a higher curvature, which consequently caused more extensive cracking.

9.1.2 Effect of Head Size

The effect of head size on cracking behavior is demonstrated by three specimens of various head size (LS-08-00.00-08-10(N)-1, LS-08-01.18-08-10(N)-1, and LS-08-04.04-08-10(N)-1). These specimens had $8d_b$, non-contact laps and were cast in the same group. Crack patterns at failure are shown for non-headed, small-headed, and large-headed specimens in Figure 9-8.

The internal crack patterns showed that all three specimens demonstrated similar behavior. Transfer of force between opposing bars was accomplished by struts propagating at roughly 55° angles to the axes of the bars. The non-headed specimen demonstrated more longitudinal bond splitting cracks at failure than did the other two. The large headed specimen demonstrated more diagonal strut cracks than did the small- and non-headed specimens. The small-headed specimen developed zig-zag crack patterns on its surface that nearly perfectly mimicked the flow of strut forces between bars. Overall, however, the basic mechanism of force transfer was unchanged by head size.

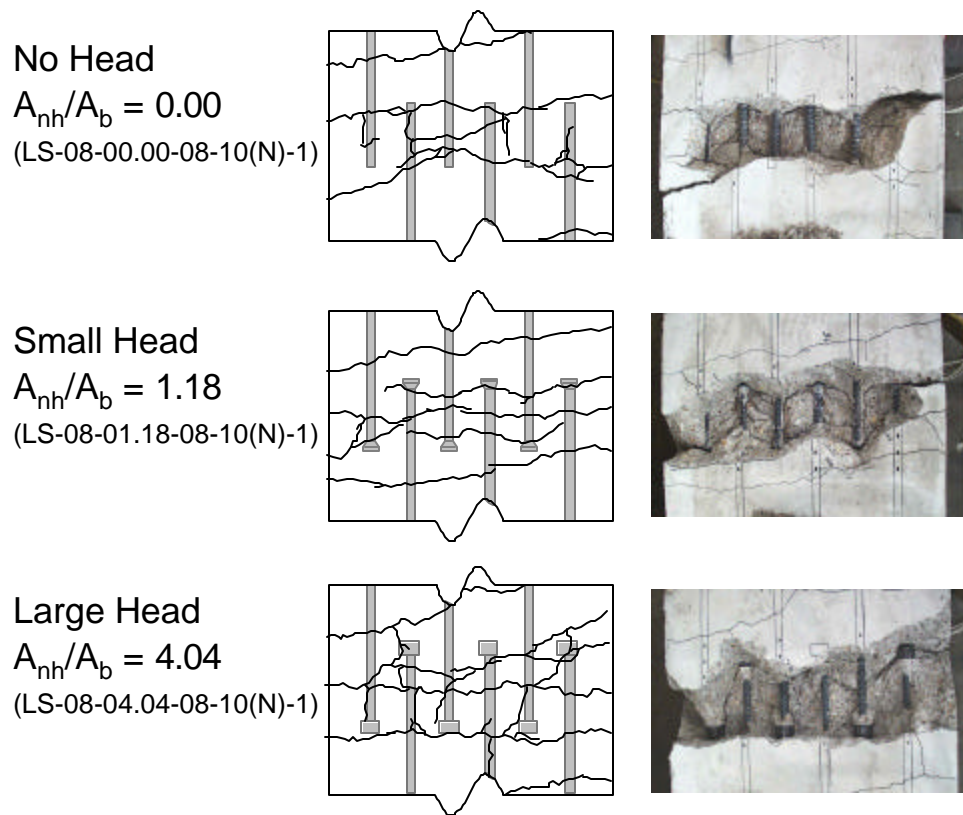


Figure 9-8: Crack patterns for specimens of different head sizes ($L_s = 8d_b$)

9.1.3 Effect of Lap Configuration

Two lap configurations were tested: contact and non-contact. Two pairs of tests with $5d_b$ lap lengths provided data on the effect of lap configuration. Small- and large-headed bars were tested under both configurations. Crack patterns at failure are presented for these specimens in Figure 9-9.

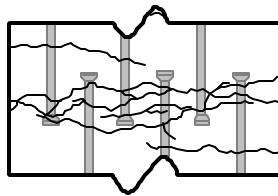
External crack patterns show that less cracking occurred when lapped bars were placed in contact with one another. External crack patterns of adjacent lap tests showed fewer longitudinal and diagonal cracks within the lap zone. Examination of the internal cracking pattern of the large-

headed contact splice shows diagonal cracks propagating between the non-adjacent opposing bars. It appears as if the headed bars developed unsymmetrical struts to the opposing bars on both sides. Thus the behavior does not seem to have differed much from the non-contact case, except that the strut mechanism of force transfer became distorted by the unsymmetrical spacing of bars.

i. Small Heads

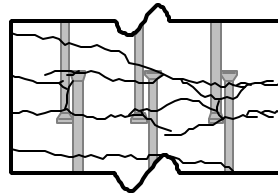
Non-Contact

(LS-08-01.18-05-10(N)-1)



Contact

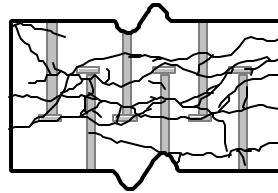
(LS-08-01.18-05-10(C)-1)



ii. Large Heads

Non-Contact

(LS-08-04.70-05-10(N)-1)



Contact

(LS-08-04.70-05-10(C)-1)

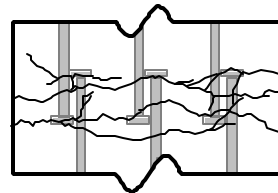


Figure 9-9: Crack patterns for contact and non-contact lap splices ($L_s = 5d_b$)

These test results derive from specimens of a very short lap length ($L_s = 5d_b$). Analysis of the effect of lap length on the mechanism of force transfer (Section 9.1.1) has shown that the $5d_b$ lap length was too short for a normal transfer of stress involving both bond and head bearing. Thus the tests presented in this section probably do not present a complete picture of the effect of lap configuration. This variable should be studied in tests of longer lap lengths.

9.1.4 Effect of Debonding

Two companion specimens provided information on the effect of debonding (LS-08-04-04-14-10(N)-1 and LS-08-04-04-14-10(N)-1-DB). These two specimens used large-headed bars with a $14d_b$, non-contact lap. Crack patterns at failure for these two specimens are shown in Figure 9-10.

Much less cracking developed in the debonded specimen. The cracks that did form, however, reached much larger crack widths than the bonded specimen. Transverse cracking in the debonded specimen occurred close to heads. Distinct diagonal cracks formed between two sets of opposing heads. Cracking around the heads in bonded specimens was typically complex with indications of bursting having occurred. This behavior was not evident in the debonded specimen. Following failure of the debonded specimen, the concrete cover in the lap zone could not be loosened even after large deformation was imposed on the specimen. Thus no photos of the internal crack pattern could be obtained.

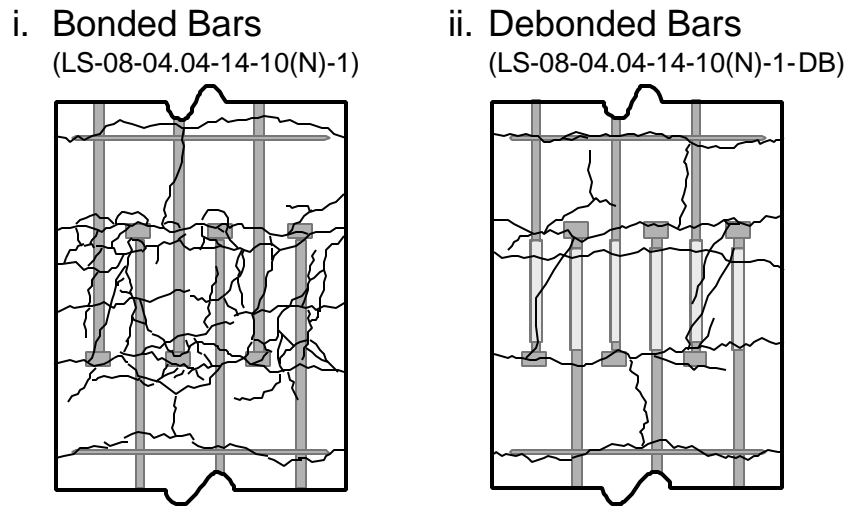


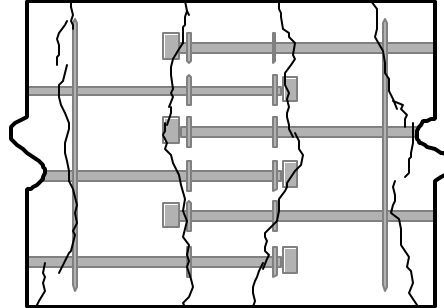
Figure 9-10: Crack patterns for bonded and debonded lap splices

9.1.5 Effect of Confinement

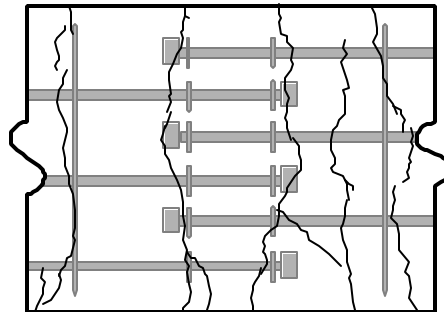
Two confinement details were tested: hairpins and the transverse tie-down detail. Crack development of a typical hairpin specimen (LS-08-04.04-12-10(N)-H0.6-1) is outlined in Figures 9-11a and 9-11b. Crack development of the hairpin specimens resembled typical unconfined specimen cracking. First cracking in the lap zone initiated near the heads (Figure 9-11a, part i). There was then gradual development of longitudinal and diagonal cracks within the lap zone as bond splitting and strut action occurred (parts ii, iii, and iv). Failure was more gradual than the unconfined case and marked by extensive cracking in the lap zone (Figure 9-11b, part v).

Examination of the internal cracking revealed that the hairpins had modified the shape of the concrete wedges at the heads (Figure 9-12). The wedges were enlarged to include the hairpins located at the heads. These hairpins seemed to have the effect of enhancing the head area. The hairpins away from the heads were located in the concrete mass outside of the anchorage length and thus were not active in the force transfer mechanism of the lap splice.

- i. P = 7.6 kips
First cracking in the lap zone occurs along the heads and the tops of the hairpins.



- ii. P = 10.9 kips
A diagonal crack forms at the edge of the lap zone. Additional transverse cracks form outside of the lap zone.



- iii. P = 14.0 kips
Diagonal cracks extend into the lap zone.

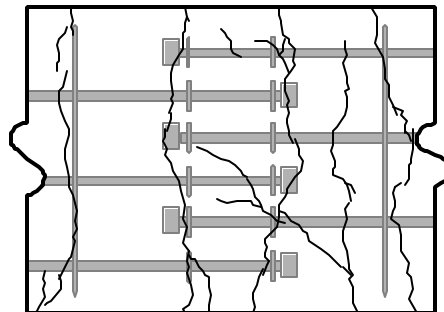
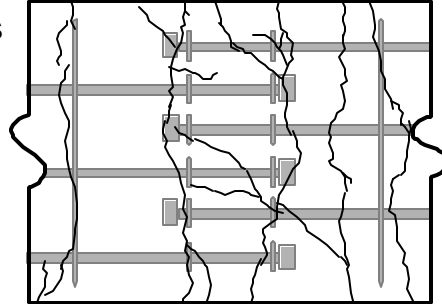


Figure 9-11a: Crack development in a typical hairpin confined lap splice test (specimen LS-08-04.04-12-10(N)-1-H0.6)

- iv. P = 17.0 kips
The first longitudinal cracks appear in the lap zone. Diagonal cracks extend across the length of the lap zone.



- v. P = 17.6 kips
Failure. Longitudinal and diagonal cracks extend across the length of the lap zone.

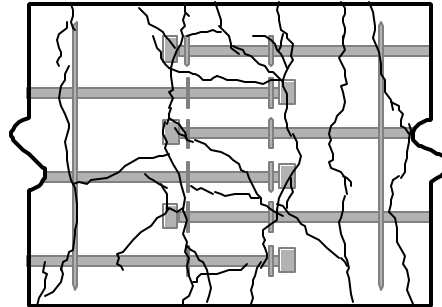


Figure 9-11b: Crack development in a typical hairpin confined lap splice test (specimen LS-08-04.04-12-10(N)-1-H0.6) (continued)

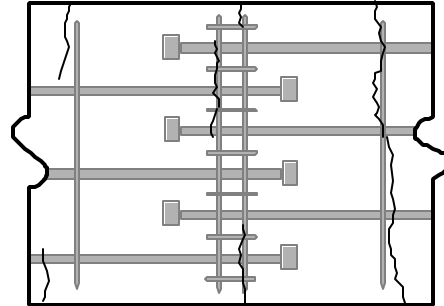


Figure 9-12: Internal cracking with hairpin confinement (specimen LS-08-04.04-12-10(N)-1-H0.6)

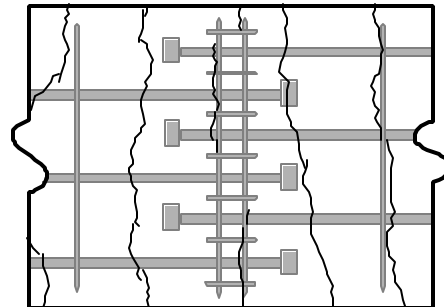
Crack development of the specimen with the transverse tie-down detail is outlined in Figures 9-13a through 9-13c. Crack development in this test did differ in some aspects from the unconfined tests and the tests with hairpin confinement. First cracking in the lap zone occurred over the transverse bars rather than the heads (Figure 9-13a, part i). These cracks never propagated across the full width of the specimen. Full width transverse cracks formed just outside of the lap zone (part ii). Longitudinal and diagonal cracks formed within the lap zone (Figure 9-13b, parts iv & v), however, their progression was checked by the presence of the transverse steel. Diagonal cracks propagated from the heads to the point on the opposing bar that crossed underneath the transverse steel rather than the head of the opposing bar (parts v & vi). At failure (Figure 9-13c, part vii), some diagonal cracks appear within the panels of the transverse stirrup cage. Residual capacity remained in the specimen after failure (part viii). The concrete cover over the lap zone could not be spalled off even after severe deflection had been imposed on the specimen.

Crack patterns at failure for unconfined, hairpin confined, and the transverse tie-down confined specimens are provided in Figure 9-14 for comparison. The transverse tie-down detail provided much more effective confinement than the hairpins. The hairpins enhanced the bearing area of the heads, but the similarities between the crack development of unconfined and hairpin confined specimens would indicate the hairpin detail did not fundamentally alter the strut-and-tie mechanism of force transfer between bars. However, the transverse tie-down did by providing a transverse tie component into the model. This method was a much more efficient means of improving the capacity of the lap splice.

- i. P = 6.5 kips
First cracking in the lap zone occurs along the transverse confining bars.



- ii. P = 8.2 kips
Transverse cracks form outside of the lap zone.



- iii. P = 12.9 kips
Transverse cracks propagate within the lap zone.

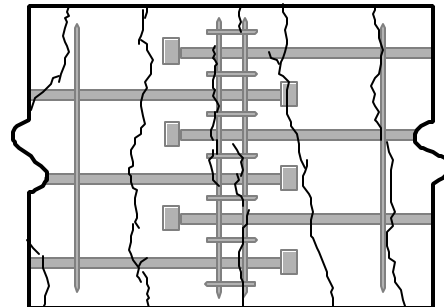
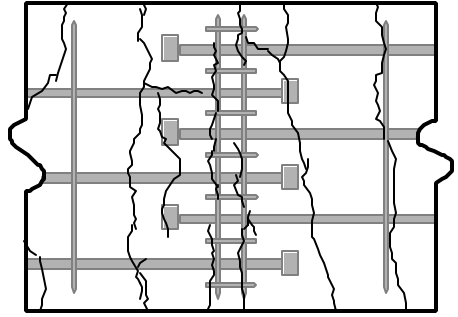
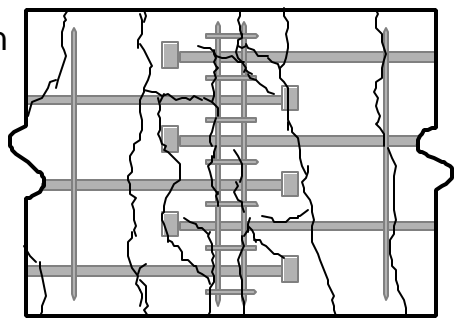


Figure 9-13a: Crack development in the transverse stirrup cage test (specimen LS-08-04.04-12-10(N)-1-TTD)

- iv. P = 15.1 kips
Longitudinal cracks begin to form at the edge of the lap zone. Transverse cracks in the lap zone continue to propagate.



- v. P = 17.3 kips
Diagonal cracks form within the lap zone.



- vi. P = 18.5 kips
Extensive cracking within and outside of the lap zone.

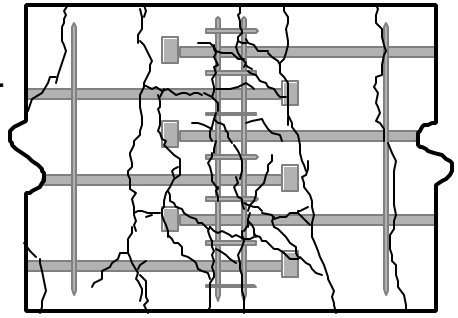
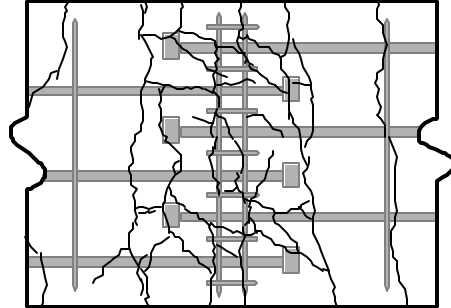


Figure 9-13b: Crack development in the transverse stirrup cage test (specimen LS-08-04.04-12-10(N)-1-TTD) (continued)

- vii. P = 19.0 kips
Maximum capacity.



- viii. P = 13.0 kips
Midspan deflection = 1.6".
Significant residual capacity exists in the specimen,
but crack formation is unrestrained.

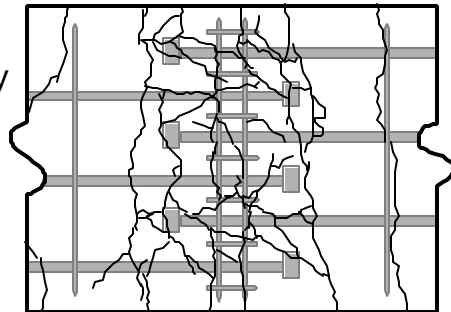
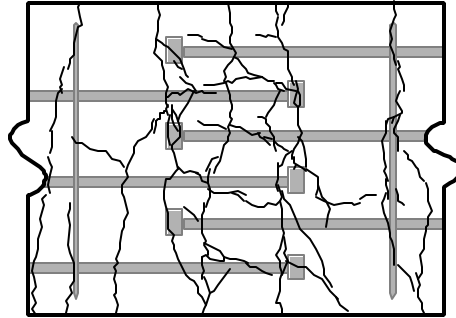
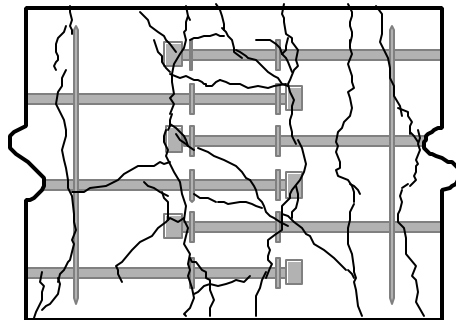


Figure 9-13c: Crack development in the transverse stirrup cage test (specimen LS-08-04.04-12-10(N)-1-TTD) (continued)

i. Unconfined
(LS-08-04.04-12-10(N)-1)



ii. Hairpin Confinement
(LS-08-04.04-12-10(N)-1-H0.6)



iii. Transverse Tie-Down Confinement
(LS-08-04.04-12-10(N)-1-TTD)

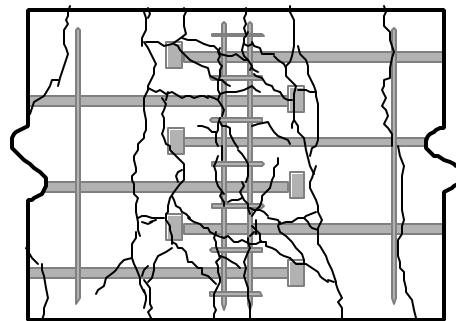


Figure 9-14: Crack patterns at failure for unconfined and confined specimens

9.2 STRESS/STRAIN DEVELOPMENT

Stresses along the headed bars in the lap splice tests developed in a manner similar to that in the CCT node tests. Anchorage consisted of a two stage process: an initial period when resistance was provided primarily by bond, then a transition in which bond deteriorated and stress was transferred to the head. The bond and head bearing components of bar stress for specimen LS-08-04.70-12-10(N)-1 (large heads, $12d_b$ lap length) are plotted in Figure 9-15. This plot closely resembles a plot for CCT node tests presented in Figure 6-14.

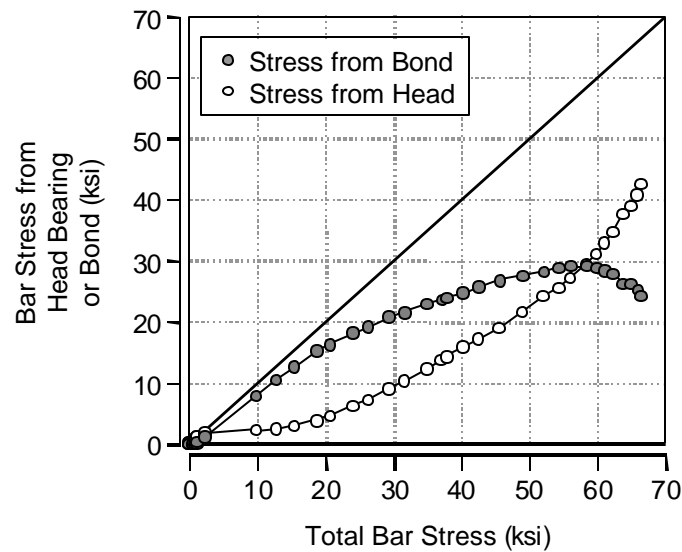


Figure 9-15: Components of bar stress provided by bond and head bearing in a typical lap splice specimen (LS-08-04.70-12-10(N)-1)

The effect of the variables on this basic stress and strain behavior is examined in the following subsections.

9.2.1 Effect of Head Size

Stress profiles along headed and non-headed lapped bars are presented in Figure 9-16. The two profiles have similar shapes: a rise in stress starting from the end of the bar and flattening in the tail end of the lap zone. The profile for the headed bars lies above the profile for the non-headed bars. The offset is due to the additional capacity provided by the heads.

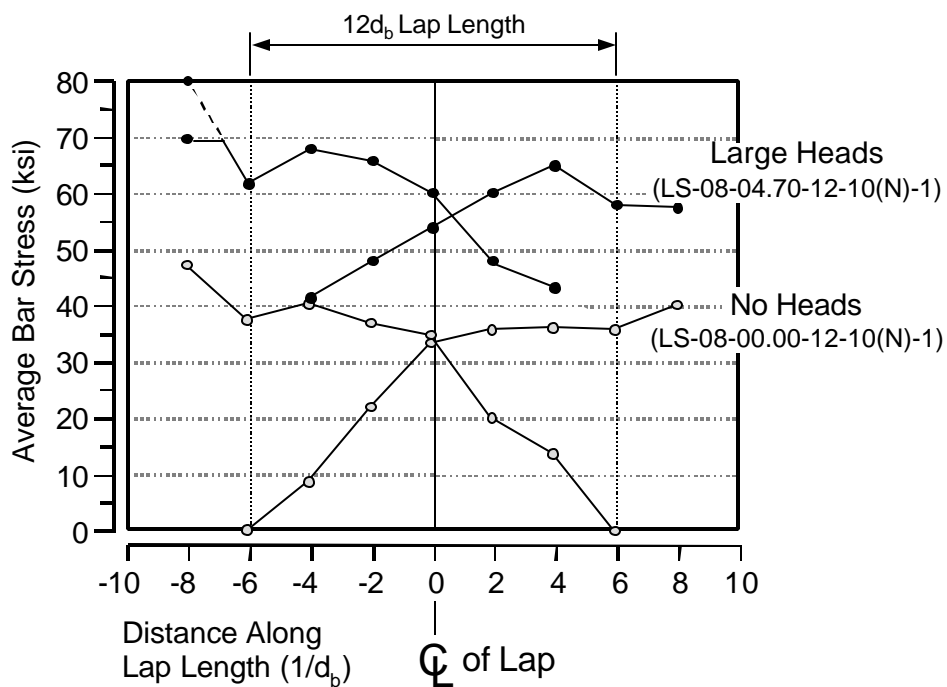


Figure 9-16: Stress profiles for headed and non-headed lap splices ($L_s = 12d_b$)

The stress data presented in Figure 9-16 were used to determine bond stress profiles for the non-headed and headed bar tests. Bond profiles for the headed bar test are plotted in Figure 9-17. The bond profile for the non-headed bar test is presented in Figure 9-18.

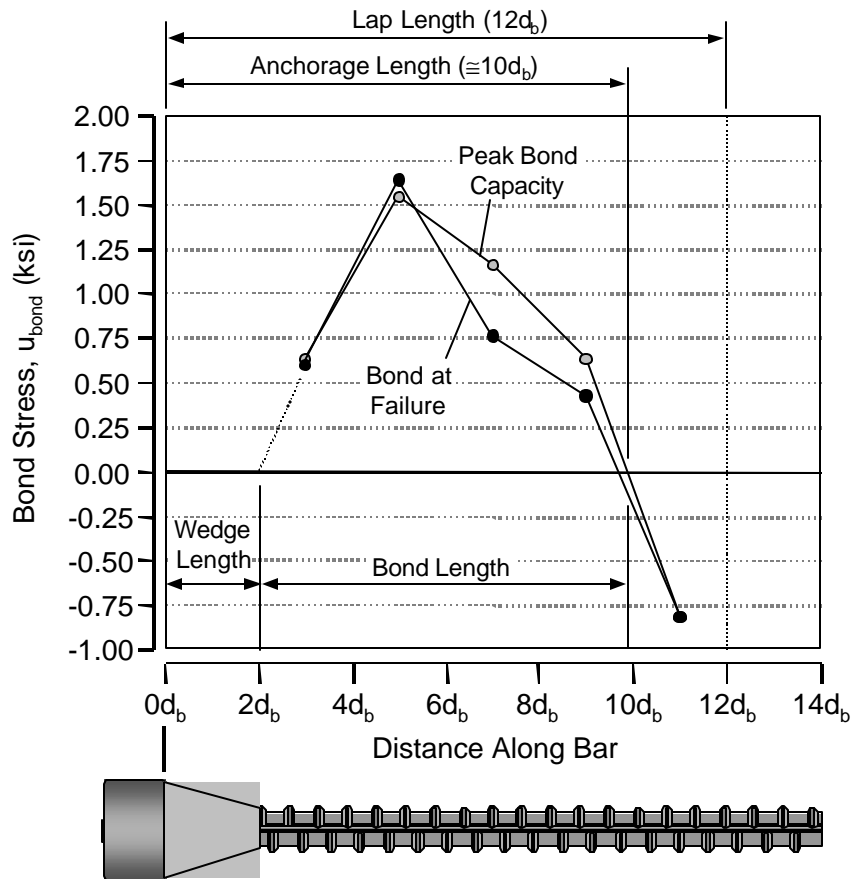


Figure 9-17: Bond profiles for a headed bar lap splice (specimen LS-08-04.70-12-10(N)-1)

The bond profile of the headed bar reinforces many of the observations gathered from the cracking behavior. Bond drops to zero at a point before the end of the lap length. That point is the anchorage point of the bar and corresponds with the distance determined by the intersection of struts drawn between opposing bars (roughly $10d_b$ for the specimen in Figure 9-17). Near the head, the drop off in bond between $3-5d_b$ suggests that bond terminates at about $2d_b$. This most likely occurs because the concrete wedge which forms between $0-2d_b$ prevents further stress transfer along that length of bar. Thus, the anchorage length available for bond should not include

the wedge length. Profiles for peak bond and bond at failure are plotted in Figure 9-17. The final bond profile (at failure) resembles the peak bond profile except for some drop in stress near the anchorage point. The change in profile indicates that bond deterioration occurs away from the head.

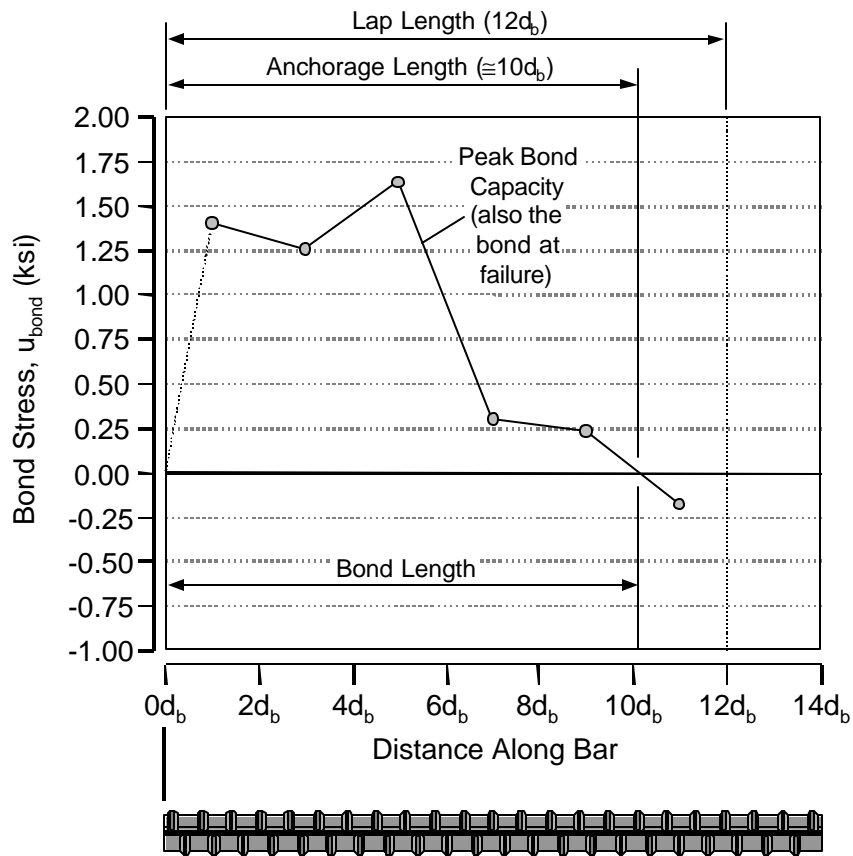


Figure 9-18: Bond profiles for a non-headed bar lap splice (specimen LS-08-00.00-12-10(N)-1)

The non-headed bond profile was different in shape from the headed bond profile. Higher bond stresses were observed closer to the end of the bar. This was expected since there was no

bearing wedge that interfered with bond. The anchorage point occurred at roughly the same location as the headed bars. The location of the anchorage point is primarily a function of lap length and the spacing between opposing bars. Head size was not expected to affect the location of the anchorage point and the data in Figures 9-17 and 9-18 support that conclusion. The magnitude of local bond stresses for the non-headed bars was approximately that found for the headed bars. The average peak bond stresses of the two specimens depicted in Figures 9-17 and 9-18 were nearly the same (0.91 ksi and 0.94 ksi respectively).

9.2.2 Effect of Lap Length

The effect of lap length on bond is illustrated in Figure 9-19. Peak bond stress profiles for $8d_b$, $12d_b$, and $14d_b$ lap lengths are plotted in the Figure (specimens LS-08-04.04-08-10(N)-1, LS-08-04.04-12-10(N)-1, and LS-08-04.04-14-10(N)-1). The plots show the anchorage point of the bars moved closer to the head as the lap length was reduced. As the lap length shrank to $8d_b$, there was little bond length left. Furthermore, the magnitude of the bond stress was lower than the bond stresses measured for the $12d_b$ and $14d_b$ lap lengths. An analogous plot for a $5d_b$ test could not be included because there was no measurable contribution from bond.

The contributions from bond and head bearing to splice bar stress are plotted for a large headed, $8d_b$ lap length test (specimen LS-08-04.70-08-10(N)-1) in Figure 9-20. The plot shows the same trend as was seen in previous plots of bond and head bearing contribution. However, in this case, the contribution from bond was less than the contribution from the head at all increments measured during the load process of the test. The lap length was too short for the maximum bond stresses to develop.

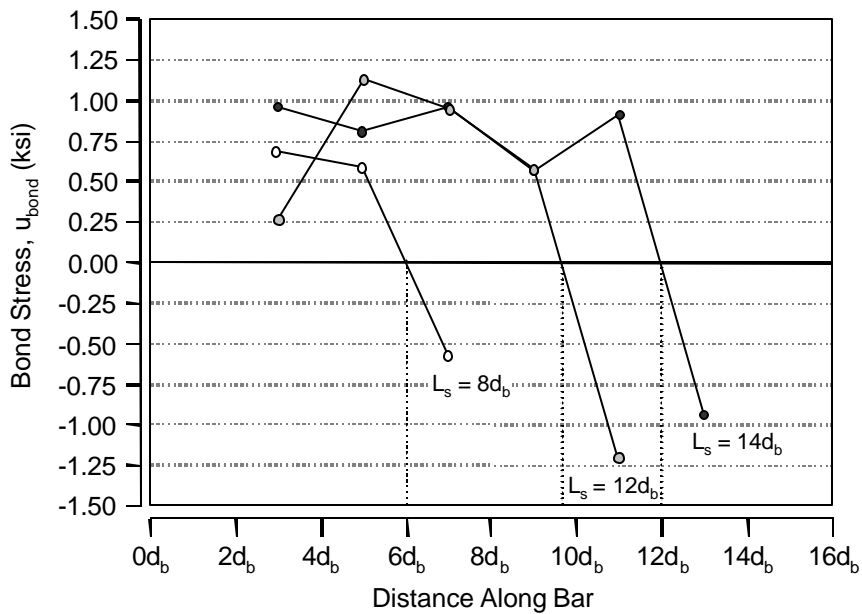


Figure 9-19: Bond profiles for a headed bar lap splices of varying lap length (specimens LS-08-04.04-08-10(N)-1, LS-08-04.04-12-10(N)-1, and LS-08-04.04-14-10(N)-1)

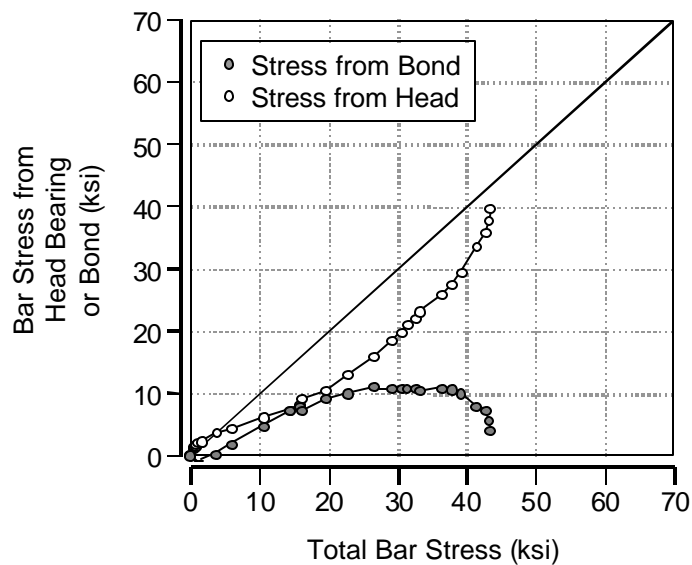


Figure 9-20: Components of bar stress provided by bond and head bearing in a lap splice of short length (LS-08-04.70-08-10(N)-1)

9.2.3 Effect of Confinement

The bond stress profile plot in Figure 9-21 for a hairpin confined specimen (LS-08-04.04-12-10(N)-1-H0.6) shows that the bond stress profile was not significantly altered by the presence of the hairpins when compared with Figure 9-17. The plot in Figure 9-21 illustrates the primary flaw of the hairpin detail that was studied in this project. No hairpins were placed along the bond length of the bars. The hairpin close to the head was located within the wedge length and the hairpin away from the head was located just outside the anchorage length. Had the two hairpins been placed along the bonded length, they may have helped prevent deterioration of the bond and thus enhanced the overall capacity of the lap splice much more efficiently. As detailed, the locations of the hairpins were poorly chosen and the full potential of the hairpin bars may have been missed by the tests performed in this study.

Bond stress profiles for the transverse tie-down specimen are shown in Figure 9-22. The peak bond stress profile resembles that of the unconfined and hairpin confined specimens, however, the bond stress at failure was much different. At failure, the bond stress had deteriorated significantly. The anchorage point had shifted to a location only $6d_b$ from the head and very little bond was measured along the remaining anchorage length. The final anchorage point was approximately midway between the transverse confining bars. The average bond over the initial $10d_b$ anchorage length was approximately zero at failure. All of the bar stress at failure was carried by the heads. The capacity of the heads was significantly improved over the unconfined and hairpin confined tests.

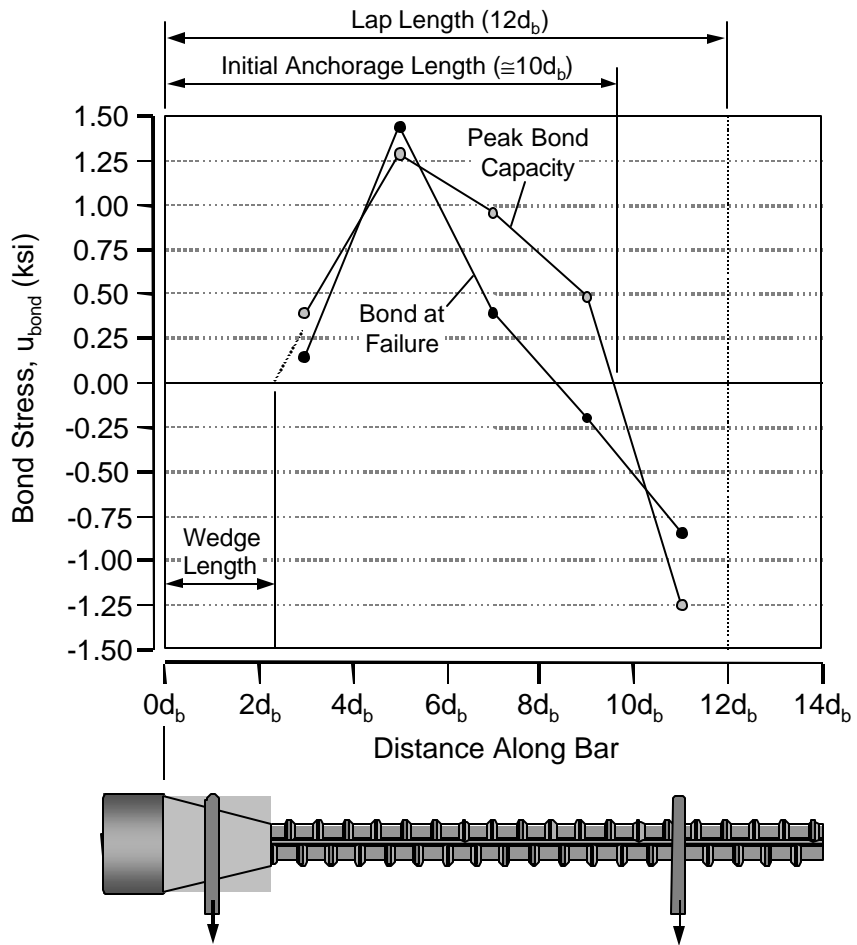


Figure 9-21: Bond profiles for a headed bar lap splice confined by hairpins (specimen LS-08-04.04-12-10(N)-1-H0.6)

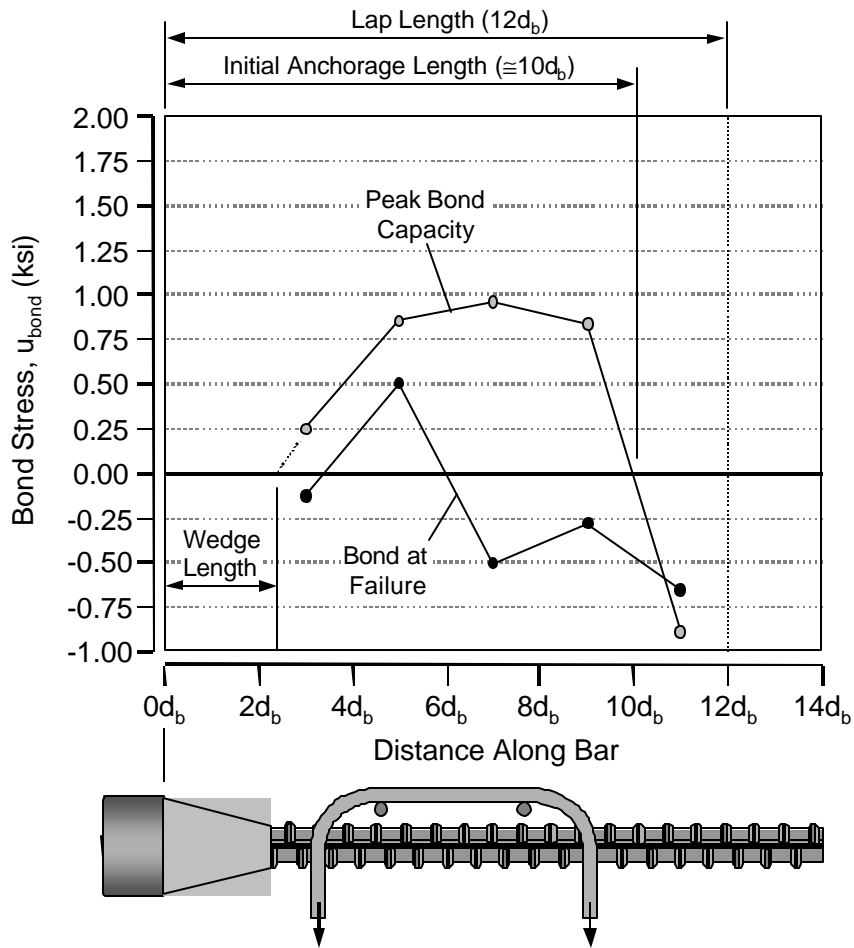


Figure 9-22: Bond profiles for a headed bar lap splice confined by transverse and tie-down bars (specimen LS-08-04.04-12-10(N)-1-TTD)

9.2.3.1 Stress Development in the Hairpins

Strain gages were placed on the hairpin bars in order to determine their activity as stress in the lap splice increased. Hairpin force is plotted against bar stress at the head in Figure 9-23. The data are from a single bar and its hairpins (bar 2) from a $12d_b$ lap splice (LS-08-04.04-12-10(N)-1-H0.6). The plot in Figure 923 shows that the hairpin further from the head did not develop any tensile force. This was due to the mistake of placing the further hairpin outside of the

anchorage length. The hairpin closest to the head did develop some force. The growth of that force did not initiate until the bar stress reached a level comparable to the maximum stress obtained by unconfined companion specimens. The head reached a stress at which the unconfined concrete would have failed in tension. Most likely, that process began and the tensile force in the concrete was transmitted into the hairpin bar. Force in the hairpin increased even after strain readings from the headed bar indicated yielding (that particular bar showed signs of yielding, but on average, the lapped bars in this specimen did not reach stresses as high as yield).

The data in Figure 9-23 represent a specimen with good results from the hairpin instrumentation. Much of the rest of the strain data from the hairpin bars were erratic and in many cases, the behavior of the hairpin bars could not be determined. Local strains and sideways deformation of the hairpins was frequently observed during the post-failure examination of the lap splice. The hairpin bars were instrumented to determine tensile strains, yet much of the strain imposed on those bars resembled dowel action. The data in Figure 9-23 suggest certain tensile behavior which is plausible, however, there may be other actions occurring between the headed bars and the hairpins which are not represented by that data.

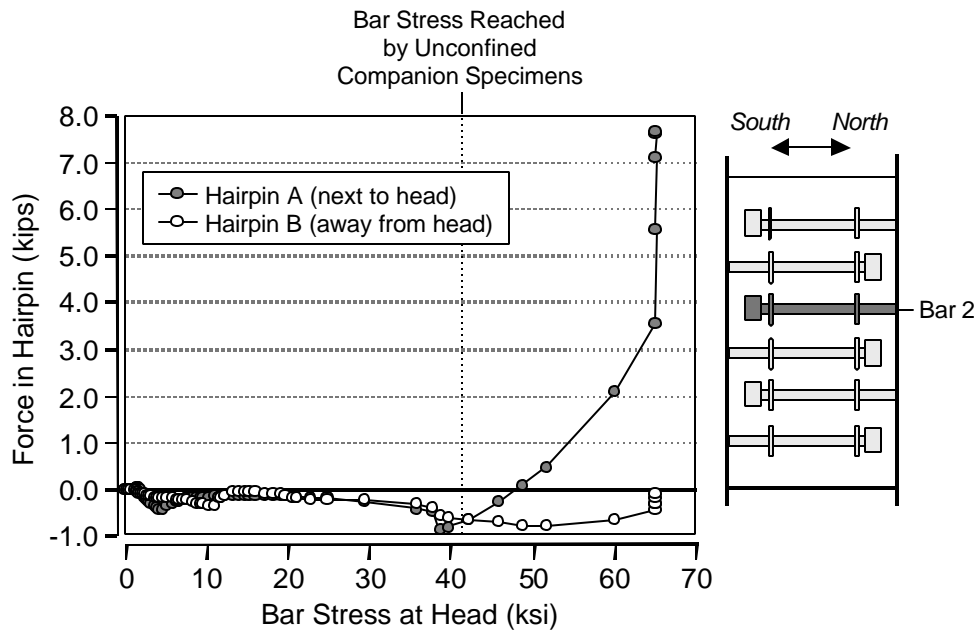


Figure 9-23: Hairpin force versus bar stress (specimen LS-08-04.04-12-10(N)-1-H0.6)

9.2.3.2 Stress Development in the Transverse Tie-Down Detail

Strain gages were placed on the transverse bars and tie-down bars of the transverse tie-down detail. Strain data from the transverse bars are presented in Figures 9-24 and 9-25. Strain data from the tie-down bars are presented in Figures 9-26 and 9-27.

Average transverse bar strain is plotted against the lapped bar stress at the heads in Figure 9-24. The plot shows that the transverse bar strain increased almost linearly with the stress at the heads of the lapped bars. This indicates a very direct link between the heads and the transverse bars. The #3 transverse bars reached about 40% of their yield strain before the specimen failed. The strain profile at failure along these transverse bars is plotted in Figure 9-25. The strains peaked slightly on the west side of the lap zone where longitudinal and diagonal cracks passed across the lap zone, but the strain profile was relatively constant across the width of the specimen.

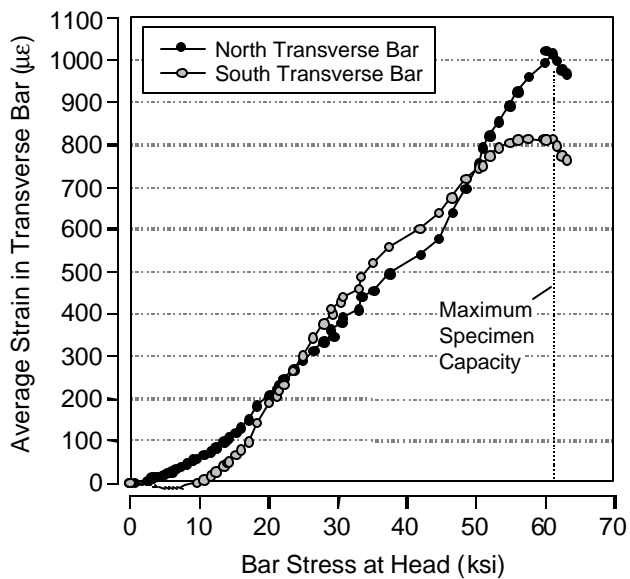


Figure 9-24: Transverse strain versus splice bar stress (specimen LS-08-04.04-12-10(N)-1-TTD)

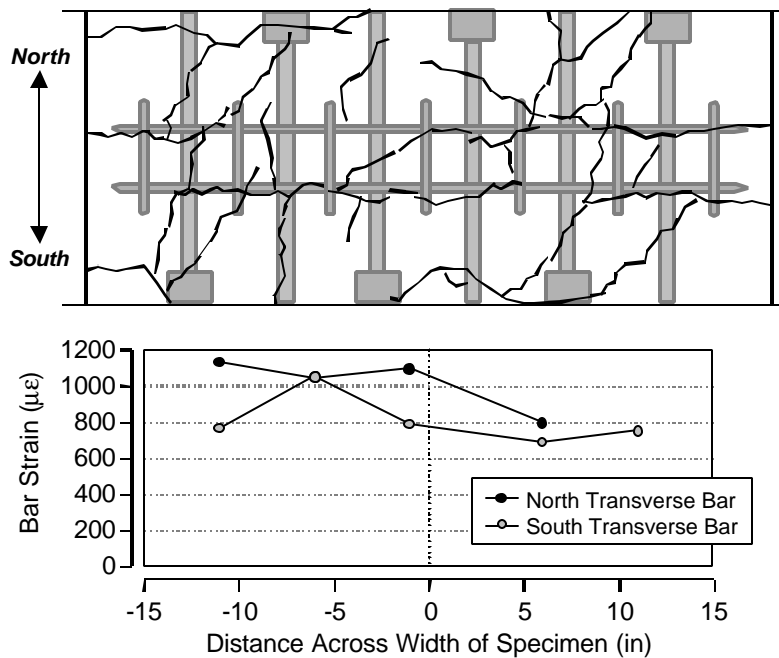


Figure 9-25: Strain profiles in transverse bars of LS-08-04.04-12-10(N)-1-TTD

Average tie-down strains are plotted against lapped bar stress at the heads in Figure 9-26. Unlike the transverse strains, the tie-down bars were not active until the lapped bars had reached stresses of about 50 ksi at their heads. Furthermore, the tie-downs near the center of the specimen developed the largest strains. Once these tie-downs became active, they did not gain significant strain (only about 15% of the yield strain) before the specimen reached its maximum capacity. The evidence shows that the tie-downs were not part of the primary strut-and-tie mechanism of force transfer like the transverse bars were. Figure 9-27 shows the strain profiles of the tie-down bars at failure. Several of the strain gages on the southern legs of the tie-downs were damaged during casting, however, a complete profile was determined for the northern legs of the tie-downs. The profile peaks in the center indicating that as the location of the greater spalling stresses produced by the lap splice.

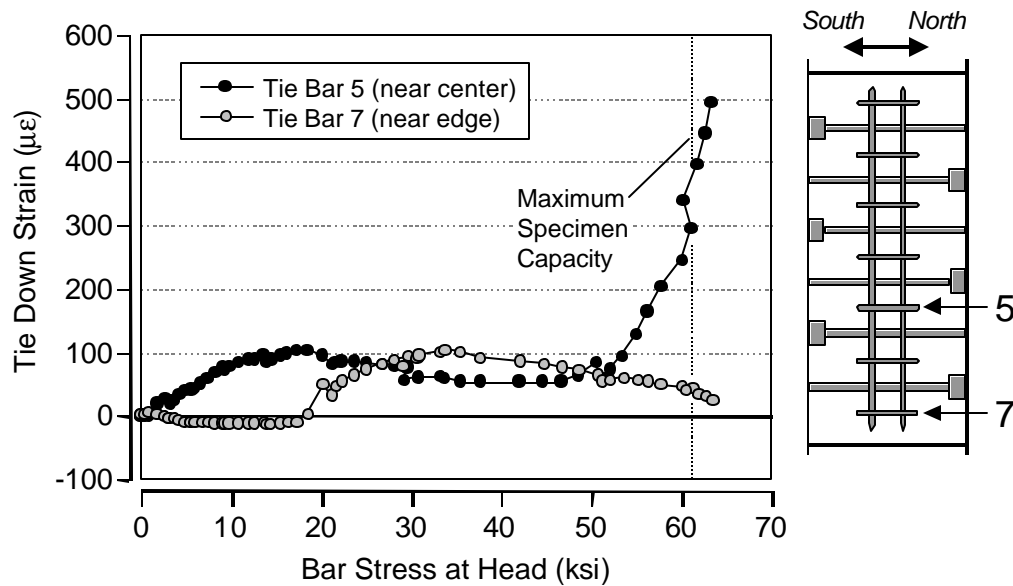


Figure 9-26: Tie-down strain versus splice bar stress (specimen LS-08-04.04-12-10(N)-1-TTD)

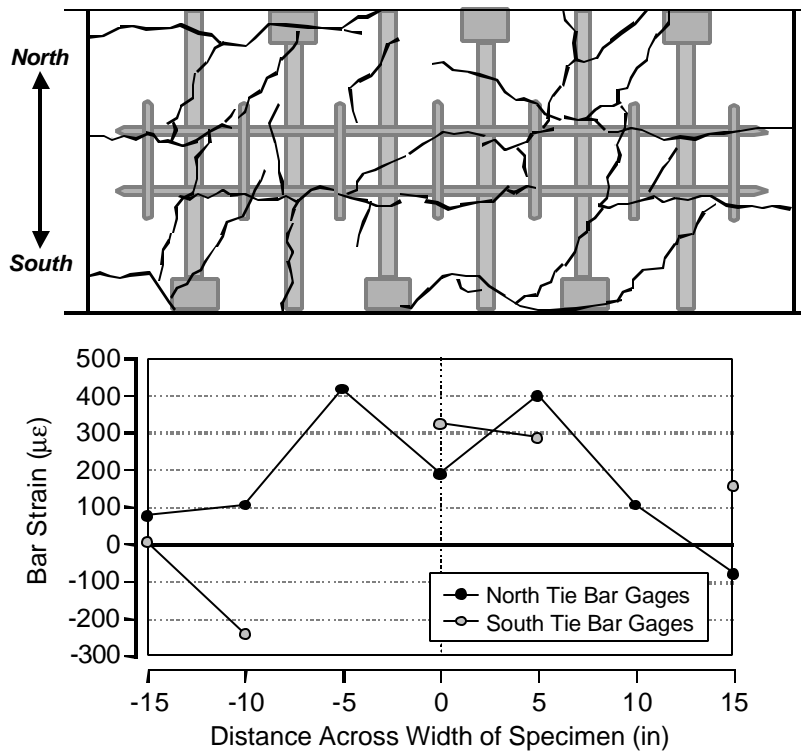


Figure 9-27: Strain profile in tie-down bars of LS-08-04.04-12-10(N)-1-TTD

9.3 LOAD-DEFLECTION BEHAVIOR

Midspan deflection was measured during each test and compared to calculated load deflection curves based on experimentally determined material properties and moment-curvature calculations. In most cases the relationship between the calculated and measured deflections was very good. The use of headed bars in the lap zone did not affect the specimen stiffness and the deflection data did not provide revealing information about the behavior of the headed bar lap splices before failure. However, the deflection data did prove useful in illustrating the post-failure response provided by the headed bar lap splices. Two interesting sets of data are discussed in this section: bonded versus de-bonded behavior and unconfined versus confined behavior.

Load-deflection curves for bonded and debonded specimens (LS-08-04.04-14-10(N)-1 and LS-08-04.04-14-10(N)-1-DB) are presented in Figure 9-28. The bonded specimen data follow the calculated load-deflection data fairly well. The debonded specimen was clearly less stiff than the bonded one or the calculated response. This behavior is typical of structural concrete with debonded tensile reinforcement and was not surprising to observe in the test behavior. The debonded specimen also had less capacity than the bonded specimen. The most interesting difference between the two specimens was in the post-failure response. The bonded specimen lost capacity quickly following its peak. The debonded specimen was slow to fail, reaching a second peak after its initial failure. The removal of the bond and the detrimental splitting caused by the bond in the de-bonded specimen allowed the head to sustain a high capacity for longer than was sustained in the bonded specimen.

Load-deflection curves for unconfined and confined specimens (LS-08-04.04-12-10(N)-1, LS-08-04.04-12-10(N)-1-H0.6, and LS-08-04.04-12-10(N)-1-TTD) are presented in Figure 9-29. The three specimens had similar behavior before failure. The confined specimens both achieved higher capacities than the unconfined specimen. The hairpin confined specimen reached its peak capacity, then lost load gradually. The transverse tie-down confined specimen first departed from the calculated load-deflection response, then reached its peak. The point where the transverse tie-down confined specimen began to re-acquire load after departing from the calculated load-deflection response corresponds with the rise in tie-down strain shown in Figure 9-26. The initiation of strain development in the tie-downs was related to mechanisms associated with failure and loss of stiffness.

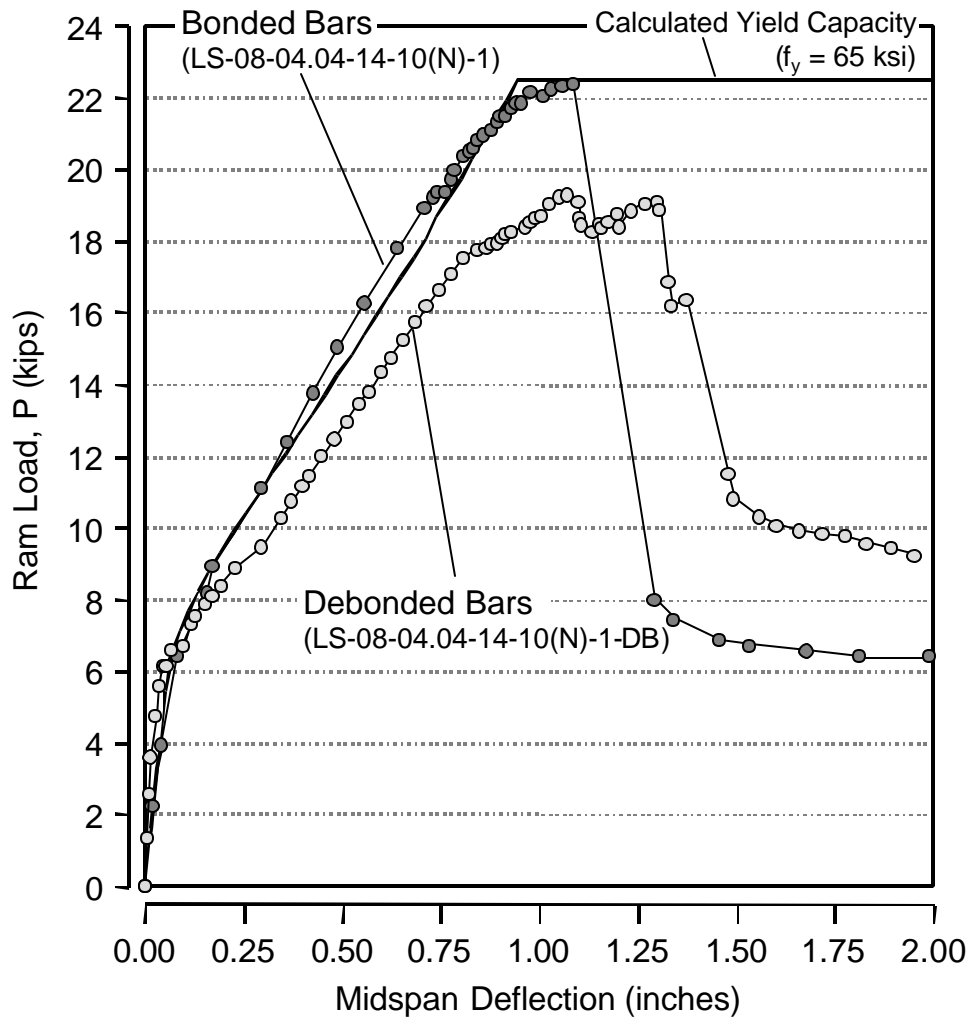


Figure 9-28: Load-deflection curves for bonded and debonded specimens

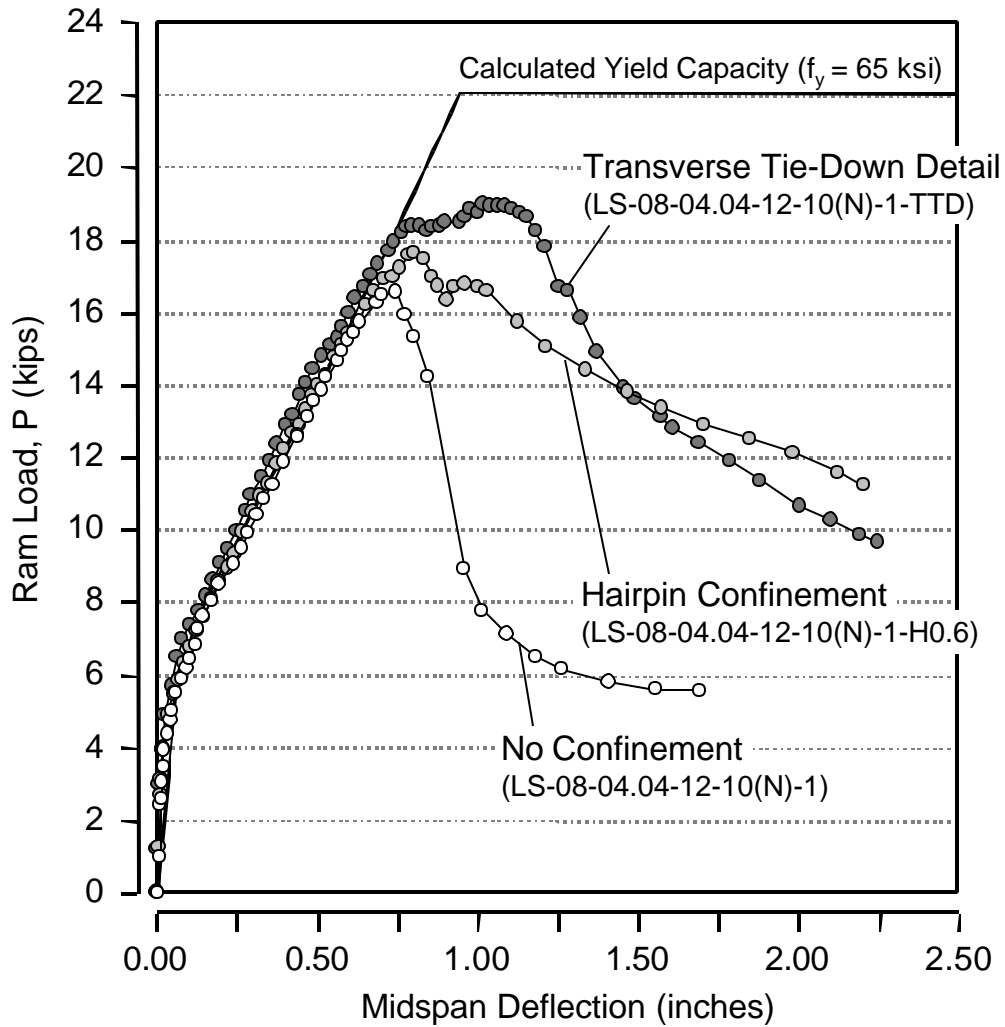


Figure 9-29: Load-deflection curves for unconfined and confined specimens

9.4 TRENDS IN THE DATA

9.4.1 Effect of Lap Length and Head Area

Normalized bar stress is plotted against lap length in Figure 9-30. Bar stress increased at a linear rate with increases in lap length. Non-headed and headed bar results fell along linear paths that paralleled one another. The relationship of headed bar stress to lap length seemed to equal that

of non-headed bar stress plus a constant. The bar stress predicted by the ACI formula for development length was generally too low compared with the non-headed test results. However, it should be kept in mind that the non-headed data set consists of only three tests.

The data from Figure 9-30 are represented in Figure 9-31 with a secondary axis for anchorage length. The strut-and-tie mechanism of force transfer between opposing lapped bars results in an anchorage length for the lapped bars that is less than the lap length. Due to the details of bar spacing and lap configuration in the test specimens of this study, the anchorage length was generally about $2d_b$ less than the lap length which is the offset used in Figure 9-31. The straight line from the x-axis intercept at $2d_b$ and passing through the non-headed data points fits that data well. The trend of the headed bar data show the same slope with a stress offset of about 20 ksi and suggests that headed bar capacity is equal to the capacity from bond of a deformed bar and a contribution from head bearing.

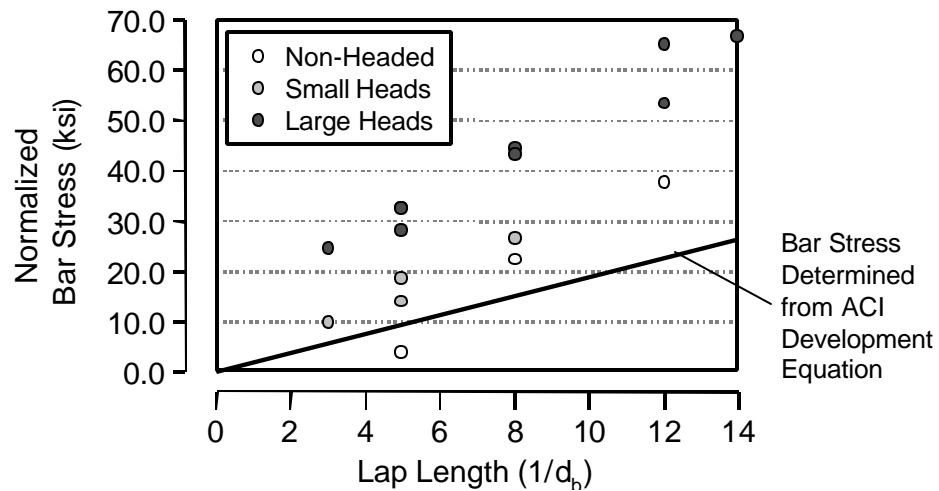


Figure 9-30: Bar stress versus lap length

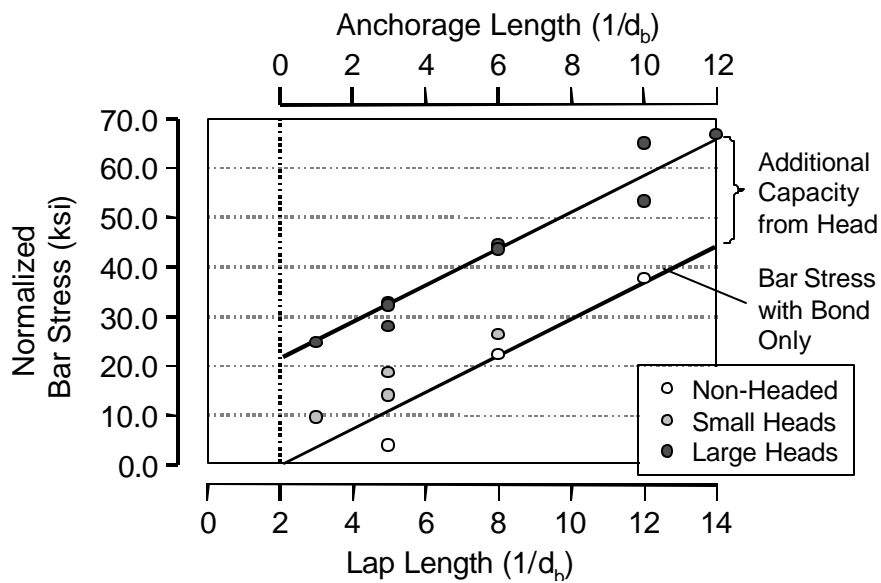


Figure 9-31: Bar stress versus anchorage length

Normalized bar stress provided by the small and large heads is plotted against lap length in Figure 932. This plot indicates that the lap length affected head capacity. The contribution from the heads was not a constant. A secondary scale at the top of the plot helps to explain the effect of lap length. All of the tests of lapped bars were performed with embedment depth to cover ratios less than 5.0. Thus the mode of failure in these many of the tests with small lap lengths ($5d_b$ or less) may be more akin to shallow embedment concrete breakout failure than the bearing failures recorded in the CCT node tests. At larger lap lengths ($8d_b$ or greater), the head capacity seems to level off and attain a constant value related to head size. Observations of cracking patterns (discussed in Section 9.1.1) support this conclusion.

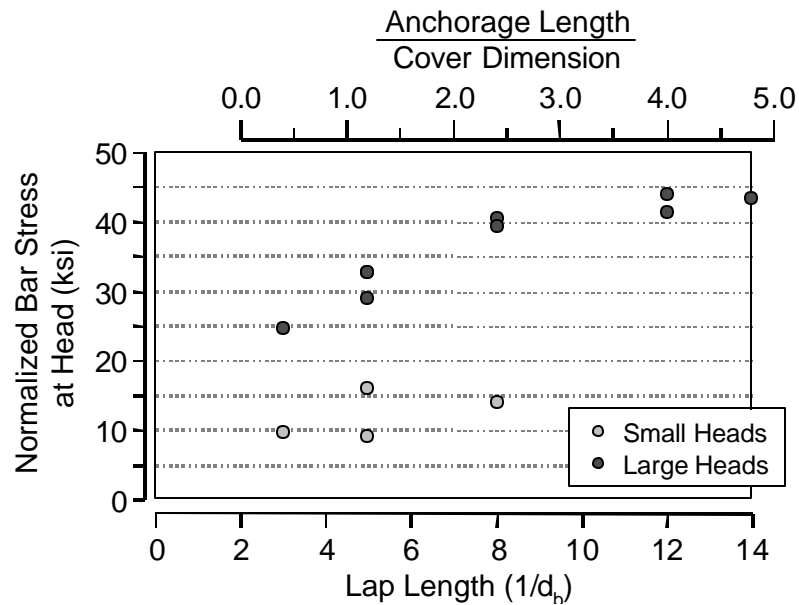


Figure 9-32: Bar stress at the head versus lap length

9.4.2 Effect of Head Shape

Two large head shapes were studied: circular and rectangular. The two shapes had nearly the same area ($A_{nh}/A_b = 4.04$ for circular heads and 4.70 for rectangular heads), thus comparison of companion specimens with circular and rectangular heads provides a reasonable indication of the effect of head shape in the lap splice tests. Load-deflection curves for circular and rectangular headed bar specimens are plotted in Figure 933 (specimens LS-08-04.04-08-10(N)-1 (circular) and LS-08-04.70-08-10(N)-1 (rectangular)). The specimens had the same lap length ($8d_b$) and were cast from the same concrete. The only difference between the two was head shape.

The load-deflection curves for the two specimens show almost identical responses. The change in head shape did not effect the capacity or stiffness of the specimens. Based on these tests,

head shape was not considered to be a significant test variable. Subsequently, data from circular and rectangular tests were considered interchangeable in analysis.

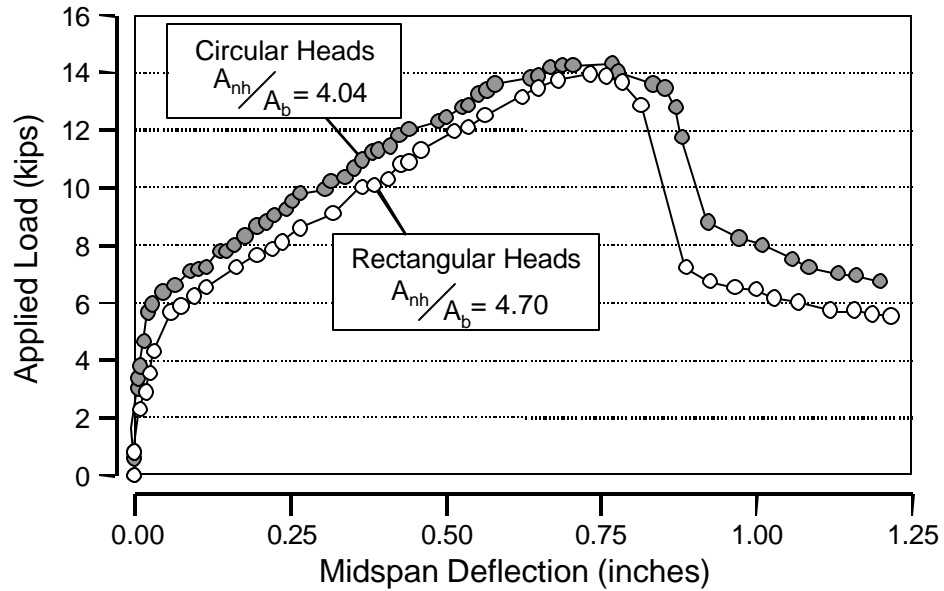


Figure 9-33: Load-deflection curves for circular and rectangular heads

Though head shape is not a consideration for bar capacity, it is a detailing concern. Head orientation is not easy to control during the construction of a reinforcement cage. Rectangular and square heads pose the problem that their orientation will change the clear cover over the heads. Thus, in detailing of square and rectangular heads, the cover should be selected such that the minimum is used in meeting code cover requirements. This problem is especially important for rectangular heads. A constant cover will be present only for circular heads. Figure 934 is reproduced from Ledesma [67] who discussed this issue.

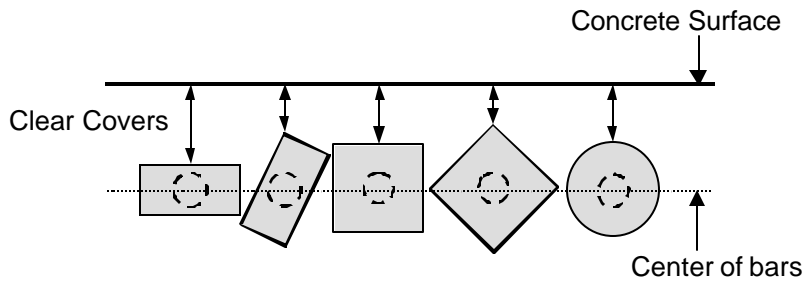


Figure 9-34: Concrete cover for various head shapes (after Ledesma [67])

9.4.3 Effect of Bar Spacing

Two specimens with bars spaced at $6d_b$ and $10d_b$ provided an indication of the effect of bar spacing (LS-08-04.70-05-06(N)-1 and LS-08-04.70-05-10(N)-1). The capacities of these two specimens are compared in Figure 9-35 and show that bar stress was reduced by about 15% with a 40% reduction in bar spacing. These results come from specimens with only a $5d_b$ lap length. At such a short lap length, the lapped bars do not develop any capacity from bond. The effect of bar spacing on specimens with longer lap lengths (in which bond would provide a greater contribution to capacity) cannot be extrapolated from these results alone.

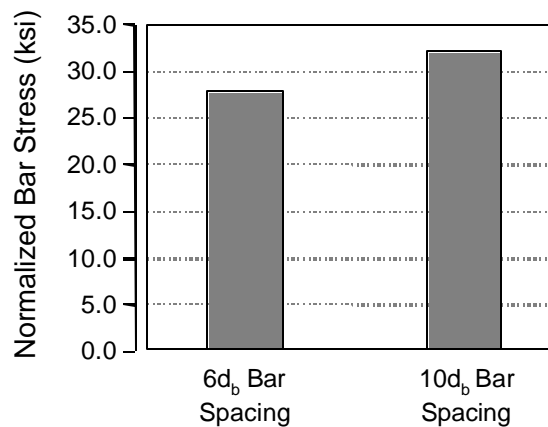


Figure 9-35: The effect of bar spacing on bar stress ($L_s = 5d_b$)

9.4.4 Effect of Lap Configuration

A non-contact lap configuration is preferable for precast applications because it minimizes the potential of overlap conflicts between opposing layers of bars. However, a contact lap configuration may provide more efficient force transfer resulting in a greater splice capacity. The effect of lap configuration was studied in two pairs of specimens: small heads (LS-08-**01.18**-05-10(C)-1 and LS-08-**01.18**-05-10(N)-1) and large heads (LS-08-**04.70**-05-10(C)-1 and LS-08-**04.70**-05-10(N)-1). The capacities of these specimens are compared in Figure 10-36. A 33% increase in bar stress resulted when small headed bars were placed in contact with one another, however, there was virtually no increase for large headed bars (only 1%). When placed in contact with one another, bars with small heads can generally be placed closer than bars with large heads, thus the small headed, contact splice results also reflect closer bar spacing than those with large heads. Since the specimens had only a short, $5d_b$ lap length, the mechanism of force transfer may not be the same as would occur for longer lap lengths. Therefore, the effect of lap configuration on specimens with longer lap lengths (in which bond would provide a greater contribution to capacity) remains to be evaluated.

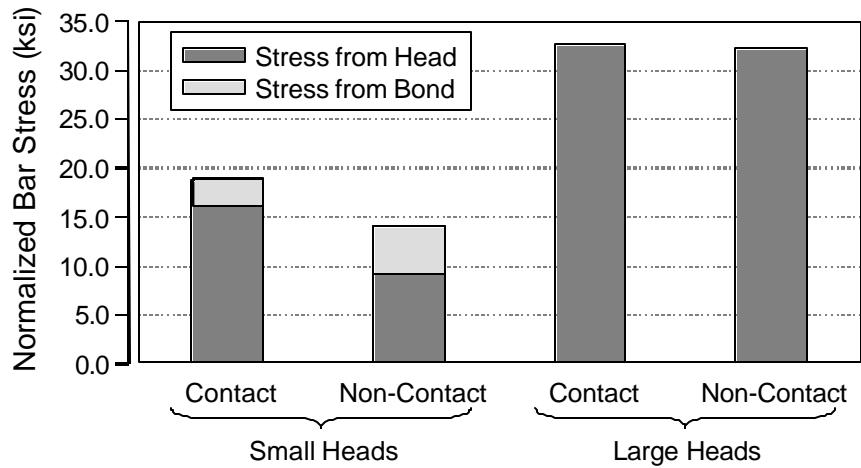


Figure 9-36: The effect of lap configuration on bar stress ($L_s = 5d_b$)

9.4.5 Effect of Debonding

In order to distinguish the capacity provided by head bearing from the capacity that is provided when bond acts in conjunction with head bearing, one specimen was tested with a debonding wrap placed over the deformations of the bars within the lap zone. The capacity of the debonded specimen (LS-08-04.04-14-10(N)-1-DB) is compared with a companion bonded specimen (LS-08-04.04-14-10(N)-1) in Figure 937. These tests were performed with long lap lengths ($14d_b$) in order to accentuate the contribution from bond.

Debonding resulted in a lower total bar stress, however, the debonded bars had a much higher (by 40%) contribution from head bearing than did the bonded bars. The reason for this increase is explained in Figure 9-38. In Chapter 7, head capacity was shown to be related to the two cover dimensions, c_1 (the minimum cover) and c_2 (the secondary cover). In the bonded specimen, bond-splitting cracks propagating from the opposing lap bars extend into the concrete region surrounding the heads. The cover dimensions are defined based on the extent of the bond splitting cracks. With bonded bars, splitting cracks may emanate from the opposing bars and the

side cover dimension is about half of the spacing between opposing lapped bars. In the debonded case, there are no bond splitting cracks and the side cover may be taken as half of the spacing between heads, or twice that in the bonded case. As a result, higher head capacities resulted when bars were debonded, but, as the data in Figure 9-37 show, a smaller total capacity results because of the corresponding loss in bond. These test results illustrate that even though bond can deteriorate dramatically as stress is transferred to the head, it can still provide a significant contribution to anchorage capacity if the lap length is long enough.

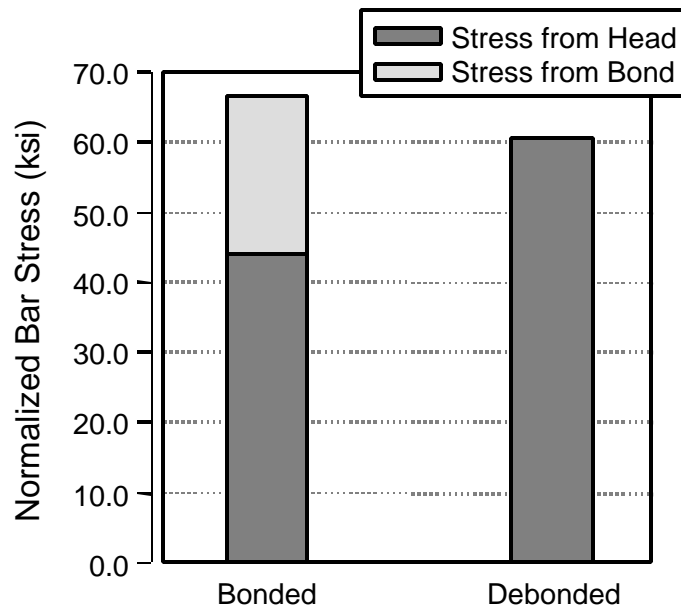
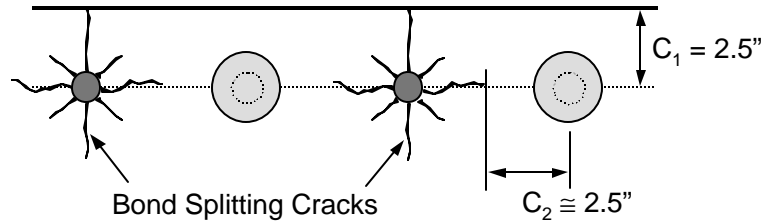


Figure 9-37: The effect of debonding on bar stress ($L_s = 14d_b$)

i. Bonded Bars



ii. De-Bonded Bars

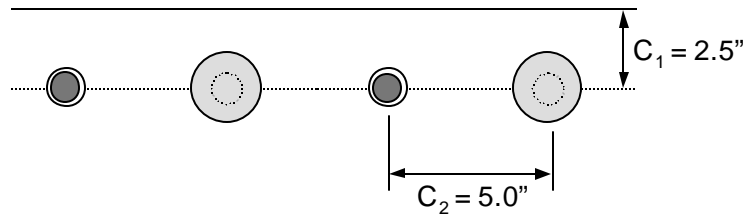


Figure 9-38: Bond splitting effect on cover dimensions

9.4.6 Effect of Confinement

The effect of confinement on capacity was examined using the results from two groups of specimens: tests with hairpin confinement and lap lengths of $8d_b$ and tests with unconfined, hairpin confined, and transverse tie-down confined splices and lap lengths of $12d_b$.

The hairpin confinement detail provided only tie-down (or tie-back) confinement for the headed bars. This type of confinement was easily defined by the tie-down confinement ratio, the ratio of tie-down steel to longitudinal steel in the lap zone. Normalized bar stress is plotted against confinement ratio in Figure 9-39 for non-headed and large headed bars with $8d_b$ lap length. The plot shows a gradual increase in bar stress with increasing confinement ratio. Hairpins with bar sizes of #2, #3, and #4 produced increases of 22%, 36%, and 43% over unconfined bars respectively. There was no corresponding increase for the single non-headed bar test; however, the

hairpins were not placed where they could enhance bond strength as discussed in Section 9.2.3. Improvements in capacity from the hairpins resulted from their influence on the head bearing capacity. Normalized bar stress at the head is plotted against confinement ratio in Figure 9-40. The bar stress provided by the head increased by 50% over unconfined bars when hairpins of #3 or greater bar size were placed next to the head.

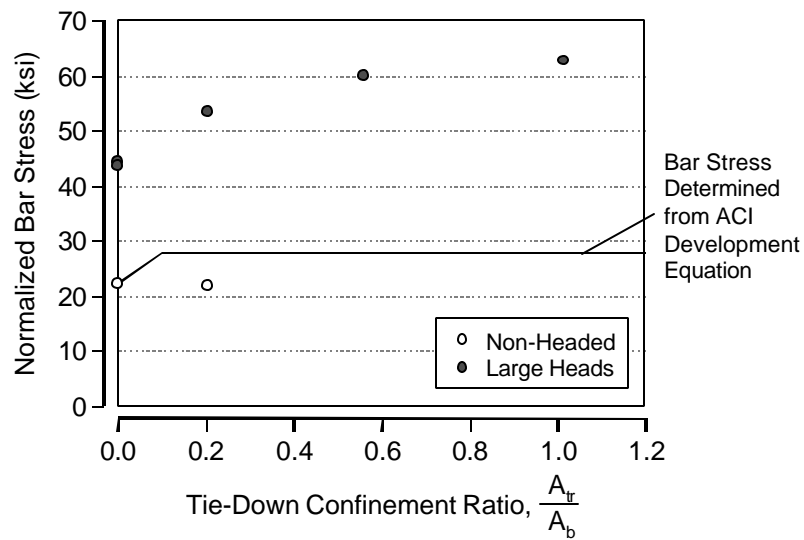


Figure 9-39: Normalized bar stress versus confinement ratio ($L_s = 8d_b$)

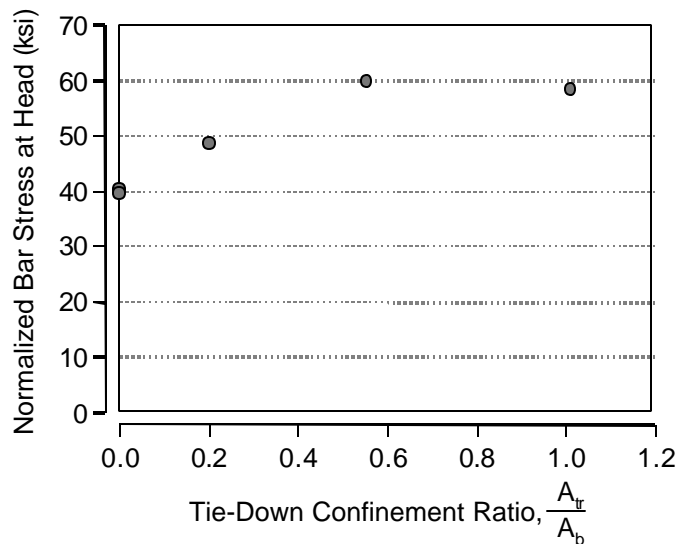


Figure 9-40: Normalized bar stress at the head versus confinement ratio ($L_s = 8d_b$)

Because none of the confined specimens achieved yield at a lap length of $8d_b$ and significant improvement from additional confining steel was unlikely, subsequent confinement studies were performed on specimens with a $12d_b$ lap length. The capacities of an unconfined specimen (LS-08-04.04-12-10(N)-1), a hairpin confined specimen (LS-08-04.04-12-10(N)-1-H0.6), and a transverse tie-down confined specimen (LS-08-04.04-12-10(N)-1-TTD) are compared in Figure 9.41. Hairpins increased the capacity by only 5% at $12d_b$ (In contrast, the capacity was increased by 36% at $8d_b$), and the capacity provided by the head declined slightly. The transverse tie-down detail improved the capacity by 11%. As discussed in Section 9.2.3, transverse bars provided a much more efficient confinement detail than did tie-down bars.

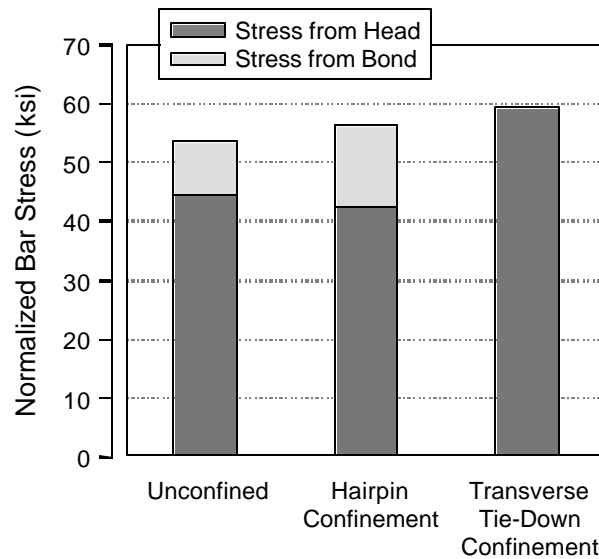


Figure 9-41: The effect of confinement type on bar stress ($L_s = 12d_b$)

9.5 SUMMARY

The behavior of the lap splice specimens during testing has revealed that the mechanism of force transfer consists of broad struts that propagated between the heads and straight bar deformations of opposing bars (Figure 9-5). These struts propagated at angles of approximately 55° from the longitudinal axes of the bars and their intersection with opposing bars determined the anchorage points (critical locations for bar development) of those bars. Development of the headed bars within the anchorage length consisted of a combination of bond and head bearing. As with the headed bars used in the CCT nodes, anchorage was a two stage process in which bar stress was first carried by bond, the gradually transferred to the head as bond deteriorated. The bonded length of the bar was equal to the anchorage length deducted by the wedge length. The wedge length was the bar length taken up by the formation of the concrete bearing wedge and was approximately equal to the side dimension of the head.

The following additional observations were noted:

- Head size did not affect the mechanism of force transfer between opposing lapped bars.
- Below a lap length of $5d_b$ (the spacing between lapped bars), the mechanism of force transfer was entirely between the heads of the lapped bars and there was no contribution from bond to the lap capacity. Furthermore, the capacity provided by the heads was less at the short ($5d_b$ or less) lap lengths.
- Head shape did not influence head capacity, but is a significant detailing concern because of clear cover considerations. Circular heads provide the smallest minimum clear cover for a given head area.
- Debonding of the lapped bars resulted in a fewer number of surface cracks that developed greater widening than for a companion bonded specimen. Debonding also resulted in a loss of stiffness. Debonding significantly increased the capacity and performance of head bearing, but the overall capacity was reduced due to the loss of a bond contribution.
- Hairpin confinement did not change the fundamental mechanism of force transfer in the lap zone. Hairpins placed near the heads helped to improve the anchorage performance of the heads, but the improvement in capacity was modest. The details of the placement of the hairpins tested in this study may not have reflected the optimal use of the hairpins. Placement of the hairpins within the center of the lap zone rather than the ends may have improved their efficiency.
- The transverse tie-down detail provided better confinement of the lap zone. The transverse bars of this detail were more active than the tie-down bars. The transverse

bars improved the lap capacity by altering the mechanism of force transfer in the lap zone. Strain development in the transverse bars was directly linked to the bar stress carried by the heads. The tie-down bars of this detail did not develop strain until failure of the specimen was imminent. The tie-down bars then became active as part of a secondary failure mechanism accompanied by a severe loss of stiffness in the specimen.

A summary of all lap splice tests is provided in Appendix D.

Chapter 10: Development of a Design Methodology for Headed Bars and Recommendations for Code Provisions

10.1 INTRODUCTION

In this chapter the lap splice data are compared with capacities computed using the proposed bearing model that was developed from the CCT node tests. Bond data from the lap splice tests are combined with data from the CCT node tests to develop modification factors for the effects of head size, lateral stress, and/or platen restraint at the node. Finally, the proposed bearing models are combined with a modified bond model and compared with the results of this and other headed bar studies.

10.2 COMPARISON OF LAP SPLICE RESULTS TO RECOMMENDED BEARING MODEL

Measured head capacities were compared to the proposed bearing model developed in Chapter 7. Two models were proposed in that chapter, the second of which was selected for use in design because of its simplicity. This model is presented below:

$$\text{Bearing Capacity, } P = A_{nh} 0.9 \Psi \left(\frac{2c_1}{\sqrt{A_{nh}}} \right) (f'_c) \quad (10-1)$$

$$\text{with } \Psi = 0.6 + 0.4 \frac{c_2}{c_1} \leq 2.0 \quad (10-2)$$

P = head capacity (kips)

Ψ = radial disturbance factor

A_{nh} = net head area (in²)

c_1 = minimum cover dimension (in)

c_2 = secondary cover dimension (measured perpendicular to c_1) (in)

f_c' = concrete cylinder strength (ksi)

The bearing capacities of the heads in bonded and de-bonded tests were calculated using cover dimensions, c_1 and c_2 , as discussed in Section 9.4.5 and shown in Figure 9-38. Measured/calculated ratios for the heads are plotted against lap length in Figure 10-1. These ratios decreased as the lap length dropped below $8d_b$. The ratios were also low for the small-headed bar tests. Only the large-headed bars with lap lengths of $8d_b$ or greater compared well with the proposed model. As discussed in Section 9.4.1, failure of the specimens with small lap length (of $5d_b$ or less) occurred by a different mode than the specimens with larger lap lengths. Thus the failure of the model to reflect measured head capacities accurately at smaller lap lengths was expected.

The distribution of the measured/calculated ratios is shown in Figure 10-2. The statistical information is also presented in Table 10-1. The data are divided between specimens of lap length less than $8d_b$ and those greater than or equal to $8d_b$. For the longer lap lengths, the average measured/calculated ratio was 0.95 and the coefficient of variation was 16%.

| | | Measured/Calculated Values | | |
|-------------|---------------------|----------------------------|-------------|--------------------|
| Lap Length | Number of Specimens | Range | Mean | Standard Deviation |
| $< 8d_b$ | 7 | 0.41 - 0.87 | 0.69 | 0.15 |
| $\geq 8d_b$ | 7 | 0.64 - 1.08 | 0.95 | 0.15 |
| All | 14 | 0.41 - 1.08 | 0.82 | 0.20 |

Table 10-1: Statistical data for accuracy of recommended bearing model (lap splice tests)

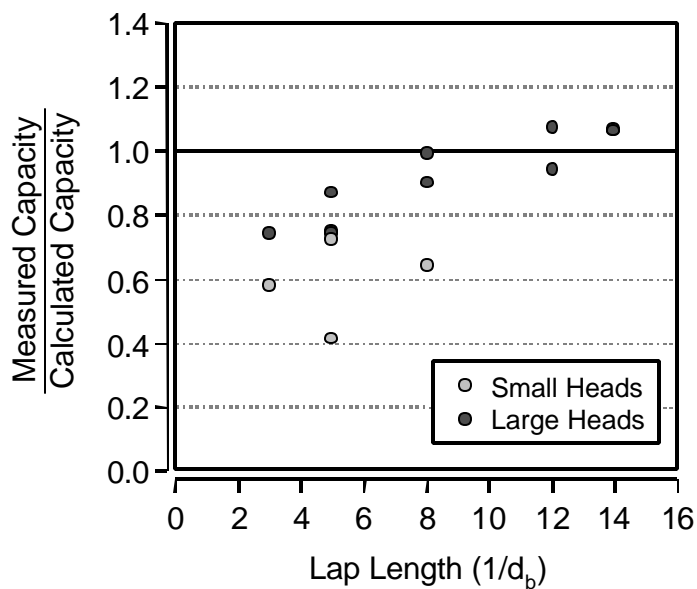


Figure 10-1: Measured/calculated ratio of recommended model versus lap length

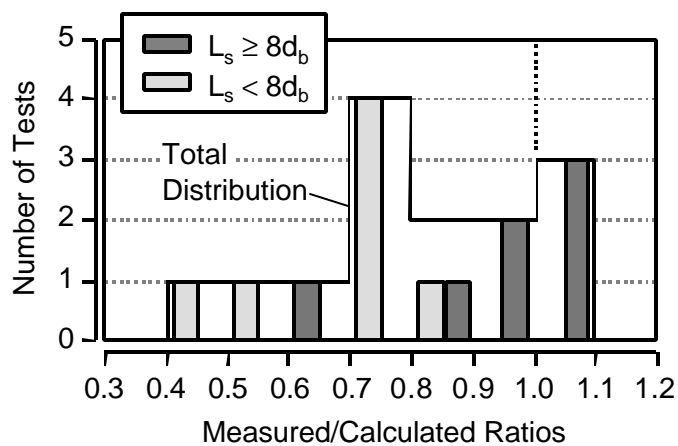


Figure 10-2: Distribution plot of measured/calculated ratios for recommended bearing model

10.3 EVALUATION OF BOND DATA

As with the CCT nodes, peak bond stresses and failure bond stresses were determined for the lap splice specimens. Lap splice peak and failure bond stress are plotted against lap length in Figure 10-3. The peak bond stress was equal to the failure bond stress for non-headed and small headed bars. However, the bond stresses at failure for the large-headed bars were substantially less than peak bond stresses for the same bars. Furthermore, much less bond was developed at failure for large headed bars than small headed or non-headed bars. This agrees with the trend seen in the CCT node data (Figure 7-34). Additionally, the failure bond stress was effected by lap length. For a given head size, the failure bond stress increased with increasing lap length. At a lap length of $5d_b$, no bond stress was developed for the bars with large heads.

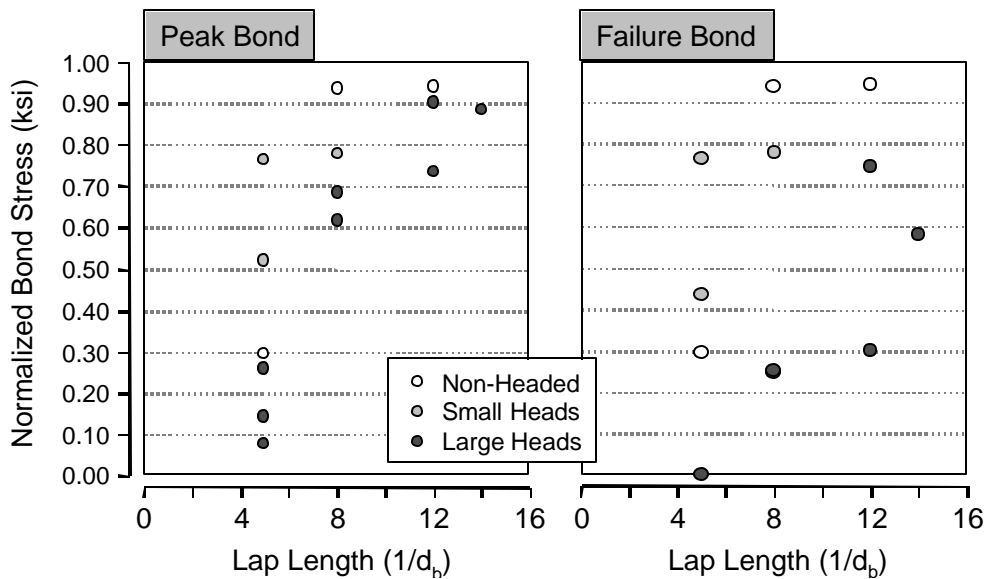


Figure 10-3: Bond stress at failure versus lap length

By combining the results of the lap splice tests with lap lengths greater than or equal to $8d_b$ and the CCT node results, a more complete picture of the bond stress behavior emerges. The

bond data from the CCT node tests were influenced by two factors: lateral compression and/or platen restraint in the CCT node and the decline in bond stress associated with head size. In the lap splice tests, only one of these factors is present: the decline in bond stress associated with head size. Peak bond stress data from the lap splice and CCT node tests were compared in order to determine a normalizing factor for the lateral compression and/or platen restraint that occurs in the CCT nodes. Distribution plots of peak bond stress for the CCT node and lap splice tests are presented in Figure 10-4. The average peak bond stresses for the two data sets were 0.81 ksi (lap splices) and 1.25 ksi (CCT nodes). The average peak bond stress in the CCT nodes was about 1.5 times the average peak bond stress that occurred in the lap splice tests. This ratio was used to normalize the CCT node failure bond data with respect to the lap splice tests.

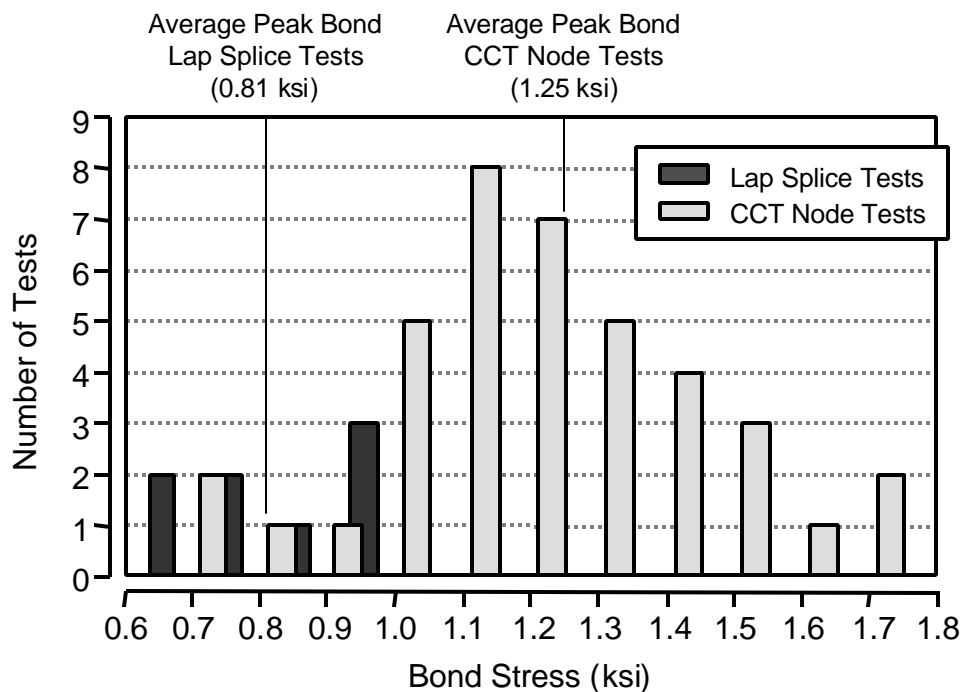


Figure 10-4: Peak bond stress distributions for lap splice and CCT node tests

Normalized failure bond stresses from the CCT node and lap splice tests were used to determine a modification factor for the reduction in bond at failure that is related to head size. Bond stress at failure is plotted against relative head area in Figure 10-5. Bond stress at failure decreased from an average value of about 1.0 ksi to 0.3 ksi over the range of relative head areas from 0.0 to 5.0. The single data value at a relative head area of 10 suggests that further reduction did not occur beyond the drop to 0.3. The following equation is proposed as a reasonable approximation of the trend in the data:

$$\text{Head Size Reduction Factor, } \chi = 1.0 - 0.7 \left(\frac{A_{nh}/A_b}{5.0} \right) \geq 0.3 \quad (10-3)$$

A_{nh} = net head area (in²)

A_b = bar area (in²)

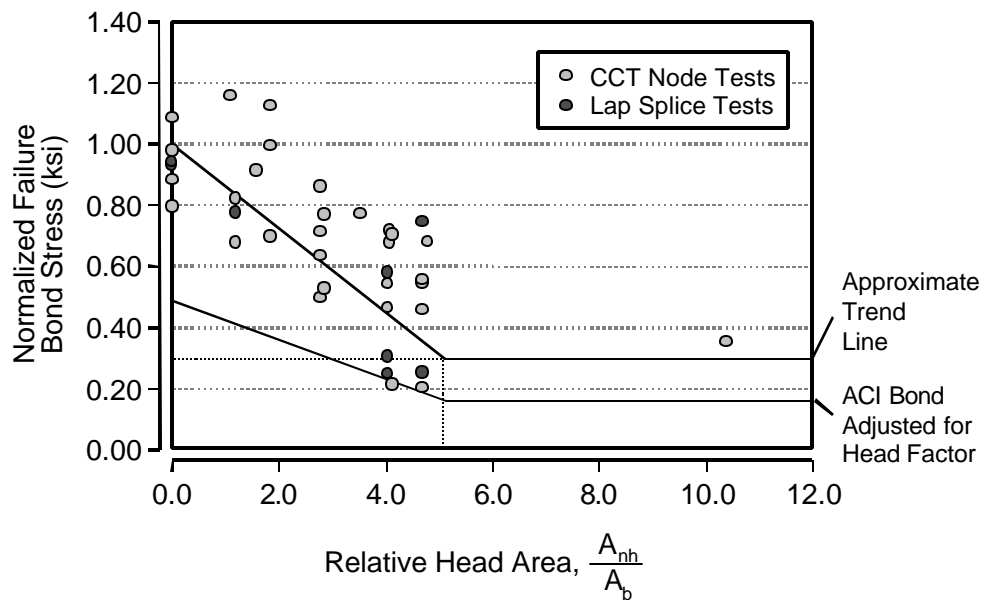


Figure 10-5: Bond stress at failure versus relative head area (lap splice and CCT node data)

Using the normalization ratio that accounts for compression stress and/or platen restraint in the CCT nodes and the head size factor proposed in equation 10-3, bond stresses at failure were predicted for all of the CCT node and lap splice tests. The measured/calculated ratios are summarized in Table 10-2. The distribution of the ratios is presented in Figure 10-6. Measured bond stresses averaged about twice the bond determined from the ACI equation for development length. The distribution plot indicates considerable scatter in the data and several tests with very high measured bond stresses. The ACI equations provided a very conservative estimate of the bond stresses that occurred in the CCT node and lap splice tests. However, some of the disparity may result from the particular reinforcing bars and concrete mixes used in this study. A broader study including reinforcing bars of different sizes from different suppliers and concrete mixes would provide better insight as to the effect of those parameters.

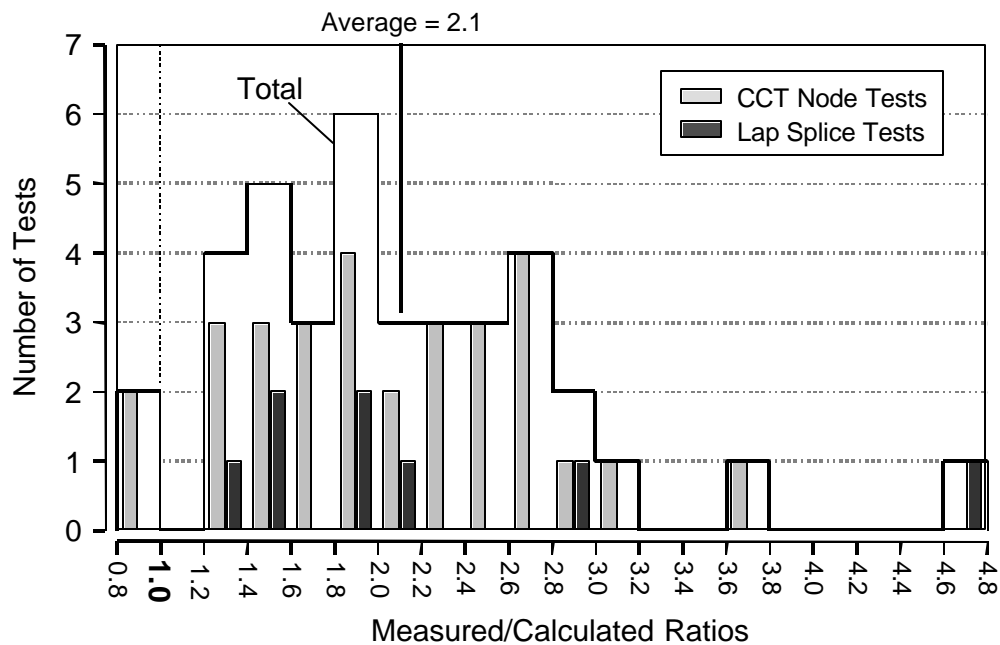


Figure 10-6: Distribution plot for bond stress at failure data

| | | Measured/Calculated Values | | |
|------------|---------------------|----------------------------|------|--------------------|
| Test Type | Number of Specimens | Range | Mean | Standard Deviation |
| CCT Node | 30 | 0.90 - 3.72 | 2.08 | 0.64 |
| Lap Splice | 8 | 1.21 - 4.65 | 2.22 | 1.10 |
| All | 38 | 0.90 - 4.65 | 2.11 | 0.75 |

Table 10-2: Statistical data for accuracy of modified ACI bond stress at failure

10.4 COMBINED BOND AND HEAD BEARING

In Section 7.4, the CCT node test data were combined with data from other studies of headed bars, anchor bolts, and bearing blocks to develop a model for head bearing capacity. In the preceding section (10.3), bond data from the CCT node and lap splice tests were combined in order to develop a modification factor bond stress in headed bars. In this section, the CCT node data and the lap splice data are combined with data from various other headed bar studies in order to evaluate the accuracy of the proposed head bearing and modified bond capacity model when they are combined to predict total headed bar anchorage capacity.

In addition to the two sets of tests from this study, three other studies provide data for headed bars that are anchored by a combination of bond and head bearing. The five test groups are listed in Table 10-3. For each study the ranges of the test variables found to be most important are listed: concrete strength (f_c'), relative head area (A_{nh}/A_b), relative cover dimension (c_1/d_b), and relative anchorage length (L_a/d_b).

| Source | Number of Data Values | Ranges for Variables | | | |
|----------------------------|-----------------------|----------------------|----------------------|-------------------|---------------------|
| | | f'_c (ksi) | $\frac{A_{nh}}{A_b}$ | $\frac{c_1}{d_b}$ | $\frac{L_a^*}{d_b}$ |
| UT CCT Node Tests | 27 | 3.1 - 4.2 | 0.0 - 10.4 | 2.8 - 3.0 | 7.0 |
| UT Lap Splice Tests | 8 | 3.6 - 4.1 | 0.0 - 4.7 | 2.5 | 6.0 - 12.0 |
| UT Deep Embedment [42] | | | | | |
| • Unconfined Tests | 15 | 3.0 - 3.9 | 4.7 - 9.0 | 1.8 - 2.4 | 7.6 - 18.3 |
| • Confined Tests | 20 | 3.0 - 3.9 | 4.7 - 9.0 | 1.8 - 2.4 | 8.7 - 12.2 |
| UT Beam-Column [26] | | | | | |
| • "Side Blow-Out Failures" | 18 | 3.2 - 5.7 | 2.1 - 7.4 | 1.6 - 2.6 | 5.8 - 12.3 |
| • Shear-Related Failures | 14 | 3.3 - 5.8 | 2.1 - 7.4 | 1.7 - 2.6 | 5.8 - 9.8 |
| Kansas Pullout Tests [119] | | | | | |
| • Unconfined Tests | 3 | 4.9 | 10.4 | 2.5 | 11.0 |
| • Confined Tests | 13 | 4.9 - 5.0 | 10.4 | 2.5 - 3.5 | 10.9 |

* h_d/d_b presented for UT Beam-Column and Kansas Pullout studies

Table 10-3: Research studies of bonded headed bars

The term anchorage length has been used occasionally throughout this report and can easily be confused with two other terms: development length and embedment depth. In order to clarify the following discussion, these three terms are defined below:

- **Development length (L_d)** is the length required for a straight bar to develop by bond. The development length can be determined from the design equations provided in the ACI [2] or ASSHTO [1] code provisions. ACI development length is frequently used throughout this report.
- **Embedment depth (h_d)** is the length measured along the bar from the bearing face of the head (or the end of a straight bar) to the surface of the member in which the bar is anchored.

- **Anchorage length (L_a)** is the length measured along the bar from the bearing face of the head (or the end of a straight bar) to the point of peak bar stress. The point of peak bar stress (or anchorage point) generally coincides with the intersection of the bar and the leading edge of the strut(s) that the bar anchors. This length often defines the available length in which the bar can be anchored and is sometimes referred to in this report as the available anchorage length.

The distinctions between embedment depth and anchorage length are clarified in Figure 10-7. As this figure shows, the anchorage length is generally shorter than the embedment depth. Furthermore, a strut-and-tie model is necessary in order to determine the available anchorage length.

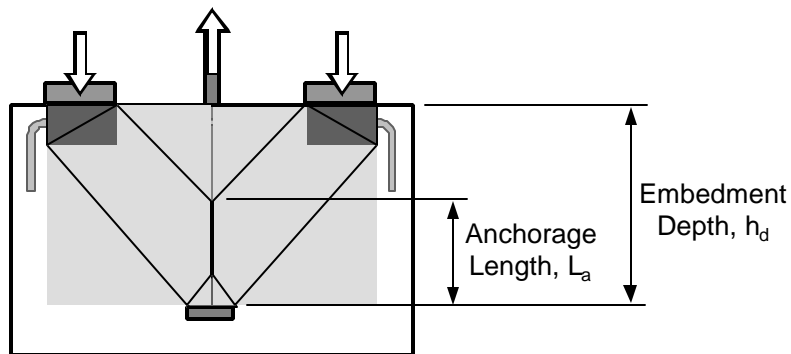


Figure 10-7: Distinction between embedment depth and anchorage length

Because the proposed models for bond and head bearing were developed from the CCT node and lap splice data, the combined model provided good estimations of the test results. The head bearing model was designed to provide an average measured/calculated ratio of 1.0 and the modified ACI bond model provided conservative estimates for the bond contribution. Thus the combined results gave average calculated values that were less than the average measured results.

Statistical results of the combined bond and head bearing analysis are listed in Table 10-4. The distribution of measured/calculated ratios for the CCT node and lap splice tests is plotted in Figure 10-9. The combined models provided an average measured/calculated ratio of about 1.3 with a coefficient of variation of 20%.

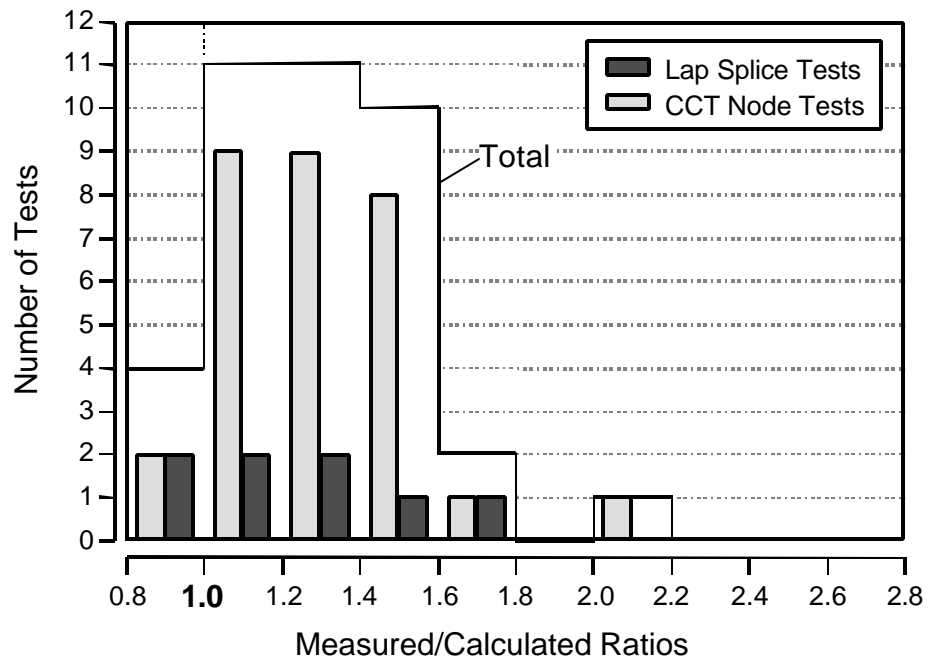


Figure 10-8: Distribution of measured/calculated ratios for CCT node and lap splice tests (bond plus bearing) (current study)

| | | Measured/Calculated Values | | |
|------------|---------------------|----------------------------|------|--------------------|
| Test Type | Number of Specimens | Range | Mean | Standard Deviation |
| CCT Node | 30 | 0.86 - 2.07 | 1.30 | 0.25 |
| Lap Splice | 8 | 0.84 - 1.60 | 1.22 | 0.29 |
| All | 38 | 0.84 - 2.07 | 1.30 | 0.26 |

Table 10-4: Statistical data for CCT node and lap splice tests (bond plus head bearing) (current study)

Thirty-five tests from the University of Texas deep embedment study [42] used bonded headed bars. These tests were analyzed using the recommended bearing model and the modified bond model. The statistical results of that analysis are listed in Table 10-5 and the distribution of the results is plotted in Figure 10-10. The combined model provided slightly more conservative results for that study than for the CCT node and lap splice tests. The average measured/calculated ratio was about 1.5 with a coefficient of variation of 25%. The distribution of the measured/calculated ratios was skewed towards a value of 1.0. The median value of test results was about 1.3, which was close to that for the CCT node and lap splice tests.

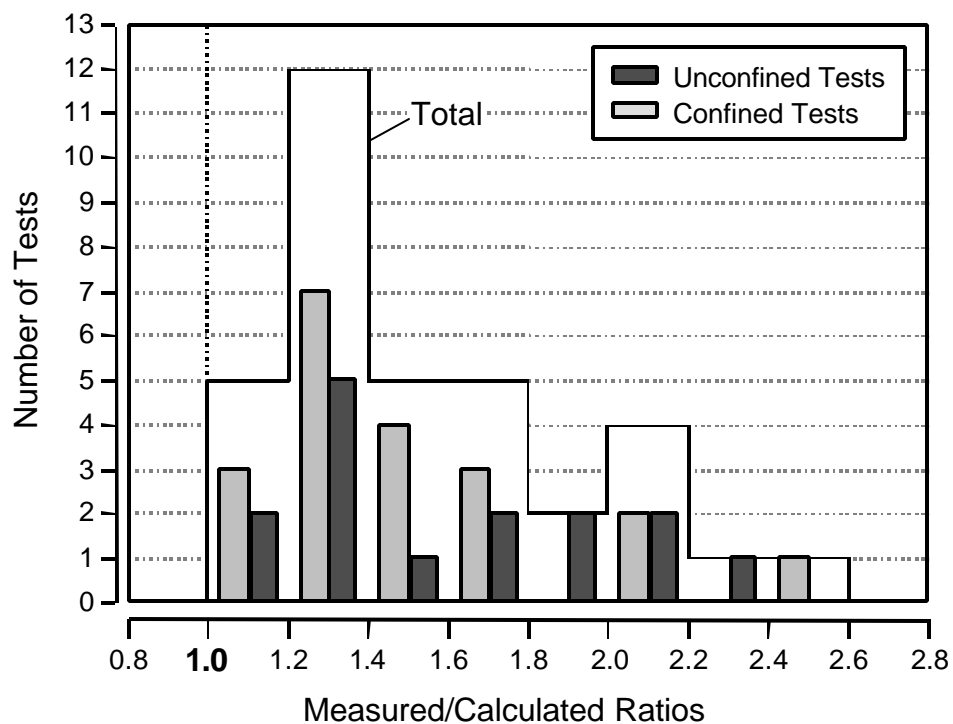


Figure 10-9: Distribution of measured/calculated ratios University of Texas deep embedment tests [42] (bond plus bearing)

| Test Type | Number of Specimens | Measured/Calculated Values | | |
|------------|---------------------|----------------------------|------|--------------------|
| | | Range | Mean | Standard Deviation |
| Unconfined | 15 | 1.04 - 2.32 | 1.58 | 0.40 |
| Confined | 20 | 1.08 - 2.51 | 1.51 | 0.38 |
| All | 35 | 1.04 - 2.51 | 1.54 | 0.39 |

Table 10-5: Statistical data for University of Texas deep embedment tests [42] (bond plus head bearing)

The two remaining studies: the University of Texas beam-column tests [26] and the University of Kansas pullout tests [119], provided an additional 48 test results to compare against

the proposed models. When analyzed, the results of these studies did not compare well with the combined bond and head bearing model. The statistical data for the beam-column and pullout studies are listed in Tables 10-6 and 10-7. The measured/calculated ratios for these two studies were 0.78 for the beam column tests (“side blow-out” failures) and 0.56 for the pullout tests. The reasons for these poor results can be found by analyzing the strut-and-tie mechanisms within these specimens and examining the results relative to embedment depth and anchorage length.

| | | Measured/Calculated Values | | |
|-----------------|---------------------|----------------------------|------|--------------------|
| Failure Mode | Number of Specimens | Range | Mean | Standard Deviation |
| “Side Blow-Out” | 18 | 0.47 - 1.21 | 0.78 | 0.21 |
| Shear Related | 14 | 0.28 - 0.89 | 0.58 | 0.19 |
| All | 32 | 0.28 - 1.21 | 0.69 | 0.22 |

Table 10-6: Statistical data for University of Texas beam-column tests [26] (bond plus bearing)

| | | Measured/Calculated Values | | |
|--------------|---------------------|----------------------------|------|--------------------|
| Failure Mode | Number of Specimens | Range | Mean | Standard Deviation |
| Unconfined | 3 | 0.39 - 0.43 | 0.41 | 0.02 |
| Confined | 13 | 0.50 - 0.66 | 0.58 | 0.06 |
| All | 16 | 0.39 - 0.66 | 0.56 | 0.09 |

Table 10-7: Statistical data for University of Kansas pullout tests [119] (bond plus bearing)

Almost all of the beam-column and Kansas pullout tests had embedment/cover ratios less than 5.0; the limit specified for deep embedment tests in the University of Texas study [42] and

for applying the side blow-out and proposed bearing capacity models. Measured/calculated ratios are plotted against embedment/cover ratio for the two studies in Figure 10-10. Almost all of the measured strength capacities were less than the computed values. There is the suggestion of an upward trend with measured/calculated ratios approaching and surpassing 1.0 at larger embedment/cover ratios. The range of embedment/cover ratios in the beam column and Kansas pullout studies is comparable to the range of anchorage length/cover ratios found in the lap splice tests for which the proposed model worked well. However, the embedment depths of the bars in the beam-column and Kansas pullout tests were probably greater than the anchorage lengths available for the bars in those tests. Thus, the anchorage length/cover ratios of the beam-column and Kansas pullout studies may be substantially less than the anchorage length/cover ratios of the lap splice tests.

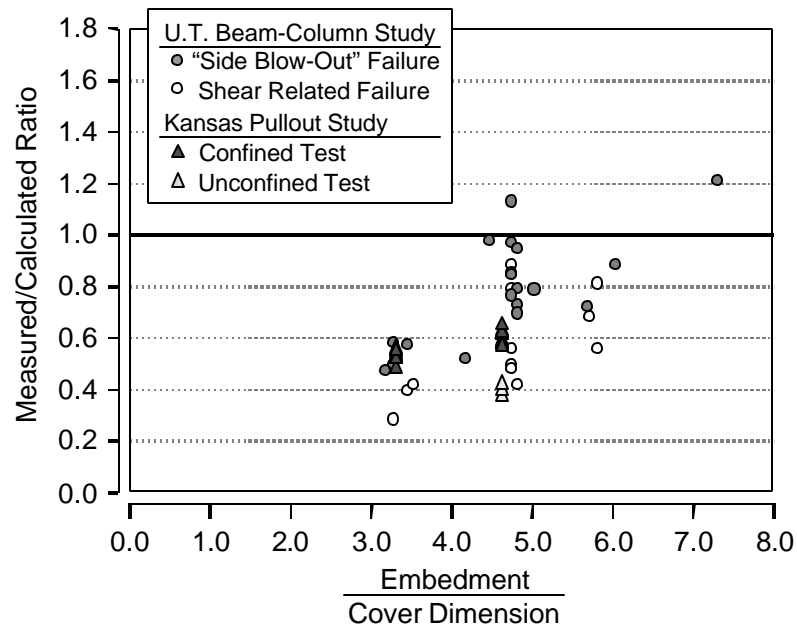


Figure 10-10: Measured/calculated ratio versus embedment/cover ratio (University of Texas beam-column and Kansas pullout studies)

The joint region of a typical beam-column specimen is reproduced in Figure 10-11. A strut-and-tie model is super-imposed onto the layout of the joint. The strut-and-tie model reveals that the critical anchorage point of the headed bar did not coincide with the edge of the column. The anchorage length of the headed bar for the specimen shown in Figure 10-11 was much less than its embedment depth. Similarly, examination of the Kansas pullout tests using strut-and-tie models revealed that the anchorage lengths of those bars were also smaller than the embedment depths (Figure 10-12). If anchorage length/cover ratios were used instead of embedment depth/cover ratios in Figure 10-10, the data would shift to the left of the plot. Examination of the beam-column test results revealed that the specimens with the best measured/predicted ratios had either long embedment depths (with corresponding long anchorage lengths) or closely spaced stirrups directly over and under the headed bars. Stirrups placed close to the headed bars facilitated strut development at shallow angles to the headed bars and allowed the anchorage (peak stress) point of the bars to move closer to the edge of the column, thus increasing the anchorage length.

The results of the beam-column tests and Kansas pullout tests highlight the importance of the distinction between embedment depth and anchorage length. This importance is further reinforced by recalling the catastrophic collapse of the Sleipner A offshore platform (which is reviewed in Section 3.4.5.1) [38, 63]. In the analysis and design of this offshore platform, the anchorage point of an important headed bar tie had been assumed at the edge of a tri-cell support wall rather than from strut-and-tie models. This assumption resulted in the detailing of the tie with a very short anchorage length that could not develop the yield capacity of the bar. The mechanism of collapse for the tri-cell wall was subsequently governed by failure of the tie. The collapse of the Sleipner A offshore platform can be attributed to a confusion between embedment depth and anchorage length. Anchorage length, not embedment depth, is the variable that governs the

contribution from bond and the governing mode of failure, which will either be the bearing mode examined in this study or concrete breakout.

i. Strut-and-Tie Model

ii. Typical Crack Pattern

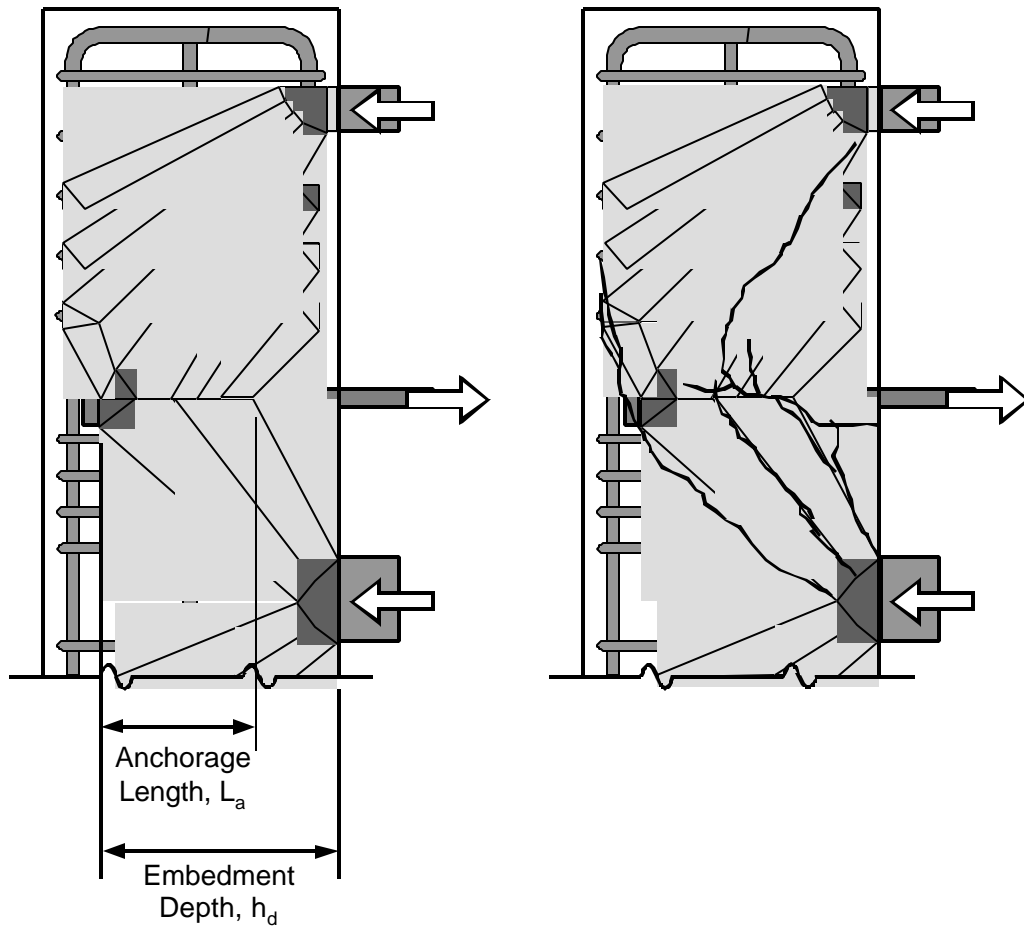


Figure 10-11: Strut-and-tie model for beam-column specimen

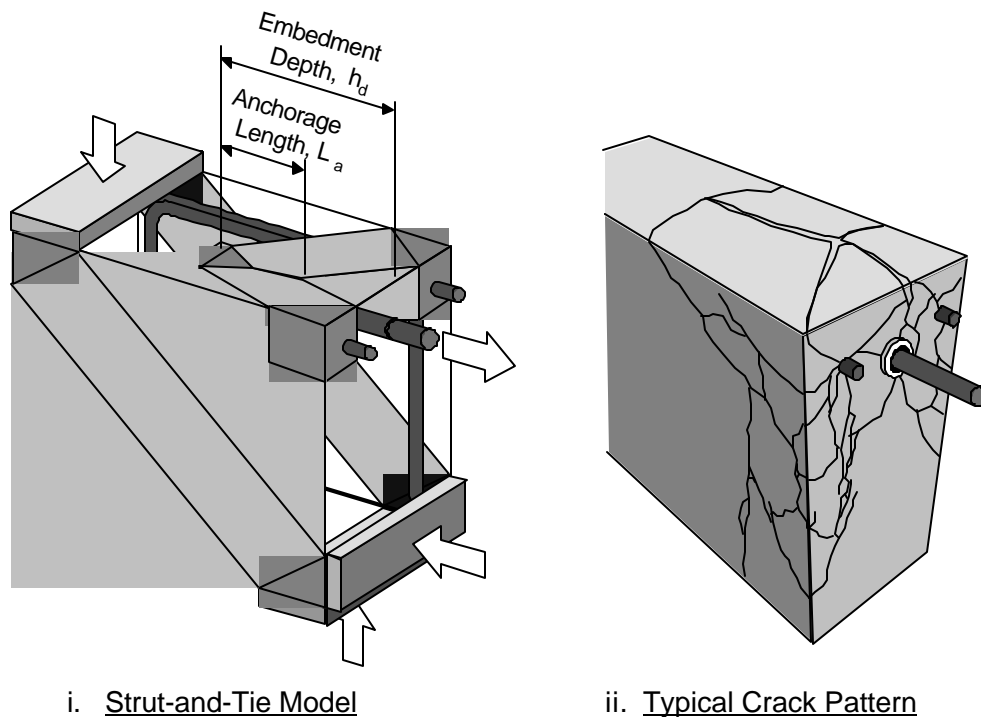


Figure 10-12: Strut-and-tie model for Kansas pullout specimen

10.5 RECONFIGURATION OF PROPOSED MODEL INTO DESIGN FORMAT

A proposed model of headed bar anchorage has been developed and compared against a wide variety of test results. The final step is to convert the model into a more usable design form and to state limitations on the applicability of the model.

From a designer's perspective, the decision to use headed bars follows from a need to shorten development length to meet dimensional limits of the structure. The designer will be faced with a situation in which the necessary development length, L_d , of a bar will not fit with the available anchorage length, L_a . Thus the designer may choose to use a headed bar to solve the problem. The next question posed by the designer is "What size head will need to be placed on this bar in order to meet the anchorage length limitation?" This question points the way to the

design form for the proposed method. The designer begins by knowing the following: basic development length, L_d , and available anchorage length, L_a . The designer will also know such variables as concrete strength, f_c' , and cover dimensions, c_1 and c_2 . The unknown variable is head size, which can be expressed by the relative head area, A_{nh}/A_b . Thus, the model equations must be re-arranged in order to solve for relative head area in terms of the known quantities listed above. The following procedure is recommended:

1. Basic development length, L_d , is calculated and compared to the available anchorage length, L_a .
2. If L_d is greater than L_a and space considerations preclude the use of a hooked bar, a headed bar becomes the most likely solution.
3. The contribution from bond to anchorage capacity, $f_{s,bond}$, is determined. The basic bar stress provided by bond can be calculated simply as:

$$f_{s,bond} = \left(\frac{L_a}{L_d} \right) f_y \cdot \chi$$

where χ = a reduction factor for the deterioration related to head size (For now, a constant value of 0.3 is assumed. The selection of this factor is discussed in Section 10.5.1.).

$(L_a/L_d)f_y$ = the bar stress that would be expected at L_a assuming linear development of stress in the bar over L_d (Figure 10-13).

4. The contribution that must be provided by the head is then $f_{s,head} = f_y - f_{s,bond}$.
5. The minimum relative head area is then determined based on $f_{s,head}$.

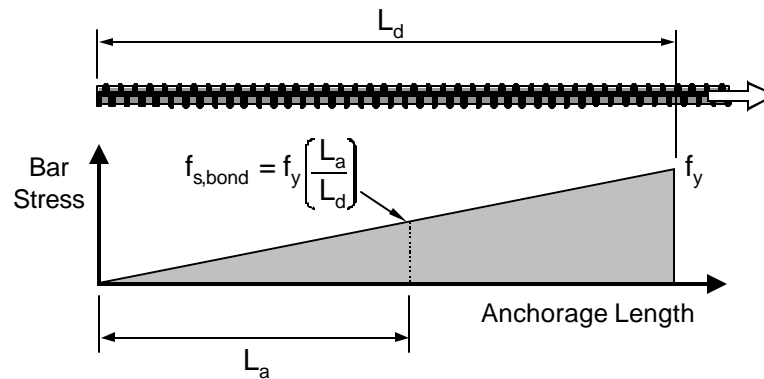


Figure 10-13: Development of bar stress for a non-headed bar

In order to use the preceding process, the modification factor for head size, χ , must be selected and the formula for head capacity must be re-arranged to solve for relative head area. Finally, a minimum anchorage length should be recommended for the method.

10.5.1 Bond Modification Factor for Head Size

In preceding sections, the modification factor for head size, χ , was related to the known relative head area of the bar. The factor would be much more convenient if it could be related to a variable such as the anchorage length, L_a , that is known before the head size is determined. Using the recommended capacity equations for bearing capacity and bond modified by the head size factor, combinations of relative head area and anchorage length that provide a bar stress of 60 ksi were plotted in Figure 10-14. The results plotted in Figure 10-14 indicate a very strange relationship between relative head area and anchorage length for low values of concrete strength ($f'_c = 3$ ksi). At 85 – 100% of the development length, the results suggest that the addition of a head can make the required anchorage length longer than the basic development length of the bar. The proposed modification factor for head size is based on test results representing a limited range

of anchorage lengths (about 30% of L_d maximum). It is unlikely that these results can be extrapolated to longer anchorage lengths. The results in Figure 10-14 are the result of doing so.

The head size modification factor is plotted against anchorage length in Figure 10-15. It can be seen that there is not a simple relationship between the modification factor and anchorage length. Furthermore, the relationship is not always unique (as for the cover dimensions listed in Figures 10-14 and 10-15 and a concrete strength of 3 ksi). For the time being, it is suggested that the modification factor for head size be taken as a constant equal to 0.3, which can be considered appropriate for anchorage lengths shorter than 30% of L_d . This conservative assumption limits the designer to consider very little bond stress over a very short anchorage length. Many designers will find that the contribution from bond under these conditions is so small that it will be easier to ignore bond altogether and design the head to carry the full yield strength of the bar. Though it is unrealistic to so severely restrict the contribution from bond and doing so will require unnecessarily large heads in many instances, there is not enough available data to provide any other recommendation at this time. The topic of bond in headed bars requires further investigation, particularly for headed bars with small relative head areas (< 3) and moderate to long anchorage lengths ($L_a = 30 - 90\%$ of L_d).

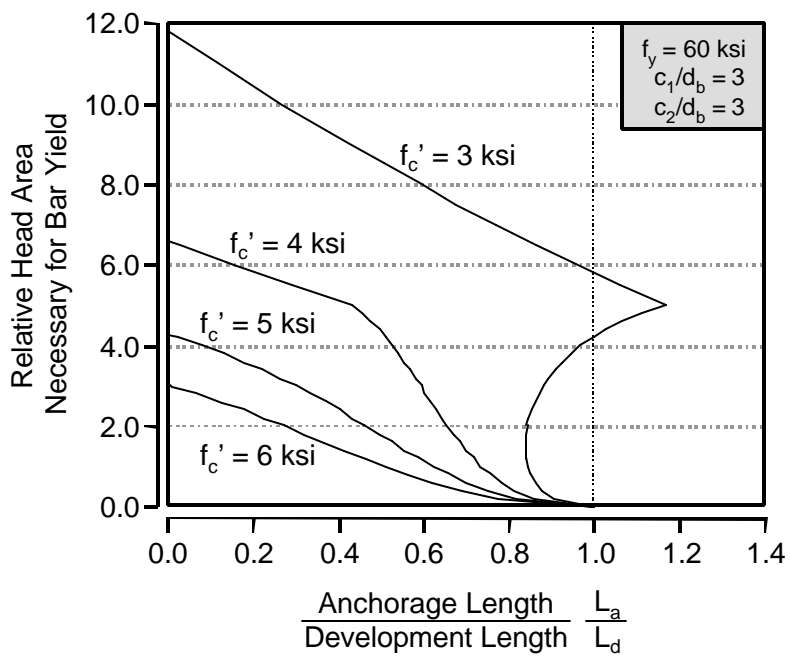


Figure 10-14: Required relative head area versus anchorage length

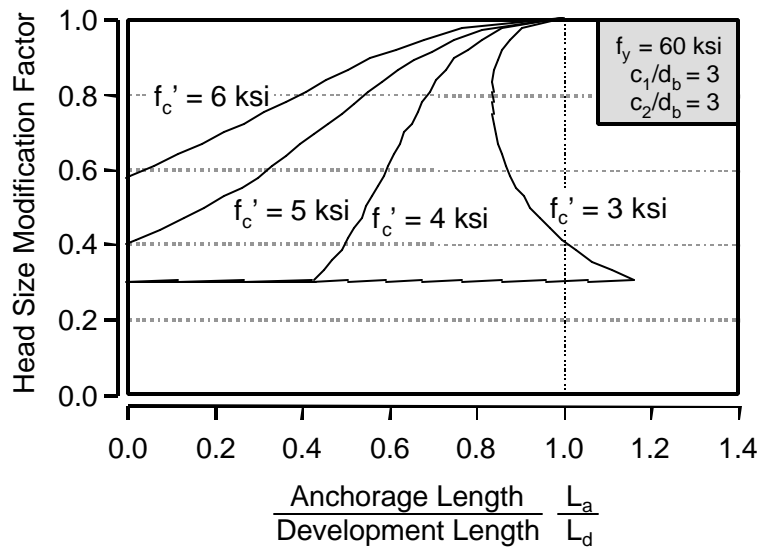


Figure 10-15: Head size modification factor versus anchorage length

10.5.2 Equation for Relative Head Area

Equation 10-1 provides a head bearing capacity (P) in kips based on several variables including net head area (A_{nh}). This equation would be more useful re-arranged to provide relative head area (A_{nh}/A_b) as a function of bar stress ($f_{s,head}$) in ksi. Equation 10-1 is so re-arranged in the following derivation (the 5% exclusion factor determined in Section 7.4.6 has been included):

$$\text{Bar Stress} = (\text{Head Capacity})/A_b = \left(0.9 \cdot n_{5\%} \cdot A_{nh} \left(\frac{2c_1}{\sqrt{A_{nh}}} \right) \psi f'_c \right) / A_b \quad (10-3)$$

$$f_{s,head} = \frac{1.26 \cdot \sqrt{A_{nh}} \cdot c_1 \cdot \psi \cdot f'_c}{\sqrt{A_b} \cdot \sqrt{A_b}} \quad (10-4)$$

$$\text{Substitute } \sqrt{A_b} = \sqrt{\frac{\pi d^2}{4}} \cong 0.9d_b,$$

$$f_{s,head} = 1.26 \cdot \sqrt{\frac{A_{nh}}{A_b}} \cdot \frac{c_1}{0.9d_b} \cdot \psi \cdot f'_c \quad (10-5)$$

$$f_{s,head} = 1.4 \cdot \sqrt{\frac{A_{nh}}{A_b}} \cdot \frac{c_1}{d_b} \cdot \psi \cdot f'_c \quad (10-6)$$

Now re-arrange to solve for the relative head area,

$$\sqrt{\frac{A_{nh}}{A_b}} = \frac{1}{1.4\psi} \cdot \frac{d_b}{c_1} \cdot \frac{f_{s,head}}{f'_c} \quad (10-7)$$

$$\frac{A_{nh}}{A_b} = \left(\frac{1}{1.4\psi} \cdot \frac{d_b}{c_1} \cdot \frac{f_{s,head}}{f'_c} \right)^2 \quad (10-8)$$

All variables are as defined at the beginning of the chapter. Equation 10-8 can be used to solve for the relative head area that is necessary to provide a given contribution to bar stress, $f_{s,head}$.

10.5.3 Minimum Anchorage Length

The proposed model for head bearing is based on tests in which the minimum anchorage length was at least $6d_b$. The model is not applicable when the anchorage length is less than $6d_b$. At shorter anchorage lengths, a different mode of failure occurs. Furthermore, analysis of the lap splice tests and the University of Texas beam-column tests revealed the importance of strut-and-tie modeling in determining the available anchorage length, l_a . It is highly recommended that the proposed headed bar anchorage model only be used when strut-and-tie modeling has been applied to determine critical anchorage points for ties and available anchorage lengths. The potential to confuse embedment length with anchorage length is great and can lead to catastrophic over-estimations of capacity.

10.6 RECOMMENDED CODE PROVISIONS

Recommended headed bar design provisions are proposed for the mechanical anchorage sections of the ACI [2] and AASHTO [1] codes. The following changes are recommended for Sections 12.6 and R12.6 of the ACI code. Similar changes are recommended for Section 5.11.3 of the AASHTO code with appropriate adjustments to article numbering. Changes and additions are italicized for emphasis:

12.6 Mechanical anchorage

12.6.1 *(no changes)*

12.6.2 Test results showing the adequacy of mechanical devices *other than headed bars* shall be presented to the building official. *Headed bars are permitted provided they conform to the provisions of 12.6.3 through 12.6.4.*

12.6.3 Development of reinforcement shall be permitted to consist of a combination of mechanical anchorage plus *bond along the anchorage length* of reinforcement between the point of maximum bar stress and the mechanical anchorage. *The stress provided by bearing of the head shall conform to 12.6.3.1 and the stress provided by bond shall conform to the provisions of 12.6.3.2.*

12.6.3.1 *The bar stress provided by bearing of the head, $f_{s,head}$, shall be computed by*

$$f_{s,head} = 1.4 \cdot \sqrt{\frac{A_{nh}}{A_b}} \cdot \left(\frac{c_1}{d_b}\right) \cdot Y \cdot f'_c$$

with

$$Y = 0.6 + 0.4 \left(\frac{c_2}{c_1}\right) \leq 2.0$$

where

A_{nh} = *net bearing area of the head (neglecting the bar area), in².*

c_1 = *the minimum cover dimension measured to the center of the bar, in.*

c_2 = *the minimum cover dimension measured perpendicular to the axis of c_1 , often referred to as the secondary cover dimension, in.*

Y = *the radial disturbance factor.*

12.6.3.2 *The bar stress provided by bond, $f_{s,bond}$, shall be computed by*

$$f_{s,bond} = \chi \cdot f_y \left(\frac{L_a}{L_d}\right)$$

where

L_a = the bonded anchorage length as determined by the provisions of 12.6.6,
in.

L_d = the development length of a non-headed bar of the same diameter as
determined from the provisions of 12.2, in.

c = the reduction factor for head size, 0.3 (a more exact expression to be
determined by future research)

The anchorage length, L_a , shall be measured from the point of maximum bar stress to the bearing face of the head. Anchorage length less than $6d_b$ shall not be permitted. Appropriate strut-and-tie models shall be used to determine critical sections at which the maximum bar stress occurs.

12.6.4 Any connection between the head and the bar shall be permitted provided the full bar stress expected from the head can be developed at the connection without slip of the reinforcement relative to the head. Furthermore, the head shall be sufficiently rigid to provide optimal bearing across the entire head area. Test results demonstrating the adequacy of the head-bar connection shall be provided to the appropriate building official. (The requirements of this provision should be addressed by ASTM. At the time when a suitable provision exists, the language of this provision can be adjusted to reference ASTM specifications.)

R12.6 Mechanical anchorage

R12.6.1 (no changes)

R12.6.3 *Total development of a bar with a mechanical anchorage is determined by summing the mechanisms that contribute to the anchorage. These are, the capacity in bearing of the mechanical anchorage and the bond along the anchorage length between the mechanical anchorage device and the critical section.*

R12.6.3.1 *The expression for the bar stress provided by the head can be rearranged to solve for the minimum head area that is necessary to provide a given bar stress requirement.*

R12.6.3.2 *A reduction factor of 0.3 is included to account for the decrease in bond that occurs as bar stress is transferred to the head. Tests indicate that bond stress generally peaks and begins to decline before the peak bearing stress on the head is developed. Test results have shown that the equation for the bar stress provided by the head is unsafe for anchorage lengths less than $6d_b$. At such short anchorage lengths, the importance of properly determining the critical section necessitates that strut-and-tie modeling techniques be used to determine the critical section. Improper determination of the critical section can lead to an over-estimation of the available anchorage length and may result in the determining of a head size that is too small or a cut-off point that does not provide sufficient anchorage length to develop the headed bar.*

R12.6.4 *The provisions assume that failure between the bar and the head are precluded. Any connection type is allowed that is sufficient to develop the strength of the bar and to engage the head without slipping. The provisions also assume failure of the head in flexure to be precluded as bearing pressure is applied.*

Sections 12.6.1 through 12.6.3 have been changed to alter terminology and to permit the use of headed bars without test results showing the adequacy of the bars for the intended application. Sections 12.6.3.1, 12.6.3.2, and 12.6.4 have been added to address the design issues of headed bars. The term anchorage length has been substituted for embedment length. The constant reduction (0.3) for bond stress is very conservative and should be examined in future research. Section 12.6.3.2 limits the minimum anchorage length and requires strut-and-tie modeling in the determination of the anchorage length. Section 12.6.4 addresses the quality assurance of the head to bar connection. It is intended to be flexible enough to permit a variety of head types. The necessary requirements for the strength and stiffness of the head to bar connection and the flexibility of the head plate have already been addressed to a limited extent in the ASTM A-970 standard for headed bar manufactures. This standard is still under development. At a time when the standard is complete, Section 12.6.4 can be replaced by a citation to ASTM A-970.

10.7 SUMMARY

The lap splice data were compared to the recommended bearing capacity model proposed in Chapter 7. The model was found to work well for tests with lap splices greater than or equal to $8d_b$. Bond data from the lap splice tests were combined with bond data from the CCT node tests in order to develop a modification factor for the reduction in failure bond that is associated with increasing head size. Data from the CCT node and lap splice tests as well as three additional headed bar studies were compared to the combined bond and head bearing model. The combined model worked well for tests with longer anchorage length/cover ratios (>2.5).

A method for using the proposed bond and bearing models in design was recommended. The modification factor for bond was found to be unrealistic for long anchorage lengths (between 85-100% of L_d) and further study was recommended. The model for bearing capacity was re-

arranged to solve for a required relative head area in terms of the bar stress that must be carried by the head. Equations 10-9 and 10-10 present the final model. Additionally, it was recommended that available anchorage length should be determined using appropriate strut-and-tie models and that a minimum anchorage length of $6d_b$ should be applied to headed bars. Draft language for code specifications was also provided.

Chapter 11: Design Examples

Three design examples are provided to illustrate the recommended design guidelines for headed bar anchorage. The first example, a bracket design, illustrates a CCT node problem. The second and third examples are of lap splice applications. Each example was chosen to emphasize important practical concerns for detailing of headed bars. For some of the examples, the shortcomings of the current recommendations are dramatized in order to underscore the necessity for additional research.

11.1 BRACKET DESIGN

The first example consists of a bracket attached to a column. The dimensions and loads are shown in Figure 11-1. The bracket supports a transfer beam with a vertical reaction of 100 kips. Horizontal restraint between the bracket and the transfer beam is prevented by use of a neoprene bearing pad. The column supports an axial load of 250 kips and a shear of 10 kips at its top. A concrete compression strength, f'_c , of 5 ksi and a steel yield stress, f_y , of 60 ksi are assumed. Due to the space limitations within the bracket, headed bars will be used for the bracket's tie bars.

Design of the column results in a 16" x 16" cross-section with #8 bars in each corner (Figure 11-2, part i). The width of the bracket is equal to the width of the column, 16". A 5" x 14" neoprene pad is assumed. Free-body forces at the section between the bracket and the column are used to design the tie steel for the bracket (Figure 11-2, part ii). The center-line of the tie is assumed to be 3" below the support surface of the bracket. This depth would provide a large cover for conventional bars, but if headed bars are used for the bracket tie then additional cover must be provided to accommodate the heads.

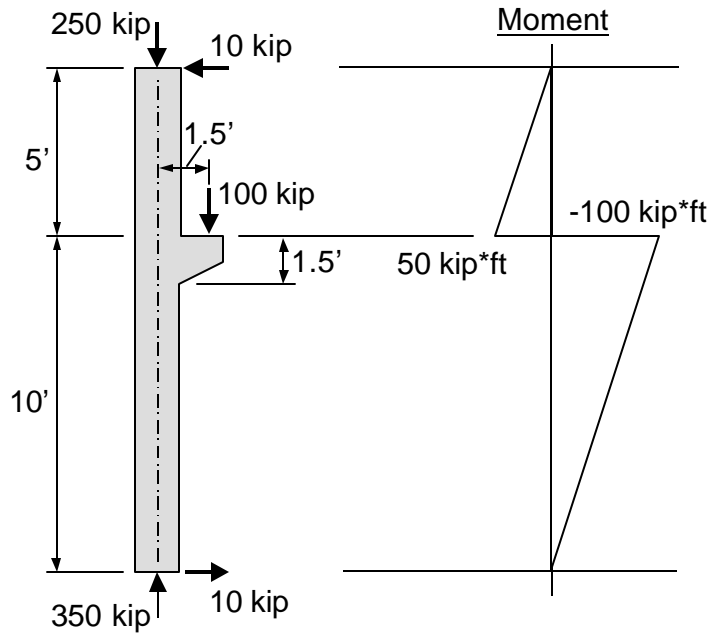


Figure 11-1: Loads and dimensions for bracket problem

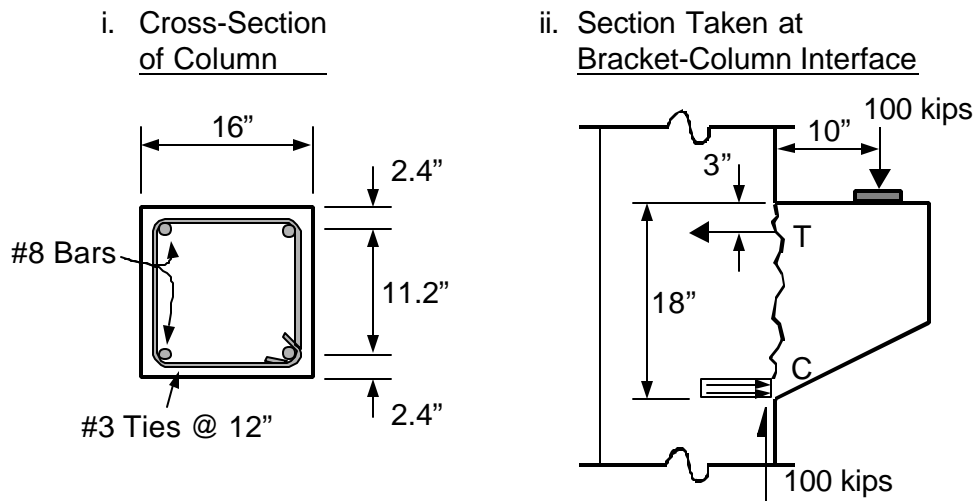


Figure 11-2: Column cross-section and free body forces on bracket

In this example, the headed bar is treated as a tie in a strut-and-tie model, and the ACI safety reduction (ϕ) factor of 0.75 is applied. The depth of the compression block is assumed to be about 2", making the tie force, T, and the required tie steel, A_s :

$$T = 100 \text{ kips} \cdot \frac{10''}{15'' - \frac{2''}{2}} = 71.4 \text{ kips}$$

$$T = 71.4 \text{ kips} = \phi A_s f_y = (0.75)(60 \text{ ksi})A_s$$

$$\text{Required tie steel, } A_s = \frac{71.4 \text{ kips}}{(0.75)(60 \text{ ksi})} = \mathbf{1.59 \text{ in}^2}$$

This tie steel can be provided by 3 #7 bars ($A_s = 3 \cdot 0.60 \text{ in}^2 = 1.80 \text{ in}^2$). These bars are spaced evenly within the available distance between the vertical column bars (Figure 11-3). This provides a center-to-center spacing of 4.6" between the #7 bars and a side cover dimension of 3.4" for the two outside bars. The top cover dimension is 3". The minimum cover dimension will be one half of the bar spacing, $c_1 = 4.6/2 = 2.3$ ". The secondary cover dimension, c_2 , is 3.0".

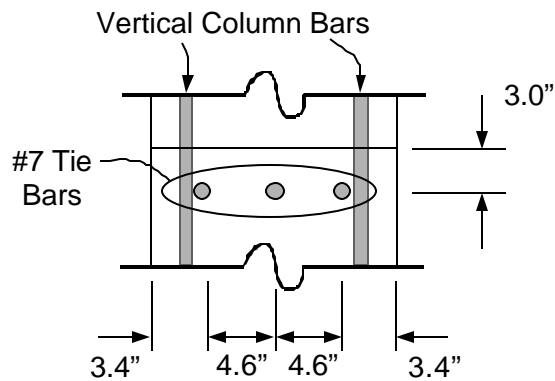


Figure 11-3: Spacing of bracket tie bars

Anchorage of the horizontal bracket tie must now be satisfied. The CCT node and the diagonal compression strut in the bracket must first be dimensioned. Because few realistic guidelines are available for dimensioning nodes, completion of this step is largely a matter of guesswork. However, in this case the pad dimensions define at least the length of the node. The CCT node was assumed to be 3" tall and as long as the bearing plate, 5". The diagonal compression strut was assumed to have a slope of about 54°, the angle defined by the centroids of the bracket forces. This geometry locates the point of critical bar development at a distance of roughly 7" from the face of the column wall (Figure 12-4). The distance from the critical development point to the far edge of the bearing plate is 6", which is equal to almost $7d_b$ for the tie steel, more than the minimum anchorage length for headed bars.

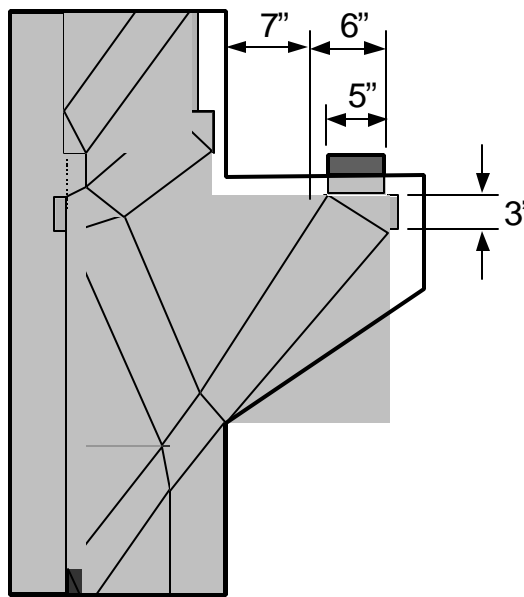


Figure 11-4: The available anchorage length within the bracket

Since the minimum anchorage length is provided, the heads can now be sized. The cover dimensions, c_1 and c_2 , have already been determined from bar spacing considerations. The anchorage length and the concrete strength are known. The bars are designed for 60 ksi of stress. First, the contribution from bond is estimated:

$$\begin{aligned} \text{Development length, } L_d &= \frac{3d_b}{40} \cdot \frac{f_y}{\sqrt{f_c}} \cdot \frac{\alpha\beta\gamma\lambda}{\left(\frac{c + K_{tr}}{d_b}\right)} \\ &= \frac{3(0.875")}{40} \cdot \frac{60,000 \text{ psi}}{\sqrt{5,000 \text{ psi}}} \cdot \frac{(1)(1.3)(1)(1)}{(2.1)} = \mathbf{34.5 \text{ in}} \end{aligned}$$

$$\text{Contribution from bond, } f_{s,\text{bond}} = 0.3 \cdot \frac{L_a}{L_d} \cdot f_y = 0.3 \cdot \frac{6"}{34.5"} \cdot 60 \text{ ksi} = \mathbf{3.1 \text{ ksi}}$$

Note, that in the calculation for the contribution from bond, the full anchorage length was used with no deduction for the wedge length in front of the head. The expected contribution from bond was only 3.1 ksi, which is about 5% of the required bar stress, a negligible amount. This example shows that the current recommendations for bond of headed bars allow such little bond that there is almost no point in performing the step of calculating the bond contribution. The head can simply be sized to carry the full bar stress, 60 ksi:

$$\text{Bar stress demand on the head, } f_{s,\text{head}} = f_y = 60 \text{ ksi}$$

$$\text{Radial disturbance factor, } \Psi = 0.6 + 0.4(c_2/c_1) = 0.6 + 0.4(3"/2.3") = 1.12$$

$$\text{Bar stress provided head, } f_{s,\text{head}} = 1.4 \sqrt{\frac{A_{nh}}{A_b} \left(\frac{c_1}{d_b} \right)} \Psi f_c'$$

$$60 \text{ ksi} = 1.4 \sqrt{\frac{A_{nh}}{(0.60 \text{ in}^2)} \left(\frac{2.3''}{0.875''} \right)} (1.12)(5 \text{ ksi})$$

$$\text{Required relative head area, } \frac{A_{nh}}{A_b} = \left[\left(\frac{60 \text{ ksi}}{5 \text{ ksi}} \right) \cdot \left(\frac{0.875''}{2.3''} \right) \cdot \frac{1}{(1.4)(1.12)} \right]^2 = 8.5$$

$$\text{The required gross head area, } A_{gh} = \left(\frac{A_{nh}}{A_b} + 1 \right) A_b = (8.5 + 1)(0.60 \text{ in}^2) = 5.7 \text{ in}^2$$

This area can be provided by a square head that is $2\frac{1}{2}'' \times 2\frac{1}{2}''$ or a circular head that is $2\frac{3}{4}''$ in diameter. The circular heads will provide a minimum clear cover of $1\frac{7}{8}''$, slightly under the requirements for exterior exposure. The square heads can provide more clear cover over the head if special attention is given to positioning and orientation of the heads during construction. The final detail is shown in Figure 11-5.

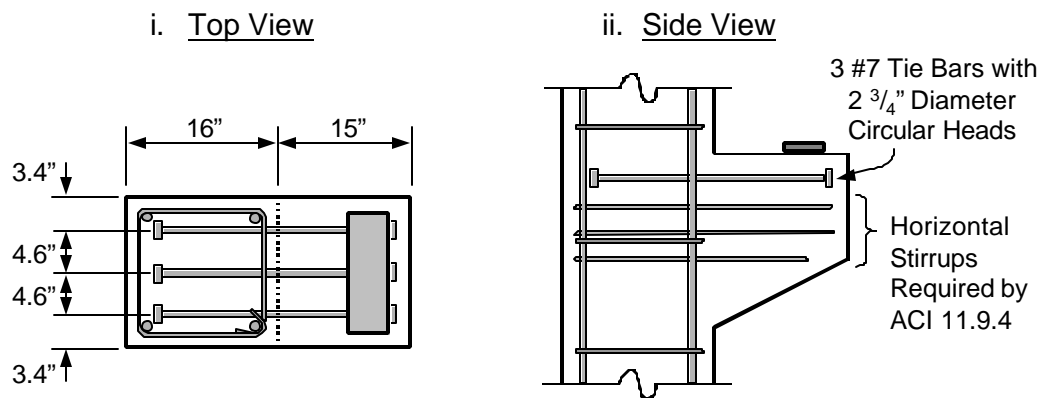


Figure 11-5: Final detail for bracket

11.2 DETAILING OF PRECAST PANEL CLOSURE STRIP

The second example is the detailing of a closure strip between precast panels of an elevated walkway. The walkway will consist of precast slab panels that will be made continuous by the casting of a closure strip at the supports. Continuity of the longitudinal bars will be achieved by lap splicing within the closure strip. The closure strip is limited to a 10" width requiring the use of headed bars for the lap splice.

Plan and elevation views of the walkway are provided in Figure 11-6. The walkway is 10'-10" wide with a 16'-8" span length. The slab is 6" thick with 13 #5 bars spaced at 10" for the longitudinal steel. The walkway supports its own weight (75 psf) plus an additional 10 psf for railing and other dead load. The live load is 85 psf. Continuous moment capacity across supports is required to carry ultimate load. A concrete strength of 5 ksi is assumed.

To facilitate the placement of the panels, the headed longitudinal bars are detailed with an offset to one side of the panel. The offset allows alternate panels to be rotated, providing a non-contact lap splice with maximum spacing between opposing bars in the closure strip. This minimizes the risk of conflicts in bar placement when the panels are dropped into place. This lap configuration provides a 5" space between opposing lapped bars (Figure 11-7). The lap length must provide room for head thickness ($\frac{3}{4}$ " or less) and some positioning tolerance ($\frac{1}{2}$ " each side). A 7.5" lap is assumed. The resulting anchorage length is determined assuming a strut angle of 55° between opposing bars. The anchorage length is 4" which is equal to $6.4d_b$, almost the minimum allowed.

i. Plan View



ii. Elevation View

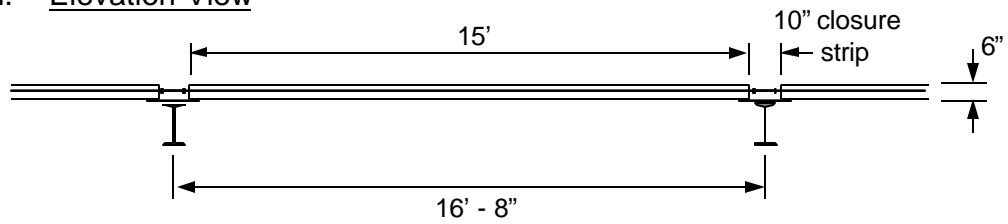


Figure 12-6: Plan and elevation views for precast slab problem

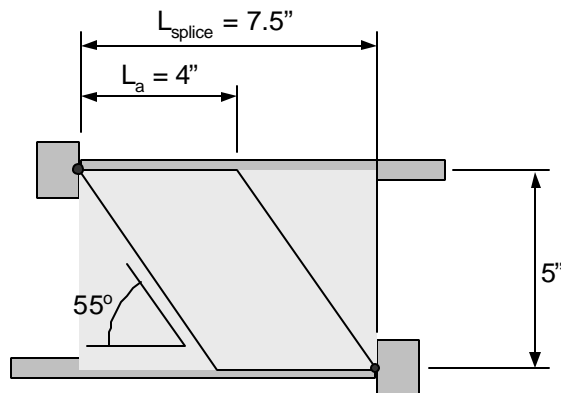


Figure 11-7: Anchorage length of lap splice

It is assumed that the bars will be epoxy coated. This should have no effect on head capacity, but will make the bond contribution negligible. For convenience, the contribution from bond is ignored and the head is sized to carry the full yield stress, 60 ksi. The side cover dimension is taken as half the distance between opposing bars: $5''/2 = 2.5''$. The top and bottom cover dimensions are half the slab thickness: $6''/2 = 3''$. Thus, $c_1 = 2.5''$ and $c_2 = 3''$. The minimum head size is calculated as follows:

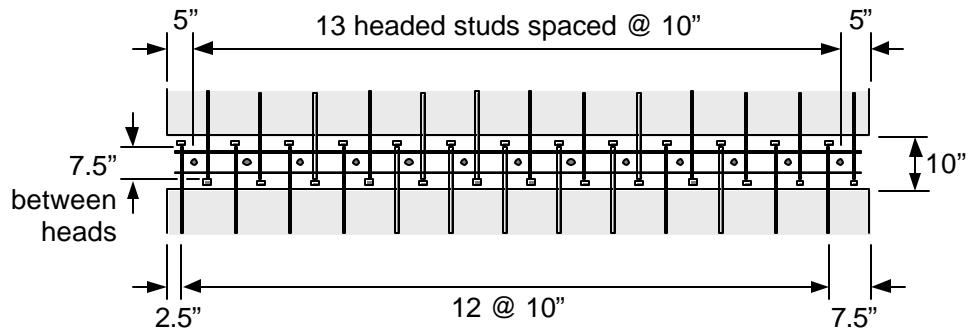
$$\text{Radial disturbance factor, } \Psi = 0.6 + 0.4(c_2/c_1) = 0.6 + 0.4(3''/2.5'') = 1.08$$

$$\begin{aligned} \text{Relative head area, } \frac{A_{nh}}{A_b} &= \left(\frac{1}{1.4\Psi} \cdot \frac{d_b}{c_1} \cdot \frac{f_{s,head}}{f'_c} \right)^2 \\ &= \left(\frac{1}{(1.4)(1.08)} \cdot \frac{0.625''}{2.5''} \cdot \frac{60 \text{ ksi}}{5 \text{ ksi}} \right)^2 = \mathbf{3.9} \end{aligned}$$

$$\text{Gross head area, } A_{gh} = \left(\frac{A_{nh}}{A_b} + 1 \right) A_b = (3.9+1)(0.31 \text{ in}^2) = \mathbf{1.5 \text{ in}^2}$$

The required head size can be provided by a circular head with a 1.4" diameter. The final detail is shown in Figure 11-8. Transverse bars in the lap zone are recommended. Additionally, headed studs welded to the support girder will provide a connection between the slab and the support and tie-down confinement for the lap.

i. Top View



ii. Side View

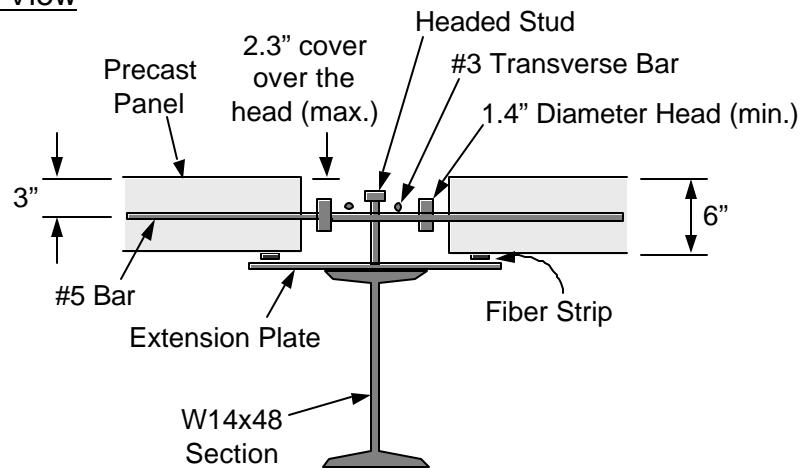


Figure 11-8: Final detail for closure strip

11.3 BENT CAP EXTENSION

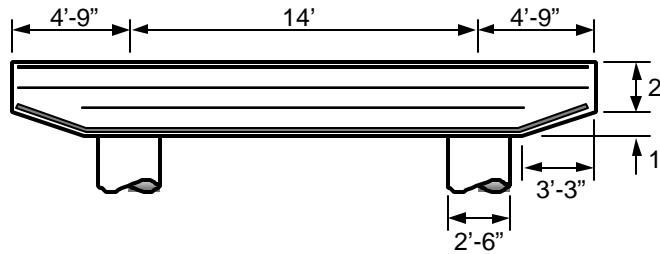
The final design example is for the extension of a typical bridge bent cap. This example will illustrate a problem that requires a different approach for the selection of head size than in the previous examples. Whereas anchorage length had been a known variable that was used to select a head size in the previous problems, this example will require the selection of a head first and then

the calculation of a required anchorage length. Furthermore, several of the shortcomings of the current research will be demonstrated. The examination of this problem will reveal that it cannot be solved using the recommendations of this report.

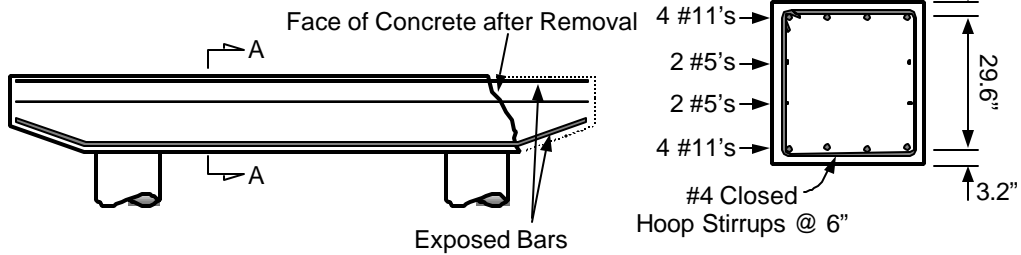
The extension of an existing bent cap requires that the existing concrete be removed to expose the longitudinal bars. This is a time consuming process for the contractor. The amount of concrete removed is dependant on the length of longitudinal bar that must be exposed for splicing. Reductions in lap length result in less concrete removal for the contractor and provides savings in time and labor. The use of headed bar lap splices shows great potential for achieving the shorter lap splices desired for this particular problem.

A standard Texas Department of Transportation plan for a bent cap supporting a 24' wide roadway is shown in Figure 11-9. The problem requires that the roadway supported by the bent cap be expanded to 38'. This requires the retrofit extension of the bent cap by 14'. The bent cap extension must have full continuity with the existing bent cap. Splicing of the new longitudinal steel with the original longitudinal steel must be accomplished. In this scenario, headed bars will be examined as a means of shortening the required lap length between the new longitudinal bars and the existing longitudinal bars.

i. Existing Bent Cap for 24' Roadway



ii. Concrete Chiseled from Bent End



iii. Retrofit Bent Cap for 38' Roadway

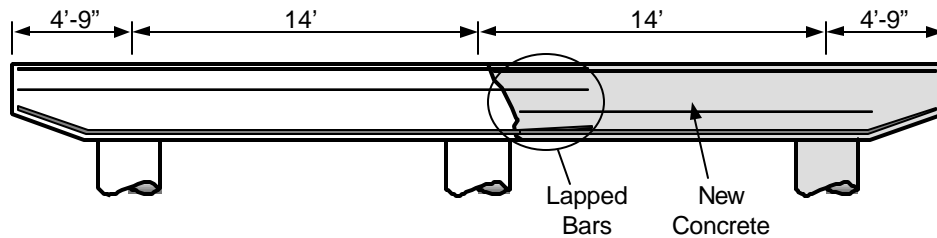


Figure 11-9: Dimensions of bent cap

The designer might wonder if the existing longitudinal bars must be retrofitted with heads in order to provide a reduced splice length or if headed bars can be lapped against the old non-headed bars and still provide a reduction in splice length. The mechanism for force transfer between a headed and non-headed bar is shown in Figure 11-10. While the anchorage length that is provided by the lap may be adequate for the headed bar, the non-headed bar will be unable to develop in that length. The full yield stress will not be developed in the non-headed bar because

the full development length has not been provided. The capacity of the lap will be limited to the capacity of the weaker anchorage, which will be provided by the non-headed bar. There is no benefit to providing a head on one lapped bar if the opposing bar is not headed. Thus, the existing bars must be retrofitted with heads, and head selection must be based on the feasibility of retrofitting a head to the existing bars. Friction-welded heads cannot be field-fitted, but the other two currently available head types can be attached in the field.

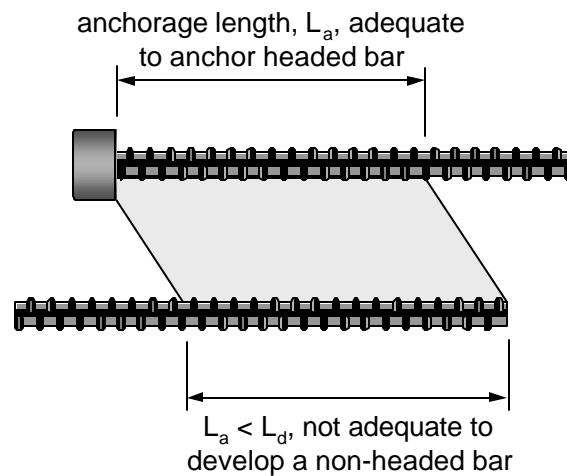


Figure 11-10: Headed/non-headed bar lap splice

Xtender forged heads can be added in the field. They provide a relatively small bearing area and would require a long bonded length to achieve yield. According to the product literature, 6 to 7 bar diameters (for #6 - #11 bar sizes) must be exposed in order to properly fit the upsetting vise over the end of the bar and apply the head. Since more than $6 - 7d_b$ would have to be exposed to develop a headed bar lap, the contractor would probably choose to use the mechanical coupling system that accompanies the Xtender heads rather than use a headed lap splice which

would require more concrete removal. The mechanical coupling system is promising for the problem but is not considered here because it does not illustrate the issues of a headed bar lap.

The Lenton Terminator threaded head can also be used in the field. These heads provide a larger bearing area and require less bonded length of bar to achieve yield. The Lenton Terminator will be used as the case study head in this example. The longitudinal bars in the bent cap are #11 size. The #11 head produced by Lenton has a 3" diameter and is $1\frac{11}{16}$ " long. The relative head area is 3.53.

The lap splice in this problem can not be as neatly arranged as the splice in the previous problem. There is not enough space for all bars with heads to fit in a single layer in the lap zone. Thus the lap has to have an "over-under" configuration (Figure 11-11). Furthermore, the bars will probably be placed in contact with one another. This research study has dealt primarily with non-contact lap splices and there is little guidance available for designing the contact splice in this problem. In the very limited series of tests in which contact splices were compared to non-contact splices, the contact splices had a capacity greater than or equal to the non-contact configuration. The splice in this example will be treated as if it were laid out in a non-contact configuration within a single layer. However, the legitimacy of this approach has not been verified by experimental investigation. The side cover dimension for a non-contact splice would be $\frac{1}{4}$ of the spacing between bars, $8.9"/4 = 2.2"$. The top and bottom cover dimensions are 3.2". A concrete strength of 5 ksi is assumed. The capacity provided by the head is:

$$\text{Radial disturbance factor, } \Psi = 0.6 + 0.4(3.2"/2.2") = 1.18$$

$$f_{s,\text{head}} = 1.4 \sqrt{\frac{A_{\text{mh}}}{A_b}} \left(\frac{c_1}{d_b} \right) \Psi f_c' = 1.4 \sqrt{3.53} \left(\frac{2.2"}{1.41"} \right) (1.18)(5 \text{ ksi}) = \mathbf{24.2 \text{ ksi}}$$

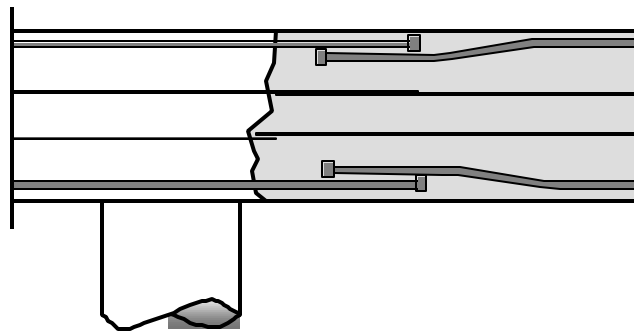


Figure 11-11: Over-under lap splice

Because the head size is known, the bond reduction factor that was determined in Chapter 10 can be used. This formula was not included in the proposed design provisions, but will be used in this example in order to determine the minimum anchorage length that might be used. The formula for the head size reduction factor was:

$$\text{Head Size Reduction Factor, } \chi = 1.0 - 0.7 \left(\frac{A_{nh}/A_b}{5.0} \right) \geq 0.3 \quad (11-1)$$

The head size reduction factor for this problem is:

$$\chi = 1.0 - 0.7 \left(\frac{3.53}{5.0} \right) = 0.51$$

The stress required from bond and the head size reduction factor are used to calculate a required anchorage length. The lap length magnification factor for this Class C splice is ignored.

$$\text{Required stress from bond, } f_{s,\text{bond}} = 60 \text{ ksi} - 24.2 \text{ ksi} = 35.8 \text{ ksi}$$

$$\text{Development length (top cast assumed), } L_d = \frac{3d_b}{40} \cdot \frac{f_y}{\sqrt{f'_c}} \cdot \frac{\alpha\beta\gamma\lambda}{\left(\frac{c + K_{tr}}{d_b} \right)}$$

$$= \frac{3(1.41")}{40} \cdot \frac{60,000 \text{ psi}}{\sqrt{5,000 \text{ psi}}} \cdot \frac{(1)(1.3)(1)(1)}{(2.5)} = 46.7 \text{ in}$$

The required anchorage length is:

$$L_a = \frac{f_{s,bond}}{f_y} \cdot \frac{L_d}{\chi} = \frac{35.8 \text{ ksi}}{60 \text{ ksi}} \cdot \frac{46.7"}{0.51} = \mathbf{54.6"}$$

The calculation shows that the addition of the head increased the necessary anchorage length from the non-headed case. This example points out one of the shortcomings of the available research. It is not expected that the anchorage length of the headed bar should be longer than its corresponding non-headed development length. This result reflects the lack of data for headed bar tests with moderate to long anchorage lengths. Furthermore, there is no guidance as yet for the analysis of contact lap splice or of the over-under lap configuration used in this problem. Further research on these issues is required. The calculation of anchorage length would provide the final step of this problem. It would tell the contractor how much of the existing bar must be exposed to provide the lap.

Chapter 12: Summary and Conclusions

12.1 SUMMARY

A test program was conducted to study the anchorage behavior of headed bars in CCT nodes and lap splices. The goal of the testing was to determine the viability of headed bars to shorten development lengths and alleviate congestion in complex structural details. CCT node and lap splice specimens were selected to simulate commonly occurring anchorage situations where development length and congestion are important factors.

Sixty-four CCT node specimens were tested. The nodes in the specimens were anchored by a single tie bar (Figure 12-1). The variables in the study were: anchorage type (straight, headed, or hooked bar), relative head area ($A_{nh}/A_b = 0.0$ to 10.4), strut angle ($\theta_{strut} = 30^\circ, 45^\circ,$ or 55°), tie bar size (#8 or #11), and the level of confinement (none or #3 closed hoop stirrups placed at 6" or 3"). Specimens were instrumented to measure the bearing reaction at the CCT node, strain along the anchorage portion of the tie bar, and head slip. The cracking behavior was also observed and recorded.

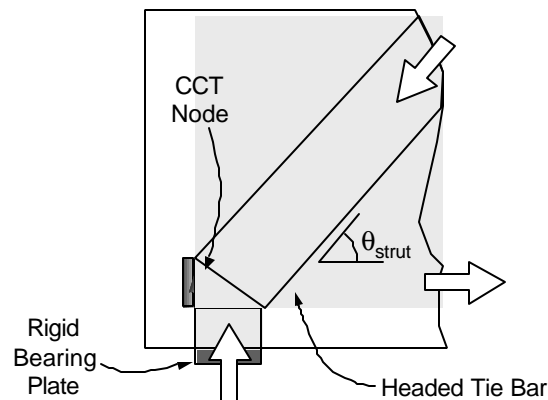


Figure 12-1: Typical CCT node from the test program

Twenty-seven lap splice specimens were also tested. Slab specimens were fabricated with a lap splice at midspan. The slabs were loaded in flexure, placing the lap splice in tension. The lap splice consisted of headed or non-headed bars placed in a single layer (Figure 12-2). The variables in the study were: head size ($A_{nh}/A_b = 0.0$ to 4.7), lap length ($L_d/d_b = 3$ to 14), bar spacing ($s_b/d_b = 6$ or 10), lap configuration (lapped bars in contact or not), debonded versus bonded bars, and confinement type (no confinement, hairpin confinement, or transverse bars in the lap zone). Specimens were instrumented to measure the load on the specimen, strain along the bars within the lap zone, and midspan deflection of the slab. The cracking behavior was also observed and recorded.

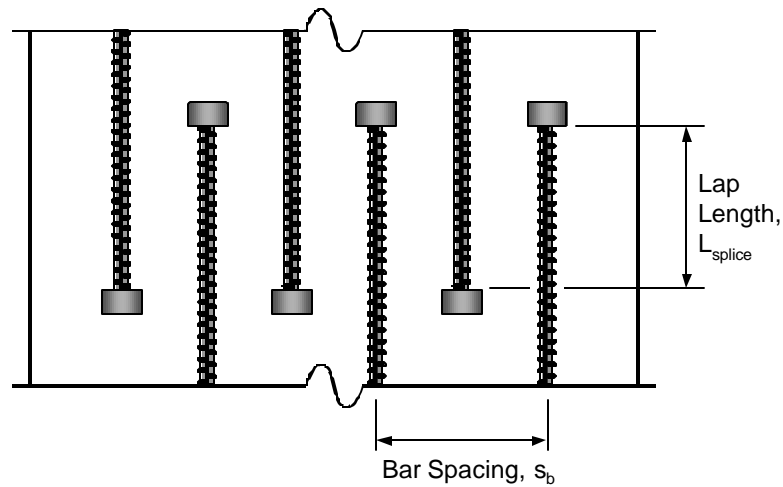


Figure 12-2: Plan view of typical lap splice

Test results were analyzed and reported. Conclusions from the tests were used to develop recommendations for the design of headed bar anchorage in CCT nodes and lap splices. Design examples were provided to illustrate the use of the design guidelines. Suggestions for future research are provided at the end of this chapter

12.2 CONCLUSIONS

Conclusions from the tests are summarized in the following subsections. The conclusions are divided into three categories: conclusions about the anchorage of headed bars that were drawn from all of the test data, specific conclusions about the behavior of CCT nodes, and specific conclusions about the behavior of lap splices.

12.2.1 Anchorage Capacity of Headed Bars

The following conclusions about the anchorage capacity of headed bars were drawn from the data collected in the study:

- **The anchorage process of headed bars consists of two stages.** In the first stage, anchorage is carried almost entirely by bond stress, which peaks as the first stage ends. In the second stage, the bond begins to deteriorate allowing bar stress to be transferred to the head. Throughout the second stage, bond declines and head bearing increases. The second stage ends with yield of the bar or bearing failure of the concrete at the head. As a result of this behavior, peak bond and peak head bearing can not occur simultaneously. The capacity of the bar at failure is determined by the peak bearing capacity plus some contribution from reduced bond along the bar between the head and the point of peak bar stress.
- **The bearing capacity of the heads** was similar to the side blow-out capacity of deeply embedded anchor bolts and the bearing capacity of rigid plates on concrete. The bearing behavior of these three elements (headed bars, anchor bolts, and bearing plates) can be treated similarly in analysis. A formula was developed to determine the bearing capacity of rigid heads and plates which is dependent on four variables: the net bearing area (A_{nh}), the cover dimensions (c_1 and c_2), and the concrete cylinder

strength (f'_c). The equations for calculating nominal bearing capacity for a rigid head are reproduced below:

$$\text{Nominal Bearing Capacity (kips)} = n_{5\%} (A_{nh}) \cdot \left(\frac{2c_1}{\sqrt{A_{nh}}} \right) \cdot \Psi \cdot f'_c \quad (12-1)$$

$$\Psi = 0.6 + 0.4 \left(\frac{c_2}{c_1} \right) \leq 2.0 \quad (12-2)$$

A_{nh} = net bearing area of the head (in^2)

c_1 = minimum cover dimension over the bar (in)

c_2 = minimum cover dimension over the bar measured orthogonal to c_1 (in)

f'_c = concrete cylinder strength (ksi)

$n_{5\%}$ = 5% exclusion factor, 0.7

Ψ = radial disturbance factor (a function of the cover dimensions)

This model was used to compute capacities obtained from bearing, anchor bolt, and headed bar studies. The average calculated strength (omitting $n_{5\%}$) was equal to the average measured strength with a coefficient of variation of 20%.

- **The model for bearing capacity can be rewritten** for determining either the bar stress ($f_{s,\text{head}}$) provided by a given relative head area (A_{nh}/A_b) or the necessary relative head area to provide a given bar stress:

$$f_{s,\text{head}} = 2n_{5\%} \cdot \sqrt{\frac{A_{nh}}{A_b}} \cdot \left(\frac{c_1}{d_b} \right) \cdot \Psi \cdot f'_c \quad (12-3)$$

$$\frac{A_{nh}}{A_b} = \left(\frac{1}{2n_{5\%}} \cdot \frac{1}{\Psi} \cdot \frac{d_b}{c_1} \cdot \frac{f_{s,head}}{f'_c} \right)^2 \quad (12-4)$$

$f_{s,head}$ = the bar stress supplied by or required from the head (ksi)

A_b = the bar cross-sectional area (in²)

d_b = the bar diameter (in)

- **A minimum anchorage length of 6d_b is required** for applicability of Equations 12-3 and 12-4 to headed bars. For short anchorage lengths, a different failure mode occurs and the model is unconservative for predicting capacity.
- **The failure bond stress can be directly related to head size.** The larger the relative size of the head, the smaller the bond stress sustained at failure. Among the CCT node tests and lap splice tests of this study, this relationship was found to be linear with a minimum bond stress of 30% the peak bond stress that occurs during the first stage of bar anchorage.
- **The bearing capacity of the head was not significantly improved by confinement in the form of hoop stirrups or hairpins.** Previous studies have shown that it is very difficult to improve the anchorage of a headed bar with confining steel. It is far more economical to improve the bearing capacity by simply increasing the size of the head.
- **Confinement appeared to help sustain bond stresses** during the second stage of headed bar anchorage when bar stress is transferred to the head. The effect of confinement on the bond stress of headed bars requires further study.

- **The anchorage length of a headed bar must be distinguished from its embedment depth.** The potential confusion between these two concepts can lead to dangerous detailing mistakes. In order to prevent unsafe anchorage conditions, strut-and-tie modeling must be used to determine the critical development points for headed bars. Anchorage length is measured from the critical development point (the point where yield capacity in the bar must be achieved) to the bearing face of the head and is frequently shorter than the actual embedment depth (which is measured from the bearing face of the head to the closest concrete surface or edge through which the bar passes). Anchorage length determines the straight length of deformed bar available for bond and reduces the bearing capacity of the head if it is too short.
- **Slip of the head** was decreased as head size was increased for a given anchorage length. Slip occurs in two stages: insignificant head slip occurs before the head attains most of its capacity. Once the capacity in bearing is reached, slip initiates and the head provides little resistance to movement with failure occurring quickly thereafter.
- **Head shape and aspect ratio** had no significant effect on capacity. However, because head orientation cannot be controlled under field conditions, circular heads provide the most reliable control of clear cover over the head. The choice of head shape should be based on detailing considerations such as clearance and congestion.
- **Headed bars provide a feasible substitute for hooks.** Headed bars can achieve equal or superior performance to comparable hooked bars depending on head size.

12.2.2 CCT Node Behavior

The following conclusions about the behavior of CCT nodes were drawn from the data collected in the study:

- **The critical development point** of the tie bar in a CCT node can be estimated as the intersection of the tie bar and the edge of the diagonal compression strut that is anchored by that tie bar (Figure 12-3).

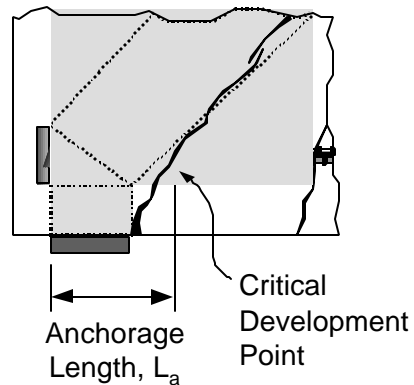


Figure 12-3: Critical development point for a CCT node

- **The state of stress at a CCT node** reverses on either side of the critical crack. Beneath the CCT node, compression stresses from the lower bearing plate neck inward to equilibrate spatially with the bearing face of the headed bar. This creates a region of vertical and transverse compression. This region begins at the bearing face of the head and extends to the surface of the critical diagonal crack where development of the bar begins. On the other side of the crack, radial splitting stresses created by bond of the reinforcing bar cause a state of tension within the concrete (Figure 12-4).

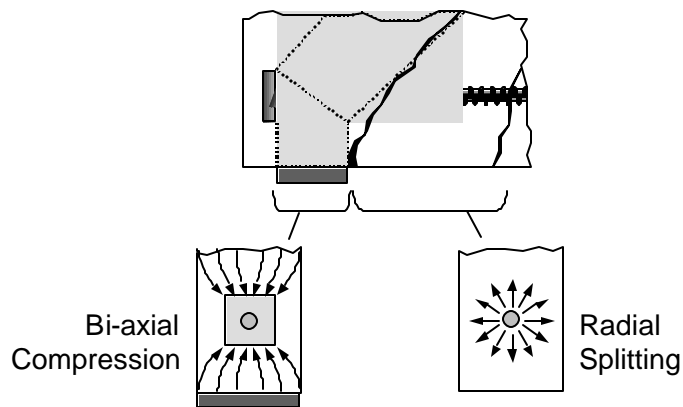


Figure 12-4: The state of stress at the CCT node

- **CCT nodes fail by mechanisms related to anchorage.** Non-headed bars fail by pullout from the node. Headed bars fail when bearing stress at the head exceeds the bearing capacity of the concrete. Failure of a CCT node anchored by a headed bar is explosive, resulting in rupture of the node and struts. Rupture is characterized by crushing just above the head and lateral splitting of the diagonal strut. The extent to which these two characteristics occur depends on head size and orientation.
- **The development of the truss mechanism is a staged process.** The strut-and-tie mechanism has a preference to transfer force along the most direct path between loads or reactions. In a D-region with stirrups or other reinforcement capable of acting as tension ties, force is initially transferred along a straight path from the point of load application to the CCT node. Only after extensive cracking and softening of the primary strut, are stirrups utilized to form secondary strut paths. The formation of secondary strut paths may not occur until after the peak capacity of the member has been reached.

- **The anchorage length in the CCT node zone can be increased by confinement.** Changes in the strut-and-tie mechanism (provided by adding vertical stirrups) allow the critical development point of the headed bar to move away from the primary CCT node. Due to the increases in anchorage length, bond stress can act over a longer portion of the bar, increasing the total anchorage capacity.
- **Variations in strut angle** do not effect the bearing capacity of the head or the bond stress developed by the bar. However, strut angle does effect the anchorage length of the bar. Shallow strut angles allow a longer length of bar to be included within the bounds of the diagonal strut, moving the critical development point away from the head and increasing anchorage length. The increase in the anchorage length of the tie bar results in a higher anchorage capacity for the tie.
- **Bond stress within a CCT node** is significantly improved by lateral compression and platen restraint. In the current study and tests reported in the literature, little change in bond stress has been observed with changes in lateral compression, which tends to indicate that lateral compression is not as influential as platen restraint. Platen restraint may provide significant increases in bond stress and should be a subject for future study.
- **CCT nodes anchored by bars with 180° hooks** are taller than analogous nodes anchored by headed or non-headed bars. The height of the node is increased to the full height of the hook. The centroid where the strut and tie forces intersect seems to occur just inside the bend of the hook. A hooked bar anchorage fails by splitting the node and struts laterally.

- **The dimensions of CCT and CCC nodes** are much smaller than the dimensions suggested in the ACI and AASHTO code provisions. Furthermore, the stresses sustained by these nodes are much higher than the stresses allowed under the current code provisions. The ultimate strength of nodes may be completely controlled by anchorage considerations. The allowable stress requirements for nodes and struts require further experimental investigation.
- **The philosophy of the current code provisions** for determining the capacity of CCT nodes may require reconsideration. The evidence from the tests shows that the failure of these nodes is primarily related to anchorage and that the current stress limits for nodes are unrealistic. It is possible that CCT nodes cannot be failed in compression if anchorage of the tie bars is satisfied. The stress limits imposed by the code provisions may be unnecessary.

12.2.3 Lap Splice Behavior

The following conclusions about the behavior of lap splices were drawn from the data collected in the study:

- **The mechanism of stress transfer** between opposing bars in non-contact lap splices is by struts acting at an angle to the direction of the bar. The resulting strut-and-tie mechanism causes the lapped bars to have anchorage lengths that are less than the lap length. The struts between lapped bars were observed to occur at an angle of about 55° to the axis of the bar (Figure 12-5).

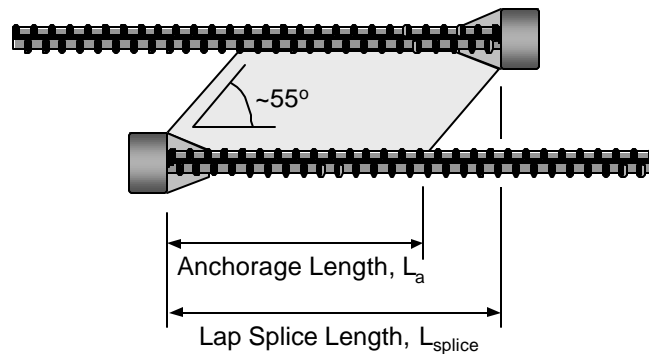


Figure 12-5: Mechanism of stress transfer between opposing lapped bars

- A **minimum anchorage length of $6d_b$** is required to properly develop the bearing capacity of the head. Provided the anchorage length is longer than $6d_b$, the lap length does not effect the basic mechanism of stress transfer. At shorter anchorage lengths, the mechanism of failure was different.
- **Head size and shape** do not effect the mechanism of stress transfer.
- **Determination of cover dimensions**, c_1 and c_2 , must account for the extent of bond splitting cracks propagating from opposing lapped bars. Data from the tests of this study indicated that the side cover dimension should be taken as half the distance between opposing lapped bars.
- **Bar spacing** effects splice capacity due to the change in side cover dimension provided for the heads. Smaller bar spacing results in reduced head capacity.
- **Debonding of the lapped bars** eliminated bond splitting cracks and increased the side cover dimension to the full center-to-center distance between opposing lapped bars. This eliminated the bond contribution to anchorage, but significantly improved the bearing capacity of the head due to the increase in side cover dimension. If the behavior of the debonded test is indicative of the behavior of epoxy coated bars (in

which the bond is partially obstructed by the epoxy coating), then less bond stress and greater head bearing capacity can be expected compared to analogous uncoated lapped bars. Tests of epoxy coated, lapped, headed bars should be conducted in order to verify this behavior and to gauge the extent of the differences from uncoated, headed bars.

- **Transverse confining bars** parallel to the plane of the lap splice and placed within the cover concrete over the splices provide the best confinement for lapped bars. Transverse bars help to reinforce the angled struts between opposing bars and are integrated into the strut-and-tie mechanism of stress transfer.
- **Tie-down or tie-back confinement** perpendicular to the plane of the lap splice does not significantly improve lap splice performance. Such confinement does not become active until peak capacity is nearly achieved and primarily helps by providing residual capacity after the peak capacity has passed. Tie-down reinforcement in the form of hairpins might be best placed along the bonded length of the headed bars where it may help to sustain peak bond stress until failure.
- **Contact lap splices** may have a greater capacity than non-contact lap splices, however, the only tests conducted with contact lap splices had very small lap lengths and anchorage lengths were less than $6d_b$. Additional tests on the effect of lap configuration should be conducted at longer lap lengths.

12.3 SUGGESTIONS FOR FUTURE RESEARCH

Further studies of headed bars are recommended. The following experimental goals are suggested:

1. The bond developed by headed bars is still uncertain. The current study has shown that the failure bond of a headed bar is less than the peak bond. However, the magnitude of the reduction in bond is unknown for many cases. Headed bars with long anchorage lengths and small heads were not studied. Additional tests of such headed bars are recommended. Furthermore, the effects of confinement and variations in concrete strength on the failure bond have not been addressed. These issues require additional experimental investigation.
2. Studies of epoxy coated headed bars should be performed. Epoxy is not expected to effect the bearing ability of the head, but its effect on bond and the magnitude of bond splitting cracks for lapped headed bars (which effects side cover and, subsequently, head capacity) is unknown.
3. Additional studies of lapped headed bars investigating the effect of lap configuration (contact versus non-contact) at long lap lengths should be performed. Primarily, the changes in the strut-and-tie mechanism of force transfer between opposing bars should be determined.
4. Proof tests that examine the ultimate and service level performance of headed bars should be conducted. Such tests should be designed for anchorage controlled failure. Previous large-scale studies have only explored the feasibility of headed bars for specific applications without examining the effects of premature anchorage failure on the ultimate capacity and behavior of the whole structural member. In all cases,

the head sizes were sufficiently large to provide yielding of the headed bars. What is needed is a verification of the proposed design models for application specific tests.

Additional node tests should also be performed. Among the goals of such research should be included:

1. Tests to determine realistic dimensions for nodes and the stress limits that can be sustained. The use of instrumentation to measure the flow of stresses around nodes may prove useful for this.
2. The determination of the critical anchorage points for bars anchored in CTT nodes.
3. The effect of anchorage on node capacity should be defined. Two specific questions should be answered: what is required to satisfy anchorage at a node and, if anchorage is satisfied, can a node fail in compression?
4. A better understanding of the effects of platen restraint and lateral compression is required. Does lateral compression by itself effect bond? When can platen restraint be relied on, and how much does it effect bond? How much does platen restraint effect allowable stresses in CCC nodes?
5. Confinement of nodes should be studied. Effective means to provide confinement for nodes should be determined, or even if confinement of nodes is practical.
6. Finally, the effectiveness of secondary steel such as stirrups in developing alternative strut paths should be determined. What degree of cracking is required for secondary strut paths to form and will they enhance capacity when they form? Will too much stiffness be lost by the time secondary strut mechanisms form?

Appendix A: Instrumentation and Mechanical Properties of Reinforcing Bars

Tensile and flexural properties were measured for the different stocks of deformed bars used in the research. Much of the data for the performance of the headed bars were determined from strain gages placed on the surface of the deformed bars. Because this type of instrumentation was so pervasive in the research, it is important to discuss it in detail. Mechanical property tests of bar samples were always calibrated with regard to strain gage measurements.

A.1 INSTRUMENTATION OF REINFORCING BARS

Reinforcing bars were instrumented by adhering foil strain gages to the surface of the bars. The strain gages were used to determine strain data for the bars and thus calculate stress and force values for the bars. Gages placed on the surface of the bars interfere with bond by covering the ribs of the deformed bar. In order to reduce any such effect, gages were placed over the main ribs of the bar (Figure A-1). Since the main rib already interferes with direct bearing on the transverse ribs, it was reasoned that placement there would produce the least interference from the gages.

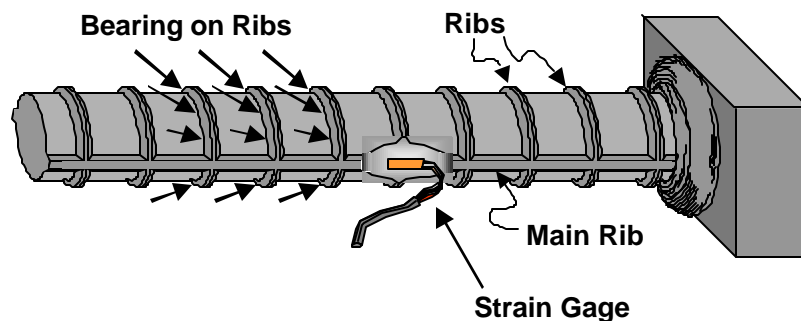


Figure A-1: Placement of strain gage on main rib of bar

Figure A-2 shows photos of a bar in the progress of being instrumented. First, a section of the main rib is ground down to a flat, level surface. This grinding was done with a hand-held grinder. Because the grinding was done by hand, the surface the gage was adhered to was not always precisely machined. Some misalignment and non-flatness could occur for each gage. This imprecision causes the gage data to have some error that will be discussed in the next section. Once the surface was cleaned, electronic foil gages were then adhered to the bar as per the instructions provided by the manufacturer (All of the gages used in the project were purchased from Measurements Group, Inc.). Once the gages had been attached and soldered to insulated three-wire leads, the gage was covered by a quick setting epoxy. The epoxy coating provided a hard, waterproof armor for the gage that protected it during the casting process.

Two different gage sizes were used. A $\frac{1}{8}$ " gage length was used for bars #4 and smaller (Measurements Group product EA-06-125BT-120). A $\frac{1}{4}$ " gage length was used for bars #8 and larger (Measurements Group product EA-06-250BG-120).

A.2 TENSILE PROPERTIES

The instrumentation placed on the tie bars used in the test specimens provides data on strain values only. In order to convert the strain data into the more useful stress and force equivalents, one must have previously measured several mechanical properties of the bars: the area (A) and first moment of inertia (I) properties of the bar cross-section and the modulus of elasticity of the steel (E). Pure tension tests of instrumented bar specimens were designed to provide values for the product AE.

- i. A flat smooth surface is ground onto the main rib of the rebar.



- ii. Electronic foil strain gages are adhered to the ground surfaces.



- iii. Insulated 3-wire leads are soldered onto the strain gages (covered by a white water-proof acrylic lacquer in this photo).



- iv. A clear epoxy coating is placed over the gages and the leads to protect them during the casting process.



Figure A-2: Steps in the bar instrumentation process

Short lengths of sample bars were instrumented with strain gages and pulled in tension in a universal load machine. Data from the gages provided information on the bar strain (ϵ). Data from the load machine provided information on the tensile force in the bar (F_{bar}). The two values are related by Hook's Law:

$$\sigma = \epsilon \cdot E \quad (\text{A-1})$$

$$F_{\text{bar}}/A = \epsilon \cdot E \quad (\text{A-2})$$

$$F_{\text{bar}}/\epsilon = AE \quad (\text{A-3})$$

These tests also provided values for the yield stress (f_y) of the bars.

Figure A-3 shows the typical layout of a tensile test specimen for a larger bar size. Between 3 to 6 strain gages were placed on each tensile specimen. No two gages will provide the exact same reading, therefore multiple gages were used on multiple bar samples to provide values for the mean bar stiffness (AE) and the standard distribution (σ). Samples of $3/16$ " diameter plain round bar and #2, #3, #4, #5, #8, and #11 deformed bar sizes were tested. Bars used in the project came from a variety of suppliers. At least one bar sample was tested for each supplier.

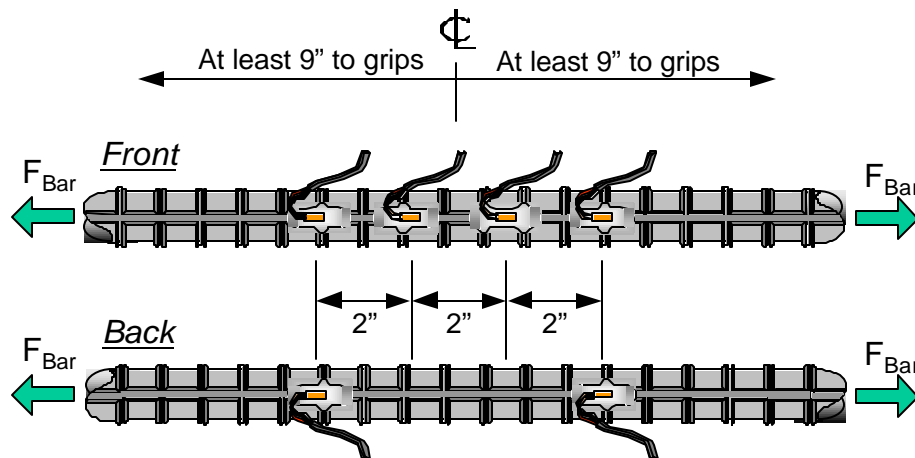


Figure A-3: Layout of strain gages for #8 and #11 tensile specimens

Figure A-4 shows typical from a tensile bar test. The data come from a #8 bar provided by ERICO. The top plot shows the force-strain relationship measured during the test. The bottom plot shows the slopes calculated from the data in the top plot. A range of slope points from $400\mu\epsilon$ to $1900\mu\epsilon$ was averaged to determine the stiffness associated with each gage.

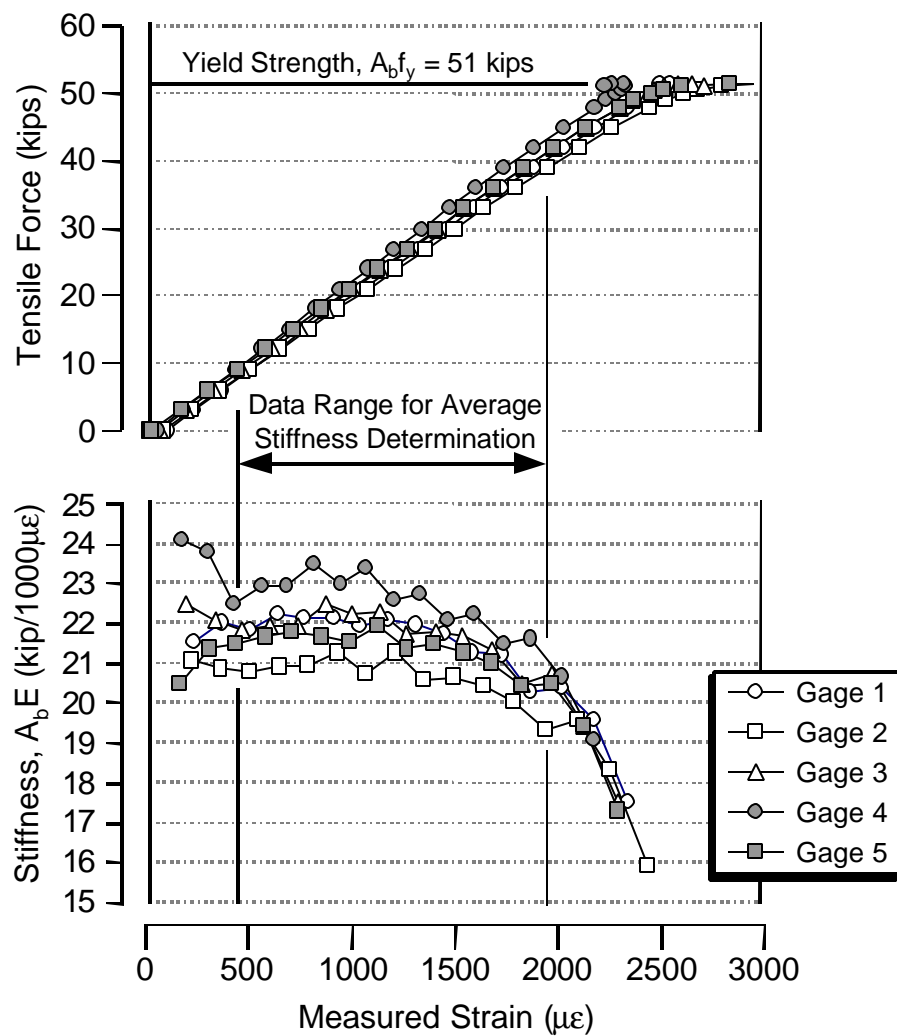


Figure A-4: Typical load-strain data from a tensile test (# 8 ERICO⁽²⁾ bar group)

The individual gage stiffnesses from all of the bars of the same size from a given supplier were averaged to determine the mean stiffness for that bar group. The data range of stiffnesses for each group was also analyzed to determine standard deviations. The standard deviation was calculated using the following formula:

$$\text{Mean Stiffness, } \overline{AE} = \frac{1}{n} \sum_{i=1}^n (AE)_i \quad (\text{A-4})$$

$$\text{Gage Variance, } \text{Var}_i = \left(\overline{AE} - (AE)_i \right)^2 \quad (\text{A-5})$$

$$\text{Standard Deviation, } \sigma = \sqrt{\frac{1}{n-1} \sum_{i=1}^n \text{Var}_i} \quad (\text{A-6})$$

n = number of working strain gages for a group

(AE)_i = stiffness value for a given gage i

Note that a denominator of n-1 is used in equation (A-6) rather than n. The subtraction of one from the number of samples acts as a penalty for smaller sample sizes.

Table A-1 summarizes the stiffness values and standard deviations for all bar groups. Bar groups are sorted by bar size and supplier. Standard deviations are also expressed as percentages for each group. The bar group with the best (in this case smallest) standard deviation was the ³/₁₆ “ diameter plain wire. This is most likely due to the fact that no grinding was required to prepare the bar surface for gage installation. Only a light sanding was needed to prepare the surface for epoxy adherence to the metal. The uniformity of the manufacture of the plain wire bars was very good.

The worst standard deviations are found in the #8 bar groups. Most of the #8 bars were tested early in the research when that bar size was the predominant one used in specimens. At that time, the skill of the researchers in placing the gages on the bars was not that good. Later tests of #5 and #11 bars showed improvement of gaging skills. A good indication of the improvement of the researchers' skills in placing gages is demonstrated by comparing two #8 bar groups: ERICO⁽¹⁾ and ERICO⁽²⁾. There are two #8 ERICO groups because the limited supply of #8 bars from ERICO was depleted and additional bars were ordered. Two samples were taken from each shipment of bars. Samples from the first shipment were tested from 2/10/2000 to 2/11/2000 along with most of the other #8 bars. Samples from the second shipment were tested on 2/27/2001, one year later. After a year of practice, the standard deviation of 10 gages placed by the researchers dropped from 10.6% to 3.4%, a significant improvement. Some of the groups have large standard deviations because of the imposed penalty for small sample sizes.

| | Bar Size | Supplier | Number of Bars Sampled | Total Working Gages | Mean Bar Stiffness $A_{\text{bar}}E_s (\pm \sigma)$ (kip/1000 $\mu\epsilon$) | $\frac{\sigma}{AE}$ (%) | Yield Stress (ksi) |
|--------------------|---|----------------------|------------------------|---------------------|---|----------------------------|-----------------------|
| Confinement Bars | Plain Wire ($\frac{3}{16}$ " ϕ) | L. Stock* | 4 | 16 | 0.831 \pm 0.007 | 0.9% | 82 |
| | # 2 | Mexican† | 4 | 12 | 1.13 \pm 0.10 | 8.4% | 80 |
| | # 3 | A.I.W.‡ | 3 | 8 | 2.61 \pm 0.21 | 7.9% | 63 |
| | # 4 | A.I.W.‡ | 3 | 9 | 4.88 \pm 0.26 | 5.4% | 60 |
| Headed Bar Samples | # 5 | HRC | 4 | 16 | 7.46 \pm 0.44 | 5.9% | 60 |
| | | ERICO | 3 | 12 | 7.50 \pm 0.31 | 4.2% | 74 |
| | # 8 | HRC | 4 | 17 | 21.3 \pm 1.8 | 8.4% | 68 |
| | | ERICO ⁽¹⁾ | 2 | 10 | 19.9 \pm 2.1 | 10.6% | 61 |
| | | ERICO ⁽²⁾ | 2 | 10 | 21.3 \pm 0.7 | 3.4% | 65 |
| | | All ERICO | 4 | 20 | 20.6 \pm 1.7 | 8.2% | - |
| | | A.I.W.‡ | 1 | 4 | 21.6 \pm 2.4 | 11.0% | 68 |
| | | All Bars | 9 | 41 | 21.0 \pm 1.8 | 8.5% | - |
| | # 11 | HRC | 4 | 19 | 39.1 \pm 2.6 | 6.6% | 63 |
| | | ERICO | 2 | 11 | 42.3 \pm 2.3 | 5.5% | 67 |

* Lab Stock

† Lab Stock, Mexican Supplier

‡ Alamo Iron Works

(Standard Hook sample for # 8's)

Table A-1: Stiffness, A_bE , and yield stress, f_y , for all specimen bar sizes

Histograms of the stiffness data ranges for each bar size are presented in Figures A-5 through A-11. The histograms are presented as indications of the normalness of each distribution of bar group data. They also give a graphical indication of the scatter.

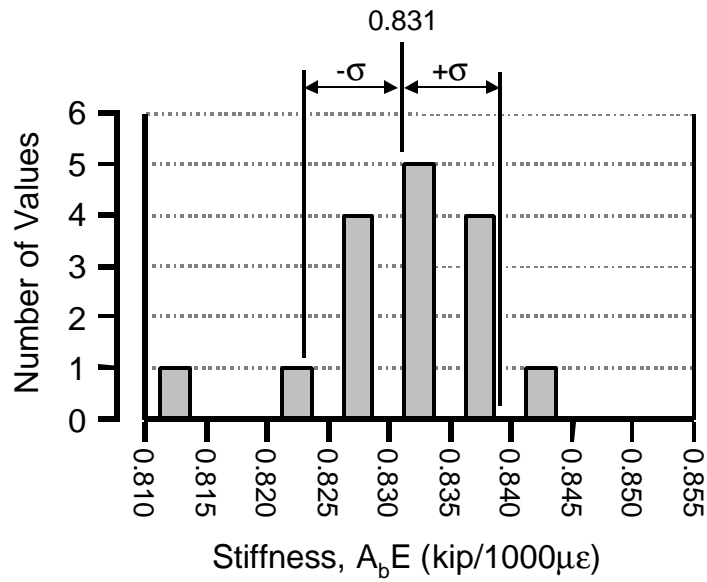


Figure A-5: Histogram of $3/16$ " diameter plain wire tensile test data

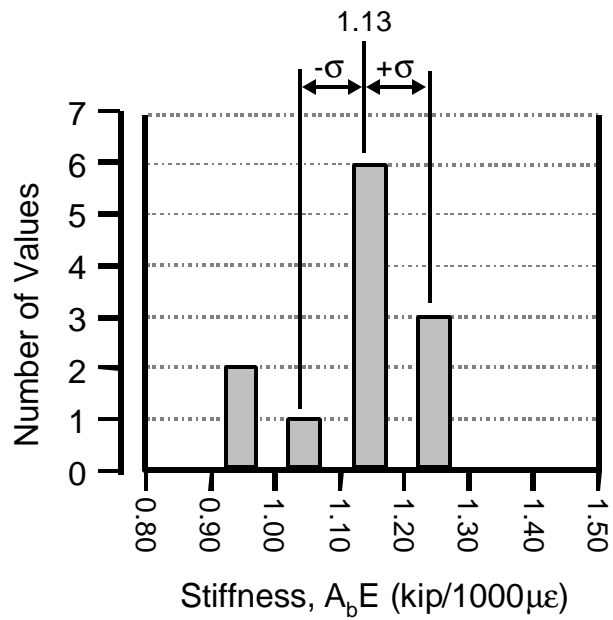


Figure A-6: Histogram of # 2 bar tensile test data

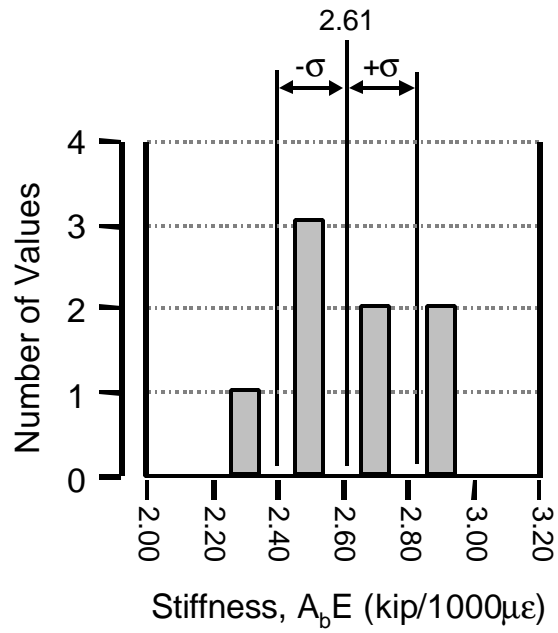


Figure A-7: Histogram of # 3 bar tensile test data

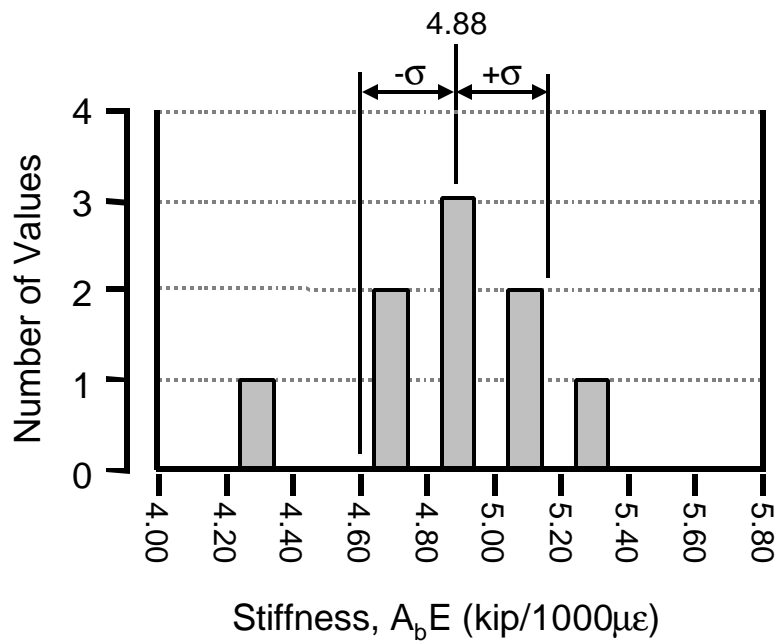


Figure A-8: Histogram of # 4 bar tensile test data

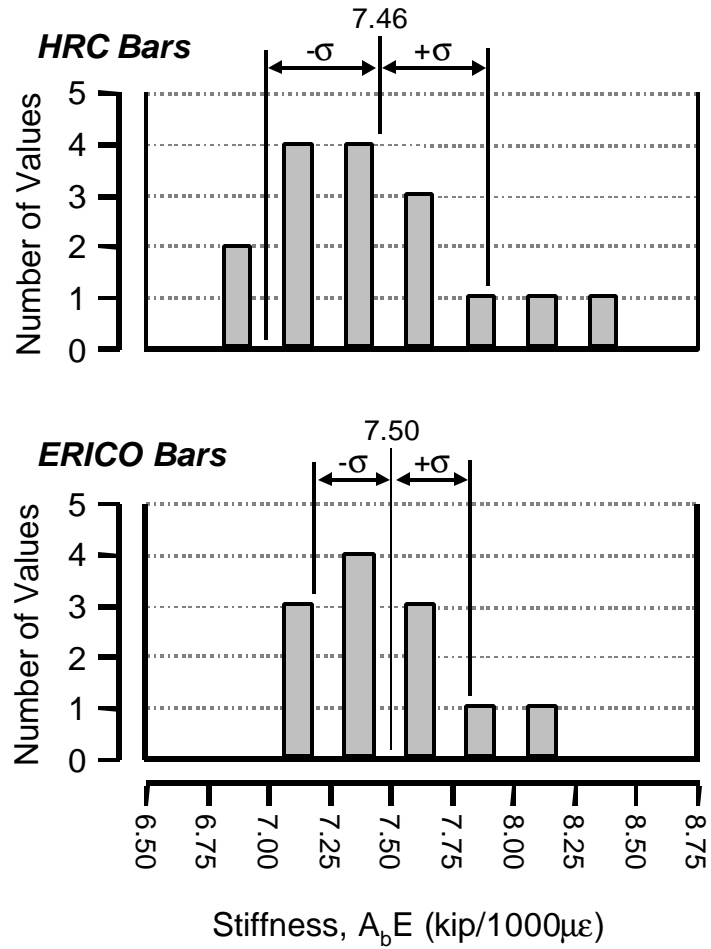
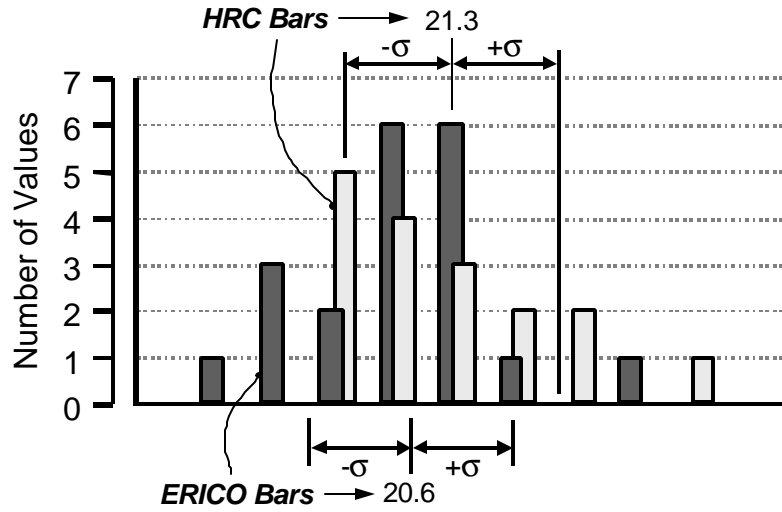


Figure A-9: Histogram of # 5 bar tensile test data

HRC & ERICO Bars



All # 8 Bars

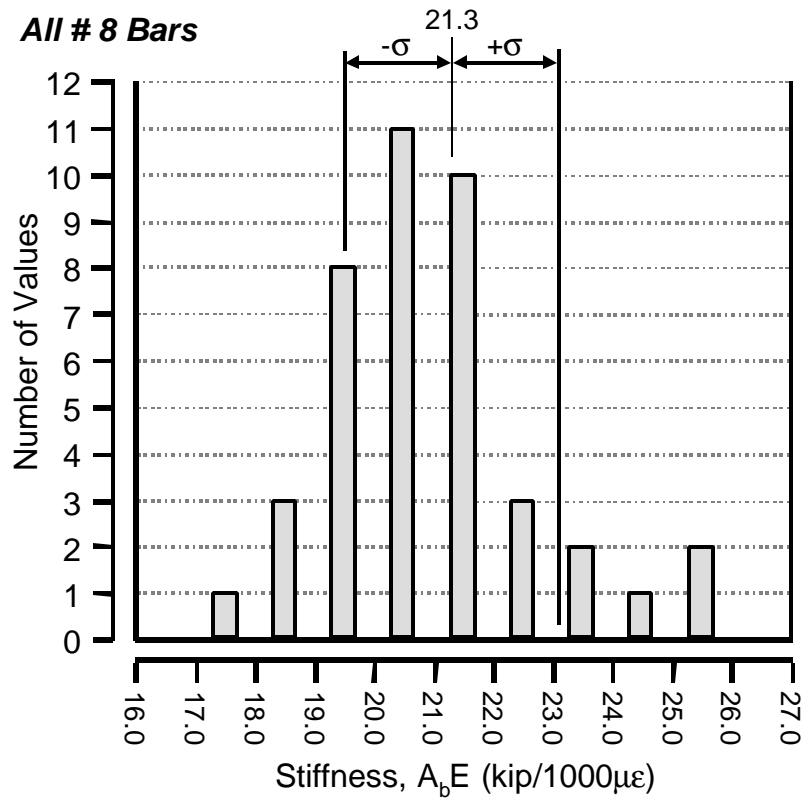


Figure A-10: Histogram of # 8 bar tensile test data

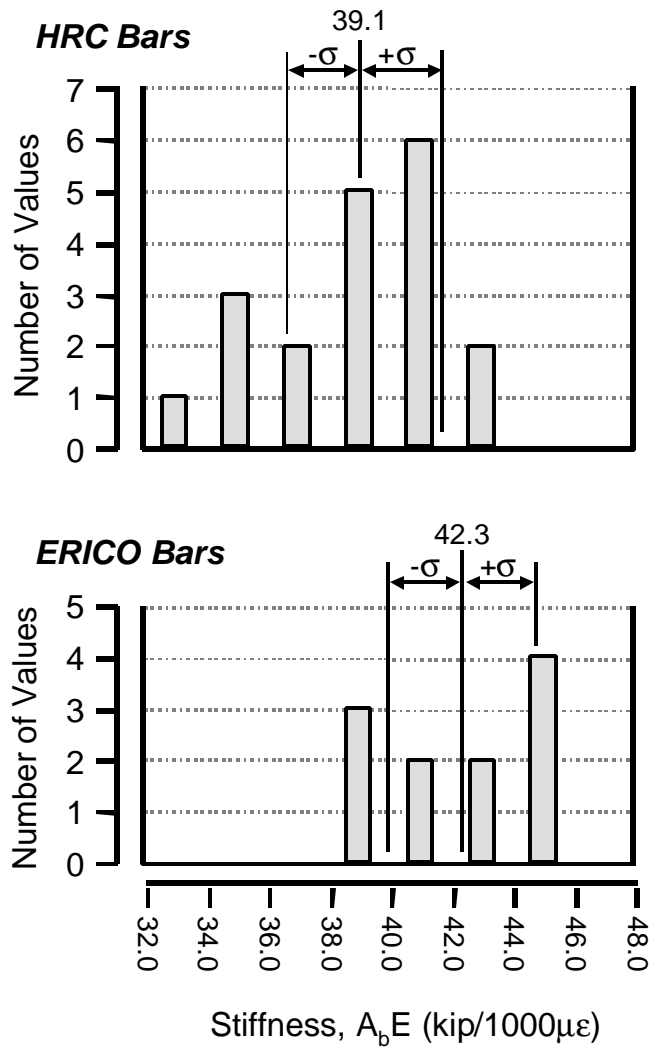


Figure A-11: Histogram of # 11 bar tensile test data

A.3 FLEXURAL PROPERTIES

The data from the bending tests were necessary in analyzing the information gathered from CCT node tests where kinking forces produced large bending strains in the specimen bars. The tensile tests of the bars provided values only for the axial stiffness of the bars. For complete

analysis of the data measured in the test specimens, information was also need on the flexural stiffness properties of the bars. Bending tests of #8 and #11 bar samples were performed to measure the flexural stiffness values, IE/r , of the various bar groups in those size ranges. Figure A-12 shows the basic configuration of a bending test for bar samples. The moment was calculated from the load placed on the bar multiplied by the shear span. Strain was measured by two strain gages placed in the constant moment region at the midspan of the bar specimen: one on the compression side of the bar, the other on the tension side.

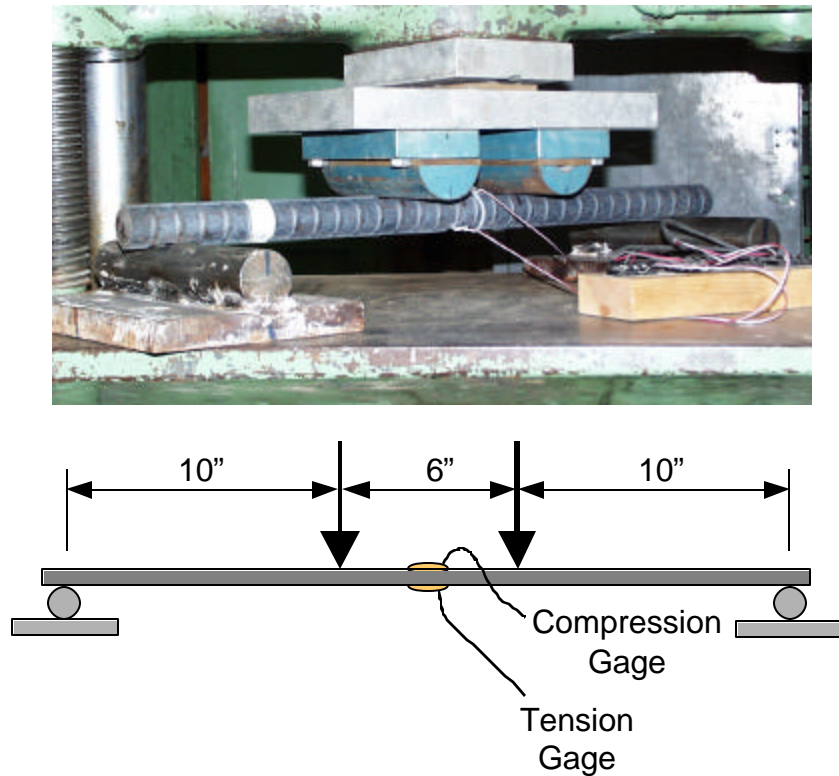


Figure A-12: Test setup for bending tests of bars

Once specimens were tested, the data were plotted and the flexural stiffness of each gage was determined. Figure A-13 shows data from a typical test. Once a strain of about $2400\mu\epsilon$ was reached, the outer fibers began to yield and the stiffness of the bar dropped towards zero. Flexural stiffness values were determined by averaging over a range from $400\mu\epsilon$ to $2400\mu\epsilon$.

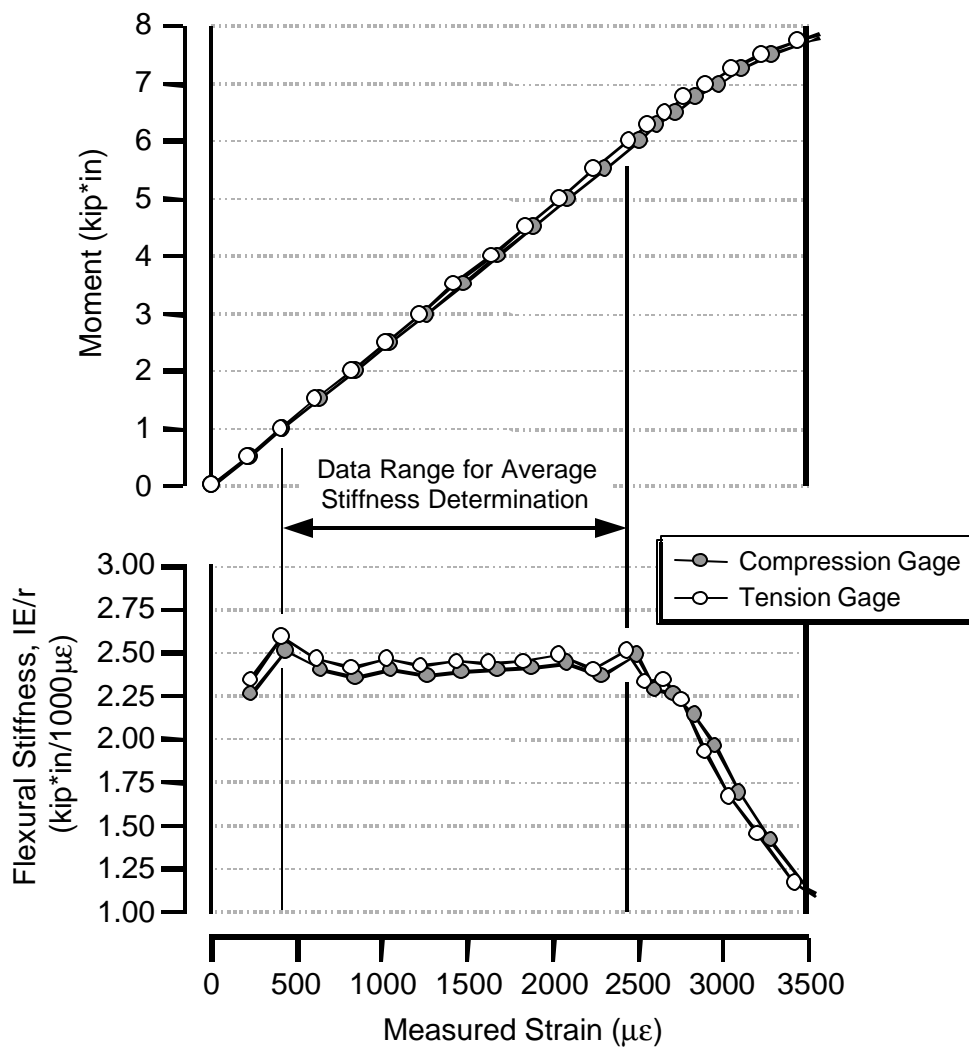


Figure A-13: Typical moment-strain data from a bending test (# 8 ERICO⁽²⁾ bar group)

Data from tensile and bending tests were used to determine the physical properties for the bars that could be used to analyze strain data for elastic and plastic behavior. The bar is assumed to have a circular cross-section and the stress-moment relationship is used to determine the radius of the bar from the axial and flexural stiffness values derived in the bar tests:

$$\text{Moment, } M = \frac{\sigma I}{r} \quad (\text{A-7})$$

$$\text{Moment, } M = (\text{Strain, } \epsilon) \frac{IE}{r} \quad (\text{A-8})$$

Substitute $I = \frac{\pi r^4}{4}$ for circular sections:

$$\frac{\text{Moment}}{\text{Strain}} = \frac{\pi r^4 E}{4r} \quad (\text{A-9})$$

$$\frac{\text{Moment}}{\text{Strain}} = \frac{(\pi r^2 E) \cdot r}{4} \quad (\text{A-10})$$

$$\frac{\text{Moment}}{\text{Strain}} = \frac{(AE) \cdot r}{4} \quad (\text{5-11})$$

r = bar radius (inches)

A = bar area (in²)

I = first moment of inertia (in⁴)

E = modulus of elasticity (ksi)

Table A-2 lists the flexural stiffness values measured from the bending tests. Calculated bar radii are also listed.

| Bar Size | Supplier | Num. of Bars | AE (kip/1000 $\mu\epsilon$) | IE/r (kip-in/1000 $\mu\epsilon$) | Radius r ($\pm \sigma$) (inches) | $\frac{\sigma}{r}$ (%) |
|----------|----------------------|--------------|------------------------------|-----------------------------------|------------------------------------|------------------------|
| # 8 | HRC | 2 | 21.3 | 2.61 | 0.490 \pm 0.024 | 4.8% |
| | ERICO ⁽²⁾ | 2 | 21.3 | 2.43 | 0.457 \pm 0.007 | 1.6% |
| | All Bars | 4 | 21.0 | 2.52 | 0.480 \pm 0.034 | 7.0% |
| # 11 | HRC | 2 | 39.1 | 7.03 | 0.719 \pm 0.016 | 2.2% |
| | ERICO | 2 | 42.3 | 7.03 | 0.664 \pm 0.014 | 2.1% |

Table A-2: Flexural stiffness, IE/r, and radii, r, for all specimen bar sizes

A.4 CALCULATION OF BAR FORCES

Given the flexural and tensile properties of the bar, the bar force can be calculated by using the extreme fiber strain data. Figure A-14 shows a bar instrumented with strain gages 1 and 2 located on the top and bottom fibers of the bar. The instrumented section of bar was located near a crack across which shear and tensile forces are transmitted. The bar was placed in both tension and flexure at this location (this was typical of a bar anchored in a CCT node specimen). Figure A-14 shows the cross-section strain and stress distribution of the bar. Because the stress distribution was non-uniform and the bar was only partially yielded, it was unrealistic to characterize the bar by its average strain. Instead, plastic analysis of the section must be performed to determine resultant axial forces and moments. If the section is assumed to be approximately circular and the strain distribution linear, then the force on the section can be determined by formulas using the top and bottom steel strains (ϵ_1 and ϵ_2 respectively) and the cross-section and material properties (area: A, radius: r, modulus: E, and yield strain: ϵ_y) determined from the bar sample tests described in the previous sections. The applicable equations are listed on the following pages.

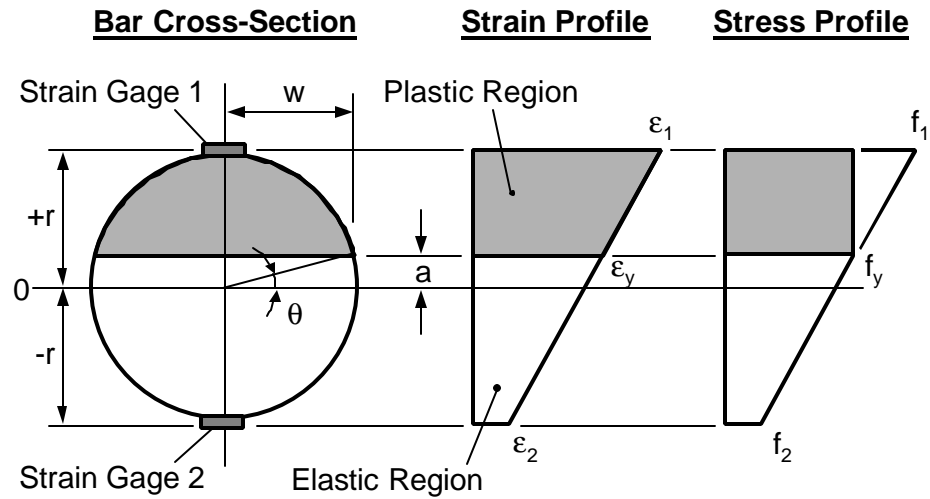


Figure A-14: Bar cross-section strains and stresses

Axial Force in Bar, P:

- Fully elastic behavior:

$$P = E \epsilon_{\text{avg}} \pi r^2 \quad (\text{A-12})$$

- Partially plastic behavior:

$$P = E \left\{ -\frac{2}{3} m w^3 + \left(\left(\frac{\pi}{2} + \theta \right) r^2 + w a \right) \epsilon_{\text{avg}} + \left(\left(\frac{\pi}{2} + \theta \right) r^2 - w a \right) \epsilon_y \right\} \quad (\text{A-13})$$

- Fully plastic behavior:

$$P = E \epsilon_y \pi r^2 \quad (\text{A-14})$$

Moment in Bar, M:

- Fully elastic behavior:

$$M = E \left(\frac{1}{4} m \pi r^4 \right) \quad (\text{A-15})$$

- Partially plastic behavior:

$$M = E \left\{ \frac{2}{3} w^3 (\epsilon_y - \epsilon_{avg}) + m \left[\frac{1}{4} \left(\frac{\pi}{2} + \theta \right) r^4 + aw \left(\frac{1}{4} r^2 - \frac{1}{2} w^2 \right) \right] \right\} \quad (A-16)$$

- Fully plastic behavior:

$$M = 0 \quad (A-17)$$

$$m = \text{strain gradient, } \frac{\epsilon_1 - \epsilon_2}{2r}$$

$$\epsilon_{avg} = \text{average strain, } \frac{\epsilon_1 + \epsilon_2}{2}$$

$$a = \text{plastic boundary, } \frac{\epsilon_y - \epsilon_2}{m} - r \quad (\text{see Figure 5-14})$$

$$w = \text{plastic width, } \sqrt{r^2 - a^2} \quad (\text{see Figure 5-14})$$

$$\theta = \text{plastic angle, } \sin^{-1} \left(\frac{a}{r} \right) \quad (\text{see Figure 5-14})$$

The above equations are very complex for partially plastic bar behavior, however, they can be programmed into a spreadsheet and performed automatically. Note also that “fully plastic behavior” refers to tension yielding of the section. Thus the moment when the section is fully plastic is zero. The necessity of these complex calculations arose from the curvature induced into the tensile reinforcement in CCT tests which is discussed in Chapter 6.

Appendix B: Distribution Plots for Bearing Capacity Database

B.1 PROPOSED BEARING CAPACITY MODEL 1

Distribution plots for proposed bearing capacity model 1 are presented in Figures B-1 through B-14. Model 1 is presented below:

$$\text{Bearing Capacity, } P = A_{nh} \left(2.6 \Psi \left(\frac{2c_1}{\sqrt{A_{nh}}} \right) \left(\frac{f_c}{2.4} \right)^{0.5 \left(1 + \sqrt{A_{nh}} / 2c_1 \right)} \right) \quad (\text{B-1})$$

$$\text{with } \Psi = 0.7 + 0.3 \frac{c_2}{c_1} \leq 1.8 \quad (\text{B-2})$$

All variables are as defined in Chapter 8.

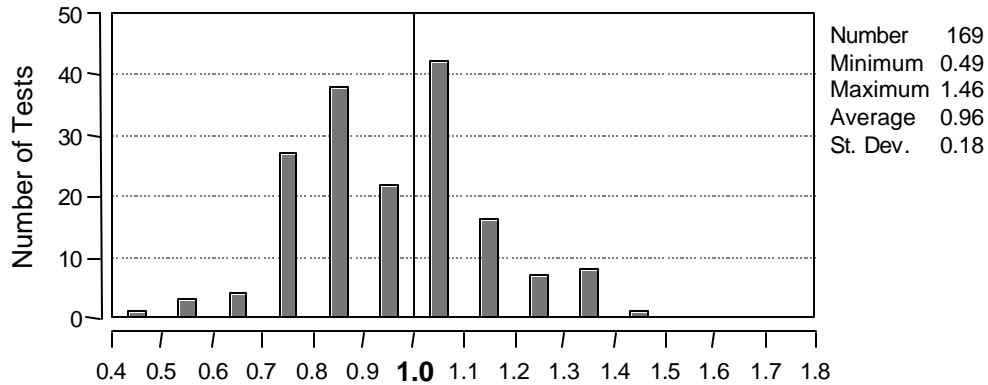


Figure B-1: All headed bar and anchor bolt tests listed in database (model 1)

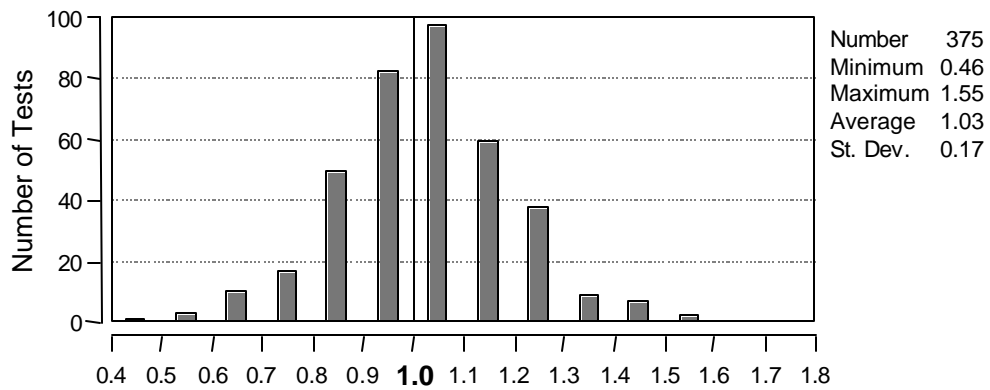


Figure B-2: All bearing block tests listed in database (model 1)

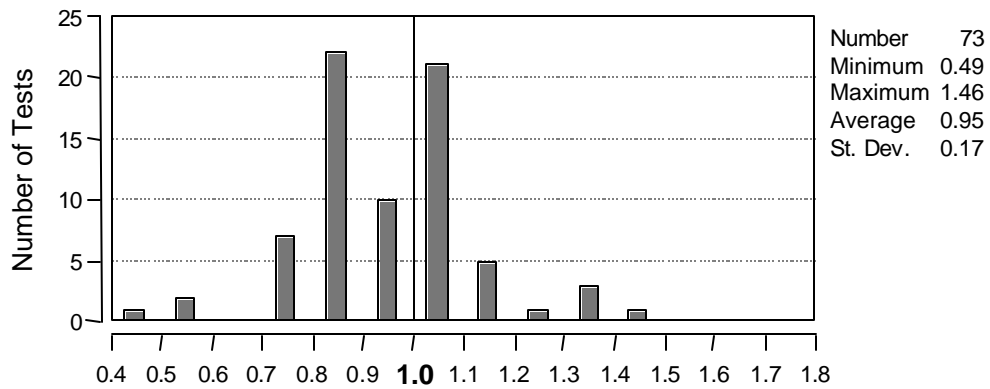


Figure B-3: University of Texas Deep Embedment Tests [42] (model 1)

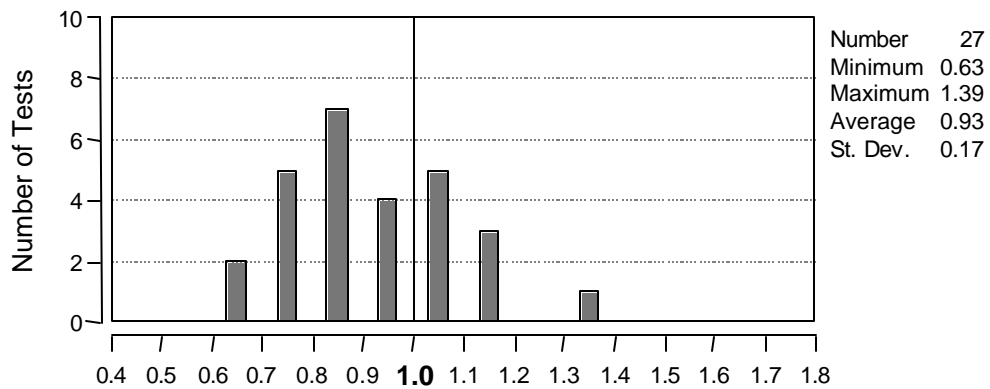


Figure B-4: University of Texas CCT node tests (current study) (model 1)

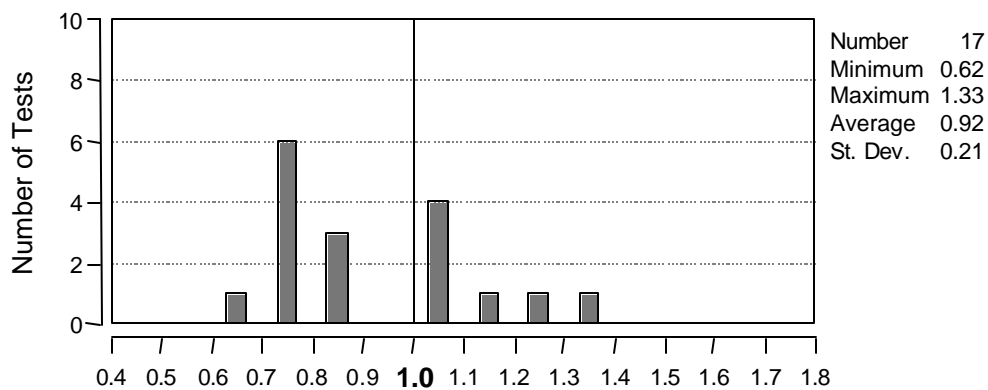


Figure B-5: Breen, 1964 [31] (model 1)

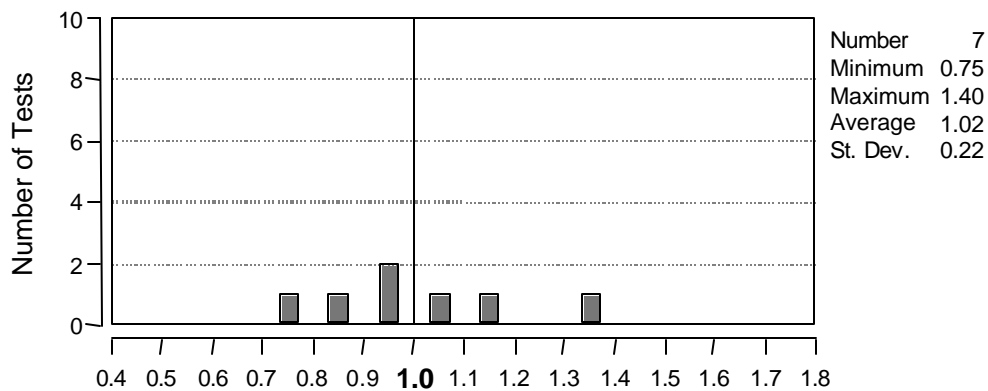


Figure B-6: Lee and Breen, 1966 [68] (model 1)

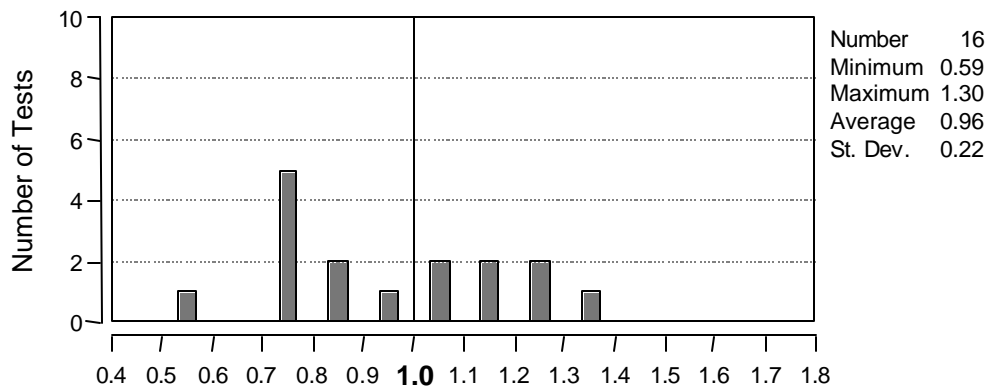


Figure B-7: Lo, 1975 [58] (model 1)

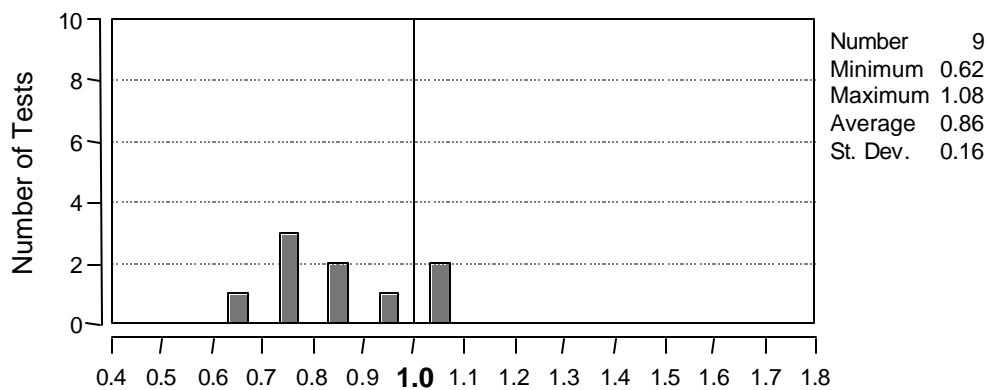


Figure B-8: Hasselwander, 1977 [58] (model 1)

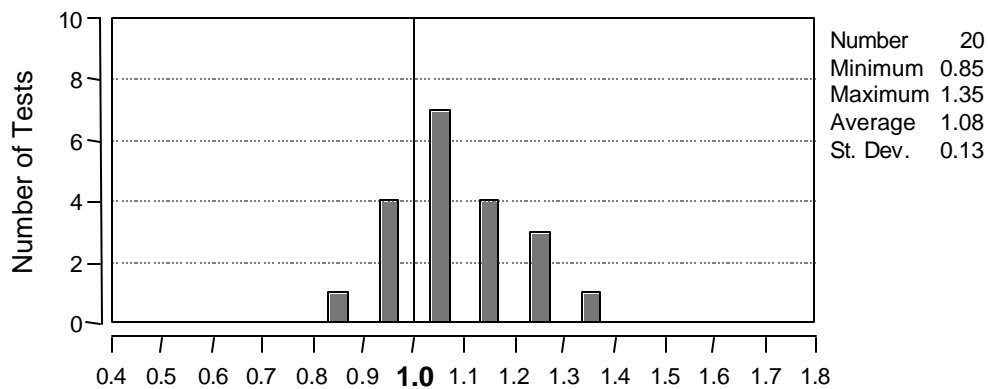


Figure B-9: Furche and Eligehausen, 1991 [49] (model 1)

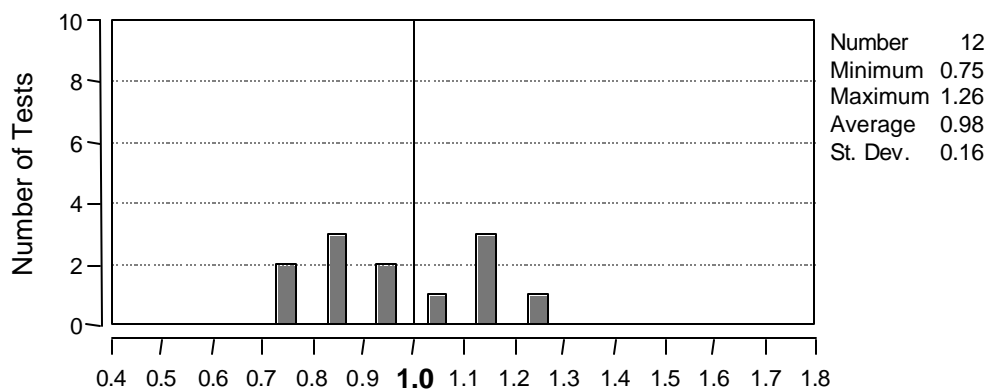


Figure B-10: Shelson, 1957 [106] (model 1)

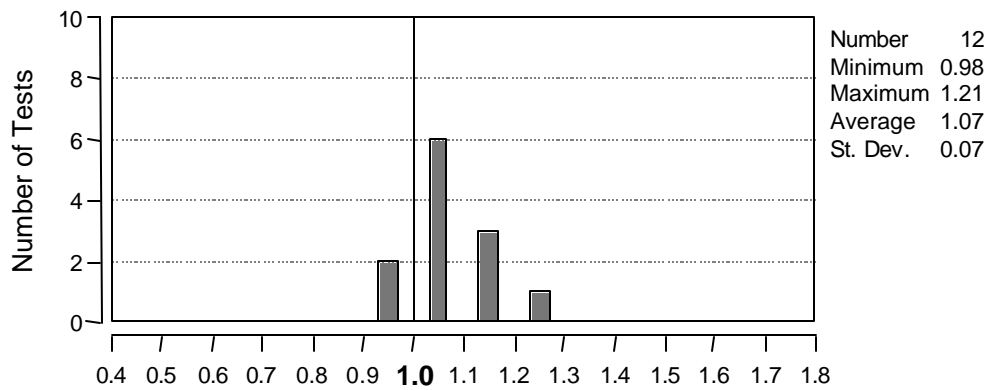


Figure B-11: Au and Baird, 1960 [24] (model 1)

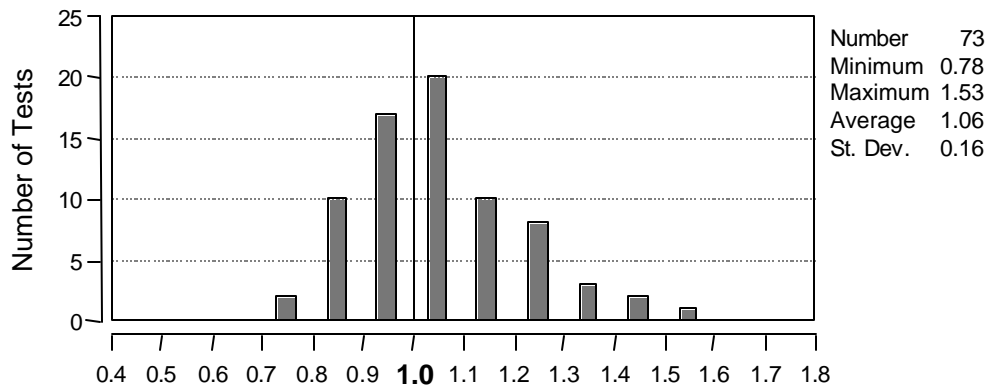


Figure B-12: Hawkins, 1968 [60] (model 1)

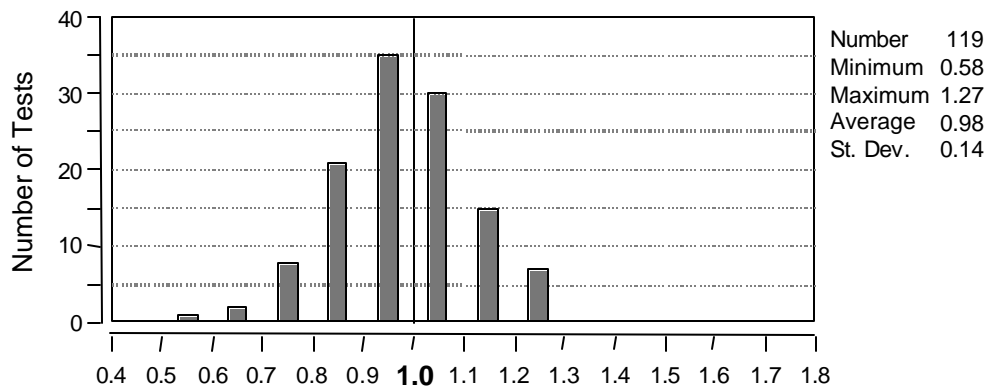


Figure B-13: Niyogi, 1973 [90, 91] (model 1)

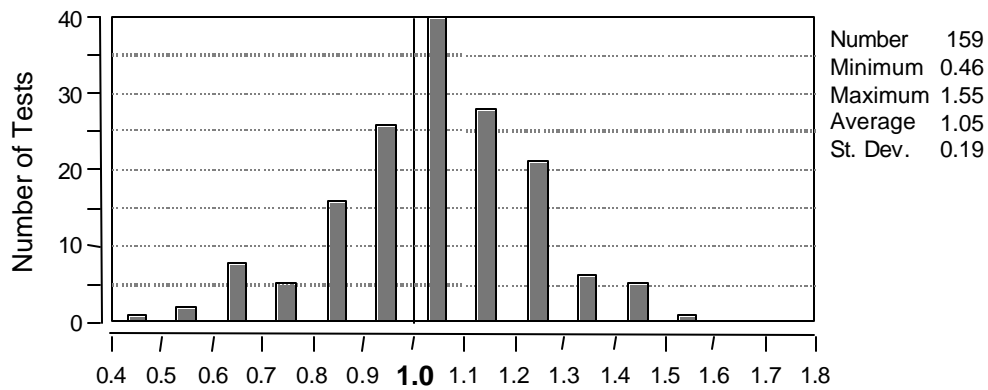


Figure B-14: Williams, 1979 [116] (model 1)

B.2 PROPOSED BEARING CAPACITY MODEL 2

Distribution plots for proposed bearing capacity model 2 are presented in Figures B-15 through B-28. Model 2 is presented below:

$$\text{Bearing Capacity, } P = A_{nh} \left(0.9 \Psi \left(\frac{2c_1}{\sqrt{A_{nh}}} \right) f'_c \right) \quad (\text{B-3})$$

$$\text{with } \Psi = 0.6 + 0.4 \frac{c_2}{c_1} \leq 2.0 \quad (\text{B-4})$$

All variables are as defined in Chapter 8.

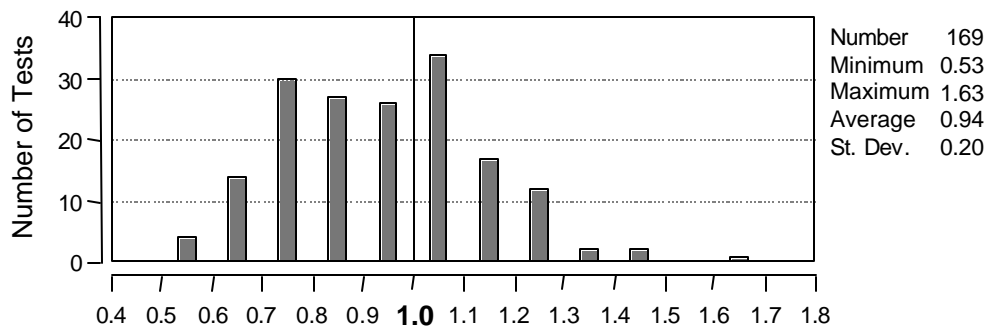


Figure B-15: All headed bar and anchor bolt tests listed in database (model 2)

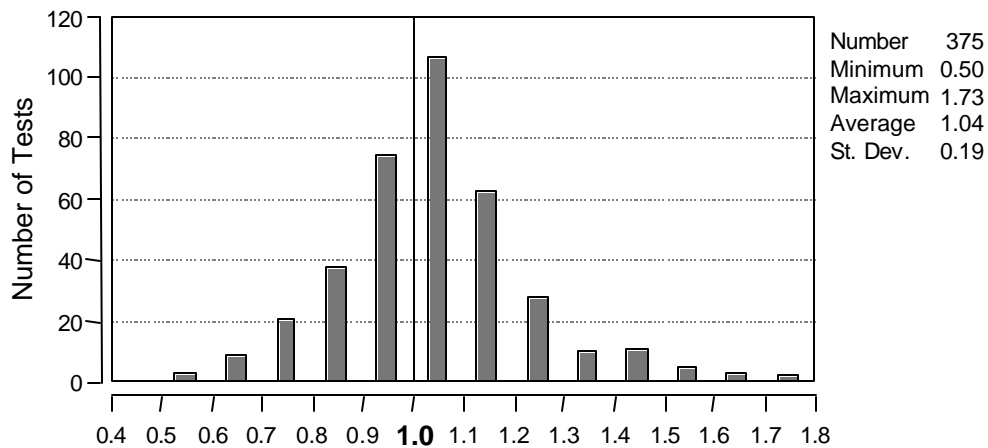


Figure B-16: All bearing block tests listed in database (model 2)

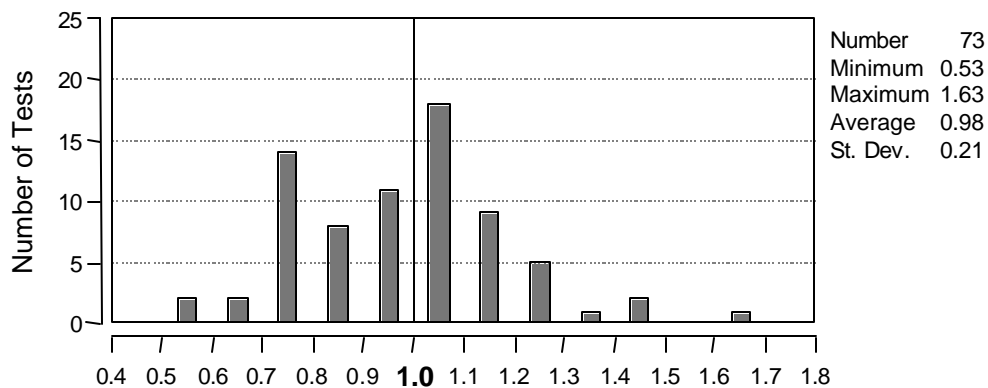


Figure B-17: University of Texas Deep Embedment Tests [42] (model 2)

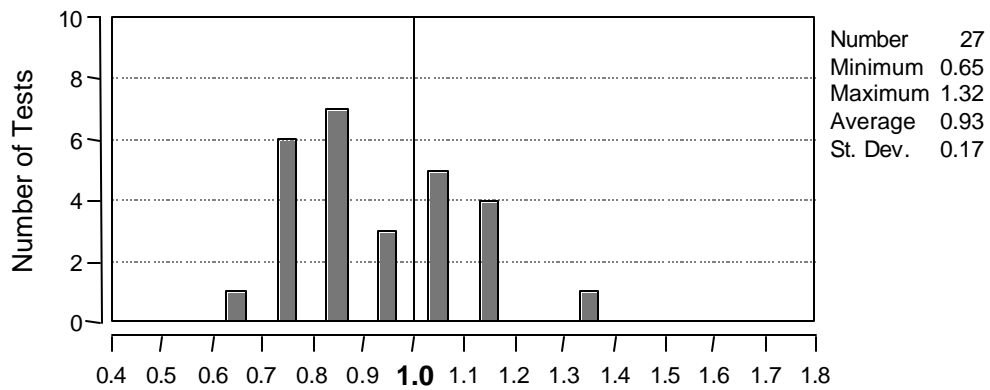


Figure B-18: University of Texas CCT node tests (current study) (model 2)

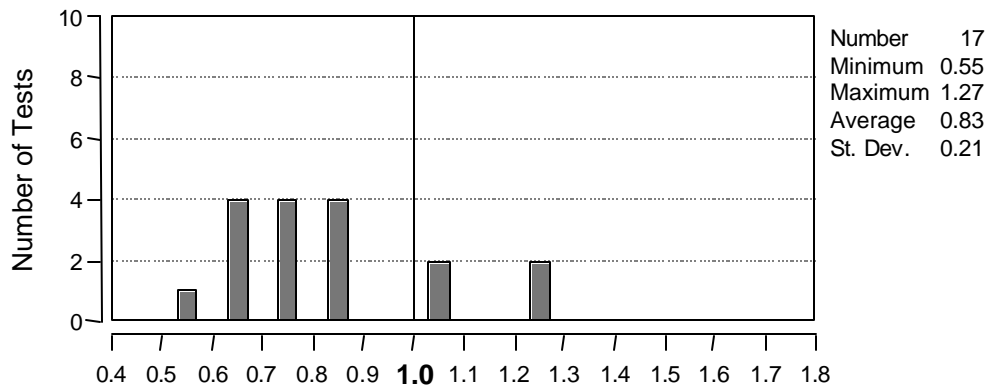


Figure B-19: Breen, 1964 [31] (model 2)

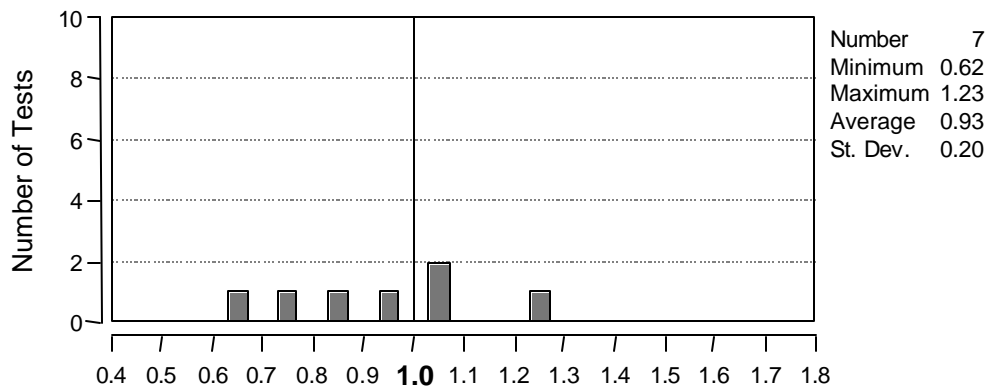


Figure B-20: Lee and Breen, 1966 [68] (model 2)

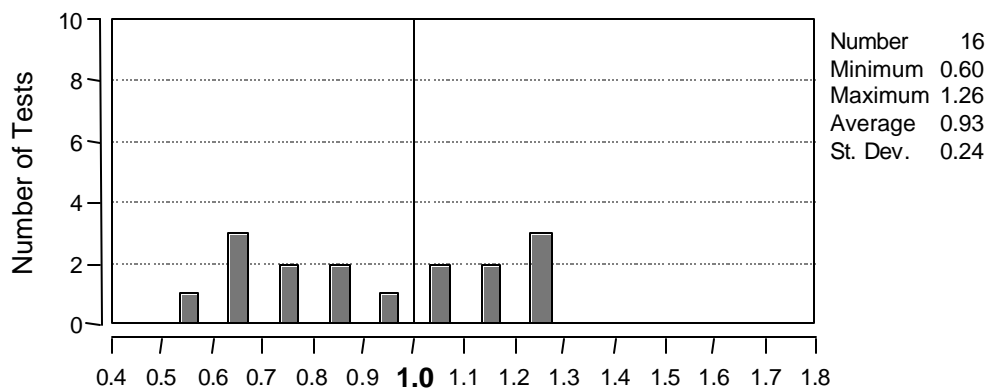


Figure B-21: Lo, 1975 [58] (model 2)

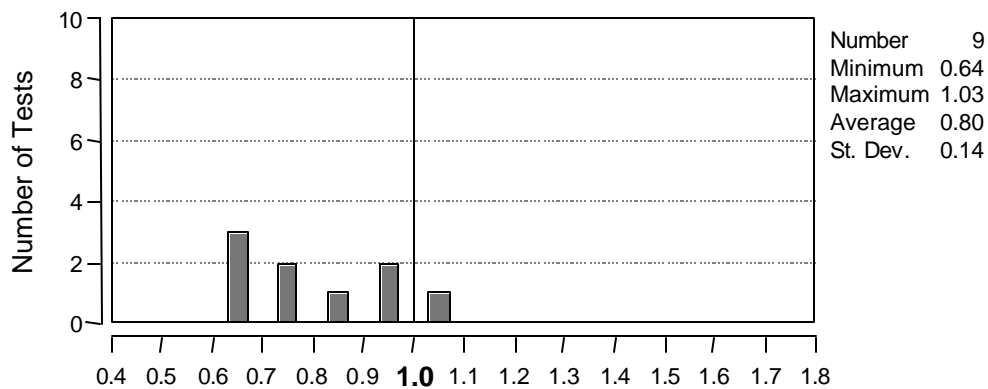


Figure B-22: Hasselwander, 1977 [58] (model 2)

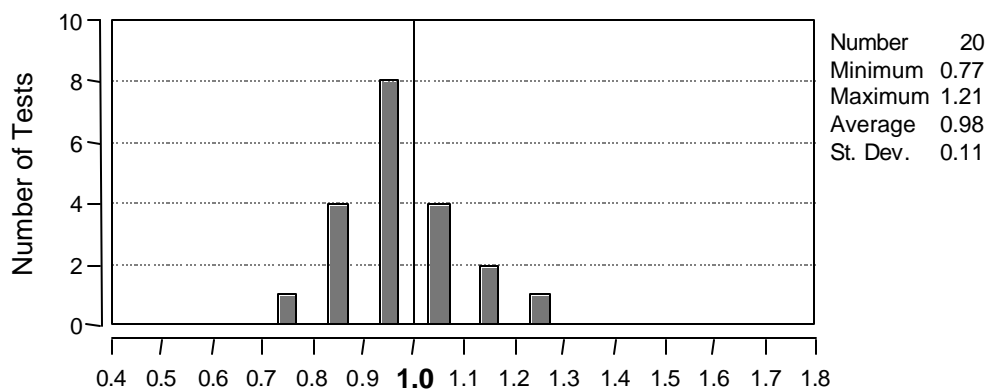


Figure B-23: Furche and Eligehausen, 1991 [49] (model 2)

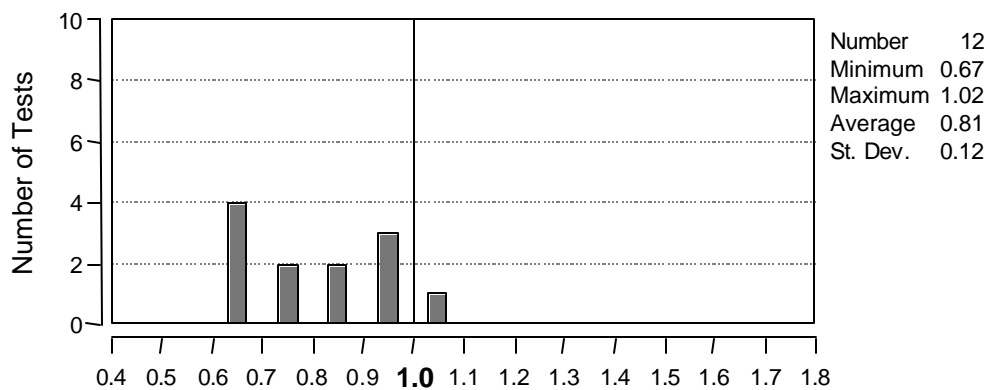


Figure B-24: Shelson, 1957 [106] (model 2)

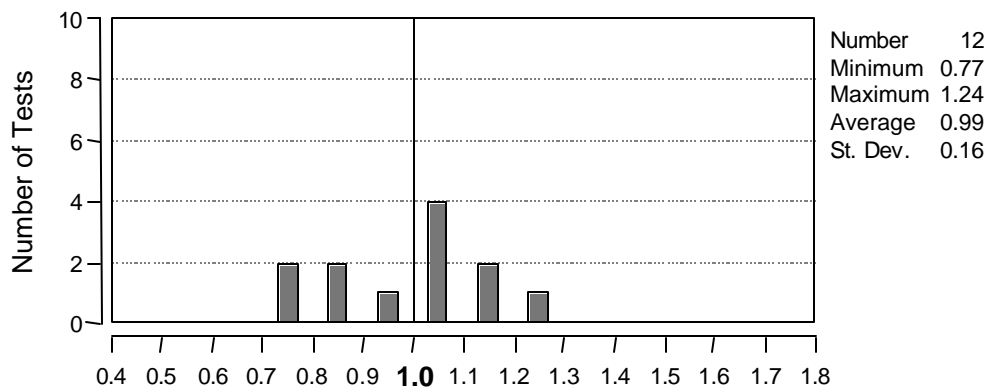


Figure B-25: Au and Baird, 1960 [24] (model 2)

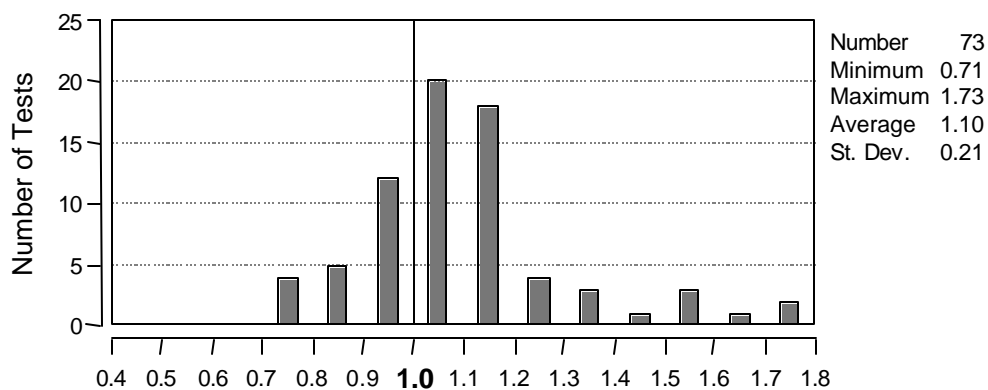


Figure B-26: Hawkins, 1968 [60] (model 2)

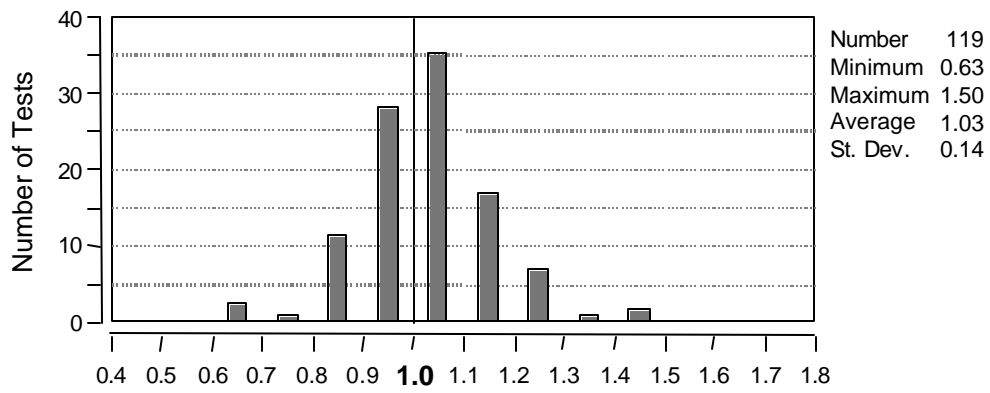


Figure B-27: Niyogi, 1973 [90, 91] (model 2)

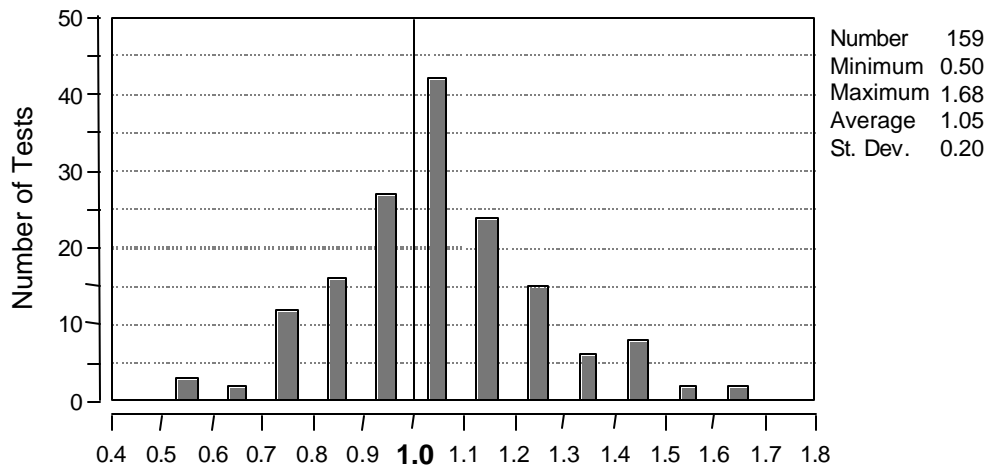


Figure B-28: Williams, 1979 [116] (model 2)

Appendix C: Summary of CCT Node Data

CCT test results are summarized in Tables C-1a through C-1c. The tables report the maximum bar stresses at $1d_b$ (next to the head) and $7d_b$ (close to the critical crack) and the maximum bearing reaction, P (see Figure C-1). Important parameters from of the specimens are also reported.

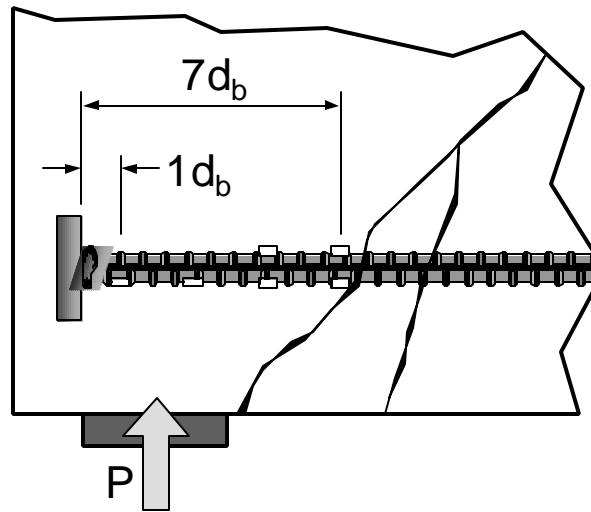


Figure C-1: Close-up of CCT node

| Specimen Identification | Head Type | θ_{strut} | $\frac{L_{plate}}{d_b}$ | $\frac{A_{nh}}{A_b}$ | $\frac{C_1}{d_b}$ | $\frac{C_2}{d_b}$ | f'_c (ksi) | f_s at $1d_b$ (ksi) | f_s at $7d_b$ (ksi) | P_{max} (kip) | Failure Mode |
|----------------------------|--------------------|------------------|-------------------------|----------------------|-------------------|-------------------|--------------|-----------------------|-----------------------|-----------------|--------------|
| CCT-08-45-00.00-1-E1,W8 | no head | 45° | 6.0 | 0.00 | 4.0 | 4.0 | 5.7 | - | - | - | shear † |
| CCT-08-45-01.18-1-E1,W8 | $d_h = 1.48"$ | 45° | 6.0 | 1.18 | 4.0 | 4.0 | 5.7 | - | - | 64.1 | shear † |
| CCT-08-45-04.70(H)-1-E1,W8 | $1.5" \times 3.0"$ | 45° | 6.0 | 4.70 | 4.0 | 4.0 | 5.7 | - | - | 53.8 | shear † |
| CCT-08-45-10.39-1-E1,W8 | $3.0" \times 3.0"$ | 45° | 6.0 | 10.39 | 4.0 | 4.0 | 5.7 | - | - | 75.0 | shear † |
| CCT-08-45-00.00-1-E2,W8 | no head | 45° | 6.0 | 0.00 | 4.0 | 4.0 | 3.0 | - | - | 45.3 | pullout |
| CCT-08-45-01.18-1-E2,W8 | $d_h = 1.48"$ | 45° | 6.0 | 1.18 | 4.0 | 4.0 | 3.0 | - | - | 51.7 | splitting |
| CCT-08-45-04.70(H)-1-E2,W8 | $1.5" \times 3.0"$ | 45° | 6.0 | 4.70 | 4.0 | 4.0 | 3.0 | - | - | 76.0 | crushing |
| CCT-08-45-10.39-1-E2,W8 | $3.0" \times 3.0"$ | 45° | 6.0 | 10.39 | 4.0 | 4.0 | 3.0 | - | - | 72.5 | crushing |
| CCT-08-45-00.00-1-E2,W6 | no head | 45° | 6.0 | 0.00 | 3.0 | 4.0 | 3.0 | - | - | 48.7 | pullout |
| CCT-08-45-04.70(H)-1-E2,W6 | $1.5" \times 3.0"$ | 45° | 6.0 | 4.70 | 3.0 | 4.0 | 3.0 | - | - | 66.7 | crushing |
| CCT-08-45-10.39-1-E2,W6 | $3.0" \times 3.0"$ | 45° | 6.0 | 10.39 | 3.0 | 4.0 | 3.0 | - | - | 57.8 | crushing |
| CCT-08-45-00.00-1-B6 | no head | 45° | 6.0 | 0.00 | 3.0 | 4.0 | 4.0 | 16.3 | 55.9 | 53.7 | pullout |
| CCT-08-55-00.00-1 | no head | 55° | 4.0 | 0.00 | 3.0 | 4.0 | 3.9 | 11.7 | 50.2 | 56.1 | pullout |
| CCT-08-55-01.18-1 | $d_h = 1.48"$ | 55° | 4.0 | 1.18 | 3.0 | 4.0 | 3.9 | 37.9 | 61.8 | 67.7 | splitting |
| CCT-08-55-01.85-1 | $1.5" \times 1.5"$ | 55° | 4.0 | 1.85 | 3.0 | 4.0 | 3.9 | 41.8 | 66.3 | 80.7 | splitting |
| CCT-08-55-02.80(H)-1 | $1.5" \times 2.0"$ | 55° | 4.0 | 2.80 | 3.0 | 4.0 | 3.9 | 38.0 | 68.4 [†] | 86.4 | splitting |
| CCT-08-55-02.80(V)-1 | $1.5" \times 2.0"$ | 55° | 4.0 | 2.80 | 3.0 | 4.0 | 3.9 | 43.2 | 65.4 | 78.3 | splitting |
| CCT-08-55-04.04-1 | $d_h = 2.25"$ | 55° | 4.0 | 4.04 | 3.0 | 4.0 | 3.1 | 30.3 | 46.3 | 63.9 | crushing |
| CCT-08-55-04.06-1 | $2.0" \times 2.0"$ | 55° | 4.0 | 4.06 | 3.0 | 4.0 | 3.1 | 34.8 | 55.9 | 69.2 | crushing |
| CCT-08-55-04.70(H)-1 | $1.5" \times 3.0"$ | 55° | 4.0 | 4.70 | 3.0 | 4.0 | 4.0 | 46.6 | 68.4 [†] | 88.7 | yield |
| CCT-08-55-04.70(H)-2 | $1.5" \times 3.0"$ | 55° | 4.0 | 4.70 | 3.0 | 4.0 | 3.1 | 52.1 | 66.5 | 82.3 | crushing |
| CCT-08-55-04.70(V)-1 | $1.5" \times 3.0"$ | 55° | 4.0 | 4.70 | 3.0 | 4.0 | 3.9 | 48.6 | 68.4 [†] | 85.4 | splitting |
| CCT-08-55-10.39-1 | $3.0" \times 3.0"$ | 55° | 4.0 | 10.39 | 3.0 | 4.0 | 4.0 | 59.0 | 68.4 [†] | 91.9 | yield |

Table C-1a: Summary of CCT node test results

| Specimen Identification | Head Type | θ_{strut} | $\frac{L_{plate}}{d_b}$ | $\frac{A_{nh}}{A_b}$ | $\frac{C_1}{d_b}$ | $\frac{C_2}{d_b}$ | f'_c (ksi) | f_s at $1d_b$ (ksi) | f_s at $7d_b$ (ksi) | P_{max} (kip) | Failure Mode |
|-------------------------|--------------------|------------------|-------------------------|----------------------|-------------------|-------------------|--------------|-----------------------|-----------------------|-----------------|--------------|
| CCT-08-45-00.00-1 | no head | 45° | 4.0 | 0.00 | 3.0 | 4.0 | 4.0 | 12.0 | 43.5 | 42.3 | pullout |
| CCT-08-45-01.18-1 | $d_h=1.48"$ | 45° | 4.0 | 1.18 | 3.0 | 4.0 | 4.0 | 18.7 | - | 46.3 | splitting |
| CCT-08-45-01.85-1 | $1.5" \times 1.5"$ | 45° | 4.0 | 1.85 | 3.0 | 4.0 | 4.0 | 26.6 | 66.7* | 43.4 | splitting |
| CCT-08-45-01.85-2 | $1.5" \times 1.5"$ | 45° | 4.0 | 1.85 | 3.0 | 4.0 | 3.1 | 29.6 | 60.9 | 52.0 | splitting |
| CCT-08-45-02.80(H)-1 | $1.5" \times 2.0"$ | 45° | 4.0 | 2.80 | 3.0 | 4.0 | 4.0 | 46.5 | 68.4 | 62.2 | yield |
| CCT-08-45-02.80(H)-2 | $1.5" \times 2.0"$ | 45° | 4.0 | 2.80 | 3.0 | 4.0 | 3.1 | 37.6 | 59.8 | 53.1 | splitting |
| CCT-08-45-02.80(V)-1 | $1.5" \times 2.0"$ | 45° | 4.0 | 2.80 | 3.0 | 4.0 | 3.9 | 49.1 | 66.5 | 59.8 | splitting |
| CCT-08-45-04.04-1 | $d_h=2.25"$ | 45° | 4.0 | 4.04 | 3.0 | 4.0 | 4.0 | 41.4 | 61.0 | 54.7 | yield |
| CCT-08-45-04.06-1 | $2.0" \times 2.0"$ | 45° | 4.0 | 4.06 | 3.0 | 4.0 | 3.1 | 44.1 | 66.6 | 62.7 | crushing |
| CCT-08-45-04.70(H)-1 | $1.5" \times 3.0"$ | 45° | 4.0 | 4.70 | 3.0 | 4.0 | 3.1 | 53.6 | 59.9 | 51.5 | crushing |
| CCT-08-45-04.70(V)-1 | $1.5" \times 3.0"$ | 45° | 4.0 | 4.70 | 3.0 | 4.0 | 3.9 | 48.8 | 68.4 | 63.9 | splitting |
| CCT-08-45-10.39-1 | $3.0" \times 3.0"$ | 45° | 4.0 | 10.39 | 3.0 | 4.0 | 3.1 | - | 54.6 | 45.8 | crushing |
| CCT-08-45-10.39-2 | $3.0" \times 3.0"$ | 45° | 4.0 | 10.39 | 3.0 | 4.0 | 3.8 | 54.7 | 68.4 | 59.5 | crushing |
| CCT-08-45-Hook1-1 | Hook 1 | 45° | 4.0 | - | 3.0 | 4.0 | 4.0 | - | - | 49.0 | splitting |
| CCT-08-45-Hook2-1 | Hook 2 | 45° | 4.0 | - | 3.0 | 4.0 | 4.0 | - | - | 52.8 | splitting |
| CCT-08-30-00.00-1 | no head | 30° | 4.0 | 0.00 | 3.0 | 4.0 | 4.1 | 6.1 | 34.0 | 20.2 | pullout |
| CCT-08-30-01.18-1 | $d_h=1.48"$ | 30° | 4.0 | 1.18 | 3.0 | 4.0 | 4.1 | 29.9 | 59.8 | 31.1 | splitting |
| CCT-08-30-01.85-1 | $1.5" \times 1.5"$ | 30° | 4.0 | 1.85 | 3.0 | 4.0 | 4.1 | 40.5 | 68.4 | 41.5 | yield |
| CCT-08-30-04.04-1 | $d_h=2.25"$ | 30° | 4.0 | 4.04 | 3.0 | 4.0 | 4.1 | 34.8 | 61.0 | 37.8 | yield |
| CCT-08-30-04.06-1 | $2.0" \times 2.0"$ | 30° | 4.0 | 4.06 | 3.0 | 4.0 | 4.1 | 49.2 | 68.4 | 40.6 | yield |
| CCT-08-30-10.39-1 | $3.0" \times 3.0"$ | 30° | 4.0 | 10.39 | 3.0 | 4.0 | 4.1 | 46.0 | 68.4 | 39.0 | yield |
| CCT-08-45-04.70(V)-1-S1 | $1.5" \times 3.0"$ | 45° | 4.0 | 4.70 | 3.0 | 4.0 | 4.1 | - | - | - | pullout |
| CCT-08-45-04.70(V)-1-S2 | $1.5" \times 3.0"$ | 45° | 4.0 | 4.70 | 3.0 | 4.0 | 4.1 | 41.3 | 58.0 | 54.8 | crushing |
| CCT-08-45-04.70(H)-1-S3 | $1.5" \times 3.0"$ | 45° | 4.0 | 4.70 | 3.0 | 4.0 | 3.8 | 54.7 | 66.0 | 58.8 | splitting |

Table C-1b: Summary of CCT node test results (continued)

| Specimen Identification | Head Type | θ_{strut} | $\frac{L_{\text{plate}}}{d_b}$ | $\frac{A_{\text{nh}}}{A_b}$ | $\frac{C_1}{d_b}$ | $\frac{C_2}{d_b}$ | f'_c (ksi) | f_s at $1d_b$ (ksi) | f_s at $7d_b$ (ksi) | P_{max} (kip) | Failure Mode |
|-----------------------------|---------------|-------------------------|--------------------------------|-----------------------------|-------------------|-------------------|--------------|-----------------------|-----------------------|------------------------|--------------|
| CCT-08-45-00.00-1-C0.006 | no head | 45° | 4.0 | 0.00 | 3.0 | 4.0 | 3.8 | 2.1 | 43.1 | 40.6 | pullout |
| CCT-08-45-00.00-1-C0.012 | no head | 45° | 4.0 | 0.00 | 3.0 | 4.0 | 3.8 | 7.2 | 41.2 | 41.6 | pullout |
| CCT-08-45-04.70(V)-1-C0.006 | 1.5" x 3.0" | 45° | 4.0 | 4.70 | 3.0 | 4.0 | 3.8 | 36.5 | 64.1 | 58.1 | splitting |
| CCT-08-45-04.70(V)-1-C0.012 | 1.5" x 3.0" | 45° | 4.0 | 4.70 | 3.0 | 4.0 | 3.8 | 39.2 | 65.6 | 66.8 | splitting |
| CCT-08-45-Hook2-1-C0.012 | Hook 2 | 45° | 4.0 | - | 3.0 | 4.0 | 3.8 | - | 59.6 | 52.5 | splitting |
| CCT-11-45-00.00-1 | no head | 45° | 4.0 | 0.00 | 2.8 | 3.0 | 4.1 | 13.6 | 38.9 | 68.4 | pullout |
| CCT-11-45-01.10-1 | $d_h = 2.04"$ | 45° | 4.0 | 1.10 | 2.8 | 3.0 | 4.1 | 21.4 | 51.3 | 91.4 | splitting |
| CCT-11-45-01.56-1 | 2.0" x 2.0" | 45° | 4.0 | 1.56 | 2.8 | 3.0 | 4.1 | 30.2 | 53.7 | 90.0 | splitting |
| CCT-11-45-02.85(H)-1 | 2.0" x 3.0" | 45° | 4.0 | 2.85 | 2.8 | 3.0 | 4.1 | 30.3 | 50.1 | 78.4 | splitting |
| CCT-11-45-02.85(V)-1 | 2.0" x 3.0" | 45° | 4.0 | 2.85 | 2.8 | 3.0 | 4.1 | 40.9 | 54.4 | 89.6 | crushing |
| CCT-11-45-03.53-1 | $d_h = 3.00"$ | 45° | 4.0 | 3.53 | 2.8 | 3.0 | 4.0 | 36.7 | 55.9 | 93.7 | crushing |
| CCT-11-45-04.13(H)-1 | 2.0" x 4.0" | 45° | 4.0 | 4.13 | 2.8 | 3.0 | 4.1 | 56.5 | 61.9 | 96.2 | crushing |
| CCT-11-45-04.13(V)-1 | 2.0" x 4.0" | 45° | 4.0 | 4.13 | 2.8 | 3.0 | 4.0 | 39.1 | 57.0 | 88.9 | splitting |
| CCT-11-45-04.77-1 | 3.0" x 3.0" | 45° | 4.0 | 4.77 | 2.8 | 3.0 | 4.0 | 39.7 | 56.8 | 84.0 | crushing |
| CCT-11-45-06.69(H)-1 | 3.0" x 4.0" | 45° | 4.0 | 6.69 | 2.8 | 3.0 | 4.0 | 54.9 | 62.8 [†] | 95.8 | yield |
| CCT-11-45-06.69(V)-1 | 3.0" x 4.0" | 45° | 4.0 | 6.69 | 2.8 | 3.0 | 4.0 | 40.0 | 62.8 [†] | 99.1 | yield |
| CCT-11-45-09.26-1 | 4.0" x 4.0" | 45° | 4.0 | 9.26 | 2.8 | 3.0 | 4.0 | 50.5 | 62.8 [†] | 107.7 | yield |

- data not available or not applicable

* questionable data point

† stress equal to f_y

‡ shear failure on back portion of specimen

Table C-1c: Summary of CCT node test results (continued)

Appendix D: Summary of Lap Splice Data

Lap splice test results are summarized in Tables D-1a and D-1b. The tables report the maximum bar stresses at $2d_b$ (next to the head) and L_a (the point of critical bar development - see Figure D-1). The maximum moment is also reported. Important parameters from of the specimens are also reported.

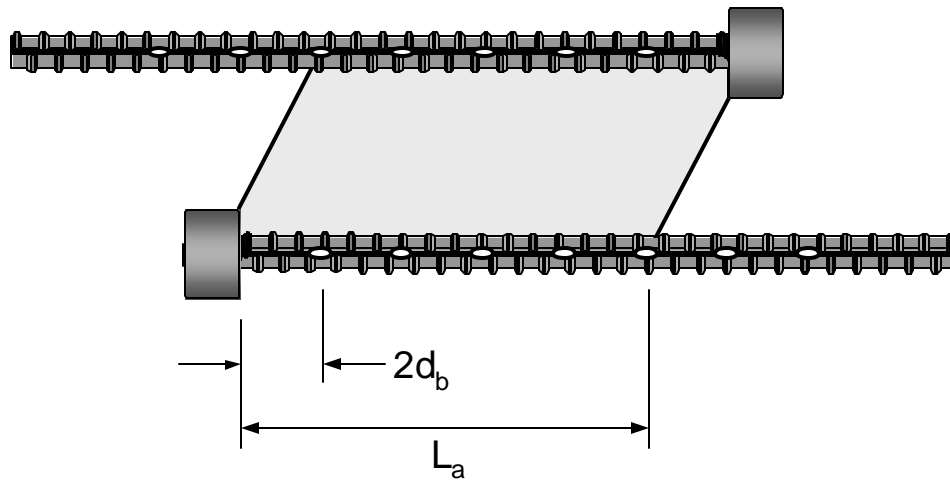


Figure D-1: Close-up of lap splice

| Specimen Identification | Head Type | $\frac{L_a}{d_b}$ | $\frac{A_{nh}}{A_b}$ | $\frac{C_1}{d_b}$ | $\frac{C_2}{d_b}$ | f'_c (ksi) | f_s at $2d_b$ (ksi) | f_s at L_a (ksi) | M_{max} (kip*in) | Failure Mode |
|---------------------------|--------------------|-------------------|----------------------|-------------------|-------------------|--------------|-----------------------|----------------------|--------------------|--------------|
| LS-05-01.39-12-16(C)-1 | $d_h = 0.97"$ | 6.5 | 1.39 | 4.0 | 4.0 | 5.7 | - | - | 826 | yield |
| LS-05-01.39-12-16(C)-2 | $d_h = 0.97"$ | 6.5 | 1.39 | 4.0 | 4.0 | 5.7 | - | - | 842 | yield |
| LS-05-01.39-12-10(C)-1 | $d_h = 0.97"$ | 8.5 | 1.39 | 2.5 | 4.0 | 5.7 | - | - | 912 | splitting |
| LS-05-11.90-11-10(C)-1 | $2.0" \times 2.0"$ | 7.5 | 11.90 | 2.5 | 4.0 | 5.7 | - | - | 1081 | yield |
| LS-08-00.00-05-10(N)-1 | no head | 3.0 | 0.00 | 2.5 | 2.5 | 3.2 | 0.9 | 3.4 | 312 | splitting |
| LS-08-00.00-08-10(N)-1 | no head | 6.0 | 0.00 | 2.5 | 2.5 | 4.0 | 17.4 | 22.4 | 473 | splitting |
| LS-08-00.00-12-10(N)-1 | no head | 10.0 | 0.00 | 2.5 | 2.5 | 4.2 | 11.1 | 38.0 | 700 | splitting |
| LS-08-01.18-03-06(N)-1 | $d_h = 1.48"$ | 1.5 | 1.18 | 1.5 | 2.5 | 3.7 | 9.0 | 9.02 | 347 | splitting |
| LS-08-01.18-05-10(N)-1 | $d_h = 1.48"$ | 3.0 | 1.18 | 2.5 | 2.5 | 3.7 | 8.4 | 13.3 | 477 | splitting |
| LS-08-01.18-05-10(C)-1 | $d_h = 1.48"$ | 3.0 | 1.18 | 2.5 | 2.5 | 3.7 | 14.8 | 17.5 | 493 | splitting |
| LS-08-01.18-08-10(N)-1 | $d_h = 1.48"$ | 6.0 | 1.18 | 2.5 | 2.5 | 4.0 | 14.1 | 26.4 | 577 | splitting |
| LS-08-04.70-03-06(N)-1 | $1.5" \times 3.0"$ | 1.5 | 4.70 | 1.5 | 2.5 | 3.2 | 18.6 | 18.6 | 415 | splitting |
| LS-08-04.70-05-06(N)-1 | $1.5" \times 3.0"$ | 3.0 | 4.70 | 2.5 | 2.5 | 3.7 | 24.1 | 27.0 | 567 | splitting |
| LS-08-04.70-05-10(N)-1 | $1.5" \times 3.0"$ | 3.0 | 3.70 | 2.5 | 2.5 | 3.2 | 24.5 | 24.1 | 581 | splitting |
| LS-08-04.70-05-10(C)-1 | $1.5" \times 3.0"$ | 3.0 | 4.70 | 2.5 | 2.5 | 3.2 | 24.6 | 24.5 | 655 | splitting |
| LS-08-04.70-08-10(N)-1 | $1.5" \times 3.0"$ | 6.0 | 4.70 | 2.5 | 2.5 | 4.0 | 39.5 | 43.5 | 659 | splitting |
| LS-08-04.04-08-10(N)-1 | $d_h = 2.25"$ | 6.0 | 4.04 | 2.5 | 2.5 | 4.0 | 40.4 | 44.4 | 673 | splitting |
| LS-08-04.70-12-10(N)-1 | $1.5" \times 3.0"$ | 10.0 | 4.70 | 2.5 | 2.5 | 4.2 | 42.4 | 66.3 | 986 | splitting |
| LS-08-04.04-12-10(N)-1 | $d_h = 2.25"$ | 10.0 | 4.04 | 2.5 | 2.5 | 3.8 | 41.6 | 51.0 | 765 | splitting |
| LS-08-04.04-14-10(N)-1 | $d_h = 2.25"$ | 12.0 | 4.04 | 2.5 | 2.5 | 3.5 | 39.1 | 65.0* | 1039 | splitting |
| LS-08-04.04-14-10(N)-1-DB | $d_h = 2.25"$ | 12.0 | 4.04 | 2.5 | 5.0 | 3.5 | 54.4 | 54.4 | 883 | splitting |

Table D-1a: Summary of lap splice test results

| Specimen Identification | Head Type | $\frac{L_a}{d_b}$ | $\frac{A_{nh}}{A_b}$ | $\frac{c_1}{d_b}$ | $\frac{c_2}{d_b}$ | f'_c (ksi) | f_s at $2d_b$ (ksi) | f_s at L_a (ksi) | M_{max} (kip*in) | Failure Mode |
|------------------------------|---------------|-------------------|----------------------|-------------------|-------------------|--------------|-----------------------|----------------------|--------------------|--------------|
| LS-08-00.00-08-10(N)-1-H0.25 | no head | 6.0 | 0.00 | 2.5 | 2.5 | 4.2 | 7.4 | 22.0 | 528 | splitting |
| LS-08-04.70-08-10(N)-1-H0.25 | 1.5" x 3.0" | 6.0 | 4.70 | 2.5 | 2.5 | 4.2 | 49.7 | 54.8 | 859 | splitting |
| LS-08-04.04-08-10(N)-1-H0.56 | $d_h = 2.25"$ | 6.0 | 4.04 | 2.5 | 2.5 | 3.5 | 56.7 | 54.1 | 845 | splitting |
| LS-08-04.04-08-10(N)-1-H1.01 | $d_h = 2.25"$ | 6.0 | 4.04 | 2.5 | 2.5 | 3.5 | 52.4 | 56.7 | 905 | splitting |
| LS-08-04.04-12-10(N)-1-H0.56 | $d_h = 2.25"$ | 10.0 | 4.04 | 2.5 | 2.5 | 3.8 | 39.9 | 53.8 | 818 | splitting |
| LS-08-04.04-12-10(N)-1-TTD | $d_h = 2.25"$ | 10.0 | 4.04 | 2.5 | 2.5 | 3.8 | 60.0 | 56.6 | 886 | splitting |

- data not available or not applicable

* questionable data value

Table D-1b: Summary of lap splice test results (continued)

References

1. "AASHTO LRFD Bridge Design Specifications, 2nd ed.," American Association of State Highway and Transportation Officials, Washington, DC, 1998.
2. ACI 318-02, "Building Code Requirements for Structural Concrete and Commentary," American Concrete Institute, Farmington Hills, Michigan, October 2002.
3. ASTM A615/A615M-96a, "Standard Specification for Deformed and Plain Billet-Steel for Concrete Reinforcement," American Society for Testing and Materials, West Conshohocken, Pennsylvania, September 1996.
4. ASTM A944-99, "Standard Test Method for Comparing Bond Strength of Steel Reinforcing Bars to Concrete Using Beam-End Specimens," American Society for Testing and Materials, West Conshohocken, Pennsylvania, September 1999.
5. ASTM A970/A970M-97, "Standard Specification for Welded Headed Bars for Concrete Reinforcement," American Society for Testing and Materials, West Conshohocken, Pennsylvania, September 1997.
6. ASTM C39/C39M-99, "Standard Test Method for Compressive Strength of Cylindrical Concrete Specimens," American Society for Testing and Materials, West Conshohocken, Pennsylvania, September 1999.
7. ASTM C496-96, "Standard Test Method for Splitting Tensile Strength of Cylindrical Concrete Specimens," American Society for Testing and Materials, West Conshohocken, Pennsylvania, September 1996.
8. ASTM C469-94, "Standard Test Method for Static Modulus of Elasticity and Poisson's Ratio of Concrete in Compression," American Society for Testing and Materials, West Conshohocken, Pennsylvania, September 1994.
9. CSA Standard CAN3-A23.3-94, "Design of Concrete Structures for Buildings with Explanatory Notes," Canadian Standards Association, Rexdale, Ontario, 1994.
10. CEB Bulletin No. 216, "Fastenings to Concrete and Masonry Structures," Lausanne, Switzerland, July 1994.
11. CEB Bulletin No. 226, "Design of Fastenings in Concrete: Draft CEB Guide – Part 1 to 3," Lausanne, Switzerland, August 1995.
12. "Fracture Mechanics of Concrete: Concepts, Models and Determination of Material Properties," Report by ACI 446, Fracture Mechanics (Z. P. Bažant, Chairman), Detroit, Michigan, December 1989.
13. International Conference of Building Officials (ICBO) Evaluation Report ER-5309, Whittier, California, May 1997.

14. "Ontario Highway Bridge Design Code, 3rd Edition," Canadian Ministry of Transportation, Toronto, Ontario, Canada, 1991.
15. PCI Design Handbook 3rd Edition, Prestressed Concrete Institute, Chicago, Illinois, 1985.
16. "Structural Concrete: The Textbook on Behavior, Design, and Performance - Volume 2: Basis of Design," Federation Internationale du Beton (FIB), Lausanne, Switzerland, July 1999.
17. Abrams, D.A., "Tests of Bond Between Concrete and Steel," Engineering Experiment Station, University of Illinois Bulletin No. 71, Urbana, Illinois, December 1913.
18. Adebar, P., Kuchma, D., and Collins, M.P., "Strut-and-Tie Models for the Design of Pile Caps: An Experimental Study," ACI Structural Journal, Proceedings Vol. 87, No. 1, pg. 81-92, Detroit, Michigan, January-February 1990.
19. Adebar, P. and Zhou, Z., "Bearing Strength of Compressive Struts Confined by Plain Concrete," ACI Structural Journal, Proceedings Vol. 90, No. 5, pg. 534-541, Detroit, Michigan, September-October 1993.
20. Adebar, P. and Zhou, Z., "Design of Deep Pile Caps by Strut-and-Tie Models," ACI Structural Journal, Proceedings Vol. 93, No. 4, pg. 437-448, Detroit, Michigan, July-August 1996.
21. Aguilar, G., Matamoros, A., Parra-Montesinos, G., Ramirez, J.A., and Wight, J.K., "Experimental and Analytical Evaluation of Design Procedures for Shear Strength of Deep Reinforced Concrete Beams," Final Report to the Reinforced Concrete Research Council, ACI, Purdue University, Lafayette, Indiana, May 2001.
22. Alshegeir, A.A. and Ramirez, J.A., "Analysis and Design of Disturbed Regions with Strut-Tie Models, Parts I and II," Purdue University, Structural Engineering Report No. CE-STR-93-1, Lafayette, Indiana, 1993.
23. Armstrong, S.D., Salas, R.M., Wood, B.A., Breen, J.E., and Kreger, M.E., "Behavior and Design of Large Structural Concrete Bridge Pier Overhangs," Center for Transportation Research Report CTR-1364-1, Austin, Texas, February 1997.
24. Au, T. and Baird, D.L., "Bearing Capacity of Concrete Blocks," Journal of the American Concrete Institute, Proceedings Vol. 56, No. 9, pgs. 869-879, Detroit, Michigan, March 1960.
25. Barton, D.L., Anderson, R.B., Bouardi, A., Jirsa, J.O., and Breen, J.E., "An Investigation of Strut-and-Tie Models for Dapped Beam Details," Center for Transportation Research Report No. CTR 3-5-87/9-1127-1, Austin, Texas, May 1991.
26. Bashandy, T.R., "Application of Headed Bars in Concrete Members," PhD Dissertation, The University of Texas at Austin, Austin, Texas, December 1996.

27. Beaupre, R.J., Powell, L.C., Breen, J.E., and Kreger, M.E., "Deviation Saddle Behavior and Design for Externally Post-Tensioned Bridges," Center for Transportation Research Report No. CTR 3-5-85/8-365-2, Austin, Texas, July, 1988.
28. Bergmeister, K., Breen, J.E., Jirsa, J.O., and Kreger, M.E., "Detailing for Structural Concrete," Center for Transportation Research Report CTR 0-1127-3F, Austin, Texas, May 1993.
29. Berner, D.E., Gerwick, B.C., and Hoff, G.C., "T-Headed Stirrup Bars," Concrete International, Vol. 13, No. 5, Detroit, Michigan, May 1991.
30. Berner, D.E. and Hoff, G.C., "Headed Reinforcement in Disturbed Strain Regions of Concrete Members," Concrete International, Vol. 16, No. 1, Detroit, Michigan, January 1994.
31. Breen, J.E., "Development Length for Anchor Bolts," Center for Transportation Research Report CTR-55-1F, Austin, Texas, April 1964.
32. Breen, J.E., Burdet, O., Roberts, C., Sanders, D., and Wollmann, G., "Anchorage Zone Reinforcement for Post-Tensioned Concrete Girders," National Cooperative Highway Research Program Report No. 356, Washington, DC, 1994.
33. Chamberlin, S.J., "Spacing of Spliced Bars in Tension Pull-Out Specimens," Journal of the American Concrete Institute, Proceedings Vol. 49, No. 4, pg. 261-274, Detroit, Michigan, December 1952.
34. Chen, W.F., "Double Punch Test for Tensile Strength of Concrete," Journal of the American Concrete Institute, Proceedings Vol. 67, No. 12, pg. 993-995, Detroit, Michigan, December 1970.
35. Chinn J., Ferguson, P.M., Thompson, J.N., "Lapped Splices in Reinforced Concrete Beams," Journal of the American Concrete Institute, Proceedings Vol. 52, No. 2, pg. 201-212, Detroit, Michigan, October 1955.
36. Clark, A.P., "Comparative Bond Efficiency of Deformed Concrete Reinforcing Bars," Journal of the American Concrete Institute, Proceedings Vol. 43, No. 4, Detroit, Michigan, December 1946.
37. Clark, A.P., "Bond of Concrete Reinforcing Bars," Journal of the American Concrete Institute, Proceedings Vol. 46, No. 3, November 1949.
38. Collins, M.R., Vecchio, F.J., Selby, R.G., and Gupta, P., "The Failure of an Offshore Platform," Concrete International, Vol. 19, No. 8, pg. 28-35, Detroit, Michigan, August 1997.
39. Cook, W. and Mitchell, D., "Studies of Disturbed Regions Near Discontinuities in Reinforced Concrete Members," ACI Structural Journal, Proceedings Vol. 85, No. 2, pg. 206-216, Detroit, Michigan, March-April 1988.

40. Darwin, D. and Graham, E.K., "Effect of Deformation Height and Spacing on Bond Strength of Reinforcing Bars," *ACI Structural Journal*, Vol. 90, No. 6, Detroit, Michigan, November-December 1993.
41. Darwin, D., Zou, J., and Tholen, M.L., "Overview of Research to Improve the Development Characteristics of Reinforcing Bars," *Proceedings of the International Symposium "Bond and Development of Reinforcement, A Tribute to Dr. Peter Gergely,"* ACI International, SP-180, pg. 299-318, Farmington Hills, Michigan, 1998.
42. DeVries, R.A., "Anchorage of Headed Reinforcement in Concrete," PhD Dissertation, The University of Texas at Austin, Austin, Texas, December 1996.
43. Dilger, W.H. and Ghali, A., "Double-Headed Studs as Ties in Concrete," *Concrete International*, Vol. 19, No. 6, pg. 59-66, Detroit, Michigan, June 1997.
44. Dilger, W.H. and Ghali, A., "Shear Reinforcement for Concrete Slabs," *ASCE Journal of Structural Engineering*, Vol. 107, No. 12, pgs. 2403-2420, New York, New York, December 1981.
45. Drågen, A., "T-Headed Bars SP2: Fatigue Tests," SINTEF Report STF18 F86048, Trondheim, Norway, 1986 (*proprietary report*).
46. Dyken, T. and Kepp B., "Properties of T-Headed Bars in High Strength Concrete," *Nordic Concrete Research*, Publication No. 7, pg. 41-51, Oslo, Norway, 1993.
47. Eibl, J. and Zeller, W., "Untersuchungen zur Traglast der Druckdiagonalen in Konsolen," *Bericht*, Institut für Massivbau und Baustofftechnologie, University of Karlsruhe, Germany, 1991.
48. Fuchs, W., Eligehausen, R., and Breen, J.E., "Concrete Capacity Design (CCD) Approach for Fastening to Concrete," *ACI Structural Journal*, *Proceedings* Vol. 92, No. 1, pg. 73-94, Detroit, Michigan, January-February 1995.
49. Furche, J. and Eligehausen, R., "Lateral Blow-Out Failure of Headed Studs Near a Free Edge," *Proceedings of International Symposium "Anchors in Concrete – Design and Behavior,"* ACI International, SP-130, pg. 235-252, Farmington Hills, Michigan, 1991.
50. Fynboe, C.C. and Thorenfeldt, E., "T-Headed Bars SP1: Static Pullout Tests," SINTEF Report STF65 F86083, Trondheim, Norway, 1986 (*proprietary report*).
51. Fynboe, C.C. and Thorenfeldt, E., "T-Headed Bars SP3: Fatigue Tests – Bars Embedded in Concrete," SINTEF Report STF65 F86088, Trondheim, Norway, 1986 (*proprietary report*).
52. Fynboe, C.C. et al, "T-Headed Bars SP4: Shear," SINTEF Report STF65 F86084, Trondheim, Norway, 1986 (*proprietary report*).
53. Gambarova, P.G., Rosati, G.P., and Schumm, C.E., "Bond and Splitting: A Vexing Question," *Proceedings of the International Symposium "Bond and Development of*

- Reinforcement, A Tribute to Dr. Peter Gergely,” ACI International, SP-180, pg. 23-44, Farmington Hills, Michigan, 1998.
54. Goto, Yukimasa, “Cracks Formed in Concrete Around Deformed Tension Bars,” Journal of the American Concrete Institute, Proceedings Vol. 68, No. 4, pg. 244-251, Detroit, Michigan, April 1971.
 55. Hamad, B.S., “Comparative Bond Strength of Coated and Uncoated Bars with Different Rib Geometries,” ACI Materials Journal, Vol. 92, No. 6, Detroit, Michigan, November-December 1995.
 56. Hamad, B.S. and Mansour, M.Y., “Bond Strength of Noncontact Tension Lap Splices,” ACI Structural Journal, Proceedings Vol. 93, No. 3, Detroit, Michigan, May-June 1996.
 57. Haroun, H., Pardoen, G., Bhatia, H., Shahi, S., and Kazanjy, R., “Structural Behavior of Repaired Pier Walls,” ACI Structural Journal, Proceedings Vol. 97, No. 2, pg. 259-267, Detroit, Michigan, March-April 2000.
 58. Hasselwander, G.B., Jirsa, J.O., Breen, J.E., and Lo, K., “Strength and Behavior of Anchor Bolts Embedded Near Edges of Concrete Piers,” Center for Transportation Research Report CTR-29-2F, Austin, Texas, May 1977.
 59. Hasselwander, G.B., Jirsa, J.O., and Breen, J.E., “Strength and Behavior of Single Cast-in-Place Anchor Bolts Subject to Tension,” Proceedings of the International Symposium “Anchorage to Concrete,” ACI International, SP-103, pg. 203-231, Farmington Hills, Michigan, 1984.
 60. Hawkins, N.M., “The Bearing Strength of Concrete: 1. Loading Through Rigid Plates Covering Part of the Full Supporting Area,” The University of Sydney, Research Report No. 54, Sydney, Australia, March 1967.
 61. Hawkins, N.M., “The Bearing Strength of Concrete: 2. Loading Through Flexible Plates,” The University of Sydney, Research Report No. 84, Sydney, Australia, August 1967.
 62. Ingham, J.M, Priestley, M.J., and Seible, F., “Seismic Performance of a Bridge Knee Joint Reinforced with Headed Reinforcement,” University of California, San Diego, Structural Systems Research Project, Report No. SSRP-96/06, La Jolla, California, September 1996.
 63. Jakobsen, B. and Rosendahl, B., “The Sleipner Platform Accident,” IABSE Structural Engineering International, Vol. 4, No. 3, pg. 190-193, Zurich, Switzerland, August 1994.
 64. Kuchma, D.A. and Collins, M.P., “The Influence of T-Headed Bars on the Strength and Ductility of Reinforced Concrete Wall Elements,” University of Toronto, Paper Presented at the Spring Conference of the American Concrete Institute, Seattle, Washington, April 1997.

65. Kupfer, H., Hilsdorf, H.K., and Rusch, H., "Behavior of Concrete Under Biaxial Stresses," *Journal of the American Concrete Institute, Proceedings* Vol. 66, No. 8, pg. 656-666, Detroit, Michigan, August 1969.
66. Lampert, P. and Thürlimann, B., "Ultimate Strength and Design of Reinforced Concrete Beams in Torsion and Bending," *IASBE Publications*, No. 31-1, pg. 107-131, Zurich, Switzerland, 1971.
67. Ledesma, A.L., "Development of Lap Splices Using Headed Reinforcement," Master's Thesis, The University of Texas at Austin, Austin, Texas, May 2000.
68. Lee, D.W. and Breen, J.E., "Factors Affecting Anchor Bolt Development," Center for Transportation Research Report CTR-88-1F, Austin, Texas, August 1966.
69. Lehman, D.E., Gookin, S.E., Nacamuli, A.M., and Moehle, J.P., "Repair of Earthquake-Damaged Bridge Columns," *ACI Structural Journal, Proceedings* Vol. 98, No. 2, pg. 233-242, Detroit, Michigan, March-April 2001.
70. Lormanometee, Sumete, "Bond Strength of Deformed Reinforcing Bar Under Lateral Pressure," Master's Thesis, The University of Texas at Austin, Austin, Texas, January 1974.
71. Lüchinger, P., "Bruchwiderstand von Kastenträgern aus Stahlbeton unter Torsion, Biegung, und Querkraft (Ultimate Strength of Box-Griders in Reinforced Concrete under Torsion, Bending, and Shear)," *Institut für Baustatik und Konstruktion-ETH, Zurich, Switzerland, Bericht Nr. 69*, 1977.
72. Lutz, LeRoy A., "The Mechanics of Bond and Slip of Deformed Reinforcing Bars in Concrete," Department of Structural Engineering, Cornell University, Report No. 324, Ithaca, New York, August 1966.
73. MacGregor, J.G., "Reinforced Concrete: Mechanics and Design (3rd Edition)," Prentice Hall, Upper Saddle River, New Jersey, 1997.
74. Mains, R.M., "Measurement of the Distribution of Tensile and Bond Stresses Along Reinforcing Bars," *Journal of the American Concrete Institute, Proceedings* Vol. 48, No. 3, pg. 225-252, Detroit, Michigan, November 1951.
75. Marques, J.L.G., and Jirsa, J.O., "A Study of Hooked Bar Anchorages in Beam-Column Joints," *Journal of the American Concrete Institute, Proceedings* Vol. 72, No. 5, pg. 198-209, Detroit, Michigan, May 1975.
76. Marti, P., "Basic Tools in Reinforced Concrete Beam Design," *Journal of the American Concrete Institute, Proceeding* Vol. 82, No. 1, pg. 46-56, Detroit, Michigan, January-February 1985.
77. Marti, P., "Size Effect in Double-Punch Tests on Concrete Cylinders," *ACI Materials Journal, Proceedings* Vol. 86, No. 6, pg. 597-601, Detroit, Michigan, November-December 1989.

78. Marti, P., "Truss Models in Detailing," *Concrete International*, Vol. 7, No. 12, pg. 66-73, Detroit, Michigan, December 1985.
79. Matsumoto, E.E., Waggoner, M.C., Sumen, G., Kreger, M.E., Wood, S.L., and Breen, J.E., "Development of a Precast Bent Cap System," Center for Transportation Research Report 1748-2, Austin, Texas, January 2001.
80. Mattock, A.H., "Effectiveness of Loop Anchorages for Reinforcement in Precast Concrete Members," *PCI Journal*, Vol. 39, No. 6, pg. 54-68, Chicago, Illinois, November-December 1994.
81. Maxwell, B.S. and Breen, J.E., "Experimental Evaluation of Strut-and-Tie Model Applied to Deep Beam with Opening," *ACI Structural Journal*, Proceedings Vol. 97, No. 1, pg. 142-148, Detroit, Michigan, January-February 2000.
82. McMackin, P.J., Slutter, R.G., and Fisher, J.W., "Headed Steel Anchor Under Combined Loading," *AISC Engineering Journal*, Vol. 10, No. 2, pg. 43-52, New York, New York, 2nd Quarter, 1973.
83. Menon, G. and Furlong, R.W., "Design of Reinforcement for Notched Ends of Prestressed Concrete Girders," Center for Transportation Research Report No. 196-1F, Austin, Texas, 1977.
84. Minor, J., and Jirsa, J.O., "Behavior of Bent Bar Anchorages," *Journal of the American Concrete Institute*, Proceedings Vol. 72, No. 4, pg. 141-149, Detroit, Michigan, April 1975.
85. Mitchell, D. and Collins, M., "Diagonal Compression Field Theory – A Rational Model for Structural Concrete in Pure Torsion," *Journal of the American Concrete Institute*, Proceedings Vol. 71, No. 8, pg. 396-408, Detroit, Michigan, August 1974.
86. Mokhtar, A.S., Ghali, A., and Dilger, W.H., "Stud Shear Reinforcement for Flat Concrete Plates," *Journal of the American Concrete Institute*, Proceedings Vol. 82, No. 5, pgs. 676-683, Detroit, Michigan, September-October 1985.
87. Mörsch, E., "Der Eisenbetonbau, seine Theorie und Anwendung (Reinforced Concrete, Theory and Application)," Stuttgart, Germany, 1902.
88. Mörsch, E., "Über die Berechnung der Gelenkquader," *Beton-und Eisen*, No. 12, pg. 156-161, Stuttgart, Germany, 1924.
89. Nielson, M.P., "Limit Analysis and Concrete Plasticity, 2nd Edition," CRC Press, Boca Raton, Florida, 1998.
90. Niyogi, S.K., "Bearing Strength of Concrete – Geometric Variations," *ASCE Journal of Structural Engineering*, Vol. 99, No. 7, pgs. 1471-1490, New York, New York, July 1973.

91. Niyogi, S.K., "Concrete Bearing Strength – Support, Mix, Size Effect," ASCE Journal of Structural Engineering, Vol. 100, No. 8, pgs. 1685-1702, New York, New York, August 1974.
92. Niyogi, S.K., "Bearing Strength of Reinforced Concrete Blocks," ASCE Journal of Structural Engineering, Vol. 101, No. 5, pgs. 1125-1137, New York, New York, May 1975.
93. Orangun, C.O., Jirsa, J.O., and Breen, J.E., "The Strength of Anchor Bars: A Reevaluation of Test Data on Development Length and Splices," Center for Highway Research, Report 154-3F, Austin, Texas, January 1975.
94. Orangun, C.O., Jirsa, J.O., and Breen, J.E., "A Reevaluation of Test Data on Development Length and Splices," Journal of the American Concrete Institute, Proceedings Vol. 74, No. 3, pg. 114-122, Detroit, Michigan, March 1977.
95. Ørjasæter, O., "T-Headed Bars: Fatigue Tests of Embedded Bars," SINTEF Report STF18 F87043, Trondheim, Norway, 1987 (*proprietary report*).
96. Ørjasæter, O., "Fatigue Tests of Friction Welded Bar / Reinforcement Bar," SINTEF Report STF18 F87042, Trondheim, Norway, 1987 (*proprietary report*).
97. Ramirez, J. and Breen, J.E., "Proposed Design Procedures for Shear and Torsion in Reinforced and Prestressed Concrete," Center for Transportation Research Report No. 248-4F, Austin, Texas, 1983.
98. Roberts, C., "Behavior and Design of the Local Anchorage Zone of Post-Tensioned Concrete Members," Master's Thesis, The University of Texas at Austin, May 1990.
99. Rogowsky, D.M. and MacGregor, J.M., "Shear Strength of Deep Reinforced Concrete Continuous Beams," The University of Alberta, Structural Engineering Report No. 110, Edmonton, Alberta, November 1983.
100. Rogowsky, D.M. and MacGregor, J.M., "Design of Reinforced Concrete Deep Beams," Concrete International, Vol. 6, No. 8, pg. 49-58, August 1986.
101. Richart, F., "An Investigation of Web Stresses in Reinforced Concrete Beams," University of Illinois Engineering Experiment Station, Bulletin No. 166, Urbana, Illinois, 1927.
102. Ritter, W., "Die Bauweise Hennebique (The Hennebique System)," Schweizerische Bauzeitung, Bd. XXXIII, No. 7, Zurich, Switzerland, 1899.
103. Rosati, G.P. and Schumm, C.E., "Modeling of Local Bar-to-Concrete Bond in RC Beams," Proceedings of the International Conference "Bond in Concrete: From Research to Practice," CEB-RTU, Vol. 3, pg. 12.34-12.43, Riga, Latvia, October 1992.
104. Schlaich, J. and Schäfer, K., "Konstruieren im Stahlbeton," Betonkalender, pg 563-715, Berlin, Germany, 1989.

105. Schlaich, J., Schäfer, K., and Jennewein, M., "Towards a Consistent Design of Structural Concrete," *PCI Journal*, Vol. 32, No. 3, pg. 74-150, Chicago, Illinois, May-June 1987.
106. Shelson, W., "Bearing Capacity of Concrete," *Journal of the American Concrete Institute, Proceedings* Vol. 54, No. 5, pgs. 405-414, Detroit, Michigan, November 1957.
107. Sritharan, S. and Priestley, M.J., "Seismic Testing of a Full-Scale Pile-Deck Connection Utilizing Headed Reinforcement," University of California, San Diego, Structural Systems Research Project, Report No. TR-98/14, La Jolla, California, August 1998.
108. Stoker, J.R., Boulware, R.L., Crozier, W.F., and Swirsky, R.A., "Anchorage Devices for Large Diameter Reinforcing Bars," Caltrans Report CA-DOT-TL-6626-1-73-30, California Department of Transportation, Sacramento, California, September 1974.
109. Talbot, A., "Tests of Reinforced Concrete Beams: Resistance to Web Stresses, Series of 1907 and 1908," University of Illinois Engineering Experiment Station, Bulletin No. 29, Urbana, Illinois, 1909.
110. Tepfers, Ralejs, "A Theory of Bond Applied to Overlapped Tensile Reinforcement Splices for Deformed Bars," Chalmers University of Technology, Publication No. 73:2, Göteborg, Sweden, 1973.
111. Thrö, Gerfried Schmidt, Stöckl, Siegfried, and Kupfer, Herbert, "Verankerung der Bewehrung am Endauflager bei einachsiger Querpressung" ("Anchorage of Reinforcement at an End Bearing with Uni-Axial Lateral Pressure"), *Deutscher Ausschus für Stahlbeton, Heft 389*, pg. 11-98, Berlin, Germany, 1988.
112. Untrauer, R.E. and Henry, R.L., "Influence of Normal Pressure on Bond Strength," *Journal of the American Concrete Institute, Proceedings* Vol. 62, No. 5, Detroit, Michigan, May 1965.
113. Vecchio, F.J. and Collins, M.P., "The Modified Compression Field Theory for Reinforced Concrete Elements Subjected to Shear," *Journal of the American Concrete Institute, Proceedings* Vol. 83, No. 2, pg. 219-231, Detroit, Michigan, March-April 1986.
114. Vecchio, F.J. and Collins, M.P., "The Response of Reinforced Concrete to In-Plane Shear and Normal Stresses," The University of Toronto, Department of Civil Engineering Publication No. 82-03, Toronto, Canada, 1982.
115. Wallace, J.W., McConnell, S.W., Gupta, P., and Cote, P.A., "Use of Headed Reinforcement in Beam-Column Joints Subjected to Earthquake Loads," *ACI Structural Journal, Proceedings* Vol. 95, No. 5, pg. 590-606, Detroit, Michigan, September-October 1998.
116. Williams, A., "The Bearing Capacity of Concrete Loaded Over a Limited Area," *Cement and Concrete Association, Technical Report 526*, Wexham Springs, Slough, The United Kingdom, August 1979.

117. Withey, M., "Tests of Plain and Reinforced Concrete, Series of 1906 and 1907," Bulletin of the University of Wisconsin, Engineering Series, Vol. 4, No. 2, Madison, Wisconsin, 1907-1908.
118. Wood, B.A., Kreger, M.E., and Breen, J.E., "Experimental Investigation of Design Methods for Large Cantilever Bridge Bents," Center for Transportation Research Report CTR-1364-3F, Austin, Texas, August 1997.
119. Wright, J.L. and McCabe, S.L., "The Development Length and Anchorage Behavior of Headed Reinforcing Bars," University of Kansas Center for Research, SM Report No. 44, Lawrence, Kansas, September 1997.
120. Young, M.J., "Performance of Headed Reinforcing Bars in CCT Nodal Regions," Master's Thesis, The University of Texas at Austin, Austin, Texas, August 2000.
121. Zeller, W., "Conclusions from Tests on Corbels," IASBE Colloquium on Structural Concrete (Stuggart 1991), IABSE Reports Vol. 62, pg. 577-582, Zurich, Switzerland, 1991.
122. Personal e-mail correspondence between Michael Keith Thompson, PhD candidate at the University of Texas at Austin, and Lou Colarusso, Senior Development Engineer, ERICO, Inc., May 30, 2001.
123. Personal e-mail correspondence between Michael Keith Thompson, PhD candidate at the University of Texas at Austin, and Steven L. McCabe, professor of Civil Engineering at the University of Kansas, June 29, 1999.
124. Company History, Metalock, <<http://www.metalock.co.uk>> (*as posted during July 2001*).

VITA

Michael Keith Thompson was born in Montgomery, Alabama on May 17, 1972, the son of Paul Yates Thompson and Gayle Hood Thompson. He attended Bay High School in Panama City, Florida and graduated from there in May of 1990. He attended two years of undergraduate study at The California Institute of Technology in Pasadena, California then another two and one half years of study at North Carolina University in Raleigh, North Carolina from which he received his Bachelor of Science degree in December of 1994. After working briefly for the segmental bridge design firm of Figg Engineering, Inc. he entered the Master's program at the University of Texas at Austin in August of 1995. He received his Master of Science in Civil Engineering in May of 1998. He subsequently entered the Doctor of Philosophy program at the University of Texas at Austin in August of 1998.

Permanent address: 1400 B West Braker Lane
 Austin, Texas 78758

This dissertation was typed by the author.